JOURNAL
OF
APPLIED PHYSICS

SEP 25 1953
PHYSICS
LIBRARY

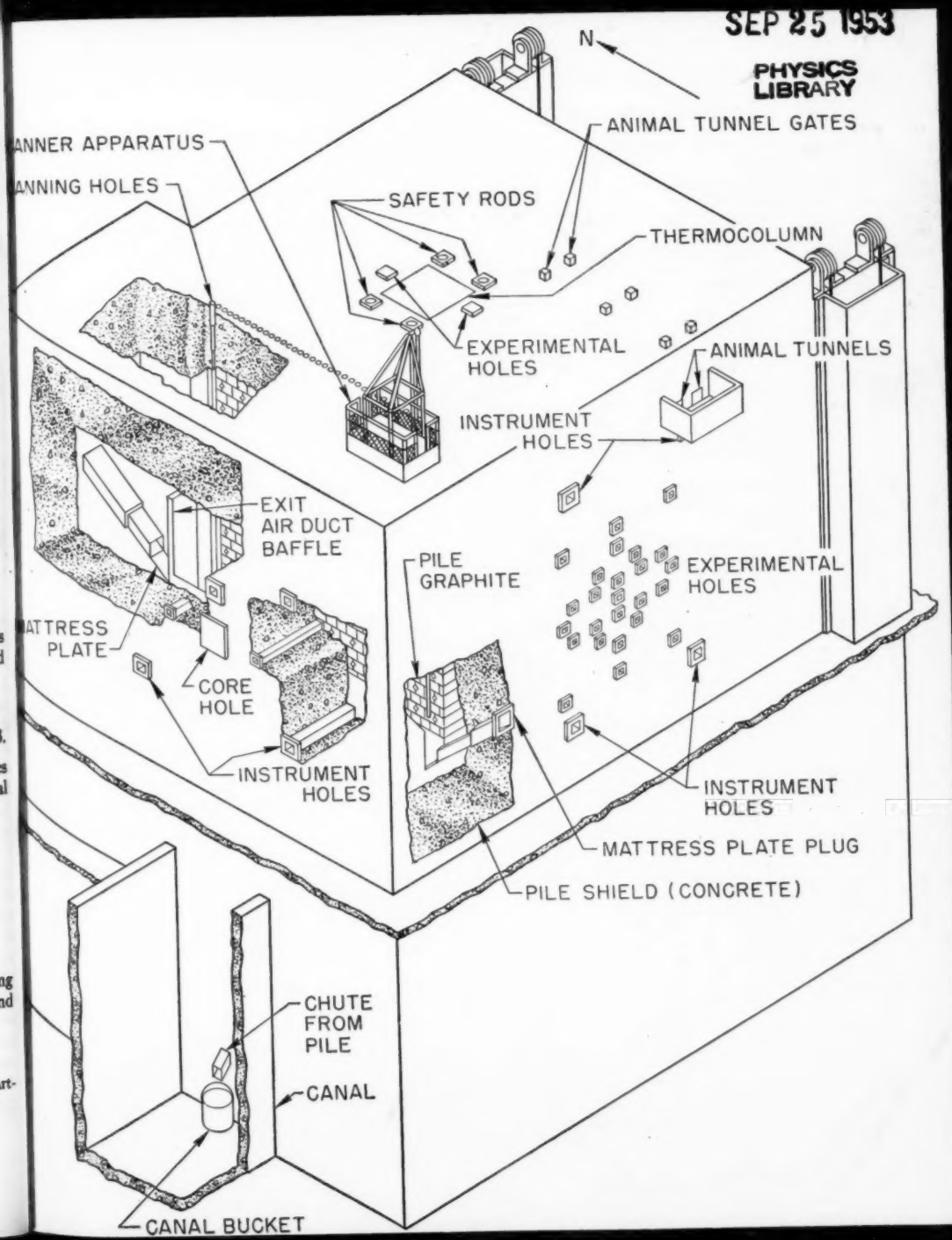

JOURNAL OF APPLIED PHYSICS

Vol. 24, No. 9 SEPTEMBER, 1953

In This Issue

		Page
Production of Radioisotopes	A. F. Rupp and F. T. Binford	1069
Formation of Black Carbon	R. O. Grisdale	1082
Effect of Stiffness and Nonuniformity on Vibroscopic Determination of Filament Cross-Sectional Area	D. J. Montgomery	1092
Identification of Individual Hygroscopic Particles in the Atmosphere by a Phase-Transition Method	S. Twomey	1099
Summation of Series Involving Roots of Transcendental Equations and Related Applications	M. R. Speigel	1103
Metallic Grating Replicas as Internal Standards for Calibrating Electron Microscopes	S. R. Rouze and John H. L. Watson	1106
Radioactive Charging Effects with a Dielectric Medium	P. Rappaport and E. G. Linder	1110
Wave Propagation in Finite Rods of Viscoelastic Material	E. H. Lee and I. Kanter	1115
Diffraction of Electromagnetic Waves by an Aperture in a Large Screen	G. Bekefi	1123
Determination of the Surface Stress by Means of Electroplating	H. Ōkubo	1130
Solution of Electromagnetic Scattering Problems as Power Series in the Ratio (Dimension of Scatterer)/Wavelength	A. F. Stevenson	1134
Electromagnetic Scattering by an Ellipsoid in the Third Approximation	A. F. Stevenson	1143
Negentropy Principle of Information	L. Brillouin	1152
Sinusoidal and Relaxation Oscillations Sustained by Nonlinear Reactances	R. Stuart Mackay	1163
First Probability Densities for Receivers with Square Law Detectors	R. C. Emerson	1168
Energy Stored in Metal Chips during Orthogonal Cutting	M. B. Bever, E. R. Marshall, and L. B. Ticknor	1176
Free Surface Motion Induced by Shock Waves in Steel	William A. Allen	1180
Electrostatic Potential Plotting for Use in Electron Optical Systems	Kuo-Chu Ho and Robert J. Moon	1186
Some Dielectric Properties of Barium-Strontium Titanate Ceramics at 3000 Megacycles	Luther Davis, Jr., and Lawrence G. Rubin	1194
More Exact Treatment of the Equations Describing Dielectric Relaxation and Carrier Motion in Semiconductors	Julian Keilson	1198
Reactor Simulators	F. E. O'Meara	1200
Crystallographic Variations of Field Emission from Tungsten	M. K. Wilkinson	1203
Static and Sliding Friction in Feedback Systems	J. Tou and P. M. Schultheiss	1210
Vector Wave Function Solution of the Diffraction of Electromagnetic Waves by Circular Disks and Apertures. I. Oblate Spheroidal Vector Wave Functions	Carson Flammer	1218
Vector Wave Function Solution of the Diffraction of Electromagnetic Waves by Circular Disks and Apertures. II. The Diffraction Problems	Carson Flammer	1224
Laminar Flow in Channels with Porous Walls	Abraham S. Berman	1232
Electron Flow Through Small Tubes with Magnetic Focusing	John L. Stewart	1236
Epicentral Displacement Caused by Elastic Waves in an Infinite Slab	Alan G. Mencher	1249
Letters to the Editor:		
Spatially Alternating Magnetic Fields for Focusing Low-Voltage Electron Beams	J. R. Pierce	1247
Mach Reflexion of Shocks at Arbitrary Incidence	H. F. Ludloff and M. B. Friedman	1247
Effect of Distribution of Lattice Defects within Crystals on Linear Expansion and X-Ray Lattice Constant	P. H. Miller, Jr., and B. R. Russell	1248
Geometrical and Apparent X-Ray Expansions of a Crystal Containing Lattice Defects	J. D. Eshelby	1249
Combustion Rate of Artificial Graphites from 700°C to 2000°C in Air	Jun Okada and Tatsuo Ikegawa	1249
Simplified Calculation for Dolph-Tchebycheff Arrays	G. J. van der Maas	1250
Some Relations between the Modulus of Rigidity and the Surface and Sublimation Energies	G. C. Kuczynski	1250
X-Ray Measurements of Radiation Damage in Black Phosphorus	D. L. Chipman, B. E. Warren, and G. J. Dienes	1251
Test for Zeros in the Unit Circle	Louis Weinberg	1251
Response of Undamped Systems to Noise	D. B. Duncan	1252
Announcements		1254
Index to Advertisers		xxii

Elmer Hutchisson, *Editor*

Earle C. Gregg, *Assistant Editor*

Board of Editors

Ray E. Bolz
Lyle D. Borst
Wallace J. Eckert
Robert D. Heidenreich
Leonard B. Loeb
W. James Lyons
Louis A. Pipes
Roman Smoluchowski
W. R. Smythe

Publication of the American Institute of Physics

OFFICERS

George R. Harrison, *Chairman*
George B. Pegram, *Treasurer*

GOVERNING BOARD

J. W. Buchta
Karl K. Darrow
G. J. Dienes
S. A. Goudsmit
George R. Harrison
Frederick V. Hunt
Deane B. Judd
Hugh S. Knowles
C. C. Lauritsen
William F. Meggers
Philip M. Morse
Brian O'Brien
George B. Pegram
I. I. Rabi
Duane Roller
Frederick Seitz
William Shockley
Richard M. Sutton
J. H. Van Vleck
Mark W. Zemansky

Consultant on Printing

Melvin Loos

ADMINISTRATIVE STAFF

Henry A. Barton, *Director*
Wallace Waterfall, *Executive Secretary*
Theodore Vorburger, *Advertising Manager*
Ruth F. Bryans, *Publication Manager*
Betty H. Goodfriend, *Assistant Secretary*
Eileen B. Neuberger, *Circulation Manager*
Kathryn Setze *Assistant Treasurer*

The Journal of Applied Physics, published monthly at Prince and Lemon Sts., Lancaster, Pa., is devoted to physics in its role as the science basic to other natural sciences and to the arts and industries. Previous to 1937 this publication was known as Physics. The Journal of Applied Physics publishes editorials and reviews, as well as technical papers of applied physics. Articles appearing in it are indexed regularly, according to their field, by Physics Abstracts, Chemical Abstracts, Engineering Index, Inc., Industrial Arts Index, etc.

Manuscripts should be submitted to Elmer Hutchisson, Editor, Case Institute of Technology, Cleveland 6, Ohio. Unless otherwise stated, submission of a manuscript is a representation that it has been neither copyrighted, published, nor submitted for publication elsewhere. The authors' institutions are requested to pay a **publication charge** of $8 per page which, if honored, entitles them to 100 reprints without further charge. Instructions will be sent with galley proofs.

Subscriptions, renewals, and orders for back numbers should be addressed to the American Institute of Physics, 57 East 55 Street, New York 22, New York.

Subscription Price	U.S. and Canada	Elsewhere
To members of the American Institute of Physics and Affiliated Societies	$10.00	$11.00
To all others	12.00	13.00

Back Number Prices

Yearly back number rate when complete year is available: $14.00. Single copies: $1.25 each.

Changes of address should be sent to the American Institute of Physics; **corrected proofs** should be sent to the Publication Manager, American Institute of Physics. **Advertising rates** supplied on request. Orders, advertising copy, and cuts should be sent to the American Institute of Physics.

Entered as second class matter January 22, 1937, at the Post Office at Lancaster, Pennsylvania, under the Act of March 3, 1879. Accepted for mailing at the special rate of postage provided for in paragraph (d-2), section 34.40, P. L. & R. of 1948, authorized May 2, 1932.

Journal
of
Applied Physics

Volume 24, Number 9 September, 1953

Production of Radioisotopes

A. F. Rupp and F. T. Binford
Oak Ridge National Laboratory, Oak Ridge, Tennessee

INTRODUCTION

SINCE the start of the program in 1946, the production of radioisotopes has grown into a business that amounts to more than 10 000 individual shipments a year. At the present time, the bulk of the material is used in medical therapy or in research in the biological sciences; however, more than 20 percent of the shipments has been directed to work concerned with pure or applied physical research. The production of radioisotopes, developed as a by-product of nuclear research, therefore makes some small contribution to furthering the science that made it possible. This paper is designed to present a few of the practical problems encountered in radioisotope production; certainly no rigorous treatment of the physical or chemical details is intended.

Radioisotopes, other than the naturally occurring ones, are produced by irradiation of target materials in a nuclear reactor or particle accelerator. Production in the reactor is of main concern in the radioisotope program, although some processing of cyclotron targets is done at Oak Ridge National Laboratory; processing of cyclotron targets has been well described by Garrison and Hamilton[1] and others.

METHODS OF IRRADIATION

Target materials that have been selected for stability, chemical purity, and production of a minimum of undesirable radioactivities are enclosed in grade 2S (high-purity) aluminum containers for insertion into the reactor. Because of volatility or possible reaction with aluminum, it is often necessary to seal the target material in a quartz ampoule; the quartz ampoules are then sealed in aluminum tubes and are protected from mechanical shock with quartz-wool wadding. Glass is not used because of its high neutron absorption. Most of the target containers used for radioisotope production are extruded aluminum tubes, which are closed with a crimped cover (Fig. 1). Larger objects (such as pieces of machinery), with dimensions of less than 3.5 by 3.5 by 10 in., may be irradiated in special, rectangular, aluminum containers. The small containers are irradiated in holes in long, rectangular, graphite blocks or stringers, that are pushed into the side of the reactor; the larger containers are pushed into special holes from which part of the graphite has been removed. No elaborate tools are used for manipulating the graphite

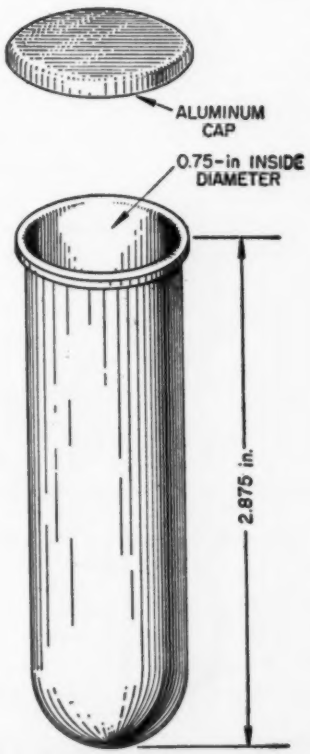

FIG. 1. Aluminum irradiation can. (Type 2S aluminum with 0.035-in. wall. Length given is working dimension; actual length is 3 inches.)

[1] W. M. Harrison and J. G. Hamilton, Chem. Revs. 49, 237 (1951).

stringers; they are merely pushed in with poles and pulled out into long lead coffins after irradiation (Fig. 2). Special short-term irradiations may also be made in capsules that are moved by gas pressure in and out of the reactor through a smooth aluminum tube.

Since decomposition often results in excessive gas pressure in the container, target materials that have reasonably good thermal stability and those that show little decomposition under irradiation should be used. The targets should not volatilize or produce forms of elements that would attack the container; for example, mercuric oxide will decompose and the mercury will attack an aluminum container. When they can be obtained with acceptable purity, solid metallic elements are usually used, and stable oxides and carbonates are also employed. Compounds containing elements that are activated to produce undesired nuclides such as chloride (which yields S^{35}, P^{32}, Cl^{36}) are usually avoided unless multiple production is desired. Salts such as nitrates (which decompose to nitrite and oxygen) are also usually avoided when possible. Organic compounds can be irradiated, but may char at reactor temperatures and are often broken down by reactor irradiation, thus producing gas pressure and an unusable mixture of compounds. In general, materials that are thermally stable are also fairly stable under neutron irradiation.

The generation of excessive heat in samples under irradiation is generally not a problem in the Oak Ridge National Laboratory graphite reactor unless some fissionable material is present; gamma heating at this flux is insufficient to materially raise the temperature above that of the surrounding graphite.

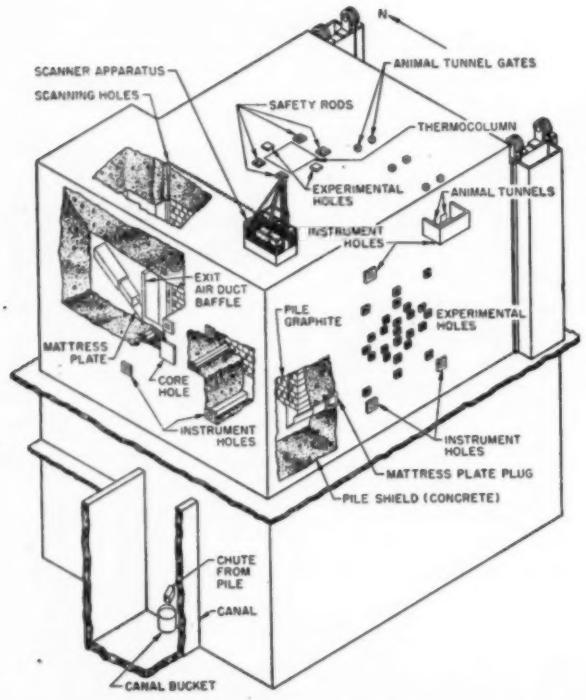

FIG. 2. Schematic diagram of the ORNL graphite reactor.

PRODUCTION RATES AND RELATED MATTERS

Radioisotopes are produced in the reactor mainly by simple neutron capture, neutron capture followed by decay to another species, neutron-proton reaction, occasionally by a neutron-alpha reaction, and fission of uranium. In each case, the production process may be described by an equation of the form,

$$A(t)=P[1-e^{-\lambda t}],$$

where A is the activity produced, expressed as a function of exposure time t, λ is the decay constant of the nuclide produced, and P is the rate of production, which is dependent upon the nuclear characteristics of the target and the neutron flux. The maximum activity obtainable as $t\rightarrow\infty$ is P, the "saturation activity."

A useful form of the production equation is

$$A(\eta)=P[1-(\tfrac{1}{2})^{\eta}],$$

where A is the activity in disintegrations per second, η is $t/t_{\frac{1}{2}}$, t is the exposure time, $t_{\frac{1}{2}}$ is the half-life, and P is the rate of formation in atoms per second. A plot of $A(\eta)/P$ *vs* η is given in Fig. 3.

If the neutron-activation cross section is known, the activation of elements being irradiated may be computed from

$$A(t)=(1.63f\sigma\phi\cdot10^{13})[1-\exp(-\lambda t)],$$

where $A(t)$ is equal to curies per gram-atom of target material at time t, f is the isotopic abundance of target isotope in the target element, σ is the isotopic activation cross section in cm^2, ϕ is the neutron flux in neutrons/cm^2·sec, λ is the decay constant of the radioisotope, and the factor $(1.63f\sigma\phi\cdot10^{13})$ is equal to P, the production rate.

In this equation, it is assumed that the amount of target material remains the same throughout the irradiation. However, some isotopes such as Eu^{151} and Sm^{149} have cross sections of several thousand barns,[2] and the burnup of the primary target material in long or very intense irradiations must be considered.

The burnup of the radioisotope itself must also be considered in the few cases where the radioisotope produced has a large neutron-capture cross section. The production equation can be corrected for the effect of product burnup as follows:

$$A(t)=\frac{P\lambda}{\lambda+\phi\sigma'}(1-\exp[-(\lambda+\phi\sigma')t]),$$

where σ' is the capture cross section of the radioisotope being formed. It is apparent that this effect need be considered only when $\phi\sigma'$ is significant compared with λ, the decay constant of the product.

The production of radioisotopes by fission, covering the range of elements Zn to Eu with mass 72 to 158,

[2] 1 barn = 10^{-24} cm^2.

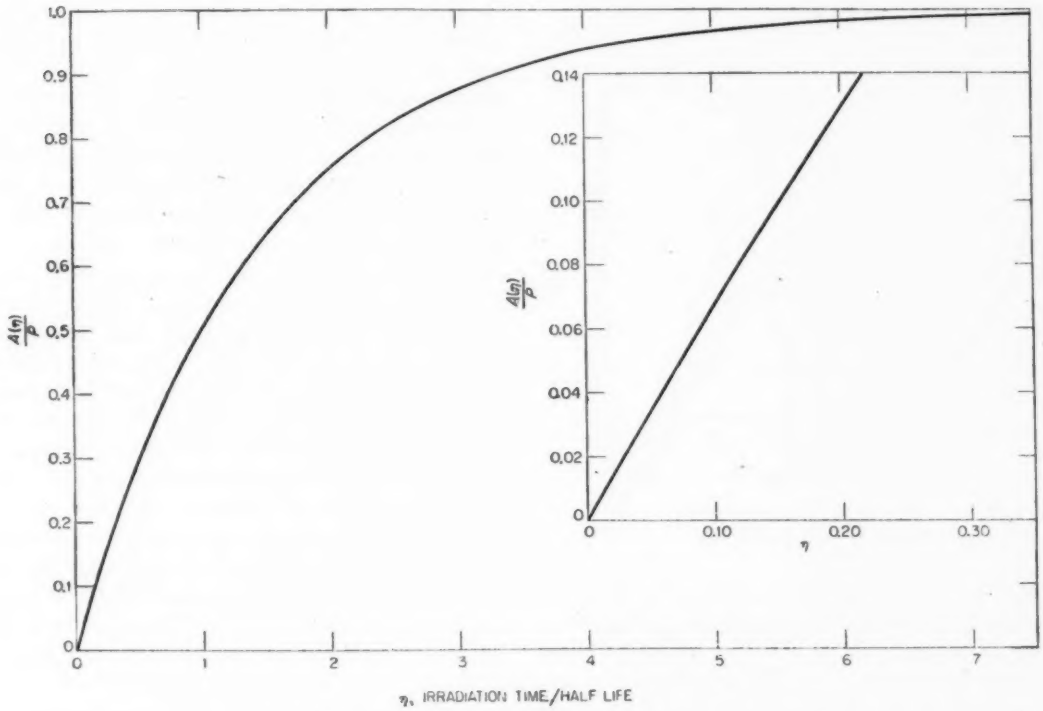

FIG. 3. Growth of a primary radioactive product during irradiation.

has been well documented.[3] The quantity of a given radioisotope formed directly from fission can be easily computed. The production rate (P) is obtained in several ways, most often from power output data, as shown by

$$A(t)=0.866Wr[1-\exp(\lambda t)],$$

where $A(t)$ is the curies per kilogram of fuel at time t, W is the power output in watts per kilogram of fuel in the region under consideration, and r is the fractional fission yield of the radioisotope.

A desired radioisotope is sometimes produced by the decay of a primary radioisotope that is formed by one of the processes discussed. The activity produced is given by

$$A_2(t)=\frac{P}{\lambda_2-\lambda_1}[\lambda_2[1-\exp(-\lambda_1 t)]-\lambda_1[1-\exp(-\lambda_2 t)]],$$

where subscripts 1 and 2 refer to the primary and secondary products. When $\lambda_1 \gg \lambda_2$, so that $\lambda_2-\lambda_1 \sim -\lambda_1$ and $[1-\exp(-\lambda_1 t)] \sim 1$, the primary product may be considered as an intermediate step of such short duration that it has no appreciable effect on the growth of the secondary product and can be ignored. When $\lambda_2 \gg \lambda_1$, so that $\lambda_2-\lambda_1 \sim \lambda_2$ and $1-\exp(-\lambda_2 t) \sim 1$, the opposite condition prevails, and the activity of the secondary product is identical with the activity of the primary product.

The general case occurs when both the half-lives are of a magnitude that is comparable to the irradiation time. The ratio of the activities then becomes

$$\frac{A_2(t)}{A_1(t)}=\frac{1}{\lambda_2-\lambda_1}\left[\lambda_2-\lambda_1\left[\frac{1-\exp(-\lambda_2 t)}{1-\exp(-\lambda_1 t)}\right]\right]$$

which approaches unity as an upper limit when t becomes large compared with the longer half-life. In Fig. 4, the reciprocal (R) of this expression is plotted against irradiation time for the production of $Zr^{95}-Nb^{95}$.

It often happens that more than one radioisotope of the same element is formed during irradiation. For example, 46-d Fe^{59} and 2.9-y Fe^{55} are produced by irradiation of natural iron. Similarly, 53-d Sr^{89} and 25-y Sr^{90} are produced in fission. These relations are plotted in Fig. 5, as determined from

$$\frac{A_1(t)}{A_2(t)}=\frac{\sigma_1 f_1[1-\exp(-\lambda_1 t)]}{\sigma_2 f_2[1-\exp(-\lambda_2 t)]}$$

which approaches $\sigma_1 f_1/\sigma_2 f_2$ as a limit with increasing t.

SOME PRACTICAL ASPECTS OF RADIOISOTOPE PRODUCTION IN THE REACTOR

The calculated production rates are often in error because of self-absorption of neutrons by relatively large pieces of target material.[4] Large absorbers in the vicinity of the sample under irradiation may also have

[3] C. D. Coryell and N. Sugarman, *Radiochemical Studies: The Fission Products*, National Nuclear Energy Series (McGraw-Hill Book Company, Inc., New York, 1951).

[4] R. Keyes, "Estimation of Self-Absorption in Neutron-Irradiated Samples," AECD—3000 (1950).

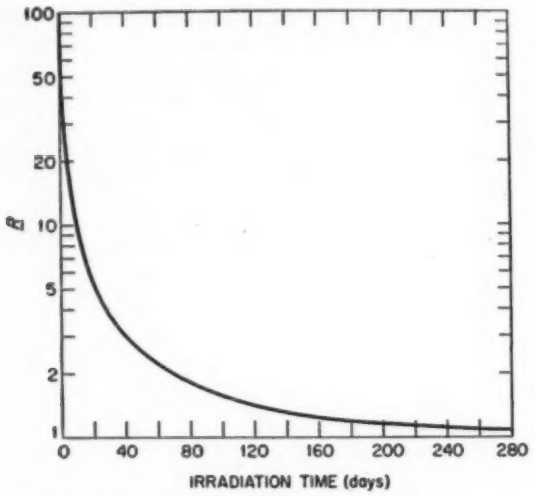

FIG. 4. Ratio of Zr^{95} activity to Nb^{95} activity as a function of irradiation time.

a great effect on the activation because of a localized flux depression. Therefore, even though calculations can be used as a guide, it is often necessary to chart the flux zones in the reactor with monitors (for example, thin films of Co) and to determine activation rates experimentally with the actual material under consideration.

From a practical standpoint, the radioactive products of a nuclear reactor fall into two broad classes: those that occur alone, free from significant contamination with other radioisotopes of the product element and free from daughter products, and those that occur in conjunction with radioisotopes of the product element other than the sought-after activity or that have one or more daughter activities; many of the fission products are in this second class.

In the first class are found those radioisotopes that are produced from monoisotopic targets, those that have significant cross section for only one radioisotope-producing reaction, those in which any extraneous activities are extremely short-lived, and those that are the last radioactive product of short-lived parents in a decay chain. Separation of such product is not too difficult, and ordinary chemical means suffice.

Separation of products in the second class, however, has certain intrinsic difficulties—as an example, the system $Sr^{89}-Sr^{90}$, in which both components are produced in fission. As shown in Fig. 5, the ratio $Sr^{90}:Sr^{89}$ is small for periods of irradiation that are short compared with the half-life of Sr^{90}. Thus, after a 12-month irradiation period, the ratio is only about 0.03, while the Sr^{89} has reached more than 99 percent of the saturation value. The mixture thus contains virtually the maximum amount of Sr^{89} that can be produced under the given conditions and contains less than 3 percent Sr^{90}. Three months after the target has been removed from the reactor, however, the ratio $Sr^{90}:Sr^{89}$ has increased to about 0.1. In fact, the ratio increases by a factor of 10 in approximately six months so that after 18 months, the ratio $Sr^{90}:Sr^{89}$ is approximately 30 and the proportions are about 96.5 percent Sr^{90} and 3.5 percent Sr^{89}. This illustrates one method of separating two isotopic products. It is applicable only when the half-lives differ greatly; the short half-lived material can be economically separated only if it is produced at a much faster rate than the material with the long half-life.

In the case of the $Fe^{55}-Fe^{59}$ system, the circumstances are not so favorable for the separation of the short-lived product. Because Fe^{54} is approximately 18 times as abundant as Fe^{58}, the ratio of the long-lived Fe^{55} to the short-lived Fe^{59} is fairly high, even for short periods of irradiation, as can be seen in Fig. 5. It is still possible to obtain Fe^{55} relatively free from Fe^{59} by performing a long irradiation and then allowing the Fe^{59} to decay. It is difficult, however, to obtain Fe^{59} that is low in Fe^{55} without resorting to electromagnetic enrichment of the target in Fe^{58}. Some fair results can be obtained by irradiating normal iron for an extremely short period of time at a high flux, thus minimizing the ratio $Fe^{55}:Fe^{59}$ but still producing appreciable amounts of Fe^{59}.

In the case of the product itself decaying to a radioactive daughter, the two can be separated chemically; however, the daughter will eventually grow back. If the daughter is very short-lived compared with the parent, the two activities will be essentially the same, and the mixture will decay with approximately the half-life of the parent. On the other hand, if the daughter is long-

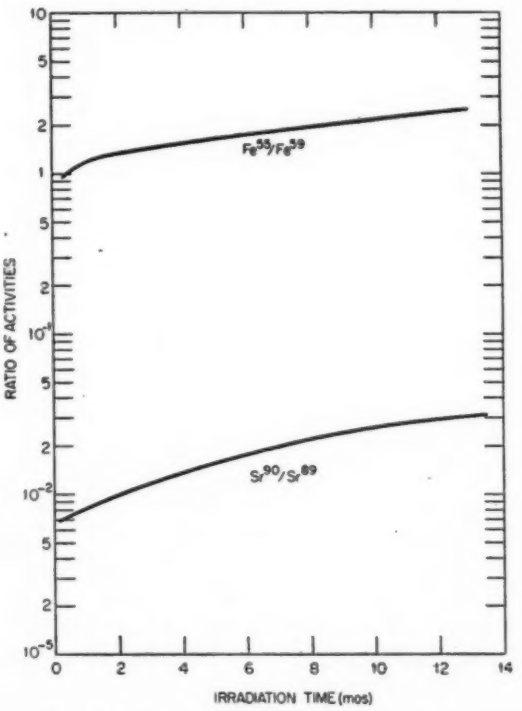

FIG. 5. Ratios of radioisotopes of same element formed during irradiation.

lived compared with the parent, the parent will eventually decay completely and leave only the daughter activity.

The case of the daughter and the parent having comparable half-lives, but the daughter being shorter lived than the parent, is illustrated in Fig. 6, which shows the fraction of Zr^{95} in a mixture of Zr^{95}—Nb^{95} as a function of decay time. Several different starting mixtures are shown. It will be noted that regardless of the fraction of Zr^{95} present in the mixture at the beginning, all mixtures approach the limit of 0.317 as t increases. Figure 7 shows the actual growth and decay of a mixture during and after irradiation.

In addition to interferences caused by simultaneous production of radionuclides of the same elements, stable elements are also produced during the fission process as a result of decay chains that end in stable isotopes. The presence of the stable isotopes materially affects the specific activity of the separated radioisotopes, even though no carrier is added during separation. Thus, I^{131} with very high specific activity cannot be made from long-irradiated uranium because of the accumulation of I^{129} and I^{127}, Cs^{137} is encumbered with comparable amounts of Cs^{133} and Cs^{135}, and Sr^{90} contains comparable amounts of Sr^{88}. Some stable isotopes produced by fission and decay are also reactivated by neutron capture.

CHEMICAL PROCESSING

The purpose of chemical processing is to isolate the product element, free from radioactive and inactive chemical contaminants, and to put it into a readily usable form. One or more of the following chemical processes are usually used for separating and purifying radioisotopes: distillation, gasification, ion exchange, precipitation and coprecipitation, solvent extraction,

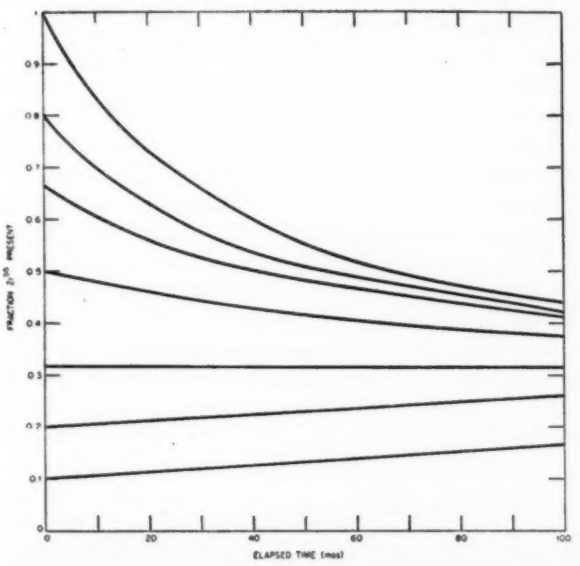

FIG. 6. Fraction Zr^{95} present in Zr^{95}—Nb^{95} mixture.

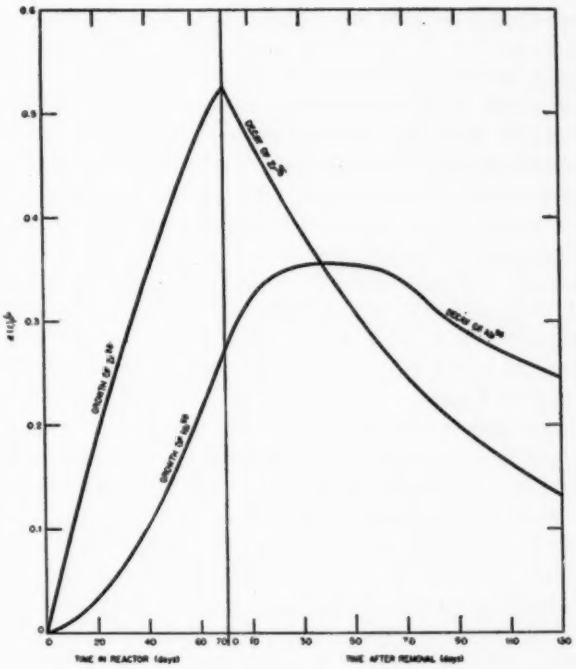

FIG. 7. Growth and decay of Zr^{95} and Nb^{95} during and after irradiation.

adsorption, electrochemical separation, and paper chromatography. In general, only the simplest chemical compounds are made at ORNL; further processing to make specific preparations needed for particular applications is done by the user or by a commercial supplier. Most preparations are simple solutions that may be easily and accurately dispensed; chloride in a slight excess of hydrochloric acid is the type of product solution usually made. The chemistry of chlorides of most elements is well known; excess hydrochloric acid may be removed by volatilization or neutralized to produce NaCl, which is required in many solutions used for injection into the body.

Target materials that are apparently quite often pure are found to have contaminating radioactivities after neutron irradiation, caused by the unsuspected presence of impurities with large neutron cross sections. An example would be the large amount of Co^{60} found upon irradiation of reagent-grade nickel, which is pure enough for ordinary chemical work. Although it is preferable and often possible to purify target materials before irradiation, induced activities are often removed from the targets after irradiation in order to use the isotopic-dilution techniques in which inactive carriers are added and to easily detect the contaminating elements by means of their radioactivity.

Separation and purification of carrier-free radioelements require special precautions because the product element may be present in only microgram amounts and must be separated from gram amounts of target material and milligram amounts of extraneous impurities; for example, P^{32} weighs 3.5μg/curie and must

be separated from a kilogram of sulfur. A large part of a carrier-free product undergoing processing may easily be lost by adsorption on the walls of the vessels and filters or on an inconspicuous bit of "crud." However, by utilizing techniques such as ion exchange, solvent extraction, or controlled adsorption, quite pure products can be obtained. Small amounts of chemical contaminants are necessarily picked up from processing chemicals and equipment and are usually those ever-present elements found in most solutions: Ca, Mg, Si, Al, Na, and Fe. Occasionally Pb is found, but most preparations to which the specification could apply are kept below 10 ppm of heavy metals, as detected by standard tests.

The total nonvolatile solids in carrier-free preparations of short half-life materials (which have very little mass per unit of activity) may be kept down to between 0.001 and 0.1 percent in most cases. When striving to obtain carrier-free materials of high activity per unit weight, which are useful in studying radiation characteristics of radioisotopes, fairly large amounts of activity (for example, several curies) should be processed, because experience has shown that about the same amount of extraneous solids per batch is obtained, whether the amount of activity is small or large. Brief descriptions of the chemical processing used at ORNL for some of the more important radioisotopes are given below.

CARBON-14

C^{14} is produced by the irradiation of beryllium nitride that is first compressed into dense pellets. The nitrogen atom is the target for the $N^{14}(n, p)C^{14}$ reaction, and beryllium nitride was chosen because it contains a large proportion of nitrogen and because the beryllium absorbs few neutrons; chemical stability is also somewhat better than that of other nitrides that might be used. The target is dissolved in sulfuric acid and hydrogen peroxide, and the gases that contain the C^{14} are swept out in a stream of pure nitrogen. The gas evolved has a variable composition and contains organic compounds such as methane, as well as CO_2; these compounds are oxidized to CO_2 over hot CuO and then absorbed in highly purified NaOH solution. $BaC^{14}O_3$ is precipitated by the addition of $Ba(OH)_2$, washed, dried, and assayed for shipment. The average isotopic ratio, $(C^{14}/\text{totalC})\times 100$, of the product is ~12 percent, with a maximum at the present time of 26 percent. Process-development work currently is largely directed toward the isolation of the various organic compounds from the gas stream and the reduction of carbon contamination in the target material in order to produce C^{14} with higher isotopic ratios.

PHOSPHORUS-32

Kilogram amounts of highly purified elemental sulfur are irradiated to produce $P^{32}[S^{32}(n, p)P^{32}]$. The carrier-free P^{32} is extracted from molten sulfur by weak HNO_3. Because sulfur melts above 120°C, this operation is necessarily done under pressure in an autoclave to prevent boiling of the aqueous phase. The extract must be purified to separate $P^{32}O_4^{---}$ from sulfate, nitrate, silicate, and contaminating cations such as Fe, Cr, Ni, Mg, Pb, Ca, and many other lesser components. Even highly purified sulfur contains organic matter that is also very troublesome when it is extracted. The purification steps are carried out entirely in Pyrex glass or quartz equipment. The extract liquor is first evaporated to near dryness and then boiled with *aqua regia* to oxidize organic matter. After a second evaporation, the residue is taken up in very weak acid and the solution is then passed through a cation-exchange column to remove most of the interfering cations. The effluent is collected in a Stang precipitator. Lanthanum carrier is added and $La(OH)_3$ is precipitated with ammonium hydroxide; PO_4^{---} coprecipitates as $LaPO_4$. The precipitate is dissolved in weak acid and passed through another cation exchanger to remove La^{+++}, thus leaving only H^+, Cl^-, and PO_4^{---} ions in the effluent. The effluent is evaporated to dryness and taken up in weak HCl as a product. Although carrier-free P^{32} can be made in this way, it is the usual practice to add 25μg of inactive phosphorus carrier per mc P^{32} in the first evaporation step to reduce losses by adsorption.

IODINE-131

The first I^{131} distributed in the radioisotope program was made by irradiating tellurium metal ($Te^{130}(n, \gamma)$ $Te^{131}\xrightarrow{\beta}I^{131}$). The demand increased rapidly beyond the production practical by this method, and fission-product I^{131} (2.8 percent fission yield) is now separated from uranium metal.

Uranium that has had a short residence in the reactor (~60 days) is dissolved, and the iodine is volatilized under controlled conditions by steam-air sparging. The condensate and alkaline-scrub liquor capture the iodine; then the liquors are further processed to concentrate and purify the I^{131} by distilling iodine from an acid-hydrogen peroxide solution and receiving the distillate in an alkaline solution. The distillate is then treated in another distilling apparatus by first oxidizing the iodine to iodate with $KMnO_4$. The oxidation step is followed by distillation, in which the volatile impurities are removed, and the iodine remains in the distilling flask as the nonvolatile iodate. The iodate is then reduced to elemental iodine by phosphorous acid, and the iodine is quickly distilled over into alkaline sodium sulfite. This concentrated product is diluted, assayed, and prepared for shipment.

SULFUR-35

S^{35} is produced by fast-neutron irradiation of KC $Cl^{35}(n, p)S^{35}$. The KCl is dissolved in water that col,

n-

tains a trace of hydrogen peroxide to ensure oxidation of all sulfur to SO_4^{--}. A trace of P^{32} is present (as a result of $Cl^{35}(n,\gamma)P^{32}$) and is removed by passage through a bed of bright aluminum shavings. The solution is passed through a cation-exchange bed where the potassium is removed and the HCl and $H_2S^{35}O_4$ are allowed to pass into the effluent. The effluent is distilled to remove HCl; the $S^{35}O_4^{--}$, which remains adsorbed on the walls of the distillation flask, is removed by boiling with weak HCl.

FISSION PRODUCTS

After uranium and plutonium have been removed, fission-product mixtures are fractionated by ion-exchange or precipitation procedures into the following groups: alkaline earth ($Sr^{89,90}$, Ba^{140}), rare earth ($Ce^{141,144}$, Nd^{147}, Pr^{143}, Pm^{147}, Y^{91}, and Eu^{155}), alkali (Cs^{137}), anionic ($Ru^{103,106}$), and radiocolloidal ($Zr^{95}-Nb^{95}$). The gases I^{131}, Xe^{133}, and Kr^{85} are removed during previous processing.

The rare-earth fraction is further fractionated by using ammonium citrate complexing agent on long, heated, ion-exchange columns that have 500 to 1000 theoretical plates. The citrate fraction containing the pure radioelements is metathesized to the chloride by ion-exchange techniques. The alkaline earths are also fractionated by ion-exchange methods or purified by classical separations in concentrated nitric and hydrochloric acids. Cs^{137} is purified by ion exchange or successive cocrystallizations with ammonium alum.

The $Zr^{95}-Nb^{95}$ system, which exists in colloidal form in strong acid solution, is separated by adsorption on silica gel and elution in oxalic acid complexing agent. Further purification is accomplished by ion-exchange methods, in which oxalic acid in various strengths is used as the complexing agent.

Ru^{106} is separated and purified primarily by oxidation with sulfuric acid and $KMnO_4$. The oxidation is followed by distillation into HCl and hydrogen peroxide solution. A number of distillations might be necessary to achieve the desired purity.

n-GAMMA-ACTIVATED PRODUCTS

An example of *n*-gamma-activated products is Ca^{45} produced by irradiation of $CaCO_3(Ca^{44}(n,\gamma)Ca^{45})$; since gram amounts are used, fairly common purification methods can be used. After the irradiated compound is dissolved in HCl, the solution is first scavenged with iron and rare-earth hydroxides and then the heavy metals are removed by sulfide precipitation. The calcium is precipitated from 80 percent HNO_3, dissolved, and then reprecipitated as the carbonate. The carbonate is dissolved in dilute HCl, and the solution is analyzed and assayed for shipment. To produce high specific-activity material, target $CaCO_3$, electromagnetically enriched in Ca^{44}, is used.

The foregoing is typical of the chemical processing methods used in this work—that of following classical methods whenever possible and introducing newer methods, such as ion exchange and solvent extraction with selective chelation, when necessary. The purification procedure selected depends upon the basic chemistry of the element involved, the nature of the target compound, the probable kind and amount of impurities, and the amount of radiation to be encountered in processing.

Some of the impurities usually found with several radioisotopes are: Co^{60} in $Fe^{55,59}$, Co^{60} in Ni^{63}, Fe^{59} in Cr^{51}, Ba^{133} in Ca^{45}, Hf^{181} in Zr^{95}, Sm^{151} in Eu^{152}, 154, Rb^{86} in K^{42}, rare earths in Sc^{46}, S^{35} in P^{32}, and Rb^{86} in Cs^{134}.

Table I gives some data on many of the other radioisotopes produced at ORNL.[5] The specific activities indicated are not necessarily the best ones obtainable, but they represent the maximum that has been attained for materials distributed in the radioisotope program.

PROCESSING FACILITIES

Other than the nuclear reactor itself, the main parts of the radioisotope production plant are the facilities for chemical processing, storing, and packaging radioactive material (Figs. 8–12). Also included are the facilities for the disposal or decontamination of radioactive wastes or chemical equipment.

Equipment for processing ranges from the simplest laboratory bench apparatus to complex, heavily shielded, remote control equipment, and the type used usually depends on the amount of material being processed, the intensity, and the kind of radiation encountered. Radioisotopes for which the demand is small and the radiation level is low are processed in temporary setups of standard laboratory equipment, the so-called "beaker and tong" method. On the other hand, I^{131}, which is produced on a regularly scheduled multicurie basis and involves processing large quantities of highly radioactive material, requires a fairly large, industrial type of unit. Radiochemical processing is based upon three types of radiation: low, intermediate, and high level. Within these general groups are many subgroups for which several of the criteria are: production requirements, toxicity of the radiochemical, type and complexity of the process, general safety considerations, and relation to other processes.

The main Radioisotope Processing Area at ORNL consists of a group of buildings that comprise a total of about 20 000 ft^2 of floor space and that are designed especially for the processing, handling, and shipping of radioisotopes. Within the area, the various facilities are roughly divided into several subareas. One building contains no processing equipment but only such services as lockers, toilet facilities, and area stores, and every effort is made to keep it completely free from contamination. Analyzing, storing, packing, and shipping of radioisotope preparations are performed in another

[5] Isotopes—Catalog and Price List, Oak Ridge National Laboratory, July, 1952.

TABLE I. Review of radioisotope preparations and methods.

Nuclide	Half-life	Production method	Present status[a]	Specific activity (units per gram) attained at ORNL	Principal purification methods used
H^3	12.1 *y*	Li–*n*–α	*R*		Gasification and absorption
Be^7	52.9 *d*	Li–*p*–*n*	*R*	Carrier-free	Coprecipitation (Fe^{+++})
Be^{10}	2.4×10^6 *y*	Be–*n*–γ	*O*	μc	Precipitation
C^{14}	5700 *y*	N–*n*–*p*	*R*	1.2 curies	Gasification
Na^{22}	2.6 *y*	Mg–*d*–α	*R*	195 mc	Ion exchange and precipitation
		Na–*p*–*d*	*D*	1 mc	Precipitation (chloride)
Na^{24}	14.8 *h*	Na–*n*–γ	*R*	115 mc	Precipitation (chloride)
P^{32}	14.3 *d*	S–*n*–*p*	*R*	Carrier-free	Precipitation [$La(OH)_3$] and ion exchange
		P–*n*–γ	*R*	50 mc	Unprocessed unit
		Cl–*n*–α	*O*	Carrier-free	Precipitation [$La(OH)_3$] and ion exchange
P^{33}	23 *d*	S–*n*–*p*	*D*	Carrier-free	(Occurs with P^{32} from S)
S^{35}	87.1 *d*	Cl–*n*–*p*	*R*	Carrier-free	Ion exchange
		S–*n*–γ	*O*	0.3 mc	Unprocessed unit
Cl^{36}	4.7×10^5 *y*	Cl–*n*–γ	*R*	0.48 mc	Distillation (HCl)
A^{37}	34.1 *d*	Ca–*n*–α	*I*	Carrier-free	Adsorption, distillation
A^{39}	Long	K–*n*–*p*	*D*		
K^{40}	1.5×10^9 *y*	K–*n*–γ	*O*		Precipitation (chloride)
K^{42}	12.4 *h*	K–*n*–γ	*R*	154 mc	Precipitation (chloride)
Ca^{45}	180 *d*	Ca–*n*–γ	*R*	6.5 curies	Precipitation (nitrate, carbonate)
		Sc–*n*–*p*	*R*	Carrier-free	Chelation, solvent extraction
Sc^{46}	85 *d*	Sc–*n*–γ	*R*	60 curies	Chelation, solvent extraction
V^{48}	16 *d*	Cr–*d*–α	*O*	Carrier-free	Ion exchange (citrate)
		Ti–*p*–*n*	*D*		
Cr^{51}	26.5 *d*	Cr–*n*–γ	*R*	4 curies	Precipitation
		V–*p*–*n*	*D*		
Mn^{52}	5.8 *d*	Cr–*d*–2*n*	*O*	Carrier-free	Ion exchange (citrate)
		Cr–*p*–*n*	*D*		
Mn^{54}	310 *d*	Cr–*d*–*n*	*O*	Carrier-free	Ion exchange (citrate)
		Cr–*p*–*n*	*D*		
Fe^{55}	3 *y*	Fe–*n*–γ	*R*	4 curies	Solvent extraction (dichloro-ether)
		Mn–*p*–*n*	*D*		
Fe^{59}	47 *d*	Fe–*n*–γ	*R*	4 curies	Solvent extraction (ether)
		Co–*n*–*p*	*D*	100 mc	Solvent extraction (ether)
		Co–*d*–2*p*	*D*	1 curie	Solvent extraction (ether)
Co^{57}	270 *d*	Fe–*d*–*n*	*O*	Carrier-free	Ion exchange (citrate)
Co^{58}	72 *d*	Fe–*d*–*n*	*O*	Carrier-free	Ion exchange (citrate)
		Ni–*n*–*p*	*D*	Carrier-free	Solvent extraction (SCN^--hexone)
Co^{60}	5.3 *y*	Co–*n*–γ	*R*	8 curies	Precipitation
Ni^{59}	2×10^5 *y*	Ni–*n*–γ	*R*	Low	Solvent extraction
Ni^{63}	85 *y*	Ni–*n*–γ	*R*	86 mc	Solvent extraction
Cu^{64}	12.8 *h*	Cu–*n*–γ	*R*	300 mc	Unprocessed unit
Zn^{65}	250 *d*	Zn–*n*–γ	*R*	900 mc	
		Cu–*p*–*n*	*I*	Carrier-free	Dithizone–CN^- complexing
Ga^{67}	78.3 *h*	Zn–*p*–*n*	*D*	Carrier-free	
Ga^{72}	14.3 *h*	Ga–*n*–γ	*O*	170 mc	Unprocessed unit
Ge^{71}	11 *d*	Ge–*n*–γ	*D*		Unprocessed unit
Ge^{77}	12 *h*	Ge–*n*–γ	*D*		Unprocessed unit
As^{73}	90 *d*	Ge–*d*–*n*	*O*	Carrier-free	Distillation
As^{74}	17.5 *d*	Ge–*d*–*n*	*O*	Carrier-free	Distillation
		Ge–*p*–*n*	*D*	Carrier-free	Distillation
As^{76}	26.8 *h*	As–*n*–γ	*D*	550 mc	Unprocessed unit
As^{77}	40 *h*	Ge–*n*–γ–β	*D*	Carrier-free	Distillation
Se^{75}	127 *d*	Se–*n*–γ	*R*	1300 mc	
		As–*p*–*n*	*D*		
Br^{82}	34 *h*	Br–*n*–γ	*R*	120 mc	Unprocessed unit
		Se–*p*–*n*	*D*		
Kr^{85}	10 *y*	U–*f*	*D*	Carrier-free	Low-temperature fractionation
		Kr–*n*–γ	*D*		
Rb^{86}	19.5 *d*	Rb–*n*–γ	*R*	20 mc	Unprocessed unit
		U–*f*	*D*	Carrier-free	
Sr^{85}	65 *d*	Rb–*d*–2*n*	*O*	Carrier-free	Precipitation (in HNO_3)
		Rb–*p*–*n*	*D*	Carrier-free	Precipitation (in HNO_3)
Sr^{89}	53 *d*	Sr–*n*–γ	*O*	0.1 mc	Precipitation
		U–*f*	*R*	Carrier-free	Ion exchange
Sr^{90}	25 *y*	U–*f*	*R*	Carrier-free	Precipitation (in HNO_3)
Y^{90}	62 *h*	Sr^{90}, β	*R*	Carrier-free	Daughter of Sr^{90}
		Y–*n*–γ	*R*	115 mc	Unprocessed unit
Y^{91}	57 *d*	U–*f*	*R*	Carrier-free	Ion exchange
Zr^{95}	65 *d*	U–*f*	*R*	Carrier-free	Adsorption and ion exchange
		Zr–*n*–γ	*R*	0.05 mc	Unprocessed unit
Nb^{95}	35 *d*	Zr^{95}, β	*R*	Carrier-free	Precipitation (MnO_2)
Te^{95}	56 *d*	Mo–*p*–*n*	*D*	Carrier-free	

TABLE I.—*Continued.*

Nuclide	Half-life	Production method	Present status[a]	Specific activity (units per gram) attained at ORNL	Principal purification methods used
Te^{99}	9.4×10^{5} *y*	U–*f*	*D*	Carrier-free	
Ru^{103}	42 *d*	U–*f*	*R*	Carrier-free	Distillation (RuO_4)
		Ru–*n*–γ	*R*	3 mc	Unprocessed unit
Ru^{106}	1 *y*	U–*f*	*R*	Carrier-free	Distillation (RuO_4)
		Ru–*n*–γ	*R*	3 mc	Unprocessed unit
Pd^{103}	17 *d*	Pd–*n*–γ	*R*		Unprocessed unit
Pd^{107}	2×10^{6} *y*	U–*f*	*D*	Carrier-free	
Ag^{105}	45 *d*	Pd–*p*–*n*	*D*	Carrier-free	
Ag^{110}	225 *d*	Ag–*n*–γ	*R*	380 mc	
Ag^{111}	7.5 *d*	Pd, β	*D*	Carrier-free	Electrolytic
Cd^{115}	43 *d*	Cd–*n*–γ	*R*	115 mc	
In^{114}	48 *d*	In–*n*–γ	*R*	70 mc	Precipitation
		Cd–*p*–*n*	*D*	Carrier-free	
Sn^{113}	105 *d*	Sn–*n*–γ	*R*	72 mc	Precipitation
		In–*p*–*n*	*D*	Carrier-free	
Sb^{124}	60 *d*	Sb–*n*–γ	*R*	2587 mc	
Sb^{125}	2.7 *y*	Sn^{125}, β	*I*	Carrier-free	Distillation
		U–*f*	*D*	Carrier-free	
Te^{125}	60 *d*	Sb^{125}, β	*O*	Carrier-free	Precipitation
Te^{129m}	32 *d*	U–*f*	*D*	Carrier-free	
		Te–*n*–γ	*R*	0.16 mc	Unprocessed unit
Te^{132}	77 *h*	U–*f*	*D*	Carrier-free	
I^{126}	56 *d*	Te–*d*	*I*	Carrier-free	Distillation
I^{129}	Very long	U–*f*	*D*	Carrier-free	Distillation
I^{131}	8 *d*	U–*f*	*R*	Carrier-free	Distillation
		Te^{131}, β	*R*	Carrier-free	Unprocessed unit
Xe^{133}	5.3 *d*	U–*f*	*D*	Carrier-free	Low-temperature fractionation
		Xe–*n*–γ	*D*		
Cs^{131}	9.6 *d*	Ba–*n*–γ–β	*D*	Carrier-free	
Cs^{134}	2.3 *y*	Cs–*n*–γ	*R*	13 curies	
Cs^{137}	37 *y*	U–*f*	*R*	Carrier-free	Cocrystallization (alum)
Ba^{131}	12 *d*	Ba–*n*–γ	*D*	0.26 mc	Precipitation
Ba^{133}	>20 *y*	Ba–*n*–γ	*D*		Precipitation
Ba^{140}	12.8 *d*	U–*f*	*R*	Carrier-free	Ion exchange
La^{140}	40.4 *h*	Ba, β	*O*	Carrier-free	Ion exchange
		La–*n*–γ	*R*	525 mc	Unprocessed unit
Ce^{141}	28 *d*	U–*f*	*I*	Carrier-free	Ion exchange
		Ce–*n*–γ	*R*	75 mc	Unprocessed unit
Ce^{144}	275 *d*	U–*f*	*R*	Carrier-free	Ion exchange
Pr^{143}	13.8 *d*	U–*f*	*I*	Carrier-free	Ion exchange
		Ce^{143}, β	*R*	Carrier-free	Unprocessed unit
Pr^{142}	18.9 *h*	Pr–*n*–γ	*R*	550 mc	Unprocessed unit
Nd^{147}	11 *d*	U–*f*	*R*	Carrier-free	Ion exchange
		Nd–*n*–γ	*R*	3.5 mc	Unprocessed unit
Pm^{147}	3.7 *y*	U–*f*	*R*	Carrier-free	Ion exchange
		Nd^{147}, β	*R*	Carrier-free	Unprocessed unit
Sm^{151}	20 *y*	U–*f*	*D*	Carrier-free	Ion exchange
$Eu^{152-154}$	13–16 *y*	Eu–*n*–γ	*R*	5 curies	
Eu^{155}	2–3 *y*	U–*f*	*I*	Carrier-free	Ion exchange
		Sm^{155}, β	*R*	Carrier-free	Unprocessed unit
Gd^{153}	155 *d*	Gd–*n*–γ	*D*		
Td^{160}	73.5 *d*	Td–*n*–γ	*D*		
Er^{169}	9.4 *d*	Er–*n*–γ	*D*		
Tm^{170}	127 *d*	Tm–*n*–γ	*D*		
Hf^{181}	46 *d*	Hf–*n*–γ	*R*	60 mc	Unprocessed unit
Ta^{182}	117 *d*	Ta–*n*–γ	*R*	1700 mc	
W^{185}	73 *d*	W–*n*–γ	*R*	622 mc	
Os^{185}	97 *d*	Os–*n*–γ	*R*		Unprocessed unit
Os^{191}	15 *d*	Os–*n*–γ	*R*	73 mc	Unprocessed unit
Ir^{192}	70 *d*	Ir–*n*–γ	*R*	6 curies	Chlorination
Au^{198}	2.7 *d*	Au–*n*–γ	*R*	3 curies	Unprocessed unit
$Hg^{203,205}$	43.5 *d*	Hg–*n*–γ	*R*	830 mc	Precipitation
Tl^{204}	2.7 *y*	Tl–*n*–γ	*R*	702 mc	Precipitation
UX_1	24.1 *d*	Natural	*O*	Carrier-free	Ion exchange

[a] Symbols refer to work within the ORNL Radioisotope Production group. *R* = routine production. *I* = produced at irregular intervals. *O* = occasionally produced on special orders. *D* = of interest in development program.

large building. Six small buildings are used for various types of radioisotope production and development. A similar building, which is kept contamination-free, is used as the supply and control point for the various services for the area, such as electricity, distilled water, etc. A somewhat larger building with garage-type doors,

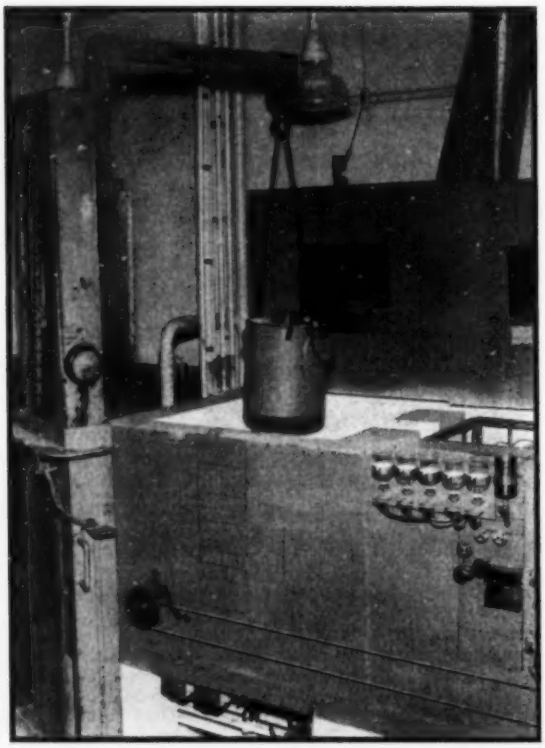

FIG. 8. Shielded carrier being lowered into high-level barricade.

big enough to accommodate the largest trailer trucks, is provided for washing and decontaminating heavy equipment. A 250-ft stack is provided, together with

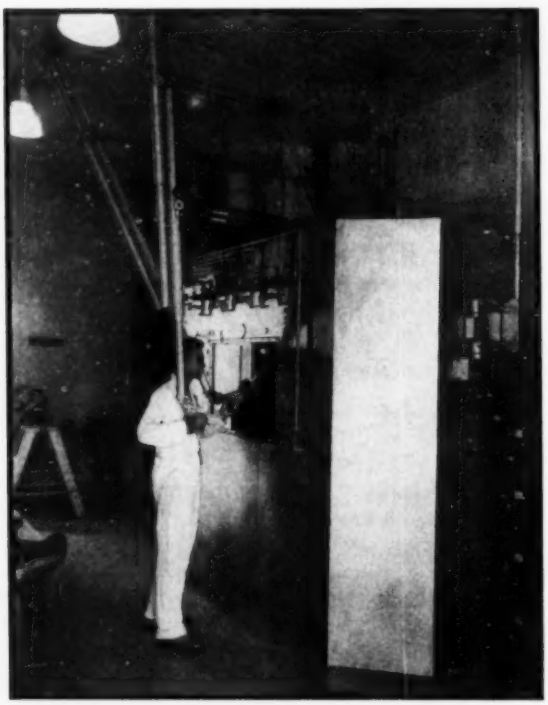

FIG. 9. High-level cell with mechanical manipulators.

associated fans, blowers, jets, filter, precipitators, and ductwork, for decontaminating and discharging the ventilating air and exhaust gases from the area. The buildings and associated areas are interconnected by a system of concrete roads and utility services.

The use of separated, small, processing buildings (Fig. 13) to minimize the effects of fire, explosion, or poisonous gases resulting from chemical processing is not new in industry; various forms of the basic design pattern have been used for many years in processing explosives, organic chemicals, and toxic biological preparations. The experience gained during a number of years of processing large and small amounts of radiochemicals indicates that the arrangement possesses a number of advantages.

The concrete roadways in the area are 20 ft wide and large enough to accommodate large trucks or ordinary two-way traffic. The roads have slightly cupped sides so that all water will flow to drains in the center. The

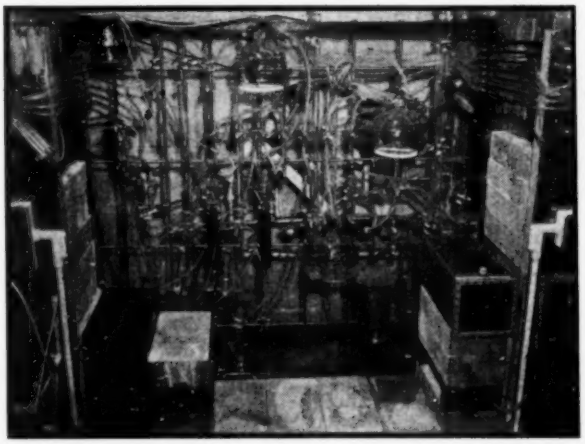

FIG. 10. Typical view of cell for radioisotope chemical processing (during construction).

entrances to the various buildings are slightly sloped ramps, about 8 ft wide with raised edges that are a continuation of those of the main road. The slopes of the ramps and the elevations of the road and building floor prevent wash water from the building floors from draining down the ramp to the road; drain water from the road, of course, cannot enter the buildings.

All space not occupied with buildings, concrete roadway, or concrete pads is graded and planted in grass. All underground lines, service lines, etc., have blanked-off branches so that the number of process buildings may be increased with no further service, ventilation, or waste facilities added.

There are three liquid-waste systems in the area, excluding the sanitary waste. The ground drainage, drinking fountains, steam condensate, and some condenser waste are discharged to a tile line that empties into a small stream on the east of the area. All other drains in the area, except the hot drains, empty into the semi-

hot waste system, which culminates in a chemical-ware line that leads to the retention pond. The concrete roadways also drain into the semihot system, because any spills of radioactive material on the roadway must be washed up and the wash water should go into the semihot waste. The hot waste from hot sinks, hoods, and equipment connections passes into an underground system of stainless steel lines, which empty into a 2500-gal, stainless steel, underground waste tank. Waste from this tank is periodically transferred to the main tank farm for disposal.

The process buildings are one-story (except the one used for column work) structures 25 by 30 ft long that are built of aluminum sheet on a structural steel frame-

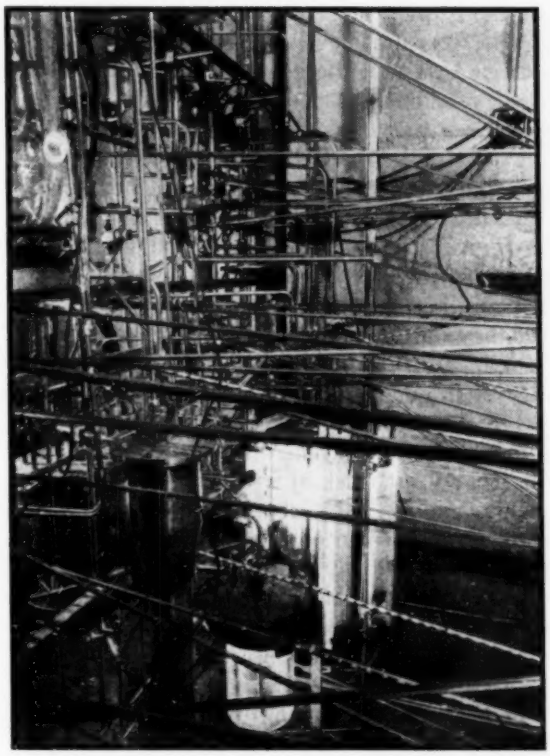

FIG. 11. View inside high-level fission product purification cell.

work. The floors are concrete, topped with a special, low-porosity concrete, and are sloped slightly toward the several semihot floors drains in the middle area of the building. A 1-ft concrete curb surrounding the floor, except at the entrance to the building, makes it possible to vigorously hose the floor for decontamination. The sides of the building are placed on this concrete curbing, and all equipment in the buildings is also placed on 4-in. high concrete pads that prevent wash water from running under the equipment. Entrance to the building is through a 5-ft wide by 10-ft high doorway, which is large enough for the electric truck-hoist to pass through with large objects.

Ventilating air is passed into the room by a heater,

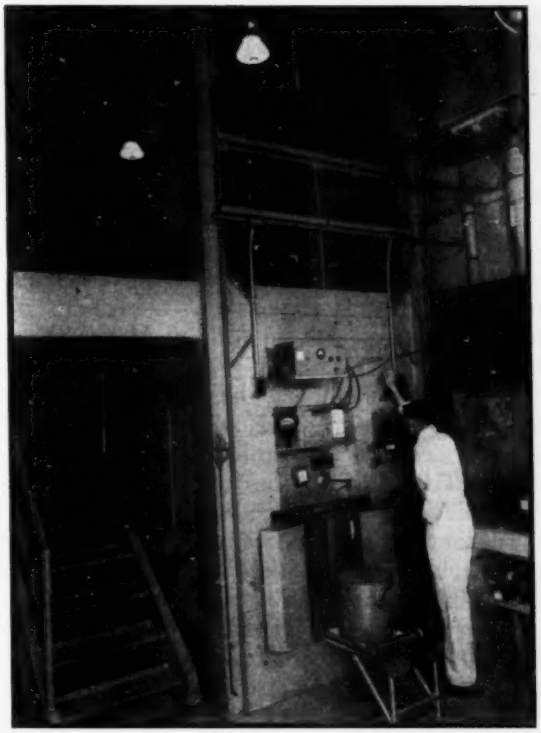

FIG. 12. Fractionation of fission product rare earths, showing transfer carrier at cell port.

fan, and filter unit located in a plenum chamber above a perforated ceiling. The air is exhausted through hoods and other partly enclosed equipment held at reduced pressure. Passage of air is always away from the worker in the room and toward the exhaust hoods.

Air, electrical, steam, and vacuum lines come into the building from a steel trestle, which runs from the distribution center into the service building, and then pass into the plenum chamber above the ceiling. Gas,

FIG. 13. View of radioisotope production area, showing small, separate, processing buildings.

water, and distilled-water lines run underground but are also piped to the overhead-plenum distribution area. The ventilating (hood exhaust) duct also passes into the building underground and extends into the space above the ceiling. The layout of the buildings is as follows. A 5-ft wide aisle runs through the middle of the entire building, and the space on each side is divided into three zones, each 10 ft wide and 10 ft long. Each zone is supplied with a hot-drain connection and a hot off-gas connection that come up through the floor and an overhead ventilating-duct connection. All services at the aisle and overhead are capped off in readiness for connection.

Although each building has somewhat different fixtures and functions (the column building differs most), the design is standardized, as has been briefly described. The keynote of the design is maximum utility and flexibility. Units of processing equipment and associated laboratory equipment are placed in the various zones of the buildings and connected as desired. For example, in the buildings used in the preparation of C^{14} and P^{32}, one zone is used for primary separations equipment, one for purification equipment, two for laboratory furniture, one open area for developmental work, and another for cleaning and storing equipment and chemicals.

The base dimensions (25 by 30 ft) and the floor construction of the building used for column work are the same as those of the process buildings, but the height is 32 ft from the floor to the ceiling. A steel superstructure, open except for three levels of floor that are 8 ft apart and are covered by steel grating, is constructed of heavy I-beams in the middle of the building. The total height of this structure is 24 ft, and it serves as a framework to hold lead-shielded, especially ion-exchange and solvent-extraction equipment.

Standard laboratory furniture, including fume hoods, is used wherever possible. However, some alterations were made; for example, stainless steel tops with a 1-in. curb are used on a number of the tables and sinks.

Three types of hood-barricades are provided, depending upon the amount of shielding required: semihot hoods, high-level barricades, and product-storage barricades. The hoods used for beta work are the same as those used for ordinary radio-chemical laboratory work.

The semihot hoods are made up of ordinary Transite hoods that are painted with a strippable coating have 3-in. thick lead floors and 6-in. curbs and are mounted on heavy supporting pedestals made of concrete. The hood contains an off-gas connection, a hot drain, and a semihot drain. The services—air, gas, electricity, vacuum, and water—are placed in a recess on the outside front of the hood. The drains and semihot trap are enclosed and shielded below, but are accessible for cleaning and repair.

The high-level barricades (Fig. 8) (sometimes referred to as "caves") are made of 6-in. lead in front and on the side and 3-in. lead on the back and bottom. The tops are 6 ft from the floor level, and the barricade interior is about 3 ft deep and 3 ft wide. The entire structure is supported on heavy concrete pedestals. There are two barricades (each in a separate high-level building) 20 ft long that may be divided by movable partitions into separate cubicles, six per unit. Each unit has a front slot 8 in. wide (one lead brick length) and $2\frac{1}{2}$ ft long, in which controls, instruments, zinc bromide windows, etc., may be placed; the space can also be completely closed with lead bricks. A movable lid fits over each cell unit; the lids are adjustable and have a mirror fitted on the underside that serves the triple purpose of regulating air flow, providing cell vision, and cutting down minor scattering out of the top of the cell. Since the cell is open on top, the portable electric hoist can move to the front and lift heavy casks in and out. The hoist can also move complete equipment units of apparatus that have been built on framework so they can be constructed outside and then set in place. Heavy, steel, scatter-shields may also be placed over the tops of the cell units. Each cell unit is equipped with a hot off-gas line, a hot drain, and a semihot drain. All services are supplied in front of each cell, and connections can be passed in through the front slot. The entire barricade is ventilated by ducts at the back.

After radioisotope preparations are made and analyzed, they must be stored until aliquots are removed for shipment. A product-storage barricade, approximately 50 ft long, 4 ft deep, and 3 ft wide is placed across the south-middle wall of the largest building in the area. It is constructed of concrete, 1 ft thick at the back and 2 ft thick in front and on the sides. The inside is heavily painted with white plastic paint. Movable, compartmented trays, which slide from under horizontally placed scatter shields, are used to contain up to 1000 preparations. Each compartment is numbered and lettered according to row and position, and the identification of the sample is recorded on a plot-plan sheet. A mechanical manually operated tong that runs on rails on the top front edge of the barricade is used for picking up product bottles, placing them in the grid, or transporting them to the east end of the barricade, where the packing machinery is located. At ceiling height over the middle of the barricade is a 3-ton monorail that is used for bringing in lead casks containing products and for general utility lifting work in the barricade. Air is drawn out of the barricade by ducts at the back. Mirrors at the back of the barricade provide viewing of the operations.

At the end of the storage barricade, backed up against a heavy concrete wall that isolates this section from the rest of the building, is the packing barricade. The remote control equipment for packaging radioisotope solutions is placed behind this barricade. The barricade is 6 ft in height, and the structure is of lead rather than concrete because of the numerous holes for controls needed for the remote equipment and the

desirability of minimizing the distance from the controls to the equipment.

A variety of remote-control equipment is installed in the packing barricade to permit transportation of the stock solution from the storage barricade, sampling for analysis, visual inspection through windows filled with dense (80 percent) zinc bromide solution, accurate measurement of radioisotope-solution volume, filling various-sized glass containers, placing and tightening plastic caps on bottles, placement in the lead shipping shield, and handling various parts of the shipping container. Monitoring instruments of various kinds are placed so that gross checks can be made on shipments in order to reduce errors in quantities shipped. Final-survey instruments are used to ensure that radiations are below the safe levels specified in shipping regulations.

The packing barricade is well ventilated by ducts in the back and is powerfully illuminated. In addition to the zinc bromide windows, mirrors and optical equipment are used to provide a good view of all equipment inside.

Shipping containers are stored under two large monorails in one large area that takes up most of the room. The boxes are placed on a portable, roller conveyor and pushed into a lead cave at the end of the packing barricade. The lead door to this compartment is operated by a hydraulic mechanism. After the radioisotope is placed in the shipping container, it is pulled out onto another roller conveyor where shipping labels are put on and a final inspection is made. At the end of the conveyor, the container is lifted by a power belt-loader onto the shipping truck.

Many of the radioisotopes are pure beta emitters such as S^{35} or P^{32}. A low-level packing load with Lucite shielding and relatively simple packing tools, together with a plain table for holding small concrete containers, are provided to speed the handling of these materials. Some materials, such as $BaC^{14}O_3$, are weighed and shipped in a dry form; therefore a dry-box type of hood containing a balance and other simple tools is used.

In addition to the equipment located in the main radioisotope processing area, several of the larger units, such as the plants used for processing I^{131} and separating fission products from waste, are located in various other sections of the laboratory. Services and specialized equipment, such as that required for analysis, testing, maintenance, and equipment fabrication, are also available in other divisions of the Laboratory.

JOURNAL OF APPLIED PHYSICS VOLUME 24, NUMBER 9 SEPTEMBER, 1953

Contributed Original Research

The Formation of Black Carbon

R. O. GRISDALE
Bell Telephone Laboratories, Inc., Murray Hill, New Jersey
(Received March 16, 1953)

Electron microscopic evidence is presented in support of the hypothesis that black carbon resulting from pyrolysis of gaseous hydrocarbons is produced through the intermediate formation of droplets of complex hydrocarbons. Electron diffraction studies further confirm this hypothesis if, as has been found for particles of carbon blacks, the droplets consist in part of graphitic nuclei arranged with their basal planes tangential to the droplet surface. The carbonization of small solid spherules of highly cross-linked organic polymers is described, and it is shown that the morphology of the carbonization products is wholly analogous to those for pyrolytic carbon and carbon blacks. It is suggested, therefore, that the formation of carbon by the carbonization of solids and by deposition from the gas phase occurs through similar mechanisms and that the two processes are simply two extremes in an infinite series of processes which are all fundamentally alike.

INTRODUCTION

THE mechanism by which carbon is formed during pyrolysis of a hydrocarbon gas, whether in a flame or in an oxygen-free enclosure, has not been clearly established; and, in addition, it is generally believed that the formation of carbon by gas pyrolysis takes place in a manner essentially different from that occurring during carbonization of an organic solid. However, study of microphone carbon produced both by deposition and by carbonization has provided physical data which clarify certain features of the mechanism of carbon deposition and suggest that the processes of deposition and carbonization may be similar and differ only quantitatively.

Previous studies of carbon deposition have been concerned with chemical aspects of the problem or with the crystalline structure of the material. While the morphology of carbon black has been widely studied, that of the more dense and coherent forms of deposited carbon has not. Further, detailed correlation of the properties of pyrolytic carbon with its crystal structure and geometry has not been available. Investigation of the behavior of microphonic carbon contacts has necessitated correlation of this behavior with the structure, composition, geometry, and properties of the carbon surfaces,[1] and from these correlations has evolved an understanding of the mechanism by which carbon is produced.

Small spherules of silica are coated with carbon to produce microphonic materials by introducing a mass of them into a rotating furnace heated to temperatures near 1000°C into which is injected a mixture of pure methane and oxygen-free nitrogen.[2] In early work rotation of the furnace, which ensures equal exposure of all spherule surfaces to the furnace atmosphere, was maintained at constant speed, and the microphonic characteristics of the carbon-coated particles then depend in a systematic fashion on the temperature of the furnace, on the concentration of methane in the furnace atmosphere, and on the thickness of the carbon film.[1] The characteristics of these microphonic materials also depend on the nature of the hydrocarbon from which the carbon is obtained; and, under otherwise identical conditions, carbons produced from methane, ethane, benzene, toluene, and a variety of other hydrocarbons possess different microphonic characteristics.

Polished silica plates coated with carbon at the same time as the silica spherules were employed in an electron diffraction determination of the carbon structure. The carbon consists of graphite-like crystallites which are more or less preferentially oriented with their basal planes parallel to the surface on which they are deposited, both the size of the crystals and their degree of orientation depending on the conditions under which the carbon is produced.[3] In virtue of the anisotropy in properties of the crystals, variations in degree of preferential orientation are reflected in systematic variations in certain properties of contacts between such carbon surfaces.[1] However, there is no observable correlation between the extent of preferred orientation and the microphonic sensitivity of the contacts, which depends on the surface geometry as determined largely by the rate at which the carbon is deposited.

The first step in pyrolysis of a hydrocarbon to yield carbon probably is the removal of a hydrogen atom from the hydrocarbon molecule in the gas phase.[2] Reaction of the resultant hydrocarbon fragments and continuation of this process of dehydrogenation leads to the production of molecular fragments which polymerize to molecular species ranging in complexity and molecular weight from methane and acetylene to anthracene and far more complex oils, tars, and solids, some with exceptionally high melting points. An essential step in the formation of pyrolytic carbon is probably the adsorption and continuing dehydrogenation of these complex substances on the surfaces of objects in the pyrolyzing chamber. Not only are these materials essential intermediates in the formation of carbon but,

[1] R. O. Grisdale, J. Appl. Phys. (to be published).
[2] The techniques of pyrolysis and the properties of pyrolytic carbon are discussed by Grisdale, Pfister, and van Roosbroeck in Bell System Tech. J. 30, 271 (1951).
[3] A. H. White and L. H. Germer, J. Chem. Phys. 9, 492 (1941).

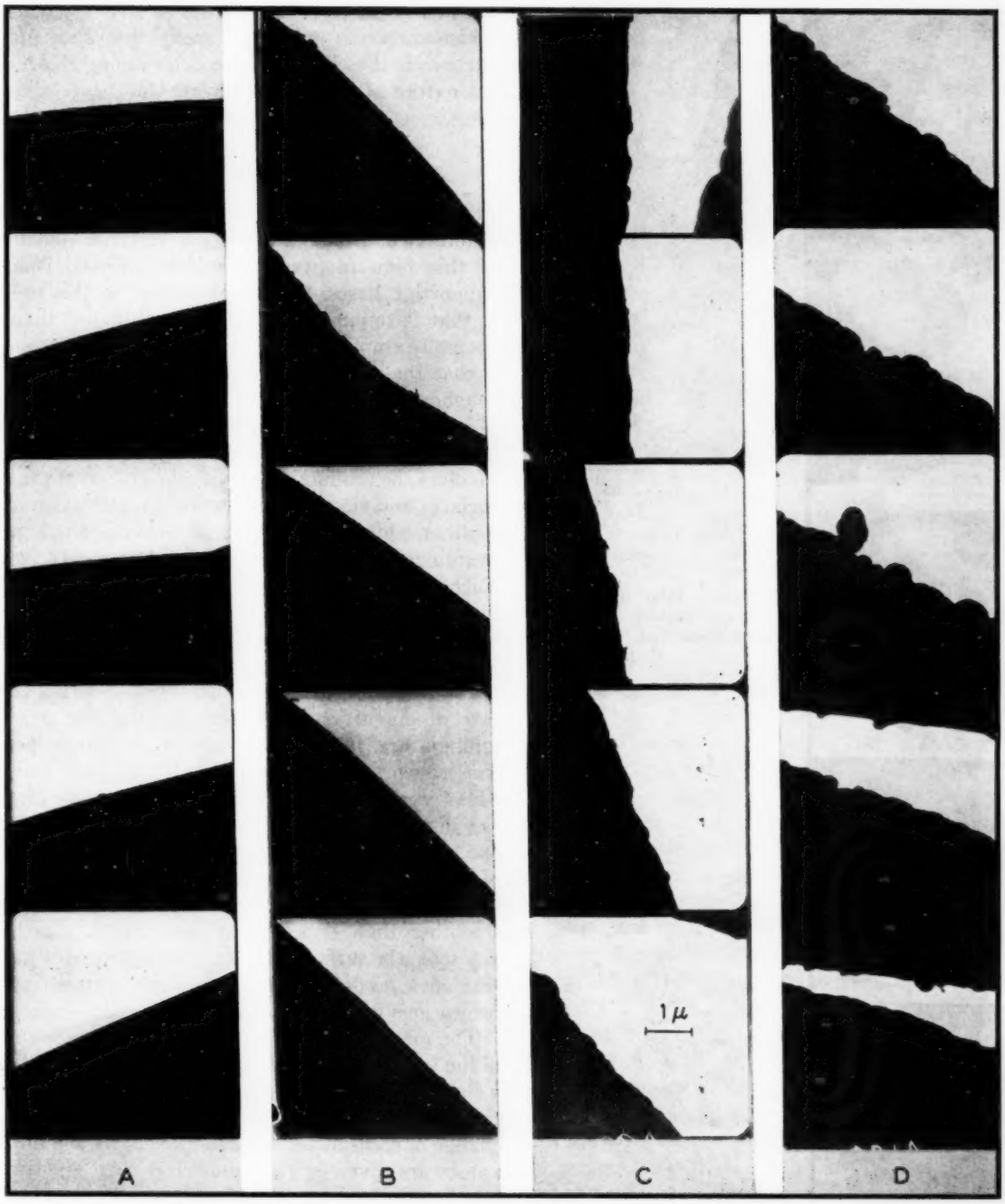

FIG. 1. Electron shadowgraphs of surfaces of pyrolytic microphone carbon showing variations in surface roughness. Correlation of roughness with microphonic behavior and with rate of carbon deposioion is shown in the following table:

Sample	A	B	C	D
Methane concentration, percent	30	30	30	30
Pyrolyzing Temperature, °C	975	1000	1050	1100
Rate of carbon deposition, gm/cm²/hr ×10⁶	1.5	2.9	7.5	14
Modulation efficiency, $\Delta R/R \times 10^3$	14.6	13.1	8.7	7.7

by suitable solvent extraction or heating in vacuum, they have been isolated from it.[2]

Because of the unsaturated valences at the edges of pure graphite-like crystals the hydrogen in pyrolytic carbon is probably largely chemically bound through these valences, thus, in effect, providing each graphitic crystal with a hydrocarbon skin separating it from its neighbors.[2] Elimination of this hydrogen through heating results in an increase in average crystal size and a decrease in intercrystal resistance. At sufficiently

FIG. 2. Edge silhouettes of carbon coated silica filaments

high temperatures this leads to graphitization of the specimen.

While the average crystal size in pyrolytic carbons is systematically variable, it does not appear to be altered in crystal size which accounts for the progressive increase of modulation efficiency with decrease in rate of deposition.[1] The "carbon" as first deposited appears to possess a certain "mobility," and the balance between the rate at which "carbon" is brought to the surface and its ability to "orient" itself determines the surface geometry. The nature of the mechanism by which carbon is produced through pyrolysis of hydrocarbons is thus important in determining the geometrical nature of the carbon surface and hence the microphonic sensitivity of carbon contacts.

THE ELECTRON MICROSCOPIC EVIDENCE

The small-scale geometry of carbon surfaces can be determined from transmission electron micrographs of thin films of pyrolytic carbon stripped from their supporting bases. One disadvantage of this procedure is that it requires films of carbon thinner than those normally employed in microphonic materials; a second is that the results obtained represent an integration of roughnesses on both sides of the film, only one of which is important to microphonic action. A second method of investigation, free from this latter disadvantage, involves the production of suitable replicas of the carbon surfaces and electron microscopic investigation of these replicas, while a third method is to obtain shadowgraphs or silhouettes of the surfaces of carbon-coated particles. Each of these methods has been successfully employed in the present study, but the most significant information has been obtained from the silhouettes.

Typical silhouettes of carbon-coated silica spheres are shown in Fig. 1which indicates that with increasing rate of deposition, as determined by the pyrolyzing temperature, the apparent surface roughness increases. The several micrographs shown for each sample in Fig. 1 were selected to give a representative picture of the distribution of rough and smooth regions on any one sample. Over the surface of any particle the degree of roughness varies, and those portions of the surface which are convex on a gross scale are, in general, smoother than those which are concave. Further, on any scale the surfaces are composed of smoothly curved segments, and in some micrographs gross globular projections from the surface can be seen.

The modulation efficiency or microphonic sensitivity of the four specimens of Fig. 1 was determined by measuring, in a standard telephone transmitter filled with the material and in a given sound field, the fractional change of transmitter resistance, $\Delta R/R$.[1] The measured values are given in the figure and they illustrate the relationship between surface geometry and modulation efficiency.

Granules of microphone carbon are small and difficult to handle, their average radius being about 0.01 cm, and to decrease the radius of curvature of the base and to obtain specimens which could easily be placed across the aperture in the microscope, silica filaments having diameters of about 0.005 cm were placed in the furnace together with silica spherules, and carbon deposition was carried out as usual. The electron microscopic silhouettes of these carbon coated filaments in Fig. 2 exhibit a range of surface roughness far greater than that illustrated in Fig. 1. In all, about ten lots of

microphonic materials and fibers were produced under identical conditions. Measurements on these carbon-coated spherules indicated that within the limits of experimental error the microphonic characteristics of all lots were the same, whereas the surface roughnesses of the fibers were extremely varied. However, edge silhouettes of the corresponding spherules are given in Fig. 3 which show that there is no wide variation in the roughnesses of the microphonic materials. Indeed from them and an examination of Fig. 1, it might be predicted that these materials would exhibit the same microphonic properties.

FIG. 3. Edge silhouettes of carbon coated silica spherules

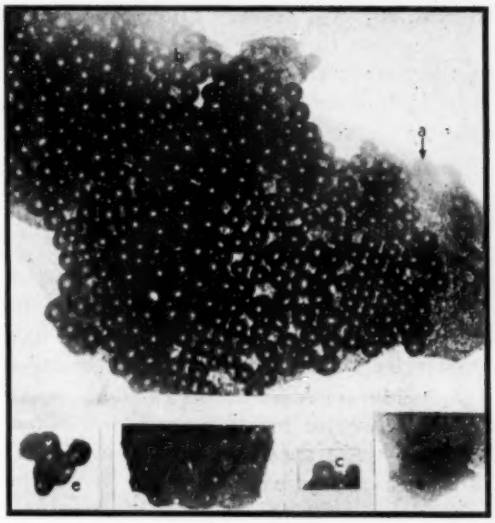

FIG. 4. Photomicrographs of carbon coated spherules produced at low speed of furnace rotation: (a) carbon film from furnace wall, (b) layers of spherules bonded to carbon film, (c) very rough spherule, (d) fragments of carbon shells embedded in film, (e) spherules bonded together with carbon.

Figures 2 and 3 indicate a very great difference between the surface geometries of carbon on silica fibers and on silica spherules, even though produced under identical conditions. It was felt that the fibers, being subject to less rubbing action during the deposition, might have floated on top of the mass of spherules during rotation of the furnace, and that this might affect the surface geometry. The influence of this rubbing was investigated by preparing a series of microphonic materials in the production of which the rate of furnace rotation was varied while all other variables in the deposition were maintained constant. Initially, a smaller-than-normal charge of silica spherules was placed in the furnace which was rotated to less than one-fifth the normal speed, but on completion of the deposition it was impossible to remove this charge. Admission of oxygen to the heated furnace burned out the carbon, and it was thereafter possible to remove the silica spherules. In a subsequent run performed under identical conditions the furnace was allowed to cool after deposition while an atmosphere of oxygen-free nitrogen was maintained in it. By scraping the furnace core it was then possible to remove a mass of carbon-coated silica spherules together with large flakes of pyrolytic carbon. Examination of this material indicated that a continuous film of carbon had been formed over the furnace walls and that in this film, imbedded in a close-packed array, were the carbon coated silica spherules. These spherules exhibited the most varied appearances and all were on the average far rougher than microphonic material made under the same conditions with higher speed of

furnace rotation, as is shown in the photomicrographs of Fig. 4. Even at this low magnification the globular character of the surface is apparent, with the spherules bonded to each other and to the furnace wall. During pyrolysis, the furnace wall and the spherule surfaces apparently were coated with a tacky layer of complex organic material, and with the small furnace charge employed the tumbling action was insufficient to free the spherules from it.

Additional lots of microphonic material were then produced, one employing the normal rate of furnace rotation, the second a rate more than twice as great. These materials, together with that discussed above, showed a regular increase in microphonic sensitivity as the rate of furnace rotation increased. Silhouettes obtained from these specimens are shown in Fig. 5, which illustrates a progressive increase in the smoothness of the surface with rate of rotation.

These complex hydrocarbon materials are deposited on the surfaces in a discontinuous fashion in the form of minute globules as is illustrated in the silhouette of Fig. 6. The average surface of the carbon is especially smooth, but extending from it in chains are aggregates of almost perfect spheres of widely varied sizes. These are spheres of complex organic materials, and by suitable mechanical action they can be smeared smoothly over the surface. That they are not carbon as such was shown by electron diffraction analysis of a clean gold surface over which they had been smeared. Such a surface showed only the diffuse features characteristic of an amorphous material, provided that the deposition temperature was not excessive. At high deposition temperatures the amorphous material was still present, but there were also features characteristic of graphitic carbon.

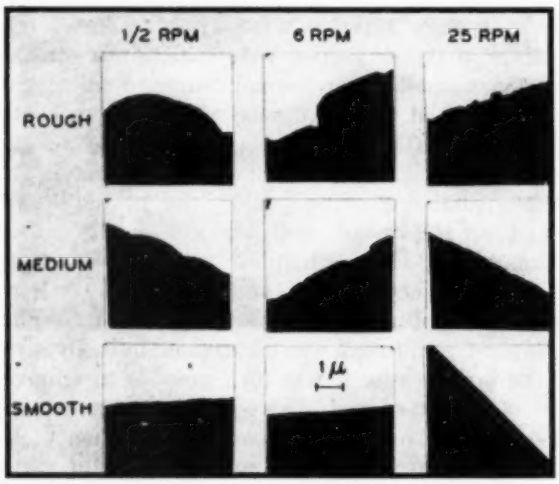

FIG. 5. Effect of speed of furnace rotation on surface geometry. The percentage of the surfaces having roughnesses as shown are

	½ rpm	6 rpm	25 rpm
Rough	35.	20	8
Medium	55.	39	29
Smooth	10.	41	63

THE ELECTRON DIFFRACTION EVIDENCE

As noted above, pyrolytic carbon is composed of very small graphite-like crystals which are, like graphite, highly anisotropic both in structure and shape. Electron diffraction analysis has shown that these crystallites can, under certain circumstances, be preferentially oriented so that their flat basal faces lie more or less parallel to the surface on which the carbon film is formed.[3] The specimens employed in the diffraction studies consisted of carbon films deposited on surfaces

FIG. 6. Spherical droplets of hydrocarbon extending from the carbon surface in chains.

of almost optically flat plates of fused silica. Diffraction patterns taken by reflection at almost grazing incidence, as well as those obtained by transmission at 45° through the film stripped from its substrate, exhibited the preferred orientation of the crystallites.[3]

To assess the degree of this orientation, a series of diffraction patterns was selected and arranged in order of increasing orientation as judged primarily by the angular intensity distribution or the degree of "arcing" of the features. The first of these showed no detectable preferential orientation and was assigned the identifying numeral 0, while the last, numbered 10, showed the highest degree of orientation observed. Three of these patterns, illustrating the variation in degree of orientation, are shown in Fig. 7. The linearity

FIG. 7. Electron diffraction patterns obtained by reflection from pyrolytic carbon showing the "arcing" resulting from preferential orientation of the graphitic crystals. Numbers represent positions of the patterns on the arbitrary scale of orientation.

of the scale of orientation thus established is unknown, but its use has enabled semiquantitative estimates of relative orientation to be made with a precision of 0.5 unit on the scale. It was estimated that in scale specimen 10 more than 90 percent of the crystals were oriented with their basal planes within 20° of parallelism with the surface of the specimen. Oxidation of the surfaces of these carbon films in air invariably increased the degree of preferred orientation, and scale specimen 10 was prepared in this way. In view of the rapid oxidation of the edges of graphite crystals relative to their basal surfaces, it appears that those crystals in pyrolytic carbon whose edges are exposed in the surface are preferentially removed by oxidation.

When pyrolytic carbon is deposited at constant methane concentration, the degree of orientation at its surface passes through a maximum value as the pyrolyzing temperature is increased. Figure 8 gives the degree of orientation on the above scale as a function of furnace temperature for films produced at a methane concentration of 30 percent by volume. Results similar to these have been obtained repeatedly at other methane concentrations, and the maximum degree of orientation occurs at about 1025°C regardless of the methane concentration. For higher methane concentrations, however, the degree of orientation at any given temperature is greater than that shown in Fig. 8 since the orientation increases regularly with increase in methane concentration as illustrated in Fig. 9 for carbon films prepared at 1000°C.

The degree of preferred orientation increases to an asymptotic limiting value when the film thickness increases as a function of time under otherwise constant pyrolyzing conditions. This asymptotic value is reached at a film thickness of about 3×10^{-5} cm, and the data of Figs. 8 and 9 are for films whose thicknesses exceed this value.[2]

The preferred orientation of the crystallites revealed by diffraction studies is confirmed by measurements of the properties of pyrolytic carbon[2] and of contacts between carbon surfaces.[1] The properties of microphonic carbon contacts depend systematically on the conditions under which the carbon is produced, and these properties are well correlated with the extent of preferential orientation in the contact region.

THE DROPLET MECHANISM OF CARBON DEPOSITION

The surfaces shown in Figs. 1 and 2 appear to have been formed from molten substances, and Fig. 6 shows that these substances are deposited in the form of minute spheroids. During pyrolysis of a gaseous hydrocarbon there appears to be formed, through multiple

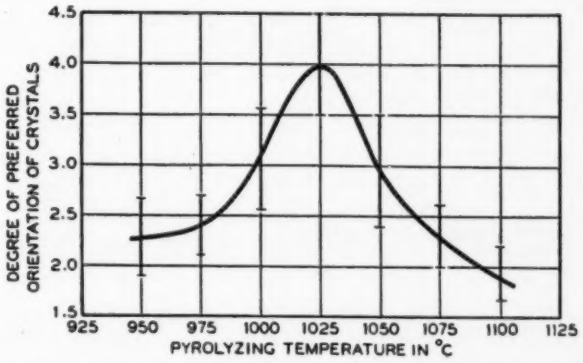

FIG. 8. Preferential orientation of pyrolytic carbon crystallites as a function of the temperature of pyrolysis at constant methane concentration (30 percent).

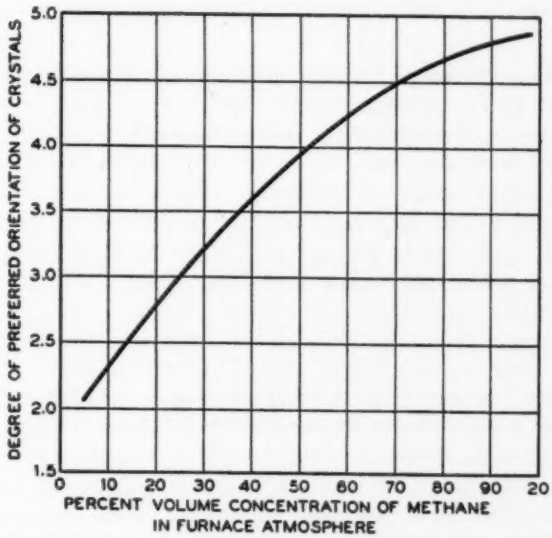

FIG. 9. Preferential orientation of pyrolytic carbon crystallites as a function of the methane concentration at constant temperature (1000°C).

collision or condensation; a suspension of droplets of complex organic materials which impinge on surfaces in the pyrolyzing chamber and provide nuclei for the formation of films of pyrolytic carbon. Their spherical shapes suggest that they are liquid or plastic, and the rubbing action of the spherules tumbling over each other in the furnace may smear them uniformly over the spherule surfaces, thus producing a smooth layer which further polymerization converts to carbon. On this basis, therefore, this rubbing action is of fundamental importance in the production of the "smooth" surfaces necessary for the highest microphonic efficiency. It is significant that, as noted above, those portions of the spherule surfaces which are convex are smooth, while those which are concave are rough and exhibit a more globular structure, because it is predominantly on convex portions of the surface that rubbing can occur.

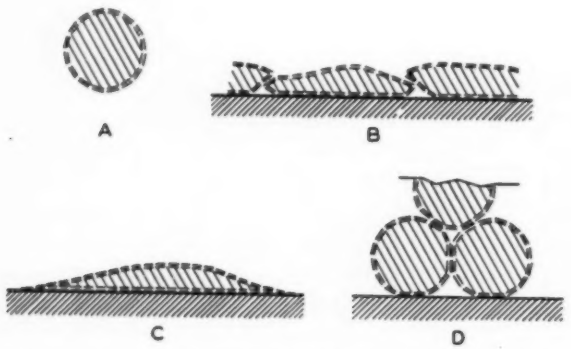

FIG. 10. (a) A spherical droplet of hydrocarbon (or of carbon) showing the graphite-like crystallites oriented tangential to its surface, (b) droplets as in (a) "smeared" over the surface without rupturing their skins, (c) a droplet such as in (a) which has wet the surface and spread over it, (d) rigid droplets as in (a) which do not wet the surface and which cannot be smeared over it as in (b) and (c). The preferential orientation of the crystallites parallel to the substrate surface is apparent in (b) and (c).

These droplets are not all of the same size nor are they all of the same age, or, what is equivalent, of the same composition. In the case of methane, for example, there is at any moment in the pyrolyzing atmosphere an entire series of molecular species ranging from methane and hydrogen through acetylene, benzene, and napthalene to very complex materials of low hydrogen content and high molecular weight which are virtually indistinguishable from carbon itself. The greater the complexity of these materials, the higher are their melting points, and the greater is their "viscosity" at any given temperature. It is possible that, until a high degree of complexity has been achieved, nuclei of the droplets are not formed, but once nucleated the drops probably increase in size and viscosity with time. The two processes—nucleation and growth—proceed simultaneously, and on their relative rates depend the properties of films formed by aggregation of the droplets.

Generally, of course, droplets of widely varied degrees of rigidity are present in the furnace atmosphere, and the more rigid ones can be incorporated in a fluid or semifluid matrix formed from droplets of lower viscosity, much as the rigid silica spheres of Fig. 4 are bonded in an otherwise virtually continuous "carbon" matrix. The bond between such rigid droplets and their matrix is not equivalent in strength either to the matrix or to the solid droplets themselves owing to an apparent inability of the solid phase to cross-link with the relatively fluid phase of lower molecular weight.

If the droplets are sufficiently fluid and are deposited at a relatively rapid rate on the surface, they merge and tend to form a continuous film of uniform composition over the surface. This merging of individual droplets is facilitated by forces tending to distort them, such as are provided by the rotation of a batch type of furnace. Actually, the older and generally larger droplets appear to be encased in skins which are relatively rigid in comparison with their interiors, and these skins prevent their coalescence unless the forces operating are sufficient to rupture them and to permit escape of their relatively fluid interiors. The skins represent a higher degree of polymerization in the surface brought about either because of more rapid loss of hydrogen there or because of the polymerizing or catalytic influence of constituents in the gas in which the droplets are immersed.

It would be desirable if the fluid droplets could be separated from the more rigid ones and used to build up a film, and such a "filtering" action can be achieved under certain circumstances. The droplets create an opaque fog over most of the coating zone cross section in pyrolyzing furnaces when the hydrocarbon concentration is high. The fog is not present at low concentrations nor immediately adjacent to the heated furnace walls or other objects in the furnace which are hotter than the gas.[2] The well-defined limits of these fog-free areas probably are the boundaries between a conduction zone contiguous to the surfaces in which diffusion processes are operative and turbulent regions in the body of the gas. The fog in the turbulent regions probably consists to a greater extent of the larger droplets which, because of gradients in temperature and viscosity, cannot usually penetrate the conduction zone. When these gradients are reversed, however, as by introducing a cooler object into the furnace atmosphere, these heavier and larger particles deposit on the cooler surface. This type of deposition results in a soft, porous, and loosely adherent film of carbon. Thus, by keeping the surface to be coated at a higher temperature than the gas, the larger and more rigid droplets do not as readily penetrate the conduction zone, and a relatively homeogeneous film is produced primarily from the smaller and more fluid particles.

With rise in temperature both the rate of nucleation and the average degree of polymerization of the droplets increase, and the increase in roughness shown in Fig. 1

is probably due to the increased rigidity of the droplets and to their correspondingly increased resistance to deformation. Figure 5 shows that, under otherwise fixed conditions, the surface becomes smoother the greater the smearing forces as determined by the rotational speed of the furnace, and that the generally spherical shapes of the roughnesses at low rotational speeds are translated into generally rectangular roughnesses at higher speeds. This is probably a consequence of the fact that the droplets in this instance are relatively rigid and are deformed into disk shape, a process occurring to a lesser extent at low speeds where the time interval between successive exposures to the turbulent furnace gases is longer and where the increase in "viscosity" between exposures is greater.

The preferred crystallite orientation in the carbon films is also explicable if they are built up by the accretion of molten droplets of complex hydrocarbons. As noted earlier, these droplets appear to be encased in "skins" in which the degree of polymerization or the extent of dehydrogenation is greater than in the sphere interiors and the number of graphitic nuclei or the lateral extent of the hexagonal networks of carbon atoms is, therefore, probably greatest near the droplet surface. These flat platelets tend to "float" in positions tangential to the droplet surface much as graphite flakes align themselves on the surfaces of liquid drops. If the droplets are dehydrogenated to carbon while still spherical, a diffraction pattern from them, which invariably results from transmission of the beam through them, should show a random orientation since equal numbers would be oriented in all directions. However, if the droplets are deformed while their centers are still relatively fluid, preferred orientation would result. Such deformation could result from the "smearing" action noted earlier or from the tendency of the droplets to coalesce and flow over the substrate surface. In these cases the crystallites would tend to orient themselves parallel to the substrate surface just as do the flakes of colloidal graphite in "aquadag." The postulated structure of the droplets and the manner in which the observed preferential crystal orientation is developed is shown schematically in Fig. 10.

The ability of the crystallites to orient themselves in this way will be dependent on the "viscosity" of the droplets and on the number of them striking the surface. The number available per unit time increases with hydrocarbon concentration, and the average viscosity probably decreases because of a decreased "transit time" between their formation and their impingement on the surface. Thus, the increase in preferred orientation with increase in concentration shown in Fig. 9 is to be expected.

As the pyrolyzing temperature increases, the time rate of production of complex hydrocarbon intermediates increases as does the molecular weight or "viscosity" of the more complex members of the series. At first, increase in the rate of nucleation or in the quantity of the lower molecular-weight material probably exceeds in its effect the increase in viscosity of the more complex materials and hence, as shown in Fig. 8, the extent of preferred orientation initially increases. With further increase in temperature, however, dehydrogenation of the already formed droplets is greatly accelerated, and their average viscosity or resistance to deformation increases correspondingly. As a result, the relationship between orientation and pyrolyzing temperature assumes the form shown in Fig. 8, the orientation passing through a maximum value as the temperature increases.

A preferential crystallite orientation of the type proposed here has been reported for crystallites in particles of carbon black. Hall has found that the parallel layer groups of graphitic planes near the surface of the roughly spherical particles of some carbon blacks are oriented approximately parallel to the surface.[4] Further, Iley and Riley, in a study of the deposition of carbon on silica, observed a filamentary type of growth in which the hexagon layer planes lie more or less parallel to the fiber axis, the maximum deviation from parallelism being about 20°.[5] These filaments grew at the downstream end in a short furnace tube of relatively small diameter through which the hydrocarbon gas was passed at a velocity in excess of 650 cm per minute at 1000°C. Under these conditions it is probable that the droplets are quite fluid so that a shearing force between droplets and a point of attachment to the tube parallel to the direction of flow provides an effective orienting influence similar to the mechanical rubbing forces described above. Filamentary growths similar to those noted by Iley and Riley have been observed during the present study, particularly under conditions where the hydrocarbon is injected into a heated enclosure through small diameter jets, the growth occurring from the edges of the jets in the direction of flow. These growths were observed to consist of rounded segments, just as do the surfaces of pyrolytic carbon films. Indeed, the "ball-chain" structures shown extending from the surface in Fig. 6 suggest how such filaments may originate.

DISCUSSION

That carbon is produced during pyrolysis of simple hydrocarbons by a process of polymerization or condensation seems to be generally accepted, but details of the process have remained obscure. As an example, Parker and Wolfhard,[6] in a study of carbon formation in flames, state the situation in the following way:

"Tentatively we suggest that carbon formation in flames occurs by one of the following two processes: (1) Higher hydrocarbons are formed by pyrolysis. The molecular weight and concentration of these increase until the saturation vapor pressure is exceeded,

[4] E. C. Hall, J. Appl. Phys. **19**, 271 (1948).
[5] R. Iley and H. L. Riley, J. Chem. Soc. (London) **1948**, 1362.
[6] W. G. Parker and H. G. Wolfhard, J. Chem. Soc. (London) **1950**, 2038.

whereupon condensation occurs and fine droplets are formed. These droplets contain nuclei of graphite, and graphite crystallites grow in the manner described by Hofmann and Wilm[7] until each droplet is converted into carbon and hydrogen is largely eliminated Since the droplets are moving in an increasing temperature gradient, the process of graphitizing must be more rapid than that of reevaporation of the droplet. (2) During pyrolysis of the hydrocarbon large unstable molecules are formed which tend to decompose again into their original material. If conditions are favorable, however, very large molecules may be formed which graphitize on entering a region of sufficiently high temperature. The graphitization process is again similar to that proposed by Hofmann and Wilm and depends on the spontaneous formation of carbon nuclei within the molecules. Each nucleus grows into a graphite crystallite until it meets the next crystallite growing from an adjacent nucleus inside the same molecule. The hydrogen atoms are freed and escape from the graphite structure."

The evidence for the occurrence of droplets of hydrocarbon postulated in (1) provided by the present study argues for the correctness of this hypothesis. Further, however, hypothesis (2) assumes a single giant molecule, or a particle in which there is a strongly developed and continuous carbon skeleton. In this latter case, because of the strong bonding between nuclei, there could be little preferential orientation of the crystallites of the type observed here, whereas in (1) the individual graphite nuclei are not connected by valence forces and they therefore are free to orient tangential to the droplet surface. From the physical data provided by the present study it consequently appears that in pyrolysis carbon is formed by the first of the two mechanisms postulated on chemical grounds by Parker and Wolfhard.

The droplet mechanism of carbon deposition also provides an explanation for the "reticulate chain structure" of carbon blacks reported by Ladd and Wiegand[8] and clearly confirmed by Watson.[9] This structure is one in which individual spherical particles of carbon black are joined to each other by short necks or rods. Necks of varied diameters have been observed and to explain them it is only necessary to postulate collision between droplets of the nature described above. The dimensions of the necks will clearly depend on the fluidity of the droplets, being large when the fluidity is large and small when they are more viscous. This partial fusion of droplets can occur on any scale, and the tightly bonded group of coated silica spheroids in Fig. 4 bears a striking resemblance to some of Watson's electron micrographs of carbon black.

A valence bonded carbon skeleton such as discussed above can, however, be produced under certain conditions, and pyrolysis of such a system leads to quantitatively different results. It has been observed in the present study that oxygen, present in small quantities during pyrolysis of a hydrocarbon, acts as a strong cross-linking agent for the materials of which the droplets are composed. In such an event, the droplets are made rigid by a three-dimensional system of valence bonds, and they cannot be smeared over surfaces to yield carbon films exhibiting a preferential crystal orientation. Films produced from such oxygenated droplets are lower in apparent density, less adherent to surfaces on which they are formed, and have higher specific resistances and larger temperature coefficients of resistance than do films formed by pyrolysis in the absence of oxygen.

An illustration on a macroscopic scale of the influence of oxygen during pyrolysis is afforded by the results of a study of the carbonization of certain highly cross-linked organic polymers. Small spherules produced by suspension polymerization of a mixture of ethyl vinyl benzene and divinyl benzene were employed in this study. The spherules were about 0.5 mm in diameter, and they were heated in suitable atmospheres in a small oven attached to the stage of a binocular microscope. With no preliminary treatment, these spheres invariably melted at about 350°C to 400°C in atmospheres of hydrogen or oxygen-free nitrogen or helium. The molten material had a relatively high vapor pressure, and further heating to higher temperatures resulted in deposition of a carbon film on the furnace walls. It is probable that this pyrolytic carbon film was produced by the same mechanism as are those deposited from methane.

Melting of the polymer could be partly or entirely prevented by subjecting the spheroids to a preliminary heat treatment in air at temperatures up to 200°C or higher. This heating produced a sufficient degree of cross-linking in the polymer surface that the spheroids could subsequently be carbonized without losing their spherical form. Cross-linking apparently occurred as a result of oxygen diffusion into the sphere, a process which could be observed by noting the radial variation of the yellow to deep red color produced by oxidation. Heating for a short time in air or oxygen produced a thin cross-linked skin which carbonized without melting even though the interior of the sphere was clearly molten. With slow heating the molten material diffused through the skin and evaporated, leaving fragile hollow spheres of carbon. The skin thickness could be controlled by varying the duration and temperature of preoxidation, and, if sufficient time was allowed for oxygen to diffuse to the center of the sphere, then it could be dehydrogenated or carbonized to yield a solid sphere of carbon. The yield of carbon, based on the original weight of the polymer, increased with the extent of oxidation, in accordance with the observations of Gibson, Holohan, and Riley on the carbonization process.[10]

When lightly oxidized polymer spheres were rapidly heated, the internal pressures developed by the shrinkage of the skin and the vapor of the molten center caused the skin to rupture. Occasionally, after rapid

[7] U. Hofmann and D. Wilm, Z. Elektrochem. **42**, 504 (1936).
[8] W. A. Ladd and W. B. Wiegand, Rubber Age **57**, 299 (1945).
[9] J. H. L. Watson, J. Appl. Phys. **20**, 747 (1949).
[10] Gibson, Holohan, and Riley, J. Chem. Soc. (London) **1946**, 456.

escape of the melt, the two or more spherical segments of the shell would be "cemented" together by the fluid to give hollow spheres showing circumferential belts. In other cases the separated segments would carbonize as cup shaped specimens. And at times the molten fluid would cement spheres or fragments of them together. The appearance after carbonization was often much similar to that for pyrolytic carbon shown in Fig. 4 with its vestiges of carbon shells cemented to the wall, or with spherules joined by necks of varying sizes. Figure 11 shows schematically the form of the products of carbonization of polymer spheres under various conditions.

It should be noted that this "polymer carbon" differs from pyrolytic carbon in having, in general, a more disorganized structure.[11] The average crystal size is also smaller, it is more microporous, its surface is smoother, there is no evidence of preferred crystal orientation, and it exhibits a remarkable thermal stability even at temperatures of 2500°C.

The hollow spheroids formed by carbonization of partially oxygenated polymer spheroids are geometrically indistinguishable from the hollow particles of carbon black observed by Watson.[9] Despite the differences in size between these polymer carbon spheres and those of carbon black, it appears highly probable that they are produced by the same fundamental mechanism. Thus, oxygen present at the proper stage in life of a hydrocarbon droplet from which carbon black or pyrolytic carbon is produced would be expected to form a cross-linked skin just as in the case of solid polymer spheres.

Recent work by Franklin has suggested that black carbons can be divided into graphitizing and nongraphitizing varieties.[12] The graphitizing varieties are those in which the graphitic crystallites are not cross-linked, while the nongraphitizing types consist of crystallites connected by valence bonds to each other. These two types correspond, in the extremes, to the pyrolytic carbon and the polymer carbon described above. But rather than being two distinct varieties, these and Franklin's carbons probably result from the same process and simply represent members near the opposite ends of a continuous series of carbons. Franklin, in confirmation of this, has found carbons intermediate between the two varieties and discusses multiphase systems to account for them.[12] It seems quite probable that these various phases differ in the same way that the droplet or spheroid skins differ from droplet centers in the present discussion. There can be no sharp phase boundary between them, and all degrees of cross-linking probably are coexistent.

It will be appreciated that no pyrolyzing atmosphere can be entirely oxygen-free and, therefore, that the differences in mechanism between the formation of pyrolytic carbon as detailed above and the carbonization of a solid hydrocarbon are quantitative rather than qualitative. All of the processes by which a solid hydrocarbon has been given its properties can occur very rapidly during pyrolysis of a gaseous hydrocarbon such as methane, especially if traces of oxygen are present. And indeed it may be that traces of oxygen, minute though they may be, are essential to the production of carbon by purely thermal means.[10] It now seems clear that the mechanisms underlying the formation of pyrolytic carbon films, of the many types of carbon black, and of soot in flames of all types are fundamentally alike in that all these forms of black carbon have as common precursors molten droplets of complex hydrocarbons. Traces of oxygen may conceivably be necessary in the formation of the nuclei, and the amount of oxygen present during pyrolysis is clearly important in determining the extent of cross-linking and hence the geometrical form of the resultant carbon particles and the extent of a preferred crystallite orientation. Gas-phase pyrolysis and the carbonization of solid organic substances, however, are not two uniquely different ways of obtaining black carbon. They simply represent two extremes in an infinite series of processes which are all fundamentally alike.

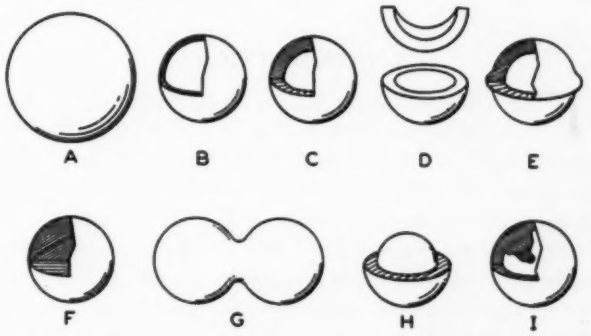

FIG. 11. Artifacts produced by carbonization of polymer spheres —(a) the original polymer sphere, (b) thin-shelled hollow carbon sphere obtained by slow carbonization of (a) after light oxidation, (c) thick-shelled hollow carbon sphere obtained by slow carbonization of (a) after more prolonged oxidation, (d) fragments of hollow spheres obtained as in (c) except with rapid carbonization, (e) fragments of hollow spheres as in (d) which have joined together to give a belted hollow sphere, (f) a solid sphere of carbon obtained by carbonization after prolonged oxidation, (g) two carbon spheres joined by a neck, (h) sphere from which thick shell has partially peeled, (i) sphere with irregular inner wall.

It is a pleasure to acknowledge the assistance of many members of the Bell Telephone Laboratories in this work. A. H. White, K. H. Storks, R. D. Heidenreich, and C. J. Calbick together with Miss S. E. Koonce were responsible for the many electron-microscopic and electron-diffraction studies. Preparation of the samples and determination of their physical properties were carried out by A. C. Pfister, J. M. Hinkel, and H. E. Earl. Finally, the solid polymers employed in the studies of carbonization were prepared by W. O. Baker and F. H. Winslow.

[11] W. O. Baker and F. H. Winslow, Proc. 12th International Congress of Pure and Applied Chem., 1951.

[12] Rosalind E. Franklin, Proc. Roy. Soc. (London) **A209**, 196 (1951).

JOURNAL OF APPLIED PHYSICS VOLUME 24, NUMBER 9 SEPTEMBER, 1953

Effect of Stiffness and Nonuniformity on Vibroscopic Determination of Filament Cross-Sectional Area

D. J. MONTGOMERY*
Textile Research Institute, Princeton, New Jersey
(Received April 9, 1953)

The presence of stiffness in a stretched string vibrating between fixed supports raises all the natural frequencies over those for a perfectly flexible string. The presence of nonuniformity in cross-sectional area along the string changes some or all of the frequencies from those for a perfectly uniform string, the amount and direction of change depending on the form of the nonuniformity. These changes in frequency may introduce error into the calculation of the average cross-sectional area of a fiber by means of the vibroscopic technique, wherein the mechanical resonance of a stretched fiber is observed under oscillating mechanical or electrostatic forces. In this paper the natural frequencies are calculated with both the stiffness and the nonuniformity taken into account to first-order terms. The relation between the average cross-sectional area and the natural frequencies is analyzed. Consideration is given to the manner in which the changes in frequency and shifts of the nodes, due to nonuniformity, determine the detailed form of the area variation. The characterization of nonuniformities in terms of certain arbitrary parameters is shown to lead to the possibility of calculating the average area by measuring the natural frequencies in only the first and second modes and of calculating the maximum or minimum area by measuring also the nodal shift in the second mode.

I. INTRODUCTION

THE vibroscopic method of determining the cross-sectional area of filaments has been described by several authors.[1–5] In this method the linear density of the filament is obtained from the values of the natural frequencies of transverse vibration of the filament under tension. In the papers cited some attention was given to the effect of stiffness in raising the natural frequencies of vibration, but no correction was attempted for the effect of possible nonuniformity in cross section along the filament. The present paper takes into account the existence of both stiffness and nonuniformity, under the restriction that they are small enough that a first-order perturbation treatment can be applied to the differential equation describing the motion of the filament.

Preceding the treatment of this equation, a short discussion on the kind of information the vibroscope might yield about the cross-sectional area is given in Sec. II. It is pointed out that one does not ordinarily wish complete information as to the detailed form of the area as a function of position along the filament, but rather that one is interested in some kind of averaged area, or other derived quantity, which reduces the total amount of information to manageable form. The treatment of the differential equation is then given in Sec. III. The relation between the mean cross-sectional area and the natural frequencies of vibration is obtained in Sec. IV. The manner in which the values of the natural frequencies and the nodal shifts permit determination of the detailed form of the variation in area is considered in Sec. V. The characterization of nonuniformities in terms of certain arbitrary parameters is treated in Sec. VI.

II. SOME ASPECTS OF THE PROBLEM OF MEASUREMENT

Although there are times when it is desirable to know in detail the area S of a fiber of length l as a function of position x along the fiber, we are usually concerned with the determination of a few derived quantities that permit the wealth of detailed information to be viewed in a readily comprehensible form. Thus in the present instance we are as a rule not so much interested in the detailed form of $S(\xi)$, the area as a function of the reduced length

$$\xi \equiv x/l, \quad (0 \leq \xi \leq 1) \tag{1}$$

as in some averaged area, say the mean area $\bar{S}$, defined as

$$\bar{S} \equiv \int_0^1 S(\xi)d\xi. \tag{2}$$

Some other quantities which are of interest in certain problems are the variance of the area from the mean, and the maximum or minimum values of the area along the fiber.

From this point of view, the first task in the general problem of physical measurement is the definition of useful functionals ϕ_i (such as $\bar{S}$) of physically interesting functions $F(\xi)$ of some variable ξ [such as $S(\xi)$]. To facilitate the mathematical analysis, the present work is restricted to functionals of the form

$$\phi_i[F(\xi)] = \int_{\xi_1}^{\xi_2} F(\xi)g_i(\xi)d\xi, \tag{3}$$

where $g_i(\xi)$ is a weighting function of some kind (equal to unity, in the definition of $\bar{S}$).

* Present address: Michigan State College, East Lansing, Michigan.

[1] V. E. Gonsalves, Textile Research J. **17**, 369 (1947).
[2] S. L. Dart and L. E. Peterson, Textile Research J. **19**, 89 (1949); **22**, 819 (1952).
[3] D. O. Sproule, J. Textile Inst. **43**, T455 (1952).
[4] D. J. Montgomery and W. T. Milloway, Textile Research J. **22**, 729 (1952).
[5] J. Lindberg, Textile Research J. **23**, 67 (1953).

In many instances, a measuring process does not give directly the quantity of interest, but rather a quantity indirectly related to it. For example, we may seek to determine the cross-sectional area of a fiber by weighing a known length on a microbalance. The mass m of the sample will be connected with the area S through the relation

$$m=\int_0^l \rho(\xi)S(\xi)l\,d\xi, \tag{4}$$

where $\rho(\xi)$ is the density of the fiber, assumed to be determinable by some independent means such as suspending fiber segments in a density gradient column. It is clear that detailed information about the form of the integrand in Eq. (4) cannot be obtained from the weighing alone. Moreover, unless the value of $\rho(\xi)$ is known, nothing can be said about the average area $\bar{S}$. However, if ρ can be taken as constant, the value of $\bar{S}$ can be got immediately; but there is still no knowledge of $S(\xi)$ other than its average, and no knowledge whatsoever of the variance of the area. Thus it is possible for the result of a given experiment to define completely the value of some functionals but to afford no knowledge of others.

The second task in the general problem of physical measurement, then, is the development of experimental techniques yielding weighting functions $h_j(\xi)$ [equal to $\rho(\xi)l$ in the case of Eq. (4)] which will generate useful functionals ψ_j [such as m of Eq. (4)] of physically interesting functions $F(\xi)$ [such as $S(\xi)$]. The functionals ψ_j will be restricted to the form

$$\psi_j[F(\xi)]=\int_{\xi_1}^{\xi_2} F(\xi)h_j(\xi)d\xi. \tag{5}$$

It is now apparent that the third task of the general problem is relating the sought ϕ_i to the observed ψ_j. There is no universal prescription for finding the relation between these functionals; indeed, there is no assurance that there is any connection except in deliberately selected instances. But often the connection is obvious, as in relating $\bar{S}$ of Eq. (2) with m of Eq. (4) when ρ is constant. Then

$$m=\rho l\int_0^1 S(\xi)d\xi=\rho l\bar{S}.$$

In other cases, some relation does exist, but it is not direct and simple. Section IV of this paper will be concerned with such a problem.

It is necessary first to determine the weighting functions h_j appropriate to the vibroscopic method. Hence, the next portion of the paper, Sec. III, takes up the problem of the vibrating nonuniform stretched string with stiffness.

III. THEORY OF TRANSVERSE VIBRATION OF NONUNIFORM STRETCHED STRING WITH STIFFNESS

The equation of motion for the transverse vibrations of a stiff string under longitudinal tension can be shown[6] to be

$$\frac{\partial}{\partial x}\left(T\frac{\partial y}{\partial x}\right)-\frac{\partial^2}{\partial x^2}\left[(QS+T)\kappa^2\frac{\partial^2 y}{\partial x^2}\right]=\rho S\frac{\partial^2 y}{\partial t^2}, \tag{6}$$

where x = distance along string, t = time, $y(x,t)$ = transverse displacement of string, T = longitudinal tension, S = cross-sectional area, Q = elastic modulus, κ = radius of gyration about neutral axis, ρ = volume density. Except for neglect of rotational inertia terms, this equation is correct for small displacements.

If T, S, Q, κ, and ρ are assumed to be independent of time, Eq. (6) may be handled by separation of variables. Thus, if we write

$$y=y_n(x,t)\equiv X_n(x)T_n(t), \tag{7}$$

the partial differential Eq. (6) breaks down into two ordinary differential equations in x and in t.

The equation involving t has the solution

$$T_n(t)\sim\sin(\omega_n t+\gamma_n), \tag{8}$$

where $-\omega_n^2$ is the constant appearing in the separation of variables, and γ_n is a constant of integration.

The equation involving x is

$$\frac{1}{\rho S}\frac{d}{dx}\left(T\frac{dX_n}{dx}\right)-\frac{1}{\rho S}\frac{d^2}{dx^2}\left[(QS+T)\kappa^2\frac{d^2X_n}{dx^2}\right]=-\omega_n^2X_n. \tag{9}$$

This equation determines the allowed values of ω_n^2, and hence the natural frequencies of vibration, when the boundary conditions are imposed. For a string of length l clamped at both ends, it is required that

$$\begin{aligned} y(0)&=y(l)=0,\\ y'(0)&=y'(l)=0. \end{aligned} \tag{10}$$

Equation (9) has simple exact solutions only in very restricted cases, and in general we shall have to resort to perturbation techniques. Accordingly, only those cases where the nonuniformities along the string are slight will be treated. To this end certain unperturbed solutions will now be developed.

[6] A. Seebeck, Abhandl. math.-phys. Kl. sächs. Akad. Wiss., Leipzig, 1852; or see Lord Rayleigh, *The Theory of Sound* (Macmillan and Company, Ltd., London, 1898), 2nd ed., Vol. 1, p. 301; reprinted by Macmillan, 1926, 1929; (Dover Publications, New York, 1945); or P. M. Morse, *Vibration and Sound* (McGraw-Hill Book Company, Inc., New York, 1948), 2nd ed., p. 170.

Uniform Stretched String with Stiffness

If T, QS, κ, and ρS are independent of x as well as t, Eq. (9) for the eigenfunctions $X_n^0(x)$ may be written

$$\frac{d^4X_n^0}{dx^4}-\frac{a^2d^2X_n^0}{\kappa^2b^2dx^2}-\frac{\omega_{n0}^2X_n^0}{b^2\kappa^2}=0, \tag{11}$$

where

$$b^2=(QS+T)/\rho S, \tag{12}$$

and

$$a^2=T/\rho S. \tag{13}$$

The exact solution of Eq. (11) which satisfies the boundary conditions (Eq. 10) is

$$X_n^0\sim(\alpha_n\sin\beta_nl-\beta_n\sinh\alpha_nl)(\cos\beta_nx-\cosh\alpha_nx)-(\cos\beta_nl-\cosh\alpha_nl)(\alpha_n\sin\beta_nx-\beta_n\sinh\alpha_nx), \tag{14}$$

wherein

$$\alpha_n^2\equiv(a^2/2b^2\kappa^2)[(1+4\omega_{n0}^2b^2\kappa^2/a^4)^{\frac{1}{2}}+1], \tag{15}$$

and

$$\beta_n^2\equiv(a^2/2b^2\kappa^2)[(1+4\omega_{n0}^2b^2\kappa^2/a^4)^{\frac{1}{2}}-1]. \tag{16}$$

The equation determining the allowed frequencies turns out to be

$$\frac{\sinh\alpha_nl\sin\beta_nl}{1-\cosh\alpha_nl\cos\beta_nl}+\frac{2\alpha_n\beta_n}{\alpha_n^2-\beta_n^2}=0. \tag{17}$$

Uniform Stretched String with Small Stiffness

For a uniform stretched string with small stiffness ($\alpha\ll1$), where

$$\alpha^2\equiv4QS_0\kappa^2/Tl^2, \tag{18}$$

the approximate solution of Eq. (14) leads to the following expression* for the eigenfrequencies $f_{n0}\equiv\omega_{n0}/2\pi$:

$$f_{n0}=nf_0(1+\alpha), \tag{19}$$

where

$$f_0\equiv(1/2l)(T/\rho S_0)^{\frac{1}{2}}.$$

Moreover, it may be shown that the solution (14) reduces to

$$X_n^0\sim\sin(n\pi x/l)+O(n\alpha), \tag{20}$$

where $O(n\alpha)$ is a term of first order or higher in $n\alpha$. This result will be of importance in simplifying the calculations for perturbing terms when nonuniformity along the string exists.

Slightly Nonuniform Stretched String with Small Stiffness

When variations in T, S, Q, κ, or ρ along the string exist, the general equation (9) becomes complicated, and it usually cannot be solved in closed form. In many practical cases, the deviation from uniformity is slight, and it is possible to calculate approximately the natural frequencies and the corresponding characteristic solutions. Here we restrict ourselves to the case where only the cross-sectional area S varies with x. We write

$$S\equiv S_0[1+\eta(\xi)], \tag{21}$$

where $\xi\equiv x/l$, as defined earlier for Eq. (1).

The usual perturbation treatment[7] is applied to Eq. (9), with the unperturbed solutions taken as the X_n^0 in Eq. (14); but if we impose the additional restriction that the stiffness be small, and if we confine ourselves to first-order corrections, the much simpler solutions as given by Eq. (20) may be used. The computation then gives the following approximation for the frequency shift Δf_n between the actual frequencies f_n and the unperturbed frequencies f_{n0} of Eq. (19):

$$\Delta f_n/f_{n0}\equiv(f_n-f_{n0})/f_{n0}=-\int_0^1\eta(\xi)\sin^2n\pi\xi d\xi. \tag{22}$$

This approximation is correct to terms in η and α, but neglects terms in η^2, α^2, and $\eta\alpha$.

Another computation furnishes an approximation for the displacement δ_{pq} of the pth node at $\xi=\xi_{pq}$ in the qth mode of vibration ($0\leq p\leq q$) from its position ξ_{pq}^0 in a uniform string,†

$$\delta_{pq}\equiv\xi_{pq}-\xi_{pq}^0=(-1)^p(2/\pi)\sum_j'\{[q\sin(j\pi p/q)]/(q^2-j^2)\}\times\int_0^1\eta(\xi)\sin j\pi\xi\sin q\pi\xi d\xi, \tag{23}$$

where the prime on the summation sign means that the term for $j=q$ is to be omitted.

Equations (22) and (23) are all the results we shall need from the theory of the vibrating string in order to have a basis for setting up the weighting functions h_j of Eq. (5).

IV. RELATION BETWEEN MEAN AREA AND NATURAL FREQUENCIES

The functional ϕ_i of interest is the mean cross-sectional area $\bar{S}$; the functionals ψ_j available will be taken as the *apparent areas* S_n, quantities to be defined below in terms of the natural frequencies of the vibrating fiber. First we put Eq. (22) into the following form, correct to first-order terms in $\eta(\xi)$:

$$1/f_n^2=(1/f_{n0})^2\left[1+2\int_0^1\eta(\xi)\sin^2n\pi\xi d\xi\right].$$

With the aid of Eqs. (19) and (21) we get

$$(1+\alpha)^2/(f_n/n)^2=(4l^2\rho/T)\left[2\int_0^1S(\xi)\sin^2n\pi\xi d\xi\right]=(4l^2\rho/T)S_n, \tag{24}$$

* Equation (19) is correct to first-order terms in α; to get the second- and third-order terms, add $(1+n^2\pi^2/8)\alpha^2$ and $(1+n^2\pi^2/6)\alpha^3$ within the parentheses in Eq. (19).

[7] See reference 6, Rayleigh, p. 115.

† In the absence of stiffness $\xi_{pq}^0=p/q$; when stiffness exists, certain nodes are shifted from these values.

where

$$S_n \equiv T(1+\alpha)^2/4l^2\rho(f_n/n)^2. \quad (25)$$

By Eq. (25) we have defined our functionals S_n in terms of measured quantities,‡ and by Eq. (24) we have related them to the function $S(\xi)$. Now we must find what relation exists between $\bar{S}$ and the S_n.

Without loss of generality $S(\xi)$ may be written as a Fourier series in $\cos k\pi\xi$,

$$S(\xi)=S_0[1+\eta(\xi)]=S_0[1+\sum_{j=1}^{\infty} a_j \cos j\pi\xi], \quad (26)$$

where in the usual way

$$a_j=2\int_0^1 \eta(\xi)\cos j\pi\xi d\xi. \quad (27)$$

It is seen immediately that

$$\bar{S}\equiv\int_0^1 S(\xi)d\xi=S_0. \quad (28)$$

By application of elementary trigonometric identities, the second equation of (24) gives

$$S_n=S_0\left[1-\int_0^1 \eta(\xi)\cos 2n\pi\xi d\xi\right]. \quad (29)$$

The insertion of relation (27) into Eq. (29) leads to the important result

$$S_n=S_0(1-\tfrac{1}{2}a_{2n}), \quad (30)$$

or to first-order terms,

$$\bar{S}=S_0=S_n(1+\tfrac{1}{2}a_{2n}). \quad (31)$$

That is, *the mean area $\bar{S}$ is equal to the apparent area S_n increased by a relative amount equal to one-half the 2nth component of the Fourier cosine expansion of the deviation of the area $S(\xi)$ from the mean area $\bar{S}$.*

To show a little more clearly how the form of $\eta(\xi)$ affects the correction term $\frac{1}{2}a_{2n}$, consider the special cases of n equal to 1 and to 2. The correction term may be written as

$$\tfrac{1}{2}a_{2n}=\int_0^1 \eta(\xi)u_n(\xi)d\xi,$$

where

$$u_n(\xi)=\cos 2n\pi\xi, \quad (0\leq\xi\leq 1).$$

When the area variation $\eta(\xi)$ is multiplied by the appropriate weighting function, the desired functional appears as the area under the resulting curve. It is clear that an inhomogeneity at $\xi=\frac{1}{2}$ or $\frac{3}{4}$ has no effect on the correction term for the first mode, but that it has a strong effect on the correction term for the second mode. In similar fashion the relative effect of an inhomogeneity at any other point can be assessed.

‡ Actually the exact value of α is not known since it involves the area and the shape of the fiber cross section. But it may be estimated satisfactorily by taking the area S_n to be the area S_0 of Eq. (18), provided of course that the shape of the fiber cross section is known.

Equation (31) is the basic equation for determining the correct value for the mean area from the knowledge of the natural frequencies of vibration. It is seen immediately that unless information besides the natural frequencies is available, $\bar{S}$ cannot be determined except to the zero-order terms S_n. It is known, of course, that the a_j go to zero as j increases beyond some fixed value j'. If j' is small enough, and the decrease of a_j is fast enough for $j>j'$, then the a_{2n} may become negligible for some nth mode, and $\bar{S}$ may be taken equal to S_n. The reason that this method cannot be followed universally is that a value of n large enough to render a_{2n} negligible may vitiate Eq. (31), in view of the neglect of second-order and higher terms in Eqs. (19) and (22). However, in many cases it is possible to work with a mode of high enough order that S_n is substantially equal to $\bar{S}$. Only experience with different types of nonuniformity will show the applicability of this procedure.

To gain an idea of the effects of specific types of nonuniformity, we consider the deviation $\eta(\xi)$ to be proportional to an integral power of ξ, to simulate *taper* along the fiber, and to be proportional to a sinusoid in ξ,

TABLE I. Values of $\frac{1}{2}a_{2k}/c_r$ when $\eta(\xi)=c_r\xi^r$.

$2k$ \ r	1	2	3	4	5
2	0	+0.05066	+0.07599	+0.08592	+0.08815
4	0	+0.01267	+0.01900	+0.02437	+0.02926
6	0	+0.00563	+0.00844	+0.01107	+0.01360
8	0	+0.00317	+0.00475	+0.00627	+0.00777
10	0	+0.00203	+0.00304	+0.00403	+0.00500

to simulate *waviness* along the fiber. First we note that if $\eta(\xi)$ is constant, then all the a_j are zero, and *thus a constant may be added to any $\eta(\xi)$ without changing the a_j.* Accordingly, it is not necessary in the immediate discussion to subtract from the assumed form of $\eta(\xi)$ its average value over the interval $0\leq\xi\leq 1$ in order to satisfy Eq. (26), since the subtraction does not alter the values of the a_j.

Effect of Taper

Suppose that the fiber has a taper which can be described by

$$\eta(\xi)=c_r\xi^r; \quad r=1, 2, 3\cdots \quad (32a)$$

then

$$\tfrac{1}{2}a_j=c_r\int_0^1 \xi^r\cos j\pi\xi d\xi=c_rC(r, j), \quad (32b)$$

where $C(r, j)$ may be computed by repeated integration by parts, or may be taken from tables.[8] Values of $\frac{1}{2}a_{2k}/c_r$ for $1\leq r$, $k\leq 5$, are given in Table I.

Examination of Table I shows that the presence of a

[8] A. N. Lowan and J. Laderman, J. Math. and Phys. 22, No. 3, 1943; reprinted by National Bureau of Standards, Math. Table MT 23, Government Printing Office, Washington, November, 1949.

taper in a fiber does not generate very large coefficients a_{2k} in the expansion (26). If the nonuniformity is proportional to the first power of ξ, all the a_{2k} are zero. If it is proportional to some higher power, say up to the fifth, the a_2/c_r do not exceed 0.10, and the a_4/c_r do not exceed 0.03. If the $|c_r|$ are limited to, say, 0.20, then in relation (31) $\bar{S}$ will not differ from S_1 by more than 2 percent, nor from S_2 by much more than $\frac{1}{2}$ percent. In reality, these limits are quite conservative, and under most circumstances *the mean area $\bar{S}$ is very nearly equal to the apparent area S_n when a taper is the only nonuniformity.*

Effect of Waviness

Suppose that the fiber has a waviness which can be described by

$$\eta(\xi)=B\cos(\beta\pi\xi+\gamma);\quad(\beta>0,\ -\pi<\gamma\leq\pi) \tag{33a}$$

then

$$\begin{aligned}\tfrac{1}{2}a_{2k}&=B\int_0^1\cos(\beta\pi\xi+\gamma)\cos 2k\pi\xi\,d\xi\\&=[B/\pi(\beta+2k)(\beta-2k)]\\&\qquad[\sin(\beta\pi+\gamma)-\sin\gamma]\qquad(\beta\neq 2k)\\&=\tfrac{1}{2}B\cos\gamma\qquad(\beta=2k).\end{aligned} \tag{33b}$$

Upon introduction of the quantity ϵ defined by

$$2\epsilon\equiv\beta\pi-2k\pi,$$

Eq. (33b) becomes

$$\tfrac{1}{2}a_{2k}/\tfrac{1}{2}B=\tfrac{1}{2}[\epsilon^{-1}+(\epsilon+2k\pi)^{-1}][\sin(\gamma+2\epsilon)-\sin\gamma].$$

The maximum value of this expression, for fixed β and k, occurs at $\tan\gamma=-[(1-\cos 2\epsilon)/(1+\cos 2\epsilon)]^{\frac{1}{2}}$, where it has the value

$$[\epsilon^{-1}+(\epsilon+2k\pi)^{-1}]\sin\epsilon.$$

The maximum of this last expression, for fixed k, occurs roughly at $\epsilon=3/2k\pi$, where it has a value decreasing from a maximum of about 1.03 at $k=1$ to unity at $k=\infty$. The expression varies slowly with respect to ϵ in the range $-\pi<2\epsilon<\pi$. Hence, when $|\epsilon|$ is less than about $\pi/2$, that is, when β differs from $2k$ by unity or less, it is possible for $|\frac{1}{2}a_{2k}|$ to get as large as $\frac{1}{2}B(1.03)$, where B is the maximum of the deviation from the mean area. If $|B|$ reaches 0.20, the difference between S_n and $\bar{S}$ can exceed 10 percent. In other words, *the difference between S_n and $\bar{S}$ may become substantial when waviness occurs along the fiber with a wavelength close to twice that of the mode under observation.* No general procedure exists for finding the correction to S_n, but special techniques may be developed in some cases, as exemplified in Sec. VI of this paper.

At points away from the "resonance" at $\beta\sim 2k$ the coefficients a_{2k} are small; even there the phase angle γ may be such as to make them vanish [see Eq. (33b)]. For the purposes of discussion, suppose that β is restricted to integral values r, and that γ is taken as zero. Then

$$\eta(\xi)=A_r\cos r\pi\xi,\quad(r=1,2,3\cdots) \tag{34a}$$

and

$$\begin{aligned}\tfrac{1}{2}a_j&=A_r\int_0^1\cos r\pi\xi\cos j\pi\xi\,d\xi=\tfrac{1}{2}A_r\quad(r=j)\\&=0\qquad(r\neq j).\end{aligned} \tag{34b}$$

Thus S_r will be just equal to $\bar{S}$ unless $r=2k$; then $\frac{1}{2}a_{2k}=0.50A_r$, and the difference between S_r and $\bar{S}$ can be as large as 10 percent if $|A_r|$ reaches 0.20.

Suppose now that β is again restricted to integral values r, but that γ is taken as $-\pi/2$. Then

$$\eta(\xi)=B_r\sin r\pi\xi,\quad(r=1,2,3\cdots) \tag{35a}$$

and

$$\begin{aligned}\tfrac{1}{2}a_j&=B_r\int_0^1\sin r\pi\xi\cos j\pi\xi\,d\xi\\&=\begin{cases}0 & (r+j\text{ even})\\ 2rB_r/\pi(r^2-j^2) & (r+j\text{ odd}).\end{cases}\end{aligned} \tag{35b}$$

Values of $\frac{1}{2}a_{2k}/B_r$ for $1\leq k,\ r\leq 5$, are given in Table II.

Examination of Table II shows that in the presence of only the even harmonics, S_n is equal to $\bar{S}$; in the presence of odd harmonics, the coefficients are small provided $|r-2k|\geq 1$. If $|B_r|<0.20$, and $|r-2k|\geq 2$, S_r will not differ from $\bar{S}$ by much more than 3 percent, for $r\leq 6$. However, if $|r-2k|=1$, the difference can become as large as 6 to 8 percent.

Hence, it may be stated that *the mean area $\bar{S}$ is very nearly equal to the apparent area S_n when the nonuniformity is a waviness with wavelength considerably different from twice that of the mode under observation.*

V. DETERMINATION OF FORM OF $S(\xi)$ FROM ANHARMONICITIES AND NODAL SHIFTS

Anharmonicity

Equation (31) contains the coefficients a_{2k} of the even terms in the Fourier expansion of the area $S(\xi)$, but it contains also the unknown quantity $\bar{S}$. To get a quantity independent of $\bar{S}$, define the *anharmonicity* ϵ_{nm} between the frequency of the nth mode and that of the mth mode $(n>m)$ as

$$\epsilon_{nm}\equiv(mf_n-nf_m)/nf_m. \tag{36}$$

By Eq. (22) it is found that to first-order terms

$$\epsilon_{nm}=\int_0^1\eta(\xi)(\sin^2 m\pi\xi-\sin^2 n\pi\xi)\,d\xi, \tag{37}$$

whence by relation (27)

$$\epsilon_{nm}=\tfrac{1}{4}(a_{2n}-a_{2m}). \tag{38}$$

Nodal Shifts

The basic equation (23) for the nodal shifts δ_{pq} becomes the following when it is transformed to contain

the Fourier coefficients a_j defined in Eq. (27):

$$\delta_{pq}=(-1)^p(q/2\pi)\sum_j' \times\{[\sin(j\pi p/q)]/(j^2-q^2)\}(a_{j+q}-a_{j-q}), \quad (39)$$

where $a_{j-q}\equiv a_{q-j}$ in cases where $q>j$. Some manipulation of Eq. (39) leads to an expression of more convenient form,

$$\delta_{pq}=(2q^2/\pi)\sum_j' a_j[\sin(j\pi p/q)]/(j-2q)j(j+2q). \quad (40)$$

Equations (38) and (40) furnish the basis for the determination of all the coefficients a_j, which together with S_0 determined from Eqs. (31) and (25) specify $S(\xi)$ in Eq. (26) completely.

To show a little more clearly how the form of $\eta(\xi)$ affects the anharmonicity and nodal shifts, consider the special case of ϵ_{21} and δ_{12}. The anharmonicity may be written as

$$\epsilon_{21}=\int_0^1 \eta(\xi)v_{21}(\xi)d\xi,$$

where by a slight transformation of Eq. (37) it is seen that

$$v_{21}(\xi)=-\sin\pi\xi\cdot\sin3\pi\xi \quad (0\leq\xi\leq1).$$

TABLE II. Values of $\frac{1}{2}a_{2k}/B_r$ when $\eta(\xi)=B_r\sin r\pi\xi$.

$2k$ \ r	1	2	3	4	5
2	−0.21221	0	+0.38197	0	+0.15158
4	−0.04244	0	−0.27284	0	+0.35368
6	−0.01819	0	−0.07074	0	−0.28937
8	−0.01011	0	−0.03472	0	−0.08162
10	−0.00643	0	−0.02099	0	−0.04244

The nodal shift may be written as

$$\delta_{12}=\int_0^1 \eta(\xi)w_{12}(\xi)d\xi,$$

where by some manipulation of Eq. (39) it is found that

$$w_{12}(\xi)=\begin{cases}-\frac{1}{4}(1-\cos4\pi\xi)=-\frac{1}{2}\sin^2 2\pi\xi & (0\leq\xi\leq\frac{1}{2})\\ \frac{1}{4}(1-\cos4\pi\xi)=\frac{1}{2}\sin^2 2\pi\xi & (\frac{1}{2}<\xi\leq1).\end{cases}$$

When the area variation $\eta(\xi)$ is multiplied by the appropriate weighting function, the desired functional appears as the area under the resulting curve. It is clear that an inhomogeneity at $\xi=\frac{1}{2}$ has no effect on the nodal shift, but that it has a strong effect on the anharmonicity. In similar fashion the relative effect on an inhomogeneity at any other point can be assessed. Analogous expressions can be derived for other modes with higher values of m, n, p, and q in Eqs. (37) and (40). In practice only a few modes can be observed, and thus only a few ϵ_{nm} and δ_{pq} are available. Then some additional information on the form of $S(\xi)$ is necessary before very much can be learned from the values of ϵ_{nm} and δ_{pq}.

As a specific example, suppose that only the first, second, and third modes are observed; then the independent anharmonicities and the nodal shifts§ available are ϵ_{21}, ϵ_{32}, δ_{12}, δ_{13}, and δ_{23}. Equations (38) and (40) specialize to the following:

$$\epsilon_{21}=\tfrac{1}{4}(a_4-a_2), \quad (41)$$

$$\epsilon_{32}=\tfrac{1}{4}(a_6-a_4), \quad (42)$$

$$\delta_{12}=-\frac{8}{\pi}\sum_{l=0}^{8}a_{2l+1}(-1)^l/(2l-3)(2l+1)(2l+5)$$

$$=-\frac{8}{15\pi}\left(a_1-\frac{5}{7}a_3-\frac{1}{3}a_5+\frac{5}{7\cdot11}a_7-\frac{1}{3\cdot13}a_9+\cdots\right), \quad (43)$$

$$\delta_{13}=\frac{18}{\pi}\sum_{k=1}'a_k[\sin(k\pi/3)]/(k-6)k(k+6)$$

$$=-\frac{9\sqrt{3}}{35\pi}\left(a_1+\frac{5\cdot7}{4\cdot16}a_2-\frac{7}{16}a_4-\frac{7}{11}a_5-\frac{5}{13}a_7+\cdots\right), \quad (44)$$

$$\delta_{23}=\frac{18}{\pi}\sum_{k=1}'a_k[\sin(2k\pi/3)]/(k-6)k(k+6)$$

$$=-\frac{9\sqrt{3}}{35\pi}\left(a_1-\frac{5\cdot7}{4\cdot16}a_2+\frac{7}{16}a_4-\frac{7}{11}a_5-\frac{5}{13}a_7+\cdots\right). \quad (45)$$

Under the *assumption* that a_7, a_8, and so on, are negligible, then the following relations hold:

$$a_1=-\frac{35\pi}{18\sqrt{3}}(\delta_{23}+\delta_{13})+\frac{7}{11}a_5,$$

$$a_2=\frac{128}{3}\epsilon_{21}+\frac{32\cdot35\pi}{27\sqrt{3}}(\delta_{23}-\delta_{13}),$$

$$a_3=\frac{21\pi}{8}\delta_{12}-\frac{49\pi}{18\sqrt{3}}(\delta_{23}+\delta_{13})+\frac{14}{33}a_5,$$

$$a_4=\frac{140}{3}\epsilon_{21}+\frac{32\cdot35\pi}{27\sqrt{3}}(\delta_{23}-\delta_{13}),$$

$$a_5=a_5,$$

$$a_6=4\epsilon_{32}+\frac{140}{3}\epsilon_{21}+\frac{32\cdot35\pi}{27\sqrt{3}}(\delta_{23}-\delta_{13}).$$

§ It must be remembered that the pth node in the qth mode for a uniform fiber necessarily lies at $\xi_{pq}^0=p/q$ only in the absence of stiffness. Hence, further analysis is necessary before the δ_{13} and δ_{23} can be obtained simply in a stiff fiber. However, δ_{12} is directly given by $\xi_{12}-\frac{1}{2}$ whether or not stiffness exists.

TABLE III. Values of $\frac{1}{2}a_{2k+1}/c_r$ when $\eta(\xi)=c_r\xi^r$.

$2k+1$ \ r	1	2	3	4	5
1	−0.20264	−0.20264	−0.18077	−0.15890	−0.14029
3	−0.02252	−0.02252	−0.03225	−0.04199	−0.04903
5	−0.00811	−0.00811	−0.01196	−0.01582	−0.01929
7	−0.00414	−0.00414	−0.00615	−0.00817	−0.01008
9	−0.00250	−0.00250	−0.00373	−0.00497	−0.00616

Hence, the a_2, a_4, and a_6 are known unequivocally, and any two of a_1, a_3, and a_5 are known in terms of a value assumed for the third. In certain circumstances, a_5 may be taken as negligible in comparison with the leading a_1; then the a_1, a_2, a_3, a_4, and a_6 are determined. Again, the validity of such an assumption can be tested only by experiment. Examination of Tables III and IV for the odd coefficients a_{2k+1} in the Fourier expansions of $c_r\xi^r$ and $B_r\sin r\pi\xi$, together with re-examination of Tables I and II for the even coefficients, shows how the a_j vary with j for these particular functions. The a_5's are indeed small.

The method of attack on the problem of finding the form of $S(\xi)$ in terms of anharmonicities and nodal shifts is clear. It is doubtful that examination of further special cases is worth while here.

TABLE IV. Values of $\frac{1}{2}a_{2k+1}/B_r$ when $\eta(\xi)=B_r\sin r\pi\xi$.

$2k+1$ \ r	1	2	3	4	5
1	0	+0.42441	0	+0.16977	0
3	0	−0.25465	0	+0.36378	0
5	0	−0.06063	0	−0.28294	0
7	0	−0.02829	0	−0.07717	0
9	0	−0.01654	0	−0.03918	0

VI. SIMPLIFIED CHARACTERIZATION OF NONUNIFORMITIES

Sometimes it is desired to characterize the nonuniformity in a fiber by specifying the values of only a few parameters. The characterization proceeds by arbitrarily assuming that the variation of the area along the length of the fiber can be described by a function containing these parameters. The values of the parameters are derived from observation of the natural frequencies and nodal shifts of the fiber in vibration in the requisite number of modes.

TABLE V. Position of Extrema of $S(\xi)$ in Eq. (46).

$\lambda\equiv\pi^{-1}\cos^{-1}(-64\delta_{12}/15\pi^2\epsilon_{21})=0.318\cos^{-1}(-0.432\delta_{12}/\epsilon_{21})$				
δ_{12}	ϵ_{21}	$\lvert 0.432\delta_{12}/\epsilon_{21}\rvert$	ξ_M	ξ_m
+	+	>1	1	0
+	+	<1	λ	0
+	−	>1	1	0
+	−	<1	1	λ
−	+	>1	0	1
−	+	<1	λ	1
−	−	>1	0	1
−	−	<1	1	λ

Suppose that the nonuniformity is considered to be the superposition of a linear taper and a sinusoidal bulge or thinning,‖

$$S(\xi)=S_0[1+c_1(\xi-\tfrac{1}{2})+B_1(\sin\pi\xi-2/\pi)]. \quad (46)$$

If the first and second modes of vibration are observed, the two natural frequencies f_1 and f_2 and the one nodal shift δ_{12} will permit the determination of c_1 and B_1 (as well as $\bar{S}=S_0$), according to the relations developed in the earlier sections of this paper.

Instead of working directly with observed frequencies f_1 and f_2, it is convenient to use the derived quantities *anharmonicity* ϵ_{21}, defined in Eq. (36), and *apparent areas* S_1 and S_2, defined in Eq. (25). To evaluate the parameters in Eq. (46), we note that the linear term generates only odd coefficients a_{2k+1} in the Fourier expansion (26), and that the sinusoidal term generates only even coefficients a_{2k} therein. The constants within the parentheses in Eq. (46), of course, do not affect any of the coefficients a_j; they have been inserted merely to ensure that Eq. (46) be of the form of Eq. (26).

The parameter c_1 is found in terms of δ_{12} by inserting the special values for a_{2k+1} as given in Eq. (32b) for $r=1$ into Eq. (43). The result is

$$c_1=16\delta_{12}. \quad (47)$$

The parameter B_1 is found in terms of ϵ_{21} by inserting into Eq. (41) the special values for a_{2k} as given in Eq. (35b) for $r=1$. The result is

$$B_1=11.78\epsilon_{21}. \quad (48)$$

The parameter $S_0=\bar{S}$ is found by expressing the quantity $\frac{1}{2}a_{2n}$ in Eq. (44) in terms of ϵ_{21} with the aid of Eqs. (41) and (35). The results are

$$\bar{S}=S_0=S_1(1-\tfrac{5}{2}\epsilon_{21}) \quad (49\text{–}1)$$

$$=S_2(1-\tfrac{1}{2}\epsilon_{21}). \quad (49\text{–}2)$$

The results expressed in Eqs. (49–1) and (49–2) are useful when Eq. (46) is an adequate representation of the area variation along the fiber, for with their aid the mean area $\bar{S}$ can be determined to first-order correction terms merely by observing the two lowest natural frequencies [provided, of course, that information is available to determine the stiffness correction, in accordance with the footnote following Eq. (25)]. Moreover, it can be seen that if no correction is made to the apparent area, the frequency for the second mode gives a considerably better approximation to the mean area $\bar{S}$. However, there is no *a priori* guarantee that Eq. (46) will describe the nonuniformity satisfactorily, and the consequences of this equation must be used judiciously. Only experience with given fiber types can determine the conditions of applicability.

Other results that may be deduced from Eq. (46) are the positions and values of the extrema of $S(\xi)$. These

‖ In the absence of nonuniformity the node is at $\xi=\frac{1}{2}$ even for a stiff fiber. Hence, the nodal shift is easily determined.

lie either at an end point of the interval $0 \leq \xi \leq 1$, or where $S'(\xi)=0$. Examination of Eq. (46), with c_1 and B_1 replaced by δ_{12} and ϵ_{21} with the aid of Eqs. (47) and (48), yields the data presented in Table V for the position ξ_M of the maximum, and the position ξ_m of the minimum, of the value of the area. The corresponding values of S are found immediately from Eq. (46). The application of this procedure is fraught with danger, since δ_{12} and ϵ_{21} are not sensitive to sharp irregularities in the fiber, while the extrema are. Hence the conclusions of this paragraph must be applied with considerable caution.

To see the effect of forms assumed for $S(\xi)$ other than that of Eq. (46), suppose that the linear term is left unchanged, but that the bulge is taken as $-A_2 \cos 2\pi\xi$ instead of $B_1 \sin\pi\xi$. It is found that Eq. (48) is replaced by $-A_2=4\epsilon_{21}$, and that the coefficients $-\frac{8}{3}$ and $-\frac{1}{2}$ of ϵ_{21} in Eqs. (49–1) and (49–2) become -2 and 0, respectively. Thus the corrections are of about the same size for either type of bulge. In the more general case where the bulge is generalized to a waviness

$$B_r \sin r\pi\xi, \quad r=1, 2, 3, \cdots$$

Eq. (48) becomes

$$B_r=(\pi/12r)(r^2-16)(r^2-4)\epsilon_{21}, \tag{50}$$

and

$$\bar{S}=S_0=S_1[1-(r^2-16)\epsilon_{21}/6] =S_2[1-(r^2-4)\epsilon_{21}/6]. \tag{51}$$

To extend the above treatment to data obtained from modes higher than the first and second is straightforward; to generalize the taper term to powers of ξ higher than the first is complicated. It is believed that further development along these lines is not warranted here.

VII. ACKNOWLEDGMENTS

The author is grateful to his colleagues at Textile Research Institute, in particular to Dr. J. H. Dillon and Dr. J. H. Wakelin for their interest and encouragement; to Miss E. T. L. Voong, for her help with the computations; and to Mr. W. T. Milloway for valuable suggestions. Dr. Paul Meier of the Department of Biostatistics, Johns Hopkins University, kindly read the manuscript. The work was sponsored in part by the Wool Research Project at Textile Research Institute.

JOURNAL OF APPLIED PHYSICS VOLUME 24, NUMBER 9 SEPTEMBER, 1953

The Identification of Individual Hygroscopic Particles in the Atmosphere by a Phase-Transition Method

S. TWOMEY
Division of Radiophysics, Commonwealth Scientific and Industrial Research Organization, Australia
(Received April 27, 1953)

It is shown that in many cases the measurement of the relative humidity at which a hygroscopic particle becomes liquid can be used to establish the chemical composition of the particle. An apparatus is described which produces a stream of air of constant temperature and variable humidity. Using this apparatus the phase-transition point was determined for particles collected on spider webs. These particles were sampled in the Sydney area on the ground and from an aircraft, and it is shown that the measured values of relative humidity for the solid-liquid phase transition agreed with the hypothesis that the hygroscopic particles were composed of sea salt. Direct microscopic observation was used to follow the behavior of the particles; the technique was capable of dealing with particles down to 10^{-12}g.

I. INTRODUCTION

CONDENSATION nuclei in the atmosphere are known to consist of a large variety of substances, a small but important proportion of which is made up of hygroscopic solid particles. The sizes of these hygroscopic nuclei cover a wide range, but those nuclei the masses of which exceed 10^{-12} g are of particular significance in the formation of rain in nonfreezing clouds. These nuclei accumulate water even in unsaturated air and in cloud grow into droplets larger than the average cloud droplet. Under suitable conditions, growth by coalescence of the relatively small number of large drops may lead to precipitation.[1,2] The size distribution of large hygroscopic nuclei has been examined by Woodcock and Grifford[3] using an "isopiestic" method. To use this method (which is based on the measurement of the equilibrium size of a dissolved nucleus in an atmosphere of known humidity), it is necessary to make an assumption concerning the nature of these nuclei. Woodcock and Grifford assumed that the nuclei consisted of sea-salt particles. They showed that this was a reasonable assumption by comparing chlorinity values for the suspended matter in the air deduced by the "isopiestic" method with corresponding values obtained by direct titration—the results agreed to within better than 50 percent.

[1] I. Langmuir, J. Meteorol. 5, 175 (1948).
[2] P. Squires, Australian J. Sci. Research Ser. A, 5, 473–499 (1952).
[3] E. G. Bowen, Australian J. Sci. Research Ser. A, 3(2), 193–213 (1950).

The investigations to be described were primarily intended to develop, if possible, a method to establish more certainly the composition of individual hygroscopic nuclei,* and also to examine the behavior of large atmospheric particles in so far as their part in condensation processes is concerned.

2. METHOD

At a fixed temperature a hygroscopic particle under increasing humidity changes to a liquid drop at a definite value of humidity, which can be used to identify the particle as a particular substance or one of a group of substances.

In the case of a single chemical compound, application of the phase rule shows that at a fixed temperature a triple point exists (humidity being taken as the remaining variable) at which solid, liquid, and vapor phases are in equilibrium. At humidities above that of the triple point, the two-phase liquid-vapor system is stable, while below it, the solid-vapor system is stable. The triple-point humidity is thus the humidity at which the solid-liquid phase change takes place and is in fact the humidity in equilibrium with a saturated solution at the environmental temperature. The effect of curvature can, of course, be neglected for drops of 1 micron diameter and greater.[4] Thus by measuring the humidity of the phase transition the particle may be identified. Table I, compounded from data drawn from a number of sources,[5–7] shows the relative humidity in equilibrium with a number of common chemical compounds at 20°C. The temperature coefficient is small in all cases.[6] Where data conflict, the range of relative humidity covered is given.

TABLE I. The relative humidity in equilibrium with some saturated aqueous solutions at 20°C.

Solute	Percent Rel. Humidity	Solute	Percent Rel. Humidity
$Pb(NO_3)_2$	98	NaCl	75
$CaSO_4 \cdot 5H_2O$	98	$NaClO_3$	75
K_2SO_4	97	$(COOH)_2 \cdot 2H_2O$	75
$CaHPO_4 \cdot 2H_2O$	95	$(CHOH \cdot COOK)_2 \cdot \frac{1}{2}H_2O$	74
$Na_2HPO_4 \cdot 12H_2O$	95	$SrCl_2 \cdot 6H_2O$	71
$Na_2SO_3 \cdot 7H_2O$	95	$CoCl_2 \cdot 6H_2O$	67
KNO_3	(93–94)	$NaNO_2$	66
$NH_4 \cdot H_2PO_4$	93	NH_4NO_3	(64–65)
Na_2SO_4	93	$(CH_3COO)_2Mg \cdot 4H_2O$	65
$Na_2CO_3 \cdot 10H_2O$	92	$NaBr \cdot 2H_2O$	58
$(CHOH \cdot COONa)_2 \cdot 2H_2O$	92	$Ca(NO_3)_2 \cdot 4H_2O$	(55–56)
$NaBrO_3$	92	$C_6H_{12}O_6 \cdot \frac{1}{2}H_2O$	55
K_2HPO_4	92	$Mg(NO_3)_2 \cdot 6H_2O$	53
$BaCl_2 \cdot 2H_2O$	90	$NaHSO_4 \cdot H_2O$	52
$ZnSO_4 \cdot 7H_2O$	90	KNO_2	45
K_2CrO_4	88	$K_2CO_3 \cdot 2H_2O$	(43–45)
$(CHOH)_2COOK \cdot COONa \cdot 4H_2O$	87	$Zn(NO_3)_2 \cdot 6H_2O$	42
KCl	(84–86)	$NaI \cdot 2H_2O$	36
$KHSO_4$	86	$MgCl_2 \cdot 6H_2O$	(33–34)
KBr	(81–84)	$CaCl_2 \cdot 6H_2O$	(32–35)
$(NH_4)_2SO_4$	(80–82)	CH_3COOK	20
$CO(NH_2)_2$	81	LiCl	(11–15)
NH_4Cl	(79–80)	$ZnCl_2$	10
$Na_2S_2O_3 \cdot 5H_2O$	78	HPO_3	10
$NaNO_3$	77.7	H_3PO_4	9
$CH_3COONa \cdot 3H_2O$	76	NaOH	(5–7)
		P_2O_5	0

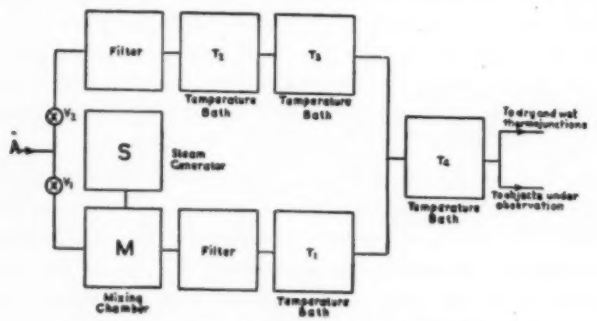

FIG. 1. Apparatus for producing a slow air stream of variable humidity.

3. APPARATUS

To measure the phase-transition humidity of atmospheric particles, an atmosphere or air stream of variable humidity was required. The apparatus, represented schematically in Fig. 1, produced a slow stream of air, the humidity of which could be controlled in a simple fashion. The apparatus operated as follows: air entering at A was split into two streams, in a proportion which could be varied by the control valves V_1 and V_2. One stream of air was saturated by mixing with steam from the generator S; it was then filtered through cotton wool and cooled back to the working (room) temperature in passing through a coil immersed in the water bath T_1. The second stream of air was filtered, dried by cooling in the bath T_2, and brought to to the working temperature in the bath T_3. The two streams were mixed in the bath T_4 to produce an air stream at the working temperature whose humidity depended on the setting of the control valves V_1 and V_2. This outgoing stream was again divided, one stream being directed on to the objects under examination; wet- and dry-bulb temperature measurements were made in the second stream using very fine, rapidly responding, copper-constantan thermocouples the emf of which could be measured by a simple potentiometric circuit which could measure differences of less than 4 microvolts (equivalent to 0.1°C). The object of carrying out temperature measurements in a separate stream was to eliminate the possibility of the humidity being changed by evaporation from the wet-bulb element.

The above method of producing humidified air had a number of advantages as compared to static methods, using, for example, solutions of known concentration:

(1) Humidity could be varied easily over a wide range.

(2) As the dimensions of the apparatus were large (all the air lines were of 1-inch copper tubing), maintaining a constant temperature presented little difficulty.

* The hygroscopic particles discussed in this paper ($>10^{-12}$ g) are referred to by some writers as "giant nuclei" (Riesenkerne).

[4] A. H. Woodcock and M. M. Gifford, J. Marine Research (Sears Foundation) **8**, 177–197 (1949).
[5] W. E. Howell, J. Meteorol. **6**, 134–149 (1949).
[6] Physik. Chem. Tab. **2**, 1288, Tab. 285A (1931).
[7] F. E. M. O'Brien, J. Sci. Instr. **25**, 73–76 (1948).

(3) As a moving stream of air was produced, such questions as the effect on temperature of the presence of the microscope (which can be a serious problem if static methods are used) did not have to be considered.

(4) The relative humidity could be measured more easily.

4. SAMPLING

Atmospheric particles were sampled by exposing spider webs mounted in a Perspex frame. The webs ranged from 1 to 5 microns in diameter and were attached to the frame by cellulose acetate cement. They could be tightly stretched by a conical tensioning bolt. For ground-level sampling the frames were mounted on a rotating arm with a peripheral speed of 75 meters per second. At higher altitudes samples were taken from an aircraft at speeds of 60–70 meters per second. At those speeds the "collection efficiency" of the coarsest webs used was very close to unity for collected particles down to 0.5 micron in diameter.[1,8]

Ten frames were exposed in aircraft observations on three days. Ground observations were made on eight days, 24 frame exposures being made. All observations were made in the Sydney area. Times of exposure averaged 2 minutes for ground observations; exposures from aircraft ranged from 5 minutes upwards.

5. EXPERIMENTAL

The exposed frames were placed on a microscope stage and the slow air stream from the humidity apparatus directed on to the frames. The behavior of individual particles on the spider webs was followed, using a magnification of 450 with dark-field illumination.

It was necessary to ensure that heating by the microscope illuminator did not introduce errors. A rise in temperature of less than 0.05°C was found to occur when the heat-filtered light beam was operated at peak power, while the microscope was focused on a small blackened thermojunction. In view of the length and very small cross-sectional area of the spider webs, conduction along the webs under the conditions of the experiment was almost certainly insignificant. Thus the particles under observation were in a condition approximating very closely to that of particles in free air at the same temperature and humidity.

When the humidity of the air stream applied was increased in small steps, all large solid particles observed were found to remain unchanged up to 70 percent relative humidity. Their subsequent behavior, however, served to divide the solid particles into two types. The first and by far the commoner type had a well-defined transition point between 71 percent and 75 percent at around 20°C; particles of the second type remained solid at all applied humidities (20 percent to 97 percent R.H.). The change from solid to liquid was usually unmistakable under dark-field illumination,

[8] I. Langmuir and K. B. Blodgett, Army Air Forces Technical Report No. 5418, pp. 68 (1946).

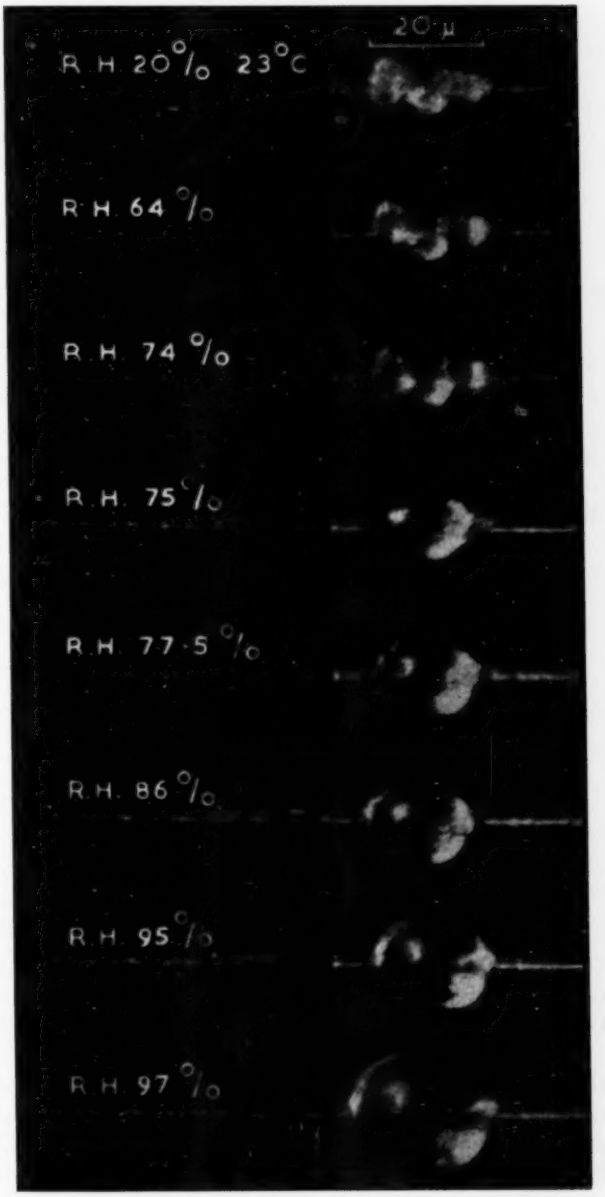

FIG. 2. A natural hygroscopic nucleus at a number of relative humidities, showing a phase change between 74 percent and 75 percent R.H.

being seen as a change from an irregularly shaped, brightly reflecting mass to an almost spherical and semitransparent state. In Fig. 2 actual photomicrographs are reproduced showing a large hygroscopic atmospheric particle at different relative humidities; in this case the phase-transition took place between 74 percent and 75 percent R.H. It is seen that the transition can be determined unambiguously within close limits. The range 71 percent–75 percent R.H. quoted above arose from the fact that sufficiently small increments in relative humidity were difficult to achieve around the critical value. If a finer control was maintained, it was thought that the transition point could

be determined within 1 percent or better. As the phase change occurs in a moment when a particle comes into contact with air of appropriate humidity, the rate of increase of the applied humidity was limited only by the time taken to make humidity measurements. Figure 3 shows a nonhygroscopic particle which was solid at 97 percent R.H.

Referring to Table I, it is seen that the following simple compounds would undergo a phase-transition between 71 percent and 75 percent R.H.: sodium chloride, sodium chlorate, oxalic acid, and potassium hydrogen tartrate. Of these compounds, sodium chloride is the only one which could reasonably be expected to occur in the atmosphere in large particle numbers. Thus the value found for the phase-transition point makes it appear very probable that the particles of the first type were in fact sea salt, as assumed by Woodcock. Sea salt, however, is not a simple compound,

FIG. 3. A nonhygroscopic particle which remained solid at 97 percent R.H.

and a further test had to be made to determine the relative humidity at which sea-salt particles become liquid. Sea water was sprayed on spider webs mounted in the usual way, the residual particles left on evaporation were exposed to the air stream and their transition point determined. The values found were in the same range (71 percent–75 percent R.H.) as given by hygroscopic atmospheric particles. The origin of the atmospheric particles was also indicated by the fact that large nuclei in maritime air consisted almost exclusively of particles of the first type. In offshore air streams the numbers of such particles were reduced approximately tenfold and were associated with approximately similar numbers of nonhygroscopic particles of the second type. A very small number of hygroscopic liquid droplets were also found. These droplets remained liquid at 20 percent R.H. and were thought to be sulfuric acid droplets from industrial pollutions—a few measurements of the variation of drop size with relative humidity agreed with this assumption. The nonhygroscopic particles of the second type were thought to be minute fragments of silica, clay, or similar substances. From a meteorological point of view, however, the particles of the first type are the only important ones.

It is surprising that at least a few hygroscopic solid particles with a different transition point—such as, for example, sodium carbonate (92 percent R.H.) or ammonium sulphate (80–82 percent R.H.)—were not found. However, of 400 particles, all collected in the Sydney area as described above, no large solid hygroscopic nuclei, other than those described, were found, and if other nuclei were present, the proportion of such must have been small.

6. LIMITATIONS OF THE METHOD

The phase-transition method provided a satisfactory check on the nature of the large hygroscopic nuclei in the atmosphere. It possesses the advantage that *individual* particles can be examined, but as used it was limited to hygroscopic particles and to particles of 10^{-12} g or greater (the latter limit was set by questions of microscopy). The method, however, may have some applications for the examination of smoke particles or similar problems. It is worth mentioning that silk, wool, Nylon, and glass fibers were tried for sampling and were not satisfactory; spider webs only gave satisfactory results. None of the alternative fibers equalled spider webs for strength, while atmospheric particles did not adhere to wool or Nylon in a satisfactory manner.

7. CONCLUSIONS

1. Hygroscopic particles greater than 10^{-12} g may be identified or partly identified by measuring the humidity at which the solid-liquid phase transition takes place.

2. More than 400 hygroscopic nuclei were sampled in the Sydney area and were found to become liquid between 71 percent and 75 percent relative humidity at 20°C. These particles apparently consisted of sea salt.

3. Large unidentified particles were found which remained solid at 97 percent relative humidity; large numbers of these were found in offshore air streams, but only small numbers occurred in maritime air.

4. No hygroscopic particles, other than those which appeared to be sea salt or sodium chloride, were found in the samples taken.

This work was part of the research program of the Division of Radiophysics. The author is indebted to the Chief of the Division, Dr. E. G. Bowen, for his encouragement and advice in connection with the project and to Mr. L. F. Clague for constructing the apparatus and assisting in the observations.

The Summation of Series Involving Roots of Transcendental Equations and Related Applications

M. R. SPEIGEL
Rensselaer Polytechnic Institute, Troy, New York
(Received March 12, 1953)

The summation of series involving the roots of certain transcendental equations having real roots is achieved by elementary considerations. The method is illustrated by several examples representative of those which may arise in applications. In addition to summing series, the method can be used to obtain the least positive root of the transcendental equation to any desired accuracy with but little computation.

I. INTRODUCTION

VERY often, in the course of some theoretical investigations, the physicist or engineer encounters series involving the sums of reciprocals of various powers of the roots of a transcendental equation which has only real roots. A very simple example involves the sums of reciprocals of fourth powers of the positive roots of $\sin x=0$. This leads to the series

$$\frac{1}{1^4}+\frac{1}{2^4}+\frac{1}{3^4}+\cdots. \tag{1}$$

This series arises in the evaluation of the integral

$$\int_0^\infty \frac{x^3}{e^x-1}dx \tag{2}$$

which has as one of its origins the Debye theory of specific heats.

Another example, slightly more complicated, involves the sum of the inverse square or inverse fourth powers of the positive roots of the equation $J_0(x)=0$, where $J_0(x)$ is the Bessel function of zero order.

A third example involves summing the inverse square or fourth powers of the positive roots of the equation $\tan x=x$.

Still another example, which arises in a problem considered by Lord Rayleigh[1] on the transverse vibrations of a clamped beam, involves the summation of the reciprocal fourth powers of the positive roots of the equation

$$\cos x \cosh x+1=0. \tag{3}$$

In this paper we shall present a very simple, but also quite general, method by which the summation of such series may be obtained. The methods whereby many authors have obtained the solutions to the problems which we shall treat are quite varied, ranging all the way from the relatively elementary Fourier Series to somewhat complicated contour integrations and unnecessarily difficult procedures involving integral equations. The method considered in this paper does not seem to be as well-known as it should be, in view of its simplicity, although Lord Rayliegh knew of it so many years ago and applied it to the special equation (3), but did not treat the general case.

We shall restrict ourselves to cases where all the zeros of the function are real[2] and distinct and where the sequence of roots have no finite limit point. The latter condition is obviously necessary since if the sequence of roots did have a limit point, the sum of reciprocals of any powers of these roots would diverge. In many cases the fact that the roots of an equation have to be real may be surmised from physical considerations although it is possible in some cases to prove this mathematically. There does not seem, however, to be any simple general method for determining whether all the roots of a transcendental equation are real.

In Sec. II we shall discuss the general treatment of the problem, and in Sec. III we shall illustrate this general discussion by several examples which may arise in practical problems. In Sec. IV we shall show how various applications of this procedure may be used to calculate to any desired accuracy with very little computation the least positive root of the transcendental equation involved. Illustrative examples showing the accuracy which is achieved are also given.

II. SOME PRELIMINARY CONSIDERATIONS

To illustrate our general method we first take a very simple case. Consider the equation

$$x^3-6x^2+11x-6=0. \tag{4}$$

We may write this equation as

$$1-\frac{11}{6}x+x^2-\frac{x^3}{6}=0. \tag{5}$$

It is clear from the theory of equations that the sum of the roots of the equation (4) is 6. Also the sum of the reciprocals of the roots of Eq. (5) is 11/6. This is easily verified for the particular equation (4) since its roots are 1, 2, and 3. Similarly it is clear that the sum of the products of the reciprocals of the roots taken two at a time is 1.

[1] Lord Rayleigh, *Theory of Sound* (Macmillan and Company, Ltd., London, 1894), Vol. I, p. 258.

[2] This is a sufficient condition but not necessary, as will be pointed out at the end of Example 4 in Sec. III.

In general, the equation $a_nx^n+a_{n-1}x^{n-1}+\cdots+a_0=0$ which may be written

$$1+\alpha_1x+\alpha_2x^2+\cdots+\alpha_nx^n=0, \tag{6}$$

where we have placed $\alpha_k=a_k/a_0(a_0\neq 0)$, has for the sum of the products of the reciprocals of its roots taken k at a time, the value $(-1)^k\alpha_k$.

It is not difficult to show from what has already been stated, that given the equation

$$1+\alpha_1x^2+\alpha_2x^4+\cdots+\alpha_nx^{2n}=0, \tag{7}$$

$(-1)^k\alpha_k$ represents the sum of the squares of the products of the reciprocals of the positive roots taken k at a time.

We now turn our attention to the following question. Given that $\lambda_1, \lambda_2, \cdots, \lambda_n$ are roots of the equation (6), how do we find the sums of the reciprocals of various powers of the λ's? This can easily be answered. We have from Eq. (6)

$$\frac{1}{\lambda_1}+\frac{1}{\lambda_2}+\cdots+\frac{1}{\lambda_n}=-\alpha_1, \tag{8}$$

$$\frac{1}{\lambda_1\lambda_2}+\frac{1}{\lambda_2\lambda_3}+\cdots+\frac{1}{\lambda_{n-1}\lambda_n}=\alpha_2 \text{ (two at a time).} \tag{9}$$

Squaring Eq. (8) and subtraction twice Eq. (9) we have

$$\frac{1}{\lambda_1^2}+\frac{1}{\lambda_2^2}+\frac{1}{\lambda_3^2}+\cdots+\frac{1}{\lambda_n^2}=\alpha_1^2-2\alpha_2. \tag{10}$$

Similarly since

$$\begin{aligned}\frac{1}{\lambda_1^3}+\frac{1}{\lambda_2^3}+\cdots+\frac{1}{\lambda_n^3}&=-\frac{3}{2}\left(\frac{1}{\lambda_1^2}+\cdots+\frac{1}{\lambda_n^2}\right)\left(\frac{1}{\lambda_1}+\frac{1}{\lambda_2}+\cdots+\frac{1}{\lambda_n}\right)\\&\quad+3\left(\frac{1}{\lambda_1\lambda_2\lambda_3}+\frac{1}{\lambda_1\lambda_3\lambda_4}+\cdots[\text{3at a time}]\right)\\&\quad-\frac{1}{2}\left(\frac{1}{\lambda_1}+\frac{1}{\lambda_2}+\cdots+\frac{1}{\lambda_n}\right)^3,\end{aligned} \tag{11}$$

we have using Eqs. (8), (9) and (10),

$$\frac{1}{\lambda_1^3}+\frac{1}{\lambda_2^3}+\cdots+\frac{1}{\lambda_n^3}=3\alpha_1\alpha_2-3\alpha_3-\alpha_1^3. \tag{12}$$

The sums of reciprocals of first and higher powers of the roots of Eq. (6) are gathered for convenient reference in the list of formulas at the end of the paper.[3]

[3] A method for calculation of these sums is given in Barnard and Child, *Advanced Algebra* (Macmillan and Company, Ltd., London, 1939), p. 48.

Thus far everything we have done has been mathematically rigorous and has been valid not only for real roots but for complex roots of polynomials as well. We shall, however, usually exclude complex roots for purposes of our applications. We are now ready to apply our results to the case where instead of having polynomial equations we have infinite power series equations. The results which we have spoken of as being true for polynomial equations will be assumed to be true for series equations, the only difference being that instead of finite n in (6) we have infinite n. Mathematically the results which we are assuming true can be proved valid by appealing to the theory of integral functions in complex variable theory.[4]

We shall illustrate the procedure involved by several illustrative examples in the next section.

III. ILLUSTRATIVE EXAMPLES

Example 1

Evaluate[5]

$$\frac{1}{1^4}+\frac{1}{2^4}+\frac{1}{3^4}+\cdots.$$

Consider the equation

$$\frac{\sin x}{x}=0.$$

The positive roots of this equation are $x=n\pi$, $n=1, 2,3,\cdots$. The sum of the inverse fourth powers of these roots is

$$\sum_1^\infty\frac{1}{(n\pi)^4}=\frac{1}{\pi^4}\sum_1^\infty\frac{1}{n^4}.$$

Now

$$\frac{\sin x}{x}=1-\frac{x^2}{6}+\frac{x^4}{120}-\frac{x^6}{5040}+\cdots.$$

Comparison with Eq. (7) [n infinite] shows that

$$\alpha_1=-1/6,\quad \alpha_2=1/120,\quad \alpha_3=-1/5040,\cdots,$$

and using Eq. (10) we have

$$\frac{1}{\pi^4}\sum_1^\infty\frac{1}{n^4}=(-1/6)^2-2(1/120)=1/90$$

so that

$$\sum_1^\infty\frac{1}{n^4}=\frac{\pi^4}{90}. \tag{13}$$

Similarly from Eq. (12) we may easily show that

$$\sum_1^\infty\frac{1}{n^6}=\frac{\pi^6}{945}. \tag{14}$$

[4] E. C. Titchmarsh, *The Theory of Functions* (Oxford University Press, New York, 1939), second edition, p. 246.

[5] The results in this example may also be obtained by use of methods shown in the author's paper, J. Appl. Phys. **23**, 906 (1952).

Example 2

Evaluate

$$\sum_1^\infty \frac{1}{p_n^4},$$

where p_n is the nth positive root of $J_0(x)=0$.

Here

$$J_0(x)=1-\frac{x^2}{2^2}+\frac{x^4}{2^2 4^2}-\frac{x^6}{2^2 4^2 6^2}+\cdots$$

and

$$\alpha_1=-1/4, \quad \alpha_2=1/64, \quad \alpha_3=-1/2304.$$

Thus we have

$$\sum_1^\infty \frac{1}{p_n^2}=\frac{1}{4}. \tag{15}$$

Using Eqs. (10) and (12) successively we find

$$\sum_1^\infty \frac{1}{p_n^4}=\frac{1}{32} \tag{16}$$

and

$$\sum_1^\infty \frac{1}{p_n^6}=\frac{1}{192}. \tag{17}$$

Example 3

Evaluate

$$\sum_1^\infty \frac{1}{p_n^4},$$

where p_n is the nth positive root of $\tan x=x$.

It can be shown that $f(x)=\tan x-x$ has an infinite number of distinct real zeros and no complex zeros. Here $\tan x$ is not an integral function, hence instead of using the equation $\tan x=x$ we use the equivalent

$$\sin x-x\cos x=0. \tag{18}$$

Using the power series expansion for $\sin x$ and $\cos x$ in Eq. (18) and simplifying we find

$$\frac{x^3}{3}-\frac{x^5}{30}+\frac{x^7}{840}-\frac{x^9}{45360}+\cdots=0.$$

Discarding the factor $x^3/3$ we have

$$1-\frac{x^2}{10}+\frac{x^4}{280}-\frac{x^6}{15120}+\cdots=0$$

so that

$$\alpha_1=-1/10, \quad \alpha_2=1/280, \quad \alpha_3=-1/15\,120, \cdots.$$

Thus from Eqs. (8), (10), and (12) we have

$$\sum_1^\infty \frac{1}{p_n^2}=\frac{1}{10}, \tag{19}$$

$$\sum_1^\infty \frac{1}{p_n^4}=\frac{1}{350}, \tag{20}$$

$$\sum_1^\infty \frac{1}{p_n^6}=\frac{1}{7875}. \tag{21}$$

Example 4

Evaluate

$$\sum_1^\infty \frac{1}{p_n^4},$$

where the p_n are the positive roots of the equation

$$\cos x\cosh x+1=0.$$

Using the series for $\cos x$ and $\cosh x$ and discarding the factor 2 which arises we find

$$1-\frac{x^4}{12}+\frac{x^8}{5040}-\cdots=0,$$

and thus

$$\sum_1^\infty \frac{1}{p_n^4}=\frac{1}{12},$$

$$\sum_1^\infty \frac{1}{p_n^8}=\frac{11}{1680}.$$

It should be pointed out that the zeros of this equation consist of reals and pure imaginaries. Thus our condition that the transcendental function have real zeros is sufficient but not necessary.

IV. SOME FURTHER APPLICATIONS OF THE METHOD

The method outlined above can be used not only to obtain the sums of series involving the roots but also to calculate the least positive root of the transcendental equations which have real distinct roots. Several of our previous examples will serve to illustrate this point.

As a first illustration, take the case of example 1. We know that the sum of the reciprocals of the fourth powers of the positive roots of $\sin x=0$ is $1/90$. Denoting these roots by p_n $n=1, 2, \cdots$, we have

$$\sum_1^\infty \frac{1}{p_n^4}=\frac{1}{90}. \tag{22}$$

Since $p_1<p_2<p_3<\cdots$, we have $1/p_1^4>1/p_2^4>1/p_3^4>\cdots$. In most cases $1/p_1^4$ is by far the most prominent term in the series of Eq. (22), so that a first approximation to the first positive root of $\sin x=0$ would be $\sqrt[4]{90}$, and in fact this would be a lower limit to the root. In Table I we have listed the approximate value of the first positive root obtained by using $\sum 1/p_n^2$, $\sum 1/p_n^4$, etc., as well as the true value of this root. It will be seen how rapidly the approximate values approach the true

TABLE I.

Illustrative example	$\Sigma\frac{1}{\rho_n^2}$	$\Sigma\frac{1}{\rho_n^4}$	$\Sigma\frac{1}{\rho_n^5}$	$\Sigma\frac{1}{\rho_n^6}$	True value
1 $\sin x=0$	2.45	3.08	3.13+	3.14+	3.14+
2 $J_0(x)=0$	2.00	2.38	2.40+	2.40+	2.40+
3 $\tan x=x$	3.16	4.30+	4.46	4.49	4.49+
4 $\cos x\cosh x+1=0$		1.86+		1.87+	1.87+

value. Similar results have been worked out for the transcendental equations of the other illustrative examples, and are included in Table I.

SUMMARY OF FORMULAS

If $\lambda_1, \lambda_2, \cdots \lambda_n$ are the roots of Eq. (6)

$$\sum_1^n \frac{1}{\lambda_k} = -\alpha_1$$

$$\sum_1^n \frac{1}{\lambda_k^2} = \alpha_1^2 - 2\alpha_2$$

$$\sum_1^n \frac{1}{\lambda_k^3} = 3\alpha_1\alpha_2 - 3\alpha_3 - \alpha_1^3$$

$$\sum_1^n \frac{1}{\lambda_k^4} = \alpha_1^4 - 4\alpha_1^2\alpha_2 + 2\alpha_2^2 + 4\alpha_1\alpha_3 - 4\alpha_4.$$

JOURNAL OF APPLIED PHYSICS VOLUME 24, NUMBER 9 SEPTEMBER, 1953

Metallic Grating Replicas as Internal Standards for Calibrating Electron Microscopes*

S. R. ROUZE,
Research Laboratories Division, General Motors Corporation, Detroit, Michigan

AND

JOHN H. L. WATSON,
Edsel B. Ford Institute for Medical Research, Henry Ford Hospital, Detroit, Michigan

(Received March 26, 1953)

It was shown earlier that plastic grating-replicas mounted upon eighth-inch specimen screens were practical internal standards and that they could be accurately calibrated independently by spectroscopic means. Metallic replicas of diffraction gratings have been made by a direct-stripped method. These can still be direct-stripped easily and without damage to the original grating, and the optical quality of these preshadowed all-metal replicas is better than that of the plastic replicas. Because of their superior optical properties, the spacing can be determined spectroscopically more conveniently and with greater accuracy. In addition, the metal-gratings are more stable than the plastic ones. The electron microscopy of the metallic replicas and the accuracy and constancy of their magnification measurement is discussed.

IT has been shown previously that plastic grating replicas mounted upon eighth-inch specimen screens are practical internal calibration standards for electron microscopes, and that they can be calibrated accurately and independently by spectroscopic means.[1] It seemed that all-metal grating replicas might be even better for the purpose and that they might not suffer the limitations of the plastic ones, *viz.*, shrinkage and inability to withstand exposure to high-intensity beams. However, the preparation of all-metal replicas involved the destruction of the specimen, and this could not be tolerated when replicating optical gratings. With a preshadowing technique, however, it was possible to make direct-stripped all-metal replicas without affecting the original grating surface, and it is the purpose of this paper to discuss the advantages and the limitations of all-metal replicas made by this process compared with the plastic ones when they both are used as internal calibration standards.

The technique used for making the all-metal grating replicas is similar to that described by one of the authors for making preshadowed plastic replicas[2] and parallels that described by Kaye.[3] Both of these techniques made use of a surface-active parting layer of Victawet 35B† between the original specimen and the shadowing layer, so that the final replica could be direct-stripped easily.

The original grating used in the present work was a Baird Associates' 15 000-line/inch grating, commonly used in electron microscopy for calibration purposes. After the parting layer was applied by vacuum evapora-

* Presented in part before the Annual Meeting of the Electron Microscope Society of America, Cleveland, Ohio, 1952.

[1] John H. L. Watson and William L. Grube, J. Appl. Phys. **23**, 793 (1952).

[2] William L. Grube and Stanley R. Rouze, Proc. Am. Soc. Testing Materials **52**, 71 (1952).

[3] W. Kaye, J. Appl. Phys. **10**, 1209 (1949).

† Victawet 35B, available from the Victor Chemical Works, Chicago, Illinois.

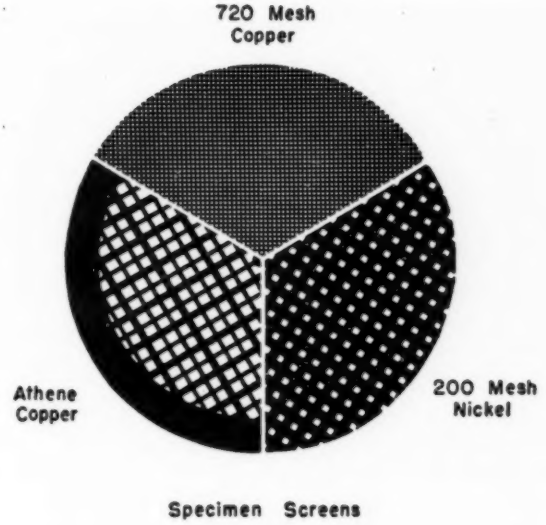

FIG. 1.

tion, the grating was shadowed with chromium at an angle of 27° from a direction perpendicular to that of the rulings. Without breaking the vacuum, this was followed by a normal evaporation of 45:55 aluminum-beryllium alloy. After removal from the vacuum chamber, the replica was floated off directly upon a water surface and picked up on eighth-inch diameter copper screens. In order to give the fragile all-metal replicas adequate support, it was necessary to use screens of 720 mesh.‡ In Fig. 1, the usual 200-mesh nickel screen and the Athene 200-mesh copper screen are compared with the 720-mesh copper screen used in this work. Although the mesh is finer, there is 50 percent open area in the 720-mesh as compared with 20 percent open area in the nickel and 35 percent open area in the Athene screens. The finer mesh does not interfere in any way with micrographs taken at magnifications greater than 2500×. Aluminum-beryllium replicas were found to be more fragile than plastic ones and rather difficult to handle, primarily due to the flexibility of the 720-mesh screen. However, exceptionally rough treatment outside the microscope, such as bending the support, did not affect the measurement of the periodicity of the grating in any detectable way. Once in the electron microscope, they were exceptionally strong and able to withstand high-electron beam intensities. Infrequently, cracks in the replicas were observed along the lines of the rulings, but these were recognizable and never affected a calibration.

As in the previous work by Watson and Grube,[1] the replicas were calibrated independently as transmission gratings in a Gaertner spectrometer using a mercury-arc lamp as the source. Figure 2 compares the spectra of an aluminum-beryllium replica with that of a plastic replica. We should like to stress that the spectra illustrated were produced by the small eighth-inch diameter grating replicas mounted on the usual specimen screen. It can be seen that the aluminum-beryllium gave spectral lines which could be measured more accurately than those from the plastic. As noted in the earlier work, the multiple lines seen in the plastic replica spectra are due to periodicity in the specimen screen itself. To eliminate or minimize this effect, the aluminum-beryllium replicas were placed upon the 720-mesh screen with the grating rulings at a 45° angle with the screen wires, causing the diffraction patterns due to the screen to lie at an angle with respect to the grating spectrum. This effect, as shown in Fig. 2, allows the central lines to be more easily identified since those due to the screen show up as only partial lines. The lines that were measured—the 4358A violet line and the 5461A green line—are also shown.

The "*d*" values were calculated by the usual formula relating grating space and diffraction angle.[1] With the

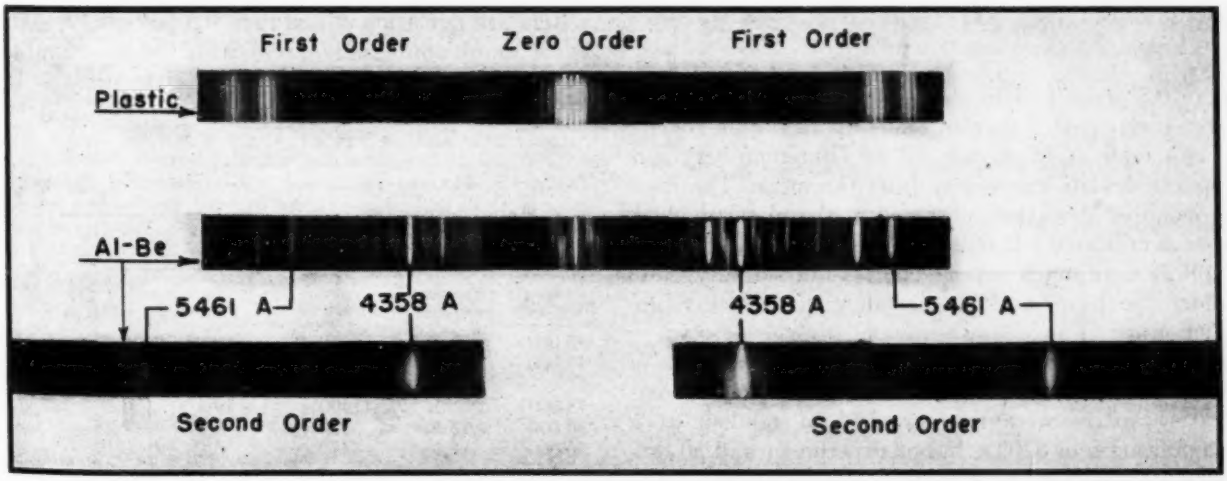

FIG. 2. Typical spectrograms of a mercury source diffracted by plastic and aluminum-beryllium grating replicas.

‡ Obtained from RCA Tube Division, Lancaster, Pennsylvania

aluminum-beryllium replicas, measurements were made using both first- and second-order spectra, and in some cases it would have been possible to have used the third order. In contrast, only the first order from the plastic replicas was measurable.

Typical spectral measurements of the aluminum-beryllium replicas are given in Table I. The average d value of the original grating, as measured in the spectrometer, was 1.696 microns; the average d value of the aluminum-beryllium replicas, for the first and second orders, was 1.700 microns, a variation between them of less than 0.3 percent. Among a total of 56 independent measurements on 14 Al–Be replicas, the maximum deviation from the mean was less than 1 percent. By comparison, the maximum deviation of plastic replicas of the same grating approached 3 percent. At the same time, the standard deviation of the measurements on aluminum-beryllium replicas was less than 0.5 percent. This showed a similar improvement over a reported 3 percent standard deviation for the plastic replicas. In no case did the aluminum-beryllium replicas deviate excessively from the mean. The more pronounced deviations observed in the plastic replicas always indicated a shrinkage. The aluminum-beryllium replicas were much superior by way of stability, both under the beam and in constancy of surface reproduction.

TABLE I. Typical spectral measurements of aluminum-beryllium replicas of 15 000-line/inch grating.

Diffraction order	Wavelength	Total diff. angle $\alpha+\beta$	Grating spacing d in microns	Deviation from mean Microns	Deviation from mean %
1	4358A	29°42′	1.701	0.001	0.06
1	5461A	37°30′	1.699	0.001	0.06
1	4358A	29°41′	1.701	0.001	0.06
2	5461A	80°04′	1.698	0.002	0.12
2	4358A	61°40′	1.701	0.001	0.06
2	5461A	80°05′	1.698	0.002	0.12

Average grating spacing—1.700 microns
Standard deviation for 56 readings less than 0.5%

TABLE II. Electron microscope measurements of the grating space of Al–Be replicas of 15 000-line/inch grating.

Magnification	Mean grating space in mm	Standard deviation (mm)	Standard deviation %
5360×	9.07	0.30	3.3
3210×	5.44	0.22	4.0

The replicas were also measured by the methods of electron microscopy. One hundred and sixty different grating spaces were micrographed at random at a magnification of 3200× in one experiment and 50 in a second experiment at a magnification of 5360×. The standard deviation of the readings was of the same order, but a little greater, than was found by one of us earlier for the plastic replicas, Tables II and IV.

TABLE III. Typical spectral measurements of aluminum-beryllium replicas of 30 000-line/inch grating.

Diffraction order	Wavelength	Total diff. Angle $\alpha+\beta$	Grating spacing d in microns	Deviation from mean Microns	Deviation from mean %
1	4358	62°02′	0.846	0.000	0.00
1	5461	80°18′	0.847	0.001	0.12
1	4358	62°02′	0.846	0.000	0.00
1	5461	80°16′	0.847	0.001	0.12
1	4358	62°10′	0.844	0.002	0.24
1	5461	80°24′	0.846	0.000	0.00

Average Grating Spacing—0.846 microns
Standard deviation for 18 readings less than 0.5 percent

Therefore, as far as the microscopy of the replicas is concerned, the aluminum-beryllium showed no improvement over the plastic for the 15 000 line/inch grating.

This could be due to any one, or combination, of three things: (a) replica reproducibility, (b) quality of the original grating, or (c) accuracy of micrograph measurements.

It has already been shown by the spectral measurements that the replica reproducibility is not at fault.

To determine whether or not the measured deviation is due to nonuniformity of the original grating spacing, it was decided to replicate another grating of different spacing, and one which was known to have a good optical quality. If the standard deviation changed significantly, it would indicate that the original grating was responsible; on the other hand, if the figure did not change, it would indicate that a limit had been reached in the accuracy with which the micrographs can be measured. Accordingly, a grating§ with 30 000 lines/inch was obtained. When this was checked on the spectrometer, it was found to deviate only 6 lines from 30 000 lines/inch (0.02 percent). Spectral calibration measurements of aluminum-beryllium replicas of this grating were difficult to make, but were found to have a standard deviation of less than 0.5 percent, the same as for aluminum-beryllium replicas of the other grating. The measurements of this grating are given in Table III.

In the electron micrographs, as shown in Fig. 3, two consecutive spaces rather than a single space were

TABLE IV. Electron microscope measurements of the grating space of Al–Be replicas and plastic replicas of diffraction gratings.

Grating lines/inch	Replica material	Magnification	Mean grating space in mm	Standard deviation Mean	Standard deviation %
*15 000	Al–Be	5360×	9.07	0.30	3.3
15 000	Al–Be	3210×	5.44	0.22	4.0
				Average	3.65
15 000	Plastic	11400×	19.3	0.56	2.9
30 000	Al–Be	5220×	8.91	0.25	2.8
30 000	Al–Be	3470×	5.88	0.13	2.2
				Average	2.5

* Single operator.

§ Ruled by R. W. Wood, Johns Hopkins University.

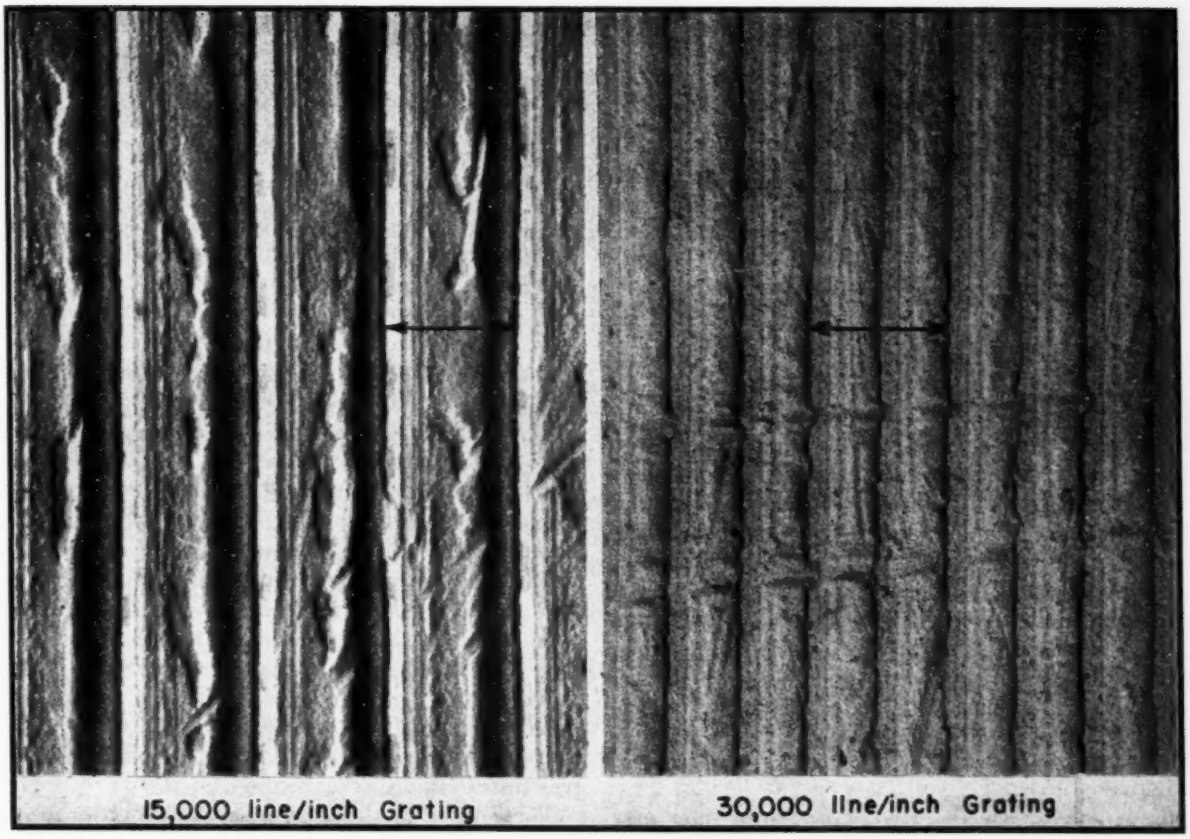

FIG. 3.

measured. This provided for measurement of the same linear distance on the 30 000-line grating as was measured on the 15 000-line grating and was done to minimize distortion and scale measurement errors. Table IV summarizes the results. The standard deviation for the 30 000-line/inch grating was found to be significantly less than for the 15 000-line/inch grating. This indicates that the electron micrograph measurements were at least partially limited in accuracy by the rulings of the original 15 000-line grating.

Certain conclusions may be drawn: first, aluminum-beryllium replicas of the 30 000-line/inch grating can be calibrated electron microscopically as accurately as, and perhaps better than, the plastic ones of the 15 000-line/inch grating; second, the reverse seems to be true of the aluminum-beryllium replicas of the 15 000-line/inch grating; and third, when calibrated spectroscopically, the superior optical qualities of the aluminum-beryllium replicas are of immense assistance to the calibrator. To take full advantage of this, however, it must be possible to make the electron microscopy measurements more accurately. For this purpose, a grating of exceptionally uniform spacing must be used. The extra cost of a grating of this type is justified since the aluminum-beryllium technique is nondestructive and has no deteriorating effect upon the grating.

Radioactive Charging Effects with a Dielectric Medium*

P. RAPPAPORT AND E. G. LINDER
Laboratories Division, Radio Corporation of America, Princeton, New Jersey
(Received April 16, 1953)

A process is described in which radioactive radiation traverses a solid dielectric medium to charge a collector electrode. This process offers a simple method of studying effects of radiation on matter such as bombardment-induced conductivity, secondary emission, charge soakage, and radiation absorption. Typical data are given. Possible application of this process for the construction of a current or voltage source for use in electronic devices is discussed.

INTRODUCTION

THIS paper discusses a new means of directly converting the energy of radioactive radiations into electrical energy, and some effects related to the passage of the charging radiation through a dielectric medium. Other means of making this conversion have been treated by several previous investigators. In 1913, Moseley[1] suspended a sphere containing radon in a vacuum and determined that it charged to as high as 150 000 volts resulting from the emission of charged particles. Using an improved method and device, Linder and Christian[2–4] obtained voltages as high as 365 000 volts with 250 millicuries of Sr^{90}-Y^{90}. A quite different approach was described by Kramer[5] in 1924, and more recently by Ohmart.[6] Their devices were similar to voltaic cells, having plates of two dissimilar metals, but instead of an electrolyte, a gas irradiated by radioactive radiation was used. The open-circuit potentials produced were of the order of one volt.

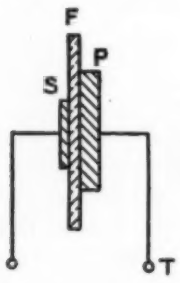

FIG. 1. Schematic diagram showing radioactive source S, dielectric separator F, and collector P.

A third method, which was an outgrowth of previous work[2–4] has been discussed briefly by the present authors.[7] In the present paper it is described more completely, and recent data are included. The method may be understood by reference to Fig. 1, which shows a schematic diagram of this type of generator. Here, S is a plane electrode containing radioactive material and emitting beta rays; F is a sheet of dielectric material such as polystyrene or mica; P is a collector electrode, thick enough to stop impinging beta particles. In operation, beta particles from the emitter S pass through the dielectric F and are collected by P. Thus, P charges negative and S becomes positive. In the absence of F, the air between S and P would become ionized and the voltage developed would be very small, because of the conductivity of the ionized air. However, when the dielectric F is present, the path from P to S has very high resistance and correspondingly higher voltages may be produced. In other words, high-energy electrons may pass easily from S to P, but low-energy particles produced by gas ionization cannot penetrate F and discharge the device.

These three methods represent possibilities for utilizing radioactive materials as sources of electrical energy. The present, and no doubt future, availability of large amounts of such materials give these attempts a special significance. As of the present date, numerous radioisotopes may be purchased from the U. S. Atomic Energy Comission in amounts up to several curies in purified form. Much larger amounts (megacuries) are being produced in unpurified form.[8] These are being stored pending the development of a suitable market. It appears that a large future supply is very probable.

THEORY

Devices of the type of Fig. 1 may be represented by an equivalent electrical circuit consisting of a constant current generator in parallel with the capacity C of the device and the resistance R of the device and load. The current of the constant current generator is equal to the beta current i_0 reaching the collector P. Such a circuit charges at an initial rate given by i_0/C and approaches asympotically a final equilibrium value given by $R\,i_0$.

The net current to the collector is given by $i=i_0-V/R_1$ where V is the potential difference between the collector and the emitter, and R_1 is the resistance of the dielectric separator. Experimentally the voltage may be varied by changing the load resistance or by applying a voltage from an external battery. A repre-

* This work was supported in large part by the Components and Systems Laboratory, Wright Air Development Center, Air Research and Development Command, United States Air Force.
[1] H. G. J. Moseley, Proc. Roy. Soc. (London) **A88**, 471 (1913).
[2] E. G. Linder, Phys. Rev. **71**, 129 (1947).
[3] E. G. Linder and S. M. Christian, Phys. Rev. **83**, 233 (1951).
[4] E. G. Linder and S. M. Christian, J. Appl. Phys. **23**, 1213 (1952).
[5] J. B. Kramer, The Electrician, **93**, 497 (1924).
[6] P. E. Ohmart, Atomic Energy Commission Report MLM 521.
[7] E. G. Linder and P. Rappaport, Phys. Rev. **91**, 202 (1953).
[8] Stanford Research Institute "Industrial Uses of Radioactive Fission Products," Project No. 361 (1951).

sentative graph is shown in Fig. 2. Characteristics of this type permit the determination of the internal resistance from the slope. They determine also the maximum charging voltage from the intersection with the horizontal axis. The current i_2 through any load R_2 is given by the intersection of the load line of slope $-1/R_2$ with the i *vs* V curve as shown in the figure.

Control of the voltage of this type of device may be obtained by several methods. For example, it may be controlled by varying the load resistance. Also, the dielectric separator may be designed to have an appropriate resistance. The dielectric film may have its resistance varied by changing its composition or dimensions. Further, since the resistance of the film depends greatly upon bombardment-induced conductivity,[9] the resistance will be importantly affected by the beta current and will decrease as the current is increased.

EXPERIMENTAL WORK

I. Apparatus

The type of device with which most of the measurements were made is shown in Fig. 3. This represents

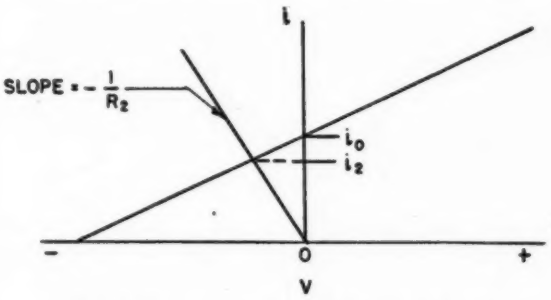

FIG. 2. Current *vs* voltage with typical load line

the practical version of the schematic sketch of Fig. 1, and parts are lettered correspondingly. The source S consisted of a cylindrical head with a shaft for handling. The head contained radioactive material A under its front surface which was a thin metallic window.[10]

The dielectric separator F consisted of polystyrene and was machined so as to form an integral part of the cylindrical case D which supported both the source S and collector P. The latter comprised an aluminum disk with a stud for handling.

Two sources were used; one contained 25 millicuries of Sr^{90}-Y^{90} and the other 250 millicuries. Faraday cage measurements of the currents emitted in the forward direction gave 1.2×10^{-11} amp and 3.2×10^{-10} amp, respectively. These values are, respectively, about 8 and 21 percent of the total current produced by the radioactive material, the loss being the result of absorption in the windows and of the angular distribution of emission. The actual current in each measurement varied from the above values because of variations in construction, and in each case individual current determinations were made. Much more efficient sources could be constructed if desired by using a thinner window and better angular geometry, such as a concentric cylinder arrangement. The approximate average energy of the electrons emitted by these sources was 0.7 Mev.

Because of the very small currents and small capacitances involved, a special type of voltmeter was devised. This is shown in Fig. 4. It consisted of a pocket-type

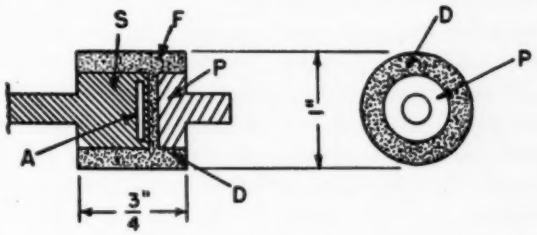

FIG. 3. Scale drawing of a typical device

quartz-fiber dosimeter of a type used for radiation monitoring. This was modified by bringing out a lead a from the fiber mounting b through a polystyrene insulator c. By slightly bending the fiber support, a 0-to-115-volt scale was obtained. By illuminating the insulator, sufficient light was transmitted into the barrel to illuminate the internal scale. By mounting special fibers, other instruments were made to cover the ranges 200 to 400, 500 to 1000, and 1000 to 2000 volts.[11] These voltmeters were found very useful. Their scales were suitably linear, their capacitance low (about $3.5\mu\mu f$) and their resistance high (about $10^{16}\Omega$ but varying with insulator surface condition).

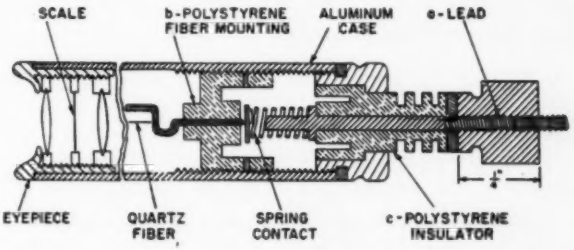

FIG. 4. Scale drawing of quartz-fiber voltmeter (modified dosimeter).

Current measurements were made using a vibrating reed voltmeter. The combination of high input resistance and one-mv voltage sensitivity allowed measurement of currents down to 10^{-14} amp.

II. Data

(1) *Charging Data*

Measurements were made by applying the probe of the quartz-fiber voltmeter to the collector shaft and

[9] L. Pensak, Phys. Rev. **75**, 472 (1949).

[10] Actually, the sources used were strontium medical applicators manufactured by Tracerlab. Inc., Boston, Massachusetts.

[11] These three instruments were made for us by the Landsverk Electrometer Company.

placing the radioactive source into the device. The collector was short-circuited to the source before each run in order to eliminate static charge and charge soakage effects. After a given time, the short circuit was removed and voltage was recorded as a function of the time. Curves so taken agreed with theory in showing the voltage rising to an asymptotic value.

The initial linear sections of several curves are shown in Fig. 5. These are for several thicknesses of dielectric and different collector materials, as indicated. The observed charging rates are in fair agreement with calculated ones when measured values of current and capacitance are used. For example, for device No. 8 with a 0.020-in. separator, the observed charging rate was 42 volts/min and the theoretical value 51 volts/min corresponding to a capacity of $13\mu\mu f$ and an intercepted current of 1.1×10^{-11} amp. This discrepancy may be due partly to leakage produced by the ionization around the charger.

For comparison purposes, an evacuated device (No. 5) was constructed having a 0.005-in. nickel window in the envelope to admit beta radiation, and a nickel collector supported in the vacuum with no dielectric separator. The charging curve is shown in Fig. 5. The capacitance (including the voltmeter and leads) was $7.5\mu\mu f$ and the intercepted current was 0.56×10^{-11} amp (see Fig. 6), which yields a charging rate of 45 volts/min, as compared with an observed value of about 40 volts/min as shown in Fig. 5.

(2) *Current vs Voltage Measurements*

A direct measurement of the current flowing through the charging device as a function of an externally applied voltage can give information concerning the following; internal impedance, limiting voltage, bombardment-induced conductivity, charge soakage, secondary emission, and beta-ray spectrum.

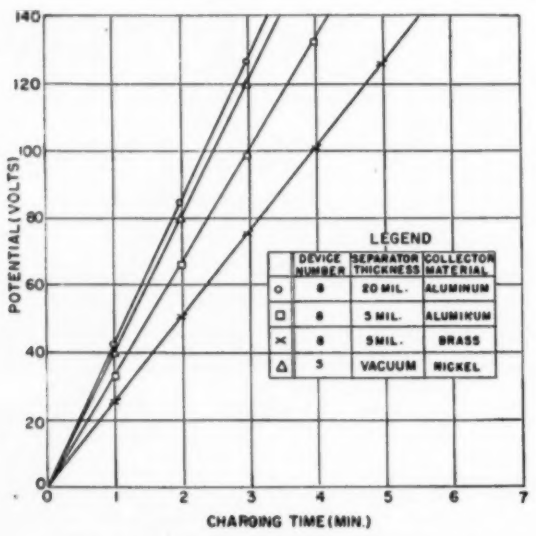

FIG. 5. Charging curves for various dielectric thicknesses and collector materials.

The net current was measured over a range from plus to minus 540 volts. Data are shown in Fig. 6 for a device with a 0.020-in. separator and also for the evacuated device mentioned above (No. 5). The charging current values at $V=0$ used in previous calculations were obtained in this manner. The curve relating to device No. 5 gives information concerning the secondary emission including low-energy front-to-back ratio of the nickel surfaces used. The sloping section of the curve is caused by the low-energy secondary electrons. Within the limits of experimental accuracy the slope of the curve is zero after ±67 volts, which means that the internal resistance of the device is very large and beyound the limit of these measurements. This indicates that a very high value of voltage is attainable as in previous high-vacuum devices.

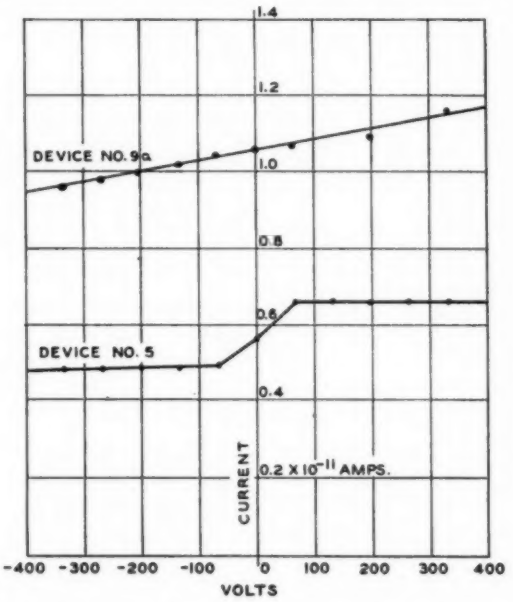

FIG. 6. Experimental current-voltage curves for a high-vacuum device (No. 5) and a polystyrene separator device (No. 9a).

The curve for device No. 9a shows an almost constant slope. The low-energy secondary emission effects are missing because of the inability of the low-energy secondaries to traverse the 20-mil polystyrene separator. The slope of the curve indicates a resistance of 3.5×10^{14} ohms for the device. This value will be discussed further in the section on bombardment-induced conductivity. By extrapolation, the limiting voltage can be obtained from the point at which the curve intersects the zero current axis. This value is seen to be 3700 volts. Using a 54-millicurie source, the limiting voltage was found to be about 6600 volts.

(3) *Resistance and Bombardment-Induced Conductivity*

Estimates of the internal resistance R_1 were made by two methods. The first was to calculate the resistance

from the slope of the current *versus* voltage graph, as described in the foregoing section. This gave a value of 3.5×10^{14} ohms for the case of device No. 9a shown in Fig. 6. The second method used was to shunt the device with known values of load resistances R_2 and to observe the effect on the maximum voltage V_m. Taking the case for $R_2=10^{13}$ and $V_m=92$, it is found that $R_1=0.6\times10^{14}$. This agreement is as good as could be expected in view of the uncertainty of the value of V_m and of R_2.

From the dimensions of the polystyrene separator used in device No. 9a, it was found that the above figures of resistance (average value 2×10^{14} ohms) yield a specific resistance of 7×10^{15} ohm-cm. It is of interest to compare this with that of unbombarded polystyrene values for which given in the literature range from 10^{18} to 10^{22} ohm-cm.[12] Thus, there is a decrease in resistivity by a factor of from 10^2 to 10^6.

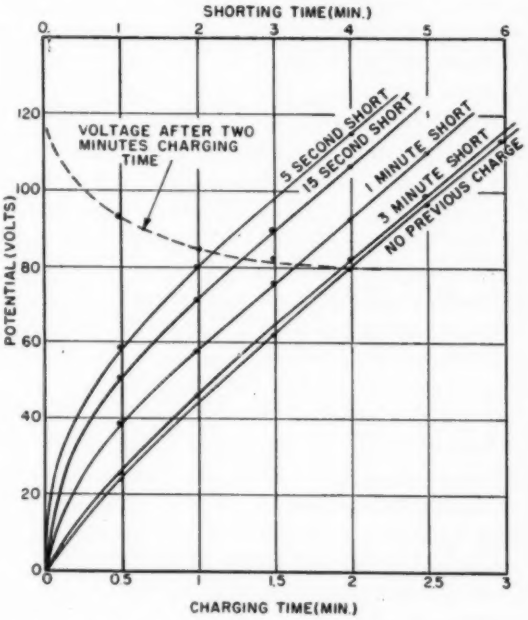

FIG. 7. Variation in charging due to soakage effect.

This is attributed to bombardment-induced conductivity.[9] Using a stronger source (54 millicuries), the internal resistance was found to be 2.7×10^{13} ohms and the corresponding specific resistance 0.5×10^{15} ohm-cm, a decrease by a factor of 14 due to the increased bombarding current.

In connection with this high value of internal resistance it may be pointed out that the utility of the device may be more as a source of constant current than one of voltage depending on the resistance R_2 of the load.

(4) *Charge Soakage*

When charging curves were made one after the other on the same device, it was sometimes found that the curves were not identical. This is believed to be caused by charges being stored in the polystyrene which require relatively long times to leak out. In Fig. 7 can be seen a family of charging curves on device No. 8 with a 0.005-in. separator which demonstrate the soakage effect. Note that the voltage to which the device charges in a fixed time is different for all curves but that the charging rate after a short time is the same for all. These curves were measured as follows: The device was first charged up to 115 volts, using the beta source, for all cases except the one labeled "no previous charge." The electrodes were then short-circuited for times of 5 seconds to 3 minutes as indicated. Charging was then measured as a function of time to give the curves in the figure. The differences in the voltages corresponding to the different shorting times are attributed to the effect of the stored charge. By replotting the information with shorting time as the independent parameter, as was done in the dashed curve in Fig. 7, information concerning the lifetime of the soaked-up charges can be obtained. Here, it can be seen that the lifetime of the charge is about 5 minutes.

The mechanism of charge soakage here is probably somewhat different from the usual type,[12] since it is caused by beta-ray absorption, rather than by merely applying a field across the dielectric. Further study of this would be desirable.

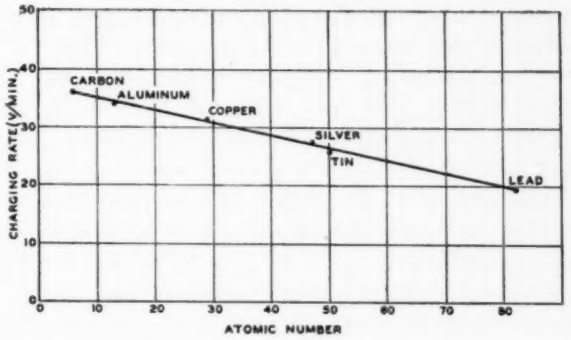

FIG. 8. Variation of charging rate with collector material.

(5) *Backscattering*

Low-energy secondary-emission electrons have no effect on the device under discussion since they are unable to penetrate the dielectric separator. However, backscattered electrons, which have substantially the same energy as the primary beta particles, can penetrate the separator and reduce the value of the charging current and hence the charging rate. It is known that the amount of backscattering is dependent upon the atomic number of the material.[13] Confirmation of this was found in measurements of charging rate with collectors of various materials. The results are shown in Fig. 8, where charging rate is plotted against

[12] L. A. Matheson and V. J. Caldecourt, J. Appl. Phys. **22**, 1176 (1951).

[13] Rutherford, Chadwick, and Ellis, *Radiations from Radioactive Substances* (Macmillan Company, New York, 1930).

atomic number for six different collector materials. Carbon is seen to have the highest rate and hence the least backscattering, whereas lead has about half the rate of carbon. The relation appears to be linear. Approximate values of backscattering coefficients calculated from these data are 0.49 for lead, 0.31 for tin, 0.25 for silver, 0.17 for copper, 0.09 for aluminum, and 0.04 for carbon. These are in satisfactory agreement with values found by Trump and Van de Graaff[14] under comparable conditions. Since backscattering is almost energy independent at high primary energies, a beta source is almost equivalent to a monokinetic electron beam and permits an easy determination of the backscattering coefficient.

(6) *Effect of Dielectric Thickness*

The charging rate depends upon both the charging current and the capacitance. Changes in the thickness of the dielectric may affect both of these. Increasing the thickness decreases the capacitance by separating the electrodes and also decreases the current due to greater beta-ray absorption. Experimental results showing the variation of charging rate with thickness are given in Fig. 9. The shape of this curve is explainable by assuming the capacitance of the device varies inversely as the dielectric thickness, and that the current drops approximately exponentially.

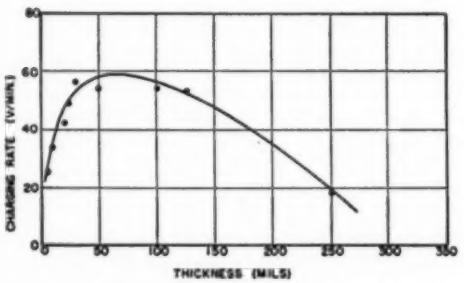

FIG. 9. Variation of charging rate with dielectric thickness.

[14] J. G. Trump and R. J. Van de Graaff, Phys. Rev. 75, 44 (1949); also Mass. Inst. Technol. Report on Contract No. AT(30-1)-905, (January 1951), pp. 14-15.

(7) *Factors Controlling the Limiting Voltage*

The discussion up to now has given little information concerning the value of the peak voltage to which the device will charge. In most cases, the voltage has been over 2000 volts, beyond the limits of the measuring equipment. For many practical uses, a limiting voltage in the range of 100 to 300 volts is desirable. This may be accomplished by such means as shunting with resistors, or by using different dielectric materials with different bombardment-induced conductivities.

CONCLUSIONS

The apparatus and techniques used in this study appear to offer new and simple methods for investigating such effects as bombardment-induced conductivity, secondary emission, charge soakage, radiation absorption, and other effects of radiation on solids. In this respect the results presented here are only of a preliminary and suggestive nature and are given mainly to elucidate the operation of the device, rather than as information on the properties of materials. It is believed that these methods are worth further consideration.

One of the purposes of the work reported in this paper was to study the possibility of making a radioactive source of current or voltage. It was thought that such a source would have several advantages, among which would be long life, simplicity of structure, and stability with respect to ordinary physical conditions. The idea of charging through a dielectric medium was thought to offer a promising approach, and, since no work on such a process appeared to have been done previously, a study was undertaken. The results reported in this article lead to the conclusion that the dielectric charging process is suitable for such applications and, in fact, that a dielectric medium is a good substitute for a vacuum. Radioactive current and voltage sources based on this principle appear to be entirely feasible. It is believed that they should find application in electronic equipment.

ACKNOWLEDGMENTS

We are indebted for valuable discussions to numerous members of the RCA Laboratories staff, especially Dr. M. J. Cohen, and also to Professor M. G. White of Princeton University.

JOURNAL OF APPLIED PHYSICS VOLUME 24, NUMBER 9 SEPTEMBER, 1953

Wave Propagation in Finite Rods of Viscoelastic Material*

E. H. LEE†, *Brown University, Providence, Rhode Island*

AND

I. KANTER,‡ *Lockheed Aircraft Corporation, Burbank, California*

(Received April 6, 1953)

The paper is concerned in the main with a Maxwell material, which corresponds to a model having a spring and dashpot in series. The equation for longitudinal wave propagation in rods is shown to be equivalent to the telegraph equation, and solutions of transient wave problems are treated briefly in the Appendix using the Laplace transform technique. Impact on a semi-infinite rod is considered in detail in the report. A method of superposition of images is discussed to use this solution to solve boundary value problems for finite rods. The resulting stress distributions are discussed and contrasted with those for an elastic rod. The natural grouping of problems is discussed according to the relative magnitude of the duration of interest, the relaxation time, and the wave traverse time. The influence of the idealization involved in the Maxwell model is briefly touched upon.

I. INTRODUCTION

IN the dynamic loading of materials and structures wave propagation effects become important if the time of loading is of the order of the wave propagation time through the body. For much slower loading, internal reflections of the stress waves smooth out the stress variation, and a satisfactory approximation to the stress distribution can generally be obtained without an analysis of the wave motion. In this paper we are concerned with the stress analysis under rapid loading conditions of rods of viscoelastic material subjected to axial stresses.

In particular we are concerned with the varying stress distribution in a rod subjected to a prescribed variation of stress or velocity at one end, the other being subjected to a boundary condition such as being fixed or free. We shall treat transient conditions, as contrasted with the response to periodic or sinusoidal stimulus. A survey of the literature indicates that while propagation of steady-state oscillatory waves in viscoelastic materials has received considerable attention in recent years, only a few problems of transient wave propagation have been investigated. Since we shall deal with linear materials, it is formally feasible to use superposition and Fourier series or integral methods for the treatment of transient problems in terms of steady-state sinusoidal response, but this would involve convergence and evaluation difficulties which are avoided by the direct study of the transient wave propagation.

The mathematical analysis involved is used in the theory of electrical cables, but it seemed worth while to give a brief statement of the theory and to discuss the application to the analysis of stress waves in viscoelastic materials, since such application has apparently not appeared in the literature. Problems of this type arise in important technological applications in which polymers are subjected to impact and dynamic stressing. The present work was carried out as part of a program to investigate the stresses produced in the solid propellant grains of rockets due to firing and handling. For this application the motion of the supported part of the grain is prescribed by the rocket motion, so that velocity boundary conditions commonly arise. This type of problem receives most attention in the following.

We shall be mainly concerned with a linear Maxwell material, that is, a material which has an elastic and viscous response to stress, the associated model being a spring and dashpot in series as shown in Fig. 1. The stress strain relation is

$$\dot{\epsilon}=(\dot{\sigma}/E)+\mu\sigma, \tag{1}$$

where σ is the stress, ϵ the strain, the dot represents differentiation with respect to time, and E and μ are material constants. E is the elastic modulus and μ the reciprocal of the viscosity. The quasi-static response of a rod of such material to a constant stress σ_0 is shown by the creep curve illustrated in Fig. 2. It consists of an instantaneous elastic strain σ_0/E which remains constant, with an additional viscous flow at constant strain rate $\mu\sigma_0$. The stress variation in a relaxation test in which the strain ϵ_0 is suddenly applied and held constant is shown in Fig. 3. This stress variation is given by Eq. (1) with $\dot{\epsilon}=0$, and the initial condition $\sigma=E\epsilon_0$. The solution is $E\epsilon_0 e^{-t/\tau_0}$, where $\tau_0=1/E\mu$ is called the relaxation time.

The Maxwell material considerably idealizes the re-

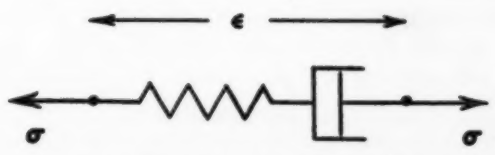

FIG. 1. Model for a Maxwell material.

* This work was sponsored under a Department of Defense Contract, NOrd 11496, with the Bureau of Ordnance, Navy Department.

† Professor of Applied Mathematics, Brown University.

‡ Applied mathematician, Lockheed Aircraft Corporation.

sponse of high polymers to stress. In general there will be a delayed elastic component, and the relaxation behavior may only be satisfactorily reproduced by a spectrum of relaxation times, and in addition nonlinear behavior may occur. However, for certain materials under certain circumstances the Maxwell model may yield useful results. The best choice of the constants E and μ will depend not only on the material and temperature, but also on the time of duration of the motion to be considered. Some discussion of this, and of the influence of deviation from the Maxwell model is given in Sec. V.

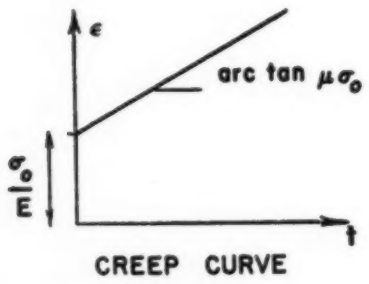

FIG. 2.

It has been mentioned already that comparatively little work seems to exist in the literature on the propagation of viscoelastic transient waves. Sips[1] gives the solution for one-dimensional waves in an infinite medium with prescribed initial conditions of displacement and velocity. No evaluations of the integrals involved are made for specific problems. The problem of impact on a semi-infinite bar of a Voigt material (a delayed elastic

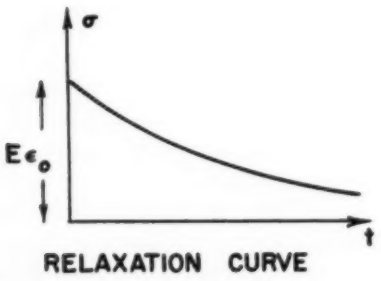

FIG. 3.

material represented by a spring and dashpot in parallel) has been considered by Zverev.[2] The analysis of a time dependent plastic material by Malvern,[3] includes the Maxwell body as a special case, but since the plastic material is nonlinear, this general case is much harder to treat than the linear Maxwell body. Malvern's work includes the solution for constant velocity impact on a semi-infinite rod of a linear Maxwell material. The present paper describes a practical method of evaluation of the stress distribution in finite rods for specific boundary conditions.

[1] R. Sips, J. Polymer Sci. 6, 285–293 (1951).
[2] I. N. Zverev, Prik. Mat. Mek. 15, 295–302 (1950), (Russian). (Brown University Translation A11-T12/16).
[3] L. E. Malvern, Quart. Appl. Math. 8, 405–411 (1951).

II. BASIC THEORY

We consider a rod with the x coordinate measured along its length. If u is the displacement in the direction of x increasing of a section specified by its position x in the unstrained rod, the equation for motion in the x direction is

$$\sigma_x=\rho u_{tt}, \tag{2}$$

where ρ is the density of the unstrained material, σ the nominal stress, the tensile force per unit initial cross-sectional area, and suffixes represent partial differentiation with respect to the corresponding variable. The use of the Lagrange type coordinate x and nominal stress ensures the validity of (2) for large strains. If true stress, the force per unit current cross-sectional area, is used, Eq. (2) is an approximation valid for small strains when the variation in cross section can be neglected. The analysis of longitudinal waves in this paper is based on (2), the equation for longitudinal motion, and in common with the usual theory for the propagation of elastic and plastic waves along rods, it neglects the influence of the inertia of the associated lateral motion. This is known to be insignificant if the length over which appreciable changes in stress take place is at least several diameters, and in practice it is found that this type of theory produces satisfactory results for transient waves in rods with a ratio of length to diameter of, say, five or more. The main influence of lateral inertia is to smooth out waves of stress discontinuity by dispersion.

The nominal strain ϵ can be expressed in terms of the displacement u,

$$\epsilon=u_x, \tag{3}$$

so that if the Maxwell relation applies for nominal values of stress and strain, Eq. (1) becomes

$$u_{xt}=(1/E)\sigma_t+\mu\sigma. \tag{1a}$$

If the Maxwell relation (1) applies for true stress and strain, the present theory can be applied only for small strains.

Elimination of u between (2) and (1a) by differentiation gives the partial differential equation for $\sigma(x, t)$,

$$\sigma_{xx}-(1/c^2)\sigma_{tt}-\mu\rho\sigma_t=0, \tag{4}$$

where $c^2=E/\rho$ is the square of the elastic wave velocity.

If we work in terms of the particle velocity $v=u_t$, Eq. (2) becomes $\sigma_x=\rho v_t$, Eq. (1a) becomes $v_x=(1/E)\sigma_t+\mu\sigma$, and by differentiation we can eliminate σ to obtain the same partial differential equation for v,

$$v_{xx}-(1/c^2)v_{tt}-\mu\rho v_t=0. \tag{5}$$

Partial integration with respect to t gives an equation for the displacement u,

$$u_{zz}-(1/c^2)u_{tt}-\mu\rho u_t=f(x), \tag{6}$$

where $f(x)$ is an arbitrary function of x. In the problems we shall consider the bar is initially unstrained and at rest, so that $f(x)=0$ and Eq. (6) has the same form as (4) and (5). Differentiation of (6) with respect to x determines an equation of the same form for the strain ϵ,

$$\epsilon_{zz}-(1/c^2)\epsilon_{tt}-\mu\rho\epsilon_t=f'(x). \tag{7}$$

Thus σ, v, ϵ, and u satisfy the same partial differential equation. It is an equation which has received considerable attention in the theory of electrical transmission lines, for it is a particular form of the so-called telegraph equation. It can be treated conveniently by operational methods, and a brief review of the Laplace transform method with some solutions is given in the Appendix.

In this section we will discuss the solution to the first problem dealt with in the Appendix, for this is a basic result from which more general solutions can be deduced. It concerns a semi-infinite rod ($x>0$), initially unstrained and at rest, and at $t=0$ subjected to impact with constant velocity V at the end $x=0$. The stress $\sigma(x, t)$ is given by Eq. (A.4) in the Appendix.

$$\sigma=-\rho cVe^{-(\mu E/2)t}I_0\left[\frac{\mu E}{2}\left(t^2-\frac{x^2}{c^2}\right)^{\frac{1}{2}}\right]H\left(t-\frac{x}{c}\right), \tag{8}$$

where I_0 is the Bessel function of imaginary argument, and H the Heaviside step function. The minus sign

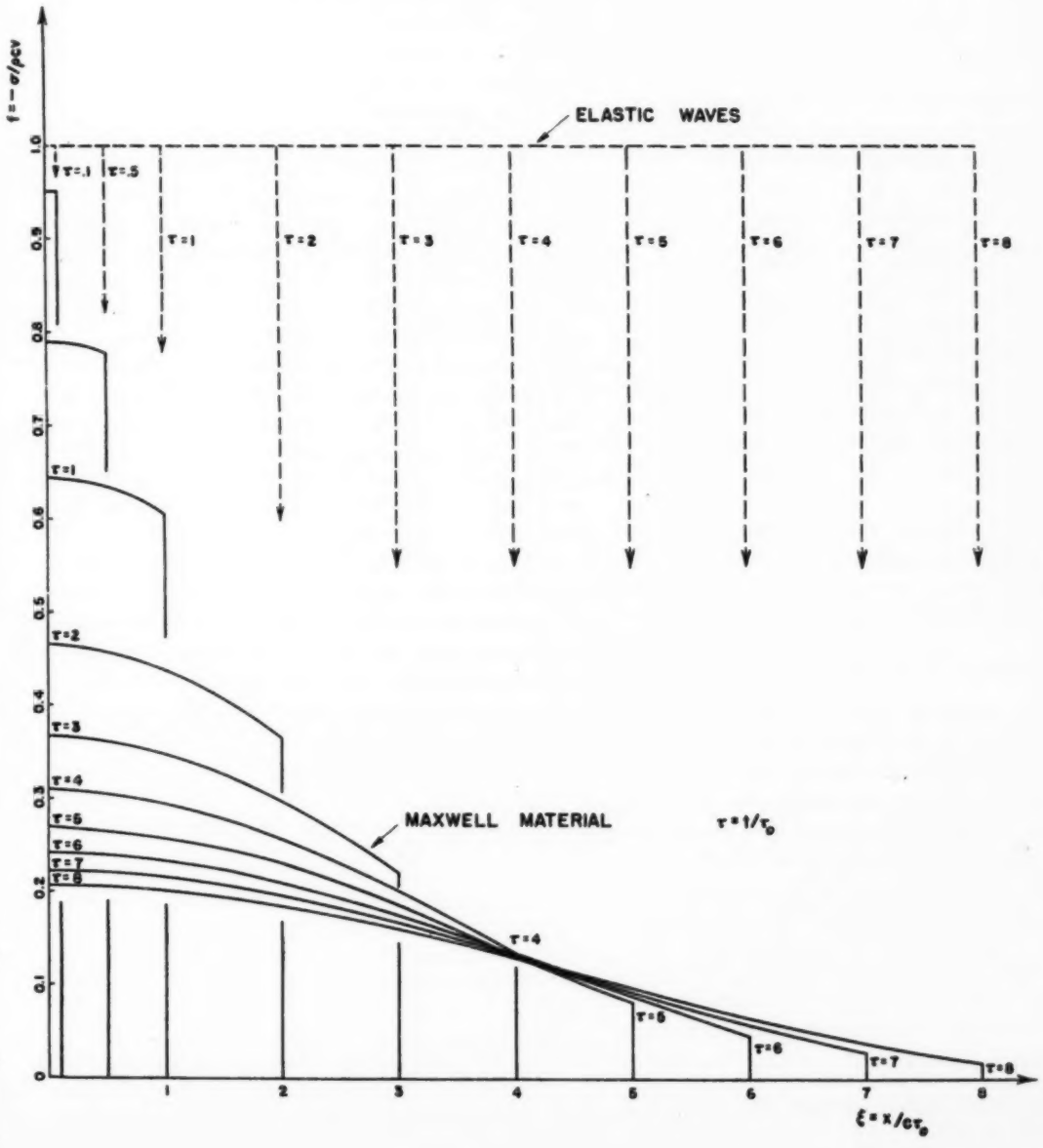

FIG. 4. Wave propagation for a Maxwell and an elastic material.

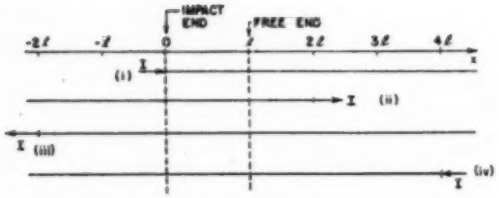

FIG. 5. Sequence of images for finite rod solution.

occurs since a positive impact velocity produces compressional waves. For the convenience of evaluation in particular cases, we express this in terms of the new variables $\tau=\mu Et=t/\tau_0$ (where τ_0 is the relaxation time discussed in Sec. I), and $\xi=\mu Ex/c=x/c\tau_0$. Equation (8) becomes

$$-\sigma/\rho cV=f=e^{-\tau/2}I_0[\tfrac{1}{2}(\tau^2-\xi^2)^{\frac{1}{2}}]H(\tau-\xi). \quad (9)$$

This function can readily be evaluated from tables of I_0,[4] and is illustrated in Fig. 4, where f is plotted against ξ for values of τ between 0 and 8. In nondimensional units, this figure depicts the spread and decay of the stress wave from the impact end of the rod in the case of a Maxwell body. The Heaviside step function H shows that the wave front is at $\xi=\tau$, for the stress is zero ahead of this front. Translating this unit velocity of the wave front in the (ξ, τ) coordinates into the physical (x, t) coordinates, we see that physically the front of the disturbance moves with the elastic wave velocity c. Since $I_0(0)=1$, a wave of stress discontinuity of amplitude $-\rho cV$ sets out from the impact face. When it has reached ξ the stress discontinuity is of magnitude $-\rho cVe^{-t/2}$. Thus it dies out exponentially as the wave progresses, as depicted in Fig. 4. The stress at the impact face also falls off as the duration of impact increases.

It is of interest to contrast this behavior with that of an elastic rod with the same density and Young's modulus. The well-known solution for elastic waves is given by choosing $\mu=0$ above, and the stress becomes

$$\sigma=-\rho cVH[t-(x/c)]. \quad (10)$$

This represents a wave of constant stress amplitude behind the front which is propagated with the elastic wave velocity. It is shown by the broken lines in Fig. 4, in which it becomes a wave of unit amplitude. We thus see that for times of the same order as the relaxation time, and times long compared with it, the effect of the viscous component in the Maxwell body is to produce an appreciable reduction in the stress wave amplitude. This is of course to be expected, since the viscous flow in the stressed region behind the wave front absorbs part of the constant velocity differential V between the impact end and the undisturbed rod, and smaller elastic strain components are therefore required. For a sufficiently long rod, as the duration of impact increases the stress magnitudes will approach zero.

In the next section it will be shown how this basic solution can be utilized to determine the stress distribution in rods of finite length.

[4] E. Jahnke and F. Emde, *Tables of Functions* (Dover Publications, New York, 1945), p. 226.

III. THE METHOD OF IMAGES

Since the analysis of the previous section and the Appendix is linear, we can use superposition, and obtain new solutions for this theory by adding basic solutions. This also applies for all linear viscoelastic materials, and is not confined to the Maxwell material already considered. The discussion of this section therefore applies to general linear materials which include materials represented by models involving any number of linear elements in series or parallel, and also to linear hereditary materials with a continuous spectrum of relaxation times, which form the limit for an infinite number of elements. As is detailed below, boundary conditions such as fixed and free ends can be satisfied by superposition and the use of symmetry arguments.

Let us first consider an impact I specified by any prescribed variation of velocity on one end $(x=0)$ of a rod, the other end $(x=l)$ being free. We take as the corresponding basic solution, this impact on a semi-infinite rod $(x>0)$. Figure 5 shows the sequence of basic solutions which when superposed satisfy the required conditions for the finite rod with a free end at $x=l$. Solution (i) of Fig. 5, the prescribed impact on the semi-infinite rod will satisfy the zero-stress conditions at the free end $x=l$ for $t<l/c$, that is, before the elastic wave front has reached that section. When $t>l/c$, the stress at $x=l$ will be neutralized by the superposition of (ii), which comprises impact I at $x=2l$ on the semi-infinite rod $-\infty<x<2l$. Since this rod extends to the left of the point of impact, the stress wave is opposite in sign to (i) and they neutralize each other at the section $x=l$. Thus if we consider the superposition of (i) and (ii) in the region $0<x<l$, the required conditions for the finite rod will be satisfied until $t=2l/c$, when the solution (ii) will disturb the prescribed velocity conditions given by I at $x=0$. This disturbance is neutralized by the superposition of (iii), but for $t>3l/c$, (iv) is also needed to neutralize the disturbance due to (iii) at the free end $x=l$. For larger values of t the sequence of images must be continued. If $\sigma_1(x,t)$ is the solution to the basic problem (i), the superposition of the sequence of images shown in Fig. 5 gives

$$\sigma(x, t)=\sigma_1(x, t)-\sigma_1(2l-x, t) -\sigma_1(2l+x, t)+\sigma_1(4l-x, t)+\cdots. \quad (11)$$

For the particular case of the Maxwell material, this sequence is represented by the two terms under the summation sign of Eq. (A.10) of the Appendix.

The determination of the stress distribution at any time can be readily carried out graphically from the basic solution using the sequence of Fig. 5. Consider the

curve $\sigma_1(x)$, giving the stress distribution for the basic problem (*i*) at the time t, to be known. For the finite rod, the required stress distribution is given by the solution of (*i*) for $0<x<l$ with the extension of (*i*) beyond $x=l$ folded back and reversed in sign, so that the section with abscissa $2l$ in (*i*) now occurs at the origin. This is again folded forward so that the section initially between $2l$ and $3l$ now spans 0 to l still with the sign reversed. This process is continued until the wave front is reached, when no more contributions to the stress distribution take place. Working with a plot of the initial stress distribution, this procedure can be readily handled graphically, and the stress distribution for the finite rod determined.

For a fixed end at $x=l$, the impact in (*ii*) must be reversed in sign in order to neutralize the velocity due to (*i*) at $x=l$. This requires (*iii*) to be reversed in sign to satisfy conditions at $x=0$, but (*iv*) will remain the same. The signs must be changed in pairs throughout the sequence of images. If the impact is prescribed by a stress variation, the sign of (*iii*) must be reversed to neutralize the stress due to (*ii*) at $x=0$. This demands a change in the sign of (*iv*) to neutralize the stress due to (*iii*) at the free end $x=l$. The sequence of images of Fig. 5 will thus be modified in pairs.

In the next section stress distributions obtained graphically by the image method will be discussed for constant velocity impact on a rod of Maxwell material.

IV. TREATMENT OF SPECIFIC PROBLEMS

The method of images discussed in the previous section is used in conjunction with the stress distributions of Fig. 4, for constant velocity impact on a Maxwell body, to determine the stress distributions in finite rods. The superposition process is carried out graphically.

For an example, a rod of length $2c\tau_0$ has been chosen, so that the rod is of length 2 in units of ξ. With this choice, relaxation effects due to the viscous component of the strain influence the motion during the first traverse of the wave front and, of course, also during subsequent reflections. Figure 6 shows the stress distribution at various times when the rod end ($x=l$) is free, so that the stress there is zero, the end $x=0$ being subjected to constant velocity impact at $\tau=0$. In this figure the same ordinate, $-\sigma/\rho cV$, is used as in Fig. 4. For $\tau<2$ the wave front has not reached the free end, and the solution depicted in Fig. 4 for the semi-infinite rod applies. The wave front initiated by the impact has an initial amplitude of unity on the $-\sigma/\rho cV$ scale, but the maximum stress ordinate has already fallen below 0.5 when the wave front has traversed the rod. The stress distributions illustrated in Fig. 6 show that reflection at the free end introduces an unloading wave which produces additional rapid stress reduction. Just prior to $\tau=5$ the stress at the impact end changes sign,

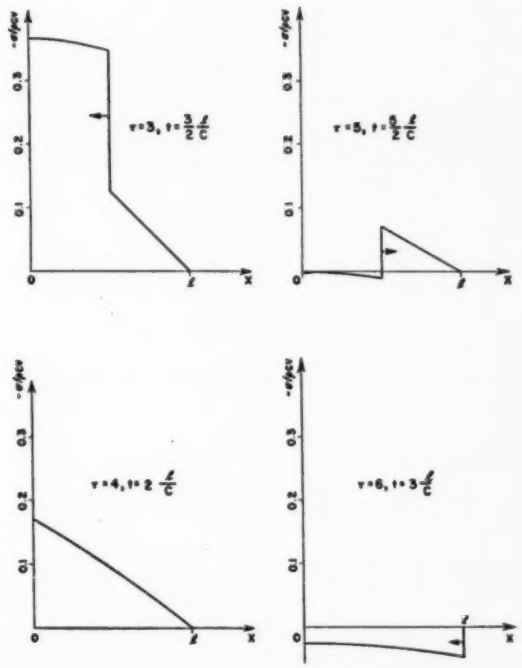

FIG. 6. Stress distribution for a rod of Maxwell material.

and this reversal is seen to have spread along the entire rod at $\tau=6$.

Figure 7 shows the corresponding stress distributions for an elastic rod. The unloading wave reflected from the free end reduces the stress behind it to zero, and at $\tau=4$ the rod is entirely unstressed. However, reflection at the impact end sends out a stress wave of opposite sign. Since there is no dissipation the stress-wave amplitude remains constant at unity on the

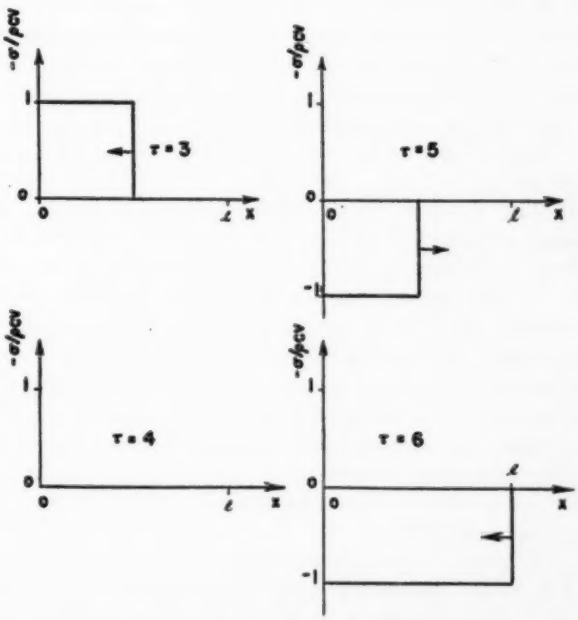

FIG. 7. Stress distribution for an elastic rod.

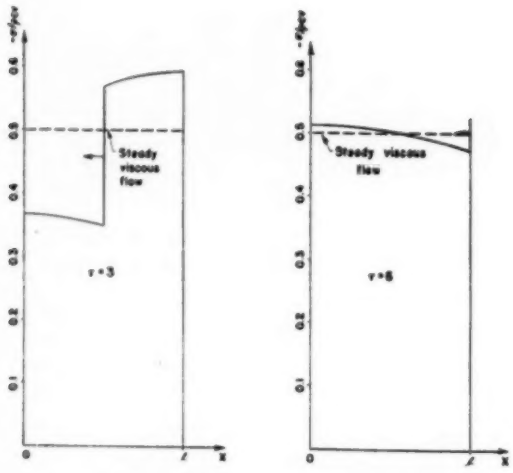

FIG. 8. Stress distribution for fixed-end rod.

$\sigma/\rho cV$ scale. Comparison of the distribution for $\tau=6$ shows the marked influence of the viscous element in the Maxwell material in absorbing the stress wave. Thus at times of the order of the relaxation time, viscous flow reduces the stress magnitudes, and throughout most of the motion they are much less than the initial stress produced at the beginning of impact.

In some cases of compressive impact, the prescribed velocity applies only as long as the stress at the impact face is compressive. Otherwise rebound occurs, and the impact end of the rod becomes a free end. In the present case, for the elastic rod corresponding to the distributions of Fig. 7, tension would occur at the impact face at $\tau=4$, and instead of a tension wave the rod would bounce forward away from the impact constraint in the unstressed condition. Figure 6 shows that for the Maxwell material tension would occur just before $\tau=5$, so that viscous flow delays the rebound. Moreover the rebound velocity will be reduced in this case, since energy is absorbed in viscous flow and less work is done by the impact constraint.

Figures 8 and 9 show stress distributions for constant velocity impact on a rod fixed at $x=l$. For an elastic rod, Fig. 9, reflection of the wave front at either the impact or fixed end produces an increase of unity in the stress ordinate amplitude. Thus, as one would expect for a continuously compressed elastic rod the stress increases indefinitely. For the Maxwell body, shown in Fig. 8, viscous flow relieves this stress increase. At $\tau=3$, the elastic wave front is still of appreciable magnitude, but at $\tau=6$, the stress wave variation has been largely dissipated and almost steady viscous flow is occurring.

One can easily calculate the steady uniform stress which will absorb the velocity difference V between the fixed and impact ends. The strain rate is V/l, and Eq. (1) gives the associated stress $-V/l\mu$. In the units of Fig. 8, this becomes $V/\rho cl\mu V$. Writing $\mu=1/E\tau_0$ and $E/\rho=c^2$, this becomes $\tau_0/(l/c)$. For the example of Fig. 8, the wave traverse time l/c was chosen to equal $2\tau_0$, so that the average stress ordinate for steady viscous flow is 0.5, as shown by the broken line in Fig. 8. It is clear that this steady flow is almost attained at $\tau=6$ so that a solution neglecting wave effects provides then a satisfactory approximation. A comparison of Figs. 8 and 9 emphasizes the relaxation potentialities of the Maxwell material in reducing the stress magnitudes.

It should perhaps be pointed out that the high initial stress at the impact face, which is not even approached following the initial traverse of the rod by the wave front, is directly associated with the wave traverse time having been chosen of the same order as the relaxation time and with the prescribed constant velocity impact. If a more gradual motion had been considered, for example constant acceleration, magnitudes of $\sigma/\rho cV$ near unity would not occur in these circumstances. Such solutions could be obtained by integration of the present solutions, considering a varying velocity as the superposition of increments as illustrated in Fig. 10. Expressed analytically, this leads to the solutions given in Eqs. (A.6) and (A.10) of the Appendix.

V. DISCUSSION

For the problems discussed above, the solution can be readily expressed in terms of the physical constants of the body and the dimensions of the system. The type of behavior in a particular case is determined by the relative magnitude of three time parameters:

t = time during which the motion is to be investigated,
$\tau_0=1/E\mu$, the relaxation time of the material,
$\tau_t=l/c$, the traverse time of an elastic wave.

If $t\ll\tau_0$, $\tau=t/\tau_0$ defined in Sec. II is small, and the behavior differs little from that of a purely elastic rod. Relaxation effects have no time to produce an appreciable influence, and elastic-wave theory will provide a satisfactory approximation. In the problems considered above, this situation occurs only immediately after impact, and, for example, the wave front in Fig. 4 for $\tau=0.1$ differs little from the elastic wave solution. However, for shorter rods or longer relaxation times this sort of approximation could apply after several wave reflections.

If $t\gg\tau_t$, many elastic wave reflections will take place in the time of interest, and a steady solution neglecting wave effects may provide a satisfactory approximation. The second diagram of Fig. 8 shows this even for a ratio t/τ_t of only 3. Comparison with the corresponding distribution for an elastic body in Fig. 9, shows that viscous flow dissipates wave fronts and accelerates the approach to the steady state. The distributions of Fig. 6 show the approach to the steady unstressed state of motion with constant velocity. In the case of the elastic rod, Fig. 7, the persistence of the elastic waves prevents the approach to the steady un-

stressed state, and the stress oscillates about the average value zero.

The problems discussed in the previous section were chosen so that both influences, relaxation and wave effects, were important. Although discussed in terms of the solutions above, the grouping of problems according to the time ratios $t:\tau_0:\tau_t$ will apply generally for other boundary conditions; it is thus important to evaluate these magnitudes in assessing a new problem.

In using the theory for a Maxwell body to approximate an actual material, the effect of the idealization involved must be considered. Since materials are known to exhibit a spectrum of relaxation times, the choice of a single value τ_0 implies grouping the longer time components with the elastic element since they will not have relaxed in times of order τ_0, and the short time components as viscous elements. Thus the selection of the best Maxwell parameters to represent a material for a given problem depends on the duration of time of interest as well as on the material properties. In general, relaxation components with a characteristic time of the order of the duration of interest in the particular problem should be considered if such exist in the spectrum of the material under consideration. Since components with long relaxation times are included with the elastic element, the equivalent Young's modulus is reduced in magnitude, compared with the instantaneous elastic modulus. This will influence wave propagation of a sharp wave front, since the initial disturbance will in fact be propagated with the true elastic wave velocity and not that based on the modified Young's modulus, and these effects will modify the shape of the computed wave front. These influences must be borne in mind in applying the results of the analysis, which can provide only an averaging out of these detailed influences. More theoretical and experimental work will be required to study this question in detail.

APPENDIX. THE SOLUTION OF THE STRESS-WAVE EQUATION USING THE LAPLACE TRANSFORM

This method of attack is discussed in detail in references 5 and 6.

We will first consider the problem of a semi-infinite rod, $x>0$, which is initially unstrained and at rest when at $t=0$ the end $x=0$ is subjected to impact with constant velocity V. The resulting stress distribution $\sigma(x, t)$ must satisfy the following conditions:

$$\left.\begin{aligned} &\sigma_{xx}-(1/c^2)(\sigma_{tt}+\mu E\sigma_t)=0,\\ &\sigma_x=\rho v_t,\\ &\sigma=0, \quad x=\infty,\\ &v=VH(t), \quad x=0,\\ &\sigma=v=0, \quad t=0, \end{aligned}\right\} \tag{A.1}$$

where $H(t)$ is the Heaviside step function $H(t)=0$, $t<0$; $H(t)=1$, $t>0$. The first of (A.1) is Eq. (4) slightly modified for convenience, making use of the relation $\rho c^2=E$. If we represent the Laplace transform with respect to t of a function by a bar over its symbol, Eq. (A.1) is replaced by conditions determining $\bar\sigma(x, s)$,

$$\left.\begin{aligned} &\bar\sigma_{xx}-(1/c^2)(s^2+\mu Es)\bar\sigma=0,\\ &\bar\sigma_x=\rho s\bar v,\\ &\bar\sigma=0, \quad x=\infty,\\ &\bar v=V/s, \quad x=0. \end{aligned}\right\} \tag{A.2}$$

This ordinary differential equation for $\bar\sigma$ can be solved directly, to give

$$\bar\sigma=-\frac{\rho cV}{(s^2+\mu Es)^{\frac12}}\exp[-(s^2+\mu Es)^{\frac12}x/c]. \tag{A.3}$$

If we write $s^2+\mu Es=(s+\mu E/2)^2-(\mu E/2)^2$, Eq. (A.3) can be expressed in a standard form, to give the inverse

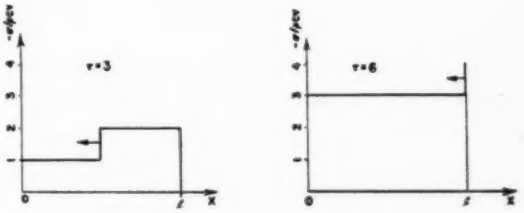

FIG. 9. Elastic rod corresponding to Fig. 8.

relation

$$\sigma=-\rho cVe^{-(\mu E/2)t}I_0\left[\mu E/2\left(t^2-\frac{x^2}{c^2}\right)^{\frac12}\right]H(t-x/c), \tag{A.4}$$

where I_0 is the zero-order Bessel function of the first kind of imaginary argument.

If we have an arbitrarily prescribed velocity on the end $x=0$, $v=V(t)$, the stress transform becomes

$$\bar\sigma=\frac{-\rho c\bar Vs}{(s^2+\mu Es)^{\frac12}}\exp[-(s^2+\mu Es)^{\frac12}x/c] \tag{A.5}$$

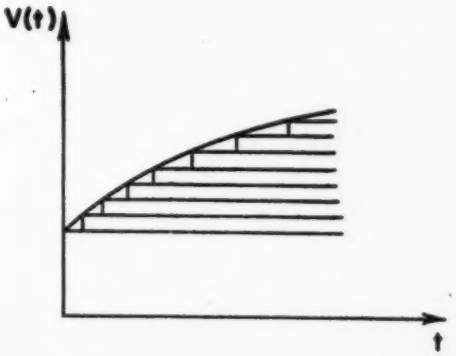

FIG. 10.

[5] H. S. Carslaw and J. C. Jaeger, *Operational Methods in Applied Mathematics* (Oxford University Press, London 1941).

[6] R. V. Churchill, *Modern Operational Mathematics in Engineering* (McGraw-Hill Book Company, Inc., New York, 1944).

which inverts into

$$\sigma=-\rho c\frac{\partial}{\partial t}\int_0^t V(t-\tau)e^{(-\mu E/2)\tau}I_0\left[\frac{\mu E}{2}(\tau^2-(x/c)^2)^{\frac{1}{2}}\right]\times H\left(\tau-\frac{x}{c}\right)d\tau=-\rho c\left\{\int_0^t V'(t-\tau)e^{(-\mu E/2)\tau}\times I_0\left[\frac{\mu E}{2}(\tau^2-(x/c)^2)^{\frac{1}{2}}\right]H\left(\tau-\frac{x}{c}\right)d\tau+V_0e^{(-\mu E/2)t}I_0\left[\frac{\mu E}{2}(t^2-(x/c)^2)^{\frac{1}{2}}\right]H\left(t-\frac{x}{c}\right)\right\},\quad(A.6)$$

where $V'(t)$ is the derivative of $V(t)$, and V_0 its initial value.

Let us now consider a finite rod of length l, subjected to a prescribed velocity $V(t)$ at $x=0$, and with the end $x=l$ free. The conditions for σ are

$$\begin{aligned}&\sigma_{xx}-(1/c^2)(\sigma_{tt}+\mu E\sigma_t)=0,\\&\sigma_x=\rho\dot{v}_t,\\&\sigma=0,\quad x=l,\\&v=V(t),\quad x=0,\\&\sigma=v=0,\quad t=0.\end{aligned}\qquad(A.7)$$

Application of the Laplace transform gives

$$\begin{aligned}&\bar{\sigma}_{xx}-(1/c^2)(s^2+\mu Es)\bar{\sigma}=0,\\&\bar{\sigma}_x=\rho s\bar{v},\\&\bar{\sigma}=0,\quad x=l,\\&\bar{v}=\bar{V},\quad x=0.\end{aligned}\qquad(A.8)$$

This ordinary differential equation can be solved directly to give

$$\bar{\sigma}=-\frac{\rho cs\bar{V}}{(s^2+\mu Es)^{\frac{1}{2}}}\frac{\exp[+(s^2+\mu Es)^{\frac{1}{2}}(l-x)/c]-\exp[-(s^2+\mu Es)^{\frac{1}{2}}(l-x)/c]}{\exp[+(s^2+\mu Es)^{\frac{1}{2}}l/c]+\exp[-(s^2+\mu Es)^{\frac{1}{2}}l/c]}.\qquad(A.9)$$

This can be inverted by the usual technique for wave problems of expanding the denominator as a binomial series,

$$\bar{\sigma}=-\frac{\rho cs\bar{V}}{(s^2+\mu Es)^{\frac{1}{2}}}\sum_{n=0}^{\infty}(-1)^n\times\left\{\exp\left[-(s^2+\mu Es)^{\frac{1}{2}}\frac{2nl+x}{c}\right]-\left[\exp-(s^2+\mu Es)^{\frac{1}{2}}\frac{2(n+1)l-x}{c}\right]\right\}$$

and inverting using standard forms

$$\sigma=-\sigma c\frac{\partial}{\partial t}\int_0^t V(t-\tau)e^{(-\mu E/2)\tau}\sum_{n=0}^{\infty}(-1)^n\times\left[I_0\left(\frac{\mu E}{2}\{\tau^2-[(2nl+x)/c]^2\}^{\frac{1}{2}}\right)H\left(\tau-\frac{2nl+x}{c}\right)-I_0\left(\frac{\mu E}{2}\left\{\tau^2-\left[\frac{2(n+1)l-x}{c}\right]^2\right\}^{\frac{1}{2}}\right)\times H\left(\tau-\frac{2(n+1)l-x}{c}\right)\right]d\tau$$

$$=-\rho c\int_0^t V'(t-\tau)e^{(-\mu E/2)\tau}\sum_{n=0}^{\infty}(-1)^n\{\tau,x\}d\tau-\rho cV_0e^{(-\mu E/2)t}\sum_{n=0}^{\infty}(-1)^n\{t,x\}.\qquad(A.10)$$

The series of waves expressed by the summation terms are the image waves discussed physically in Sec. III.

Diffraction of Electromagnetic Waves by an Aperture in a Large Screen*

G. BEKEFI
The Eaton Electronics Research Laboratory, Department of Physics, McGill University, Montreal, Canada
(Received February 16, 1953)

It has been shown that an approximate solution for the diffraction of an electromagnetic wave by an aperture in a plane conducting screen can be obtained from a single component of the Hertz vector and that the results can be applied to calculating the field of apertures which are sufficiently large as compared to the wavelength of the incident radiation. The solution rests upon an evaluation of an inhomogeneous scalar boundary-value problem. An infinitesimal wavelength approximation leads to a simple Kirchhoff-like formula which is found to be identical to that obtained by Neugebauer who derived it from geometrical optics as first approximation. The special case of diffraction by a circular aperture is treated in detail, and experimental measurements by which the theory was checked are cited.

I. INTRODUCTION

RECENT developments in microwave techniques have led to a renewal of interest in the diffraction of electromagnetic waves by an aperture in a conducting screen. In particular, the experimental work of Andrews,[1] who measured the field within and in the neighborhood of circular openings, has stimulated many of the theoretical investigations.

Despite the fact that the mathematical formalism for solving this problem has been laid down some time ago by Bethe[2] and Copson,[3] the difficulties encountered in evaluating the appropriate integral equations are such that in the general three-dimensional diffraction problem (as that of a circular aperture), the range of applicability of these methods is limited to apertures that are small as compared to the wavelength of the incident radiation. The most complete analysis of this type has been given by Bouwkamp.[4] Meixner and Andrejewski's[5] approach has met with success in so far that these authors are now able to push their solution to include apertures as large as about one wavelength in radius. Furthermore there is the well-known Kirchhoff theory extensively used at optical wavelengths and the vector-Huygens theory of Stratton and Chu,[6] both of which were thought to be good "large hole" approximations. Near-field measurements reveal however that neither of these predict the correct results. Hence there is at the present time a great number of diffraction problems and many measurements dealing with apertures of intermediate and large size for which no satisfactory theory is available. This paper and the work of Woonton[7] and Neugebauer[8] are concerned with approximate solutions applicable to diffracting holes sufficiently large with respect to the wavelength. Measurements made on circular apertures support the theoretical conclusions.

II. THE GENERAL FORMULATION OF THE PROBLEM

Consider an idealized, perfectly reflecting screen of infinite extent and zero thickness denoted by S_m (Fig. 1), lying in the x, y plane of a rectangular coordinate system. The screen is pierced by an aperture of arbitrary shape whose area is designated by S_0 and which is bounded by a contour C. The aperture and screen therefore occupy the whole x, y plane S. A monochromatic wave $\mathbf{E}_i$, $\mathbf{H}_i$ originating from a source situated in the negative half-space ($z<0$) is incident upon the screen. Harmonic time variation $\exp(j\omega t)$, where ω is the angular frequency, is implicitly assumed. The mks system of units is used throughout.

A mathematically exact solution of the diffraction problem, subject to the above idealizations, should satisfy the following requirements:

(a) The total field must be a solution of Maxwell's equations.

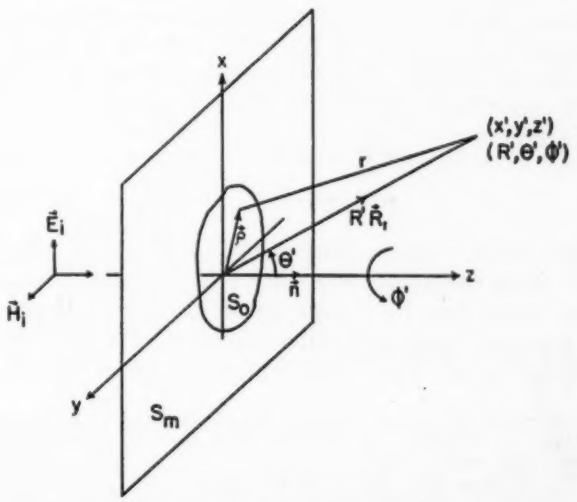

FIG. 1.

* This research forms part of a project on microwave optics that is supported at McGill University by the United States Air Force through its Cambridge Research Center under contract AF 19(122)-81. The contents of this paper have been briefly described in a Letter to the Editor, J. Appl. Phys. **23**, 1403 (1952).

[1] C. L. Andrews, J. Appl. Phys. **21**, 761 (1950).
[2] H. A. Bethe, Phys. Rev. **66**, 163 (1944).
[3] E. T. Copson, Proc. Roy. Soc. (London) **A186**, 100 (1946).
[4] C. J. Bouwkamp, Philips Research Reports **5**, 401 (1950).
[5] J. Meixner and W. Andrejewski, Ann. Physik (6) **7**, 157 (1950); also W. Andrejewski, Naturwiss. **38**, 406 (1951).
[6] J. A. Stratton and L. J. Chu, Phys. Rev. **56**, 99 (1939).
[7] G. A. Woonton, J. Appl. Phys. **23**, 1405 (1952).
[8] H. E. J. Neugebauer, J. Appl. Phys. **23**, 1406 (1952).

(b) In order that the final solution be a unique one, the field components in the half-space $z>0$ must satisfy the well-known radiation conditions at infinity,[9] and the energy density must be finite everywhere in space.[10]

(c) On the perfectly conducting screen S_m postulated in the theory it is required that

$$\left.\begin{aligned}\mathbf{n}\times\mathbf{E}&=0 \quad (1a)\\ \mathbf{n}\cdot\mathbf{H}&=0 \quad (1b)\end{aligned}\right\} \text{ on } S_m,$$

where $\mathbf{n}$ is a unit vector, normal to the plane S, directed into the half-space $z>0$.

(d) All components of the electromagnetic field must be continuous in crossing the aperture from the half-space $z<0$ to the half-space $z>0$. The continuity within S_0 is uniquely fulfilled by certain conditions[2,11] regarding the symmetry of the perturbed field about the x, y plane. These conditions can be stated as follows: The electromagnetic field $\mathbf{E}$, $\mathbf{H}$, at any point in space is split up into an incident field $\mathbf{E}_i$, $\mathbf{H}_i$, a partial field $\mathbf{E}_r$, $\mathbf{H}_r$, associated with the reflected wave that exists when the screen is complete, and a perturbed field $\mathbf{E}_p$, $\mathbf{H}_p$, due to the aperture alone. It is then found that in $z<0$,

$$\left.\begin{aligned}\mathbf{E}^-&=\mathbf{E}_i^-+\mathbf{E}_r^-+\mathbf{E}_p^-,\\ \mathbf{H}^-&=\mathbf{H}_i^-+\mathbf{H}_r^-+\mathbf{H}_p^-,\end{aligned}\right. \quad (2a)$$

and in $z>0$,

$$\left.\begin{aligned}\mathbf{E}^+&=\mathbf{E}_p^+,\\ \mathbf{H}^+&=\mathbf{H}_p^+.\end{aligned}\right. \quad (2b)$$

The superscripts "+" and "−" describe the appropriate half-space. From symmetry considerations it follows that

$$\mathbf{n}\cdot\mathbf{E}_p^+=-\mathbf{n}\cdot\mathbf{E}_p^-, \quad (3a)$$

$$\mathbf{n}\times\mathbf{H}_p^+=-\mathbf{n}\times\mathbf{H}_p^-. \quad (3b)$$

As a result of these relations, Bethe and others have shown that within the aperture the components of $\mathbf{H}$ parallel to the screen and the component of $\mathbf{E}$ normal to the screen are to be identified with the respective components of the incident radiation. If the subscript "0" describes the field in the plane $z=0$, then

$$\left.\begin{aligned}\mathbf{n}\times\mathbf{H}_0&=\mathbf{n}\times\mathbf{H}_i \quad (4a)\\ \mathbf{n}\cdot\mathbf{E}_0&=\mathbf{n}\cdot\mathbf{E}_i \quad (4b)\end{aligned}\right\} \text{ in } S_0.$$

The physical implications of (4a, b) should be noted. If a plane electromagnetic wave is incident normally on the screen then the tangential components of $\mathbf{H}$ show a uniform aperture distribution equal to that of the incident wave. This theoretical result was verified experimentally by Silver and Ehrlich.[12] However, nothing is known about the remaining three vector components within S_0 and to determine their distribution is one of the tasks of this paper.

The electromagnetic field can be everywhere represented by the Hertz vector $\mathbf{\Pi}$ from which the field components $\mathbf{E}$, $\mathbf{H}$, are derived through the relations,

$$\mathbf{E}=k^2\mathbf{\Pi}+\nabla\nabla\cdot\mathbf{\Pi}, \quad (5a)$$

$$\mathbf{H}=-\frac{k^2}{j\omega\mu}\nabla\times\mathbf{\Pi}. \quad (5b)$$

Consider now the special case of a homogeneous plane wave irradiating the aperture normally from the negative half-space, polarized with its electric vector parallel to the plane S. This specialization of the problem will be assumed throughout the remainder of this paper. Without further loss of generality, the direction of the incident $\mathbf{E}$ can be chosen to lie along the positive direction of the x coordinate. The assumption will now be made, and its consequences examined, that the total electromagnetic field at any point in space can be described by the x component of the Hertz vector alone, namely, that the field can be determined from that component of $\mathbf{\Pi}$ which is oriented in the direction of the incident electric field.† It is then found from Eqs. (5a, b) that the magnitudes of the components of $\mathbf{E}$ and $\mathbf{H}$ are

$$E_x=k^2\Pi_x+\frac{\partial^2\Pi_x}{\partial x^2}, \quad (a) \qquad H_x=0, \quad (d)$$

$$E_y=\frac{\partial^2\Pi_x}{\partial y\partial x}, \quad (b) \qquad H_y=-\frac{k^2}{j\omega\mu}\frac{\partial\Pi_x}{\partial z}, \quad (e) \quad (6)$$

$$E_z=\frac{\partial^2\Pi_x}{\partial z\partial x}, \quad (c) \qquad H_z=\frac{k^2}{j\omega\mu}\frac{\partial\Pi_x}{\partial y}, \quad (f)$$

where Π_x satisfies the scalar wave equation

$$\nabla^2\Pi_x+k^2\Pi_x=0. \quad (7)$$

It is found by inspection of (6) that relations (4a, b) pertaining to the field within the aperture are fulfilled if

$$\left(\frac{\partial\Pi_x}{\partial z}\right)_0=\left(\frac{\partial\Pi_{ix}}{\partial z}\right)_0 \quad \text{in } S_0, \quad (8)$$

where the subscript "0" denotes the value of Π_x and its derivatives at $z=0$. On both surfaces of the conducting screen the tangential components of $\mathbf{E}$ and the normal component of $\mathbf{H}$ must vanish (Eqs. 1a, b). It

[9] S. Silver, *Microwave Antenna Theory and Design* (Radiation Laboratory Series v. 12) (McGraw-Hill Book Company, Inc., New York, 1949), p. 85.

[10] J. Meixner, Ann. Physik (6) **6**, 1 (1949).

[11] S. Silver, Antenna Laboratory Report No. 163 (1949), Department of Engineering, University of California.

[12] S. Silver and M. J. Ehrlich, Antenna Laboratory Report No. 185 (1952), Department of Engineering, University of California.

† The author is indebted to Dr. C. J. Bouwkamp for pointing out that the use of a single component of the Hertz vector was already discussed briefly by F. Möglich, Ann. Physik (4) **83**, 609 (1927).

follows from (6) that a sufficient condition is that

$$\Pi_z=0 \quad \text{on } S_m. \tag{9}$$

In the Appendix it is shown in some detail that (8) and (9) fulfil requirements over the surfaces S_0 and S_m and that furthermore the solution is in accord with the symmetry conditions (3a, b).

The vector diffraction problem has thus been reduced to a scalar form in which the homogeneous wave equation (7) is to be solved subject to the conditions (8) and (9). The form of this boundary-value problem, into which the electromagnetic case has been thrown, is well known in the diffraction of scalar waves. For instance, for circular apertures Bouwkamp[13] and others have obtained solutions over a large range of aperture radius to wavelength ratio, by separating the wave equation in spheroidal coordinates. Also an integral equation representation for an aperture of arbitrary shape has been given by Rayleigh,[14] Levine and Schwinger,[15] and Baker and Copson.[16] Applying their method, the field in space is determined as follows.

If the wave function Π_z is regular at every point in the half-space $z\geqslant 0$, satisfies the prescribed boundary conditions (8) and (9), and is a solution of the wave equation (7), then the field at any point (x', y', z') in $z\geqslant 0$ is given by

$$\Pi_z(x', y', z') = -\frac{1}{2\pi}\frac{\partial}{\partial z'}\int_{S_0}\Pi_z(x, y)\frac{\exp(-jkr)}{r}dxdy, \tag{10a}$$

and in $z\leqslant 0$ by

$$\Pi_z(x', y', z')=\Pi_{iz}(x', y', z')-\Pi_{iz}(x', y', -z') + \frac{1}{2\pi}\frac{\partial}{\partial z'}\int_{S_0}\Pi_z(x, y)\frac{\exp(-jkr)}{r}dxdy. \tag{10b}$$

The unknown function $\Pi_z(x, y)$ which appears under the integral signs is determined through the integral equation,

$$\left(\frac{\partial\Pi_{iz}}{\partial z'}\right)_0 = -\frac{1}{2\pi} \times\left(\frac{\partial^2}{\partial z'^2}\int_{S_0}\Pi_z(x, y)\frac{\exp(-jkr)}{r}\right)_0 dxdy. \tag{10c}$$

In Eqs. (10), r is the distance from an element of area ($dxdy$) of S_0 to the field point (x', y', z') and is given by

$$r=[(x-x')^2+(y-y')^2+z'^2]^{\frac{1}{2}}.$$

Since Eqs. (10) fulfil boundary conditions over all finite areas of S and since furthermore the field components obtained from Π_z are solutions of Maxwell's relations, it appears as if an exact formulation of the diffraction problem had been found. Nevertheless in the general three-dimensional case the results are approximate because the initial assumption of using only one component of $\mathbf{\Pi}$ imposes a not necessarily true restriction (6d) that $H_z=0$ at every point in space. [Note that within the aperture (6d) is correct as required by relation (4a).] However experimental measurements indicate that when the aperture dimensions are at least several wavelengths, the cross-polarized component H_x in the diffraction field is very small compared to that lying parallel to the incident H_y. Although it is difficult to assess on theoretical grounds alone the magnitude of the error produced by the assumptions, it is expected that for sufficiently large apertures, the errors in the final solution will in general be small. The largest discrepancies in the prediction of the field components will probably be confined to a region close to the diffracting edge; here one finds from the scalar solution of Bouwkamp and others that the wave function Π_z tends to zero as $r^{\frac{1}{2}}$ where r is the distance from the edge to a neighboring field point situated in S_0. It is then found in general that an evaluation of the field components from Π_z leads to field singularities of an order which is not in conformity with requirements of Meixner[10] and Bouwkamp.[17] This failure of the solution causes the energy density of the field to become infinite at the rim and this in effect results in sources being generated there.

A derivation of the distant field relations in general terms will permit a verification of the radiation conditions in $z>0$. Let ϱ be a vector from the origin of the coordinates to a point (x, y) in S_0. Let R', θ', ϕ' be the spherical coordinates of the field point (Fig. 1) and finally let $\mathbf{R}_1$ be a unit vector along R' directed from the origin to the field point. In order to obtained from (10a) the field components given by (6) it is necessary to perform the required differentiations with respect to the primed coordinates. Thus to find E_x for instance, we require

$$\frac{\partial}{\partial z'}\frac{\partial^2}{\partial x'^2}\left[\frac{\exp(-jkr)}{r}\right] = jk^3\frac{\exp(-jk\{R'-\varrho\cdot\mathbf{R}_1\})}{R'}\sin^2\theta'\cos\theta'\cos^2\phi'+O\left(\frac{1}{R'^2}\right)$$

and similarly for the other derivatives. Inserting these into Eq. (10a) and transforming from a rectangular to a spherical system of field components, it then follows

[13] C. J. Bouwkamp, dissertation, University of Groningen (1941).

[14] Lord Rayleigh, *Scientific Papers* **4**, 283 (1903); **6**, 161 (1920).

[15] H. Levine and J. Schwinger, Phys. Rev. **74**, 958 (1948); **75**, 1423 (1949).

[16] B. B. Baker and E. T. Copson, *The Mathematical Theory of Huygens' Principle* (Clarendon Press, Oxford, 1950), second ed., pp. 163, 185.

[17] C. J. Bouwkamp, Physica **12**, 467 (1946).

from (6) that to the order of R'^{-1},

$$E_R=0, \qquad H_R=0,$$

$$E_\theta=g(\theta')\cos^2\theta'\cos\phi', \qquad H_\theta=-\left(\frac{\epsilon}{\mu}\right)^{\frac{1}{2}}E_\phi,$$

$$E_\phi=-g(\theta')\cos\theta'\sin\phi', \qquad H_\phi=\left(\frac{\epsilon}{\mu}\right)^{\frac{1}{2}}E_\theta,$$

where $g(\theta')$ is given by

$$g(\theta')=\frac{jk^3}{2\pi}\frac{\exp(-jkR')}{R'}\times\int_{S_0}\Pi_x(x,y)\exp(jk\boldsymbol{\rho}\cdot\mathbf{R}_1)dxdy. \quad (11)$$

Provided that the integral in (11) is finite, the radiation conditions have been satisfied.

So far consideration has been given only to that Hertz vector whose source can be traced to a distribution of electric polarization. In free space the transformation $\mathbf{D}\rightarrow\mathbf{B}$ and $\mathbf{B}\rightarrow-\mathbf{D}$ is permissible and this leads to the fact that the electromagnetic field can also be formulated in terms of a magnetic Hertz vector $\mathbf{\Pi}^*$.[18]

By reasoning similar to that given previously, it is possible to construct an electromagnetic field from the vector component Π_y^* alone which in this case fulfils the boundary requirements,

$$\Pi_{o_y}^*=\Pi_{i_y}^* \quad \text{in } S_0,$$
$$(\partial\Pi_y^*/\partial z)_0=0 \quad \text{on } S_m,$$

and which is characterized by the fact that $E_y=0$ everywhere. It appears that the whole diffraction problem as formulated here is ambiguous insofar that it can be expressed in terms of either Π_x or Π_y^*. Calculations based upon the latter are found to be in complete disagreement with experimental measurements. Below is given a possible explanation as to why results based on Π_y^* are not permissible.

As mentioned above, $E_y=0$ at every point in space, when Π_y^* is chosen to represent the vector field. It then follows from (2) that within the aperture

$$E_{o_y}=E_{i_y}=0.$$

This relation represents in general an erroneous restriction imposed upon the problem because Eqs. (4) fully determine all requirements that are necessary in S_0.

III. THE CIRCULAR APERTURE

In the special case of diffraction by a circular aperture, it is helpful to use the King[19] and Sommerfeld[20] integral representation of describing the wave function, instead of employing the formulation as given by (10), from which however the formulas that will be stated can be derived.

Let a be the radius of the circular aperture and let (ρ', z') be the field point in a cylindrical coordinate system. Since the diffraction space $z\geqslant 0$ is of main interest, attention will be restricted to that region. It is then found that the wave function $\Pi_x(\rho', z')$ at any point in $z'\geqslant 0$ is given by,

$$\Pi_x(\rho', z')=\int_0^\infty J_0(\lambda\rho')f(\lambda a)\exp(-\mu z')\frac{\lambda d\lambda}{\mu}. \quad (12)$$

Here λ is a variable of integration and $J_0(x)$ is a Bessel function of the first kind and order zero; μ is defined as

$$\mu=j(k^2-\lambda^2)^{\frac{1}{2}} \quad \lambda<k,$$
$$=(\lambda^2-k^2)^{\frac{1}{2}} \quad \lambda>k.$$

The unknown function $f(\lambda a)$ is usually termed the "radiation characteristic" and it can be shown to be proportional to $g(\theta')$ defined in (11) on setting $\lambda=k\sin\theta'$; the magnitude of $f(\lambda a)$ is determined from the boundary values that exist on the surface S. On substituting conditions (8) and (9) into (12), it follows immediately that, in the plane $z'=0$,

$$\left(\frac{\partial\Pi_{i_x}}{\partial z'}\right)_0=-\int_0^\infty J_0(\lambda\rho')f(\lambda a)\lambda d\lambda, \quad \rho'<a, \quad (13a)$$

$$0=\int_0^\infty J_0(\lambda\rho')f(\lambda a)\frac{\lambda d\lambda}{\mu}, \quad \rho'>a, \quad (13b)$$

and these are dual integral equations which must be evaluated. Once $f(\lambda a)$ has been determined, a substitution into (12), formally concludes the solution of the problem.

The evaluation of (13a, b) is difficult and it has as yet been unsuccessful when the aperture is larger than the wavelength. Nevertheless a very useful approximation can be obtained by proceeding to the high-frequency geometrical optics limit, $ka\rightarrow\infty$. Although it seems impossible to establish theoretically the range of validity of such an approximation, field measurements on apertures from $ka=\pi$ to $ka=40\pi$ substantiate the results. The final formulas are found to be the same as those obtained by Neugebauer[8] who used strict geometrical optics as first approximation and who then applied corrections in order to eliminate field discontinuities at the boundary of the geometrical shadow.

Writing (13b) in terms of its real and imaginary parts, it follows that

$$0=-j\int_0^k J_0(\lambda\rho')f(\lambda a)\frac{\lambda d\lambda}{(k^2-\lambda^2)^{\frac{1}{2}}}+\int_k^\infty J_0(\lambda\rho')f(\lambda a)\frac{\lambda d\lambda}{(\lambda^2-k^2)^{\frac{1}{2}}}, \quad \rho'>a. \quad (14)$$

[18] J A Stratton, *Electromagnetic Theory* (McGraw-Hill Book Company, Inc., New York, 1941), p. 28.
[19] L. V. King, Can. J. Research 11, 135 (1934).
[20] A. Sommerfeld, Ann. Physik (5) 42, 389 (1943).

If k is very large the second term of (14) becomes very small as compared to the first (see Sommerfeld[20]), and in the limit as $k\to\infty$ (this being synonymous with the assumption that $ka\to\infty$ as can be seen by a change of variable, $\lambda=t/a$), Eq. (14) simplifies to

$$0=\int_0^\infty J_0(\lambda\rho')f(\lambda a)\lambda d\lambda, \quad \rho'>a. \tag{15}$$

Fourier-Bessel transforms of (13a) and (15) lead to the result,

$$f(\lambda a)=-\int_0^a J_0(\lambda\rho')\cdot\left(\frac{\partial\Pi_{ix}}{\partial z}\right)_0\rho' d\rho'. \tag{16}$$

It has in effect been shown [as seen from Eq. (16)], that in the limit of infinite frequencies the mixed boundary conditions (8) and (9) used in the derivation of the dual integral equations approximate to the simple homogeneous form,

$$\left(\frac{\partial\Pi_x}{\partial z}\right)_0=\left(\frac{\partial\Pi_{ix}}{\partial z}\right)_0 \quad \text{in } S_0, \tag{17a}$$

$$=0 \quad \text{on } S_m^+, \tag{17b}$$

where S_m^+ denotes the shadow side of the screen.

The boundary condition (17a) has remained unchanged, it is exact and it ensures the continuity of the field in passing through the aperture. The approximation process outlined above has however affected conditions on the shadow side of the screen, and it is of interest to examine the implications of (17b). On turning to Eq. (6e) it becomes immediately obvious that the tangential component of the magnetic field (H_y) has been made to vanish on S_m^+. Experiment indicates that such an approximation to exact boundary conditions is reasonable, if the dimensions of the diffracting aperture are sufficiently large as compared to the wavelength in which case it is known that the field on S_m^+ drops off to zero very rapidly as the distance from the diffracting edge is increased.‡ Lastly it should be mentioned that although (17a, b) were obtained for the special case of a plane wave incident normally on a circular aperture only, these conditions also hold for apertures of any shape and for incident waves not necessarily plane.[21]

A plane wave incident normally on the screen is represented by [see Eqs. (6)],

$$k^2\Pi_x=E_c\exp(-jkz), \tag{18}$$

where E_c is a constant equal to the amplitude of the incident electric vector at $z=0$. Substituting (18) into the integrand of (16) and performing the integration, it follows that

$$f(\lambda a)=j\frac{E_c a}{k}\left(\frac{J_1(\lambda a)}{\lambda}\right).$$

The wave function $\Pi_x(\rho', z')$ at any point in $z'\geqslant 0$ is obtained by inserting the above value of $f(\lambda a)$ into (13); thus

$$\Pi_x(\rho', z')=j\frac{E_c a}{k}\int_0^\infty J_0(\lambda\rho')J_1(\lambda a)\exp(-\mu z')\frac{d\lambda}{\mu}. \tag{19}$$

Although Eq. (19) is useful in computing the wave function at $z=0$, it does not lend itself readily to evaluating Π_x in the near field ($0<z<\infty$). Furthermore the equation applies to circular holes only, while requirements (17) are true for any shape of aperture. For these reasons other forms will be given from which the wave function can be calculated.

(a) An application of Neumann's problem to the infinite plane boundary results in the fact that subject to conditions (17), Π_x at any point (x', y', z') in $z\geqslant 0$ is given by a surface integral over the aperture area,

$$\Pi_x(x', y', z')=-\frac{1}{2\pi}\int_{s_0}\left(\frac{\partial\Pi_{ix}(x, y)}{\partial z}\right)_0\frac{\exp(-jkr)}{r}dxdy, \tag{20}$$

with the same notation as used in Sec. II. Formula (20) has the appearance of a Kirchhoff type of approximation. There are however two major differences between the classical formulation of diffraction and the above equation: first, the field components derived from (20) obey Maxwell's relations, and secondly, the requirement of field continuity through the aperture is preserved; both of these are not satisfied simultaneously by either the Kirchhoff formulation or by the vector-Huygens theory of Stratton and Chu.[6] For a plane wave at normal incidence, it follows from (18) and (20) that

$$\Pi_x(x', y', z')=j\frac{E_c}{2\pi k}\int_{s_0}\frac{\exp(-jkr)}{r}dxdy. \tag{21}$$

(b) Schoch[22] has shown that for an aperture of arbitrary shape the surface integral in (21) can be transformed into a line integral. Using his results and applying them to Eq. (21), it is found that

$$\Pi_x(\rho', z')=\frac{E_c}{k^2}\left[\exp(-jkz')-\frac{1}{2\pi}\int_0^{2\pi}\exp(-jkr_0)d\alpha\right], \quad \rho'\leqslant a, \tag{22}$$

‡ In the course of preparation of this paper a recent report by S. Silver and M. J. Ehrlich (Antenna Laboratory Report No. 181, (1951), Department of Engineering, University of California) has come to the present writer's attention. In that report the boundary conditions (17a, b) derived above were made the basis of a theoretical investigation of diffraction. Many of the results there deduced can be obtained from the present analysis.

[21] Field measurements made by D. C. Hogg at the Eaton Electronics Research Laboratory, McGill University, checked well against theoretical predictions, when spherical waves were used to illuminate the aperture (private communication).

[22] A. Schoch, Akust. Z. 6, 318 (1941).

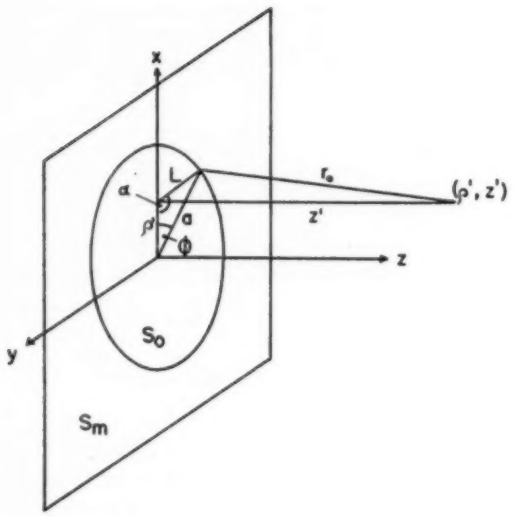

FIG. 2.

for the case when the field point (ρ', z') lies in the illuminated region; a similar expression applicable to the geometrical shadow region $\rho' > a$ is discussed by Carter and Williams.[23] In Eq. (22) r_0 is the distance from the field point to an element δs of the diffracting edge; for the special case of the circular aperture,

$$r_0^2 = z'^2 + L^2,$$

where

$$L^2 = a^2 + \rho'^2 - 2a\rho' \cos\phi,$$

or

$$L = \rho' \cos\alpha + (a^2 - \rho'^2 \sin^2\alpha)^{\frac{1}{2}},$$

and

$$\rho'^2 = x'^2 + y'^2,$$

the angles α and ϕ are defined in Fig. 2. A useful alternative form of Eq. (22) is obtained if the integration over the angle α is replaced by an integration over ϕ; it is then readily shown that

$$\Pi_z(\rho', z') = \frac{E_c}{k^2}\left[\exp(-jkz') - \frac{1}{2\pi}\int_0^{2\pi} \frac{\exp(-jkr_0)}{L^2}(a - \rho' \cos\phi) a d\phi\right] \quad (23)$$

for a circular aperture of radius a. This equation is the infinite frequency approximation to the relations derived in the previous section and it was obtained by Neugebauer[8] by an independent method.

Any one of Eqs. (19) to (23) inclusive can be used in the evaluation of the wave function Π_z. The choice rests upon the ease with which the calculation can be carried out. Within the aperture $z' = 0$, Eq. (19) is the most convenient. In fact Stenzel[24] has already given a solution of the integral since it also occurs in the problem of the vibrating circular "Rayleigh plate." Except for constants of proportionality which are different from the present case, his results can be applied. It is then found that within the circular diffracting aperture,

$$\Pi_z(\rho', 0) = \frac{E_c}{k^2}\left[1 - \sum_{m=0}^{\infty} t_m (k\rho')^m J_m(k\rho')\right], \quad (24)$$

where

$$t_m = \left(\frac{ka}{2}\right)^{\frac{1}{2}} \frac{\Gamma(m+1/2)}{m!} \frac{1}{(ka)^m} \{J_{m-1/2}(ka) - (-1)^m j J_{-m+1/2}(ka)\}.$$

The infinite series of Bessel functions are convergent for all $\rho' \leqslant a$. The three unknown field components E_x, E_y, and H_z are found from (6) and (24) on performing the required differentiations,

$$E_x(x', y', 0) = E_c\left[1 - \sum_{m=0}^{\infty} t_m (k\rho')^m \left\{J_m(k\rho') + \frac{J_{m-1}(k\rho')}{(k\rho')} + \left(\frac{x'}{\rho'}\right)^2 J_{m-2}(k\rho')\right\}\right], \quad (25a)$$

$$E_y(x', y', 0) = E_c[k^2 (x'y') \times \sum_{m=0}^{\infty} t_m (k\rho')^{m-2} J_{m-2}(k\rho')], \quad (25b)$$

$$H_z(x', y', 0) = jH_c[(ky') \times \sum_{m=0}^{\infty} t_m (k\rho')^{m-1} J_{m-1}(k\rho')], \quad (25c)$$

where

$$\rho' = (x'^2 + y'^2)^{\frac{1}{2}} \quad \text{and} \quad H_c = (\epsilon/\mu)^{\frac{1}{2}} E_c.$$

In Fig. 3 are shown a few representative aperture-field measurements of the E_x component of the electromagnetic field, which were carried out independently by Andrews,[1] Silver and Ehrlich[12], and Bekefi and Woonton.[25] The theoretical curves were computed from Eq. (25a). For the four apertures shown ($ka = \pi$, 3π, 7π, and 8π), the electric field intensity is plotted along the ordinate and the field point $(x', y', 0)$, in units of wavelength along the abscissa. In view of the experimental difficulties, the general agreement with theory is good. It is surprising to find that even for an aperture as small as one wavelength in diameter, there is fair agreement between the measured and calculated values. A comprehensive set of measurements made outside the aperture plane and the corresponding theoretical predictions will be published later.

[23] A. H. Carter and A. O. Williams, J. Acoust. Soc. Am **23**, 179 (1951)

[24] H. Stenzel, Ann. Physik (5) **41**, 245 (1942).

[25] G. Bekefi and G. A. Woonton, The Eaton Electronics Research Laboratory Report No. b7 under contract AF 19(122)-81 to the United States Air Force, Cambridge Research Center.

A further comparison of the theoretical results derived above was made with calculations based on the exact theory of Meixner and Andrejewski and published by the latter author[5] for the case $ka=10$. The graphical comparison is shown in Fig. 4.

CONCLUSIONS

It has been shown that an approximate solution of the three-dimensional electromagnetic diffraction problem is obtained by using a single component of the Hertz vector and that the results may be applied to calculating the field of apertures sufficiently large as compared to the wavelength. The solution rests upon the evaluation of an inhomogeneous scalar, boundary value problem. A high-frequency approximation ($ka\to\infty$) was found to lead to a Kirchhoff-like formula which, however, differs from the latter in so far that it satisfies Maxwell's relations and the requirement of field continuity. Experiments made on circular apertures verify much of the theoretical work.

The writer wishes to thank Professor G. A. Woonton and Dr. H. E. J. Neugebauer for the many helpful discussions of this problem. Thanks are also due to Miss E. Major who did the numerical computations.

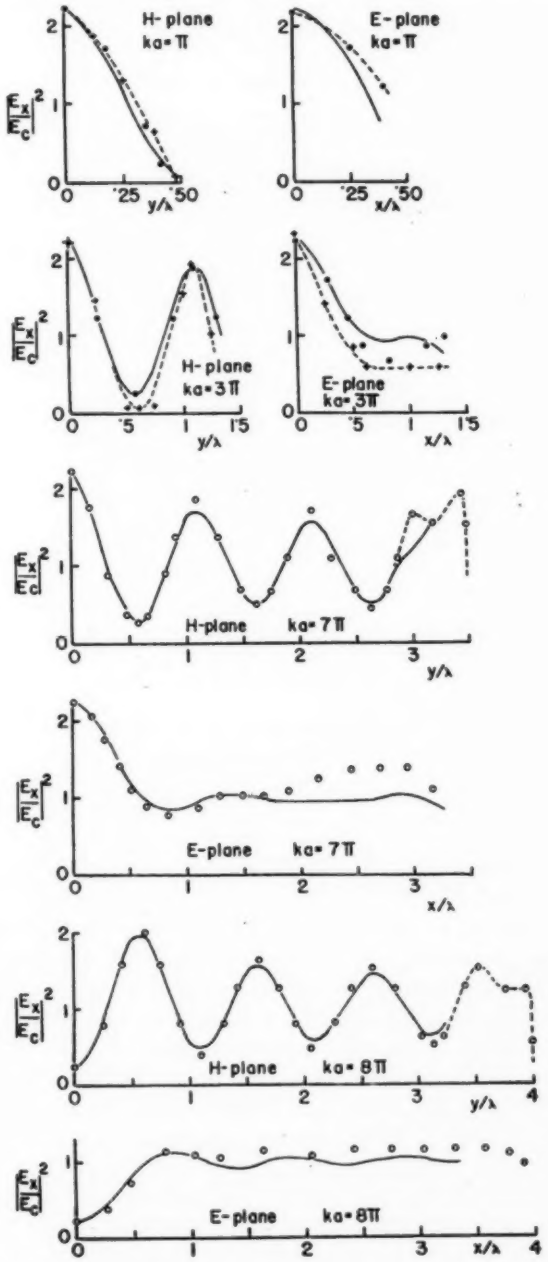

FIG. 3. The electric field intensity in the plane of circular apertures, normalized to the unperturbed incident wave. (—— calculated from Eq. (25a); ●● measured by Andrews; + - - - + measured by Silver and Ehrlich; ○ - - ○ measured by Bekefi and Woonton).

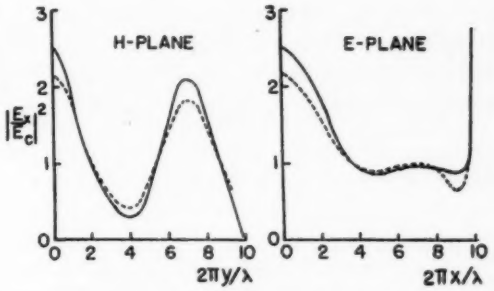

FIG. 4. The amplitude of the electric field within a circular aperture, $ka=10$. [—— as calculated from exact theory by Andrejewski; - - - calculated from Eq. (25a)].

APPENDIX

(i) It is required to show that the integral equations (10) satisfy the requirements of the vanishing of the tangential components of **E** and the normal components of **H** [Eqs. (1)] on both surfaces of screen S_m. Consider first the positive side of the screen; on carrying out the differentiation in (10a) it follows that

$$\Pi_x(x', y', z') = \frac{1}{2\pi} z' \int_{S_0} \Pi_x(x, y) \frac{\exp(-jkr)}{r^2} \left(jk + \frac{1}{r}\right) dx dy. \quad (26)$$

The components E_x, E_y, and H_z are obtained from (6) by performing the appropriate differentiations with respect to either the x' or the y' coordinates, as the case may be. This will introduce into the integrand of (26) terms similar to those that are already present and new terms of the form $(x-x')/r$ or $(y-y')/r$. Since $\Pi_x(x, y)$ is a bounded function and since on the surface of the screen the remainder of the integrand is regular ($r\neq 0$), it follows directly that as $z'\to 0$, E_x, E_y, and H_z likewise tend to zero on the positive side of S_m. This result can be derived in the same way on the negative side of the screen with the help of Eq. (10b), on noting that $\Pi_{ix}(x', y', z')$ is only a function of z' as seen from (18).

(ii) Within the aperture S_0, Eqs. (10) must satisfy conditions (4), namely, $H_{ox}=H_{ix}$, $H_{oy}=H_{iy}$, and $E_{oz}=E_{iz}$. The first of these relations is automatically

fulfilled as a result of the original postulate that H_x is zero everywhere in space and mention of this fact has already been made in Sec. II. The component H_y in the half-space $z \geqslant 0$ is found by combining (6e) with (10a),

$$-\frac{j\omega\mu}{k^2}H_y(x', y', z') = -\frac{1}{2\pi}\frac{\partial^2}{\partial z'^2}\int_{S_0}\Pi_x(x, y)\frac{\exp(-jkr)}{r}dxdy,$$

and from the integral equation (10c) it follows directly that within the aperture

$$-\frac{j\omega\mu}{k^2}H_y(x', y', 0) = \left(\frac{\partial\Pi_{ix}}{\partial z'}\right)_0 = -\frac{j\omega\mu}{k^2}H_{iy}(x', y', 0).$$

The same result is obtained from (10b) if the aperture is approached from the negative half-space. A similar proof can be given for the z component of the electric vector.

(iii) The symmetry conditions (3) can be verified by comparing expressions (10a, b) with relations (2a, b), respectively; this reveals that the perturbed fields Π_p^+ and Π_p^- in the appropriate half-spaces are

$$\Pi_{pz}^{\mp} = \pm\frac{1}{2\pi}\frac{\partial}{\partial z'}\int_{S_0}\Pi_x(x, y)\frac{\exp(-jkr)}{r}dxdy.$$

Since in the above equation the differentiation with respect to z' in the negative half-space results in a reversal of sign, Π_{pz} is a function which is symmetric about the x, y plane such that

$$\Pi_{pz}(x', y', -|z'|) = \Pi_{pz}(x', y', |z'|).$$

Since, furthermore, a calculation of the components H_{py} and E_{pz} from Π_{pz} involves an additional differentiation with respect to z', it follows that these components satisfy a relation of the form

$$-F(x', y', -|z'|) = F(x', y', |z'|)$$

which is in conformity with (3).

JOURNAL OF APPLIED PHYSICS VOLUME 24, NUMBER 9 SEPTEMBER, 1953

Determination of the Surface Stress by Means of Electroplating

H. Ōkubo
Tōhoku University, Sendai, Japan
(Received April 9, 1953)

This paper presents a new method for the measurement of surface stress. By the use of test pieces plated with copper, the stress is measured by observing the flecks on the surface produced by cyclic stress. The variation in the appearance of flecks which is due to the change of load is very sensitive at a proper load, so an accurate determination of the surface stress is feasible.

The stress concentration factor in torsion is obtained experimentally by the method described for circular shafts with a circumferential notch in each. The results are compared with theoretical values, calculated from two different formulas previously derived by the author and Sonntag, respectively. It is confirmed that the experimental results obtained here are in good agreement with those calculated by the author's formula.

INTRODUCTION

COMPLETE theoretical solutions for stress concentration problems due to fillets, notches, etc., have been found only in a few of simple cases, owing to mathematical difficulties. In the majority of cases, information regarding stress concentration has been obtained by experiment. For this purpose, strain measurements with sensitive extensometers and the method of brittle coatings are now widely used. By means of the former method, however, technical difficulty arises from the highly localized character of the stress concentration for an accurate determination of the strain at the point in question. In using the latter method, it requires high technique to have a coating of uniform thickness if the shape of a specimen is irregular, while the uniformity of a coating immediately affects results. Moreover, the sensitivity of coatings is considerably affected by various conditions of the coating material, namely, drying time of coating material, atmospheric conditions during the testing period, and many other conditions.

This paper presents a new method for the measurement of surface stress, quite free from these technical difficulties. When a specimen, plated with copper which contains some impurities, is subjected to a suitable load, the surface of the plating metal changes in color owing to the flecks produced by loading. These flecks are produced only in a very thin surface layer of the plating metal, the mechanical properties of which are somewhat different from those of the inner part. In statical loading, faint flecks begin to appear at a certain load, and with the increase of the load the density and depth of color of the flecks are increased. But if a specimen is loaded until the flecks appear very clearly, yielding starts at the inner part of the plating metal, the variation of the density and depth of color of the flecks as a result of the change of load is rather gradual.

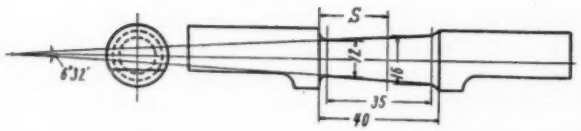

FIG. 1. Dimensions of the test piece.

Consequently, by means of a statical loading, the determination of load corresponding to a certain appearance of flecks is not sharp. But when a specimen is subjected to a cyclic load of proper magnitude, the color of flecks becomes deeper with the increase of the number of cycles, while the inner part of the plating metal remains within elastic range. The increasing rate of the depth of color and density of flecks abruptly changes at a proper load. These flecks do not appear within a certain load, but if a load slightly exceeds the proper value, the flecks of deep color abruptly come in sight. This value of the load is characteristic for the plating metal and the metal contained as an impurity in the plating solution, if the surfaces of the specimens be maintained under the same conditions. To have a distinct appearance of flecks, as a plating solution, the solution of cupric phosphate mixed with a small quantity of zinc sulfate has been used. The surface conditions of a copper-plated specimen are affected by the surface finish of the specimen before plating and also by the conditions of deposition, namely, composi-

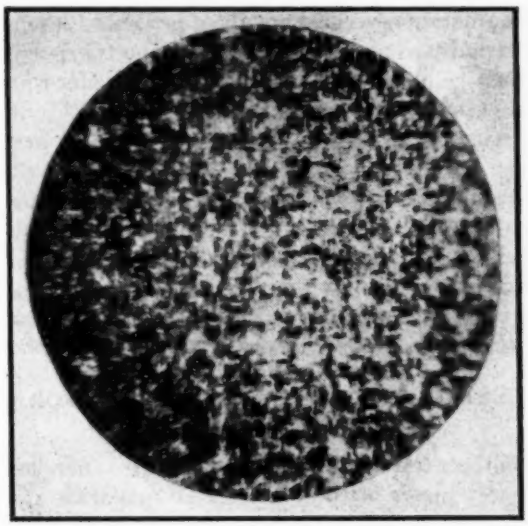

(a)
Stress ±11.5 kg/mm², flecks very dense.

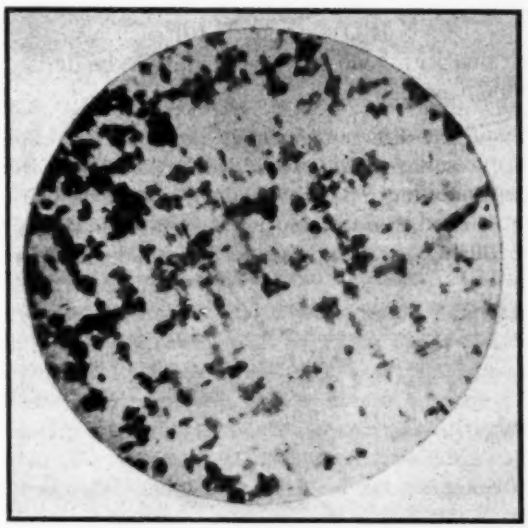

(b)
Stress ±10.0 kg/mm², flecks dense.

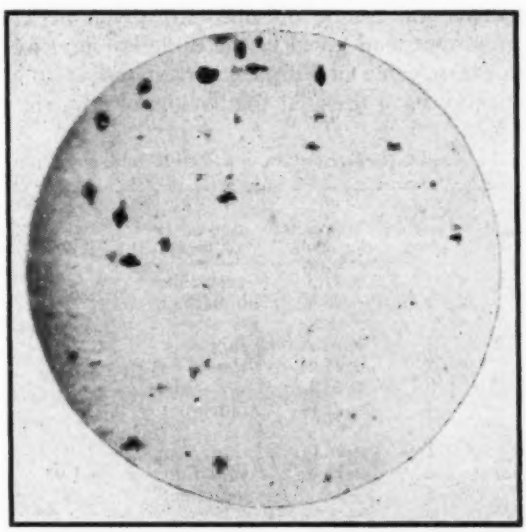

(c)
Stress ±9.1 kg/mm², flecks thin.

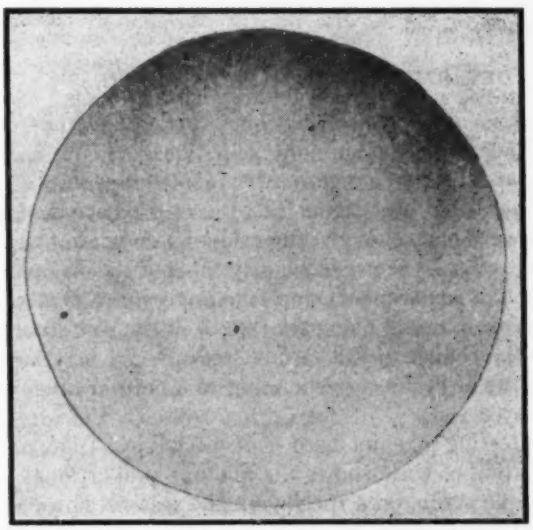

(d)
Stress ±8.4 kg/mm², flecks indistinct.

FIG. 2. Flecks on the surface of a test piece produced by fatigue.

tion of the plating solution, current density, and temperature during the period of deposition. To have the same surface conditions, specimens are carefully polished with emery-paper of fine mesh before plating, and the conditions for deposition are kept constant throughout the investigation. Specimens are prepared by treatments in dilute sulfuric acid and caustic alkali and then receive a preliminary deposit of copper from a cyanide copper vat.

The conditions for deposition used are as follows:

Solution: $CuSO_4 \cdot 5H_2O$ 250 grams
H_2SO_4 80 grams
$ZnSO_4 \cdot 7H_2O$ 0.2 gram
(Added at the end of the operation of deposition)
H_2O 1 liter
Current density: 3 amperes per square decimeter
Temperature: 15°C.

To avoid the disarrangement of the results, the solution of zinc sulfate is always added in the plating solution just one minute before the operation of deposition comes to an end, and the solution is agitated in the same manner during the last minute. The thickness of the plating has been taken to be moderate, namely, almost 0.015 mm, keeping the current density and the duration for deposition in exactly the same way. However, the thickness of the plating is not likely to affect the results appreciably.

TABLE I.

No. of test piece	Torque (kg/mm²)	S (mm)	τ_p (kg/mm²)	Mean value of τ_p (kg/mm²)
1	±22.8	18.0	±8.73	±8.70
2	±25.6	23.1	±8.66	

DETERMINATION OF PROPER STRESS

A torsional fatigue test has been carried out to determine the proper value for cyclic shearing stress, at which an abrupt change occurs in the appearance of flecks produced by fatigue. Test pieces used are conical rods of carbon steel, with dimensions as shown in Fig. 1. For test pieces, the use of slightly tapered rods is favorable in this experiment, since the appearance of flecks varies continuously along the length of the rod according to the change of the surface stress, so we may have the status of flecks corresponding to a certain range of stress by a test.

The testing machine used is of mechanical type, and the reading of scale shows the amount proportional to the torque acting on a specimen. The scale is, however, so graduated as to allow the direct reading of the maximum shearing stress for a cylindrical specimen of the diameter 10 mm. Accordingly, the reading for torque is always given in the dimensions of stress, namely, kg/mm². For abbreviation, the limiting value of stress, within which the flecks are not produced by fatigue, will be termed "proper stress" and is denoted by τ_p in this paper. Tests have been done for two test pieces. The distance S from one end to the point corresponding to the proper stress, Fig. 1, is measured by a reading micrometer observing carefully the surface of a test piece. S is measured at four counterpoints in every test piece and their mean value is taken. From the torque acting on the specimen and the diameter of rod corresponding to S, the proper stress has been calculated. In every measurement, the discrepancy between the values of S at the four points remains almost within 0.5 mm, which corresponds to the proper stress of 0.1 kg/mm². The data obtained in connection with the program described are given in Table I, the number of repetitions of the cyclic stress being taken as 5×10^6. From the results in Table I, we shall take for the proper stress the value

$$\tau_p = \pm 8.7 \text{ kg/mm}^2.$$

Figure 2 shows the microphotographs of the flecks produced on the surface of the plating metal by cyclic stress. It may be seen from the figure that when a test piece is subjected to the reversal of stress, the appearance of flecks changes sensitively by a slight variation of the cyclic stress.

STRESS CONCENTRATION FACTOR FOR A CIRCUMFERENTIAL NOTCH

Further tests have been done in the manner described, for test pieces of the diameter 20 mm with a circumferential notch in each. The dimensions of notches are shown in Fig. 3. To have accurate dimensions for the notches, they are checked by plate gauges which have been measured carefully by a Zeiss comparator. The experimental results obtained are given in Table II. The proper load given in the table is found by taking the mean value of torques, corresponding to the two appearances of flecks at the bottom of a notch, the one

TABLE II. The values of α, $r_0=10$ mm, $\rho=2$ mm.

Depth b (mm)	No. of test piece	Torque (kg/mm²)	Appearance of flecks	τ_p' (kg/mm²)	α
1.5	1	±27.3	very thin	±3.36	2.6
	2	±26.4	indistinct		
2.0	1	±24.2	thin	±2.82	3.1
	2	±23.4	thin		
	3	±23.1	very thin		
	4	±22.0	indistinct		
3.0	1	±16.0	thin	±1.93	4.5
	2	±15.6	very thin		
	3	±15.3	indistinct		
4.0	1	±10.6	thin	±1.26	6.9
	2	±10.2	very thin		
	3	± 9.9	indistinct		
	4	± 9.7	indistinct		

of which is very thin and the other indistinct. Figures for proper load shown in the table, however, are the ones reduced to those for a rod of the diameter 10 mm. They are denoted by τ_p' and are given in the dimensions of stress according to the reading of scale used.

If α is the stress concentration factor for a notch, then

$$\alpha=\tau_p/\tau_p', \tag{1}$$

since, according to the consideration described, the value of stress within which the flecks will not be produced is characteristic for the plating metal and is independent of the shape of the specimen. The values of α, calculated from Eq. (1), are also given in the same table.

The formulas for the estimation of stress concentration factor, where the depth and the radius of a notch are specified, have been introduced by several previous writers for convenience of practical use.[1] Some of them hold exactly in the extreme case where the dimensions of a notch are infinitely small in comparison with those of the shaft. According to the deriving process for the formulas, however, it is obvious that these formulas do not hold exactly for moderate dimensions of a notch, which are likely to be those of practical importance. In the previous paper, the author pointed out that for the particular case of a semicircular notch the author's

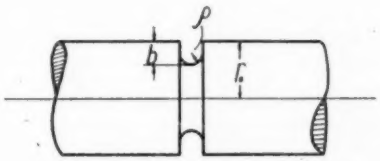

FIG. 3. Dimensions of notches.

$r_0=10mm$ $\rho=2mm$,
$b=1.5mm$, $2mm$, $3mm$, $4mm$.

formula agreed most closely with the exact values given by Willers[2] in the range of moderate dimensions of the notch and that the formula obtained by Sonntag followed it. These two formulas for the stress concentration factor are as follows:

$$\text{Author's}\quad \alpha=\frac{1+(b/\rho)^{\frac{1}{2}}}{(1-b/r_0)^2}, \tag{2}$$

$$\text{Sonntag's}\quad \alpha=\frac{r_0^2(r_0-b+\rho)^2(b+\rho)+r_0^2\rho^2(b-\rho)}{\rho(r_0-b)^3(r_0-b+2\rho)}, \tag{3}$$

[1] R. Sonntag, Z. angew. Math. Mech. **9**, 3 (1929). H. Neuber, *Kerbspannungslehre* (Julius Springer, Berlin, 1937), p. 127. H. Okubo, J. Appl. Mech. **19**, 16 (1952).

[2] F. A. Willers, Z. Math. Phys. **55**, 251 (1907).

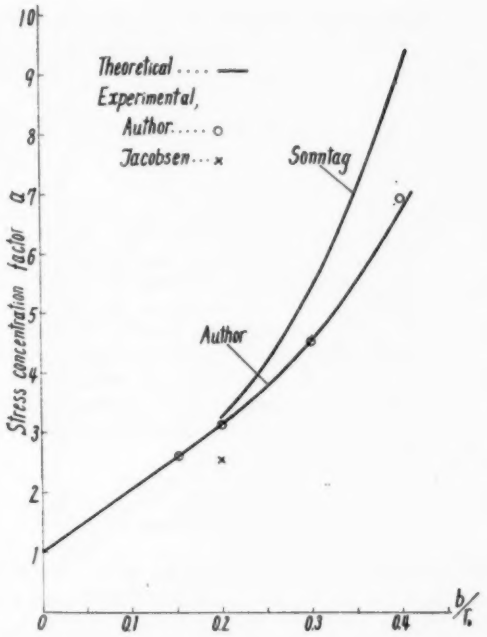

FIG. 4. Relation between the stress concentration factor and depth of notch, when $\rho/r_0=0.2$.

where r_0 is the radius of the shaft and b, ρ represent the depth and radius of a notch, respectively. The values of α given by these formulas, almost agree in the particular case of a semicircular notch, but they become considerably different with the increase of the ratio of b to ρ. The discrepancy, for larger value of b/ρ, is too large even for practical use, and yet theoretical justification for the two would not be easily found, since the two formulas are approximate ones, derived from somewhat different assumptions, respectively. Accordingly, the experimental data obtained in this paper may be a good reference for the justification of the two formulas. The values of α taken from Table II, together with those calculated from Eqs. (2) and (3), are shown in Fig. 4. It may be seen from the figure that the experimental results obtained here are in good agreement with theoretical ones, calculated from the author's formula. For the experimental determination of α, an electrical analogy has been used previously by Jacobsen.[3] The value for a shaft with fillet taken from his results is also shown in the same figure; it is rather small in comparison with the corresponding one obtained here.

A grant-in-aid of scientific research was given for this study by the Education Department of Japan. The author wishes to take this opportunity to thank Mr. S. Momma, his assistant, for his help in this study.

[3] L. S. Jacobsen, Trans. Am. Soc. Mech. Engrs. **47**, 619 (1925).

Solution of Electromagnetic Scattering Problems as Power Series in the Ratio (Dimension of Scatterer)/Wavelength

A. F. STEVENSON
Departments of Mathematics and Physics, Wayne University, Detroit, Michigan
(Received May 1, 1953)

It is shown that the scattered field and the field inside the body can be expressed formally as power series in the above ratio, the calculation of successive terms in the series requiring the solution of standard problems in potential theory, together with the evaluation of certain potential integrals, so that the process can be carried as far as desired if Laplace's equation can be solved in the coordinate system appropriate for the body. The convergence of the series for the scattered field becomes progressively worse as we recede from the body, but an alternative expression for the field, also proceeding in powers of the same parameter, gives a representation which is valid everywhere except in the immediate neighborhood of the body (in particular, in the wave zone) and which does not suffer from this defect. The case of a perfect conductor, or diffraction through a hole in a perfectly conducting screen, can be treated as particular cases of the general theory. The paper can be regarded as an extension of Rayleigh's work, which confines itself to the first terms in the series.

1. INTRODUCTION

THE problem of the scattering of an electromagnetic wave by a body of given shape and electromagnetic constants can be solved rigorously only in very special cases, and even then simplifications are usually necessary before the solution can be reduced to calculable form. It was shown long ago by Rayleigh[1] that if the dimensions of the body are small compared with the wavelength, a first approximation to the solution can be obtained by solving the corresponding problem for *static* electric and magnetic fields, so that only a solution of Laplace's equation, rather than the general system of Maxwell's equations, is involved.

The present paper can be regarded as an extension of Rayleigh's work. It is shown that a formal solution can be obtained as a power series in the ratio (dimension/wavelength), each term in the series requiring only the solution of standard problems in potential theory, together with the evaluation of certain potential integrals. Thus, if the scattering body is such that Laplace's equation can be solved in the appropriate coordinate system, the series can be continued as far as desired, though the calculation of successive terms becomes increasingly complicated.

In solving the problems relating to Laplace's equation a "condition at infinity" must, as always, be imposed in order to make the problem mathematically determinate, and it is shown how this condition can be unambiguously obtained. It may be remarked that in Rayleigh's original paper[1] this point is not entirely clear.

Probably the most general shaped body of practical interest in three dimensions for which Laplace's equation can be solved is an ellipsoid, and in an accompanying paper the first three terms in the series are calculated for this case. In two-dimensional problems, however, the range of soluble problems is greatly increased, since one can then use the methods of complex variable theory. A similar, though simpler, analysis applies to the scattering of acoustic, instead of electromagnetic, waves.

It is known that the problem of diffraction through a hole in a perfectly conducting screen can be solved if the complementary problem of scattering by a perfectly conducting lamina in the shape of the hole can be solved. The method therefore gives the solution of the diffraction problem as a series in the ratio (dimension of hole)/wavelength, if Laplace's equation can be solved for the lamina.

Tai[2] has recently considered a series solution for the scattering problem, for the particular case of a perfectly conducting spheroid with the incident wave propagated in the direction of the axis of symmetry, the method used being somewhat different. Tai's paper is referred to briefly at the end of Sec. 3, and some features of it are criticized.

2. CALCULATION OF SUCCESSIVE TERMS IN THE SERIES

We consider scattering by a body, whose surface is denoted by S, which is characterized by a (in general complex) dielectric constant ϵ and a permeability μ and confine ourselves to a steady state with a time factor $\exp(-i\omega t)$. The constant ϵ is related to the ordinary dielectric constant ϵ' and the conductivity σ by

$$\epsilon=\epsilon'+4\pi i\sigma/\omega.$$

The external medium is taken to be a vacuum.[3]

Let the given exciting field (which need not necessarily be a plane wave) be denoted by $\mathbf{E}^{(0)}$, $\mathbf{H}^{(0)}$, the scattered field by $\mathbf{E}$, $\mathbf{H}$ (so that the total field outside S is $\mathbf{E}^{(0)}+\mathbf{E}$, $\mathbf{H}^{(0)}+\mathbf{H}$), and the field inside S by $\mathbf{E}^{(i)}$, $\mathbf{H}^{(i)}$. Mathematically, the problem is then to solve the

[1] Lord Rayleigh, Phil. Mag. 44, 28 (1897).

[2] C. T. Tai, Trans. Inst. Radio Engrs. PGAP-1, p. 13 (February, 1952).

[3] The case where the external medium is characterized by constants ϵ_0, μ_0 can be deduced by replacing ϵ, μ, k of the text by ϵ/ϵ_0, μ/μ_0, $k(\epsilon_0\mu_0)^{\frac{1}{2}}$, respectively, and multiplying all electric fields (including the exciting field) by $(\epsilon_0)^{-\frac{1}{2}}$ and all magnetic fields by $(\mu_0)^{-\frac{1}{2}}$.

Maxwell equations

$$\begin{aligned} \text{curl}\mathbf{E}&=ik\mathbf{H}, & \text{curl}\mathbf{H}&=-ik\mathbf{E},\\ \text{div}\mathbf{E}&=0, & \text{div}\mathbf{H}&=0, \end{aligned} \tag{2.1a}$$

outside the body, and

$$\begin{aligned} \text{curl}\mathbf{E}^{(i)}&=ik\mu\mathbf{H}^{(i)}, & \text{curl}\mathbf{H}^{(i)}&=-ik\epsilon\mathbf{E}^{(i)},\\ \text{div}\mathbf{E}^{(i)}&=0, & \text{div}\mathbf{H}^{(i)}&=0, \end{aligned} \tag{2.1b}$$

inside the body, where

$$k=\omega/c=2\pi/\lambda,$$

λ being the wavelength in vacuum, together with the following boundary conditions, to be satisfied on S:

$$\mathbf{n}\times(\mathbf{E}-\mathbf{E}^{(i)})=-\mathbf{n}\times\mathbf{E}^{(0)}, \tag{2.2}$$

$$\mathbf{n}\cdot(\mathbf{E}-\epsilon\mathbf{E}^{(i)})=-\mathbf{n}\cdot\mathbf{E}^{(0)}, \tag{2.3}$$

$$\mathbf{n}\times(\mathbf{H}-\mathbf{H}^{(i)})=-\mathbf{n}\times\mathbf{H}^{(0)}, \tag{2.4}$$

$$\mathbf{n}\cdot(\mathbf{H}-\mu\mathbf{H}^{(i)})=-\mathbf{n}\cdot\mathbf{H}^{(0)}, \tag{2.5}$$

where $\mathbf{n}$ denotes a unit vector along the outward normal to S; and subject further to the condition that the $(\mathbf{E}, \mathbf{H})$ field is that of an outgoing wave at infinity.

The "divergence" equations in (2.1) follow from the remaining Maxwell equations, and the boundary conditions (2.3), (2.5) follow from Eqs. (2.2), (2.4) and the Maxwell equations; but we shall have occasion to use these additional equations and boundary conditions explicitly. We note that, from Eqs. (2.3), (2.5), (2.1b), it follows that

$$\int\mathbf{n}\cdot\mathbf{E}dS=0, \quad \int\mathbf{n}\cdot\mathbf{H}dS=0. \tag{2.6}$$

In Eq. (2.6), and throughout the paper unless the contrary is stated, $\int\cdots dS$ means a surface integral taken over S.

We now assume that the required fields, and also the exciting field, are expansible in powers of k, in the form

$$\begin{aligned} \mathbf{E}&=\sum_p\mathbf{E}_p(ik)^p, & \mathbf{H}&=\sum_p\mathbf{H}_p(ik)^p,\\ \mathbf{E}^{(i)}&=\sum_p\mathbf{E}_p^{(i)}(ik)^p, & \mathbf{H}^{(i)}&=\sum_p\mathbf{H}_p^{(i)}(ik)^p,\\ \mathbf{E}^{(0)}&=\sum_p\mathbf{E}_p^{(0)}(ik)^p, & \mathbf{H}^{(0)}&=\sum_p\mathbf{H}_p^{(0)}(ik)^p, \end{aligned} \tag{2.7}$$

the summations being, in each case, from 0 to ∞. $\mathbf{E}_p^{(0)}$, $\mathbf{H}_p^{(0)}$ are, of course, known functions. The series are probably convergent at all points in their respective regions; but it will appear later that the convergence of the series for the *scattered* field $\mathbf{E}$, $\mathbf{H}$ becomes progressively worse as we recede from S. In particular, Eqs. (2.7) gives no indication of the behavior of the scattered field in the wave zone. We shall, however, give in Sec. 3 alternative series for the scattered field which are valid everywhere outside a sphere which completely surrounds S, and which do not suffer from this disadvantage. The series of Sec. 3, combined with Eqs. (2.7), then give a representation of the field everywhere which proceeds essentially in powers of $kl=2\pi l/\lambda$, where l denotes, say, the maximum linear dimension of the body.[3a]

Substituting Eqs. (2.7) in (2.1), the Maxwell equations become

$$\text{curl}\mathbf{E}_0=0, \quad \text{curl}\mathbf{H}_0=0, \tag{2.8a, b}$$

$$\text{curl}\mathbf{E}_p=\mathbf{H}_{p-1}, \quad \text{curl}\mathbf{H}_p=-\mathbf{E}_{p-1}\ (p>0), \tag{2.9a, b}$$

$$\text{div}\mathbf{E}_p=0, \quad \text{div}\mathbf{H}_p=0, \tag{2.10a, b}$$

$$\text{curl}\mathbf{E}_0^{(i)}=0, \quad \text{curl}\mathbf{H}_0^{(i)}=0, \tag{2.11a, b}$$

$$\text{curl}\mathbf{E}_p^{(i)}=\mu\mathbf{H}_{p-1}^{(i)}, \quad \text{curl}\mathbf{H}_p^{(i)}=-\epsilon\mathbf{E}_{p-1}^{(i)}\ (p>0), \tag{2.12a, b}$$

$$\text{div}\mathbf{E}_p^{(i)}=0, \quad \text{div}\mathbf{H}_p^{(i)}=0, \tag{2.13a, b}$$

while the boundary conditions (2.2)–(2.5) become

$$\mathbf{n}\times(\mathbf{E}_p-\mathbf{E}_p^{(i)})=-\mathbf{n}\times\mathbf{E}_p^{(0)}, \tag{2.14}$$

$$\mathbf{n}\cdot(\mathbf{E}_p-\epsilon\mathbf{E}_p^{(i)})=-\mathbf{n}\cdot\mathbf{E}_p^{(0)}, \tag{2.15}$$

$$\mathbf{n}\times(\mathbf{H}_p-\mathbf{H}_p^{(i)})=-\mathbf{n}\times\mathbf{H}_p^{(0)}, \tag{2.16}$$

$$\mathbf{n}\cdot(\mathbf{H}_p-\mu\mathbf{H}_p^{(i)})=-\mathbf{n}\cdot\mathbf{H}_p^{(0)}. \tag{2.17}$$

Further, from (2.6),

$$\int\mathbf{n}\cdot\mathbf{E}_pdS=0, \quad \int\mathbf{n}\cdot\mathbf{H}_pdS=0. \tag{2.18a, b}$$

Equations (2.8)–(2.18) give, for $p=0, 1, 2, \cdots$, a succession of differential equations and boundary conditions for the determination of the successive terms in the series (2.7). To make the problem determinate, a condition at infinity for the scattered field $\mathbf{E}$, $\mathbf{H}$ is required. We shall use the condition that this field represents an outgoing wave at infinity in the following way:

The field $\mathbf{E}$, $\mathbf{H}$ is given in terms of its values on S by[4]

$$4\pi\mathbf{E}=ik\int(\mathbf{n}\times\mathbf{H})fdS+\text{curl}\int(\mathbf{n}\times\mathbf{E})fdS-\nabla\int\mathbf{n}\cdot\mathbf{E}fdS, \tag{2.19}$$

$$4\pi\mathbf{H}=-ik\int(\mathbf{n}\times\mathbf{E})fdS+\text{curl}\int(\mathbf{n}\times\mathbf{H})fdS-\nabla\int\mathbf{n}\cdot\mathbf{H}fdS, \tag{2.20}$$

[3a] The coefficients of the powers of kl will, of course, be functions of ϵ, μ (as well as of other dimensionless constants entering into the problem). A consideration of the way in which these constants enter into the successive terms of the series shows that, if $|\epsilon|$, μ are not of the order unity, the rapidity of convergence of the series is determined by the magnitude of $kl|(\epsilon\mu)^{\frac{1}{2}}|$, rather than of kl itself—i.e., the wavelength *in the body*, rather than the wavelength in vacuum, must be considered.

[4] J. A. Stratton, *Electromagnetic Theory* (McGraw-Hill Book Company, Inc., New York, 1941), p. 466. Our expressions are

where $f=\exp(ikr)/r$, r denoting the distance from the field point to a point on S. Substituting Eq. (2.7) in Eqs. (2.19) and (2.20), expanding f in powers of k, and equating coefficients of like powers of k, we have

$$4\pi\mathbf{E}_p=\sum_{j=0}^{p-1}\int(\mathbf{n}\times\mathbf{H}_{p-j-1})r^{j-1}/j!dS+\text{curl}\sum_{j=0}^{p}\int(\mathbf{n}\times\mathbf{E}_{p-j})r^{j-1}/j!dS-\nabla\sum_{j=0}^{p}\int(\mathbf{n}\cdot\mathbf{E}_{p-j})r^{j-1}/j!dS, \quad (2.21)$$

$$4\pi\mathbf{H}_p=-\sum_{j=0}^{p-1}\int(\mathbf{n}\times\mathbf{E}_{p-j-1})r^{j-1}/j!dS+\text{curl}\sum_{j=0}^{p}\int(\mathbf{n}\times\mathbf{H}_{p-j})r^{j-1}/j!dS-\nabla\sum_{j=0}^{p}\int(\mathbf{n}\cdot\mathbf{H}_{p-j})r^{j-1}/j!dS. \quad (2.22)$$

The first summations in Eqs. (2.21) and (2.22) are absent if $p=0$ ($0!=1$). It will be shown that, with the addition of (2.21) and (2.22), the problem of solving Eqs. (2.8)–(2.18) for the successive terms in the series becomes completely determinate.

Consider first the problem of finding the first terms in the series for the electric field. By Eqs. (2.8a), (2.10a), (2.11a), (2.13a), (2.14), (2.15), (2.18a), these are given by

$$\mathbf{E}_0=\nabla V_0, \quad \mathbf{E}_0^{(i)}=\nabla V_0^{(i)}, \quad (2.23)$$

where V_0, $V_0^{(i)}$ are harmonic functions to be found, which satisfy the boundary conditions

$$\mathbf{n}\times\nabla(V_0-V_0^{(i)})=-\mathbf{n}\times\mathbf{E}_0^{(0)}, \quad (2.24)$$

$$\frac{\partial}{\partial n}(V_0-\epsilon V_0^{(i)})=-\mathbf{n}\cdot\mathbf{E}_0^{(0)}, \quad (2.25)$$

on S, and the condition

$$\int\frac{\partial V_0}{\partial n}dS=0. \quad (2.26)$$

Since the exciting field satisfies equations analogous to Eqs. (2.8) and (2.10), we can put

$$\mathbf{E}_0^{(0)}=\nabla V_0^{(0)},$$

where $V_0^{(0)}$ is some known harmonic function, so that Eq. (2.24) becomes (to within an additive constant which can be absorbed in $V_0^{(0)}$)

$$V_0-V_0^{(i)}=-V_0^{(0)}, \quad (2.27)$$

and Eq. (2.25) becomes

$$\frac{\partial}{\partial n}(V_0-\epsilon V_0^{(i)})=-\frac{\partial}{\partial n}V_0^{(0)}. \quad (2.28)$$

Further, substituting Eq. (2.23) in (2.21) with $p=0$, we have

$$4\pi\mathbf{E}_0=\text{curl}\int(\mathbf{n}\times\nabla V_0)/rdS-\nabla\int\frac{\partial V_0}{\partial n}\Big/rdS. \quad (2.29)$$

Now it is shown in Appendix I that, if V is any function which is well behaved on S and in the immediate neighborhood exterior to S, then

$$\text{curl}\int(\mathbf{n}\times\nabla V)/rdS=\nabla\int V\frac{\partial}{\partial n}(1/r)dS. \quad (2.30)$$

Hence (2.29) gives

$$4\pi\mathbf{E}_0=\nabla\int\left[V_0\frac{\partial}{\partial n}\left(\frac{1}{r}\right)-\frac{\partial V_0}{\partial n}\frac{1}{r}\right]dS. \quad (2.31)$$

Equation (2.31) expresses $\mathbf{E}_0$ as the gradient of an *external* harmonic function (i.e., one which vanishes at infinity to an order $1/r$ or higher), so that the function V_0 in Eq. (2.23) is also an external harmonic function (apart from an additive constant which can be dropped).

The problem of determining the harmonic functions V_0, $V_0^{(i)}$, of which V_0 is an external function and $V_0^{(i)}$ an internal function, which satisfy the boundary conditions, Eqs. (2.27) and (2.28), is now a standard problem in potential theory, the additive constant in $V_0^{(0)}$ being fixed by the condition (2.26). This is, in fact, just the problem of determining the *static* electric fields inside and outside the body, the exciting electric field being replaced by its static limiting value obtained by making $k\to 0$. This is the principle enunciated by Rayleigh,[1] who took it for granted that the external field $\mathbf{E}_0$ (or the potential V_0) vanishes at infinity. No reason was given for this, although it was shown that the continuation of this field into the wave zone satisfied the outgoing-wave condition (see Sec. 3). It was not, however, shown that no other solution for $\mathbf{E}_0$ would satisfy this condition. The above demonstration, by means of Eq. (2.21), that $\mathbf{E}_0$ must vanish at infinity, seems to be more satisfactory. The use of (2.21), (2.22) is particularly advantageous for the higher terms in the series, as we shall see.

Similarly, from Eqs. (2.8b), (2.10b), (2.11b), (2.13b), (2.16), (2.17), (2.18b), and use of (2.22) with $p=0$, we find for the first terms in the series for the magnetic field

$$\mathbf{H}_0=\nabla U_0, \quad \mathbf{H}_0^{(i)}=\nabla U_0^{(i)}, \quad (2.32)$$

where U_0, $U_0^{(i)}$ are, respectively, an external and an internal harmonic function, which satisfy the boundary

slightly different from Stratton's but are easily deducible from his. Note that our direction for $\mathbf{n}$ is the opposite to Stratton's. The outgoing wave condition at infinity is required to deduce Eqs. (2.19) and (2.20) for an external region, though this fact is not mentioned by Stratton. In applying Eqs. (2.19) and (2.20), it will be assumed, where necessary, that the field point is not actually *on* S; but the final results are always valid for this limiting case.

conditions

$$U_0 - U_0^{(i)} = -U_0^{(0)}, \tag{2.33}$$

$$\frac{\partial}{\partial n}(U_0 - \mu U_0^{(i)}) = -\frac{\partial}{\partial n}U_0^{(0)} \tag{2.34}$$

on S, where $U_0^{(0)}$ is the potential of the static part of the exciting magnetic field ($\mathbf{H}_0^{(0)} = -\nabla U_0^{(0)}$), the additive constant to $U_0^{(0)}$ being determined by the condition

$$\int \frac{\partial U_0}{\partial n} dS = 0. \tag{2.35}$$

The problem defined by Eqs. (2.33)–(2.35) is again a standard problem in potential theory and is just the problem of determining the static magnetic fields inside and outside the body under the excitation of the static part of the exciting magnetic field.

Consider now the problem of determining the subsequent terms in the series (2.7). Suppose that we have found the first p terms, so that $\mathbf{E}_0, \cdots, \mathbf{E}_{p-1}, \mathbf{E}_0^{(i)}, \cdots, \mathbf{E}_{p-1}^{(i)}, \mathbf{H}_0, \cdots, \mathbf{H}_{p-1}, \mathbf{H}_0^{(i)}, \cdots, \mathbf{H}_{p-1}^{(i)}$ are known, and we wish to determine the $(p+1)$th terms for the electric field $\mathbf{E}_p, \mathbf{E}_p^{(i)}$. Suppose, for the moment, that we can find *some* solution of Eqs. (2.9a) and (2.12a) for $\mathbf{E}_p, \mathbf{E}_p^{(i)}$, say $\mathbf{E}_p = \mathbf{F}_p$, $\mathbf{E}_p^{(i)} = \mathbf{F}_p^{(i)}$, where $\mathbf{F}_p, \mathbf{F}_p^{(i)}$ are well behaved in the regions exterior and interior to S, respectively (but where $\mathbf{F}_p$ need not necessarily vanish at infinity). Suppose, further, that these solutions satisfy the equations

$$\operatorname{div}\mathbf{F}_p = 0, \quad \operatorname{div}\mathbf{F}_p^{(i)} = 0. \tag{2.36a, b}$$

Then (2.9a), (2.10a), (2.12a), (2.13a) show that

$$\mathbf{E}_p = \mathbf{F}_p + \nabla V_p, \quad \mathbf{E}_p^{(i)} = \mathbf{F}_p^{(i)} + \nabla V_p^{(i)}, \tag{2.37a, b}$$

where $V_p, V_p^{(i)}$ are harmonic functions to be found.

Substituting Eqs. (2.37a) in (2.21) and using (2.30), we have

$$\mathbf{E}_p = \mathbf{F}_p' + \nabla V_p', \tag{2.38}$$

where

$$\begin{aligned} 4\pi\mathbf{F}_p' = &\sum_{j=0}^{p-1} \int (\mathbf{n}\times\mathbf{H}_{p-j-1}) r^{j-1}/j!\, dS \\ &+ \operatorname{curl} \sum_{j=1}^{p} \int (\mathbf{n}\times\mathbf{E}_{p-j}) r^{j-1}/j!\, dS \\ &- \nabla \sum_{j=1}^{p} \int (\mathbf{n}\cdot\mathbf{E}_{p-j}) r^{j-1}/j!\, dS \\ &+ \operatorname{curl} \int (\mathbf{n}\times\mathbf{F}_p)/r\, dS \\ &- \nabla \int (\mathbf{n}\cdot\mathbf{F}_p)/r\, dS, \end{aligned} \tag{2.39}$$

$$4\pi V_p' = \int \left[V_p \frac{\partial}{\partial n}\left(\frac{1}{r}\right) - \frac{\partial V_p}{\partial n}\frac{1}{r} \right] dS. \tag{2.40}$$

According to our supposition, $\mathbf{F}_p'$, defined by Eq. (2.39), is a *known* function, while Eq. (2.40) shows that V_p' is an *external* harmonic function.[5] Further, the boundary conditions (2.14) and (2.15) become

$$\mathbf{n}\times\nabla(V_p' - V_p^{(i)}) = -\mathbf{n}\times(\mathbf{F}_p' - \mathbf{F}_p^{(i)} + \mathbf{E}_p^{(0)}), \tag{2.41}$$

$$\frac{\partial}{\partial n}(V_p' - \epsilon V_p^{(i)}) = -\mathbf{n}\cdot(\mathbf{F}_p' - \epsilon\mathbf{F}_p^{(i)} + \mathbf{E}_p^{(0)}). \tag{2.42}$$

Equation (2.41) determines $V_p' - V_p^{(i)}$ to within an additive constant, say,

$$V_p' - V_p^{(i)} = W_p. \tag{2.43}$$

The finding of the function W_p from (2.41) requires only the integration of functions of position on S and should cause no difficulty in the case where Laplace's equation is soluble in the appropriate coordinate system.[6] The condition of consistency of Eqs. (2.41) is

$$\mathbf{n}\cdot\operatorname{curl}(\mathbf{F}_p' - \mathbf{F}_p^{(i)} + \mathbf{E}_p^{(0)}) = 0$$

on S. But

$$\begin{aligned} \operatorname{curl}\mathbf{F}_p' &= \mathbf{H}_{p-1}, \\ \operatorname{curl}\mathbf{F}_p^{(i)} &= \mu\mathbf{H}_{p-1}^{(i)}, \\ \operatorname{curl}\mathbf{E}_p^{(0)} &= \mathbf{H}_{p-1}^{(0)}, \end{aligned}$$

so that the required condition is satisfied by virtue of Eq. (2.17).

The finding of external and internal harmonic functions $V_p', V_p^{(i)}$ which satisfy the boundary conditions (2.42), (2.43) is now a standard problem in potential theory quite analogous to that encountered in finding the first terms in the series. The additive constant to the function W_p in (2.43) is determined by the condition (2.18a). Having found $V_p', V_p^{(i)}$, the $(p+1)$th terms in the series for the electric field are given by Eqs. (2.37b), (2.38), and (2.39).

We see from (2.37a), (2.38) that $\mathbf{F}_p$ and $\mathbf{F}_p'$ can only differ by the gradient of a harmonic function, so that in calculating $\mathbf{F}_p' - \mathbf{F}_p$ from (2.39), it is sufficient to retain only those terms which do not vanish at infinity in both $\mathbf{F}_p'$ and $\mathbf{F}_p$; the remaining terms can be absorbed in V_p'. We further see that it is actually not necessary to suppose that $\mathbf{F}_p$ satisfies the condition (2.36a): the same results follow as before, except that V_p is not now a harmonic function and consequently the complete expression (2.39) for F_p' must be used.[7] Usually, however, it will be simpler to make our solutions $\mathbf{F}_p, \mathbf{F}_p^{(i)}$ satisfy (2.36a, b).

[5] By a well-known theorem in potential theory, it follows from Eq. (2.40) that $V_p' = V_p$ if V_p is also an external harmonic function. This cannot be assumed in advance, however, and is in general not the case.

[6] In any case, the problem is reduced to finding the appropriate solutions of Laplace's equation. We might, alternatively, assume solutions for $V_p', V_p^{(i)}$ containing adjustable constants and then use (2.41), (2.42) directly.

[7] We can also dispense with the condition (2.36b) for $\mathbf{F}_p^{(i)}$ by putting $\mathbf{E}_p^{(i)} = \mathbf{F}_p'^{(i)} + \nabla_p'^{(i)}$, where $V_p'^{(i)}$ is an internal harmonic function and $\mathbf{F}_p'^{(i)}$ is given by an expression similar to that for $\mathbf{F}_p'$ in (2.39), using internal instead of external fields.

For the second and third terms in the series ($p=1, 2$), it is not necessary to find $\mathbf{F}_p'$ from (2.39); we can proceed more simply as follows. It can be shown from Eq. (2.21) (see Appendix II) that $\mathbf{E}_p$ vanishes at infinity for $p=1, 2$. Hence, if our solution $\mathbf{F}_p$ of (2.9a) also vanishes at infinity and satisfies (2.36a), it follows that, for $p=1, 2$, the function V_p in (2.37a) is an external harmonic function. Thus we can use (2.37a) instead of (2.38) and work with V_p instead of V_p'. The terms in the series beyond the third do not vanish at infinity, and use of Eq. (2.39) (or something equivalent) cannot be avoided.

The magnetic field is treated in exactly the same way. The $(p+1)$th terms in the series are given by

$$\mathbf{H}_p=\mathbf{G}_p'+\nabla U_p', \quad \mathbf{H}_p^{(i)}=\mathbf{G}_p^{(i)}+\nabla U_p^{(i)},$$

where

$$4\pi\mathbf{G}_p'=-\sum_{j=0}^{p-1}\int(\mathbf{n}\times\mathbf{E}_{p-j-1})r^{j-1}/j!dS$$

$$+\operatorname{curl}\sum_{j=1}^{p}\int(\mathbf{n}\times\mathbf{H}_{p-j})r^{j-1}/j!dS$$

$$-\nabla\sum_{j=1}^{p}\int(\mathbf{n}\cdot\mathbf{H}_{p-j})r^{j-1}/j!dS$$

$$+\operatorname{curl}\int(\mathbf{n}\times\mathbf{G}_p)/rdS-\nabla\int(\mathbf{n}\cdot\mathbf{G}_p)/rdS,$$

and $\mathbf{H}_p=\mathbf{G}_p$, $\mathbf{H}_p^{(i)}=\mathbf{G}_p^{(i)}$ are particular solutions of (2.9b), (2.12b), respectively, which satisfy

$$\operatorname{div}\mathbf{G}_p=0, \quad \operatorname{div}\mathbf{G}_p^{(i)}=0.$$

The functions U_p', $U_p^{(i)}$ are, respectively, an external and an internal harmonic function which satisfy the boundary conditions

$$\begin{aligned}&\mathbf{n}\times\nabla(U_p'-U_p^{(i)})=-\mathbf{n}\times(\mathbf{G}_p'-\mathbf{G}_p^{(i)}+\mathbf{H}_p^{(0)}),\\&\frac{\partial}{\partial n}(U_p'-\mu U_p^{(i)})=-\mathbf{n}\cdot(\mathbf{G}_p'-\mu\mathbf{G}_p^{(i)}+\mathbf{H}_p^{(0)})\end{aligned}\qquad(2.44)$$

on S. This gives a similar problem in potential theory to that encountered in dealing with the electric field, and quite similar remarks apply. Equation (2.44) determines $U_p'-U_p^{(i)}$ to within an additive constant which is fixed by (2.18b).

Actually, it is not necessary to find both the electric and magnetic fields separately. For the Maxwell equations (2.1) and the boundary conditions (2.2)–(2.5) are invariant under the substitutions

$$\mathbf{E}\to\mathbf{H}, \quad \mathbf{H}\to-\mathbf{E}, \quad \epsilon\leftrightarrow\mu. \qquad(2.45)$$

Hence if we have found the electric field (say) with a given exciting field $\mathbf{E}^{(0)}$, $\mathbf{H}^{(0)}$, it is only necessary to write $\mathbf{H}^{(0)}$, $-\mathbf{E}^{(0)}$ in place of $\mathbf{E}^{(0)}$, $\mathbf{H}^{(0)}$ for the exciting field, and then carry out the substitutions (2.45) to pass from the electric to the magnetic fields (scattered and internal) or vice versa. Thus we can find, say, $\mathbf{E}_0$, $\mathbf{H}_1$, $\mathbf{E}_2$, $\cdots$ in succession and then find $\mathbf{H}_0$, $\mathbf{E}_1$, $\mathbf{H}_2$, $\cdots$ by means of this principle (and similarly for the internal field).

We have thus shown that the terms in the series (2.7) can be calculated successively as far as desired, each term requiring only the solution of standard problems in potential theory, together with the evaluation of integrals such as those occurring in (2.39) and the finding of particular solutions of equations such as (2.9) and (2.12) which satisfy (2.36). As regards the integrals in (2.39), we see that they are all of the form

$$\int\phi r^m dS, \qquad(2.46)$$

where ϕ is a known function of position on S, determined by the preceding terms in the series. If m is even, we can express r^m as a polynomial in the Cartesian coordinates of the field point and a point in the domain of integration, so that Eq. (2.46) can be expressed as a linear combination of integrals of the form $\int\phi x^\alpha y^\beta dS$, etc., where α, β are positive integers. The evaluation of such integrals should present no difficulty in the case where Laplace's equation is soluble in the coordinate system appropriate to S. In any case, our solution is expressed in terms of definite integrals (which do not contain a parameter).

On the other hand if m in (2.46) is odd, the integral can, in a similar way, be expressed as a linear combination of integrals of the form

$$\int\phi x^\alpha y^\beta/rdS,$$

etc., which is a potential integral, the evaluation of which can be reduced to a standard problem in potential theory.

The problem of finding a particular solution of Eqs. (2.9) and (2.12) which satisfies (2.36) is dealt with elsewhere,* where it is shown that a solution can always be found by solving a Neumann problem and evaluating certain potential integrals, though volume, rather than surface potential integrals are required in general.

The Case of a Perfect Conductor

The case where the scattering body is a perfect conductor can be treated as a special case of the general one.

* See a forthcoming note in Quart. Appl. Math. There it is pointed out that the solution usually given is not always valid.

In place of Eqs. (2.2)–(2.5), the boundary conditions are now

$$\mathbf{n}\times\mathbf{E}=-\mathbf{n}\times\mathbf{E}^{(0)}, \tag{2.47}$$

$$\mathbf{n}\cdot\mathbf{H}=-\mathbf{n}\cdot\mathbf{H}^{(0)}. \tag{2.48}$$

Now (2.48) follows from (2.5) if we put $\mu=0$, provided that $\mathbf{H}^{(i)}$ remains finite; also (2.47) follows from (2.2), (2.3) by making $|\epsilon|\to\infty$, provided that $\epsilon\mathbf{E}^{(i)}$ remains finite. A consideration of the way in which the successive terms in the series are obtained shows that, if we put $\mu=0$ and then make $|\epsilon|\to\infty$, $\mathbf{H}^{(i)}$ and $\epsilon\mathbf{E}^{(i)}$ *do*, in fact, remain finite. Thus the scattered field in the case of a perfectly conducting body is obtained if, in the general formulas, we put $\mu=0$ and make $|\epsilon|\to\infty$.[8]

Alternatively, we can use the boundary conditions (2.47), (2.48) from the beginning in place of (2.2)–(2.5) and then proceed as before. The determination of successive terms in the series then leads to a Dirichlet problem for the electric field and a Neumann problem for the magnetic field. We cannot now, of course, deduce the magnetic field from the electric (or vice versa) as we can in the general case.

3. THE DISTANT FIELD

It appears from Eqs. (2.21) and (2.22) that the integrals determining $\mathbf{E}_p$, $\mathbf{H}_p$ contain powers of r which increase with p. Consequently, as we recede from the body, the convergence of the series (2.7) for the scattered field becomes worse and worse, independently of the value of kl. In particular, the series (2.7) give no indication of the behavior of the scattered field in the wave zone. We shall now give alternative series for the field, valid outside any sphere completely surrounding the body, which do not suffer from this disadvantage.

The most natural procedure would be to use Eqs. (2.19) and (2.20), which express the field at any point outside S in terms of the field on S. We would then use the series (2.7) for the surface field and, in the wave zone, write in (2.19), (2.20),

$$\frac{\exp(ikr)}{r}=\frac{\exp(ikR)}{R}\exp(-ik\mathbf{r}'\cdot\boldsymbol{\alpha}),$$

where R is the distance of the field point from some fixed origin, $\mathbf{r}'$ the position vector of a point on S, and $\boldsymbol{\alpha}$ a unit vector in the direction of the field point. We can then expand $\exp(-ik\mathbf{r}'\cdot\boldsymbol{\alpha})$ as a series in ik, and hence, on rearranging, express the field in the wave zone as a series in ik multiplied by $\exp(ikR)/R$. The disadvantage of this procedure is that it is then found that to obtain even the first term in the series in the wave zone, it is necessary to know *two* terms in the series (2.7) for the surface field, and, generally, to obtain p terms in the wave zone, we must know $p+1$ terms in the surface field. We thus lose accuracy in carrying through this procedure.

We shall therefore employ an alternative method which is an extension and refinement of Rayleigh's[1] original method. Outside any sphere completely surrounding the body, the scattered field can be expressed as the superposition of an E wave (or TM wave) and an H wave (or TE wave). Using polar coordinates (R,θ,ϕ) with the center of the sphere as origin, the field components for an E wave can be expressed in the form[9]

$$\begin{aligned}
E_R&=\sum S_p\frac{1}{R}h_p(kR),\\
E_\theta&=\sum\frac{1}{p(p+1)}\frac{\partial S_p}{\partial\theta}\frac{1}{R}[kRh_p(kR)]',\\
E_\phi&=\frac{1}{\sin\theta}\sum\frac{1}{p(p+1)}\frac{\partial S_p}{\partial\phi}\frac{1}{R}[kRh_p(kR)]',\\
H_R&=0,\\
H_\theta&=-\frac{ik}{\sin\theta}\sum\frac{1}{p(p+1)}\frac{\partial S_p}{\partial\phi}h_p(kR),\\
H_\phi&=ik\sum\frac{1}{p(p+1)}\frac{\partial S_p}{\partial\theta}h_p(kR),
\end{aligned} \tag{3.1}$$

while for an H wave[9]

$$\begin{aligned}
H_R&=\sum\bar{S}_p\frac{1}{R}h_p(kR),\\
H_\theta&=\sum\frac{1}{p(p+1)}\frac{\partial\bar{S}_p}{\partial\theta}\frac{1}{R}[kRh_p(kR)]',\\
H_\phi&=\frac{1}{\sin\theta}\sum\frac{1}{p(p+1)}\frac{\partial\bar{S}_p}{\partial\phi}\frac{1}{R}[kRh_p(kR)]',\\
E_R&=0,\\
E_\theta&=\frac{ik}{\sin\theta}\sum\frac{1}{p(p+1)}\frac{\partial\bar{S}_p}{\partial\phi}h_p(kR),\\
E_\phi&=-ik\sum\frac{1}{p(p+1)}\frac{\partial\bar{S}_p}{\partial\theta}h_p(kR).
\end{aligned} \tag{3.2}$$

[8] It might be thought that it would be sufficient to make $|\epsilon|$ (or, to be more precise, the imaginary part of ϵ)$\to\infty$, and that the results would then be independent of μ. This must actually be the case; but our method of expansion in powers of k makes it impossible to see what the limit would be: it would be necessary to sum the series before proceeding to the limit and then expand *again* in powers of k. The procedure given here obviates the necessity for summing the series.

[9] Reference 4, pp. 555, 557.

In Eqs. (3.1) and (3.2) the summations are, in each case, with respect to p from 1 to ∞, h_p denotes the spherical Hankel function of the first kind of order p, and S_p, $\bar{S}_p$ are surface harmonics of order p.

In particular, in the wave zone, we have, for an E wave,

$$\left.\begin{aligned} E_\theta = H_\phi &= \frac{\partial P}{\partial \theta}\frac{\exp(ikR)}{R}, \\ E_\phi = -H_\theta &= \frac{1}{\sin\theta}\frac{\partial P}{\partial \phi}\frac{\exp(ikR)}{R}, \end{aligned}\right\} \tag{3.3}$$

where

$$P=\sum \frac{(-i)^p}{p(p+1)}S_p;$$

and for an H wave

$$\left.\begin{aligned} E_\theta = H_\phi &= \frac{1}{\sin\theta}\frac{\partial \bar{P}}{\partial \phi}\frac{\exp(ikR)}{R}, \\ E_\phi = -H_\theta &= -\frac{\partial \bar{P}}{\partial \theta}\frac{\exp(ikR)}{R}, \end{aligned}\right\} \tag{3.4}$$

where

$$\bar{P}=\sum \frac{(-i)^p}{p(p+1)}\bar{S}_p.$$

The scattered field is thus completely determined outside the sphere if the surface harmonics S_p, $\bar{S}_p$ are known. Further, we see that the radial components E_R, H_R in (3.1), (3.2) determine completely the E wave and H wave, respectively.

We shall now suppose that the field components are expanded as power series in k, as in Sec. 2. Consider first the E wave. The expansion of the spherical Hankel function is given by

$$h_p(x)=(-1)^{p+1}2^p i x^{-p-1}\sum_{m=0}^{\infty}\frac{(-1)^m\pi^{\frac{1}{2}}}{m!\Gamma(-p+m+\frac{1}{2})}\left(\frac{x}{2}\right)^{2m}$$

$$+2^{-p-1}x^p\sum_{m=0}^{\infty}\frac{(-1)^m\pi^{\frac{1}{2}}}{m!\Gamma(p+m+\frac{3}{2})}\left(\frac{x}{2}\right)^{2m}, \tag{3.5}$$

or

$$h_p(x)=x^{-p-1}\sum_{m=0}^{\infty}a_{pm}x^m, \tag{3.6}$$

say, where the a_{pm} in Eq. (3.6) can be read off from (3.5). We note that $a_{pm}\neq 0$ if m is even (or zero). In particular

$$a_{10}=-i, \quad a_{20}=-3i, \quad a_{32}=-3i/2. \tag{3.7}$$

The surface harmonics S_p in Eqs. (3.1) will depend on k, and we shall suppose that they are expansible as power series. Since the lowest power of k in the expansion of $h_p(kR)$ is k^{-p-1}, we see from (3.1) that, in order for the field to remain finite as $k\to 0$, the expansion of S_p must start off with k^{p+1} (or a higher power of k). We therefore write

$$S_p=\sum_{m=0}^{\infty}S_p^{(m)}k^{p+m+1}, \tag{3.8}$$

where the $S_p^{(m)}$ are surface harmonics of order p which are independent of k, the superscript m distinguishing different surface harmonics of the same order.

If we now substitute Eq. (3.8) in the first of (3.1), use (3.6), and then rearrange in powers of k, we find, for the E wave,

$$E_R=\sum_{p=0}^{\infty}\sum_{q=3-p}^{\infty}R^{-q}\sum_j a_{j,\,p-m}S_j^{(m)}, \tag{3.9}$$

where

$$j+m=p+q-2, \tag{3.10}$$

and the summation with respect to j is from max $(q-2, 1)$ to $p+q-2$. We now compare this result with that of Sec. 2. Using the notation of (2.7), we have

$$E_R=\sum_{p=0}^{\infty}(ik)^pE_{pR}. \tag{3.11}$$

Suppose, then, that E_{pR} (the radial component of the $(p+1)$th term in the series for **E**) is expanded in the form

$$E_{pR}=\sum_q R^{-q}\sum_j S_j^{(p,\,q)}, \tag{3.12}$$

where $S_j^{(p,q)}$ is a surface harmonic of order j, the first superscript p referring to the power of k and the second superscript q to the power of R. Substituting Eq. (3.12) in (3.11) and comparing with (3.9), we find

$$S_j^{(m)}=i^pS_j^{(p,\,q)}/a_{j,\,p-m}, \tag{3.13}$$

provided that $a_{j,\,p-m}\neq 0$ (in the contrary case, $S_j^{(p,q)}$ must vanish). Thus, knowing the $S_j^{(p,q)}$ from the "near-field" series (2.7), we can find the $S_j^{(m)}$ from (3.13), and hence from (3.8) and (3.1) [or (3.3)] a representation of the E-wave part of the scattered field which proceeds in powers of kl and can be used anywhere outside a sphere completely surrounding the body ("distant-field" series). Moreover, in (3.13) p can have any value such that $p-m\geqslant 0$ and $a_{j,\,p-m}\neq 0$, so that, by using different values of p (or q), checks can be obtained [note that j, m, p, q are connected by (3.10)].

A check is also obtained by noting that the ranges of summation for q, j in (3.12) must be the same as in (3.9).

Further, if we know, say, N terms in the "near-field" series, so that $S_j^{(p,q)}$ is known for $p=0, 1, \cdots, N-1$, then, by putting $p=m$ in (3.13), we can (since $a_{j0}\neq 0$) find $S_j^{(m)}$ for $m=0, 1, \cdots, N-1$. Hence, *if N terms of the "near-field" series are known, N terms of the "distant-field" series are also known.* There is thus no loss of accuracy in passing from the near-field representation to the distant-field representation.

In the wave zone, if Eq. (3.8) be substituted in (3.3) and the result rearranged in powers of k, we find

$$P=\sum_{s=2}^{\infty} k^s \sum_{j=1}^{s-1} \frac{(-i)^j}{j(j+1)} S_j^{(s-j-1)}. \tag{3.14}$$

The first term in the series for the wave-zone field is proportional to k^2, in accordance with the familiar result of Rayleigh. To find the Nth term in the series (3.14) (i.e., the term proportional to k^{N+1}), we must calculate $S_j^{(N-j)}$ for $j=1, \cdots, N$. These surface harmonics can all be found from Eq. (3.13) by putting $q=3$ or 4 according as j is odd or even (since $a_{jm}\neq 0$ if m is even). Thus, taking account of (3.10),

$$\begin{aligned} S_j^{(N-j)} &= i^{N-1} S_j^{(N-1,3)}/a_{j,j-1}, \quad (j \text{ odd}) \\ &= i^{N-2} S_j^{(N-2,4)}/a_{j,j-2}. \quad (j \text{ even}) \end{aligned} \tag{3.15}$$

Hence, *the Nth term in the wave-zone series can be found from the Nth and $(N-1)$th terms in the near-field series.* To make the connection, we require only the term in $1/R^3$ in the expansion (3.12) for the Nth term of the near-field series, and the term in $1/R^4$ for the $(N-1)$th term. Checks can, of course, be obtained by taking other values of q in Eq. (3.13).

The H-wave part of the solution can be dealt with in exactly the same way: there are formulas completely analogous to Eqs. (3.8)–(3.15), using the radial component H_R instead of E_R and the surface harmonics $\bar{S}_p$ of (3.2) instead of the S_p of (3.1). Alternatively, H_R can be deduced from E_R, and hence the H wave from the E wave, by the principle mentioned in Sec. 2.

In conclusion, we shall consider briefly Tai's[2] paper treating the scattering of a plane wave by a perfectly conducting spheroid, the direction of propagation being parallel to the axis of symmetry. In this paper, the scattered "near field" is also expanded as a power series in k, but instead of using the differential equations (2.9) for the successive terms, Tai uses the equations (in our notation)

$$\text{curl}\mathbf{E}_0=0, \quad \text{curl}^2\mathbf{E}_1=0, \quad \text{curl}^3\mathbf{E}_2=0, \cdots, \tag{3.16}$$

together with the divergence equations (2.10), for the electric field, with similar equations for the magnetic field. Evidently Eq. (3.16) follows from (2.9), but the contrary is not the case. Tai further assumes without proof that the required solutions of (3.16) vanish at infinity. We have seen that this is the case for the first three terms in the series (which are all that Tai considers), but is not the case for the higher terms. In passing from the "near-field" to the "distant-field" representation Tai also makes use of the equivalent of (3.1), (3.2), but does not make the connection via the radial components alone, as we do. No use is made of Eqs. (2.19) and (2.20).

It will be found that Tai's solutions of (3.16) *do*, in fact, satisfy our Eqs. (2.9), but it is not clear that this agreement is not partly fortuitous, since the solutions chosen of (3.16) are by no means the most general ones which satisfy the boundary conditions on S and which vanish at infinity. Further, Tai's method of connecting the near field with the distant field seems to lead to difficulties, since explicit expressions for the wave-zone field are not given except in the case of the sphere. Our method of using (2.19), (2.20) to impose an additional condition on the near-field solution, and use of the radial field components to pass to the distant-field representation, seems to be preferable, leading as it does to a determinate mathematical problem of standard type at each stage of the calculation.

APPENDIX I

We wish to prove the relation (2.30), where V is any function which is well behaved on S and in the immediate neighborhood exterior to S. Let us, for clarity, denote the coordinates of a point on S by (x, y, z) and those of the field point by (x', y', z'). Now

$$\int (\mathbf{n}\times\nabla V)/r dS = \int \mathbf{n}\times\nabla(V/r) dS - \int [\mathbf{n}\times\nabla(1/r)] V dS.$$

The first integral on the right-hand side vanishes by Stokes' theorem.[10] Hence, employing Cartesian coordinates,

$$\begin{aligned} \text{curl}' \int (\mathbf{n}\times\nabla V)/r dS &= -\int V[\mathbf{n}(\nabla\cdot\nabla')(1/r) - \nabla(\mathbf{n}\cdot\nabla'(1/r))] dS \\ &= \int V[\mathbf{n}\nabla^2(1/r) + \nabla'(\mathbf{n}\cdot\nabla(1/r))] dS \\ &= \nabla' \int V \frac{\partial}{\partial n}\left(\frac{1}{r}\right) dS, \end{aligned}$$

[10] To apply Stokes' theorem in the usual form, we imagine a small hole made in S. The integral taken over the remainder of S is then equal to a line integral taken round the rim of the hole. Making the hole shrink to zero, the required result follows.

which is the required relation. The restriction to Cartesian coordinates can now be removed. Evidently the same relation holds if V is defined in the immediate neighborhood interior, instead of exterior, to S.

APPENDIX II

We wish to show that $\mathbf{E}_p$, $\mathbf{H}_p$ defined by Eqs. (2.21), (2.22) vanish at infinity for $p=1, 2$. Let us consider $\mathbf{E}_p$; the proof is entirely similar for $\mathbf{H}_p$. For $p=1$, the result follows at once, since the only integrals in Eq. (2.21) which do not vanish at infinity are independent of the coordinates of the field point, and these vanish when the operators curl, ∇ are applied. For $p=2$, the only terms which need be considered are

$$\int \mathbf{n}\times\mathbf{H}_0 dS + (1/2)\,\mathrm{curl}\int(\mathbf{n}\times\mathbf{E}_0)r dS - (1/2)\nabla\int \mathbf{n}\cdot\mathbf{E}_0 r dS. \quad \text{(II, 1)}$$

The first integral in (II, 1) vanishes by Stokes' theorem, since $\mathbf{H}_0=\nabla U_0$.[10] In the second integral, omitting terms which vanish at infinity when the operator curl is applied, we can put r equal to a constant as far as the integration is concerned. The integral then vanishes since $\mathbf{E}_0=\nabla V_0$. The second term in (II, 1) therefore vanishes at infinity. A similar argument shows that the third term also vanishes at infinity. The required result is therefore proved.

Announcement

Conference on Applied Mass Spectrometry

A CONFERENCE on applied mass spectrometry organized by the Mass Spectrometry Panel of the Institute of Petroleum Hydrocarbon Research Group is to be held in London on Thursday and Friday, 29 and 30 October, 1953. The venue of the Conference is the Institution of Electrical Engineers, Savoy Place, London, and its main object is to bring together American, British, and European workers in the field of applied mass spectrometry to discuss problems of current and future interest. The majority of papers are designed to interest those who use mass spectrometers in their daily work, but all the papers on the first day are devoted to subjects in analytical chemistry where mass spectrometry has proved particularly valuable. It is hoped that these papers will give rise to discussions between mass spectrometrists and those who carry out similar analyses by alternative methods.

In all there will be 18 papers from workers in the U. K., the U. S. A., Canada, France, Germany, and Holland, and these will cover broadly:—

1. Quantitative analysis of gases, liquids, and solids, including the continuous monitoring and control of production composition by mass spectrometry;
2. Applications to the study of molecular structure, free radicals, and electron/molecule collision processes;
3. Recent developments in instrumentation and computing techniques.

In order to cover the cost of papers and other conference expenses a registration fee of £2 2s. 0d. will be charged. Applications for further particulars and for registration forms should be made to W. J. Brown, c/o Metropolitan-Vickers Electrical Co. Ltd., Trafford Park, Manchester 17, as soon as possible.

JOURNAL OF APPLIED PHYSICS VOLUME 24, NUMBER 9 SEPTEMBER, 1953

Electromagnetic Scattering by an Ellipsoid in the Third Approximation

A. F. STEVENSON
Departments of Mathematics and Physics, Wayne University, Detroit, Michigan
(Received May 1, 1952)

The method previously described of solving electromagnetic scattering problems as power series in k is here applied to the ellipsoid, the first three terms in the series being obtained. The second term in the series for the wave zone field (that proportional to k^2) vanishes, and the same is true of any body possessing a center of symmetry. Thus the terms in k^3, k^4 in the wave zone field are here obtained. The direction and polarization of the incident wave, and the electromagnetic constants of the ellipsoid, are arbitrary. The final results are expressed in terms of certain elliptic integrals which are functions of the three principal axes of the ellipsoid. These integrals can all be expressed simply in terms of just two such integrals; they become elementary integrals in the case of a spheroid. Various special cases are considered, including that of a perfectly conducting elliptical disk and the complementary problem of diffraction through an elliptical hole in a perfectly conducting screen.

1. INTRODUCTION

THE problem of the scattering of an electromagnetic plane wave by an ellipsoid has been considered by Möglich,[1] who showed that the *scalar* wave equation is separable in ellipsoidal coordinates. His solution is a purely formal one, however, as explicit solutions of the differential equations were not obtained, and a great deal of additional calculation would be required to bring it to a form suitable for numerical computation.

The special case of a perfectly conducting spheroid, with the incident wave propagated parallel to the axis of symmetry, has recently been considered by Schultz[2] (for the prolate spheroid) and Tai[3] (for the oblate spheroid). In neither of these papers, however, were calculations carried to a point where numerical computation could be easily applied—at least until more extensive tables of spheroidal functions are available. Schultz's results are expressed as infinite series of spheroidal functions, while Tai gave explicit expressions for the scattered field which are only of use near the spheroid.[3a]

A first approximation to the solution when the linear dimensions of the ellipsoid are small compared with the wavelength was given long ago by Rayleigh[4], and to this approximation the problem has also been considered by Gans.[5] But the only cases for which the solution has been carried further than this approximation and reduced to calculable form appear to be those of the sphere[6] and the perfectly conducting circular disk (or the complementary problem of diffraction through a circular hole in a perfectly conducting screen).[7]

The present paper attacks the problem from the point of view of a general method developed by the author,[8] in which the solution of a scattering problem is expressed as a power series in the ratio dimension/(wavelength), the calculations at each stage requiring only solutions of Laplace's equation (together with the evaluation of certain potential integrals), rather than the more complicated Maxwell's equations. The method is applicable to the ellipsoid, since the theory of ellipsoidal harmonics has been fairly extensively developed.

The first three terms in the series are here obtained, and attention is focused mainly on the field in the wave zone. It turns out that in the wave zone the second term (proportional to k^3) vanishes. Thus the wave zone field obtained here contains the terms in k^2 and k^4. In other respects the calculation is quite general: the electromagnetic constants of the ellipsoid, the ratios of the three axes, and the polarization and direction of propagation of the incident wave are all arbitrary.

The final results for the wave zone field are expressed in terms of certain elliptic integrals which are functions of the lengths of the axes of the ellipsoid and lend themselves readily to numerical computation. In the case of a spheroid the elliptic integrals become elementary integrals; and in any case the integrals can all be simply expressed in terms of only two of these integrals. Various special cases are considered, including

[1] F. Möglich, Ann. Phys., **83**, 609 (1927).
[2] F. V. Schultz, *Scattering by a Prolate Spheroid*, Report UMM-42, University of Michigan (1950).
[3] C. T. Tai, Trans. Inst. Radio Engrs. (February, 1952).
[3a] *Note added in proof:*—Dr. K. M. Siegel has since informed me that numerical calculations, based on Schultz's work, have now been made for the prolate spheroid and that similar calculations are in progress for the oblate spheroid.
[4] Lord Rayleigh, Phil. Mag. **44**, 28 (1897). Rayleigh only considered the case where the direction of propagation was along a principal axis of the ellipsoid, with the electric vector along another principal axis. But to this approximation the general case can be deduced by superposition.
[5] R. Gans, Ann. Physik **62**, 331 (1920).
[6] J. A. Stratton, *Electromagnetic Theory* (McGraw-Hill Book Company, Inc., New York), p. 563 and following. References to the original papers are given.
[7] C. J. Bouwkamp, Philips Research Repts. **5**, 401 (1950); J. Meixner and W. Andrejewski, Ann. Physik **7**, 157 (1950); H. Levine and J. Schwinger, *Theory of Electromagnetic Waves*, (Interscience Publishers, Inc., New York, 1951), p. 1; J. W. Miles, J. Appl. Phys. **20**, 760 (1949); **21**, 468 (1950).
[8] A. F. Stevenson, J. Appl. Phys. **24**, preceding paper (1953). We shall refer to this paper as "EMS."

that of a perfectly conducting elliptical disk and diffraction through an elliptical hole in a perfectly conducting screen.

2. CALCULATION OF FIRST THREE TERMS IN NEAR FIELD SERIES

Let the equation of the ellipsoid be

$$x^2/a^2+y^2/b^2+z^2/c^2=1, \tag{2.1}$$

where a, b, c are the principal semi-axes. We suppose in the first place that a, b, c are all unequal, but this restriction can be removed in the final results. Let the (in general complex) dielectric constant and permeability of the ellipsoid be ϵ, μ, respectively, the external medium being a vacuum. We suppose a plane-polarized electromagnetic wave of unit amplitude incident on the ellipsoid. Let us define the incident wave by the three sets of direction cosines:

(l, m, n): direction of propagation,
(l_1, m_1, n_1): electric vector,
(l_2, m_2, n_2): magnetic vector.

These nine direction cosines are, of course, subject to the usual relations between the direction cosines of three mutually perpendicular directions.

We consider a steady state with time factor $e^{-i\omega t}$. The incident field is then given by

$$\mathbf{E}^{(0)}=(l_1, m_1, n_1)e^{ik(lx+my+nz)},$$

$$\mathbf{H}^{(0)}=(l_2, m_2, n_2)e^{ik(lx+my+nz)},$$

where $k=2\pi/\lambda$, λ being the wavelength in vacuum.

According to the method of EMS, we expand the incident field in powers of ik in the form

$$\mathbf{E}^{(0)}=\sum_{p=0}^{\infty}\mathbf{E}_p^{(0)}(ik)^p,$$

$$\mathbf{H}^{(0)}=\sum_{p=0}^{\infty}\mathbf{H}_p^{(0)}(ik)^p. \tag{2.2}$$

The first three terms in the expansions are

$$\mathbf{E}_0^{(0)}=(l_1, m_1, n_1),$$

$$\mathbf{E}_1^{(0)}=(l_1, m_1, n_1)\,(lx+my+nz), \tag{2.3}$$

$$\mathbf{E}_2^{(0)}=\tfrac{1}{2}(l_1, m_1, n_1)(lx+my+nz)^2,$$

with similar expressions for $\mathbf{H}_{0,1,2}^{(0)}$ obtained by replacing (l_1, m_1, n_1) by (l_2, m_2, n_2).

Let $(\mathbf{E}, \mathbf{H})$ be the scattered field and $(\mathbf{E}^{(i)}, \mathbf{H}^{(i)})$ the field inside the ellipsoid. We suppose these expanded in a form similar to Eq. (2.2),

$$\mathbf{E}=\sum_{p=0}^{\infty}\mathbf{E}_p(ik)^p, \text{ etc.} \tag{2.4}$$

We shall now calculate the first three terms in the expansions in Eq. (2.4). For this, as explained in EMS, it is necessary to calculate only $\mathbf{E}_0$, $\mathbf{E}_0^{(i)}$, $\mathbf{H}_1$, $\mathbf{H}_1^{(i)}$, $\mathbf{E}_2$, $\mathbf{E}_2^{(i)}$, since Maxwell's equations are invariant under the substitutions $\mathbf{E}\to\mathbf{H}$, $\mathbf{H}\to-\mathbf{E}$, $\epsilon\leftrightarrow\mu$. This means that if we make the substitutions

$$\begin{aligned}&(l_1, m_1, n_1)\to(l_2, m_2, n_2),\\ &(l_2, m_2, n_2)\to-(l_1, m_1, n_1), \quad \epsilon\leftrightarrow\mu,\end{aligned} \tag{2.5}$$

we change $\mathbf{E}_p$, $\mathbf{E}_p^{(i)}$, $\mathbf{H}_p$, $\mathbf{H}_p^{(i)}$ into $\mathbf{H}_p$, $\mathbf{H}_p^{(i)}$, $-\mathbf{E}_p$, $-\mathbf{E}_p^{(i)}$, respectively. Hence we can pass from the electric to the magnetic field or vice versa.

According to EMS, and using the notation of that paper, $\mathbf{E}_0, \cdots, \mathbf{E}_2^{(i)}$ are given by the equations

$$\mathbf{E}_0=\nabla V_0, \qquad \mathbf{E}_0^{(i)}=\nabla V_0^{(i)}, \tag{2.6}$$

$$\mathbf{H}_1=\mathbf{G}_1+\nabla U_1, \quad \mathbf{H}_1^{(i)}=\mathbf{G}_1^{(i)}+\nabla U_1^{(i)}, \tag{2.7}$$

$$\mathbf{E}_2=\mathbf{F}_2+\nabla V_2, \quad \mathbf{E}_2^{(i)}=\mathbf{F}_2^{(i)}+\nabla V_2^{(i)}, \tag{2.8}$$

$$\mathrm{curl}\mathbf{G}_1=-\mathbf{E}_0, \quad \mathrm{curl}\mathbf{G}_1^{(i)}=-\epsilon\mathbf{E}_0^{(i)}, \tag{2.9}$$

$$\mathrm{curl}\mathbf{F}_2=\mathbf{H}_1, \qquad \mathrm{curl}\mathbf{F}_2^{(i)}=\mu\mathbf{H}_1^{(i)}, \tag{2.10}$$

$$\mathrm{div}\mathbf{G}_1=\mathrm{div}\mathbf{G}_1^{(i)}=\mathrm{div}\mathbf{F}_2=\mathrm{div}\mathbf{F}_2^{(i)}=0, \tag{2.11}$$

where $\mathbf{G}_1$, $\mathbf{F}_2$ vanish at infinity, V_0, U_1, V_2 are external harmonic functions, and $V_0^{(i)}$, $U_1^{(i)}$, $V_2^{(i)}$ internal harmonic functions, which satisfy the boundary conditions on the ellipsoid,

$$\begin{aligned}&\mathbf{n}\times\nabla(V_0-V_0^{(i)})=-\mathbf{n}\times\mathbf{E}_0^{(0)},\\ &\mathbf{n}\cdot\nabla(V_0-\epsilon V_0^{(i)})=-\mathbf{n}\cdot\mathbf{E}_0^{(0)},\\ &\mathbf{n}\times\nabla(U_1-U_1^{(i)})=-\mathbf{n}\times(\mathbf{G}_1-\mathbf{G}_1^{(i)}+\mathbf{H}_1^{(0)}),\\ &\mathbf{n}\cdot\nabla(U_1-\mu U_1^{(i)})=-\mathbf{n}\cdot(\mathbf{G}_1-\mu\mathbf{G}_1^{(i)}+\mathbf{H}_1^{(0)}),\\ &\mathbf{n}\times\nabla(V_2-V_2^{(i)})=-\mathbf{n}\times(\mathbf{F}_2-\mathbf{F}_2^{(i)}+\mathbf{E}_2^{(0)}),\\ &\mathbf{n}\cdot\nabla(V_2-\epsilon V_2^{(i)})=-\mathbf{n}\cdot(\mathbf{F}_2-\epsilon\mathbf{F}_2^{(i)}+\mathbf{E}_2^{(0)}),\end{aligned} \tag{2.12}$$

where $\mathbf{n}$ denotes a unit vector along the outward normal. Further

$$\int\mathbf{n}\cdot\mathbf{E}_0dS=\int\mathbf{n}\cdot\mathbf{H}_1dS=\int\mathbf{n}\cdot\mathbf{E}_2dS=0, \tag{2.13}$$

where the integrals are taken over the surface of the ellipsoid.

The method of solution has been fully explained in EMS. The calculations are somewhat long and involved, but are fairly straightforward applications of ellipsoidal harmonics. We shall omit the details and

give only the results (which can be verified),

$$V_0=A_1xI_a(\xi)+A_2yI_b(\xi)+A_3zI_c(\xi), \tag{2.14}$$

$$V_0^{(i)}=A_1^{(i)}x+A_2^{(i)}y+A_3^{(i)}z, \tag{2.15}$$

$$(\mathbf{G}_1)_x=A_2zI_c(\xi)-A_3yI_b(\xi), \tag{2.16}$$

$$(\mathbf{G}_1^{(i)})_x=\frac{\epsilon}{2}(A_3^{(i)}y-A_2^{(i)}z), \tag{2.17}$$

$$U_1=BX_\nu T_\nu(\xi)+B'X_{\nu'}T_{\nu'}(\xi)+B_1yzI_{bc}(\xi)+B_2zxI_{ca}(\xi)+B_3xyI_{ab}(\xi), \tag{2.18}$$

$$U_1^{(i)}=B^{(i)}X_\nu+B'^{(i)}X_{\nu'}+B_1^{(i)}yz+B_2^{(i)}zx+B_3^{(i)}xy, \tag{2.19}$$

$$\mathbf{F}_2=\mathbf{F}_2'+\nabla V_2'', \tag{2.20}$$

$$(\mathbf{F}_2')_x=-\tfrac{1}{2}A_1[x^2I_a(\xi)+y^2I_b(\xi)+z^2I_c(\xi)-I(\xi)]-\tfrac{1}{2}B_1[x^2I_{ac}(\xi)+y^2I_{bc}(\xi)+3z^2I_{cc}(\xi)-I_c(\xi)]+B_2xyI_{ab}(\xi)+C_1yzI_{bc}(\xi), \tag{2.21}$$

$$V_2''=A_1\phi_x+A_2\phi_y+A_3\phi_z, \tag{2.22}$$

$$\phi_x=\frac{1}{10}(x^2+y^2+z^2)xI_a(\xi)-\frac{1}{5}xI(\xi)-\frac{1}{50}(3a^2+b^2+c^2)xI_a(\xi), \tag{2.23}$$

$$(\mathbf{F}_2^{(i)})_x=\frac{\epsilon\mu}{4}A_1^{(i)}(y^2+z^2)-\frac{\mu}{2}B_1^{(i)}(y^2-z^2)+C_1^{(i)}y^z, \tag{2.24}$$

$$V_2=D_1xI_a(\xi)+D_2yI_b(\xi)+D_3zI_c(\xi). \tag{2.25}$$

The y and z components of Eqs. (2.16), (2.17), (2.21), (2.23), (2.24) are given by cyclic permutations of x, y, z; a, b, c and of the suffixes 1, 2, 3 in the constants A_1, A_2, A_3, etc. The complete expression for V_2 is not given, terms which vanish at infinity to an order higher than $1/R^3$ being omitted. These terms do not contribute to the first three terms in the wave zone field, by EMS. The value of $V_2^{(i)}$ does not concern us here.

The notation in Eqs. (2.14)–(2.25) is as follows: ξ is one of the ellipsoidal coordinates of the point (x, y, z), defined as the greatest root of the equation

$$\Theta(\xi)\equiv\frac{x^2}{a^2+\xi}+\frac{y^2}{b^2+\xi}+\frac{z^2}{c^2+\xi}-1=0. \tag{2.26}$$

Further

$$X_\nu=(a^2+\nu)(b^2+\nu)(c^2+\nu)\Theta(\nu),$$

ν, ν' = roots of equation

$$\frac{1}{a^2+\nu}+\frac{1}{b^2+\nu}+\frac{1}{c^2+\nu}=0$$

$$I(\xi)=\int_\xi^\infty\frac{du}{R(u)},$$

$$R(u)=[(a^2+u)(b^2+u)(c^2+u)]^{\frac{1}{2}},$$

$$I_a(\xi)=\int_\xi^\infty\frac{du}{(a^2+u)R(u)},$$

$$I_{ab}(\xi)=\int_\xi^\infty\frac{du}{(a^2+u)(b^2+u)R(u)}, \text{ etc.}$$

$$T_\nu(\xi)=\int_\xi^\infty\frac{du}{(u-\nu)^2R(u)},$$

$$\left.\begin{aligned} I&=\int_0^\infty\frac{du}{R(u)},\\ I_a&=\int_0^\infty\frac{du}{(a^2+u)R(u)},\\ I_{ab}&=\int_0^\infty\frac{du}{(a^2+u)(b^2+u)R(u)}, \text{ etc.}\end{aligned}\right\} \tag{2.27}$$

$$T_\nu=T_\nu(0),$$

$$A_1=-(\epsilon-1)f_1(\epsilon)l_1,$$

$$A_1^{(i)}=(2/abc)f_1(\epsilon)l_1,$$

$$f_1(\epsilon)=\left[(\epsilon-1)I_a+\frac{2}{abc}\right]^{-1}, \tag{2.28}$$

$$B=\frac{\mu-1}{(\mu-1)T_\nu-(1/\nu abc)}\frac{1}{6(\nu-\nu')}\left(\frac{ll_2}{a^2+\nu}+\frac{mm_2}{b^2+\nu}+\frac{nn_2}{c^2+\nu}\right),$$

B' = same as B with ν, ν' interchanged,

$$B_1=g_1(\mu)\left\{-\frac{\mu}{2}(b^2+c^2)(m_2n+n_2m)+m_2nc^2+n_2mb^2+\left[b^2I_b-c^2I_c-\frac{\mu}{2}(b^2+c^2)(I_b-I_c)\right]A_1+\frac{\epsilon\mu}{2}(b^2-c^2)A_1^{(i)}\right\},$$

$$g_1(\mu)=\left[(\mu-1)(b^2+c^2)I_{bc}+\frac{2}{abc}\right]^{-1}, \tag{2.29}$$

$$B^{(i)}=\frac{B}{(\mu-1)\nu abc},\quad B'^{(i)}=\frac{B'}{(\mu-1)\nu' abc},$$

$$B_1^{(i)}=g_1(\mu)\left\{\frac{m_2n+n_2m}{abc}-\frac{b^2-c^2}{2}I_{bc}l_1+\left[\frac{I_b-I_c}{abc}+\frac{b^2-c^2}{2}(I_b+I_c)I_{bc}\right]A_1+\frac{\epsilon\mu}{2}(b^2-c^2)I_{bc}A_1^{(i)}\right\},$$

$$C_1=(b^2-c^2)[(a^2+\nu)B+(a^2+\nu')B'],$$

$$C_1^{(i)}=-(\tfrac{2}{5})\mu(b^2-c^2)[(a^2+\nu)B^{(i)}+(a^2+\nu')B'^{(i)}],$$

$$D_1=(1/10)f_1(\epsilon)\{(1-\epsilon)l_1(a^2l^2+b^2m^2+c^2n^2)+\epsilon(b^2mn_2-c^2nm_2)+[(2-\epsilon)I-\epsilon a^2I_a+4a/bc]A_1+(\epsilon I_a+2I_c)B_1+(\tfrac{1}{2})\epsilon^2\mu(b^2+c^2)A_1^{(i)}-\epsilon\mu(b^2-c^2)B_1^{(i)}\}.$$

Any constants or functions not defined can be obtained by cyclic permutation of suffixes in these constants or functions and of the quantities $a, b, c; l, m, n; l_1, m_1, n_1; l_2, m_2, n_2$.

Various relations connect the elliptic integrals (2.27) (and T_ν, $T_{\nu'}$), of which we mention the following:[9]

$$\left.\begin{aligned} I_a+I_b+I_c&=2/abc\\ a^2I_a+b^2I_b+c^2I_c&=I,\\ I_{ab}&=(I_a-I_b)/(b^2-a^2),\\ 3I_{aa}+I_{ab}+I_{ac}&=2/a^3bc,\\ 3a^2I_{aa}+b^2I_{ab}+c^2I_{ac}&=3I_a,\end{aligned}\right\}\qquad(2.30)$$

$$T_\nu=\frac{1}{2}\left(\frac{I_a}{a^2+\nu}+\frac{I_b}{b^2+\nu}+\frac{I_c}{c^2+\nu}\right)-\frac{1}{\nu abc}.$$

The relations in Eq. (2.30) enable us to calculate all of the integrals $I, I_a, \cdots$ in terms of only *two* of them, say I_a, I_b; while in the case of a spheroid, all integrals can be calculated in terms of only *one* of them (in the case of a sphere the formulae give the integrals without calculation). Our results for the wave zone field will be expressed in terms of these integrals.

3. THE WAVE ZONE FIELD

According to EMS, the expansion of the wave zone field in powers of k can be found by expanding the radial components E_{0R}, etc., of the scattered near field in (positive and negative) powers of R and picking out the coefficients of $1/R^3$, $1/R^4$, where R denotes the distance of the field point from the origin. To find the first three terms in the wave zone expansion, we require the coefficients of $1/R^3$, $1/R^4$ in E_{0R}, E_{1R}, and the coefficient of $1/R^3$ in E_{2R}.[10] This necessitates expanding the integrals $I(\xi)$, etc., in powers of $1/R$. We write

$$\alpha=x/R,\quad \beta=y/R,\quad \gamma=z/R,$$

so that (α, β, γ) are the direction cosines of the radius vector to the field point.

From Eq. (2.26), when R is large,

$$\xi=R^2-(a^2\alpha^2+b^2\beta^2+c^2\gamma^2)+0(1/R^2).$$

Hence, expanding the integrals $I(\xi)$, etc., in inverse powers of ξ, we find

$$I(\xi)=2/R+(1/R^3[-\tfrac{1}{3}(a^2+b^2+c^2)+a^2\alpha^2+b^2\beta^2+c^{22}\gamma]+0(1/R^5),$$

$$I_a(\xi)=2/3R^3+(1/R^5)[-(1/5)(3a^2+b^2+c^2)+a^2\alpha^2+b^2\beta^2+c^2\gamma^2]+0(1/R^7),$$

$$I_{ab}(\xi)=2/5R^5+0(1/R^7),$$

$$I_a(\xi)=2/5R^5+0(1/R^7).$$

We can hence find the required coefficients in the expansions of E_{0R}, E_{1R}, E_{2R} from the formulas of the previous section. We thus find that the coefficient of $1/R^4$ in E_{0R} and the coefficient of $1/R^3$ in E_{1R} both vanish. Hence, from EMS, *the second term (proportional to k^3) in the expansion of the wave zone field vanishes.* It can be shown that the same is true for any body which possesses a center of symmetry. For the remaining coefficients, when expressed in terms of surface harmonics, we find, using the notation of EMS:

$$\left.\begin{aligned} S_1^{(0,3)}&=-(4/3)(A_1\alpha+A_2\beta+A_3\gamma),\\ S_2^{(1,4)}&=p_1\alpha^2+p_2\beta^2+p_3\gamma^2+q_1\beta\gamma+q_2\gamma\alpha+q_3\alpha\beta,\\ S_1^{(2,3)}&=r_1\alpha+r_2\beta+r_3\gamma,\\ S_3^{(2,3)}&=(\tfrac{2}{5})A_1\alpha[a^2\alpha^2+b^2\beta^2+c^2\gamma^2-(\tfrac{1}{5})(3a^2+b^2+c^2)]\\ &\quad+(\tfrac{2}{5})A_2\beta[a^2\alpha^2+b^2\beta^2+c^2\gamma^2-(\tfrac{1}{5})(3b^2+c^2+a^2)]\\ &\quad+(\tfrac{2}{5})A_3\gamma[a^2\alpha^2+b^2\beta^2+c^2\gamma^2-(\tfrac{1}{5})(3c^2+a^2+b^2)],\end{aligned}\right\}\qquad(3.1)$$

where

$$\left.\begin{aligned} p_1&=(6/5)[(b^2+\nu)(c^2+\nu)\bar{B}+(b^2+\nu')(c^2+\nu')\bar{B}'],\\ q_1&=(2/5)[(b^2-c^2)\bar{A}_1+3\bar{B}_1],\\ r_1&=(2/75)[(9a^2-2b^2-2c^2)A_1+5B_1-50D_1].\end{aligned}\right\}\qquad(3.2)$$

In Eq. (3.2), $\bar{B}$, $\bar{B}'$, $\cdots$ are to be obtained from B, B', $\cdots$ by carrying out the substitutions (2.5). The remaining constants $p_2, \cdots, r_3$ are obtained from Eqs. (3.2) by cyclic permutation.

[9] These relations are special cases of relations which connect the integrals $I(\xi)$, $I_a(\xi)$, $\cdots$, and which are useful in deriving and checking the solutions. We shall not give these more general relations, however.

[10] The coefficients of $1/R^5$ in E_{0R} and of $1/R$ in E_{2R} were also calculated, as these furnish checks on the work.

The quantity P of formula (3.3) of EMS, which determines the "E-wave" part of the wave zone field, is now obtained in terms of the harmonics of Eqs. (3.1), as far as the term in k^4, as follows [formulas (3.14), (3.15), (3.7) of EMS]:

$$P=k^2[\tfrac{1}{2}S_1^{(0,3)}]+k^4\left[-\frac{1}{2}S_1^{(2,3)}+\frac{1}{18}S_2^{(1,4)}+\frac{1}{18}S_3^{(2,3)}\right].$$

The term in k^3 vanishes, as mentioned before.

The E-wave part of the wave zone field is thus completely determined as far as the term in k^4, and the H-wave part of the solution can be deduced by making the substitutions (2.5). There remains the somewhat tedious task of collecting our results and simplifying them by means of the formulas of this and the preceding sections. The final results are given in the next section.

4. FINAL RESULTS

By Eqs. (3.3) and (3.4) of EMS and the formulas developed in the preceding two sections, we have for the wave zone field:

$$E_\theta=H_\phi=\left(\frac{\partial P}{\partial\theta}+\frac{1}{\sin\theta}\frac{\partial\bar{P}}{\partial\phi}\right)\frac{e^{ikR}}{R},$$
$$E_\phi=-H_\theta=\left(\frac{1}{\sin\theta}\frac{\partial P}{\partial\phi}-\frac{\partial\bar{P}}{\partial\theta}\right)\frac{e^{ikR}}{R}, \tag{4.1}$$

where, as far as the term in k^4,

$$P=k^2(K_1\alpha+K_2\beta+K_3\gamma)+k^4[L_1\alpha+L_2\beta+L_3\gamma$$
$$+M_1\alpha^2+M_2\beta^2+M_3\gamma^2+N_1\beta\gamma+N_2\gamma\alpha+N_3\alpha\beta$$
$$-(1/30)(K_1\alpha+K_2\beta+K_3\gamma)(a^2\alpha^2+b^2\beta^2+c^2\gamma^2)], \tag{4.2}$$

and $\bar{P}$ is obtained from P by making the substitutions (2.5). Here (R, θ, ϕ) are polar coordinates of the field point, while (α, β, γ) are direction cosines of the radius vector to the field point, and are therefore functions of θ, ϕ which depend on the choice of the polar axis. The constants $K_1, L_1, \cdots$ are defined as follows:

$$K_1=(\tfrac{2}{3})(\epsilon-1)f_1(\epsilon)l_1,$$
$$15L_1=f_1(\epsilon)\{(\epsilon-1)l_1[(\tfrac{1}{3})(6a^2-b^2-c^2)$$
$$-(a^2l^2+b^2m^2+c^2n^2)]+\epsilon(b^2mn_2-c^2nm_2)\}$$
$$+[f_1(\epsilon)]^2l_1\{(\epsilon-1)[(\epsilon-2)I+\epsilon a^2I_a-4a/(bc)]$$
$$+\epsilon^2\mu(b^2+c^2)/(abc)\}+f_1(\epsilon)g_1(\mu)\{(I_b-I_c)$$
$$\times[(\mu/2)(b^2+c^2)(mn_2+nm_2)-mn_2b^2-nm_2c^2]$$
$$-\epsilon\mu(b^2-c^2)(mn_2+nm_2)/(abc)\}+[f_1(\epsilon)]^2$$
$$\times g_1(\mu)(I_b-I_c)l_1[(\epsilon-1)k_1(\mu)$$
$$+\epsilon\mu(\epsilon\mu-2)(b^2-c^2)/(abc)],$$

$$M_1=\frac{\epsilon-1}{45Q}\Big[(\epsilon-1)(I_{ab}nn_1+I_{ac}mm_1-2I_{bc}ll_1)$$
$$+\frac{2\epsilon}{abc(\sum a^2b^2)}(2a^2ll_1-b^2mm_1-c^2nn_1)\Big],$$

$$15N_1=-(\tfrac{1}{3})(\mu-1)f_1(\mu)(b^2-c^2)l_2+g_1(\epsilon)$$
$$\times[(\epsilon/2)(b^2+c^2)(mn_1+nm_1)-b^2mn_1-c^2nm_1]$$
$$+f_1(\mu)g_1(\epsilon)l_2[\epsilon\mu(b^2-c^2)/(abc)-(\mu-1)k_1(\epsilon)],$$

where

$$k_1(\epsilon)=b^2I_b-c^2I_c-(\epsilon/2)(b^2+c^2)(I_b-I_c),$$

$$Q=(\epsilon-1)^2(I_{ab}I_{bc}+I_{bc}I_{ca}+I_{ca}I_{ab})$$
$$-\frac{4\epsilon(\epsilon-1)}{abc}\left(J+\frac{\sum a^2}{\sum a^2b^2}J'\right)+\frac{4\epsilon^2}{a^2b^2c^2(\sum a^2b^2)},$$

$$J=\int_0^\infty\frac{du}{[R(u)]^3}=(I_{ab}-I_{ac})/(c^2-b^2),$$

$$J'=\int_0^\infty\frac{udu}{[R(u)]^3}=I_{ab}-c^2J, \text{ etc.}$$

$$\sum a^2=a^2+b^2+c^2,$$

$$\sum a^2b^2=a^2b^2+b^2c^2+c^2a^2.$$

I, I_a, etc., are the elliptic integrals defined in Eq. (2.27) and are connected by the relations (2.30); they are functions of a, b, c. The functions f_1, g_1 of ϵ or μ are defined in Eqs. (2.28) and (2.29). The remaining constants $K_2, K_3, \cdots$ of Eq. (4.2) are obtained by cyclic permutation of a, b, c; l, m, n; l_1, m_1, n_1; l_2, m_2, n_2, as in Sec. 2.

If we write, in analogy with Eq. (4.2),

$$\bar{P}=k^2(\bar{K}_1\alpha+\cdots)+k^4[\bar{L}_1\alpha+\cdots], \tag{4.3}$$

then $\bar{K}_1, \cdots$ are obtained from $K_1, \cdots$ by making the substitutions (2.5).

For a nonabsorbing ellipsoid (ϵ-real), the scattered radiation is plane-polarized, to this approximation, since our formulas show that E_θ/E_ϕ is then real. The same is true of the perfectly conducting ellipsoid, considered in Sec. 6.

5. SCATTERING COEFFICIENT

The scattering coefficient s (ratio of energy scattered by ellipsoid to energy incident on ellipsoid) is easily

found from Eqs. (4.1), (4.2), (4.3) to be

$$s=(l^2b^2c^2+m^2c^2a^2+n^2a^2b^2)^{-\frac{1}{2}}$$
$$\times\Big\{(8/3)k^4\sum_{j=1}^{3}(|K_j|^2+|\bar{K}_j|^2)+(16/3)k^6$$
$$\times\Big[\mathrm{Re}\sum_{j=1}^{3}(K_jL_j^*+\bar{K}_j\bar{L}_j^*)-(1/150)$$
$$\times((3a^2+b^2+c^2)(|K_1|^2+|\bar{K}_1|^2)$$
$$+(3b^2+c^2+a^2)(|K_2|^2+|\bar{K}_2|^2)$$
$$+(3c^2+a^2+b^2)(|K_3|^2+|\bar{K}_3|^2))\Big]\Big\}+0(k^7). \quad (5.1)$$

6. PARTICULAR CASES

In what follows we shall make the usual choice of the z axis as polar axis and the zx plane as the plane $\phi=0$, so that

$$\alpha=\sin\theta\cos\phi, \quad \beta=\sin\theta\sin\phi, \quad \gamma=\cos\theta.$$

(1) Spheroid

If two of the principal axes of the ellipsoid are equal, the elliptic integrals become elementary integrals. We find for the

prolate spheroid $(a=b<c)$:

$$I=(c^2-a^2)^{-\frac{1}{2}}\log\frac{c+(c^2-a^2)^{\frac{1}{2}}}{c-(c^2-a^2)^{\frac{1}{2}}};$$

while for the

oblate spheroid $(a=b>c)$:

$$I=2(a^2-c^2)^{-\frac{1}{2}}\cos^{-1}(c/a).$$

In either case, the remaining integrals can be calculated from Eqs. (2.30). There is also no loss of generality in taking the direction of propagation to lie in, say, the zx plane. There is no great simplification in the formulas, however, and we shall not write down detailed expressions for the field.

(2) Sphere

If $a=b=c$, we find easily

$$I=2/a, \quad I_a=2/(3a^3), \quad I_{aa}=2/(5a^5),$$
$$J=2/(7a^7), \quad J'=4/(35a^5).$$

There is further no loss of generality in taking the z axis as the direction of propagation and the x axis as the direction of the electric vector, so that

$$n=l_1=m_2=1,$$

the other direction cosines vanishing. We then find from Eqs. (4.1) and (4.3) for the field:

$$E_\theta=H_\phi=\Big\{k^2a^3\Big(\frac{\epsilon-1}{\epsilon+2}\cos\theta+\frac{\mu-1}{\mu+2}\Big)+k^4a^5$$
$$\times\Big[F(\epsilon,\mu)\cos\theta+F(\mu,\epsilon)+\frac{\epsilon-1}{6(2\epsilon+3)}\cos2\theta$$
$$+\frac{\mu-1}{6(2\mu+3)}\cos\theta\Big]\Big\}\cos\phi\frac{e^{ikR}}{R},$$
$$E_\phi=-H_\theta=-\Big\{k^2a^3\Big(\frac{\epsilon-1}{\epsilon+2}+\frac{\mu-1}{\mu+2}\cos\theta\Big)+k^4a^5$$
$$\times\Big[F(\epsilon,\mu)+F(\mu,\epsilon)\cos\theta+\frac{\epsilon-1}{6(2\epsilon+3)}\cos\theta$$
$$+\frac{\mu-1}{6(2\mu+3)}\cos2\theta\Big]\Big\}\sin\phi\frac{e^{ikR}}{R},$$

where

$$F(\epsilon,\mu)=(3/10)(\epsilon+2)^{-2}(\epsilon^2-6\epsilon+4+\epsilon^2\mu).$$

This field agrees with the rigorous solution for the sphere, if powers of ka above the fourth are neglected.[11]

(3) Perfectly Conducting Ellipsoid

As explained in EMS, we can deduce this case by putting $\mu=0$ and making $|\epsilon|\to\infty$ in our general results. The field is thus still given by Eqs. (4.1), (4.2), and (4.3), where now

$$K_1=(2/3I_a)l_1,$$
$$L_1=(1/15I_a)\{l_1[(\tfrac{1}{3})(6a^2-b^2-c^2)-(a^2l^2+b^2m^2+c^2n^2)]$$
$$+b^2mn_2-c^2nm_2\}+(l_1/15I_a^2)(I+a^2I_a),$$
$$M_1=\frac{1}{45Q'}\Big[I_{ab}nn_1+I_{ac}mm_1-2I_{bc}ll_1$$
$$+\frac{2}{abc(\sum a^2b^2)}(2a^2ll_1-b^2mm_1-c^2nn_1)\Big],$$
$$Q'=I_{ab}I_{bc}+I_{bc}I_{ca}+I_{ca}I_{ab}$$
$$-\frac{4}{abc}\Big(J+\frac{\sum a^2}{\sum a^2b^2}J'\Big)+\frac{4}{a^2b^2c^2(\sum a^2b^2)},$$
$$N_1=\frac{1}{18}\frac{b^2-c^2}{I_b+I_c}l_2+\frac{1}{15I_{bc}}(mn_1+nm_1),$$
$$\bar{K}_1=-\frac{2}{3}\frac{l_2}{I_b+I_c},$$

[11] Expansions from which the field can be determined to this order are given by Stratton (reference 6), p. 571, but some of Stratton's formulas are in error.

$$\bar{L}_1=\frac{l_2}{15(I_b+I_c)}[a^2l^2+b^2m^2+c^2n^2-\tfrac{1}{3}(6a^2-b^2-c^2)]$$
$$+\frac{2l_2}{15(I_b+I_c)^2}\left[I+\frac{2a}{bc}+\tfrac{1}{4}(b^2-c^2)^2I_{bc}\right]$$
$$+\frac{b^2-c^2}{30(I_b+I_c)}(mn_1+nm_1),$$

$$\bar{M}_1=\frac{1}{45}\frac{I_{ab}nn_2+I_{ac}mm_2-2I_{bc}ll_2}{I_{ab}I_{bc}+I_{bc}I_{ca}+I_{ca}I_{ab}},$$

$$\bar{N}_1=\frac{b^2-c^2}{45I_a}l_1+\frac{1/15}{(b^2+c^2)I_{bc}-2/(abc)}$$
$$\times[b^2mn_2+c^2nm_2-(l_1/I_a)(b^2I_b-c^2I_c)].$$

The remaining constants K_2, K_3, $\cdots$ are obtained by cyclic permutation as before.

(4) Perfectly Conducting Elliptical (or Circular) Disk

The case of a perfectly conducting disk whose boundary is the ellipse

$$x^2/a^2+y^2/b^2=1, \tag{6.1}$$

follows from the preceding one by making $c\to 0$. In this case the integrals I_c, I_{ac}, and I_{bc} become infinite like $1/c$, but we can use the relations (2.30), where necessary, in proceeding to the limit. We thus find for this case:

$$K_1=(2/3I_a)l_1,\quad K_2=(2/3I_b)m_1,\quad K_3=0,$$
$$L_1=(1/15I_a)\{l_1[\tfrac{1}{3}(6a^2-b^2)-(a^2l^2+b^2m^2)]+b^2mn_2\}$$
$$+(l_1/15I_a^2)(I+a^2I_a),$$
$$L_2=(1/15I_b)\{m_1[\tfrac{1}{3}(6b^2-a^2)-(a^2l^2+b^2m^2)]-a^2ln_2\}$$
$$+(m_1/15I_b^2)(I+b^2I_b),$$
$$L_3=0,$$
$$M_1=(1/45R)[(6I_{bb}+I_{ab})ll_1-(3I_{aa}+2I_{ab})mm_1],$$
$$M_2=(1/45R)[(6I_{aa}+I_{ab})mm_1-(3I_{bb}+2I_{ab})ll_1],$$
$$M_3=(1/45R)[(I_{ab}-3I_{bb})ll_1+(I_{ab}-3I_{aa})mm_1],$$
$$R=9I_{aa}I_{bb}-I_{ab}^2+4(a^2+b^2)/a^6b^6, \tag{6.2}$$
$$N_1=N_2=0,$$
$$N_3=(1/18)(a^2-b^2)n_2/(I_a+I_b)+(1/15I_{ab})(lm_1+ml_1),$$
$$\bar{K}_1=\bar{K}_2=0,$$
$$\bar{K}_3=-(2n_2/3)/(I_a+I_b),$$
$$\bar{L}_1=\bar{L}_2=0,$$
$$\bar{L}_3=\frac{n_2}{15(I_a+I_b)}[a^2l^2+b^2m^2+\tfrac{1}{3}(a^2+b^2)]$$
$$+\frac{2n_2}{15(I_a+I_b)^2}[I+\tfrac{1}{4}(a^2-b^2)^2I_{ab}]$$
$$+\frac{a^2-b^2}{30(I_a+I_b)}(lm_1+ml_1),$$
$$\bar{M}_1=\bar{M}_2=\bar{M}_3=0,$$
$$\bar{N}_1=(b^2/45I_a)l_1+(1/15)(3I_{bb}+I_{ab})^{-1}[(I_b/I_a)l_1-mn_2],$$
$$\bar{N}_2=-(a^2/45I_b)m_1-(1/15)(3I_{aa}+I_{ab})^{-1}$$
$$\times[(I_a/I_b)m_1+ln_2],$$
$$\bar{N}_3=0.$$

The integrals I_a, I_{ab}, $\cdots$ are here to be evaluated with $c=0$.

In particular, for a circular disk ($a=b$), we have

$$I_a=\pi/(2a^3),\quad I_{aa}=3\pi/(8a^5).$$

In this case, we can, without loss of generality, take the zx plane parallel to the direction of propagation, so that

$$l=\sin\psi,\quad m=0,\quad n=\cos\psi,$$

where ψ is the angle of incidence (angle between the direction of propagation and the normal to the disk). We may now further advantageously consider the special cases where the incident wave is polarized with the electric vector parallel or perpendicular to the plane of incidence (where by "plane of incidence" we mean the zx plane). The general case can be deduced by superposition from these two cases. We characterize them more percisely by requiring that in the first (parallel) case the magnetic vector is parallel to the y axis, and in the second case the electric vector is anti-parallel to the y axis. Hence,

Parallel polarization:

$$l_1=\cos\psi,\quad m_1=0,\quad n_1=-\sin\psi,$$
$$l_2=n_2=0,\quad m_2=1.$$

Perpendicular polarization:

$$l_1=n_1=0,\quad m_1=-1,$$
$$l_2=\cos\psi,\quad m_2=0,\quad n_2=-\sin\psi.$$

We thus find for the circular disk:

Parallel polarization:

$$E_\theta=H_\phi=\{k^2a^3(4/3\pi)\cos\theta\cos\phi$$
$$+k^4a^5[(2/45\pi)(16-3\sin^2\psi)\cos\theta\cos\phi$$
$$+3\delta\sin2\theta(1+2\cos2\phi)$$
$$-(2/15\pi)\sin^2\theta\cos\theta\cos\phi]\}\cos\psi\frac{e^{ikR}}{R},$$

$$E_\phi=-H_\theta=\{-k^2a^3(4/3\pi)\sin\phi$$
$$+k^4a^5[-(2/45\pi)(16-3\sin^2\psi)\sin\phi$$
$$+(2/9\pi)\sin^2\theta\sin\phi$$
$$-12\delta\sin\theta\sin2\phi]\}\cos\psi\frac{e^{ikR}}{R},$$

where

$$\delta=\pi\sin\psi/[15(9\pi^2+64)].$$

Perpendicular polarization:

$$E_\theta=H_\phi=\{-k^2a^3(4/3\pi)\cos\theta\sin\phi$$
$$+k^4a^5[(2/45\pi)(5\sin^2\psi-16)\cos\theta\sin\phi$$
$$+(2/15\pi)\sin^2\theta\cos\theta\sin\phi$$
$$-(4/45\pi)\sin\psi\sin2\theta\sin2\phi]\}\frac{e^{ikR}}{R},$$

$$E_\phi=-H_\theta=\{k^2a^3[-(4/3\pi)\cos\phi+(2/3\pi)\sin\psi\sin\theta]$$
$$+k^4a^5[(2/45\pi)(5\sin^2\psi-16)\cos\phi$$
$$+(2/45\pi)(5+2\sin^2\psi)\cos\phi\sin^2\theta$$
$$-(3/45\pi)\sin\psi(3+\sin^2\psi)\sin\theta$$
$$+(3/45\pi)\sin\psi\sin\theta\cos^2\theta$$
$$-(8/45\pi)\sin\psi\sin\theta\cos2\phi]\}\frac{e^{ikR}}{R}.$$

In the case of normal incidence ($\psi=0$), the formulas for a circular disk agree with those of Bouwkamp[7] to the order (ka).[4] The case of oblique incidence does not seem to have been considered before to this order.

(5) Diffraction through an Elliptical or Circular Hole in a Perfectly Conducting Screen

If the ellipse, Eq. (6.1), represents the boundary of a hole in a perfectly conducting screen, the diffracted field ($z>0$) can be deduced from the complementary *disk* problem by making the substitutions[12]

$$\left.\begin{aligned}(l_1, m_1, n_1)&\rightarrow(l_2, m_2, n_2),\\(l_2, m_2, n_2)&\rightarrow-(l_1, m_1, n_1),\end{aligned}\right\}\qquad(6.3)$$

$$\mathbf{E}\rightarrow-\mathbf{H},\quad \mathbf{H}\rightarrow\mathbf{E}\qquad(6.4)$$

Instead of Eq. (6.4), we can keep the expressions (4.1) for the diffracted field and make the substitutions $P\rightarrow-\bar{P}$, $\bar{P}\rightarrow P$, or

$$K_1\rightarrow-\bar{K}_1,\quad \bar{K}_1\rightarrow K_1,\text{ etc.}\qquad(6.5)$$

Using Eqs. (6.3), (6.5) and the results for the elliptical disk, the diffracted field (for the same incident field as before) is therefore given by the formulas of Sec. 4, where now:

$$K_1=K_2=0,\quad K_3=(2n_1/3)/(I_a+I_b),$$
$$L_1=L_2=0,$$
$$L_3=-(n_1/15)(I_a+I_b)^{-1}[a^2l^2+b^2m^2+\tfrac{1}{3}(a^2+b^2)]$$
$$-(2n_1/15)(I_a+I_b)^{-2}[I+\tfrac{1}{4}(a^2-b^2)^2I_{ab}]$$
$$+(1/30)(a^2-b^2)(I_a+I_b)^{-1}(lm_2+ml_2),$$
$$M_1=M_2=M_3=0,$$
$$N_1=b^2l_2/(45I_a)+(1/15)(3I_{bb}+I_{ab})^{-1}[(I_b/I_a)l_2+mn_1],$$
$$N_2=-a^2m_2/(45I_b)-(1/15)(3I_{aa}+I_{ab})^{-1}$$
$$\times[(I_a/I_b)m_2-ln_1],$$
$$N_3=0,$$
$$\bar{K}_1=-(2/3I_a)l_2,\quad \bar{K}_2=-(2/3I_b)m_2,\quad \bar{K}_3=0,$$
$$\bar{L}_1=-(1/15I_a)\{l_2[\tfrac{1}{3}(6a^2-b^2)-(a^2l^2+b^2m^2)]$$
$$-b^2mn_1\}-(l_2/15I_a^2)(I+a^2I_a),$$
$$\bar{L}_2=-(1/15I_b)\{m_2[\tfrac{1}{3}(6b^2-a^2)-(a^2l^2+b^2m^2)]$$
$$+a^2ln_1\}-(m_2/15I_b^2)(I+b^2I_b),$$
$$\bar{L}_3=0,$$
$$\bar{M}_1=(1/45R)[(3I_{aa}+2I_{ab})mm_2-(6I_{bb}+I_{ab})ll_2],$$
$$\bar{M}_2=(1/45R)[(3I_{bb}+2I_{ab})ll_2-(6I_{aa}+I_{ab})mm_2],$$
$$\bar{M}_3=(1/45R)[(3I_{bb}-I_{ab})ll_2+(3I_{aa}-I_{ab})mm_2],$$
$$\bar{N}_1=\bar{N}_2=0,$$
$$\bar{N}_3=(n_1/18)(a^2-b^2)(I_a+I_b)^{-1}-(1/15I_{ab})(lm_2+ml_2),$$

R being given by Eq. (6.2).

In particular, for a circular hole, and using the same notation as for the circular disk, we find, using an obvious notation:

Parallel polarization:

$$E_\theta=H_\phi=(E_{\phi\perp})_{\text{disk}},$$
$$E_\phi=-H_\theta=-(E_{\theta\perp})_{\text{disk}}.$$

Perpendicular polarization:

$$E_\theta=H_\phi=-(E_{\phi//})_{\text{disk}},$$
$$E_\phi=-H_\theta=(E_{\theta//})_{\text{disk}}.$$

The transmission coefficient t of the elliptical hole (ratio of energy transmitted by hole to energy incident on hole) is given by one-half the scattering coefficient s of Eq. (5.1), using the appropriate values of the constants. For a circular hole this gives

Parallel polarization:

$$t=(16/27\pi^2)\sec\psi(ka)^4[4+\sin^2\psi$$
$$+(1/25)(ka^2)(88-54\sin^2\psi-5\sin^4\psi)].$$

[12] See, for instance, J. Meixner, Z. Naturforsch., 3A, 506 (1948).

Perpendicular polarization:

$$t=(64/27\pi^2)\cos\psi(ka)^4[1+(1/25)(ka)^2(22-5\sin^2\psi)].$$

The tangential electric field *in* the hole is of some interest. This can be found from the formulas of Sec. 2 for the near field, by first finding the magnetic field on a perfectly conducting elliptical disk and then making the substitutions (6.3) and (6.4). To calculate the magnetic field on the disk, we take the case of a perfectly conducting ellipsoid and then proceed to the limit:

$$c\to 0,\quad z\to+0,$$
$$z/c\to(1-x^2/a^2-y^2/b^2)^{\frac{1}{2}}.$$

We can only find two terms in the series, as the third term in the near field series has not been found completely. We thus obtain for the electric field in the elliptical hole:

$$E_x=(2n_1/a^3b)(I_a+I_b)^{-1}x(1-x^2/a^2-y^2/b^2)^{-\frac{1}{2}}$$
$$+ik[-(f_1+2m_2/abI_b)(1-x^2/a^2-y^2/b^2)^{\frac{1}{2}}$$
$$+(1/a^2)(f_1x^2+f_2xy)(1-x^2/a^2-y^2/b^2)^{-\frac{1}{2}}],$$
$$E_y=(2n_1/ab^3)(I_a+I_b)^{-1}y(1-x^2/a^2-y^2/b^2)^{-\frac{1}{2}}$$
$$+ik[(-f_2+2l_2/abI_a)(1-x^2/a^2-y^2/b^2)^{\frac{1}{2}}$$
$$+(1/b^2)(f_1xy+f_2y^2)(1-x^2/a^2-y^2/b^2)^{-\frac{1}{2}}],$$

where

$$f_1=(2/a^3b)(I_{ab}+3I_{aa})^{-1}(ln_1-I_am_2/I_b),$$
$$f_2=(2/ab^3)(I_{ab}+3I_{bb})^{-1}(mn_1+I_bl_2/I_a).$$

For the circular hole, this gives

Parallel polarization:

$$E_x=-(2/\pi)\sin\psi(x/a)(1-r^2/a^2)^{-\frac{1}{2}}$$
$$-(4/3\pi)ika[(2-\sin^2\psi)(1-r^2/a^2)^{\frac{1}{2}}$$
$$+(1+\sin^2\psi)(x^2/a^2)(1-r^2/a^2)^{-\frac{1}{2}}],$$
$$E_y=-(2/\pi)\sin\psi(y/a)(1-r^2/a^2)^{-\frac{1}{2}}$$
$$-(4/3\pi)ika(1+\sin^2\psi)(xy/a^2)(1-r^2/a^2)^{-\frac{1}{2}},$$

where $r=(x^2+y^2)^{\frac{1}{2}}$ denotes distance from the center of the hole.

Perpendicular polarization:

$$E_x=(4/3\pi)ika\cos\psi(xy/a^2)(1-r^2/a^2)^{-\frac{1}{2}},$$
$$E_y=(4/3\pi)ika\cos\psi$$
$$\times[2(1-r^2/a^2)^{\frac{1}{2}}+(y^2/a^2)(1-r^2/a^2)^{-\frac{1}{2}}].$$

The foregoing results for a circular hole are in agreement with those of Bouwkamp[7] in the case of normal incidence ($\psi=0$) to the order in ka here considered.

The Negentropy Principle of Information

L. BRILLOUIN
I.B.M.—Watson Laboratory, New York, New York
(Received April 21, 1953)

The statistical definition of information is compared with Boltzmann's formula for entropy. The immediate result is that information I corresponds to a negative term in the total entropy S of a system.

$$S=S_0-I.$$

A generalized second principle states that S must always increase. If an experiment yields an increase ΔI of the information concerning a physical system, it must be paid for by a larger increase ΔS_0 in the entropy of the system and its surrounding laboratory. The *efficiency* $\mathcal{E}$ *of the experiment* is defined as $\mathcal{E}=\Delta I/\Delta S_0\leq 1$. Moreover, there is a lower limit k ln2 (k, Boltzmann's constant) for the ΔS_0 required in an observation. Some specific examples are discussed: length or distance measurements, time measurements, observations under a microscope. In all cases it is found that higher accuracy always means lower efficiency. The information ΔI increases as the logarithm of the accuracy, while ΔS_0 goes up faster than the accuracy itself. Exceptional circumstances arise when extremely small distances (of the order of nuclear dimensions) have to be measured, in which case the efficiency drops to exceedingly low values. This stupendous increase in the cost of observation is a new factor that should probably be included in the quantum theory.

1. DEFINITIONS[1]

A THEORY of information has been recently developed and has been found to have many important applications in the field of telecommunications. The present author has shown that this theory also can be extremely useful in pure physics.[2-6] A certain expression can be defined that measures the amount of information in a given operation. It will be proved that this quantity is very closely connected with the physical entropy of statistical thermodynamics. The aim of the present paper is to examine and discuss this very important connection. A theoretical relation will be derived first, and the exact meaning of this formula will be discussed on a variety of examples that will give a clear understanding of the physical content of the theory.

We start with the definition of the measure of information, as it results from the previous work of mathematicians and communication engineers. The definition is based on statistical considerations and we select the simplest possible example. We consider a certain system, which could initially obtain P_0 different structures, all of them having equal *a priori* probabilities. With the information, the number of possible states is reduced to P_1, and we take the logarithm of the ratio P_0/P_1 as a measure of the information.

Initially: Information $I_0=0$, number of possible structures P_0.

Finally: Information $I_1>0$, number of possible structures P_1.

$$I_1=K\ln\frac{P_0}{P_1}$$

$$=K\,(\ln P_0-\ln P_1)\cdots\ln\text{ natural logarithm, base }e. \quad (1)$$

The coefficient K may differ, according to the unit system. For instance

$$K=\log_2 e \quad \text{gives} \quad I=\log_2(P_0/P_1) \quad (1a)$$

and measures information in bits (binary digits). Let us now recall the statistical definition of entropy and the famous formula of Boltzmann and Planck. A quantized physical system is able to take a number of discrete microscopic structures, which Planck calls the distinct "complexions" of the system. These complexions are assumed to be equally probable *a priori*. Let P be their number. The entropy of the system is given by the expression

$$S=k\ln P, \quad (2)$$

where k is Boltzmann's constant

$$k=1.38\quad 10^{-16}\text{ cgs centigrade degrees.}$$

We may now compare this entropy formula with the definition (1) of information, using similar units in both formulas and taking

$$K=k.$$

We obtain

$$S_1=S_0-I_1, \quad (3)$$

$S_0=k\ln P_0$, initial entropy of the system,
$S_1=k\ln P_1$, final entropy with the information I_1.

This proves directly that "information" corresponds to a negative term in the final entropy of a physical system.

$$\text{Information}=\text{negentropy (negative entropy)}. \quad (4)$$

[1] Paper read at the Harvard Physics Colloquium (October 1, 1951); at Brown University (February, 1952); and before the Am. Phys. Soc. (May 3, 1952) (see also Phys. Rev. **87**, 221 (1952).
[2] L. Brillouin, J. Appl. Phys. **22**, 334 (1951).
[3] L. Brillouin, J. Appl. Phys. **22**, 338 (1951).
[4] L. Brillouin, J. Appl. Phys. **22**, 1108 (1951).
[5] C. E. Shannon and W. Weaver, *Mathematical Theory of Communication* (University of Illinois Press, 1949).
[6] L. Brillouin, Am. Scientist **38**, 594 (1950).

This point of view was developed by the present author in some recent papers,[2–4] where the following points were stressed:

(A) Information can be changed into negentropy and vice versa. If the transformation is reversible, there is no loss, but an irreversible transformation always corresponds to a loss.

(B) Any experiment by which an information is obtained about a physical system corresponds *in average* to an increase of entropy in the system or in its surroundings. This average increase is always larger than (or equal to) the amount of information obtained. In other words, an information must always be paid for in negentropy, the price paid being larger than (or equal to) the amount of information received. Vice versa, when the information is lost, the entropy of the system is increased.

(C) The smallest possible amount of negentropy required in an observation is of the order of k. A more detailed discussion (see next section) gives the value

$$k \ln 2 = 0.69k = \text{minimum of information} \qquad (5)$$

as the exact limit, a result which checks with a previous discussion of L. Szilard.[7] In binary digits, this minimum represents just one bit.

(D) These remarks lead to an explanation of the problem of the Maxwell's demon, which simply represents a device changing negentropy into information and back into negentropy.

(E) When definition (1) is applied to a system of signals sent on a cable (or on any telecommunication channel), the information formula used by Shannon[5] is obtained. The average information per signal is

$$I = -K \sum_j p_j \ln p_j, \qquad (6)$$

when a set of signals, $a, b, \cdots j \cdots$ appear with the *a priori* probabilities $p_a, p_b, \cdots p_j \cdots$. Summarizing these results we may state a *generalization of the second principle:* In any transformation of a closed system, the quantity "entropy minus information" must always increase, or may at best remain constant,[6]

$$\Delta S_1 = \Delta(S_0 - I_1) \geq 0. \qquad (7a)$$

We may define the quantity N (negentropy)

$$N = -S, \quad \Delta(N + I) \leq 0. \qquad (7b)$$

The sum of negentropy plus information must always decrease. Negentropy corresponds to the "grade" of energy in Kelvin's principle of "degradation of energy," and it is no wonder that the importance of negentropy was recognized by a close friend of Kelvin, who wrote:[8]

"It is very desirable to have a word to express the *Availability* for work of the heat in a given magazine; a term for that possession, the waste of which is called *Dissipation*. Unfortunately the excellent word *Entropy*, which Clausius has introduced in this connection, is applied by him to the *negative* of the idea we most naturally wish to express. It would only confuse the student if we were to endeavour to invent another term for our purpose. But the necessity for some such term will be obvious from the beautiful examples which follow. . . ."

An isolated system contains *negentropy* if it reveals a possibility for doing mechanical or electrical work. If the system is not at a uniform temperature T, but consists of different parts at different temperatures, it contains a certain amount of negentropy. This negentropy can be used to obtain some mechanical work done by the system, or it can be simply dissipated and lost by thermal conduction. A difference in pressure between different parts of the system is another case of negentropy. A difference of electrical potential represents another example. A tank of compressed gas in a room at atmospheric pressure, a vacuum tank in a similar room, a charged battery, any device that can produce high-grade energy (mechanical work) or be degraded by some irreversible process (thermal conduction, electrical resistivity, friction, viscosity) is a source of negentropy.

The physicist working in his laboratory uses such sources of negentropy and obtains information. With the help of this information he may make an appropriate decision by which he decreases the entropy of the laboratory, thus recuperating part of the negentropy previously used in getting the information (remarks A, B, D).

Our general viewpoint agrees completely with similar discussions by D. Gabor[9] who states:[10]

"one cannot get something for nothing, not even an observation."

2. ENTROPY LIMIT FOR AN OBSERVATION

We want to discuss in the present paper a variety of examples of applications of the principle of negentropy of information, and to show how it applies in different branches of physics, technology, and even in some very general problems of human knowledge.

The first problem is to discuss more accurately the question raised under (C) in the preceding section: What is the smallest amount of negentropy required to perform an observation and to obtain a certain information? The question was discussed in general terms in a previous paper,[2] where it was shown (Eq. 22) that the limit was of the order of magnitude of k. In order to

[7] L. Szilard, Z. Physik **53**, 840 (1929).

[8] P. G. Tait, *Sketch of Thermodynamics* (Edmonston and Douglas, Edinburgh, 1868), p. 100.

[9] D. Gabor, J. Inst. Elec. Engrs. **93III**, 429 (1946); **94III**, 369 (1947); D. Gabor, Phil. Mag. **41**, 1161 (1950); and D. Gabor, *La Théorie des Communications et la Physique, La Cybernétique*, (Editions Revue d'Optique, Paris 1951), p. 115.

[10] D. Gabor, "Light and information" (Edinburgh lecture, 1951 to be published). Also M.I.T. lectures, October, 1951.

obtain a more accurate limit, we must consider some specific examples. We may read, for instance, an indication from an ammeter. The needle and its spring represent an oscillating system with a very low proper frequency. The needle exhibits a Brownian motion of oscillation, with an average kinetic energy $\frac{1}{2}kT$ and an average total energy

$$\bar{E}_i = kT.$$

G. Ising[11] considers that an additional energy,

$$E_I \geq 4\bar{E}_i = 4kT, \tag{8}$$

is required to obtain a correct reading. This energy will be dissipated in friction, Joule effect, and viscous damping of the ammeter after the physicist has performed the reading. This means an increase of entropy, for the whole system

$$\Delta S = E_I/T \geq 4k. \tag{9}$$

If $4k$ is needed for an accurate observation, we want to show that $0.7k$ is the limit, for which we just obtain a 50 percent chance that the observation is correct, with a 50 percent chance that the deflection observed might simply be the result of thermal agitation. Let us consider a harmonic oscillator of frequency ν with quantized energy levels $E_n = nh\nu$. The problem of the ammeter will correspond to the limit of very low frequency. The energy level $nh\nu$ has a probability

$$p_n = Be^{-nx} = e^{-nx} - e^{-(n+1)x}$$

with

$$x = h\nu/kT, \quad B = 1 - e^{-x}, \tag{10}$$

$$\sum_{n=0}^{\infty} p_n = \sum_{n=0}^{\infty} Be^{-nx} = 1. \tag{11}$$

Hence

$$P_{n \geq q} = p_q + p_{(q+1)} + \cdots = e^{-qx} \tag{12}$$

$$P_{0 \leq n < q} = p_0 + p_1 + \cdots p_{(q-1)} = 1 - e^{-qx} \tag{13}$$

for the probabilities of states below q or above $q-1$. We may define a *median quantum number* m by the condition

$$P_{0 \leq n < m} = P_{n \geq m} \text{ (hence } e^{-mx} = \tfrac{1}{2}), \tag{14}$$

$$mx = \ln 2 \approx 0.7, \quad E_m = mh\nu = kT \ln 2. \tag{15}$$

This median value can be compared with the average value

$$\bar{n} = \sum_{n=0}^{\infty} np_n = \frac{1}{e^x - 1}. \tag{16}$$

For *low frequencies*, this gives

$$h\nu \ll kT, \quad x \ll 1, \quad \bar{n}x = 1, \quad \bar{E} = \bar{n}h\nu = kT, \tag{17}$$

and we notice that the median value is smaller than the average value. The situation is different for high frequencies. Next we compute the average quantum value for states $n \geq q$

$$\bar{n}_q = \frac{\sum_{n=q}^{\infty} np_n}{P_{n \geq q}} = \frac{Be^{-qx} \sum_{r=0}^{\infty} (q+r)e^{-rx}}{e^{-qx}}, \quad \text{with } n = q+r, \tag{18}$$

but we have conditions (11) and (16) to use and we obtain

$$\bar{n}_q = q + \bar{n} \quad \text{since} \quad \bar{r} = \bar{n}. \tag{19}$$

The average quantum value $\bar{n}_q'$ for the group of states $n < q$ is directly obtained from the relation,

$$P_{n<q}\bar{n}_q' + P_{n \geq q}\bar{n}_q = \bar{n},$$

which yields

$$\bar{n}_q' = \bar{n} - \frac{q}{e^{-qx} - 1} \quad \text{for} \quad n < q. \tag{20}$$

Let us apply these results to the median value

$$\left.\begin{aligned} q = m, \quad \bar{n}_m &= m + \bar{n}, \quad n \geq m \\ \bar{n}_m' &= \bar{n} - m, \quad n < m \end{aligned}\right\}. \tag{21}$$

For low frequencies

$$\left.\begin{aligned} \bar{n}_m &= \bar{n}(1 + \ln 2) \approx 1.7\bar{n} \\ \bar{n}_m' &= \bar{n}(1 - \ln 2) \approx 0.3\bar{n} \end{aligned}\right\}. \tag{22}$$

We may now consider the problem of making an observation and discussing its reliability. Suppose we observe, at a certain instant of time t, an energy corresponding to $n \geq q$ quanta. The chance that this high quantum number may be due to thermal fluctuations is $P_{n \geq q}$. The chance that the resonator would have obtained normally $n < q$ and absorbed some additional quanta (to reach a level above q) is $P_{n<q}$. If we accept equal chances for these two cases we must choose for q the median value

$$q = m = (1/x)\ln 2.$$

If we take the Ising value (Eq. 8), we have

$$q_I = (1/x) \cdot 4$$

and

$$\frac{P_{n \geq q}}{P_{n<q}} = \frac{e^{-4}}{1 - e^{-4}} = \frac{1}{e^4 - 1} \approx \frac{1}{54}, \tag{23}$$

which gives about 2 percent chance for errors caused by thermal agitation.

At time t we observe more than q quanta on the resonator. In case this has been caused by thermal fluctuations, the average excess energy has been obtained from the surrounding medium, and according to Eq. (19) it will be

$$\bar{E}_q = \bar{n}_q h\nu = qh\nu + \bar{n}h\nu. \tag{24}$$

[11] G. Ising, Phil. Mag. **51**, 827 (1926); M. Courtines, *Les Fluctuations dans les Appareils de Mesures* (Congres d'Electricité, Paris, 1932), Vol. 2.

If we had actually q quanta absorbed from an outside source, the excess energy $qh\nu$ came from this source and was added to the normal $\bar{n}h\nu$ average, giving again (24). At any rate, the excess energy $qh\nu$ is dissipated later on and absorbed by the surrounding thermostat at temperature T. If Eq. (24) was the result of fluctuations, this means simply that the thermostat gets back some energy it had previously lost. If Eq. (24) results from actual absorption, we have q quanta finally absorbed by the thermostat, hence an entropy increase

$$\Delta S = qh\nu/T = qkx = \begin{cases} k \ln 2 & \text{if } q = m \\ 4k & \text{Ising} \end{cases}. \tag{25}$$

This entropy increase of the surrounding thermostat is the *cost paid for the observation*. Its lowest value $k \ln 2$ or approximately $0.7k$ is obtained when we accept a 50 percent chance of error.

It is very curious that by selecting a limit $m < \bar{n}$ (Eqs. 15 and 17) we nevertheless have a certain amount of energy absorbed to bring the resonator back to normal. This is because the limit m may be lower than the average $\bar{n}$, but (Eq. 22) the average $\bar{n}_m$ of quanta above m is larger than $\bar{n}$. The result is general and applies to low or high frequencies, although our special numerical examples were selected for low frequencies.

3. HIGH FREQUENCY RESONATOR, AND THE LIMIT OF OBSERVATION

Let us now consider a resonator with high frequency, when $h\nu$ can be of the order of kT or larger than kT. The quantity x is no more a small quantity, and condition (15) for the median value will usually not yield an integer value. We thus have to choose the next integer up

$$q \geq m \quad \text{integer}. \tag{26}$$

The accuracy of the observation is then better than 50 percent and the ΔS higher than $k \ln 2$ (Eq. 25).

Let us now select a different case that corresponds to the problem of Maxwell's demon. We have molecules in an enclosure at temperature T, and we use an additional source of light, emitting quanta $h\nu$, in order to see the molecules. A molecule is observed when it scatters at least one quantum $h\nu$, which is later on absorbed by a photoelectric cell or in the eye of the observer. This quantum $h\nu$ must be above the limit of the blackbody radiation in order to be distinguishable from that general background.

We previously assumed (2) that these requirements lead to a condition

$$h\nu \geq kT.$$

We now want to show that we may lower the limit down to

$$h\nu \geq kT \ln 2 \tag{27}$$

if we again accept a 50 percent chance of error. Condition (27) gives

$$x = h\nu/kT = \ln 2, \quad m = \bar{n} = 1, \tag{28}$$

as can be seen readily from Eqs. (15) and (16). The average value and the median value coincide and correspond to just one quantum.

The ground state with zero quanta has a probability $\frac{1}{2}$, equal to the total probability of all states with 1, 2, 3 or more quanta. If we observe one quantum (or more) on the resonator, the chance that it might be the result of actual absorption is 50 percent, the chance that it may be the result of fluctuations is 50 percent. When this quantum is dissipated and reabsorbed by the surrounding medium at temperature T, we obtain an entropy increase

$$\Delta S = k \ln 2 \tag{29}$$

for this medium.

In these examples, the observation gives us just one "bit" of information—namely, a "yes" or "no" answer to a certain question: Has energy been absorbed by a certain resonator? Is there a gas molecule on a certain location? One binary digit of information represents

$$k \ln 2 \approx 10^{-16}, \quad \text{cgs centigrade degree} \tag{30}$$

in thermodynamical units and must be paid for by more than $k \ln 2$ in negentropy. The same limit of $k \ln 2$ per bit of information was also obtained in the discussion of the capacity of a channel in the theory of telecommunications.[12]

We must note that the information obtained is valid for a short period of time only: the resonator's damping soon dissipates the excess energy, or the molecule moves away from the observed position. This law of decay corresponds to another character of the second principle.

The preceding discussion definitely shows that *the second principle holds only in average*, as was specified in Sec. 1B. The second principle is always limited by the possibility of unpredictable *fluctuations*. It may happen that one particular observation could be made at an exceptionally low cost, but we have no way to foresee when and how this may happen. Only averages can be safely predicted.

An amount of information corresponding to a sizable number of bits results in an extremely small contribution to the entropy of the system on account of the 10^{-16} factor in Eq. (30). The problems we discuss are of no great importance for thermodynamics, but the connection between entropy and information is fundamental for the theory of information, which cannot be built consistently without it. Furthermore, we shall consider special conditions where the entropy cost of an observation may become enormously higher than the limit (30).

[12] J. A. Felker, Proc. Inst. Radio Engrs. **40**, 728 (1952); D. A. Bell, Am. Scientist **40**, 682 (1952).

4. ENTROPY COST OF A MULTIPLE OBSERVATION, RELIABILITY OF AN OBSERVATION

In the preceding sections we considered the case of an experiment requiring only one observation and we found that it resulted in an entropy increase of the laboratory.

$$\Delta S \geq A_1 k \tag{31}$$

with

$$A_1 = \begin{cases} \ln 2 & \text{low frequencies } h\nu \leq kT \\ h\nu/kT & \text{high frequencies } h\nu > kT. \end{cases}$$

The limit corresponded to a 50 percent chance of error.

Our next problem is to discuss an experiment involving n simultaneous readings. At the same time we want to introduce a different limit for the permissible errors caused by thermal fluctuations. We define the "*reliability*" r of an observation by the following condition:

$$\begin{cases} \text{Probability of a correct observation} & P_c = 1 - (1/r) \\ \text{Probability of an incorrect reading caused by thermal fluctuations} & P_i = 1/r. \end{cases} \tag{32}$$

Our previous discussion was based on the assumption that the reliability r had been given its lowest possible value, 2. We now want to consider the general case

$$r \geq 2.$$

Ising's condition (Eqs. (8) and (25)) corresponds to the case of a single observation with $r = 54$.

The *reliability* of an observation should not be confused with the *accuracy* of an experiment, which will be discussed in the next section and represents quite a different quantity. Let us start with the case of low frequencies, and assume that we must observe n oscillators. On each of them, we select a limit

$$E_e = q h\nu, \quad h\nu \ll kT$$

for the amount of energy required in the observation. According to (12) we compute the following probabilities:

$$P_1 = e^{-E/kT} = e^{-A_n} \quad \text{for} \quad E \geq E_e \text{ resulting from fluctuation,} \tag{33}$$

$$P_2 = 1 - P_1 \quad \text{for a correct observation,}$$

on any one of the oscillators. We introduce the notation

$$E_e = A_n kT. \tag{34}$$

The probability for a correct result on all n oscillators is

$$P = P_2^n = (1 - e^{-A_n})^n, \tag{35}$$

and there are $1 - P$ cases where one or more of our observations are incorrect. We want the total observation to have a probability P_e of being correct (Eq. 32).

$$P = (1 - e^{-A_n})^n = \left(1 - \frac{1}{r}\right). \tag{36}$$

If we consider an observation requiring only one reading, we have

$$n = 1, \quad A_1 = \ln r.$$

The results of Sections 2 and 3 correspond to

$$n = 1, \quad r = 2, \quad A_1 = \ln 2.$$

Higher r and n values lead to higher A values. For instance, with $r = 2$ (50 percent chance of errors), we compute

$$(r=2) \quad \begin{array}{c|ccccc} n & 1 & 2 & 4 & 100 & 10\,000 \\ \hline A_n & 0.69 & 1.23 & 1.84 & 4.95 & 9.58 \end{array}. \tag{37}$$

For large r or n values we certainly obtain large A numbers, and we may compute an *asymptotic expression*. We take the logarithms of both sides of Eq. (36) and compute

$$r \gg 1, \quad n \gg 1,$$

$$n \ln(1 - e^{-A_n}) \approx -n e^{-A_n} = \ln\left(1 - \frac{1}{r}\right) \approx -\frac{1}{r};$$

hence

$$n e^{-A_n} \approx \frac{1}{r}, \qquad A_n \approx \ln(r \cdot n). \tag{38}$$

We thus must take a limit $A_n kT$ on each of the n oscillators which we want to observe. The total energy required in the experiment is

$$E = n A_n kT, \tag{39}$$

and this energy is finally dissipated in the damping mechanism of the oscillators. The total entropy increase for the observation is thus

$$\Delta S = E/T = nkA_n. \tag{40}$$

In conclusion, A_n may vary practically between 0.7 and a few tens or may be one hundred.

The case of *high frequencies* is different. One single quantum $h\nu$ per resonator is enough for a reliable observation since these frequencies do not practically appear in the blackbody radiation

$$E_e = h\nu = AkT, \quad A = h\nu/kT, \quad h\nu \gg kT.$$

We thus end up with a coefficient

$$A = \begin{cases} A_n & \text{low frequencies } h\nu \ll kT \\ h\nu/kT & \text{high frequencies } h\nu \gg kT \end{cases}. \tag{41}$$

The transition from low to high frequencies would be more difficult to discuss and should depend upon the special problem under consideration.

5. EXPERIMENTAL ERRORS, ACCURACY, AND INFORMATION

The amount of information to be obtained from an experiment is closely related with the accuracy of the experimental setup. We started with the definition of nformation

$$I_1 = k \ln(P_0/P_1), \tag{1}$$

where P_0 = number of equally probable possibilities before observation, P_1 = number of equally probable possibilities after observation, and I_1 = information obtained from the observation. We now want to discuss the general problem of *accuracy, experimental errors, and information*. Let us start with a simple and well-defined example. On a total length l we observe that the position of a certain point is at x (error Δx) (Fig. 1). We define

$$\left.\begin{array}{ll}\text{Absolute error} & \mathcal{E}_a = \Delta x \\ \text{Relative error} & \mathcal{E}_r = \Delta x/x \\ \text{Comparative or proportional error} & \mathcal{E}_c = \Delta x/l\end{array}\right\}. \tag{42}$$

The first two quantities are familiar to the physicist, but the last one does not seem to have been mentioned very often. Nevertheless, it is the quantity that really matters in connection with information theory. It contains the ratio of the uncertainty Δx (that remains after the observation was made) to the original uncertainty l, corresponding to the whole field of observation (ratio of separating power to the field of the instrument). This ratio $l/\Delta x$ will also play a role in the entropy cost of the observation.

We define the *accuracy* $\mathfrak{a}$ of the experiment

$$\mathfrak{a} = (1/\mathcal{E}_c) = (l/\Delta x). \tag{43}$$

This definition fulfills the requirement that increasing accuracy should correspond to smaller and smaller comparative errors. The amount of information obtained from the observation, according to our definition, Eq. (1), is

$$\Delta I = k \ln \frac{l}{\Delta x} = k \ln \mathfrak{a} = -k \ln \mathcal{E}_c. \tag{44}$$

The *accuracy* should not be confused with the *reliability* defined in the preceding section. The accuracy is limited by a number of physical reasons: separating power of the instrument, thickness of the marks along a yardstick, and stability of the instrument. If the system under observation is very heavy and very stable, thermal agitation will not be of importance, but if we observe the position of the needle of an ammeter, the brownian motion of the needle may play a role.

Reliability is based exclusively on the role of thermal agitation and Brownian motion. It accounts for the possibility of completely wrong indications resulting from thermal fluctuations only.

The distinction will be made clear on the following example: Let us assume we use pulses propagating along a line. The total duration of the observation is θ, and the

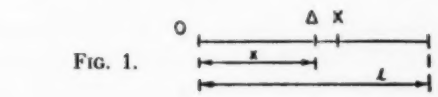

FIG. 1.

shortest pulse our receiver can detect is Δt. The accuracy is $\theta/\Delta t$. In setting up the receiver we select a lower limit E_e to the intensity it can record. If E_e is very much higher than kT, reliability is high, but when E_e approaches kT, reliability is low. This situation is explained in Fig. 2.

6. LENGTH MEASUREMENTS

Let us start with a well-defined problem, which corresponds to measuring a length with a yardstick. We assume that we know that there is a certain test object in our field of observation, and we want to measure the position of this particle with an error Δx. We divide the total length l into n intervals, Δx,

$$n = l/\Delta x = 1/\mathcal{E}_c = \mathfrak{a} \quad \text{accuracy.} \tag{45}$$

The problem is to discover which one of these cells Δx contains the particle. We may use n beams of light of

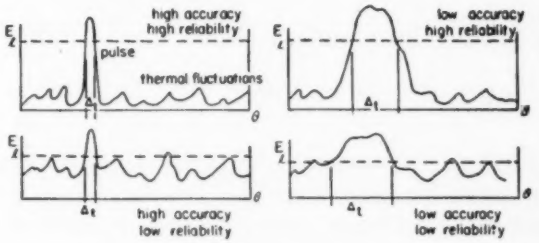

FIG. 2.

frequency ν falling down upon the n cells and received in n resonators below the cells. If the cell is empty, the resonator is excited. If the cell contains the particle, the light is absorbed by the particle and does not reach the resonator, which is in the shadow. We thus examine successively the first, second, third . . . cells, until we find the particle. This means scanning the distance l by steps Δx.

Particle in cell number	1	2	3 ···	m ···	$n-1$	n
Chance	$1/n$	$1/n$	$1/n$	$1/n$	$1/n$	$1/n$
Number of attempts required	1	2	3	m	$n-1$	$n-1$
"A" coefficient	A_{n-1}	A_{n-1}	A_{n-1}	A_{n-1}	A_{n-1}	A_{n-1}.

The coefficient A_{n-1} appearing in this table was defined in Section 4 and depends both on the reliability r and on the accuracy $\mathfrak{a}$ required in the experiment. It takes into account the fact that our experiment requires $(n-1)$ individual observations.

If the particle is in the mth cell, we will discover it after m trials, thus using an energy $mAkT$. We assume that we can use low frequencies and take the A values from Eqs. (37) and (38). If we have reached the cell $(n-1)$ without finding the particle, we know it must be in the last nth cell, and no additional experiment is required. Hence, our coefficient A is A_{n-1} and the average energy required in the experiment is

$$\langle \Delta E \rangle_{Av} = kT\frac{A_{n-1}}{n}[1+2+3\cdots+n-1+n-1] = kT\frac{A_{n-1}}{n}\left[\frac{n(n+1)}{2}-1\right],$$

and the average entropy increase, after the light has been absorbed in the different resonators, is

$$\langle \Delta S \rangle_{Av} = \langle \Delta E \rangle_{Av}/T = kA_{n-1}\left[\frac{n+1}{2}-\frac{1}{n}\right]. \tag{46}$$

Let us compare this entropy increase with the information obtained [Eq. (44)]:

$$\frac{1}{k}\Delta(S-I) = A_{n-1}\left[\frac{n+1}{2}-\frac{1}{n}\right]-\ln n \geq 0. \tag{47}$$

The following table proves that the difference is always positive and that our generalized Carnot Principle holds. We use the A values from Eq. (37) corresponding to a reliability 2 (50 percent chance of errors resulting from fluctuations)

$n=1$	2	3	$\cdots$	$n \gg 1$
$\frac{1}{k}\Delta S=0$	$\ln 2$	$\frac{5}{3}=1.23$	$\cdots$	$\frac{n+1}{2}\ln 2(n-1)\approx\frac{n+1}{2}\ln n$
$\frac{1}{k}\Delta I=0$	$\ln 2$	$\ln 3\approx 1.1$	$\cdots$	$\ln n$
$\frac{1}{k}\Delta(S-I)=0$	0	0.95	$\cdots$	$\frac{n-1}{2}\ln n.$

(48)

On the average, the entropy increase is larger than the information obtained, but if the particle happens to be in one of the first cells we may exceptionally observe its position at a lower cost. This corresponds to the general remarks made at the end of section 3.

The *efficiency* of the experimental method can be defined as the ratio of ΔI (information obtained) to ΔS (entropy increase—negentropy loss),

$$\mathcal{E}=\frac{\Delta I}{\Delta S}=\frac{\ln n}{A_{n-1}\left(\frac{n+1}{2}-\frac{1}{n}\right)}\approx\frac{2}{n+1}$$

for large n, and $r=2$. (49)

The higher the accuracy, the lower the efficiency. Our discussion was based on the assumption that our error Δx was not too small and that we could use low frequencies $h\nu \ll kT$. If Δx became very small, we would need short wavelengths and high frequencies in the illuminating beams in order not to throw light on more than one cell. The quanta $h\nu$ would become large and the efficiency would be much smaller.

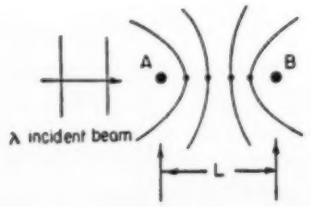

FIG. 3.

7. HOW TO MEASURE A DISTANCE?

We shall come to similar conclusions when we consider a different problem: how can we experimentally define a distance L between two points A and B? We first must have some material particles at both A and B, and the physical way to measure the distance AB is to send a beam of light on the particles A, B and observe the scattered waves with their interference pattern. The number n of fringes between A and B gives the number of half wavelengths $\lambda/2$ over the distance L (Fig. 3),

$$n\lambda/2 = L. \tag{50}$$

If we want to be more specific, we must consider an actual interferometer, for instance a Perot-Fabry apparatus used for measuring the length of a standard meter. Reducing the method to its essential features (Fig. 4) we may think of two parallel reflecting plates A and B, and a system of standing waves between them. The problem is to count the number of planes of maximum intensity between both plates A and B. This could be done by using a photocell P and moving it progressively from A to B. The relation (50) gives the frequency of the light

$$\nu = nc/2L. \tag{51}$$

We need q quanta $h\nu$ absorbed in the photocell P to observe properly the position of one plane of maximum intensity. Altogether, the radiation energy absorbed during the experiment is

$$E=nqh\nu=n^2qhc/2L. \tag{52}$$

Hence the corresponding entropy increase during the observation,

$$\Delta S=\frac{E}{T}=\frac{n^2q}{2}\frac{hc}{LT}=k\frac{n^2q}{2}\frac{\Delta x_T}{L}, \tag{53}$$

introducing the characteristic distance Δx_T for a temperature T, defined by the relation

$$\Delta x_T=hc/kT\approx 1.44/T \text{ cm Kelvin centigrade degree.} \tag{54}$$

Let us assume that we use the smallest number q of quanta under certain experimental conditions. We shall discuss this point later on. We thus measure the length L with an error that may not exceed $\lambda/4$,

$$\Delta L\approx\lambda/4=L/2n, \quad \mathfrak{a}=2n, \quad \text{accuracy.}$$

Hence,

$$\Delta S=\tfrac{1}{4}knq\Delta x_T/\Delta L. \tag{55}$$

Let us now discuss the question of the number q of quanta required to observe the position of a fringe.

(A) Large Distance—Low Accuracy—High Temperature

These conditions correspond to small quanta and low frequencies $h\nu\ll kT$.

$$\frac{h\nu}{kT}=\frac{n}{2L}\frac{hc}{kT}=\frac{1}{4}\frac{\Delta x_T}{\Delta L}\ll 1. \tag{56}$$

We are here working under the conditions specified in Sec. 4, where we discussed in a general way an experimental device using a large number n of simultaneous observations. We obtained the following result:

$$E_e=qh\nu=A_nkT, \quad A_n>0.7.$$

Hence

$$q=A_n\frac{kT}{h\nu}=4A_n\frac{\Delta L}{\Delta X_T}\gg 1.$$

The coefficient A_n was given in Eqs. (37) and (38).

Finally, we compute from Eq. (55) the entropy increase on this case A.

$$\Delta S=A_nkn. \tag{57}$$

The "information" obtained is

$$\Delta I=k\ln\frac{L}{\Delta L}=k\ln 2n \tag{58}$$

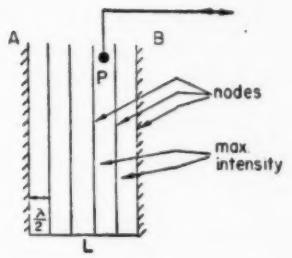

FIG. 4.

and the efficiency of the observation

$$\mathcal{E}=\Delta I/\Delta S=\ln 2n/A_n n\leq 1. \tag{59}$$

If we had required higher reliability, and a lower chance for spurious observations caused by thermal fluctuations, we should have taken the A_n coefficient from Eq. (38). The entropy cost would be higher, the efficiency lower.

Let us be satisfied with a reliability 2 (50 percent chance for errors) and use Eq. (37). A_n is always larger than $\ln 2n$, but for the case $n=1$ when A_n is $\ln 2$ and the efficiency unity, the negentropy principle of information yields our generalized Carnot principle,

$$\Delta(S-I)=k(A_n n-\ln 2n)\geq 0, \tag{60}$$

a formula very similar to our previous Eq. (47).

(B) Short Distances or High Accuracy and Low Temperature

This means a high frequency

$$h\nu\gg kT,$$

$$\frac{h\nu}{kT}=\frac{1}{4}\frac{\Delta x_T}{\Delta L}\gg 1. \tag{61}$$

Here we are operating well beyond the limit of the spectrum of blackbody radiation at temperature T. We may use one quantum only on each fringe, and Eq. (55) yields

$$q=1,$$

$$\Delta S=\tfrac{1}{4}kn\frac{\Delta x_T}{\Delta L}. \tag{62}$$

The information is still given by Eq. (58), and the efficiency is

$$\mathcal{E}=\frac{\Delta I}{\Delta S}=4\frac{\ln 2n}{n}\frac{\Delta L}{\Delta x_T}<1. \tag{63}$$

We may write, in this case, a relation which reminds us of the uncertainty relation

$$\Delta S\cdot\Delta L\approx\tfrac{1}{4}kn\Delta x_T,$$

with

$$n=L/2\Delta L=\tfrac{1}{2}\mathfrak{a} \quad (\mathfrak{a}, \text{ accuracy}). \tag{64}$$

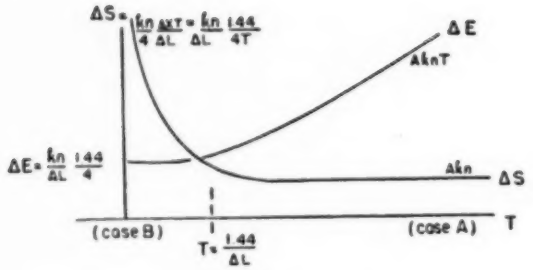

FIG. 5.

The entropy cost ΔS may become extremely large when really small distances L are being measured with reasonable accuracy. For instance, let us take
$L=10^{-13}$ cm, $n=L/2\Delta L=100$,

$$\Delta x_T=510^{-3} \text{ cm for } T=300^\circ \text{ Kelvin.} \quad (65)$$

Hence

$$\Delta S=2.5k \quad 10^{14}.$$

Comparing case (A) [Eq. (57)] and case (B) [Eq. (62)] we note that the coefficient A_n (nearly unity) has been replaced by $\Delta x_T/4\Delta L$ which may increase without limits and has the numerical value 2.5 10^{12} in our preceding example. Figure 5 summarizes the results and shows the entropy cost ΔS or the energy degraded ΔE, in our problems of length measurement, as functions of temperature. The transition between cases (A) and (B) occurs approximately when $\Delta L\approx\Delta x_T=1.44/T$.

The range of temperatures, from a fraction of an absolute degree to some thousand degrees, may introduce a factor varying from 1 to 10^4. This does not seem to be of great importance when compared to the wide variations provided by the factors depending on length.

8. DISCUSSION OF OTHER SCHEMES FOR MEASURING DISTANCE

The preceding discussion emphasizes the great difficulty of measuring extremely small distances. One might think that these difficulties came from the experimental procedure, where short wavelengths were needed to measure short distances. It is possible to imagine a different method, using long wavelengths, larger than the distance L, and observing the difference in the intensities of forward scattering and backward scattering. When this problem is properly discussed, it gives in case (A) ($\Delta L\gg\Delta x_T$) a result of the same order of magnitude as the one computed in Sec. 7. As for case (B) ($\Delta L\ll\Delta x_T$), the new method is much worse than the previous one and yields an entropy increase ΔS going up like ΔL^{-2} instead of ΔL^{-1} with the method of Sec. 7. Altogether, it seems that the very large ΔS corresponding to the observation of extremely small distances represents a new and fundamental difficulty.

Another problem was investigated, and the results will be summarized briefly—that of the observation of a particle under a microscope. According to the general remarks of Sec. 5, we have to limit the field of observation in order to be able to define the accuracy of the experiment and the amount of information obtained. This can be done by assuming that the light received in the microscope was propagated in a wave guide of limited cross section (Fig. 6). Such a wave guide has a certain set of proper waves, and, when the frequency ν of the light and the aperture θ are specified, the number of proper waves that can be excited is finite. A well-chosen superposition of these proper waves yields a focus F in the focal plane ($z=0$), and short pulses can be used to define the time of observation. With these specifications, the number of degrees of freedom of the optical system is defined. An energy larger than kT is required on each degree of freedom for a correct observation, and this energy is absorbed in the eye of the observer, hence giving an increase ΔS in entropy for the observation.

Here again one must distinguish two cases

(A) $\Delta x>\Delta x_T$ and $\Delta y>\Delta x_T$.

The separating power is not very high, and light of low frequency ($h\nu<kT$) can be used, giving a moderately large ΔS.

(B) $\Delta x<\Delta x_T$ and $\Delta y<\Delta x_T$.

High separating power requires light of high frequency ($h\nu>kT$) and the entropy cost is increased by a factor $(h\nu/kT)^2$ or $(h\nu/kT)^3$, depending upon the accuracy in time and the short light pulses required.

These results are in complete agreement with those obtained in Sec. 7 for the simpler case of one-dimensional length measurements. Details of these discussions will be given elsewhere.

9. MEASUREMENT OF TIME INTERVALS

After discussing length measurements, we now turn to another fundamental problem—time measurement. In most usual clocks, some mechanism is used to move hands in front of a dial. This simply reduces the observation of a time interval to the measurement of an angle or of a length. The observation, in such a case, proceeds as in the preceding sections.

This procedure, however, is not very accurate, and we shall consider another type of time measurements, which corresponds essentially to the method used in electronic timing devices, where very high accuracy can be achieved. A time interval t is defined as the distance in time between two pulses, which may be electric pulses sent along a line to a receiver. The situation is sketched in Fig. 7. The first pulse coincides with a pulse coming from an electronic timing device. This electronic clock sends a succession of short pulses, at intervals θ, and θ is also the length of the signal pulse at time t. Each pulse from the clock is used to switch on a certain receiver. Receivers numbered $1\cdot2\cdot3\cdots n$ are successively connected to the line from which the signal pulse is supposed to come. If there is no signal during the interval when the receiver is switched on, nothing

happens. If there is a signal, the receiver is actuated. We thus note, for instance, that receiver No. 0 and receiver No. n have been actuated, and we conclude that the length of the time interval t was

$$t=n\theta. \tag{66}$$

The switching mechanism does not require, in principle, any amount of energy. It can be obtained by changing the voltage on a crystal diode, with no current flowing unless a signal pulse comes in. The operation can also be reduced to changing the voltage on a gating grid in an electron tube. When the signal pulse arrives, it must be recorded, and this means energy dissipation. We may think of using a tuned receiver, but usually an amplifier is needed. This is just an auxiliary device to increase the power and we are not going to consider the energy required in the amplifying system itself.

In such a problem we have to specify the *total duration* τ of the experiment, in order to be able to define the amount of information and the entropy cost. We use definitions similar to those introduced in Sec. 5. We

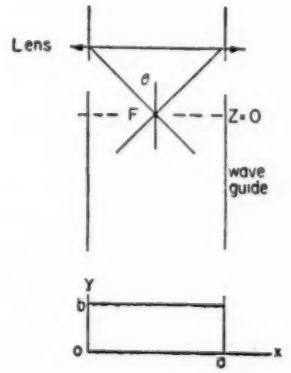

FIG. 6.

consider the *comparative error* $\mathcal{E}_c$ and the accuracy $\mathcal{A}$,

$$\mathcal{E}_c=\Delta t/\tau=\theta/\tau=1/\mathcal{A}. \tag{67}$$

The over-all situation is exactly similar to the one previously discussed in connection with length measurements.

The *information* obtained amounts to

$$\Delta I=k\ln\mathcal{A} \quad \text{(see Eq. 44)}. \tag{68}$$

The *entropy* cost (Eq. 46) is

$$\Delta S=kA_{n-1}\left[\frac{n+1}{2}-\frac{1}{n}\right] \tag{69}$$

with A_{n-1} given by (37) for the case of reliability 2 or

$$A_{n-1}=\ln r(n-1)$$

for a problem requiring high reliability r (Eq. 38). The generalized Carnot principle holds

$$\Delta(S-I)\geq 0. \tag{70}$$

In the problem of time measurements, we always remain under conditions corresponding to case (A) of Sec. 7. Pulses of duration θ require a band width

$$\Delta\nu=2\nu_M=1/\theta \qquad \nu_M, \text{ maximum frequency.}$$

We want to prove that this condition yields *low frequencies*

$$h\nu_M<kT. \quad \text{Hence,} \quad \theta=1/2\nu_M>h/2kT, \tag{71}$$

a condition which can be written

$$\theta>\frac{1}{2c}\Delta x_T=\frac{1.44}{6}\frac{10^{-10}}{T}$$

seconds, T Kelvin temperature. (72)

Δx_T is the characteristic length at temperature T defined in Eq. (54). Condition (72) is practically always fulfilled. This condition can be examined from the point of view of the uncertainty relations. It is well known that time t and energy E represent a couple of complementary variables. Hence, when we measure t with an accuracy Δt we certainly introduce an unknown perturbation ΔE in the energy E

$$\Delta E\Delta t\approx h. \tag{73}$$

The uncertainty ΔE must be compared with the normal energy fluctuations resulting from thermal agitation at the temperature T

$$\langle\Delta_1 E\rangle_{\text{av}}\approx(\langle\mathcal{E}^2\rangle_{\text{av}})^{\frac{1}{2}}=n^{\frac{1}{2}}kT, \tag{74}$$

where n represents the number of "active" degrees of freedom of the system—namely, the number of vibrations of low frequency ($h\nu\leq kT$). High-frequency vibrations are not practically excited and contribute very little to energy fluctuations. We thus have to compare ΔE and $\langle\Delta_1 E\rangle_{\text{av}}$.

$$\Delta E\ll\langle\Delta_1 E\rangle_{\text{av}}, \quad \Delta t\gg\frac{h}{n^{\frac{1}{2}}kT}. \quad \text{(75, Case (A))}$$

This is the case considered in this section. The perturbation resulting from the time measurement is negligible and can be ignored. Conditions (72) and (75) are similar but for the factor $n^{\frac{1}{2}}$.

$$\Delta E\geq\langle\Delta_1 E\rangle_{\text{av}}, \quad \Delta t\leq\frac{h}{n^{\frac{1}{2}}kT}. \quad \text{(76, Case (B))}$$

These conditions would result in a large perturbation of the system. Too much accuracy in the definition of time

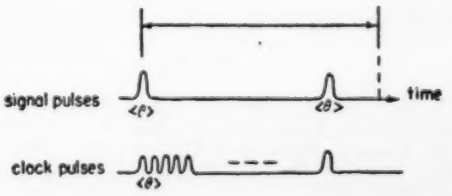

FIG. 7.

might even destroy the system under observation, since it would require high frequencies, yielding large quanta $h\nu$, of the order of $\langle\Delta_1 E\rangle_{Av}$ or more. The general problem of the perturbation introduced by observation will be discussed in the next section.

10. GENERAL REMARKS—CONNECTION WITH QUANTUM CONDITIONS

There are two levels to be distinguished in physics, the classical level and the quantum level. Physics starts on the classical level and all our apparatus are described with classical ideas (Bohr and Rosenfeld, and Bohm).[13] From this point of departure the physicist proceeds to atomic problems and quantum theory. Consistency requires that quantum theory should, in the limit of large quantum numbers, reduce to classical theory (correspondence principle).

Elsasser[14] characterizes the *classical level* by the possibility of "*nonperturbing experiments*" of limited accuracy. These classical experiments can be performed if the following conditions are satisfied:

$$\Delta q\Delta p\rangle\rangle\rangle h \quad \text{and} \quad \Delta E\Delta t\rangle\rangle\rangle h. \tag{77}$$

This means that the accuracy is low enough to permit independent determinations of p, q, E, and t. Our discussion enables us to add another requirement,

$$\Delta I\leq\Delta S\ll S_0. \tag{78}$$

The information ΔI obtained is always smaller than the entropy cost ΔS, and this should remain much smaller than the initial entropy S_0 of the system under observation. This condition is needed in order to insure that no large change in the entropy of the system might ever occur.

In all our discussions we had to use quantum conditions, because we actually live in a quantized world. When, however, the experiment performed was on the classical level, we noted that Planck's constant h dropped out from the final results, which contained only Boltzmann's constant k. This proves that our "Negentropy Principle of Information" really is a new principle and cannot be reduced to quantum conditions.

However, when the quantum level was reached, the constant h could no longer be eliminated, and information theory exhibited a strong interaction with quantum theory. In the problem of length's measurement, case (A) was on the classical level and case (B) on the quantum level.

On the classical level, the general situation is as follows. We define the *accuracy* $\mathcal{A}$ of the experiment (Sec. 5) and obtain the *information* ΔI.

$$\Delta I=k\ln\mathcal{A}. \tag{79}$$

The observation dissipates a certain amount of energy and results in an increase of entropy (loss of negentropy) ΔS in the laboratory. We found, on a variety of examples, expressions of the general type

$$\Delta S=a\mathcal{A}+b, \tag{80}$$

where a and b differ in each special case. These coefficients may be constant, or a may vary as $\ln\mathcal{A}$. At any rate, we could always prove

$$\Delta S\geq\Delta I \quad \text{generalized second principle} \tag{81}$$

and define the efficiency of the experiment

$$\mathcal{E}=\Delta I/\Delta S\leq 1. \tag{82}$$

We discussed extensively and exclusively the problems of length and time measurements. The reader may convince himself that any physical experiment can be described in terms of time intervals and lengths. A mass can be obtained from a collision process (angles to be measured). Any quantity (mass, current, force, field) is finally measured by the displacement of a pointer in front of a scale (length measurement). The results obtained are quite general and apply over the whole field of mechanics, physics, and chemistry.

11. CONCLUSIONS—THE LIMITS OF EUCLIDEAN SPACE

In addition, we discovered some special difficulties for measurements of very high accuracy, especially when extremely small distances were involved. We defined a characteristic length Δx_T at a given temperature T (Eq. 54)

$$\Delta x_T=hc/kT\approx 1.44/T \text{ cm Kelvin degrees.} \tag{83}$$

Normal (classical) conditions were found when the error ΔL in the observation of a distance L was larger than Δx_T [Sec. 7, case (A)], and efficiencies were comprised between unity and 10^{-5}, roughly speaking.

When, however, extremely small distances had to be measured, requiring $\Delta L\ll\Delta x_T$, the efficiency of the observation was enormously lower and could drop to 10^{-15} [see example (65), Sec. 7, case (B)]. Similar situations were found in many other examples, sketched in Sec. 8. In our example of Sec. 7, case (B), the entropy cost increased in proportion to ΔL^{-1} (Eq. 64).

We are thus led to the conclusion that extremely small distances represent a mathematical abstraction corresponding to impossible physical conditions. Euclidean space is an idealization which does not correspond to physical reality. It can be used on the classical level but becomes completely unrealistic on the atomic or nuclear level. The physicist operating in a given laboratory disposes of a limited supply of negentropy, which results in a limit to the small distances he can actually measure.

The very large variation in the efficiency of observa-

[13] N. Bohr and L Rosenfeld, Phys. Rev. **78**, 794 (1950). D. Bohm, *Quantum Theory* (Prentice Hall, New York, 1951).

[14] W. Elsasser, Phys. Rev. **52**, 987 (1937). Phil. Sci. **18**, 300 (1951). *Louis de Broglie physicien et penseur*, Albin Michel, (Paris, 1953), p. 87.

tions, which we emphasized, cannot be safely ignored, and it seemed to remain unnoticed until now. These remarks indicate clearly that the actual cost in equipment and machinery required in nuclear experimentation corresponds to the increased cost in entropy. After all, the cost of operating a big cyclotron or synchrocyclotron is in proportion to the high energy needed for each observation and dissipated in the target. Hence, it sounds reasonable to discuss it in terms of entropy, and the expense in dollars really depends upon the physical expense in entropy.

The conclusion is that there is no precise limitation to the small distances that can be measured but that the entropy cost increases enormously when distances become really small.

It often has been suggested that many of the difficulties of quantum theory could be eliminated by the introduction of some sort of minimal length. The preceding remarks indicate that a precise minimum length could hardly be justified. What they emphasize is the increasing difficulty of measurements for shorter and shorter distances, and they suggest that the increasing cost of the observation might be the new factor needed in the theory. Since entropy is always related to probability, it seems that very short distances and times should be given a very low probability coefficient.

JOURNAL OF APPLIED PHYSICS VOLUME 24, NUMBER 9 SEPTEMBER, 1953

Sinusoidal and Relaxation Oscillations Sustained by Nonlinear Reactances

R. STUART MACKAY
Division of Electrical Engineering, University of California, Berkeley 4, California
(Received April 13, 1953)

A duality between the two types of negative resistance is noted. It is demonstrated that with series or parallel "resonant circuits" one can form either class by using either a nonlinear choke or nonlinear condenser. This ac characteristic can be converted to a similar dc one by using a bridge rectifier. With such an arrangement one can excite oscillations in a resonant circuit or produce relaxation oscillations. Several quite general oscillatory circuits are described, as are some multistable and counter circuits. The interaction with mechanical systems are considered.

IN a previous paper some rather novel experimental results were described. These experiments showed that simple circuits, mostly involving iron cored chokes, can produce oscillations, bistability, etc.[1] The present paper is an attempt to systematize and generalize these results somewhat, and also to present some new observations.

NEGATIVE RESISTANCE

A region of negative slope on the current-voltage characteristic of a device is referred to as a region of negative resistance. The extent of this region cannot be indefinite since infinite power cannot be controlled; and there are two possible ways in which the curve can bend into the surrounding regions of positive slope. These are shown in the first and last diagrams of Fig. 1. For convenience we will refer to these curves as types 1 and 2. We should note that the circuits represented display markedly different properties in their action.[2] These drawings make clear a duality between the two types that has proven a practical help in suggesting new circuits. In a class 1 negative resistance, current is a single valued function of voltage, while voltage is a multiple valued function of current. The opposite is true of class 2. Thus a constant current source (high internal impedance) is preferred while measuring the properties of a second-class device, exemplified by a neon bulb, while an adjustable voltage source is used with elements of the first class, such as the plate characteristics of a tetrode vacuum tube. The data on a device of the second class might appear as in the center part of Fig. 1 and could be replotted as in the right-hand graph. If one tried to take the data directly as shown in Fig. 1(C) the plot would follow the dotted lines, i.e., display discontinuous jumps separated by hysteresis depending on whether the voltage was increasing or decreasing, and the region of negative slope would not be traced out.

The properties of circuits involving such elements are all made obvious by drawing load lines on the curves

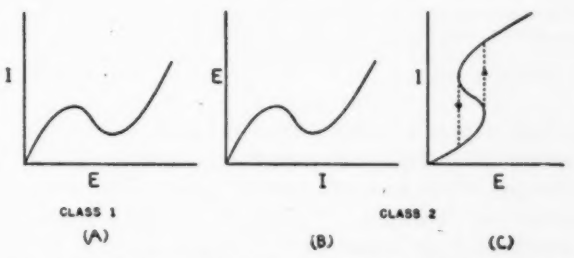

FIG. 1. Though each is characterized by a region of negative slope on the E–I curve, the two types of negative resistance are vastly different in their behavior. The shallower the $-R$ region, the slower will be a discontinuous transition between opposite sides.

[1] R. S. Mackay, J. Appl. Phys. **24**, 311 (1953).
[2] G. Crisson, Bell System Tech. J. **10**, 485 (1931).

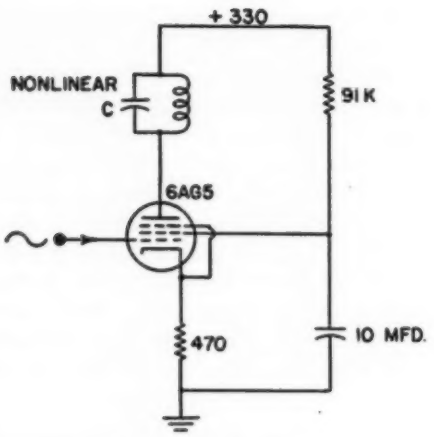

FIG. 2. Current drive for demonstrating negative resistance in nonlinear condenser circuits. In the above case discontinuous jumps in the ac voltage across the condenser are observed as the current (grid excitation) is steadily increased or decreased. The parallel connection is thus of class 1.

and noting the number of intersections or possible states of the circuit with given applied voltages. For example, a class 1 negative resistance placed in series with a sufficiently large impedance yields a combination whose characteristics are such that an increase in applied

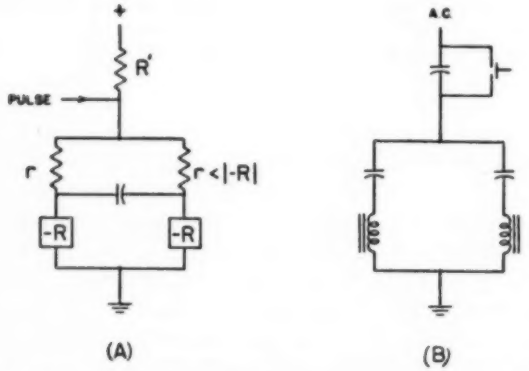

FIG. 3.(A) Counting or scaling circuit (as distinguished from a bistable circuit). Any two second-class negative resistances are used. The corresponding connection for two elements in which voltage is a multiple valued function of current places the elements in series. (B) Nonlinear reactance form showing a push button as an example of a pulse source. This circuit is also tristable at high supply voltages and, counting distortion of the wave shape (observed across one condenser) or triggered oscillations, it can display four indefinitely stable states. At certain voltages the more stable form, containing a light bulb in each arm, can be pulsed into a steady state of oscillation from a steady condition of both bulbs being on.

voltage causes a sudden snap down in current and a decrease in voltage causes an abrupt increase in current (the opposite of a class 2 element alone). Ferroresonant circuits of this type, using a small series condenser, have displayed characteristic times of seconds.

NONLINEAR REACTANCES

In the previous paper the use of a series combination of saturating choke and linear condenser to produce some rather unexpected oscillations was described. This oscillatory state was maintained because of the region of negative slope on the plot of ac voltage (average over a cycle) *vs* ac current. For ac currents and voltages a nonlinear choke in series with an ordinary (suitably tuned) condenser will display a region of negative impedance of class 2. (The fact that this negative region does not appear on an instantaneous volt-ampere curve will be seen to limit the simplicity with which one can maintain oscillations in other components). A maximum dip is achieved when the condenser is large and the voltage at the high end of the range. If the same two components are connected in parallel there will then be displayed a class 1 negative impedance. It might be worth pointing out that, with a given set of components, the external voltage to reach this region will be several times as high in the parallel resonant case. Placing a resistor in series with the parallel combination deepens the negative resistance observed with a voltage source, while it is made smaller by resistance placed in the parallel loop. In the series or class 2 case, series resistance decreases the effect which can be returned with a parallel resistor.

These observations also apply if the condenser is the nonlinear element. If one purchases a ceramic condenser of fairly high capacity, it will probably, at the time of this writing, be quite nonlinear. They can easily be checked by any standard capacitance bridge that is coupled to the test condenser through a much larger capacity condenser. An adjustable dc voltage is then fed to the junction of the two condensers through a megohm resistor and the capacity noted as a function of applied voltage. Those used by the author (a random selection of 0.01-mf Centralab "Hi-Kaps" rated at 600 volts, and collected over a period of time) usually showed an increase in capacity, followed by a decrease to about one fourth, as one approached the rated voltage. They have given satisfactory results at 50 megacycles (incrementally as a frequency or other modulator) while, in the magnetic case, even ferrite cores begin to fail near 10 megacycles.

The experiments with condensers are somewhat more difficult because of their smaller nonlinearity. Also, they must be done at higher frequencies (the following were done at 500–5000 cycles rather than 60 cycles) when using the capacities readily available (though heating produces misleading effects if the frequency is too high). Because sources of several hundred volts in this frequency range are not common, the constant current drive of Fig. 2 was used. It is a pentode with current feedback that forces the load current to follow the grid voltage. When a 3-volt signal, from any oscillator, is applied to the grid of the pentode, a 600-volt swing can be observed across the condenser with an oscilloscope. The inductor with which the condenser was resonated was a General Radio type 940c decade inductor. This parallel circuit displayed discontinuous jumps as the grid excitation was

varied and so, for ac current and voltage, it is a class 1 negative impedance. A series circuit is of the other class.

Another interesting and possibly useful effect is the hysteresis and discontinuity observed if one graphs the voltage across the paralleled nonlinear condenser and coil as the exciting frequency is varied. The curve shows a maximum whose approach from the left is discontinuous and double valued, depending on whether frequency is increasing or decreasing. Corresponding effects are found in the other cases.

It might be noted that the effect of a nonlinear C can be obtained with a parallel combination of linear C and saturating L, the latter supplying an increasing portion of the capacitive current as the voltage increases (as one approaches parallel resonance).

BISTABILITY AND OSCILLATION

A region of negative resistance implies a double valuedness or bistability that can be used to give a counting action or to produce relaxation oscillations. If one is to build a counter or scaler one must, in addition to providing distinct steady states, also supply a short time "memory" that allows the circuit to progress in the direction it was headed, once it has reached a symmetrical intermediate state, i.e., provision must be made so that a pulse will first turn an element on and later, an identical pulse at the same point must turn the same element off. A general scheme combining two separate bistable units in parallel is shown in Fig. 3(A). The condenser, acting into the load resistors r, switches off one element when its neighbor goes on and, by maintaining a reduced voltage for a time rc, assures proper counting action if the input signals are not too closely spaced. The negative resistance can be any pair of two terminal elements from class 2, e.g., neon lamps, thermistors, back-biased germanium diodes, $n-p$ junctions, etc. An excellent low-speed counter was made using a pair of old spark plugs in the position designated $-R$. In the nonlinear reactance

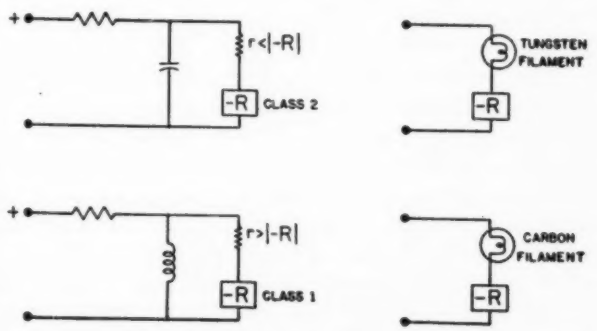

FIG. 4. Some general relaxation oscillator circuits for use with these or other negative resistances. The upper pair of connections is for class 2 elements and the lower two are the corresponding ones for class 1. The lower left figure brings out a comparison between types but there is a closer correspondence with a simple series connection of choke and $-R$. The lamps can also be used in a parallel connection.

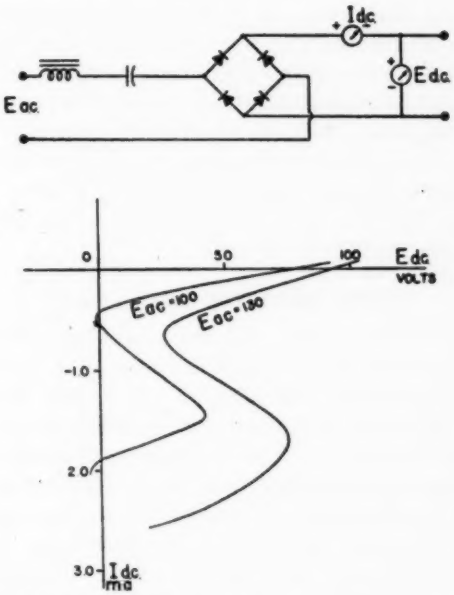

FIG. 5. A full-wave bridge can be used to convert an ac negative slope characteristic to a similar dc one. Thus a series connection involving a nonlinear reactance can be used to give a class 2 negative resistance as shown.

case no commutating condenser is needed since the transient carries the circuit through the symmetrical state in which both halves are conducting equally. Each time the circuit in Fig. 3(B) is momentarily pulsed the arms will interchange heavy and light currents, and then remain in that state until the next impulse. The light bulbs, rather than an rc time constant, determined the switching action in the cases previously reported. If the supply voltage is made too high, these circuits will tend to "free-run" (switch between end states) just as do the corresponding multivibrators.

Figure 4 depicts a few configurations leading to relaxation oscillations and brings out some differences in the two classes of negative resistance in this respect. The upper pair of figures applies to elements of the second class, and the left-hand one is actually the general case of the familiar neon-lamp relaxation oscillator. The upper right connection corresponds to the previously reported relaxation oscillations in ferroresonant circuits. With a piece of very fine wire the same can be done using a nonlinear dielectric to provide the regions of negative slope. The lower figures show the corresponding circuits applicable to first-class elements. In the left-hand circuit the application of voltage brings about an increasing flow of current in the choke, thus dropping the voltage across the negative resistance and its load resistor. At some critical voltage the negative resistance will then switch to its other state in which it draws more current and drops the voltage on the choke and its resistance, thus causing its current to start decreasing and the voltage rising, etc. The lower-right figure represents the connection suitable for

producing oscillations in parallel connected resonant circuits. The circuit is of course less satisfactory because the negative temperature coefficient of carbon is so low. If one replaces this light with a frankfurter it will cook itself and, when done, automatically switch to a low "keep warm" current because of its electrolytic thermistor action (the increased ionic mobility causing a drop in resistance by a factor of four). A hot dog oscillator is possible but difficult to adjust.

STATIC NEGATIVE RESISTANCE

It is well known that negative resistances can excite oscillations in tuned circuits. Class 1 negative resistances can excite parallel resonant circuits while those of class 2 are used with the lower impedances of series resonant circuits. At first thought one might think that these nonlinear reactance circuits might be suitable for maintaining oscillations in circuits tuned to frequencies much below the supply frequency. A little thought shows this to be untrue. A sixty-cycle wave, amplitude modulated at 1 cycle per second, has no Fourier components suitable for exciting a 1-cps resonant circuit, i.e., one could not excite oscillations in

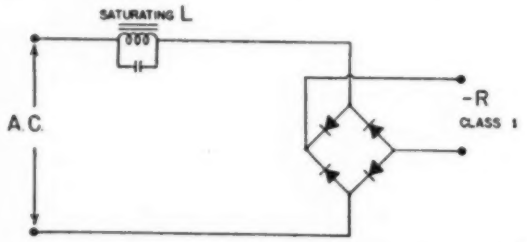

FIG. 6. The parallel ferroresonant circuit giving a class 1 negative resistance on the dc volt-ampere curve.

the circuit by placing it in series with a variable resistor across the ac line and cranking the resistance up and down at a one cycle rate. Similarly a negative resistance that is to produce oscillations (except in a light bulb which is similarly affected by current flow in either direction) must display its region of negative slope to dc meters in a static measurement.

A full-wave bridge rectifier (selenium rectifier stack) was placed in series with one of the resonant circuits. Thus alternating current could flow freely in both directions through the resonant circuit while yet having dc flow in the load or output. (The half-wave connection requries two rectifiers, not one). A dc negative resistance of the same class as the original was thus produced (Fig. 5). Possibly a more fundamental way of considering this action is to say that the switching action of the four diodes interchanges the output connections every half cycle, and thus any external dc voltage helps or hinders the flow of ac in a similar manner on each half cycle. In these experiments the nonlinear element was a small audio choke occupying about a 1.5-inch cube and rated at 200 henrys (one would not wish to use a filter choke because of its air gap). A parallel connection

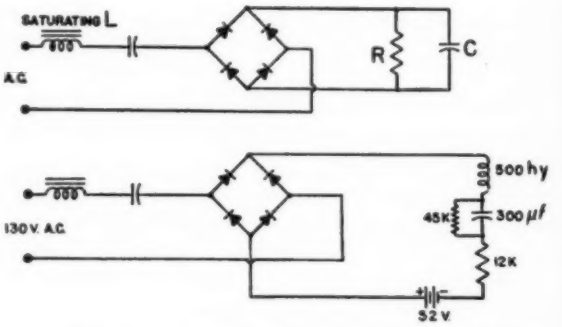

FIG. 7. Oscillator connections. In the upper figure relaxation oscillations are produced with a period of approximately *RC*. The lower connection depicts a series resonant circuit being excited at its natural frequency.

of choke and condenser gave an instantaneous class 1 negative resistance when used in conjunction with the bridge rectifier (Fig. 6).

Figure 7 depicts the oscillatory circuits used with the series connection. Placing a resistor and condenser across the output resulted in relaxation oscillations of a period close to *RC*. This is a bit different from the situation in Fig. 4(A), and corresponds to the oscillations noted when a neon bulb is placed in series with a battery and a parallel combination of resistance and capacitance.

This class of negative resistance was also expected to be capable of exciting low-frequency (compared with the rectified supply frequency) oscillations in a series tuned circuit. The lower diagram of Fig. 7 represents a successful experiment. Sinusoidal oscillations having the proper dependence on $(LC)^{\frac{1}{2}}$ were excited when the dc bias was proper. If the 12-k-ohm resistor was left out the amplitude of oscillation was greater but the wave shape became somewhat distorted. The condenser was shunted by a resistor to give a dc path. Different (large) values of L and C were tried and worked.

It is known that different electromechanical systems (e.g., D'arsonval meter movements, loudspeaker-like structures, etc.) can appear as huge inductances, the flow of current temporarily storing energy in the work done against mechanical restoring forces rather than in magnetic fields. These negative resistances might be very suitable for producing oscillations in such systems and might well prove to be a practical way of maintaining periodic or oscillatory motion in certain mechanical systems.

The unrectified form of negative resistance can also maintain oscillation in many mechanical systems. For example the classic floating ring experiment can be converted into a perpetually jumping ring by resonating the iron cored coil that does the lifting.[3] As the ring drops the increasing coupling with the shorted turn causes the circuit to suddenly switch to the high current state thus causing the ring to again rise; after which the current switches down again allowing the ring to

[3] R. S. Mackay, "Coupled electrical-mechanical oscillatory systems," Am. J. Phys. (to be published).

drop back. The hysteresis in the changes of field maintain motion. Rather than a triggering action, smaller sinusoidal oscillations can also be produced in this and many other circuits of magnets placed near movable metal.

If the tungsten filament lamp of Fig. 4 is replaced by a "universal" motor, which has related delay and variable effective impedance properties, the motor speed and current will vary cyclically, the former possibly dropping to zero for appreciable intervals. The capacity must be adjusted to the load, an increase in which can cause steady running (this system being velocity rather than position switched). Many transducers can be driven thus. A wound-field galvanometer (above) need not require a rectifier.

Two other interesting circuits are shown in Fig. 8. The first is derived from Fig. 3 by replacing the commutating condenser with a 7.5-watt incandescent lamp. The second replaces the common load impedance by a 300-watt lamp. Both circuits used filament transformers

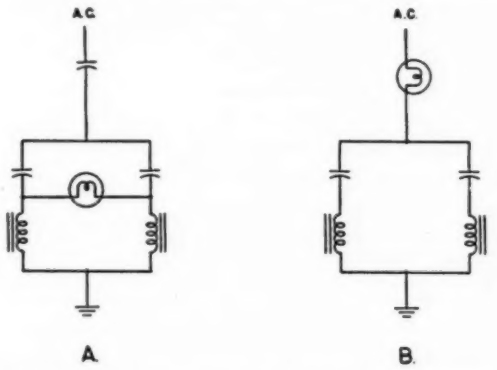

FIG. 8. Two oscillatory circuits derived from the counter circuit of Fig. 3. Rather unusual effects are observed if the two halves are not perfectly balanced.

for the nonlinear elements as in the previous paper. Both display relaxation oscillations. Possibly their most unexpected properties come from the slight asymmetry of the two halves due to commercial tolerances on the components.

The first circuit was studied by noting the voltage across one of the two lower condensers as the supply voltage was adjusted by a Variac. First a 50-ohm resistor was placed in series with the common condenser. A small increase in input voltage caused an abrupt jump in the condenser voltage which was followed, in 1 second, by another large abrupt jump during which the light flashed on and remained on. Removal of the 50 ohms led to some strange actions. An increase in voltage caused a sudden jump in condenser voltage. A decrease in input from this point caused the voltage to jump up more and the light to go on. However a further increase in input, rather than a decrease after the first mentioned jump, caused the voltage to drop and the light to go on. If the input was then dropped the light flashed on and off at about 5 cycles per second.

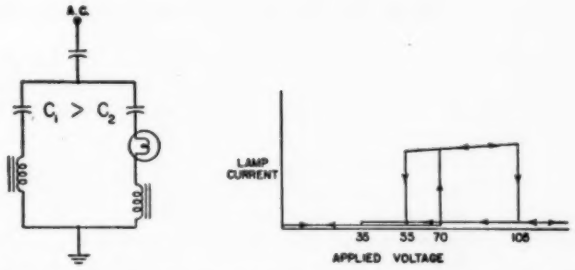

FIG. 9. Assymetric circuit showing unusual discontinuity and hysteresis which, among other things, turns on the bulb over only a restricted range of voltages.

In the second circuit an increase in input caused the "off" side to "fire". A further increase brought about a small rise in voltage followed by a sudden drop as the bulb went on. A drop in input then resulted in oscillation. The oscillation of both these circuits was much faster and less stable than the previously reported ones.

Figure 9 shows a circuit in which the bulb is fully on over a limited range of voltages, and not for higher or lower ones. This is for increasing applied voltages. If the applied voltage is steadily dropped from maximum the bulb will never come on. This circuit could be used as a maximum reading voltmeter, the bulb being off if the input voltage has ever exceeded a critical value.

OTHER POSSIBILITIES

The use of a saturating choke in series with a saturating condenser might result in higher gain since the flow of power in either one has a similar effect on the resonant frequency of the combination. It might be noted that, unlike a nonlinear resistor such as a thermistor, a nonlinear C or L alone (unresonated) cannot show a region of $-R$, even though the degree of nonlinearity be great and the Q high. The inclusion of an instantaneously nonlinear resistor might improve the above circuits.

One might build more stable multistable circuits and circuits of higher gain when using nonlinear condensers by using not the ac voltages automatically fed back to the condenser, but the rectified output purposely fed back as dc across the condenser. Thus the condenser would expose all of each cycle to a particular degree of saturation rather than just approaching it as the cycle progressed. The analog of a self-saturating magnetic amplifier could also be built to supply limited feedback.

In closing it might be noted that in the series resonant cases, when one is above the discontinuity, the nonlinearity is usually such that changes in applied voltage tend to appear across the linear element, often enlarged, while leaving the voltage across the nonlinear one regulated to a constant value.

Thanks are to be extended to Mr. Carter Collins and Mr. Harold Morris for their help in making some of these observations.

First Probability Densities for Receivers with Square Law Detectors

R. C. EMERSON
The Rand Corporation, Santa Monica, California

(Received February 9, 1953; revised manuscript received May 28, 1953)

The method of Kac and Siegert for finding the output probabi ity density characteristic function for receivers with square law envelope detections is discussed, and a parallel development is given for the square law rectifier. Procedures are then outlined for determining the probability density functions directly, i.e., without solving the eigenvalue problem or inverting the characteristic function. The method depends on expanding the density function in an orthonormal series, the coefficients of which are expressed in terms of cumulants, which in turn are obtained from the system kernel by straightforward quadratures.

As an example to illustrate the procedure, a receiver with Gaussian IF and Gaussian audio-frequency pass characteristics is treated in detail, and the output probability density functions are found for various sinusoidal input signal strengths and IF *vs* audio band-width ratios.

INTRODUCTION

THE upper limit on radio receiver performance is often determined by the ability of the equipment to detect weak signals in the presence of system, or presystem noise. Since this noise is basically random in its fine structure, the degree of signal contamination and consequent equipment malfunction must be described statistically, i.e., by means of expectations, probability distributions, etc. Considerable attention has been given in recent years to statistical analysis of electronic circuitry and particularly, because of the common requirement for "detectors" in systems, to nonlinear circuits. Some of the names in the literature associated with this work are Rice,[1] Middleton,[2] Van Vleck,[3] North,[4] Marcum,[5] Goudsmit,[6] Fubini, and Johnson[7] as well as Smith[8] in England, to mention only a few.

The springboard for this paper is a work by M. Kac and A. J. F. Siegert[9] who have investigated the statistical effects of uncorrelated Gaussian (white) noise with and without signal for a system comprising an IF amplifier, a square law envelope detector, and an audio-amplifier. They have derived an exact formula for the first probability distribution of the output voltage for such a system—an important result because of its generality both with respect to IF and audio pass band characteristics, and the unrestricted form of the signal wave assumed. Their expression for the probability distribution is, however, unsuitable for most engineering applications, first because it depends on inverting a rather complicated characteristic function which may not be possible in closed form, and secondly the explicit expression for the characteristic function depends on the solution of a certain eigenvalue problem which none but the most experienced in dealing with integral equations are equipped to solve.

This paper provides a means for using the Kac-Siegert method in its widest generality without the necessity of finding eigenvalues, and without dealing with the characteristic function at all. It depends on the fact that the cumulants of the output distribution are rather simply related to the system operator so that by employing any of the well-known orthonormal systems for expanding density functions, i.e., Gram-Charlier, Laguerre, etc., one may compute the output probability distribution to any desired degree of accuracy by straightforward techniques. The procedure is illustrated in Sec. IV for a system in which the IF and audio-amplifiers possess Gaussian band pass characteristics of arbitrary band width.

This treatment will depart from that of Kac and Siegert in one important respect. As was previously mentioned, their detector is an "envelope detector," that is, it consists of a square law rectifier followed by an appropriate smoothing circuit to attenuate the high-frequency residue. This action is accomplished mathematically by resolving the input voltage into sine and cosine components which are then squared and added to give the output voltage. This approach appears to be a carry-over from the original derivations of the detector output probability density where no separate audio-amplifier is considered. Since this treatment is to include audio filtering as a specific function, the smoothing circuitry referred to above will be included in the audio-filter. This point of view leads to a simplification of the mathematics. In addition, the theory will be slightly more flexible, since it will be possible by removing the audio-amplifier completely to determine the probability density function for the detector alone, i.e., without smoothing circuits, or to obtain the result of Kac and Siegert by modifying the audio filter so as to account for the additional smoothing action.

[1] S. O. Rice, Bell System Tech. J., **23**, 282 (1944); **25**, 46 (1945).
[2] D. Middleton, Quarterly Appl. Math., **5**, 445–98, Jan. 1948.
[3] J. H. Van Vleck and D. Middleton, Radiation Research Lab. (M.I.T.) Report No. 411–86, May 1944.
[4] D. O. North, R. C. A. Technical Report PTR 6-C, June, 1943.
[5] J. I. Marcum, *A Statistical Theory of Target Detection by Pulsed Radar: Mathematical Appendix*, The RAND Corporation, Research Memorandum RM-753, July 1, 1948.
[6] S. A. Goudsmit, Radiation Research Lab. (M.I.T.) Report No. 43–20, Jan. 1943.
[7] E. G. Fubini and D. C. Johnson, Proc. Inst. Radio Engrs. **36**, 1461–1467 (1948).
[8] R. A. Smith, Proc. Institution Elect. Engrs. (London) Part IV, **98**, 43–54 (Oct. 1951).
[9] M. Kac and A. J. F. Siegert, J. Appl. Phys. **18**, 383–397 (1947).

SECTION I

The System Operator

Figure 1 illustrates the system under investigation. The IF amplifier is characterized by the voltage-frequency function $F_{if}(\omega)$ or its Fourier transform $f_{if}(t)$; similarly for the audio-amplifier. The voltage, $E(t)$, applied to the square law detector is given by the familiar formula,

$$E(t)=\int_{-\infty}^{\infty} f_{if}(t-x)E_i(x)dx. \tag{1}$$

The output, $E^2(t)$, of the detector is obtained by squaring the input. It may be expressed by the double integral formula,

$$E^2(t)=\int_{-\infty}^{\infty}\int f_{if}(t-x)E_i(x)E_i(y)f_{if}(t-y)dxdy. \tag{2}$$

This voltage is applied to the audio-amplifier. The output voltage of this amplifier is given by the linear operation,

$$E_0(t)=\int_{-\infty}^{\infty} f_a(t-x)E^2(x)dx. \tag{3}$$

On substituting from Eq. (2) and after making certain substitutions of variables, one obtains the following formula for the output in terms of the input voltage:

$$E_0(t)=\int_{-\infty}^{\infty}\int E_i(t-u)g(u,v)E_i(t-v)dudv \tag{4}$$

where,

$$g(u,v)=\int_{-\infty}^{\infty} f_{if}(u-z)f_a(z)f_{if}(v-z)dz. \tag{5}$$

Equation (4) r.h.s. is the system operator, and the function $g(u,v)$, the system kernel.

One comment concerning the limits of integration seems in order at this point. The realizability of the IF and audio filters implies their inability to predict; consequently, the functions f_{if} and f_a vanish for negative arguments, and so the integrals may be extended over the entire time domain. Notice also that the so-called "high-frequency terms" produced by frequency addition in the detector have not been neglected. They are included in $E_0(t)$ to the extent they are passed by the audio amplifier. This residue need not be given special attention in the derivation of the characteristic function but may be discarded later on if desired.

Expansion of the System Kernel

The next step in the development is to expand the function $g(u,v)$ into the uniformly convergent bilinear series,

$$g(u,v)=\sum_j \lambda_j h_j(u)h_j(v), \tag{6}$$

where the $h_j(x)$ and λ_j are respectively the jth normal orthogonal eigenfunction and corresponding eigenvalue of the integral equation

$$\lambda h(x)=\int_{-\infty}^{\infty} g(x,y)h(y)dy. \tag{7}$$

For such an expansion to exist it is sufficient, first, that $g(u,v)$ be symmetric which can be verified by appealing to Eq. (5), and secondly, that $g(u,v)$ be positive semidefinite. On referring to Eq. (4) it will be verified that $g(u,v)$ will be positive semidefinite if for all input functions, E_i, the output is non-negative. Since the detector output is always non-negative, one has as a sufficient condition for positive semidefiniteness on $g(u,v)$ that

$$f_a(x)\geq 0. \tag{8}$$

This restriction on the audio-amplifier characteristic may actually be too stringent for particular IF amplifiers, but it will be carried along in order to guarantee the validity of the general result.

On substituting Eq. (6) into Eq. (4) the system

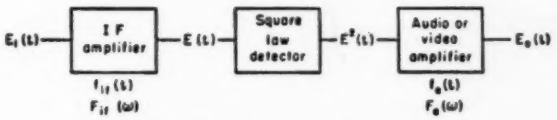

FIG. 1. Block diagram of receiver.

operator reduces to

$$E_0(t)=\sum \lambda_j[e_j(t)]^2 \tag{9}$$

where

$$e_j(t)=\int_{-\infty}^{\infty} E_i(t-x)h_j(x)dx. \tag{10}$$

The input voltage is now expressed as the sum of signal plus noise, *viz.*,

$$E_i(t)=S(t)+N(t) \tag{11}$$

so that for the output one gets,

$$E_0(t)=\sum_j \lambda_j[s_j(t)+\eta_j(t)]^2 \tag{12}$$

where

$$s_j(t)=\int_{-\infty}^{\infty} S(t-x)h_j(x)dx \tag{13}$$

and

$$\eta_j(t)=\int_{-\infty}^{\infty} N(t-x)h_j(x)dx. \tag{14}$$

We are now in a position to find the characteristic function for $E_0(t)$ for the case where $N(t)$ is an uncorrelated Gaussian process.

The Characteristic Function

For any fixed t, let $N(t)$ be normally distributed. Further, let

$$\langle N(t_1)N(t_2)\rangle_{Av}=\phi_0\delta(t_1=t_2), \tag{15}$$

where ϕ_0 is the noise power per unit frequency and $\delta(t_1=t_2)$ is a unit impulse function at $t_1=t_2$. Then, by Eq. (14), for any fixed t, the $\eta_j(t)$ will be normally distributed. And, furthermore, since the functions h_j are orthogonal,

$$\langle \eta_j(t)\eta_k(t)\rangle_{Av}=\phi_0\delta_{jk}, \tag{16}$$

where δ_{jk} is the Kronecher delta. Consequently, for any fixed time, t, the vector $\eta(t)$ defined by

$$\eta(t)=[\eta_1(t), \eta_2(t), \cdots] \tag{17}$$

has a multi-dimensional probability distribution given by,

$$dP[\eta(t)]=\prod_j \frac{d\eta_j(t)}{\sqrt{2\pi\phi_0}}\exp\left[-\frac{\eta_j(t)^2}{2\phi_0}\right]. \tag{18}$$

The characteristic function $\Phi(\xi, t)$ of $E_0(t)$ is now given by,

$$\Phi(\xi, t)=\text{ave}e^{i\xi E_0(t)}=\int_{-\infty}^{\infty}\cdots\int \exp\{i\xi\Sigma\lambda_j[s_j(t)+\eta_j]^2\}\times\prod_j \frac{d\eta_j}{(2\pi\phi_0)^{\frac{1}{2}}}\exp\left(-\frac{\eta_j^2}{2\phi_0}\right), \tag{19}$$

which may be integrated by completing the squares, giving

$$\Phi(\xi, t)=\prod_j[1-2i\xi\lambda_j\phi_0]^{-\frac{1}{2}}\times\exp\left(\frac{s_j(t)^2}{2\phi_0}\cdot\frac{2i\xi\lambda_j\phi_0}{1-2i\xi\lambda_j\phi_0}\right). \tag{20}$$

This is the result for the square law rectifier corresponding to that of Kac and Siegert for the square law envelope detector. Their result can be obtained directly from this by observing that in the case of the envelope detector for each variate of noise present in the input an extra independent variate of noise corresponding to the "out of phase" voltage component is added to the output. And, since the η_j are independent, this has the effect of multiplying the characteristic function, Eq. (20), by its value for noise alone. Under these conditions the noise power per cycle must be split equally between the two components. For Kac and Siegert the noise power per cycle is taken to be unity, so letting $\phi_0=\frac{1}{2}$, $s_j(t)^2=p^2(t)+q^2(t)=\alpha^2+\beta^2$ (in their notation), and changing the exponent of the term in brackets from $-\frac{1}{2}$ to -1, yields their formula.

The Case of No Audio-Filter

The output probability density function, $P'(E_0)$, can be derived in this case by inverting the characteristic function. Here we have

$$F_a(\omega)=1 \tag{21}$$

$$f_a(x)=\delta(x=0). \tag{22}$$

From Eq. (5) we get

$$g(u, v)=f_{ij}(u)f_{ij}(v), \tag{23}$$

and from Eq. (6) we see that there is but one eigenvalue, λ, and eigenfunction, $h(u)$. These are found to be

$$\lambda=\int_{-\infty}^{\infty}f_{ij}(x)^2dx=\int_{-\infty}^{\infty}|F_{ij}(\omega)|^2df, \tag{24}$$

and

$$h(u)=\frac{f_{ij}(u)}{\sqrt{\lambda}}. \tag{25}$$

The inversion of the characteristic function is then found to be

$$P'(E_0)=\int_C e^{-i\xi E_0}\cdot\frac{\exp\left[\frac{s(t)^2}{2\phi_0}\frac{2\phi_0\lambda i\xi}{1-2\phi_0\lambda i\xi}\right]}{(1-2\phi_0\lambda i\xi)^{\frac{1}{2}}}d\xi=\frac{\exp\left\{-\frac{1}{2\phi_0}\left[\frac{E_0}{\lambda}+s(t)^2\right]\right\}\cosh\left[\frac{s(t)}{\phi_0}\left(\frac{E_0}{\lambda}\right)^{\frac{1}{2}}\right]}{(2\pi\phi_0\lambda E_0)^{\frac{1}{2}}}. \tag{26}$$

Now, $\phi_0\lambda$ and $s(t)^2\lambda$ are respectively the rms noise power and signal power entering the detector. So, normalizing these variables as follows:

$$s(t)^2\lambda/\phi_0\lambda=X \tag{27}$$

$$E_0/\phi_0\lambda=Y, \tag{28}$$

we get

$$P'(Y)=\frac{e^{-\frac{1}{2}(X+Y)}\cosh\sqrt{XY}}{(2\pi Y)^{\frac{1}{2}}}. \tag{29}$$

This result may be verified easily by taking the distribution for the noise voltage, η, into the detector to be

$$dP(\eta)=\frac{d\eta}{(2\pi)^{\frac{1}{2}}}\exp\left(-\frac{\eta^2}{2}\right). \tag{30}$$

For rectification in the detector, make the substitution,

$$Y=(\eta+\sqrt{X})^2. \tag{31}$$

This gives,

$$dP(Y)=\frac{dY}{2(2\pi Y)^{\frac{1}{2}}}$$
$$\times\{\exp[-\tfrac{1}{2}(Y^{\frac{1}{2}}+X^{\frac{1}{2}})^2]+\exp[-\tfrac{1}{2}(Y^{\frac{1}{2}}-X^{\frac{1}{2}})^2]\} \quad (32)$$

which reduces immediately to Eq. (29).

SECTION II

The Cumulants for the Output Probability Density

In principle, the probability density function for the output voltage can be obtained from the characteristic function, Eq. (20), by a Fourier inversion. However, except in very special cases, i.e., infinitely wide audio pass band, it is a very difficult problem to find the λ_j and h_j required to determine $\Phi(\xi, t)$ explicitly, let alone to accomplish the inversion. The alternative is to find suitable methods for approximating the density function directly.

There are several well-known orthonormal systems suitable for approximating probability density functions. Two of these systems, the Gram-Charlier and the Laguerre, are discussed in Sec. III.

Particularly simple coefficients for these approximating series arise when they are expressed in terms of the cumulants of the probability density function. The cumulants, K_n, are defined by the following identity:

$$\exp\left(\sum_{n=1}^{\infty} K_n\frac{(i\xi)^n}{n!}\right)=\Phi(\xi), \quad (33)$$

where $\Phi(\xi)$ is the characteristic function.* So, taking the logarithm of $\Phi(\xi, t)$, Eq. (20), and expanding in powers of $i\xi$, we get

$$K_n(t)=(2\phi_0)^n\frac{(n-1)!}{2}\sum_j \lambda_j{}^n + (2\phi_0)^{n-1}n!\sum_j \lambda_j{}^n s_j(t)^2. \quad (34)$$

The n times iterated kernel, $g^n(u, v)$, is defined by

$$g^n(u, v)\equiv\int_{-\infty}^{\infty}\cdots\int g(u, x_1)g(x_1, x_2)\cdots \times g(x_{n-1}, v)dx_1\cdots dx_{n-1}. \quad (35)$$

By virtue of Eq. (6) it is easily verified that

$$\sum_j \lambda_j{}^n=\int_{-\infty}^{\infty} g^n(u, u)du \quad (36)$$

and

$$\sum_j \lambda_j{}^n s_j(t)^2=\int_{-\infty}^{\infty}\int S(t-u)g^n(u, v)S(t-v)dudv. \quad (37)$$

Thus, the formula for the nth cumulant becomes

$$K_n(t)=(2\phi_0)^n\frac{n!}{2}\left\{\frac{1}{n}\int_{-\infty}^{\infty} g^n(u, u)du + \frac{1}{\phi_0}\int_{-\infty}^{\infty}\int S(t-u)g^n(u, v)S(t-v)dudv\right\}, \quad (38)$$

which may be evaluated by straightforward quadratures.

Now, Eq. (38) can be derived by a more direct process. This is accomplished by noting that K_n is equal to a certain algebraic expression involving the first n moments, each of which can be evaluated by raising $E_0(t)$ as expressed in Eq. (4) to the appropriate power and then averaging.

The formulas for the higher moments become progressively more complicated because of the large number of ways noise can be paired with noise, but on forming the required algebraic combination, Eq. (38) results. Since this procedure is extremely tedious, a derivation of Eq. (38) along these lines will not be included. It is mentioned, however, because it illustrates that the condition of positive semi definiteness imposed on the kernel $g(u, v)$ via Eq. (8) to insure uniform convergence of the Mercer series, Eq. (6), is mathematically sufficient but not necessary and does not constitute a restriction on the validity of Eq. (38). In fact, Eq. (38) is valid for any kernel if the corresponding system output voltage has moments up to and including the nth. This will be the case in any practical receiver.

SECTION III

Two Orthonormal Systems

For approximating the output probability density functions two different orthonormal systems are especially useful. The first, the Weber-Hermite system which gives rise to the Gram-Charlier series, type A, is particularly suited to those functions which approximate the normal. In terms of this series, $P'(E_0)$ is given by†

$$P'(E_0)\approx\frac{1}{\sqrt{K_2}}\sum_{j=0}^{\infty}\alpha_j\phi^{(j)}\left(\frac{E_0-K_1}{\sqrt{K_2}}\right), \quad (39)$$

where

$$\phi^{(j)}(x)=\frac{d^j}{dx^j}\left\{\frac{1}{(2\pi)^{\frac{1}{2}}}\exp\left(-\frac{x^2}{2}\right)\right\} \quad (40)$$

* See M. G. Kendall, *The Advanced Theory of Statistics* (Charles Griffin and Company Ltd., London, 1943), Vol. I, for a complete discussion of cumulants and their relation to statistical approximation methods.

† See reference * and reference 5 for discussions of convergence, methods of grouping terms, evaluation of additional α_j and further details.

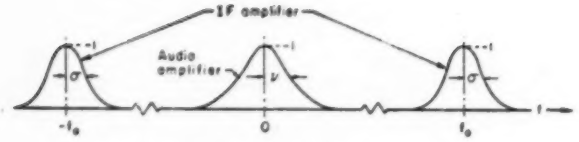

FIG. 2. Frequency characteristics of the Gaussian system.

and

$$\left.\begin{aligned}\alpha_0&=1\\ \alpha_1&=\alpha_2=0\\ \alpha_3&=-\frac{K_3}{6K_2^3}\end{aligned}\right\}. \tag{41}$$

For density functions which approximate the Rayleigh distribution, the following series‡ which derives from the orthonormal system of Laguerre is useful:

$$P'(E_0)\approx\frac{K_1}{K_2}\sum_{i=0}^{\infty}\beta_i\psi^{(i)}\left(\frac{K_1E_0}{K_2}\right), \tag{42}$$

where

$$\psi^{(i)}(x)=\frac{d^i}{dx^i}\{x^{(K_1^2/K_2)-1}e^{-x}\} \tag{43}$$

and

$$\left.\begin{aligned}\beta_0&=\frac{1}{\Gamma(K_1^2/K_2)}\\ \beta_1&=\beta_2=0\\ \beta_3&=\frac{K_1^2}{6K_2}\frac{2-(K_1K_3/K_2^2)}{\Gamma[(K_1^2/K_2)+3]}\end{aligned}\right\}. \tag{44}$$

SECTION IV

The Case of Gaussian IF and Audio with Sinusoidal Signal

To illustrate the method consider the case in which the IF has a Gaussian pass band of width σ centered at the very high frequency, f_0. Similarly let the audio have a Gaussian pass band of width ν, centered at zero frequency (see Fig. 2). Thus

$$F_{if}(f)=\exp\left[-\frac{(f+f_0)^2}{2\sigma^2}\right]+\exp\left[-\frac{(f-f_0)^2}{2\sigma^2}\right] \tag{45}$$

$$F_a(f)=\exp\left(-\frac{f^2}{2\nu^2}\right) \tag{46}$$

and

$$f_{if}(x)=2(2\pi\sigma^2)^{\frac{1}{2}}\exp\left[-(2\pi\sigma)^2\frac{x^2}{2}\right]\cos\omega_0x \tag{47}$$

$$f_a(x)=(2\pi\nu^2)^{\frac{1}{2}}\exp\left[-(2\pi\nu)^2\frac{x^2}{2}\right]. \tag{48}$$

‡ In this form, the series seems to be due to Marcum, reference 5, which see for evaluation of additional β_i and details concerning the derivation.

By means of Eq. (5) and (35) we calculate§

$$g(u,v)=\frac{4\pi\sigma^2\cos\omega_0(u-v)}{(1+2\gamma^2)^{\frac{1}{2}}}\times\exp-\frac{(2\pi\sigma)^2}{4}\left\{(u-v)^2+\frac{1}{1+2\gamma^2}(u+v)^2\right\}, \tag{49}$$

$$g^2(u,v)=\frac{4\pi^{\frac{1}{2}}\sigma^3\cos\omega_0(u-v)}{[(1+2\gamma^2)(1+\gamma^2)]^{\frac{1}{2}}}\times\exp-\frac{(2\pi\sigma)^2}{4}\left\{\frac{1+\gamma^2}{1+2\gamma^2}(u-v)^2+\frac{1}{1+\gamma^2}(u+v)^2\right\}, \tag{50}$$

$$g^3(u,v)=\frac{8\pi^2\sigma^4\cos\omega_0(u-v)}{[(1+2\gamma^2)(2+\gamma^2)(2+3\gamma^2)]^{\frac{1}{2}}}\exp-\frac{(2\pi\sigma)^2}{4}\times\left\{\frac{2+\gamma^2}{2+3\gamma^2}(u-v)^2+\frac{2+3\gamma^2}{(2+\gamma^2)(1+2\gamma^2)}(u+v)^2\right\}, \tag{51}$$

where

$$\gamma=\sigma/\nu \tag{52}$$

From these equations we get

$$\int_{-\infty}^{\infty}g(u,u)du=2\sigma\sqrt{\pi}=\Delta f \tag{53}$$

$$\int_{-\infty}^{\infty}g^2(u,u)du=\frac{2\sigma^2\pi}{(1+2\gamma^2)^{\frac{1}{2}}}=\frac{1}{2}\frac{\Delta f^2}{(1+2\gamma^2)^{\frac{1}{2}}} \tag{54}$$

$$\int_{-\infty}^{\infty}g^3(u,u)du=\frac{4\sigma^3\pi^{\frac{1}{2}}}{2+3\gamma^2}=\frac{1}{2}\frac{\Delta f^3}{2+3\gamma^2}, \tag{55}$$

where the noise band width of the IF is defined to be

$$\Delta f=\frac{\int_{-\infty}^{\infty}|F_{if}(f)|^2df}{\{\frac{1}{2}[F_{if}(f_0)+F_{if}(-f_0)]\}^{\frac{1}{2}}}=2\sigma\sqrt{\pi}. \tag{56}$$

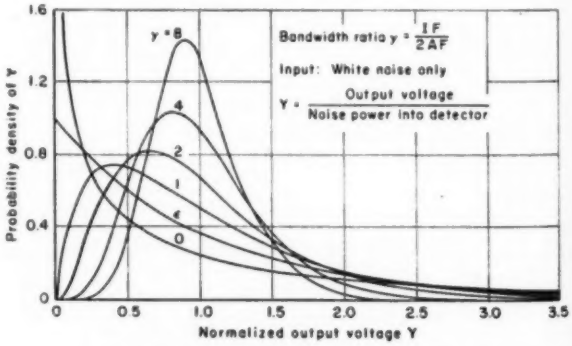

FIG. 3. Output probability densities for the Gaussian system (signal absent).

§ These formulas have been obtained by neglecting the terms in $\cos\omega_0(u+v)$ which represent the high-frequency residue. They are vanishingly small for sufficiently large ω_0.

Let the input signal voltage be

$$S(t)=(2S)^{\frac{1}{2}}\cos\omega_0 t, \tag{57}$$

where S is the average power. [This is also the average signal power applied to the detector because of Eq. (45)]. We then calculate‖

$$\int_{-\infty}^{\infty}\int S(t-u)g(u,v)S(t-v)dudv=S \tag{58}$$

$$\int_{-\infty}^{\infty}\int S(t-u)g^2(u,v)S(t-v)dudv=\frac{1}{2}\frac{\Delta f}{(1+\gamma^2)^{\frac{1}{2}}}S \tag{59}$$

$$\int_{-\infty}^{\infty}\int S(t-u)g^3(u,v)S(t-v)dudv$$

$$=\frac{1}{2}\frac{\Delta f^2}{[(2+\gamma^2)(2+3\gamma^2)]^{\frac{1}{2}}}S. \tag{60}$$

Thus, by means of Eq. (38) we get for the first three cumulants,

$$K_1=N[1+X] \tag{61}$$

$$K_2=\frac{N^2}{(1+2\gamma^2)^{\frac{1}{2}}}\left[1+2X\left(\frac{1+2\gamma^2}{1+\gamma^2}\right)^{\frac{1}{2}}\right], \tag{62}$$

$$K_3=\frac{4N^3}{2+3\gamma^2}\left[1+3X\left(\frac{2+3\gamma^2}{2+\gamma^2}\right)^{\frac{1}{2}}\right], \tag{63}$$

where

$$N=\phi_0\Delta f \tag{64}$$

is the average noise power at the input to the detector, and

$$X=S/N \tag{65}$$

is the signal-to-noise power ratio at the input to the detector.

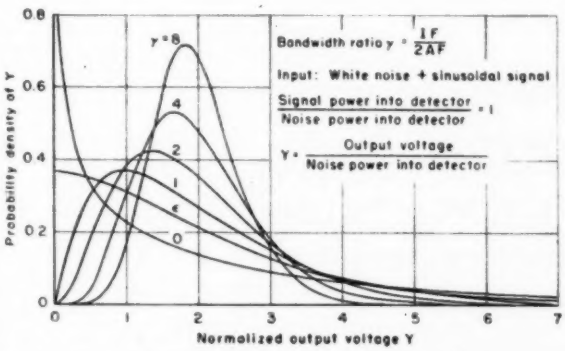

FIG. 4. Output probability densities for the Gaussian system (signal-to-noise ratio=1).

‖ Again, omitting the high-frequency terms in $\cos\omega_0(2t-u-v)$.

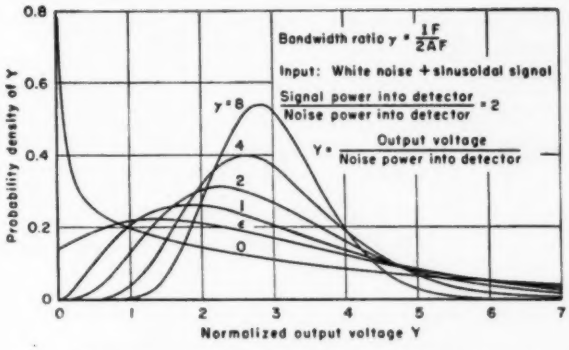

FIG. 5. Output probability densities for the Gaussian system (signal-to-noise ratio=2).

The output probability density functions are now expressed in terms of the orthonormal series discussed in Sec. III. They have been plotted in Figs. (3), (4) and (5) for selected values of the input signal-to-noise ratio X and band-width ratio γ. As was pointed out in the preceding footnotes, the treatment in this section neglects the high-frequency detector residue terms. Consequently, on letting γ pass to zero we do not obtain the case of infinite audio band width discussed in Sec. I. Rather we obtain in the limit the well-known density function for the square law envelope detector with no additional audio filtering. These curves are labeled $\gamma=\epsilon$, and the notation $\gamma=0$ is reserved for the curves of Eq. (29).

The curves labeled $\gamma=0$ and $\gamma=\epsilon$ are exact. Those for $\gamma=1$ and $\gamma=2$, were computed with the Laguerre series, and those for $\gamma=4$ and $\gamma=8$ were obtained from the Gram-Charlier series. In each case the convergence is fairly rapid (three terms were the most required) for graphical accuracy in the interior regions. Accuracy for the extremes, i.e., $Y\sim O$ and Y very large is not claimed. For the region $Y\sim O$ the series do not converge to zero rapidly enough for practical computation. In this region the curves have been corrected so as to go to zero in a sensible way. The tails for Y large appear as computed with the terminated series.

It will be noted that the tendency toward normality with increased γ (i.e., reduced audio band width) is pronounced. This is an illustration of general behavior of integrated noise derivable from the Central Limit Theorem. The tendency toward normality with increased signal-to-noise ratio is somewhat evidenced on passing through Figs. 3, 4 and 5. This phenomenon is also well known. It is due to the tendency of the detector characteristics toward linearity with the resulting duplication in the output statistics of the Gaussian IF distribution.

Appendix I. General Formula for K_n for the Gaussian System

We will now derive the Mercer series, Eq. (6), for $g(u,v)$ and obtain the general expression for the nth

cumulant. This will serve as a check on formulas (61) through (63).

To start with, write

$$g(u,v)=\frac{4\pi\sigma^2\cos\omega_0(u-v)}{(1+2\gamma^2)^{\frac{1}{2}}}\exp\left[-\frac{(2\pi\sigma)^2}{2}\right]\times\left\{\frac{1+\gamma^2}{1+2\gamma^2}(u^2+v^2)-\frac{2\gamma^2}{1+2\gamma^2}uv\right\} \quad (66)$$

and make the substitutions,

$$u=\frac{(1+2\gamma^2)^{\frac{1}{2}}}{2\pi\sigma}x, \quad (67)$$

$$v=\frac{(1+2\gamma^2)^{\frac{1}{2}}}{2\pi\sigma}y, \quad (68)$$

$$t=\frac{(1+2\gamma^2)^{\frac{1}{2}}-1}{(1+2\gamma^2)^{\frac{1}{2}}+1}. \quad (69)$$

Then Eq. (66) becomes,

$$g(u,v)=\frac{4\pi\sigma^2\cos\omega_0(u-v)}{(1+2\gamma^2)^{\frac{1}{2}}}\exp\left(-\frac{x^2+y^2}{2}\right)\cdot\exp-\left\{\frac{t^2(x^2+y^2)-2txy}{1-t^2}\right\}. \quad (70)$$

We now make use of Mehler's formula,¶ i.e.:

$$\exp-\left\{\frac{t^2(x^2+y^2)-2txy}{1-t^2}\right\}=(1-t^2)^{\frac{1}{2}}\sum_{j=0}^{\infty}H_j(x)H_j(y)\frac{t^j}{j!2^j} \quad (71)$$

and, after expanding $\cos\omega_0(u-v)$, we obtain the eigenvalue pairs

$$\lambda_j{}^S=\lambda_j{}^C=\frac{2\sigma\sqrt{\pi}}{1+(1+2\gamma^2)^{\frac{1}{2}}}\left[\frac{(1+2\gamma^2)^{\frac{1}{2}}-1}{(1+2\gamma^2)^{\frac{1}{2}}+1}\right]^j \quad (72)$$

and the corresponding pairs of eigenfunctions,

$$h_j{}^{S,\,C}(u)=(4\pi\sigma)^{\frac{1}{2}}\frac{\exp\left(-\frac{(2\pi\sigma)^2}{(1+2\gamma^2)^{\frac{1}{2}}}\frac{u^2}{2}\right)\cdot H_j\left(\frac{2\pi\sigma u}{(1+2\gamma^2)^{\frac{1}{2}}}\right)}{[2^j j!\sqrt{\pi}(1+2\gamma^2)^{\frac{1}{4}}]^{\frac{1}{2}}}\left\{\begin{matrix}\sin\omega_0 u\\ \cos\omega_0 u\end{matrix}\right\}. \quad (73)$$

Here $H_j(x)$ is the Hermite polynomial defined by

$$H_j(x)=(-)^j e^{x^2}\frac{d^j}{dx^j}e^{-x^2}. \quad (74)$$

On summing with Eq. (72), we get

$$\sum_{j=0}^{\infty}\lambda_j{}^n=\sum_{j=0}^{\infty}(\lambda_j{}^S)^n+\sum_{j=0}^{\infty}(\lambda_j{}^C)^n=\frac{2(2\sigma\sqrt{\pi})^n}{[(1+2\gamma^2)^{\frac{1}{2}}+1]^n-[(1+2\gamma^2)^{\frac{1}{2}}-1]^n}. \quad (75)$$

For the sinusoidal input signal defined by Eq. (57) we get

$$\left.\begin{aligned}s_j{}^{S,\,C}(t)&=(2S)^{\frac{1}{2}}\int_{-\infty}^{\infty}\cos\omega_0(t-x)h_j{}^{S,\,C}(x)dx\\&=\left(\frac{2S}{2\sigma\sqrt{\pi}}\right)^{\frac{1}{2}}(1+2\gamma^2)^{1/8}\frac{(j!)^{\frac{1}{2}}}{2^{j/2}(j/2)!}\left\{\begin{matrix}\sin\omega_0 t\\ \cos\omega_0 t\end{matrix}\right\}\text{for } j \text{ even}\\&=0 \text{ for } j \text{ odd.}\end{aligned}\right\}. \quad (76)$$

This result is valid for ω_0 sufficiently high to justify neglecting the high-frequency residue.

On summing with Eq. (72) and (76) we get

$$\sum_{j=0}^{\infty}\lambda_j{}^n s_j(t)^2=\sum_{j=0}^{\infty}(\lambda_j{}^S)^n s_j{}^S(t)^2+\sum_{j=0}^{\infty}(\lambda_j{}^C)^n s_j{}^C(t)^2=\frac{2S(2\sigma\sqrt{\pi})^{n-1}(1+2\gamma^2)^{\frac{1}{2}}}{\{[(1+2\gamma^2)^{\frac{1}{2}}+1]^{2n}-[(1+2\gamma^2)^{\frac{1}{2}}-1]^{2n}\}^{\frac{1}{2}}}. \quad (77)$$

Finally, by means of Eqs. (34), (56), (64), and (65) we get for the nth cumulant,

$$K_n=\frac{(2N)^n(n-1)!}{[(1+2\gamma^2)^{\frac{1}{2}}+1]^n-[(1+2\gamma^2)^{\frac{1}{2}}-1]^n}\left(1+nX\left\{\frac{[(1+2\gamma^2)^{\frac{1}{2}}+1]^n-[(1+2\gamma^2)^{\frac{1}{2}}-1]^n}{[(1+2\gamma^2)^{\frac{1}{2}}+1]^n+[(1+2\gamma^2)^{\frac{1}{2}}-1]^n}\right\}^{\frac{1}{2}}(1+2\gamma^2)^{\frac{1}{4}}\right), \quad (78)$$

which reduces for $n=1$, 2, and 3 to Eqs. (61), (62), and (63), respectively.

¶ See Watson, J. London Math. Soc., 8, 189 (1933).

Appendix II. Signal Detectability for the Gaussian System

Lawson and Uhlenbeck[10] in discussing various detection criteria suggest a "deflection criterion" which is based on measuring the change in the average output brought about by the signal. It is suggested that this change should be comparable to the standard deviation due to noise alone in order that the signal be "detectable." In terms of the cumulants, then, we have for detectability

$$S_0=\frac{K_1^{S+N}-K_1^{N}}{(K_2^{N})^{\frac{1}{2}}}\sim 1. \tag{79}$$

Related to this criterion is one obtained by using the standard deviation of the signal plus noise, i.e.,

$$S_s=\frac{K_1^{S+N}-K_1^{N}}{(K_2^{S+N})^{\frac{1}{2}}}\sim 1. \tag{80}$$

These quantities have been investigated by Smith[8] for a variety of filter shapes and detector characteristics. By direct substitution from Eq. (61) and (62) we get for the Gaussian square law system,

$$S_0=X(1+2\gamma^2)^{\frac{1}{2}} \tag{81}$$

$$S_s=\frac{X(1+2\gamma^2)^{\frac{1}{2}}}{\left[1+2X\left(\frac{1+2\gamma^2}{1+\gamma^2}\right)^{\frac{1}{2}}\right]^{\frac{1}{2}}}. \tag{82}$$

For relatively narrow audio band width, i.e., γ large, which is the region of interest for the reference, these expressions reduce to

$$S_0\sim\frac{X}{2^{\frac{1}{4}}}(2\gamma)^{\frac{1}{2}} \tag{83}$$

$$S_s\sim\frac{X(2\gamma)^{\frac{1}{2}}}{2^{\frac{1}{4}}(1+2\sqrt{2}X)^{\frac{1}{2}}}. \tag{84}$$

These are in agreement with the formulas given by Smith.

The "Ideal or Threshold Detector" provides another means for determining signal detectability. With this device a "detection" is called if the output voltage at any particular time exceeds a certain threshold. The level of this threshold is then adjusted so that "false alarms," i.e., detections in the absence of signal, are relatively infrequent. The probability of a detection at any instant can then be written

$$P_d(X,\tau)=\int_{\tau}^{\infty}P'(E_0,X)dE_0. \tag{85}$$

[10] J. L. Lawson and G. E. Uhlenbeck, *Threshold Signals* (Rad. Lab. Series), No. 24, p. 161.

Marcum[5] has considered the case of a square law envelope detector with video integration, i.e., successive samples of the detector output are numerically averaged rather than applied to a filter. The probability density function for this average output is given (in our notation) by the formula,

$$P'(E_0,X,\alpha)=\frac{\alpha}{N}\left(\frac{E_0}{NX}\right)^{(\alpha-1)/2}\times\exp\left[-\alpha\left(\frac{E_0}{N}+X\right)\right]I_{\alpha-1}\left[2\alpha\left(\frac{E_0X}{N}\right)^{\frac{1}{2}}\right], \tag{86}$$

where α is the number of samples averaged. The cumulants for this distribution are given by the formula,

$$K_n^{*}=\frac{N^n(n-1)!}{\alpha^{n-1}}(1+nX), \tag{87}$$

the first few of which are

$$K_1^{*}=N(1+X), \tag{88}$$

$$K_2^{*}=\frac{N^2}{\alpha}(1+2X), \tag{89}$$

$$K_3^{*}=\frac{2N^3}{\alpha^2}(1+3X). \tag{90}$$

We now set

$$\alpha=(1+2\gamma^2)^{\frac{1}{2}}, \tag{91}$$

and notice that fairly good agreement exists between these cumulants and those for the Gaussian audio system. Consequently, $(1+2\gamma^2)^{\frac{1}{2}}$ can be interpreted as the approximate number of samples averaged by the audio filter.**

It is now possible to obtain a fairly good first approximation to the probability of detection, $P_d(X,\tau)$, by referring to the appropriate curves in reference 5.

List of Symbols

$E_i(t)$	IF input voltage
$E(t)$	IF output (detector input) voltage
$E^2(t)$	Detector output (audio input) voltage
$E_0(t)$	Audio output voltage
$F_{if}(\omega)$	IF voltage transfer function
$f_{if}(t)$	Fourier transform of $F_{if}(\omega)$
$F_a(\omega)$	Audio voltage transfer function
$f_a(t)$	Fourier transform of $F_a(\omega)$
$g(u,v)$	System kernel defined by Eq. (5)
$h_j(u)$	jth normal eigenfunction of $g(u,v)$
λ_j	Eigenvalue corresponding to $h_j(u)$

** This is not an exact treatment because the probability density function for the Gaussian system cannot be put precisely into the form of Eq. (86) unless $\gamma=0$. However, the mean values will correspond exactly, the variance will be correct to within a factor of less than $\sqrt{2}$ in X, and the asymmetry will be in error by a factor less than 4/3 in K_3 and $\sqrt{3}$ in X.

$e_j(t)$	Component of $E_i(t)$ along $h_j(x)$ [see Eq. (10)]	σ	Band-width measure for Gaussian IF amplifier
$S(t)$	Signal component of $E_i(t)$	ν	Band-width measure for Gaussian audio-amplifier
$N(t)$	Noise component of $E_i(t)$	γ	σ/ν
$s_j(t)$	Signal component of $e_j(t)$ [see Eq. (13)]	Δf	Noise band width of IF amplifier
$\eta_j(t)$	Noise component of $e_j(t)$ [see Eq. (14)]	$H_j(x)$	jth Hermite polynomial [defined by Eq. (74)]
ϕ_0	IF input noise power per unit frequency	ω_0	Center frequency of the IF amplifier
$\Phi(\xi, t)$	Characteristic function of the probability density of $E_0(t)$	K_1^{S+N}	First output cumulant for signal plus noise
S	Signal power at input to the detector	K_1^N	First output cumulant for noise alone
N	Noise power at input to the detector	K_2^{S+N}	Second output cumulant for signal plus noise
X	Signal-to-noise power ratio at input to the detector	K_2^N	Second output cumulant for noise alone
Y	Audio output voltage measured in units of N	S_0, S_x	Detectability criteria [see Eqs. (79) and (80)]
K_n or $K_n(t)$	nth cumulant [defined by Eq. (33)]		
$g^n(u, v)$	n times iterated kernel [defined by Eq. (35)]		

JOURNAL OF APPLIED PHYSICS VOLUME 24, NUMBER 9 SEPTEMBER, 1953

The Energy Stored in Metal Chips during Orthogonal Cutting

M. B. Bever, E. R. Marshall, and L. B. Ticknor*
Department of Metallurgy, Massachusetts Institute of Technology, Cambridge, Massachusetts
(Received February 23, 1953)

Chips of a gold-silver alloy were made by orthogonal cutting with apparatus which permitted the determination of the chip geometry and cutting forces. From these data the stresses and strains and the shear and friction energies were calculated. Three rake angles were used to obtain different shear strains. The energy stored in the chips was determined as the difference in the heat effects associated with the dissolution in liquid tin of samples of cold worked and annealed chips in an isothermal calorimeter of high precision. With increasing strain the stored energy increased, but the ratio of the stored energy to the shear energy decreased.

INTRODUCTION

THE orthogonal (two-dimensional) cutting process, illustrated schematically in Fig. 1(a), is an effective experimental procedure for subjecting metals to precisely known amounts of plastic deformation. Piispanen[1,2] and Merchant[3,4] have demonstrated that a continuous chip forms by a process of shear, as shown in Fig. 1(b). The energy expended in cutting goes into plastic deformation of the chip and friction between the chip and tool; by comparison the energy expended in generating the new surfaces is negligible.[4] Part of the energy of deformation appears as heat and the remainder is stored in the chip. In the investigation reported here, the energy stored was determined as a function of the amount of plastic deformation.

Epifanov and Rebinder[5] have investigated the energy stored in chips by drilling in a calorimeter. They simultaneously measured the energy input to the drill and the heat evolved and considered the difference as the energy retained in the chips.

A variety of methods has been employed to measure the energy stored in metals deformed by various processes. A recent paper[6] reviews past work and reports on an investigation of the energy retained during rolling of a gold-silver alloy. The method of measuring this energy had previously been described briefly[7] and is identical with the one used in the investigation reported here.

The determination of the retained energy by this method differs from that of Epifanov and Rebinder[5] in that the measurements are conducted in two steps rather than simultaneously. In the first step chips are formed by machining and the forces on the tool and the chip geometry are measured. From these measurements the stresses and strains, and the shear and friction energies are calculated. In the second step the heat

* Present address: Department of Chemistry, Swarthmore College, Swarthmore, Pennsylvania.
[1] V. Piispanen, Teknillinen Aikakauslehti **27**, 315 (1937).
[2] V. Piispanen, J. Appl. Phys. **19**, 876 (1948).
[3] M. E. Merchant, J. Appl. Mech. **11**, A168 (1944).
[4] M. E. Merchant, J. Appl. Phys. **16**, 267 and 318 (1945).
[5] G. I. Epifanov and P. A. Rebinder, Doklady Akad. Nauk S.S.S.R. **66**, 653 (1949).
[6] M. B. Bever and L. B. Ticknor, Acta Met. **1**, 116 (1953).
[7] M. B. Bever and L. B. Ticknor, J. Appl. Phys. **22**, 1297 (1951).

effect associated with the dissolution of the chips in a calorimeter is determined. The corresponding effect for an equal quantity of annealed chips is also determined. The difference between these heat effects, adjusted to infinite dilution, is the stored energy of cold work.

The advantage of this method derives from the fact that the heat of solution of the gold-silver alloy in liquid tin is small. The stored energy, therefore, is the difference of two small quantities. Simultaneous methods, on the other hand, depend on the difference between the energy input and heat evolved, quantities large compared with the stored energy. The advantage of the present method, however, is restricted to combinations of solutes and solvents having small heats of solution.

Orthogonal cutting permits a simple analysis whereby basic information, such as stresses, strains, and energies,

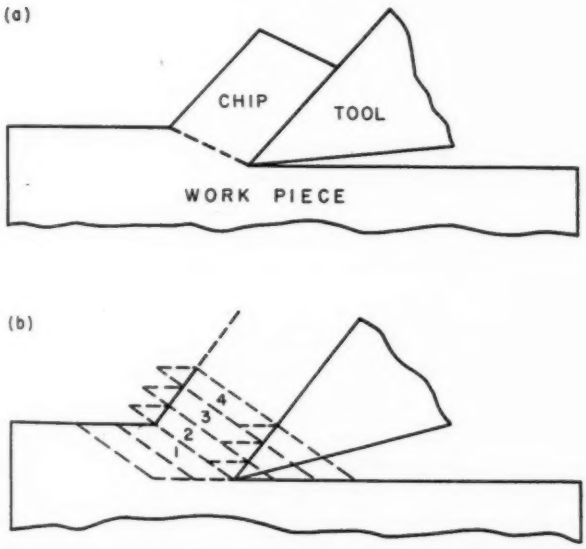

FIG. 1. (a). Elements of orthogonal cutting and (b). Formation of chips by shear.

can be found. Since the amount of energy going into plastic straining can be calculated, the stored energy can be expressed as a fraction of the strain energy. For a complex process such as drilling, it is not possible to divide the energy input between deformation and friction and consequently the stored energy cannot be calculated as a fraction of the energy of deformation.

Data on the stored energy of cold work have fundamental interest, for example in connection with the kinetics of recrystallization, x-ray diffraction measurements on worked metals and the theory of dislocations. Such data also have practical value in predicting the temperature at the tip of a tool in cutting[8] or at a grit in grinding.[9]

[8] K. J. Trigger and B. T. Chao, Trans. Am. Soc. Mech. Engrs. 73, 57 (1951).

[9] J. O. Outwater and M. C. Shaw, Trans. Am. Soc. Mech. Engrs. 74, 73 (1952).

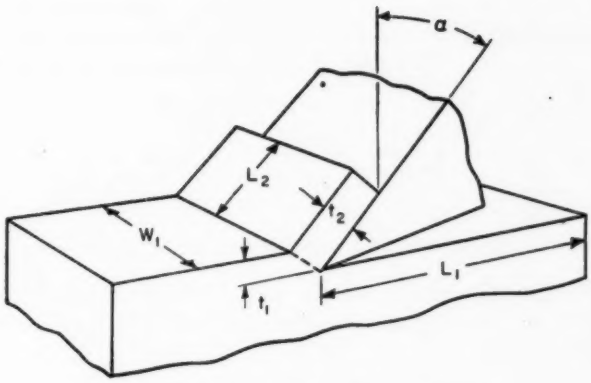

FIG. 2. The geometry of orthogonal cutting [after Merchant (reference 4)].

PROCEDURES

A. Orthogonal Cutting

The equations for calculating the stresses, strains and energies involved in continuous chip formation have been derived by Merchant.[3,4] The following geometric quantities, also shown in Fig. 2, are required for the calculations: α = the rake angle of the tool, w_1 = the width of cut (or chip), t_1 = the depth of cut, L_1 = the length of cut, and L_2 = the chip length.

The angle φ between the direction of shear and the work surface is calculated from the following equation:

$$\tan\varphi=\frac{(L_2/L_1)\cos\alpha}{1-(L_2/L_1)\sin\alpha}. \tag{1}$$

The shear strain ϵ in forming a chip is given by

$$\epsilon=\cot\varphi+\tan(\varphi-\alpha). \tag{2}$$

The cross-sectional area of cut is

$$A_0=w_1t_1. \tag{3}$$

The forces exerted by the chip on the tool were measured by a force dynamometer of the electric strain gauge type. A similar planing dynamometer has been described by Loewen, Marshall, and Shaw.[10] The two force components measured were F_c, the cutting force (along the work surface), and F_t, the thrust force (perpendicular to the work surface).

The shear stress S_s during chip formation is

$$S_s=(F_c\sin\varphi\cos\varphi-F_t\sin^2\varphi)/A_0, \tag{4}$$

and the shear energy W_s per unit volume removed is

$$W_s=S_s\epsilon. \tag{5}$$

The total work expended in cutting per unit volume removed, W_c, is

$$W_c=(F_c\cdot L_1)/(A_0\cdot L_1)=F_c/A_0. \tag{6}$$

[10] Loewen, Marshall, and Shaw, Proc. Soc. Exptl. Stress Anal. 8, 1 (1951).

TABLE I. Forces and related quantities in cutting experiments.

Width of cut, $w_1 = 0.187$ in.; depth of cut, $t_1 = 0.003$ in.; area, $A_0 = 5.61 \times 10^{-4}$ in^2; length of cut, $L_1 = 2.02$ in.

	Observed					Calculated			
α	L_2 in.	F_c lb	F_t lb	φ	ϵ	S_s psi.	W_s in. lb per in.^{3}	W_c in. lb per in.^{3}	W_f in. lb per in.^{3}
45°	1.235	41.7	−0.12	37.25°	1.179	35 400	41 800	74 300	32 500
30°	0.972	77.6	12.37	28.75°	1.801	53 100	95 500	138 200	42 700
15°	0.519	274	12.73	14.88°	3.759	119 700	450 000	488 300	38 300

Finally, the friction energy per unit volume removed, W_f, is the difference between the total work and the shear work

$$W_f = W_c - W_s. \tag{7}$$

In the experimental work an annealed alloy of 74.9 weight percent gold and 25.1 percent silver was used. This alloy was a homogeneous solid solution. Three different shear strains were obtained by using rake angles of 45°, 30°, and 15°. A decrease in rake angle increases the shear strain. The width, depth, and length of cut (w_1, t_1, L_1, respectively) were held constant in all tests. The cutting speed was 12 inches per minute. Carbon tetrachloride was used as a cutting fluid in order to insure a continuous chip with a sharply defined shear plane. Approximately eighty chips were obtained for each rake angle. Table I gives the observations (each one representing an average for eighty chips) and a summary of the calculations based on these data. The chips were stored in dry ice during the interval of one or two days, which elapsed between the cutting operation and the calorimetric measurement.

B. Calorimetric Measurements

The stored energy was determined as the difference in the heat effects of dissolution in liquid tin of a sample of cold worked chips and of an equal sample of fully annealed chips. The isothermal calorimeter used, its operation and the method of calculation have been described.[11] The use of this method for measuring the energy stored in rolled specimens of a gold-silver alloy has also been reported.[6,7] The experimental procedure and the calculations, therefore, will be described here only briefly.

The calorimeter consisted of a bath of tin held at 240°C in a Dewar flask immersed in a constant-temperature salt bath. Samples could be added under vacuum from a holder maintained at 0°C. The temperature changes of the tin bath resulting from an addition were followed with an accuracy of about 0.01°C by a thermocouple and potentiometer. After an initial drop in temperature owing to the absorption of heat by the cold addition, the exothermic dissolution of the gold-silver alloy in tin raised the temperature nearly to its original value. The complete return to the original tin bath temperature was brought about by heat transfer from the salt bath following approximately an exponential relation. A calibrating addition of tungsten furnished information on the coefficient K for this exponential heat transfer and the energy equivalent ("water value") of the calorimeter C_p.

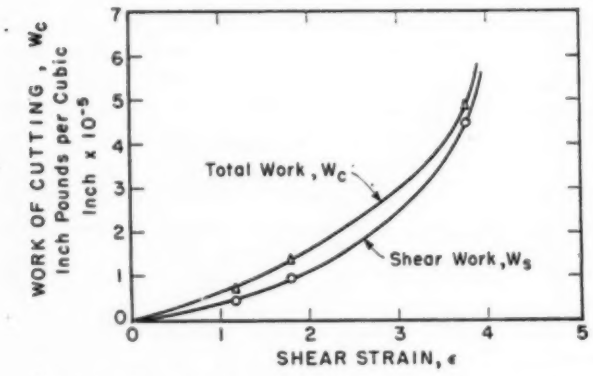

FIG. 3. The work of cutting as a function of shear strain for a gold-silver alloy.

[11] L. B. Ticknor and M. B. Bever, Trans. Am. Inst. Mining Met. Engrs. **194**, 941 (1952).

TABLE II. Measured values of the energy stored in gold-silver alloy chips and related quantities.

Rake angle α	Strain ϵ	Stored energy, E_{st} cal per gram-atom	cal per gram	in. lb per in.^{3}	Fraction stored E_{st}/W_c (percent)
45°	1.179	39	0.24	2300	5.6
30°	1.801	48	0.29	2800	2.9
15°	3.759	56	0.34	3300	0.73

The heat effect of an alloy addition was calculated in two parts: (1) the heat corresponding to the product of the energy equivalent C_p and the decrease in the temperature of the calorimeter after complete dissolution of the sample at time t_2 and (2) the heat exchanged between the salt bath and the tin solution in the interval from the addition of the sample at t_1 to time t_2. Thus,

$$Q = \int_{T_1}^{T^2} C_p dT + K \int_{t_1}^{t_2} \Delta T dt. \tag{8}$$

The heat effects of additions of cold worked and annealed chips were measured in a single run. A number of possible errors were thereby minimized. The heat effect of dissolution of the alloy in tin is a function of the composition of the resulting tin-gold-silver solution.

In the dilute range of interest here, this function is of the form $A+Bx$, where B has been found by a large number of measurements[6,11] to be -36 and x is the composition (in atomic percent solute); A is the heat effect per gram-atom of alloy at infinite dilution and can be calculated. The difference in A for the cold worked and annealed samples is equal to the stored energy E_{st} of cold work (in cal per gram-atom of alloy). Values of E_{st} determined in this manner for samples of chips are listed in Table II.

DISCUSSION OF RESULTS

Figure 3 shows the work of cutting plotted against shear strain. Both the total work W_c and the shear work W_s rise at an increasing rate with shear strain, while their difference, equalling the friction energy, remains approximately constant for strains ranging from 1 to 4. The total work is considerably larger than the shear work, except at high strains. Thus, the total work is not

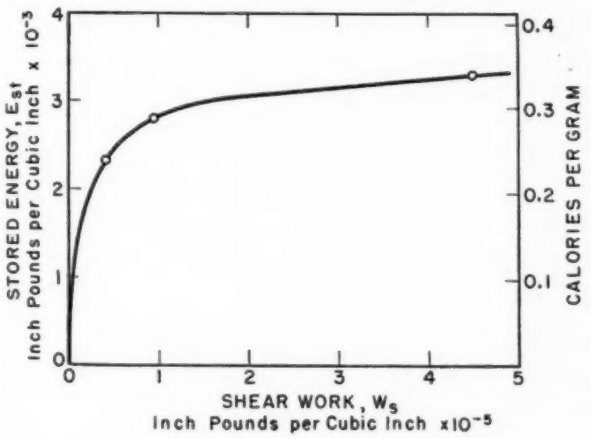

FIG. 4. The energy stored in chips of a gold-silver alloy as a function of shear work.

a good approximation to the shear work over most of the range of strains of interest here.

Since the friction work does not contribute appreciably to the plastic deformation of the bulk of the chip, the stored energy should be expressed as a function of shear work rather than of total work. This relation is shown in Fig. 4. The stored energy tends to level off with increasing shear work. Figure 5 shows the stored energy against shear strain. The rate of increase of the energy stored decreases markedly with increasing shear

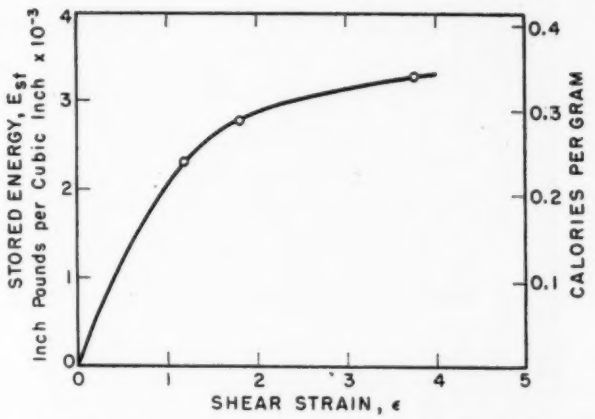

FIG. 5. The energy stored in chips of a gold-silver alloy as a function of shear strain.

strain. Neither of these graphs, however, clearly indicates a saturation value for the stored energy. Clarification of this point was desirable, but it was not possible to obtain higher strains, because the smaller rake angles necessary (e.g., 0°) caused the chip to become discontinuous.

Table II gives the stored energy as a fraction of the energy of deformation. This fraction drops from over 5 percent at a shear strain of roughly 1 to less than 1 percent at a shear strain of nearly 4. These fractions of stored energy may be compared with those obtained with rolled specimens of the same alloy.[6] These values ranged from 4–5 percent for rolling strains between 0.2 and 0.8, to 2 percent for a rolling strain of 1.4, and 1.3 percent for a rolling strain of 2.5. The fractions of stored energy reported here also agree as to order of magnitude with the results of Epifanov and Rebinder,[5] who found that the stored energy was a few percent of the total work of drilling.

For comparable strains the amount of energy stored was less in the rolled specimens of this alloy[6] than in in the chips. This difference can be attributed to the difference in the mechanism of the deformation processes.

ACKNOWLEDGMENTS

The authors are indebted to Professor M. C. Shaw for use of facilities of the M.I.T. Metals Cutting Laboratory. They also gratefully acknowledge contributions made by Dr. J. S. L. Leach and L. R. Rubin. The work was performed under Contract No. AT-30-Gen-1002 with the U. S. Atomic Energy Commission.

Free Surface Motion Induced by Shock Waves in Steel*†

WILLIAM A. ALLEN
Michelson Laboratory, U. S. Naval Ordnance Test Station, Inyokern, China Lake, California
(Received March 9, 1953)

An optical technique, reported in a previous paper, has been used to measure surface oscillations on a series of thick 5.5-in. diam steel plates of different thicknesses while they deform under explosive attack. Data obtained from the four 1025 steel specimens illustrated in the previous paper, and data obtained from two additional specimens have been analyzed partially. Results are compared with predictions from the theory of elasticity for the case of a diverging pulse. Elementary theory, known to be incorrect in the physical regime studied, is shown to give many satisfactory predictions for large distances from the charge.

INTRODUCTION

THE phenomenon studied[1] is produced when an explosive charge is detonated in intimate contact with a steel plate. Figure 1 illustrates the sequence of events that occur when a typical 4-in. specimen is fired. Initially, a curved shock-like compression pulse ($A-A$) propagates into the specimen. Later, the pulse interacts with the free surface to produce deformation ($B-B$); the compression pulse is reflected from the free surface as a tension pulse. Time-dependent histories of the slopes associated with twelve equally spaced points on a diam of the free surface have been recorded for several μsec after arrival of the initial pulse. The equipment used consists of a sweeping-image camera that views the virtual images of point light sources in the polished surface of the specimen. During the time in which the specimen is undisturbed, the camera maps the virtual images into twelve straight line *traces* on the film. The straight lines are deflected when the deformation propagates across the surface; the deflection amplitude is a measure of the radial slope of the free surface.

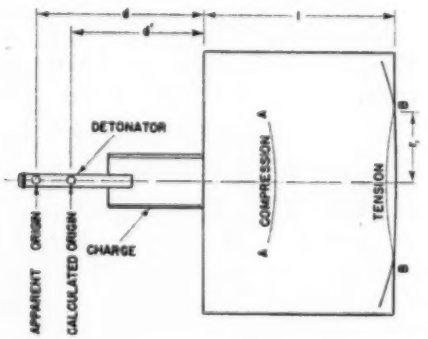

FIG. 1. Interaction of high explosive with 4-in. steel specimen to produce a shock wave. The initial pulse is shown for two different times.

* Supported in part by Armament and Mechanics Branches, U. S. Office of Naval Research.

† Presented as a paper at the American Physical Society meeting at Salt Lake City, Utah, June 25–27, 1952. For Abstract, see Phys. Rev. 87, 910 (1952).

[1] W. A. Allen and C. L. McCrary, Rev. Sci. Instr. 24, 165 (1952).

THE PHOTOGRAPHIC RECORD

A typical photographic record from a 4-in. specimen is reproduced in Fig. 2. The sketch, which represents a reproduction of the photographic data as interpreted by a recording microdensitometer, illustrates some of the principal events that occur during the first few μsec. The origin of time is chosen when the initial longitudinal pulse arrives along the axis at the free surface (A). The deformation produced by the initial pulse persists for about 4.24 μsec. At time$=2$ μsec, the initial longitudinal pulse arrives at the edge (B) of the specimen. At time$=7$ μsec, an unusual disturbance originates at the edge (D) of the specimen and travels, apparently with constant velocity of about 5 mm/μsec, toward the center (E). At time$=9$ μsec, a pulse that originates earlier at the edge of the specimen has arrived at the center (C), where it appears to be reflected (F) with reversed amplitude.

Assume that the radius r_1 of the deformation intersection with the free surface at time t, Fig. 1, can be represented by the relation developed in the previous paper,[1]

$$r_1^2=(ct)^2+2(l+d)(ct), \tag{1}$$

where c is the sound velocity in the steel, 6.2 mm/μsec. The distance $l+d$, Fig. 1, represents the apparent origin of a spherical pulse that arrives at the edge of the specimen 2 μsec later than its arrival on the axis. Substitute known values into Eq. (1) and solve for the apparent origin of the pulse,

$$l+d=190.5 \text{ mm}. \tag{2}$$

As suggested in the previous paper,[1] a spherical wave decreases its curvature when it passes from a high sound velocity medium into a low sound velocity medium. Consequently, the actual calculated origin d' of the spherical disturbance is indicated in Fig. 1 by the distance

$$d'=d/\nu, \tag{3}$$

where ν is the ratio of the detonation velocity in high explosive, 7.8 mm/μsec, to the longitudinal wave velocity in steel. Equation (1), with appropriate constants, has been plotted in Fig. 2 as the hyperbola AB. The excellent agreement between theoretical and experi-

mental data is taken as evidence that the incident pulse is spherical as assumed.

DATA ANALYSIS

The principal method used to analyze the data essentially is the same as reported.[1] It has been found slightly more expeditious, however, to perform the required integrations by numerical hand methods than by use of the REAC. In addition to the reported method, a supplementary method of data analysis has been devised that offers certain conceptual advantages over the basic method. The previously reported method involved an integration over distance r_1 to obtain particle displacement $y=u$. A subsequent differentiation was made with respect to time t to obtain particle velocity $\dot{y}=v$. The supplementary method of data analysis allows calculation of particle velocity v without the necessity to calculate displacement u. The intrinsic experimental data contained in Fig. 2 can be represented by the symbolic equation

$$y_r=f(r, t), \tag{4}$$

where the subscript indicates partial differentiation with respect to radius r. To a close approximation, $f(r, t)$ is considered to be proportional to the trace amplitude that passes through (r, t). Integrate Eq. (4) to obtain the relation

$$y=\int_{r_0(t)}^{r_1(t)} f(r, t)dr, \tag{5}$$

where the arbitrary function of time has been interpreted as plate displacement at infinity and has been set equal to zero. Differentiate Eq. (5) with respect to time to obtain the relation

$$\dot{y}\equiv v=\int_{r_0(t)}^{r_1(t)} f_t dr-\dot{r}_0 f(r_0, t)+\dot{r}_1 f(r_1, t). \tag{6}$$

The limit $r_0(t)$ can represent any definite point on the plate; the limit $r_1(t)$ has been specified by Eq. (1). In Eq. (6), $\dot{r}_0\equiv 0$ because r_0 is a constant. The function $f(r_1, t)$ also vanishes because the trace amplitude has value zero along AB, Fig. 2. Equation (6) can be written in the form

$$\dot{y}\equiv v=\int_{r_0}^{r_1} f_t dr. \tag{7}$$

Since f is proportional to the deflection amplitude of a trace, $f_t(r, t)$ is proportional to the slope of a trace that passes through (r, t). The particle velocity $\dot{y}\equiv v$, Eq. (7), is the space integral over the deformation. If neighboring traces are assumed to be similar, an average value $\bar{f}_t$ can be chosen, and Eq. (7) can be written in the form

$$\dot{y}\sim\bar{f}_t(r_1-r_0). \tag{8}$$

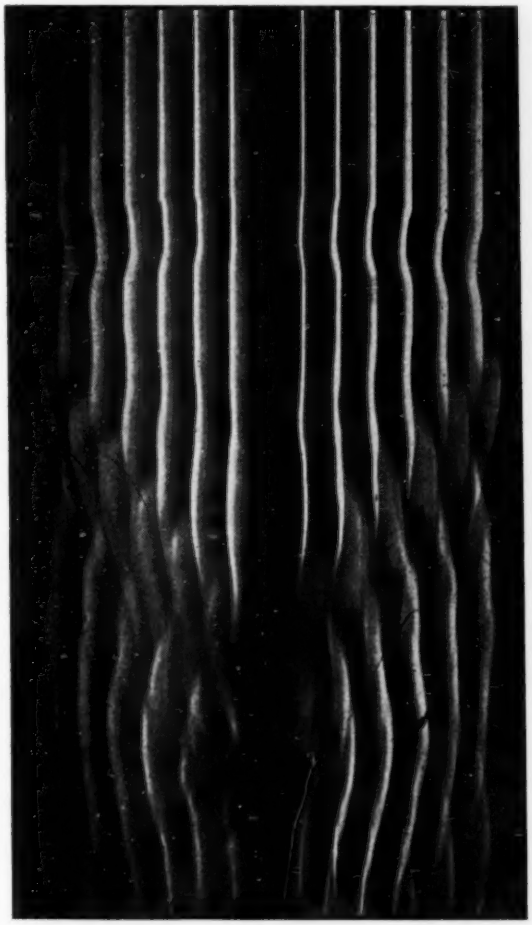

(a)

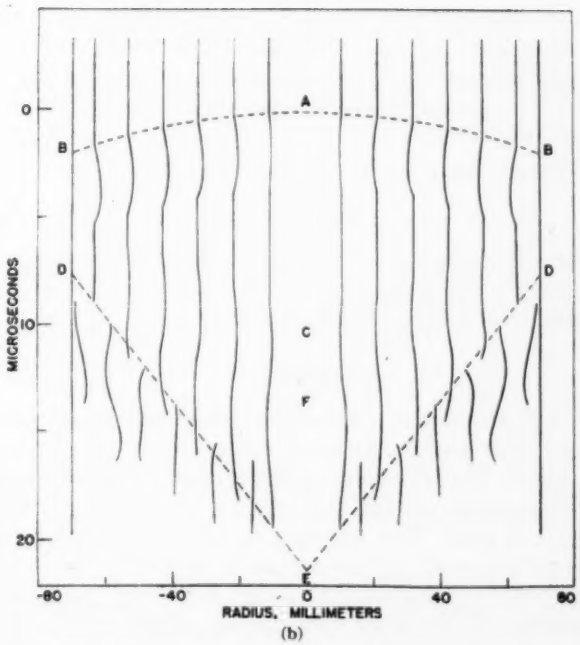

(b)

FIG. 2. Photographic record of 4-in. specimen from sweeping image camera.

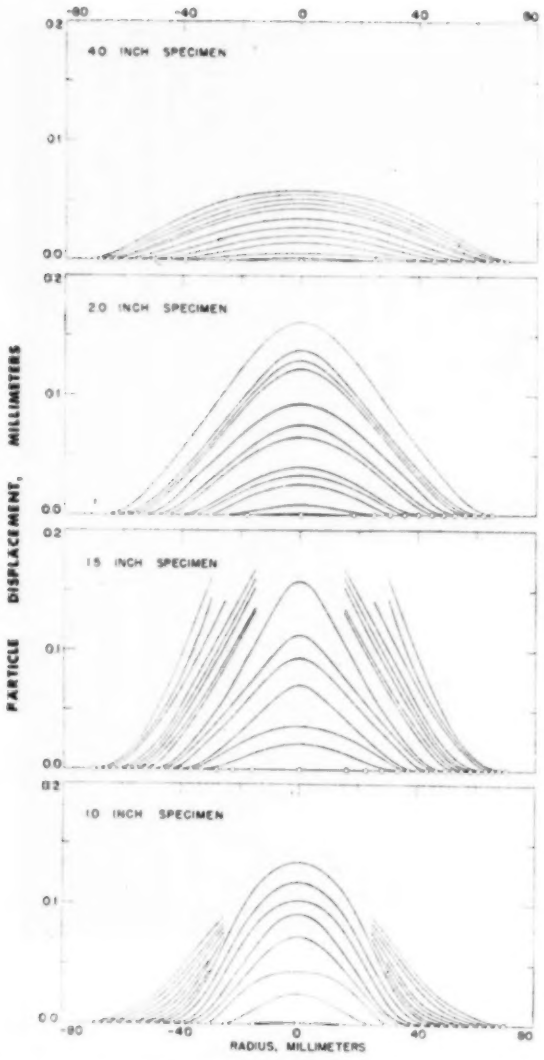

FIG. 3. Transient configurations of free surfaces of family of steel specimens for time intervals $\Delta t = 0.26$ μsec.

Integrate Eq. (8) to obtain the relation

$$y \equiv u \sim \bar{f}(r_1 - r_0), \tag{9}$$

where distance $r_1 - r_0$ has been treated as a constant. Equation (9) states that trace deflection is a rough measure of particle displacement.

RESULTS

The deformation curves associated with four specimens illustrated in the previous paper[1] are reproduced in Fig. 3. The successive curves represent the transient configurations of the free surface at time intervals $\Delta t = 0.26$ μsec. The smoothness of the displacement curves is a result of the numerical integration process. The broken curves associated with the 1.0-in. and $1\frac{1}{2}$-in. specimens indicate the deformation regime where the measuring technique breaks down. For both specimens, however, it was possible to measure the axial displacement over a time interval in excess of 1 μsec. The data of Fig. 3 have also been plotted in Fig. 4 to illustrate the probable experimental scatter connected with the measurements. Figure 4 represents particle displacements of representative points located at distances $r = 0$, 10, $\cdots$, 60 mm, respectively, from the center of the specimens. Data for even distances in cm are differentiated from data at odd distances by use of a different symbol. Figure 4 suggests that initial curvature of all lines is either constant or concave upward. This result is interpreted to mean that particle velocity v, and consequently stress, does not begin to decrease immediately behind the front of the pulse, but tends to maintain or increase its value. Experimental points of Fig. 4 suggest existence of a sinusoidal fine structure departure from the curves as drawn.

Figure 5 represents two additional specimens fired to determine the reproducibility of the experiment.

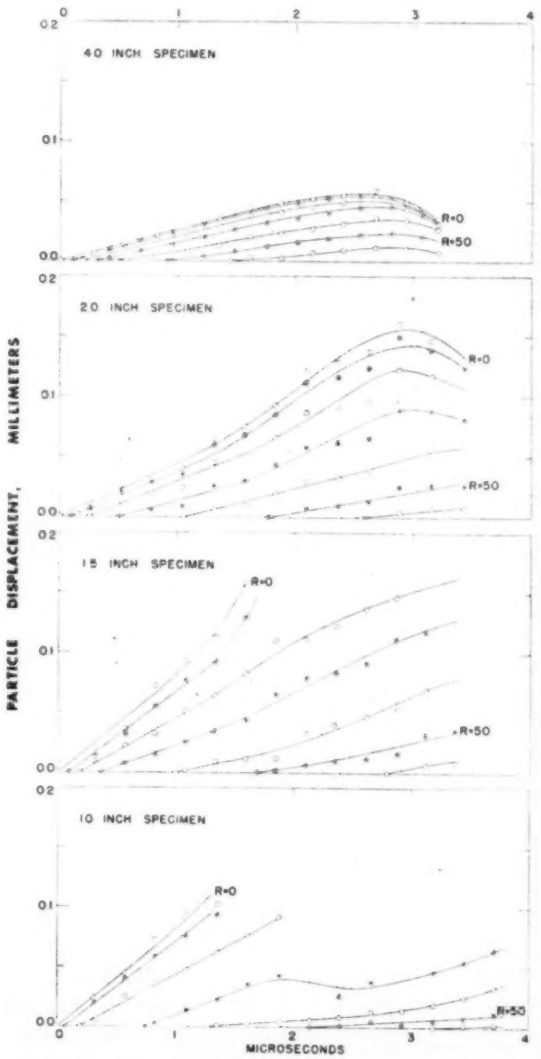

FIG. 4. Displacements for particles at various distances from axis of steel specimens.

Figure 6 is the alternative method of data presentation. Note that the initial behavior during the first 2 μsec of the two 2-in. specimens is similar, although subsequently the auxiliary specimen deformed considerably more than the original specimen. Agreement between the two $1\frac{1}{2}$-in. specimens is good. Figure 7 represents a sketch of axial particle velocity associated with the 2-in. specimens. This curve was obtained by differentiation of the axial displacement curve of Fig. 6. It is probable that the particle velocity curve of Fig. 7 gives a rough idea of the initial shape of the pressure pulse p through the relation

$$p=\rho cv, \tag{10}$$

applicable to plane flow. Figure 7 indicates a plastic pulse that travels at 4.6 mm/μsec. For a 2-in. specimen,

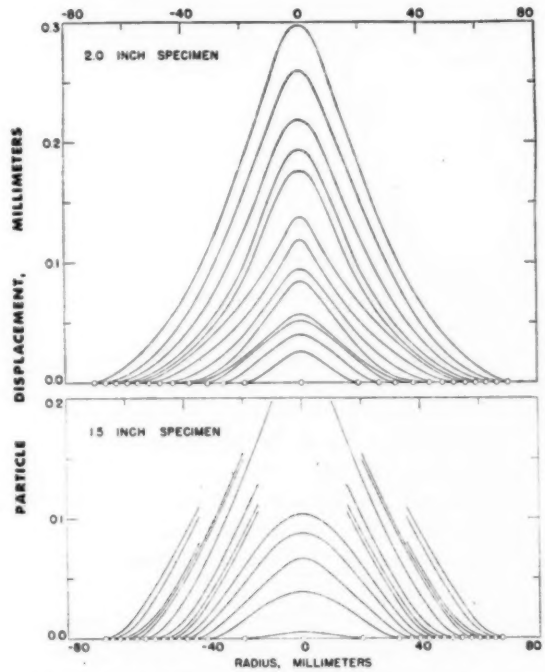

FIG. 5. Transient configurations of free surfaces of two auxiliary steel specimens for time intervals $\Delta t=0.26$ μsec.

this velocity accounts for the observed time delay T in μsec between arrival times of the elastic (E) and plastic (P) pulses at the free surface. The quantity T can be evaluated by the relation

$$T=\left(\frac{1}{4.6}-\frac{1}{6.2}\right)50.8\equiv 2.86. \tag{11}$$

Note that the critical points (E) and (P) in Fig. 7 represent the respective free surface velocities 0.048 mm/μsec and 0.125 mm/μsec. Convert these velocities to stresses by means of the formal relation, Eq. (10), where the value v used is one-half the measured value to account for the effect of the free surface. In English units, these stresses amount, respectively, to 169 000 psi

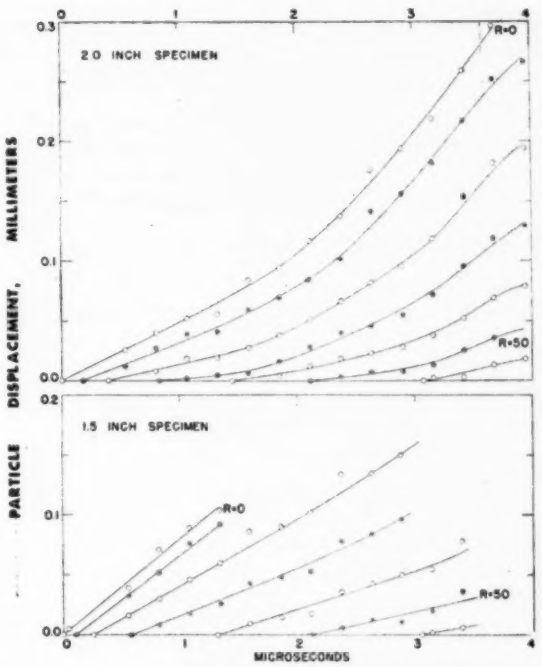

FIG. 6. Displacements for particles at various distances from axis for two auxiliary steel specimens.

and 441 000 psi. Previous investigators[2] have obtained, for essentially the same geometrical configuration used in this experiment, a maximum stress of about 330 000 psi by means of the Hopkinson bar technique. Use of Eq. (10) to calculate stress is of doubtful validity since the formula was derived for the acoustic case; the relation is known not to apply to conditions behind the front of a divergent pulse.[3] It is clear that free surface particle velocity has no ready translation into stress in the cases where actual fracture of the specimens has occurred. The 2-in. specimen of Fig. 6 suffered a slight 4-mm thick spall that extended about 1 cm in both directions from the axis. It is not believed, however,

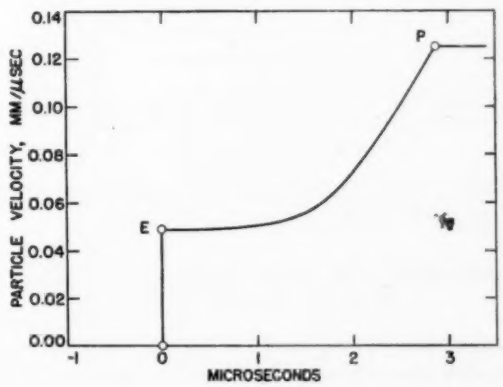

FIG. 7. Axial particle velocity of 2-in. steel specimen whose displacement curve is shown in Fig. 6. The elastic (E) pulse appears to be followed by a plastic (P) pulse.

[2] J. S. Rinehart, J. Appl. Phys. **22**, 555 (1951).
[3] F. G. Blake, Jr., J. Acoust. Soc. Am. **24**, 211 (1952).

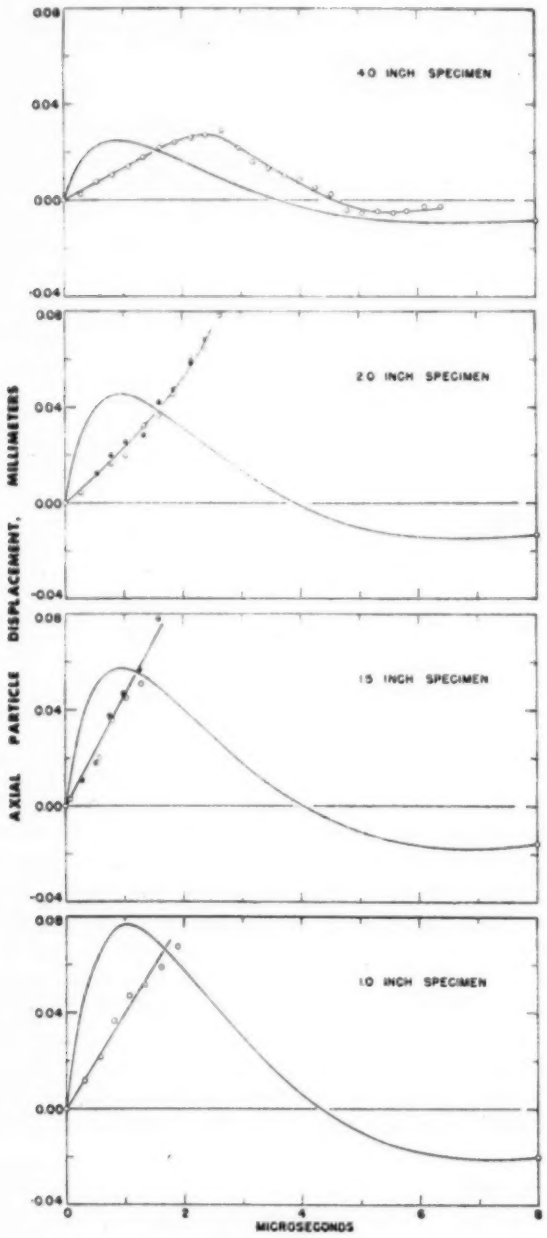

FIG. 8. Comparison between experimental and theoretical data for axial particle displacement of steel specimens.

that this fracture contributed appreciably to observed transient deformation of the free surface.

COMPARISON OF RESULTS WITH ELASTICITY THEORY PREDICTIONS

Comparison of experimental results with theory requires adoption of a set of theoretical assumptions that lead to physically realistic predictions. In the physical regime studied, effects of plastic flow, finite elastic deformations, and actual mechanical deployment of fragments fractured from the specimen properly should be given considerable attention. For the present, however, certain experimental results will be compared with those predicted from elementary elasticity theory. This comparison requires that elementary linear theory be extrapolated into a regime where it is known not to be applicable; considerable deviation of theoretical predictions from experimental results will be expected.

The theoretical problem will be specified as follows:[4] *Given a spherical cavity of radius* a *within a homogeneous ideally elastic infinite medium, find the elastic wave motion that results from application of a pressure pulse to the interior of the cavity.* This simplified problem will be considered because the actual problem, that is, interaction of a cylinder of high explosive with a metal plate, essentially is insolvable. It is not unduly restrictive to assume the actual phenomena to be spherically symmetric since experiment has shown the initial pulse diverges from a point. Elastic properties of the steel will be specified by the following quantities:[5] $E=2.139$ megabars/cm^2, $\rho=7.849$ g/cc, and $\sigma=0.310$, where E, ρ, and σ, respectively, are Young's modulus, density, and Poisson's ratio. The pressure p imparted by high explosive to the steel is assumed to be expressible in the form

$$p=0 \quad \text{for} \quad t<0, \tag{12}$$

$$p=p_0e^{-\alpha t} \quad \text{for} \quad t>0, \tag{13}$$

where p_0 is peak pressure, α is a time-decay constant, and time t is measured from arrival time of the detonation wave at the high explosive-steel interface. The properties of the high explosive are specified by the quantities: $p_0=0.283$ megabar/cm^2, $\alpha=2$ μsec^{-1}. The value of the peak pressure p_0 has been calculated in a previous paper[6] for a high explosive-steel interface from an assumed pressure of 0.17 megabar/cm^2 in the detonation front. The value of the time-decay constant α has been inferred from published theoretical data,[7] where curves are given that describe the dynamics of the combustion products behind plane and spherical detonation fronts in explosives. Specifically, it has been shown that pressure behind a detonation front decays to $1/e$ of its peak value in the distance $0.31a$ and $0.14a$ for plane and spherical flow, respectively, where distance is measured from the detonation front toward the origin. The quantity a is defined as the distance traveled by the detonation wave. The time-decay constant α for plane and spherical flow is assumed to be given by the respective relations:

$$\alpha=7.8/0.31a, \tag{14}$$

$$\alpha=7.8/0.14a. \tag{15}$$

To fit the conditions of the problem, an origin a of the disturbance must be chosen. There are at least two

[4] J. A. Sharpe, Geophysics **7**, 144 (1942).
[5] A. E. H. Love, *A Treatise on the Mathematical Theory of Elasticity* (Dover Publications, Inc., New York, 1944), fourth ed., p. 105.
[6] Pack, Evans, and James, Proc. Phys. Soc. (London) **60**, 1 (1948).
[7] G. I. Taylor, Proc. Roy. Soc. (London) **200**, 235 (1950).

alternatives: first, a can be taken equal to either d or d' of Fig. 1; second, the high explosive mass of the original 1-in. diam 2-in. charge can be expressed in terms of an *equivalent sphere* of high explosive placed in contact with the metal. A spherical charge is certain to be more effective than an actual cylindrical charge of the same mass because the center of mass of a spherical charge is closer to the metal. Consequently, an *equivalent spherical* charge will contain less high explosive than the actual cylindrical charge. A radius,

$$a=15 \text{ mm}, \tag{16}$$

was chosen arbitrarily, and calculation has shown that this choice simulates the actual results of the experiment with fair accuracy. In addition, an actual experiment was performed which confirmed that such a sphere produces physical effects on a steel plate equivalent to those produced by a standard cylindrical charge. Substitute Eq. (16) into Eqs. (14) and (15) to obtain the values of the time-decay constant α for plane and spherical flow, respectively,

$$\alpha=1.68, \tag{17}$$

$$\alpha=3.71. \tag{18}$$

The actual value $\alpha=2$ chosen for the time-decay constant represents a weighted average between the respective theoretical values of Eqs. (17) and (18).

Solution of the theoretical problem is well known.[3,4,8,9] In Fig. 8, the experimental curves indicated by circles represent one-half the measured displacement of the axial particles on the free surfaces of the four different-sized specimens. The curves for the 2-in. and $1\frac{1}{2}$-in. specimens each contain data for two separate experiments. The theoretical curves indicated by solid lines are predictions from elasticity. Calculation of the theoretical curves involved considerable labor using an electronic calculator. This machine, the IBM CPC, has been described elsewhere in connection with another problem.[10]

CONCLUSIONS

As expected, elementary elasticity theory does not give in all respects an accurate account of the complex physical phenomena associated with this experiment. It has been inferred, however, that the initial particle velocity approximately follows the r^{-1} attenuation law predicted by theory[3] provided the origin is chosen $a=15$ mm. At the distance where the initial pulse has decayed to sonic proportions, the theoretical displacement curve has several features of similarity with the experimental curve. For example, the theoretical and experimental curves associated with the 4-in. specimen of Fig. 8 have the following points of similarity:

1. The respective pulse lengths are approximately the same.
2. The respective pulse amplitudes are approximately the same.
3. Both curves have a negative phase.
4. The rising portions of both curves have curvature of the same sign.
5. The decaying portions of both curves have curvature of the same sign.

The principal discrepancy between theoretical and experimental curves of the 4-in. specimen of Fig. 8 is the fact that the experimental curve attains its maximum at a later time. This fact implies that the actual particle velocities, and consequently the actual stresses, are considerably less than predicted values. In English units, the actual calculated stress is 94 000 psi; although this value exceeds the static yield point of the steel, the recovered specimen acquired no permanent deformation. The calculated stress level for the 4-in. specimen compares favorably with the maximum stress 140 000 psi obtained by previous investigators[2] at the free surface of a 3-in. specimen. Figure 8 suggests that the wavelength of the actual pressure pulse is longer than the predicted value. This conclusion implies either that the assumed form of the initial pulse is wrong and/or that the plastic flow mechanism increases the pulse length.

No great progress has been made in interpretation of the wave phenomena indicated in Fig. 2. The phenomenon is a result of the initial longitudinal wave and its interaction with the free surfaces of the specimen because any transverse wave that may be induced at the high explosive-steel interface will not arrive at the free surface in time to affect the initial phenomena. The only known wave velocity in steel that corresponds to the measured value of 5 mm/μsec is the transverse wave velocity associated with rods[4] which can be determined by the relation

$$v=(E/\rho)^{\frac{1}{2}}. \tag{19}$$

It is significant that this wave velocity is the same as that associated with the 2-in. specimen illustrated in the previous paper.[1]

ACKNOWLEDGMENT

The writer wishes to acknowledge the helpful suggestions of Professor Werner Goldsmith, University of California. It is also a pleasure to acknowledge the technical assistance of Mr. J. W. Rogers who designed much of the equipment, machined and polished the steel specimens, measured the photographic data by means of the microdensitometer, and made most of the illustrations.

[8] Kawasumi and Yosiyama, Earthquake Research Inst. (Tokyo) 13, 496 (1935).
[9] H. L. Selberg, Arkiv Fysik 5, 97 (1952).
[10] W. A. Allen and R. H. Stark, J. Opt. Soc. Am. 41, 636 (1951).

JOURNAL OF APPLIED PHYSICS VOLUME 24, NUMBER 9 SEPTEMBER, 1953

Electrostatic Potential Plotting for Use in Electron Optical Systems*

KUO-CHU HO AND ROBERT J. MOON
Institute of Radiobiology and Biophysics, University of Chicago, Chicago, Illinois
(Received April 21, 1953)

A noniterative numerical method has been found for solving a partial differential equation when its boundary conditions are not known on the entirety of a closed boundary. Under such conditions, the iterative numerical methods which are generally used, such as the relaxation technique, are not applicable. As an example, this noniterative numerical method has been used to calculate the shapes of a pair of beam forming electrodes for use in an electron gun in which rectilinear flow is desired. The calculated shapes are in almost complete agreement with Pierce's experimental results. Equipotential surfaces calculated by this method have been checked by means of an electrolytic trough which employs a semiautomatic detecting and plotting system.

INTRODUCTION

THE electron optical study of the motion of charged particles, electrons or ions, is primarily a problem of the determination of the potential distribution which will yield the desired electron or ion trajectory. The potentials may either be calculated theoretically or plotted experimentally by means of an electrolytic trough or some other model experiments. The usual procedure employed in the analytical determination of the potential in a charge-free region often results in the solution of the Laplace equation by the method of separation of variables. The solution obtained in this method is generally expressed by a series of special functions whose coefficients are determined by the given boundary conditions. Because of the difficulty of finding coefficients even for a limited number of terms of such a series which satisfies the prescribed boundary conditions, only a few cases which have simple geometrical boundary shapes have been solved in this way. For more complicated boundary shapes, the problem is usually treated by means of iterative numerical methods. Among the different iterative methods known at the present time, Southwell's relaxation technique is the most powerful and commonly used one. However, as mentioned by Fox,[1] the success of the relaxation method can be guaranteed only if the boundary conditions are given on a closed boundary. Unfortunately, for many problems, boundary conditions are not known on the entirety of a closed boundary. Instead, it frequently happens that boundary values and their derivatives are given only on certain parts of the boundary. For such cases, the relaxation method will, in general, require some assumption about the unknown boundary values. An example of the difficulties involved in this type of approach is given below.

In the design of a high-current density electron gun such as those used in the cathode-ray tube or electron microscope, it is found that electrons emitted from the cathode diverge because of the effect of space charge. In order to obtain a rectilinear flow, Pierce[2] has proposed to incorporate an electrode which is at the cathode potential and is exterior to the cathode, and an accelerating electrode with an aperture through which the electron beam passes, wherein both the cathode electrode and the accelerating electrode are shaped so as to produce suitable forces on the electrons along the edge of the electron beam in order to keep them from diverging. These electrodes for electron guns with different geometrical shapes of the cathode and anode, such as those with planar, cylindrical, and of the spherical-type cathode and anode systems, have been found experimentally by Pierce with the help of an electrolytic trough. By means of the same experimental methods Helm, Spangenberg, and Field[3] have also obtained the shapes of electrodes for an electron gun which employs a spherical cap cathode and in which different ratios of cathode and anode radii as well as different sizes of cathode and anode are used. From their experiments, they claimed that while for any geometry of the electrodes there is theoretically only one correct shape for both electrodes, but that there are actually a large number of shapes departing slightly from the correct shape, that will produce very nearly the correct potential at the edge of the beam. In consideration of the above, it seems to be desirable to attempt to find the shapes of these electrodes entirely by theoretical means and to compare these results with the experimental shapes. This problem is of particular interest in the design of an electron optical system capable of producing a high current density focal spot; a focal spot that has diameters less than 0.1 mm and with a current of 100 ma or more.

Since the electrodes of the electron gun system are equipotential surfaces in the field, the shapes of the electrodes may be found by solving the Laplace equation. As pointed out by Pierce, the boundary conditions that this system must satisfy are: (*i*) The potentials inside and along the edge of the beam should satisfy

* This research was supported in part by the U. S. Air Force under contract No. AF18(600)-566 monitored by the Office of Scientific Research, Air Research and Development Command; in part by the U. S. Public Health Service, under contracts No. C-815CR and C-815CRS, and in part by the U. S. Office of Naval Research, under contract N6-ori-02029.

[1] L. Fox, Quart. J. Mech. Appl. Math. **1**, 253 (1948).

[2] J. R. Pierce, J. Appl. Phys. **11**, 548 (1940).

[3] Helm, Spangenberg, and Field, Elec. Commun. **24**, 103 (1947).

the current-voltage relation for the space-charge limited current flow. Such current-voltage relations have been known for current flow between parallel planes, concentric cylinders, and concentric spheres. (*ii*) The field normal to the beam, or the first derivative of the potential, should be zero, in order to have no electrons diverging from the edge.

For the case of a flat-disk cathode, the beam would be of a constant circular cross section and be surrounded by a charge-free region. Figure 1 shows a cross-sectional view of such an electron-gun system in a plane which passes through the axis of symmetry. As the beam and equipotentials in the system are axially symmetrical, i.e., $\partial V/\partial\theta=0$, the problem of determining the equipotentials is a two-dimensional one.

An investigation of potentials in this plane will give complete information about the entire field. The boundary conditions which must be satisfied along the

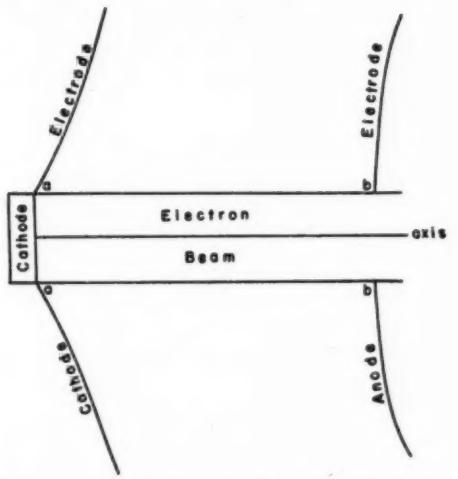

FIG. 1. A cross-sectional view of a flat-disk cathode electron-gun system in a plane which passes through the axis of symmetry.

cylindrical boundary *ab* then become

$$(\partial V/\partial r)_{r=r_0}=0, \quad V_0=V_0(z),$$

where r is the distance measured from the beam surface and normal to it, and z is the distance from the cathode. The current-voltage relation $V_0(z)$ is, according to Child's law, equal to $Az^{4/3}$, where A is a constant.

As is seen for this particular case, boundary values and their first derivatives are known on beam edge *ab* only and are not given for the remaining bounds of space surrounding the beam. Therefore, it does not lend itself to the relaxation method. However, as will be shown in the following paragraphs, problems of this type can be solved by a noniterative numerical method. We shall discuss mostly the application of the noniterative method to the particular electron-gun problem in which two independent variables in cylindrical coordinates are used. It is obvious, that this method can be extended for the treatment of problems which have more independent variables as well as in any other kind of coordinates,

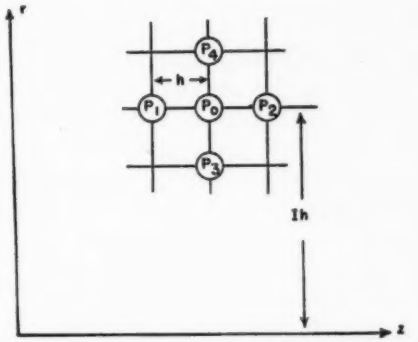

FIG. 2. The cross arrangement of the five points of the net.

though it may be more algebraically complex in some cases.

NONITERATIVE NUMERICAL METHOD

It is known that the potential at a point P_0 can be calculated in term of the potentials of its surrounding points P_1, P_2, P_3, and P_4. One simple arrangement for a two-dimensional system is shown as in Fig. 2. This is usually done by expanding the potentials ϕ_1, ϕ_2, ϕ_3, and ϕ_4 which correspond to the points P_1, P_2, P_3, and P_4 respectively, by means of Taylor's theorem at the point P_0. This together with the fact that ϕ_0 satisfies Laplace's equation leads to a formula which connects these potentials. For cylindrical coordinates, the following formula can be derived:

$$-4\Phi_0+\Phi_1+\Phi_2+\left(1-\frac{1}{2I}\right)\Phi_3+\left(1+\frac{1}{2I}\right)\Phi_4-\frac{1}{6I}\left(\frac{\partial^3\Phi}{\partial r^3}\right)_0 h^3-\frac{1}{12}\left[\left(\frac{\partial^4\Phi}{\partial r^4}\right)_0+\left(\frac{\partial^4\phi}{\partial z^4}\right)_0\right]h^4+\cdots=0, \quad (1)$$

where h is the uniform spacing between P_0 to any of the surrounding points, and Ih is the radial distance of P_0.

By Eq. (1), the potential of any point, say ϕ_4, can be calculated from the potentials of remaining four points and the derivatives at the center point P_0, provided ϕ_0 satisfies the Laplace equation. Now consider the case of the flat-disk cathode electron gun. Let P_1, P_0, and P_2 be located on the boundary between the electron beam and the charge-free region and let P_3 be located inside the beam as shown in Fig. 3. It is known from the boundary condition that ϕ_1, ϕ_0, and ϕ_2 satisfy the current-voltage relation $V_0(z)=Az^{4/3}$ and therefore are known. From the other boundary condition $(\partial V/\partial r)_0=0$, the equipotentials must be perpendicular to the edge of the electron beam at points along the beam. In the particular case for rectilinear flow, this is also true for the equipotentials inside the beam; then ϕ_3 has the same potential as ϕ_0. It is also known that the derivatives of one independent variable can be expressed in terms of finite differences which again,

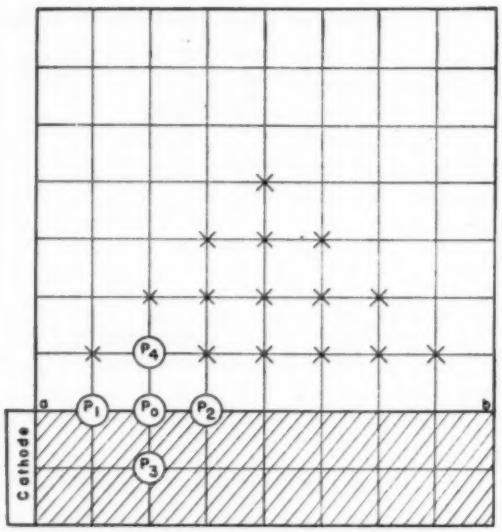

FIG. 3. The truncation of the field calculation which results from the use of the cross arrangement. Shaded area represents the electron beam.

as will be shown later, can be calculated in terms of the known potentials at points in the electron beam. Therefore potential ϕ_4 of a point outside the beam can be determined in terms of known potentials at points in the beam by Eq. (1). As a matter of fact it should be possible to evaluate the potentials at all the points which are indicated by cross signs in Fig. 3 by means of the same formula. The shaded area in Fig. 3 represents the electron beam.

In order to find potentials for points outside the field of points shown as cross marks, another expression is needed. One of the simplest arrangements is shown in Fig. 4. The connecting formula for ϕ_0, ϕ_1, ϕ_2, ϕ_3, and ϕ_4 in this arrangement can be found in the same way as was used in the derivation of Eq. (1), except that here Taylor's theorem of two independent variables has to be used. The following equation results:

$$\left(1+\frac{1}{2I}\right)\Phi_1+\left(1+\frac{1}{2I}\right)\Phi_2+\left(1-\frac{1}{2I}\right)\Phi_3+\left(1-\frac{1}{2I}\right)\Phi_4-4\Phi_0-\frac{h^3}{I}\left[\frac{1}{3}\left(\frac{\partial^3\Phi}{\partial r^3}\right)_0+\left(\frac{\partial}{\partial r}\frac{\partial^2\Phi}{\partial z^2}\right)_0\right]-h^4\left\{\frac{1}{6}\left[\left(\frac{\partial^4\Phi}{\partial r^4}\right)_0+\left(\frac{\partial^4\Phi}{\partial z^4}\right)_0\right]+\left(\frac{\partial^2}{\partial r^2}\frac{\partial^2\Phi}{\partial z^2}\right)_0\right\}-\cdots=0, \quad (2)$$

where $2h$ is the length of one side of the square mesh and again Ih is the radial distance of P_0.

With the help of Eq. (2), the potential at any point, say P_1, within the group can be calculated in terms of potentials at the rest of the points, provided the partial derivatives can be calculated by means of finite differences in the same way as before. As is seen, however, in Eq. (2) the partial derivatives of two independent variables are involved. It was therefore necessary to derive formulas which would express the partial derivatives with two variables in terms of finite differences. Since such formulas for high-order derivatives do not seem to have been reported in the literature, these will be derived in the following section.

DERIVATIVES IN TERMS OF DIFFERENCES

The expression of partial derivatives of two independent variables x and y, in terms of differences can be derived by using Bierman's[4] general formula for double interpolation. This formula can be written in the following notation:

$$f(x,y)=f(x_0,y_0)+\frac{x-x_0}{h}\Delta_x f_{00}+\frac{y-y_0}{k}\Delta_y f_{00}+\frac{1}{2!}\left[\frac{(x-x_0)(x-x_1)}{h^2}\Delta_x^2 f_{00}+\frac{2(x-x_0)(y-y_0)}{hk}\Delta_x\Delta_y f_{00}+\frac{(y-y_0)(y-y_1)}{k^2}\Delta_y^2 f_{00}\right]+\cdots+\frac{1}{m!}\left[\frac{(x-x_0)(x-x_1)\cdots(x-x_{m-1})}{h^m}\Delta_x^m f_{00}+\frac{m(x-x_0)(x-x_1)\cdots(x-x_{m-2})(y-y_0)}{h^{m-1}k}\Delta_x^{m-1}\Delta_y f_{00}+\frac{m(m-1)(x-x_0)(x-x_1)\cdots(x-x_{m-3})(y-y_0)(y-y_1)}{2h^{m-2}k^2}\times\Delta_x^{m-2}\Delta_y^2 f_{00}+\cdots+\frac{(y-y_0)(y-y_1)\cdots(y-y_{m-1})}{k^m}\Delta_y^m f_{00}\right]+R(x_0,y_0)$$

Here h and k are the intervals between the equidistant values of x and y, respectively, and $R(x_0, y_0)$ is the remainder term, and Δ's are double or two-way differ-

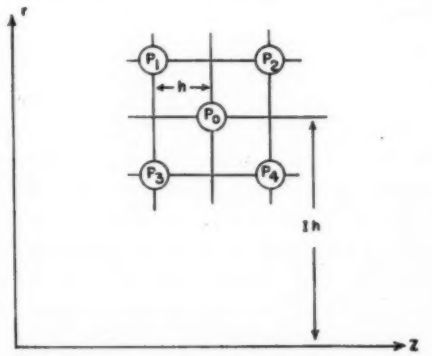

FIG. 4. The diagonal arrangement of the five points of the net.

[4] O. Biermann, *Mathematische Näherungsmethoden*. (Friedrich Vieweg Sohn, Braunschweig, Germany, 1905), p. 138.

ences.[5] The definitions of these double differences are reviewed in the Appendix along with this system of notation. As may be seen, Biermann's formula is for forward interpolation only. Similar formula can be also derived for backward and central interpolations. This will not be shown here.

In order to obtain the partial derivatives, this interpolation formula is simply differentiated the required number of times with respect to x and y, and after this x is set equal to x_0 and y is set equal to y_0. By doing this, the partial derivatives of two independent variables for different orders will be obtained as follows:

$$h\left(\frac{\partial f}{\partial x}\right)_0=\Delta_x f_{00}-\tfrac{1}{2}\Delta_x^2 f_{00}+\tfrac{1}{3}\Delta_x^3 f_{00}-\tfrac{1}{4}\Delta_x^4 f_{00}+\cdots,$$

$$k\left(\frac{\partial f}{\partial y}\right)_0=\Delta_y f_{00}-\tfrac{1}{2}\Delta_y^2 f_{00}+\tfrac{1}{3}\Delta_y^3 f_{00}-\tfrac{1}{4}\Delta_y^4 f_{00}+\cdots,$$

$$h^2\left(\frac{\partial^2 f}{\partial x^2}\right)_0=\Delta_x^2 f_{00}-\Delta_x^3 f_{00}+\frac{11}{12}\Delta_x^4 f_{00}+\cdots,$$

$$k^2\left(\frac{\partial^2 f}{\partial y^2}\right)_0=\Delta_y^2 f_{00}-\Delta_y^3 f_{00}+\frac{11}{12}\Delta_y^4 f_{00}+\cdots,$$

$$hk\left(\frac{\partial^2 f}{\partial x\partial y}\right)_0=\Delta_x\Delta_y f_{00}-\tfrac{1}{2}\Delta_x^2\Delta_y f_{00}-\tfrac{1}{2}\Delta_x\Delta_y^2 f_{00}+\tfrac{1}{3}\Delta_x^3\Delta_y f_{00}+\tfrac{1}{3}\Delta_x\Delta_y^3 f_{00}+\tfrac{1}{4}\Delta_x^2\Delta_y^2 f_{00}+\cdots,$$

$$h^3\left(\frac{\partial^3 f}{\partial x^3}\right)_0=\Delta_x^3 f_{00}-\tfrac{3}{2}\Delta_x^4 f_{00}+\cdots,$$

$$k^3\left(\frac{\partial^3 f}{\partial y^3}\right)_0=\Delta_y^3 f_{00}-\tfrac{3}{2}\Delta_y^4 f_{00}+\cdots,$$

$$h^2k\left(\frac{\partial^2}{\partial x^2}\frac{\partial f}{\partial y}\right)_0=\Delta_x^2\Delta_y f_{00}-\Delta_x^3\Delta_y f_{00}-\tfrac{1}{2}\Delta_x^2\Delta_y^2 f_{00}+\cdots,$$

$$hk^2\left(\frac{\partial}{\partial x}\frac{\partial^2 f}{\partial y^2}\right)_0=\Delta_x\Delta_y^2 f_{00}-\Delta_x\Delta_y^3 f_{00}-\tfrac{1}{2}\Delta_x^2\Delta_y^2 f_{00}+\cdots,$$

$$h^4\left(\frac{\partial^4 f}{\partial x^4}\right)_0=\Delta_x^4 f_{00}+\cdots,$$

$$k^4\left(\frac{\partial^4 f}{\partial y^4}\right)_0=\Delta_y^4 f_{00}+\cdots,$$

$$h^3k\left(\frac{\partial^3}{\partial x^3}\frac{\partial f}{\partial y}\right)_0=\Delta_x^3\Delta_y f_{00}+\cdots,$$

$$hk^3\left(\frac{\partial}{\partial x}\frac{\partial^3 f}{\partial y^3}\right)_0=\Delta_x\Delta_y^3 f_{00}+\cdots,$$

$$h^2k^2\left(\frac{\partial^2}{\partial x^2}\frac{\partial^2 f}{\partial y^2}\right)_0=\Delta_x^2\Delta_y^2 f_{00}+\cdots.$$

[5] J. B. Scarborough, *Numerical Mathematical Analysis* (The Johns Hopkins Press, Baltimore, 1950), second edition, p. 116.

It follows that the formulas just derived can be used to express the partial derivatives of Eqs. (1) and (2) in terms of finite differences by the substitution of z for x and r for y. In addition, square meshes may be chosen, that is $h=k$. Equations (1) and (2) become, respectively,

$$\Phi_4=\frac{2I}{2I+1}\left[4\Phi_0-\Phi_1-\Phi_2-\left(1-\frac{1}{2I}\right)\Phi_3+\frac{1}{6I}\Delta_r^3 f_{00}+\frac{1}{12}\Delta_r^4 f_{00}+\left(\frac{1}{12}-\frac{1}{4I}\right)\Delta_r^4 f_{00}+\cdots\right], \quad (3)$$

$$\Phi_1=\frac{2I}{2I+1}\left[4\Phi_0-\left(1+\frac{1}{2I}\right)\Phi_2-\left(1-\frac{1}{2I}\right)(\Phi_3+\Phi_4)+\frac{1}{3I}\Delta_r^3 f_{00}+\frac{1}{I}\Delta_r\Delta_z^2 f_{00}+\frac{1}{6}\Delta_z^4 f_{00}-\frac{1}{I}\Delta_r\Delta_z^3 f_{00}+\left(1-\frac{1}{2I}\right)\Delta_r^2\Delta_z^2 f_{00}+\left(\frac{1}{6}-\frac{1}{2I}\right)\Delta_r^4 f_{00}+\cdots\right]. \quad (4)$$

Equations (3) and (4) make it possible to calculate the potentials at all mesh points of the whole plane shown in Fig. 3. Finally the shapes of the cathode and anode electrodes and the equipotential lines between them can be easily plotted by interpolation.

The accuracy of this step-ahead numerical method is limited by two types of errors, namely, truncation errors and numerical errors. The truncation error arises because of the replacement of a differential equation by a difference equation. This error obviously depends upon the size of the mesh and how many terms in Eqs. (3) and (4) are used in the calculations. The numerical error is introduced in the process of solving the partial difference equation by the numerical method. A sufficient number of decimal places must be employed in order to reduce this type of error.

CALCULATION OF THE EQUIPOTENTIAL SURFACES

Figure 5 shows the results of the calculations of the electrostatic equipotentials by means of Eqs. (3) and (4) for parallel flow of electrons within a cylindrical beam which originates from a flat-disk cathode. The geometrical dimensions of the cathode and anode system are chosen so that they can be compared directly with Pierce's experimental curves.[2] Along the axis, potentials have been calculated according to the space-charge equation $V_0=Az^{4/3}$ and in order to minimize the numerical error, all the calculations have been carried out up to eight decimal places. The first five decimal places of the calculated potentials at each mesh point has been written down as shown in Fig. 5.

The side of the square meshes was chosen to be one-half of the radius of the cathode. With such a size of the meshes the value of the potential is known for a sufficient number of mesh points in the beam in order to evaluate the finite differences up to fourth order. Con-

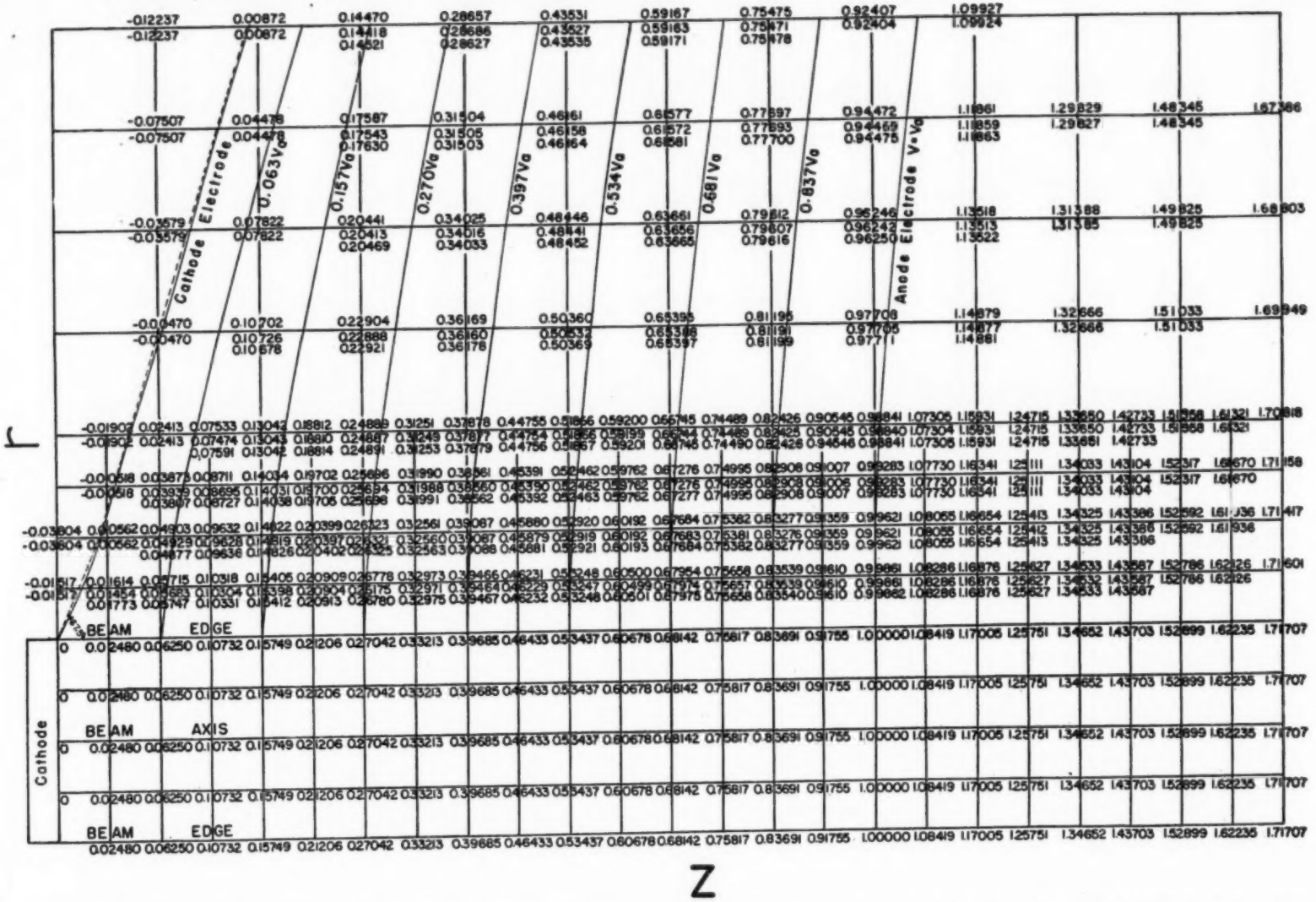

FIG. 5. Calculated potentials and interpolated equipotential surfaces about a cylindrical rectilinear space-charge limited electron beam which originates from a plane cathode. The potentials within the beam varies as $V_0 = Az^{4/3}$. The numbers at the mesh points, calculated by means of a step-ahead numerical method, are the relative potentials in the field. The first number below each mesh point is derived from Eq. (3) and the second number from Eq. (4). The average of these two numbers is given above the mesh point. The two dotted straight lines are an approximation of the cathode shape.

sequently the potentials outside of the beam are immediately given by Eqs. (3) and (4) up to and including the fourth-order derivative terms. After the first four rows of the potentials are calculated, the size of the meshes can be enlarged such as shown in Fig. 5, and the subsequent calculations will still include the fourth-order terms. Since the formulas for the determination of potentials by using different order of finite differences have been derived by the use of forward interpolation formula, some potentials of mesh points beyond the anode in the axial direction may be evaluated if needed for maintaining the higher-order terms in the calculations for points in the anode region.

In order to avoid any discrepancy of the results obtained by the use of Eqs. (3) and (4), the potential at each point has been calculated by both formulas. Mean values have been used for further calculations. The first number under each mesh point is the value calculated by Eq. (3), and the second number is that according to Eq. (4). The mean value of those two numbers is given above each of the mesh points. All the points shown in Fig. 5 have been calculated by carrying the formulas to fourth-order terms. Equipotential lines have been plotted by means of interpolation. These equipotential lines thus obtained are almost in perfect agreement with Pierce's experimental curves. It is interesting to see that the cathode electrode surface which was found by the above calculations does meet the normal to the cathode with the required angle of 67.5° as pointed out by Pierce; and also the cathode electrode shape can be approximated by two straight lines joining each other as the dotted lines shown in Fig. 5. One straight line meets the normal to the cathode at an angle of 67.5°, and the other at about 74° as Pierce proposed,[6] except the joining point of these two straight lines in our calculation is located closer to the cathode than Pierce suggested.

Certainly high-speed electronic computing devices would permit the calculations to be carried out so as to involve higher-order finite difference terms, and the use of smaller mesh sizes in order to obtain more accurate results. Theoretically it is possible to obtain potential values as accurately as is desired.

Because of the apparent precision of the above calculations, it was deemed worth while to construct an exact electrolytic trough model in which the shapes of the cathode and anode surfaces as well as that of the electron beam were accurately made to scale in order to have an experimental check on the calculations.

EXPERIMENTAL APPARATUS

The Electrolytic Trough

An electrolytic tank with a tilted bottom and constructed of Lucite served to contain a dilute solution of potassium chloride which was used as the electrolyte in these experiments. A cylindrical section of a piece of insulating material was inserted in the electrolyte to represent the edge of the beam. The cathode and anode electrodes are of brass, and were turned in a lathe and shaped according to the theoretical calculations such that the faces of the electrodes were surfaces of revolution. Consequently, more accurate results were to be expected than any heretofore obtained by means of experiments which employed flat metal sheet electrodes empirically shaped.

The thin edge of the wedge-shaped body of the electrolyte is the axis of the system. It was found that a fine line engraved along the axis on the bottom of the tank helps to eliminate the meniscus which usually exists along the axis. A sharp edge may then be produced by overflowing the electrolyte beyond this axis and then draining it out slowly. As the electrolyte passes the engraved line, due to the surface tension effect, a perfect straight line is formed along the axis.

As can be seen, if the calculated shapes of the electrodes are correct, the potentials along the electron beam should satisfy the space-charge equation $V_0=Az^{4/3}$. A measurement of potentials along the insulating piece which represents the beam will give a good check of the calculated electrode shapes. This can be done by measuring the ac potentials directly by a calibrated precision voltmeter through a probe, or else these ac potentials may be compared with the voltages from a voltage divider made from precision resistors or a shaped resistance card.†

The potentials thus measured at points along the electron beam edge of the electrolyte model agree with the required function $V_0=Az^{4/3}$ within the accuracy of the measuring devices. Hence it may be concluded that the electrode shapes which have been calculated through the use of even such large meshes as shown in Fig. 5 have proved to be more definite and accurate, when checked in the electrolytic trough, than those determined by the empirical bending of thin metal electrodes until the required voltage distribution is obtained.

Mapping Device

In order to check the calculated equipotential lines between the electrodes, an experimental mapping of the equipotentials in the electrolyte is desired. For the purpose of mapping the equipotentials on a drawing board, a one-to-one pantograph which links rigidly the probe to the writing device has been designed and constructed as shown in Fig. 6. The probe P, is made to be able to move freely in two dimensions by sliding along

[6] J. R. Pierce, Patent No. 2268,197, Part 4.

† The shaped resistance card can be made as follows: The first derivative of the desired voltage function is plotted on a graph sheet. Then a thin insulating piece is cut according to the shape of the graph, and then a thin high-resistance Manganin wire is wound around this piece. If the winding is made so close together that all the surface of this insulating piece is covered entirely by the wire without overlapping, then the total length of the wire used between any two positions will be proportional to the area it covered. This is essentially an integrating process. Consequently, along the axis of the graph the desired voltage function appears.

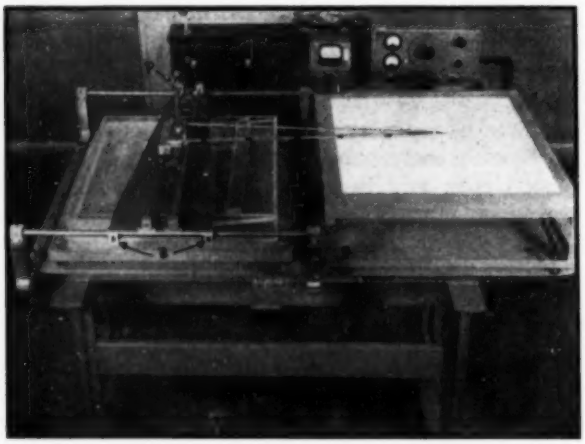

FIG. 6. Photograph of the one-to-one pantograph and the plotting device.

two pairs of ground drill rods. The smoothness of the movement is insured by the use of the ball bearing B and rollers at the joints to reduce friction. Accurate mapping is made possible by this design. The pantograph is mounted on a heavy table which makes it rigid and unshakable, and incorporates the necessary leveling screws both for the table, the trough, and the pantograph. The probe which is made of 0.001-inch tungsten wire is shielded and was designed to be adjustable up and down to give any desirable penetration into the electrolyte. The whole system could be leveled horizontally so that the probe will always penetrate into the electrolyte with the same depth for the entire surface.

Bridge Network

In order to avoid nonlinear conduction due to polarization at the electrode surfaces, an ac voltage (as is the customary practice) was used for the bridge. In our experiments, a frequency of 1000 cycles per second was employed. However, for any ac bridge network, stray admittances introduce considerable error in the balance point of the bridge. There are mainly two kinds of stray admittances, namely, the earth-admittance and the inter-branch admittances. In general, the stray earth-admittance is by far the more important one, and its effect on the bridge balance can be improved by the use of a Wagner ground device.

In the common form of Wagner ground, a transformer is used to couple the bridge and the detector. A transformer in such a position is unsatisfactory for the following reasons: (*i*) It has a low sensitivity if the bridge presents a high impedance to the detector. (*ii*) A high-impedance transformer introduces stray voltage by magnetic coupling with other parts of the circuit or with external circuits, and it is therefore necessary that this transformer be doubly shielded. If this detector input transformer is eliminated, then the difficulty arises as to how the amplifier is to be grounded properly. The grounding on one terminal of capacity coupled input amplifier makes the Wagner ground useless. An ordinary ungrounded amplifier usually introduces an intolerable amount of stray signals.

Austin's[7] method of separate balancing has been found to be applicable here. This method of connecting and balancing the Wagner ground circuit involves two steps; first, the Wagner ground W and the reference-bridge arm A are connected to the detector amplifier input as shown in Fig. 7 and balanced, and secondly the probe P and the Wagner ground are connected to the detector amplifier input and the equipotentials may then be traced out.

The elimination of the transformer which was employed between the bridge and the detector was made possible by means of this method and also permits one of the input leads of the amplifier to be grounded.

Plotting Device

The equipotential lines were electrically recorded in these experiments on an electrosensitive paper.‡ For a moderate recording speed, an open circuit voltage of approximately 100 volts and 10 to 15 milliamperes, when applied across this paper, causes a tiny spark to occur and as a result a distinctly fine point is made on the paper. The scriber was a stylus of long-wearing hard-drawn tungsten wire. Figure 7 shows a semi-schematic diagram of the circuit for the plotting device. After amplification by a two-stage amplifier, the output of the bridge is rectified by a diode T_1. A small bias has been placed on the cathode of the diode T_2 to eliminate any small current which may flow through the diode due to either contact difference of potentials or the finite velocity of emission of the electrons from the cathodes of the diodes. The negative dc voltage thus generated is applied to the grid of a thyratron. When the bridge is at balance, the dc bias is removed from the grid of the thyratron and conduction occurs. The steady bias of the thyratron can be adjusted to be just slightly above the potential needed in order that the thyratron fires. Under this condition the plate circuit of the thyratron gives enough voltage and current to make a spot on the recording paper. When the bridge

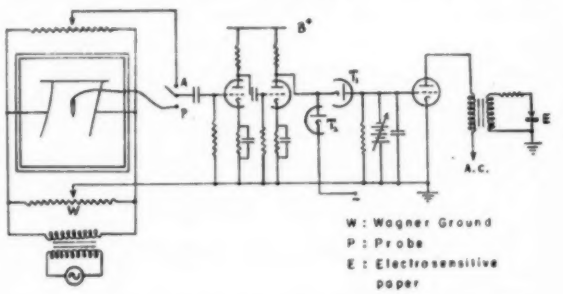

FIG. 7. A sketch of the electronic circuit for the bridge network and the plotting device.

[7] A. V. Austin, Bur. Standards J. Research 21, 425 (1938).

‡ "Teledelto" paper manufactured by Western Union Telegraph Company was employed.

is slightly off balance, a negative dc voltage is developed on the grid which cuts off the thyratron when the ac plate voltage next becomes negative. Consequently no mark will show on the electrosensitive paper. If the bridge potentiometer is set at a given potential and the probe is moved in a zig-zag fashion in the electrolytic trough, then whenever it passes a point in the electrolyte which has a potential equal to that of the reference potential a spot will be formed on the electrosensitive paper. Equipotential lines can be plotted very quickly this way.

The shapes of the electrodes and the equipotential lines which have been obtained experimentally are shown in Fig. 8. If Fig. 5 and Fig. 8 are compared, it is seen that the equipotentials thus determined experimentally follow very closely to the theoretically calculated curves.

APPENDIX

Definitions of the Double or Two-way Differences

Let $f(x, y)$ be any function of two independent variables x and y, and let $f_{rs}=f(x_r, y_s)$. A function table (Table I) can be constructed as follows.

TABLE I.

	x_0	x_1	x_2	x_3	$\cdots$	x_m
y_0	f_{00}	f_{10}	f_{20}	f_{30}	$\cdots$	f_{m0}
y_1	f_{01}	f_{11}	f_{21}	f_{31}	$\cdots$	f_{m1}
y_2	f_{02}	f_{12}	f_{22}	f_{32}	$\cdots$	f_{m2}
y_3	f_{03}	f_{13}	f_{23}	f_{33}	$\cdots$	f_{m3}
.	.	.	.	.	.	.
.	.	.	.	.	.	.
y_n	f_{0n}	f_{1n}	f_{2n}	f_{3n}	$\cdots$	f_{mn}

The double or two-way differences are defined as follows:

$$\Delta_x f_{00}=f_{10}-f_{00},$$
$$\Delta_x f_{01}=f_{11}-f_{01},$$
$$\Delta_x f_{02}=f_{12}-f_{02};$$

$$\Delta_y f_{00}=f_{01}-f_{00},$$
$$\Delta_y f_{10}=f_{11}-f_{10},$$
$$\Delta_y f_{20}=f_{21}-f_{20};$$

$$\Delta_x\Delta_y f_{00}=\Delta_x f_{01}-\Delta_x f_{00}=\Delta_y f_{10}-\Delta_y f_{00},$$

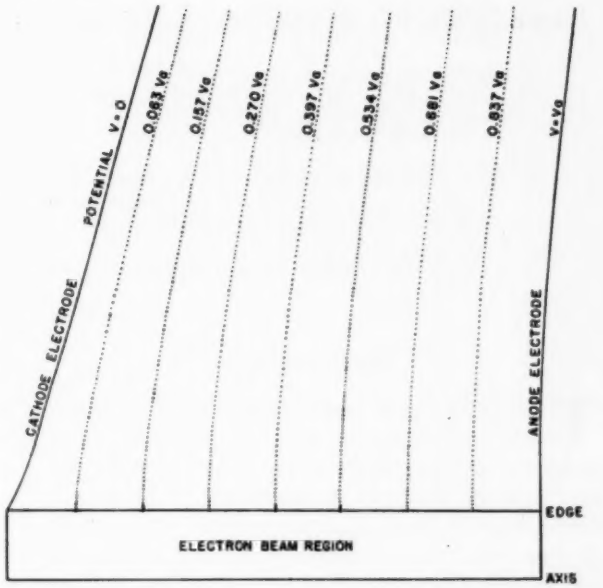

FIG. 8. Experimentally determined equipotential surfaces about a cylindrical rectilinear space-charge limited electron beam which originates from a plane cathode. Cathode and anode shapes are the calculated ones from Fig. 5.

$$\Delta_x^2 f_{00}=(f_{20}-f_{10})-(f_{10}-f_{00})=f_{20}-2f_{10}+f_{00},$$
$$\Delta_x^2 f_{01}=f_{21}-2f_{11}+f_{01};$$

$$\Delta_y^2 f_{00}=f_{02}-2f_{01}+f_{00},$$
$$\Delta_y^2 f_{10}=f_{12}-2f_{11}+f_{10}.$$

$$\Delta_x^2\Delta_y f_{00}=\Delta_x^2 f_{01}-\Delta_x^2 f_{00},$$
$$\Delta_x\Delta_y^2 f_{00}=\Delta_y^2 f_{01}-\Delta_y^2 f_{00}.$$

The general formula for writing down these double differences is easily seen to be

$$\Delta_x^m\Delta_y^n f_{00}=\Delta_x^m f_{0,n}-n\Delta_x^m f_{0,n-1}+\frac{n(n-1)}{2!}\Delta_x^m f_{0,n-2}+\cdots+\Delta_x^m f_{00}$$
$$=\Delta_y^n f_{m,0}-m\Delta_y^n f_{m-1,0}+\frac{m(m-1)}{2!}\Delta_y^n f_{m-2,0}+\cdots+\Delta_y^n f_{00}.$$

Some Dielectric Properties of Barium-Strontium Titanate Ceramics at 3000 Megacycles

LUTHER DAVIS, JR., AND LAWRENCE G. RUBIN
Raytheon Manufacturing Company, Waltham, Massachusetts
(Received April 16, 1953)

The dielectric constant ϵ'/ϵ_0 and loss tangent $\tan\delta$ of barium-strontium titanate ceramics were measured as a function of temperature and static electric field at frequencies of 10 kc, 500 kc, and 3000 Mc. No frequency dependence of ϵ'/ϵ_0 was apparent at temperatures above the Curie point. An increase in $\tan\delta$ was observed in going from the low frequencies to 3000 Mc, but above the Curie point the values were not excessively large. A description of the 3000 Mc bridge construction and operation is given.

INTRODUCTION

THE behavior of barium titanate, strontium titanate, and mixtures of the two as high dielectric ceramics has been investigated by many.[1–4] Published data has included the temperature and electric field dependence of the dielectric constant and loss tangent of these materials at various frequencies. This paper will be primarily concerned with the results of further measurements made on the mixtures 73 percent barium titanate: 27 percent strontium titanate (designated BS-73) and 60 percent barium titanate: 40 percent strontium titanate (BS60) at a frequency of 3000 Mc.

A coaxial microwave bridge technique was used to measure the complex propagation constants and hence complex dielectric constants of these materials.

The experiments were undertaken to establish whether these materials could be used for circuit elements at 3000 Mc.

METHOD

A block diagram of the 3000 Mc bridge is shown in Fig. 1. The beyond-cutoff variable attenuator, calibrated up to 60 db, was used so that variation of attenuation would not be associated with a phase change. The slotted line probe, in conjunction with a spectrum analyzer used as a null detector, made it possible to follow the movement of a given null point as the electrical length of the left bridge arm, and hence the phase angle of the wave traversing it, was changed. Since the value of ϵ'/ϵ_0 depended on the temperature and on applied dc field, a change in either variable resulted in a shift of position of the null point.

As long as this change was continuous, the difficulty arising from following a given null point for more than the length of the slotted line (5 cm) was avoided by keeping count of succeeding null points and adding a half-wavelength for each. However, operation of the bridge depended on having an initial condition of an unfilled sample holder ($\epsilon'/\epsilon_0=1$). Subsequently, the first reading of the bridge with the sample in place represented a discontinuous change from the zero condition. Therefore, an ambiguity existed in so far as the exact number of electrical half-wavelengths of sample and corresponding to the initial temperature field was not known.

The equation governing the operation of the bridge was[5]

$$(n-1)L_s=2(x_0-x)+N\lambda_0/2. \quad (1)$$

Here x_0 and x denoted the positions of the probe with sample holder empty and with the sample in place, respectively; N was an integral number of electrical half-wavelengths in the sample; L_s was the sample length in centimeters, and λ_0 the free space wavelength of the frequency used. The difficulty centered about resolving the uncertainty in N so that n, the index of refraction of the sample, could be determined.[5]

The solution to this problem was facilitated by the use of the Curie-Weiss law,

$$\epsilon_0/\epsilon'=(T-T_c)/C, \quad (2)$$

where ϵ_0/ϵ' is equal to the reciprocal of dielectric constant, T the temperature in degrees K, T_c the Curie temperature and C a constant.[6]

The procedure consisted of making a temperature run on a sample, which had a physical length L_{s1}. Using a series of arbitrary values of N, it was possible to make a corresponding series of Curie-Weiss plots of the data, only one of which was correct. This procedure was repeated on the same sample after it had been cut to a new length L_{s2} and the two series of plots were compared. Due to the obvious fact that, for a given sample, a change in its physical length could not change its dielectric properties, comparison had to indicate a match between one and only one plot of each series, thus fixing the correct value of N.

It was possible to check this method by measuring a sample cut sufficiently thin to insure its being less than one electrical half-wavelength at high temperatures.

An approximate formula for the loss tangent (tan

[1] Von Hippel, Breckenridge, Chesley, and Tisza, Ind. Eng. Chem. 38, 1097 (1946).
[2] S. Roberts, Phys. Rev. 71, 890 (1947).
[3] M.I.T. Laboratory for Insulation Research Tables of Dielectric Materials (1948).
[4] Powles and Jackson, Proc. Inst. Elec. Engrs. Pt. III 96, 383 (1949).

[5] See Appendix.
[6] A distinction should be made between T_c and the temperature of maximum ϵ'/ϵ_0 often called T_m or the Curie point, since the two are in general not equal.

$\delta = \epsilon''/\epsilon'$) was given by

$$\tan\delta = \alpha'\lambda_0/27.2L_s n, \quad (3)$$

where α' was the reading of the variable attenuator in decibels.

EXPERIMENTAL PROCEDURE

The coaxial section sample holder is shown in Fig. 2. The samples themselves were fabricated in the form of ceramic cylinders of 2.1 cm o.d., 1.6 cm i.d., and having lengths ranging from about 0.5 cm to 2 cm. Conductive coatings of silver were baked on outer and inner surfaces, which were then tinned with low temperature (125°C) solder. This same procedure was followed for the ceramic quarter-wavelength sections,

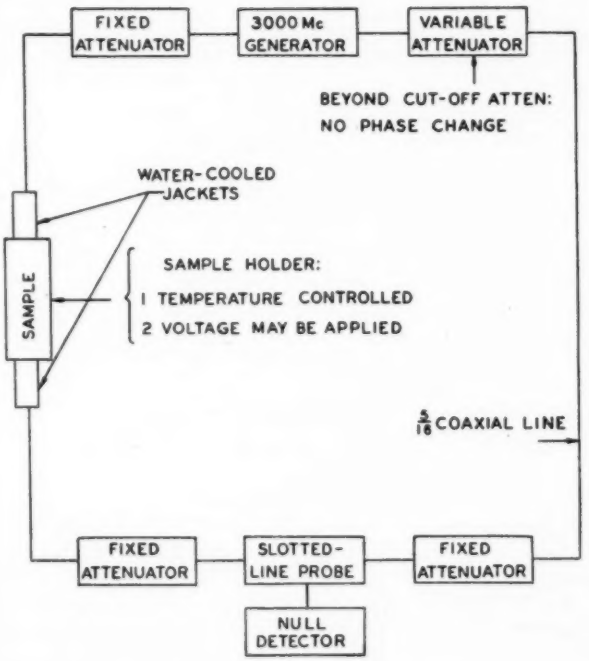

FIG. 1. Block diagram of 3000 Mc bridge.

which were employed to properly match the high dielectric material to the line and thus avoid large standing wave ratios. These sections were made from mixtures of strontium titanate and magnesium titanate, with dielectric constants in the range of 40–60. This corresponded approximately to the square root of the dielectric constant of the samples through most of the range of measurement and thus afforded satisfactory matching.

After cementing the matching sections to the faces of the sample, the three piece assembly was soldered in the holder. A great deal of care was exercised in

1. Choosing a cement which could withstand the temperature extremes and the electric field without breakdown.

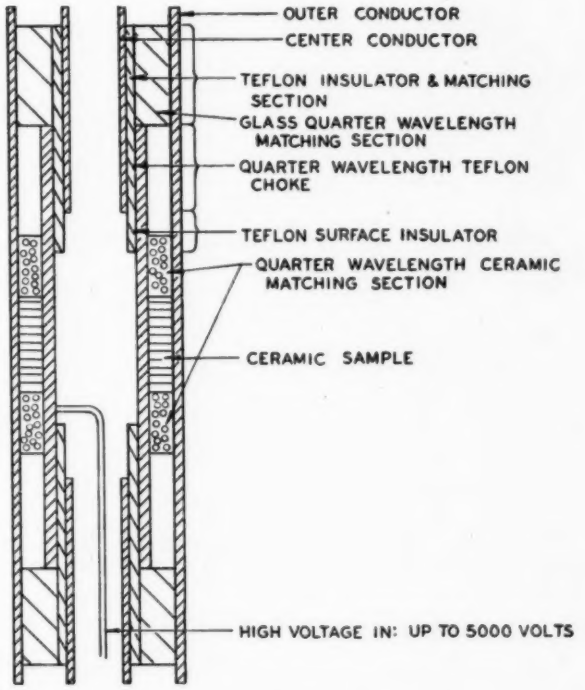

FIG. 2. $\frac{7}{8}$ inch coaxial section sample holder.

2. Cleaning the end faces of the assembly to prevent leakage of the high dc voltage.
3. Soldering so as to not harm the ceramics.

The sample holder was held in place in an insulated box, the temperature of which could be varied from −70°C to +100°C by means of dry ice and strip heaters. Temperature was determined by a copper-constantan thermocouple soldered to the outer conductor, directly in line with the sample. Thermal lag was held to a minimum by the good thermal configuration (ceramic-solder-copper jacket-solder-thermocouple) and the low time rate of change of temperature. The left bridge arm was completed by connecting the external $\frac{5}{16}$-in. coaxial line to the $\frac{7}{8}$-in. sample holder through tapered sections. A water-cooled jacket protected those parts of the line adjacent to the sample holder.

In the high voltage circuit, the outer conductor was grounded, and the dc voltage fed through the inside of the center conductor.

For purposes of comparison, low-frequency data were taken on several samples. This was felt to be necessary despite the abundance of such data in the literature, because the results in general vary with the methods of preparation of samples. A General Radio type 650A impedance bridge was used to measure the capacitance of the ceramic rings at 10 kc. To make similar measurements at 500 kc, a General Radio type 916AL bridge was employed. Corrections for edge effects were made in all cases.

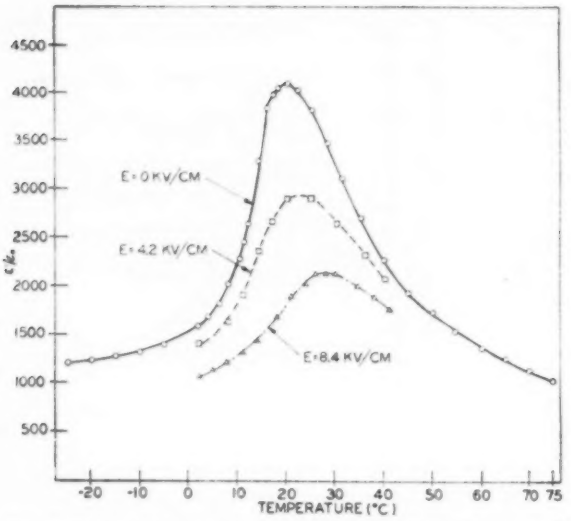

FIG. 3. Temperature dependence of dielectric constant at 3000 Mc of 73 percent $BaTiO_3$:27 percent $SrTiO_3$ for three values of electric field.

RESULTS AND CONCLUSIONS

Figure 3 demonstrates the temperature dependence of ϵ'/ϵ_0 at 3000 Mc of a sample of BS73 for three values of electric field. As the field increases, T_m shifts to the right from its zero field value of 20°C, while $\epsilon'/\epsilon_{0max}$ is depressed, particularly at the peak.

The corresponding curves for tanδ are shown in Fig. 4. The zero field curve exhibits a peak at 10°C but tanδ drops off rapidly to about 0.05 at 60°C. The large value of tanδ below the peak is a behavior quite different from that exhibited at low frequencies. Powles and Jackson[4] have witnessed a similar behavior for barium titanate at 9450 Mc, with a peak at about 110°C.

The sample on which the data of Figs. 3 and 4 were taken was one of the results of an earlier fabrication technique which improved rapidly with time. As the ceramic bodies become more dense, $(\epsilon'/\epsilon_0)_{max}$ increased, and the bodies were able to withstand higher fields. Figure 5 shows the data taken on one of the later samples, with fields up to almost 20 kv per cm and $(\epsilon'/\epsilon_0)_{max}$ equal to 5300. It may be seen that the depression of $(\epsilon'/\epsilon_0)_{max}$ and shift upwards in temperature of T_m with increasing E is very marked.

The results of a comparison of low frequency and microwave data can be stated as follows: for a given sample of BS73 in the temperature range 25° to 100°C (above the Curie point), ϵ'/ϵ_0 as determined at 3000 Mc was identical (within 5 percent) with its values at 10 kc and 500 kc; this same behavior was observed for BS60 in the range −20° to 100°C (again above the Curie point).

Previous investigators have reported on the variation of the *Curie point* with composition of barium-strontium titanate mixtures.[7–9] They discovered an almost linear relationship to exist between the two variables. As a secondary result of the present work, the authors have determined the *Curie temperatures* of nine barium-strontium titanate compositions and have obtained similar results. Table I lists these results derived from measurements performed at 500 kc. Strontium titanate appeared to have a Curie temperature of 33°K, as derived from extrapolation of its Curie-Weiss plot past 77°K (lowest point taken). It is necessary to emphasize that the Curie temperature, as defined by Eq. (2), was determined by extrapolation of the ϵ_0/ϵ' *vs* T curve. For this purpose, ϵ'/ϵ_0 was measured over a large range above the Curie point to insure the accuracy of the extrapolation.

At this point, it is worth mentioning that the authors have observed a dependence of their results on raw material lot, firing temperature, and firing schedule. Any comparison of results of different authors should certainly take into account the possible variation of such factors from one investigator to the next.

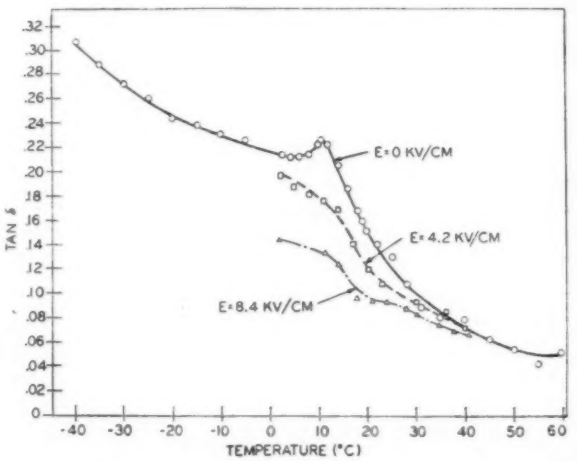

FIG. 4. Temperature dependence of loss tangent at 3000 Mc of 73 percent $BaTiO_3$:27 percent $SrTiO_3$ for three values of electric field.

The authors believe the following conclusions may be drawn on the basis of the experimental results.

1. The barium-strontium titanate ceramics studied above their respective Curie points possessed a dielectric constant which, for a given temperature and applied field, was identical at the frequencies 10 kc, 500 kc, and 3000 Mc. It is interesting to compare this result with the measurements on ceramics presumably similar to BS73 reported by Powles and Jackson.[4] At 20°C, they observed a large decrease in ϵ'/ϵ_0 at a frequency of 9450 Mc, as compared with their own low-frequency data for ϵ'/ϵ_0 at 1.5 Mc. This may indicate the existence of a relaxation frequency above the Curie temperature for this composition in the range 3000 Mc to 9450 Mc.

[7] Jackson and Reddish, Nature **156**, 717 (1945).
[8] Rushman and Strivens, Trans. Faraday Soc. **42A**, 231 (1946).
[9] Jonker and Van Santen, Philips Tech. Rev. **11**, 183 (1949).

However, their data gives ϵ'/ϵ_0 for this composition only at 20°C.

2. The loss tangent of the ceramics was higher at 3000 Mc than at the low frequencies, but not excessively so above the Curie point, at least not so large as to prevent the use of this material as a circuit element at 3000 Mc. However, the values were larger than would be desired for some purposes. The increase of tanδ below the Curie point would seem to be similar to the behavior of barium-titanate at room temperature.[3]

The authors extend their appreciation and sincere thanks to J. H. Saunders and R. M. Boutilier of this laboratory for assisting with measurements and with preparation of samples.

TABLE I. Curie temperatures of various barium-strontium titanate compositions.

Mole percent $BaTiO_3$	Curie temperature T_c(°K)
100.0	378
75.9	305
68.0	284
64.9	272
59.5	254
54.0	243
49.0	233
44.0	213
0.0	33

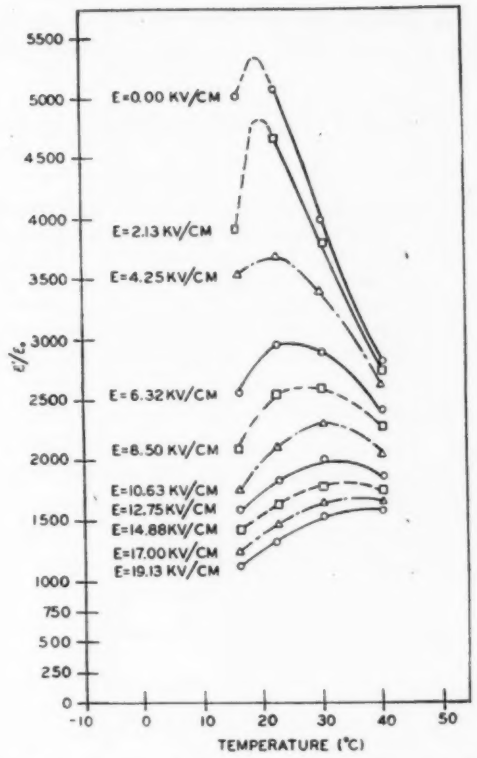

FIG. 5. Temperature and electric field dependence of dielectric constant at 3000 Mc of 73 percent $BaTiO_3$:27 percent $SrTiO_3$.

APPENDIX

Consideration of the complex propagation constant

$$\gamma=\alpha+j\beta=j(\epsilon/\epsilon_0)^{\frac{1}{2}}2\pi/\lambda_0 \tag{4}$$

and the definitions

$$\epsilon=\epsilon'-j\epsilon'' \tag{5}$$

$$\tan\delta=\epsilon''/\epsilon' \tag{6}$$

lead to the relations

$$\tan\delta=\frac{2\alpha}{\beta(1-\alpha^2/\beta^2)} \tag{7}$$

$$\epsilon'/\epsilon_0=n^2(1-\alpha^2/\beta^2). \tag{8}$$

For $\tan\delta<\frac{1}{3}$, approximations correct to better than about 2.5 percent may be made for (7) and (8) as follows:

$$\tan\delta=2\alpha/\beta \tag{9}$$

$$\epsilon'/\epsilon_0=n^2. \tag{10}$$

After conversion of α and β to experimentally measurable quantities,

$$\alpha=\alpha'/8.686L_s \tag{11}$$

$$\beta=2\pi n/\lambda_0 \tag{12}$$

Eq. (3) of the text is obtainable from (9).

Equation (2) results from equating phase change in the sample to the observed shift in the null point. The factor of two in the equation arises from the configuration whereby the probe is moving toward the signal source in one bridge arm but away from it in the other. To the approximation (10), Eq. (1) may be written as

$$\epsilon'/\epsilon_0=\{[2(x_0-x)+N\lambda_0/2]/L_s+1\}^2. \tag{13}$$

A More Exact Treatment of the Equations Describing Dielectric Relaxation and Carrier Motion in Semiconductors*

JULIAN KEILSON †
Lincoln Laboratory, Massachusetts Institute of Technology, Cambridge, Massachusetts
(Received April 16, 1953)

Previous treatments of the linearized equations describing hole and electron flow in a homogeneous semiconductor have not been wholly satisfying mathematically. An exact treatment of these equations is undertaken and it is demonstrated that the departure from complete local charge neutrality implicit in the equations corresponds to a polarization attributable to local variations of conductivity. The dielectric relaxation is described and exact expressions for the effective mobility and diffusion coefficients are obtained. The corrections to the older values are of magnitude τ_r/τ, where τ_r is the relaxation time and τ the lifetime. For semiconductors, these corrections are negligible.

VAN Roosbroeck and, independently, Brooks, have treated the linearized first-order equations describing hole and electron flow in a general homogeneous semiconductor. Similar equations are of interest in gas discharge theory. The equations are:

$$\frac{\partial n}{\partial t}=-r(n_0p+p_0n)+\mu_nE_0\frac{\partial n}{\partial x}+\mu_nn_0\frac{4\pi q}{\kappa}(p-n)+D_n\frac{\partial^2n}{\partial x^2}, \quad \text{(A)}$$

$$\frac{\partial p}{\partial t}=-r(n_0p+p_0n)-\mu_pE_0\frac{\partial p}{\partial x}-\mu_pp_0\frac{4\pi q}{\kappa}(p-n)+D_p\frac{\partial^2p}{\partial x^2}. \quad \text{(B)}$$

Here p_0 and n_0 are the equilibrium hole and electron densities; p and n are the excess densities; μ_n, μ_p, D_n, D_p are the respective mobilities and diffusion coefficients; r is the recombination coefficient and κ the dielectric constant. E_0 is the electric field present.

It has been shown that since relaxation sets in quickly, injection gives rise to the diffusion of a neutral irregularity in the crystal, described to a high degree of approximation, by

$$n=p=\frac{\lambda}{(4\pi D't)^{\frac{1}{2}}}e^{-t/\tau}\exp\left(-\left\{\frac{(x-\mu'E_0t)^2}{4D't}\right\}\right), \quad (1)$$

where λ is a constant of proportionality, and the effective lifetime, diffusion coefficient and mobility are

$$\tau=1/r(n_0+p_0), \quad (2)$$

$$D'=\frac{n_0+p_0}{(n_0/D_p)+(p_0/D_n)}, \quad (3)$$

$$\mu'=\frac{n_0-p_0}{(n_0/\mu_p)+(p_0/\mu_n)}. \quad (4)$$

Previous treatments of Eqs. (A) and (B) have not been wholly satisfying mathematically. In this paper, an exact treatment of Eqs. (A) and (B) is undertaken, and it is demonstrated that the departure from complete local charge neutrality implicit in our equations corresponds to a polarization of excess carrier density. The dielectric relaxation is described, and exact expressions for the mobility and diffusion coefficient are obtained. It is shown that corrections to the values above are of magnitude τ_r/τ where τ_r is the relaxation time.

Our equations may be rewritten compactly in the following way:

$$\frac{\partial n}{\partial t}=-\alpha_1n-\gamma_1p+b\mu_pE_0\frac{\partial n}{\partial x}+bD_p\frac{\partial^2n}{\partial x^2}, \quad \text{(A')}$$

$$\frac{\partial p}{\partial t}=-\alpha_2p-\gamma_2n-\mu_pE_0\frac{\partial p}{\partial x}+D_p\frac{\partial^2p}{\partial x^2}, \quad \text{(B')}$$

where

$$\theta=4\pi q\mu_p/\kappa r \qquad b=\mu_n/\mu_p \quad (5)$$

$$\alpha_1=r(p_0+b\theta n_0) \quad \gamma_1=rn_0(1-b\theta)$$
$$\alpha_2=r(n_0+\theta p_0) \quad \gamma_2=rp_0(1-\theta). \quad (6)$$

We assume that, at $t=0$,

$$n=N_0\delta(x-x_0) \quad p=P_0\delta(x-x_0). \quad (7)$$

If (A') and (B') are integrated over all space, and we use the notation

$$N=\int ndx, \quad P=\int pdx, \text{ we find}$$

$$dN/dt=-\alpha_1N-\gamma_1P, \quad (8)$$

$$dP/dt=-\alpha_2P-\gamma_2N, \quad (9)$$

whose solution, obtained by use of Laplace transforms, is

$$N=K_{1n}e^{-t/\tau_r}+K_{2n}e^{-t/\tau}, \quad P=K_{1p}e^{-t/\tau_r}+K_{2p}e^{-t/\tau}. \quad (10)$$

* The research in this document was supported jointly by the Army, Navy, and Air Force under contract with the Massachusetts Institute of Technology.
† Staff member.

The relaxation time, τ_r, is found to be

$$\tau_r=\frac{1}{\theta r(p_0+bn_0)}=\frac{\kappa}{4\pi q(n_0\mu_n+p_0\mu_p)}=\frac{\kappa}{4\pi\sigma}, \quad (11)$$

and the lifetime τ is

$$\tau=1/r(n_0+p_0). \quad (12)$$

One also finds that

$$K_{2n}=K_{2p}=\frac{N_0[(4\pi\sigma_n/\kappa)-n_0r]+P_0[(4\pi\sigma_p/\kappa)-p_0r]}{(4\pi\sigma/\kappa)-\tau^{-1}}, \quad (13)$$

where $\sigma_n=n_0\mu_nq$ and $\sigma_p=p_0\mu_pq$. Equation (13) implies that over-all charge neutrality (but not local charge neutrality) sets in within the relaxation time τ_r. It is noted that excess majority carriers placed in a strongly n- or p-type semiconductor decay, i.e., disappear almost completely, but that excess minority carriers are neutralized, leaving a neutral spike in the carrier distributions. When hole-electron pairs are injected by light, over-all charge neutrality is already present and no *decay* takes place.

We now consider the behavior of the first moments of our distribution. We deal with the neutral case $N_0=P_0=\lambda$. We multiply (A′) and (B′) by x and integrate again over all space. We employ the notation

$$x_n^{(1)}=\int xn\,dx \quad x_p^{(1)}=\int xp\,dx.$$

Our equation becomes

$$\frac{d}{dt}x_n^{(1)}=-\alpha_1x_n^{(1)}-\gamma_1x_p^{(1)}-b\mu_pE_0N(t),$$

$$\frac{d}{dt}x_p^{(1)}=-\alpha_2x_p^{(1)}-\gamma_2x_n^{(1)}+\mu_pE_0P(t).$$

In terms of the Laplace transform variable s, our equations are

$$(s+\alpha_1)x_n^{(1)}+\gamma_1x_p^{(1)}=\frac{-\mu_nE_0\lambda}{s+\tau^{-1}},$$

$$(s+\alpha_2)x_p^{(1)}+\gamma_2x_n^{(1)}=\frac{\mu_pE_0\lambda}{s+\tau^{-1}}.$$

When the second of these equations is subtracted from the first, we find

$$(s+\tau_r^{-1})(x_n^{(1)}-x_p^{(1)})=\frac{-(\mu_n+\mu_p)E_0\lambda}{s+\tau^{-1}},$$

so that

$$x_p^{(1)}-x_n^{(1)}=\left\{\frac{1}{s+\tau^{-1}}-\frac{1}{s+\tau_r^{-1}}\right\}\frac{(\mu_n+\mu_p)}{\tau_r^{-1}-\tau^{-1}}E_0\lambda.$$

This result implies that, after relaxation, each injected hole-electron pair has a dipole moment given by

$$p=q(x_p^{(1)}-x_n^{(1)})=\frac{q(\mu_n+\mu_p)}{\tau_r^{-1}-\tau^{-1}}E_0e^{-t/\tau}, \quad (14)$$

i.e., each excess hole-electron pair has a "polarizability" given by

$$\alpha=\frac{q(\mu_n+\mu_p)}{\tau_r^{-1}-\tau^{-1}}\simeq\frac{q(\mu_n+\mu_p)}{4\pi\sigma/\kappa}.$$

This "polarization" corresponds simply to the charge densities associated with local conductivity changes in the semiconductor.

It is also found that, after relaxation,

$$\frac{dx_n^{(1)}}{dt}=\frac{dx_p^{(1)}}{dt}=\frac{\gamma_2\mu_n-\gamma_1\mu_p}{\tau_r^{-1}-\tau^{-1}}E_0\lambda e^{-t/\tau}, \quad (15)$$

i.e., the effective mobility is

$$\frac{n_0-p_0}{(p_0/\mu_n)+(n_0/\mu_p)}\left[\frac{1}{1-(\tau_r/\tau)}\right]+\left(\frac{\tau_r}{\tau-\tau_r}\right)\frac{p_0\mu_n-n_0\mu_p}{n_0+p_0}. \quad (16)$$

We see that μ' differs from the older result by terms of the order of τ_r/τ. For germanium and silicon, $\tau_r\simeq10^{-12}\rho$ seconds, where ρ is the resistivity in ohm-cm. For our differential equations to be valid, τ will be at least 10^{-6} second, so that τ_r/τ corrections will be very small.

The effective diffusion coefficient D' may be found from the second moments. For simplicity we will assume $E_0=0$. The dependence of D' on E_0 should be small. Our equations are:

$$\frac{d}{dt}x_n^{(2)}=-\alpha_1x_n^{(2)}-\gamma_1x_p^{(2)}+2D_nN^{(1)},$$

$$\frac{d}{dt}x_p^{(2)}=-\alpha_2x_p^{(2)}-\gamma_2x_n^{(2)}+2D_pP^{(1)}. \quad (17)$$

Then, in terms of the Laplace transform variable s,

$$x_n^{(2)}=\frac{\dfrac{2\lambda}{s+\tau^{-1}}\begin{vmatrix}D_n & \gamma_1\\ D_p & s+\alpha_2\end{vmatrix}}{(s+\tau^{-1})(s+\tau_r^{-1})}.$$

We want the coefficient of $1/(s+\tau^{-1})^2$ whose inverse transform is $te^{-t/\tau}$. This we find to be

$$dx_n^{(2)}/dt=2D',$$

where

$$D'=\frac{-\gamma_2 D_n-\gamma_1 D_p}{\tau_r^{-1}-\tau^{-1}}=\frac{n_0+p_0}{(n_0/D_p)+(p_0/D_n)}\left[\frac{1}{1-(\tau_r/\tau)}\right]$$
$$-\left(\frac{\tau_r}{\tau-\tau_r}\right)\frac{n_0D_p+p_0D_n}{n_0+p_0}, \quad (18)$$

again the older result with τ_r/τ corrections.

The process outlined may be used as the basis of a recursion process providing the lifetime parts of all the higher moments, i.e., the parts remaining after relaxation has taken place. It is then seen that for this case of $E_0=0$,

$$p\simeq n\simeq\frac{\lambda e^{-t/\tau}}{(4\pi D't)^{\frac{1}{2}}}e^{-x^2/4D't}.$$

I would like to thank Professor H. Brooks of Harvard University and Professors W. P. Allis, R. B. Adler, and J. E. Thomas, Jr., for their interest and helpful discussion.

JOURNAL OF APPLIED PHYSICS VOLUME 24, NUMBER 9 SEPTEMBER, 1953

Reactor Simulators

F. E. O'MEARA
Bendix Aviation Research Laboratories, Detroit, Michigan
(Received February 16, 1953)

Reactor kinetic equations are given together with the equations for fission product poisoning and temperature effects. A conceptual design of a reactor simulator is presented and the numerical values of the coefficients are listed.

ANALOG computers for the solution of complex physical problems have become increasingly important in many branches of applied physics. Where the analytical solution is difficult or tedious, the analog computer provides a rapid and accurate answer over a wide range of dynamic variables.

Coincident with the growth of analog computer techniques has been the birth and development of nuclear reactor dynamics. There have been some recent attempts to use these techniques in reactor studies, and there is undoubtedly much to be gained in the use of analog computers in preference to analytical methods. With the declassification of certain nuclear data it has seemed worthwhile to present a general conceptual design of a reactor simulator. The treatment of the reactor equations follows that of Glasstone and Edlund[1] while the computer terminology and conventions are from Korn and Korn.[2]

In order to simulate the dynamic response of a pile it is not only necessary to design an analog computer for the kinetic equations[3] but it is also desirable to design computing circuits for the fission product poisoning effects and temperature effects.[4] It is convenient, both mathematically and in practice, to evaluate these effects in terms of excess reactivity (δk). They will therefore be derived on that basis and the resulting function of δk will be fed into the kinetic analog.

FISSION PRODUCT POISON

The outstanding fission product poison is xenon 135 with an absorption cross section of 3.5×10^6 barns at thermal energy. It is formed by the following process[5]

$$\begin{array}{l}\qquad\qquad\qquad\qquad\rightarrow 15.3m\mathrm{Xe}^{135m}\\ \qquad\qquad\qquad\qquad\quad\downarrow\\ \text{fission}\rightarrow 2m\mathrm{Te}^{135}\rightarrow 6.7\mathrm{hr}\mathrm{I}^{135}\rightarrow 9.2\mathrm{hr}\mathrm{Xe}^{135}\rightarrow 10^6\mathrm{yr}\mathrm{Cs}^{135}.\end{array}$$

Since the tellurium half-life is quite short compared to the iodine, it is customary to ignore it and consider the iodine as formed directly on fission with a yield of 5.6 percent. By the same reasoning the isomeric Xe^{135m} is usually ignored because of its comparatively short half-life.

The equation for the iodine is

$$dP_i/dt=\gamma_i n v k\Sigma_a-\lambda_i P_i-\sigma_i n v P_i.$$

Since the iodine absorption cross section is small, the last term may be dropped and the resulting equation is

$$dP_i/dt=\gamma_i n v k\Sigma_a-\lambda_i P_i.$$

To adapt this equation for analog operation it is rewritten as

$$\frac{dP_i}{dt}=\frac{\gamma_i\exp(B^2\tau)}{l^*}n-\lambda_i P_i.$$

The analog is shown in Fig. 1(a).

[1] S. Glasstone and M. C. Edlund, *The Elements of Nuclear Reactor Theory* (D. Van Nostrand Company, Inc., New York, 1952).
[2] G. A. Korn and T. M. Korn, *Electronic Analog Computers* (McGraw-Hill Book Company, Inc., New York, 1952).
[3] P. R. Bell and H. A. Straus, Rev. Sci. Instr. **21**, 760 (1950).
[4] J. D. Trimmer and W. H. Jordan, Nucleonics **9**, No. 4, 60 (1950).
[5] C. D. Coryell and N. Sugraman, *Radiochemical Studies: The Fission Products* (McGraw-Hill Book Company, Inc., New York, 1951), pp. 526–534.

The xenon dynamic equation is

$$dP_x/dt=\gamma_x nvk\Sigma_a+\lambda_i P_i-\lambda_x P_x-\sigma_x P_x nv.$$

The first term on the right side gives the direct fission yield of xenon (0.3 percent) and is often ignored. Including it is no particular problem however, so the revised equation is

$$\frac{dP_x}{dt}=\frac{\gamma_x \exp(B^2\tau)}{l^*}n+\lambda_i P_i-\lambda_x P_x-\sigma_x P_x nv$$

The analog for this equation is shown in Fig. 1(b).

In order to express the effect of xenon poisoning in terms of reactivity it is convenient to expand the expression for δk in terms of a fixed absorption characteristic of the unpoisoned reactor and a varaible absorption due to the xenon buildup. We can redefine k and L^2 in these terms as

$$k=\eta\Sigma_u/(\Sigma_a+\Sigma_p) \quad L^2=[3\Sigma_t(\Sigma_a+\Sigma_p)]^{-1}.$$

The reactivity is now

$$\delta k=1-\frac{\{[3\Sigma_t(\Sigma_a+\Sigma_p)]^{-1}B^2+1\}\exp(B^2\tau)}{\eta\Sigma_u/(\Sigma_a+\Sigma_p)}.$$

This may be simplified to

$$\delta k=1-\frac{B^2\exp(B^2\tau)}{3\eta\Sigma_u\Sigma_t}-\frac{\Sigma_a\exp(B^2\tau)}{\eta\Sigma_u}-l^*v\Sigma_p.$$

The first three terms on the right side are just the ordinary expression for δk without poisoning, which we will call δk_0. We thus have

$$\delta k=\delta k_0-l^*v\Sigma_p.$$

Now Σ_p is simply $\sigma_x P_x$, which is generated by the xenon analog.

TEMPERATURE EFFECT

It is not always possible to design a generalized temperature analog since the possible heat removal schemes for a reactor are too varied. It is possible however to introduce the effect of a general temperature change in the moderator. Since the effective change in neutron cross sections with temperature is due almost entirely to the change in neutron velocity with moderator temperature, the change in moderator temperature alone will be considered as the variable T.

Since most absorption cross sections vary as $1/v$ whereas scattering cross sections are almost velocity independent, the largest effect of a temperature variation is to change L^2. This change may be expressed in terms of a function $R=(T/T_0)^1$ so that the effective diffusion length squared is L^2R. The reactivity is thus

$$\delta k=1-\frac{(L^2B^2R+1)\exp(B^2\tau)}{k}.$$

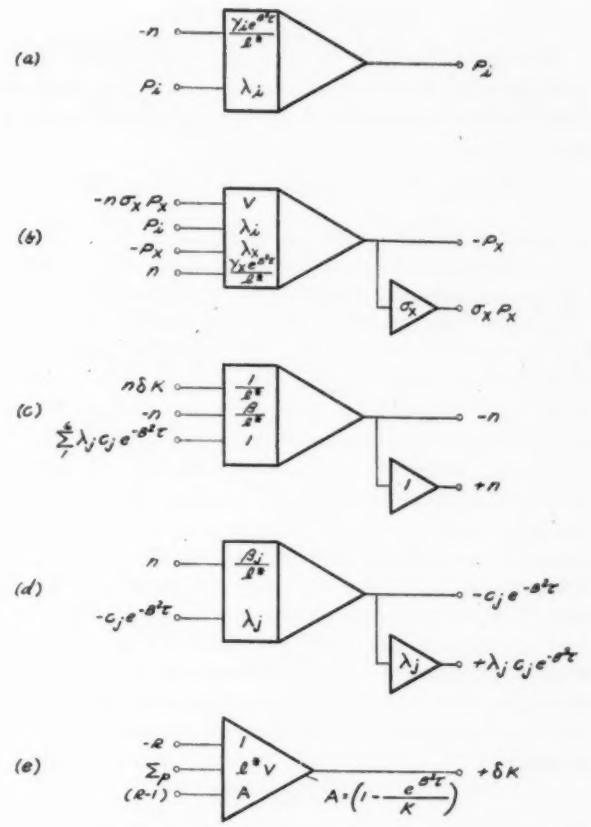

FIG. 1. Block diagram of simulator components.

This may be simplified to

$$\delta k=(1-R)(1-\exp(B^2\tau)/k)+R\delta k_0.$$

DELAYED NEUTRON EQUATIONS

The basic equations for the time dependent thermal neutron flux with a Fermi source are

$$dn/dt=nvk\Sigma_a\exp(-B^2\tau)+\Delta nv/3\Sigma_t-nv\Sigma_a$$

$$dc/dt=nvk\beta\Sigma_a-\lambda c.$$

These may be simplified to

$$\frac{dn}{dt}=\frac{\delta k}{l^*}n-\frac{\beta}{l^*}n+\sum_1^6\lambda_j c_j\exp(-B^2\tau)$$

$$e^{-B^2\tau}\frac{dc_j}{dt}=\frac{\beta_j}{l^*}n-\lambda_j c_j\exp(-B^2\tau)$$

where the second equation is the general form for each of the six delayed neutron emitters. The analog for the first equation is shown in Fig. 1(c). The analog for the second equation is shown in Fig. 1(d). There are six of these analogs for the six separate delayed neutron periods.

REACTIVITY CONTROL

The input variable for the complete system is δk_0, corresponding to the operation of the control rods, etc. Combining the xenon and temperature coefficients, we have

$$\delta k = (1-R)(1-\exp(B^2\tau)/k) - l^*v\Sigma_p + R\delta k_0.$$

The analog for this is shown in Fig. 1(e).

It is necessary to multiply δk by n in order to obtain $n\delta k$ for the delayed neutron analog; the multiplication of Σ_p by n is necessary for the xenon analog. The temperature function R may be generated by some other analog of the heat transfer system or it may be set at some fixed value. The temperature variation of the xenon cross section has not been declassified by the U. S. Atomic Energy Commission, however it appears obvious that it is not a simple $1/v$ function but rather has some sort of resonance structure. When this information is available the fixed σ_x coefficient could be replaced by a servo-driven tapped potentiometer to reproduce the xenon cross section variation with R.

So far nothing has been said about the actual values of the variables since in theory these have no effect on the analog operation. In practice however these values are of great importance if satisfactory performance is desired.

COEFFICIENTS

In the design of the operational analog it is necessary first of all to adjust the variables so that the constant multipliers do not have excessively large or small values and second to arrange that the variable multipliers have similar voltage values even though their equivalent functions have widely divergent values. The fixed constants are as follows (in the cgs system):

$v=2.2\times10^5$	
$\lambda_j=14$	$\beta_j=0.00025$
$=1.61$	$=0.00085$
$=0.456$	$=0.00241$
$=0.154$	$=0.00213$
$=0.0315$	$=0.00166$
$=0.0125$	$=0.00025$
	$\beta=\sum\beta_j=0.00755$
$\gamma_i=0.0224$	
$\lambda_i=2.9\times10^{-5}$	
$\gamma_x=0.0012$	
$\lambda_x=2.1\times10^{-5}$	
$\sigma_x=3.5\times10^{-18}$.	

In addition there are some adjustable coefficients which vary within definite limits:

$$1<k<2.1$$

$$33<\tau<400$$

$$0<B^2<0.025.$$

One adjustable coefficient that may be quite widely varied is l^*

$$10^{-5}<l^*<10^{-2}.$$

The values of the variables that are of interest are $n>10^7$, and dynamic changes in δk_0 not greater than ±0.1. (The criterion for n is that it be high enough so that the xenon loss by neutron absorption shall be equal to or greater than the loss by decay. This occurs at a flux (nv) of 6×10^{12}.)

SYMBOLS

n = Neutron density.
v = Thermal neutron velocity.
Σ_a = Macroscopic absorption cross section of reactor.
Δ = Laplacian operator.
c = Total number of delayed neutron emitters per cc.
k = Ratio of thermal neutrons produced per generation to thermal neutrons captured per generation $(\eta\Sigma_u/\Sigma_a)$.
λ = Decay constant. Probability per second for emission.
τ = Fermi age.
l^* = Mean life of thermal neutrons in finite geometry $(v\Sigma_a k e^{-B^2\tau})^{-1}$.
L^2 = Diffusion length squared.
β = Fraction of neutrons which are delayed.
B^2 = Buckling.
P_i = Number of iodine atoms per cc.
γ_i = Fractional yield of iodine per fission neutron.
λ_i = Decay constant for iodine.
σ_i = Iodine capture cross section.
P_x = Number of xenon atoms per cc.
γ_x = Fractional yield of xenon per fission neutron.
λ_x = Decay constant of xenon.
σ_x = Xenon capture cross section.
η = Number of neutrons produced per thermal neutron absorbed in fuel.
Σ_u = Macroscopic uranium absorption cross section.
Σ_p = Macroscopic xenon absorption cross section.
δk = Reactivity $\left[1-\dfrac{(L^2B^2+1)}{k}\exp(B^2\tau)\right]$.
Σ_t = Macroscopic transport scattering cross section.

Crystallographic Variations of Field Emission from Tungsten*

M. K. WILKINSON†
Research Laboratory of Electronics, Massachusetts Institute of Technology, Cambridge, Massachusetts
(Received May 20, 1953)

A photometric method has been developed and used to measure field-emission electron currents as a function of the crystallographic directions found in a tungsten single crystal emission point. Data obtained indicate that the appearance of bright and dark areas on the pattern of a field-emission projection tube can be explained by the differences in the work functions of the various crystallographic directions. The experiments also suggest that the value of the exponent of the work function needed to relate the field-emission equation to observed data is $(\frac{3}{2})$ as predicted by theory. The method of analysis is independent of the need for high accuracy of electric field determination. However, it does depend on a knowledge of the electric field distribution about the surface of the emission point. In these experiments, the field distribution was an assumption based on experimental data.

To insure the constancy of the electron emission required for measurement it was necessary to maintain an excellent vacuum. A method is given for the attainment and maintenance of a pressure in the region of 10^{-12} mm of Hg.

I. INTRODUCTION

THE most generally accepted theoretical explanation of field emission was first given by Fowler and Nordheim.[1] This theory was modified by Nordheim,[2] and subsequently, Sommerfeld and Bethe[3] gave a complete derivation. The expression obtained by them for the field-emission current was:

$$J=1.55\times10^{-6}F^{2}\varphi^{-1}\exp[-6.86\times10^{7}\varphi^{\frac{1}{2}}F^{-1}v(y)] \quad (1)$$

where J = current density in amp/cm^2, φ = surface work function in electron volts, F = electric field at the surface in volts/cm, $y=3.62\times10^{-4}F^{\frac{1}{2}}/\varphi$, and $v(y)$ = a slowly varying elliptic function of y.

Since $v(y)$ varies such a small amount for the normal experimental range in the surface field, data that fit this equation will fall on a nearly straight line when values of $\log(J/F^2)$ are plotted as a function of $1/F$, and the plot of $\log(J/F^2)$ against $1/F$ is generally called the field-emission characteristic. Certain aspects of the theoretical equation have been proved, but there is disagreement on the type of dependence of the current density on the work function. Results by Muller[4] disagree with the theory and indicate that the current density depends exponentially on the third power of the work function, while later results by Haefer[5] require the $\frac{3}{2}$ power as predicted by the theory. Experiments with the field-emission projection tube have led to a question concerning the type of pattern obtained. A photograph of a typical field-emission pattern for clean tungsten is shown in Fig. 1 (a). Such a pattern portrays bright and dark spots which can be associated with emission along the various crystallographic directions, some of which are labeled in corresponding positions in Fig. 1 (b). The puzzling feature of these patterns is the reason for the dark spots. Most observers have felt that the differences in electron emission between bright and dark spots are much too large to be explained by the normal differences in the work functions of the crystallographic directions.

The purpose of this research was to measure the relative field-emission currents along the main crystallographic directions of tungsten. A projection tube was used so that the state of contamination of the cathode would always be known from the pattern on the phosphor, and the study was made by photometering the light output along the various crystallographic directions.

II. EXPERIMENTAL TECHNIQUES

A. Construction of the Experimental Vacuum Tube

The first experimental tubes were constructed according to the conventional design, in which the phosphor is deposited directly on the glass envelope and the high voltage is applied to a separate anode structure. These tubes were found to be unsatisfactory for quantitative measurements. The potential of the phosphor was measured[6] and found to be considerably lower than that of the anode structure, and it was not uniform throughout the phosphor.

The experimental tube from which quantitative data were obtained was constructed with a layer of "conducting glass" on the inside of the glass envelope, and the phosphor was deposited on top of this layer. Such a tube allowed the voltage to be applied directly to the spherical surface and thereby eliminated the difficulties

* This material is taken from a thesis submitted to the Department of Physics, Massachusetts Institute of Technology, in partial fulfillment of the requirements for the degree of Doctor of Philosophy. This work was supported in part by the Signal Corps, the Air Materiel Command, and the U. S. Office of Naval Research.

† Present address: Oak Ridge National Laboratory, Oak Ridge, Tennessee.

[1] R. H. Fowler and L. Nordheim, Proc. Roy. Soc. (London) A119, 173 (1928).

[2] L. Nordheim, Proc. Roy. Soc. (London) **121**, 628 (1928).

[3] A. Sommerfeld and H. A. Bethe, *Handbuch der Physik*, **24**, Part 2, Sec. 3, p. 436 (1934).

[4] E. W. Muller, Z. Physik **102**, 734 (1936).

[5] R. Haefer, Z. Physik **116**, 604 (1940).

[6] M. K. Wilkinson, Technical Report No. 228, R.L.E., M.I.T. (1952).

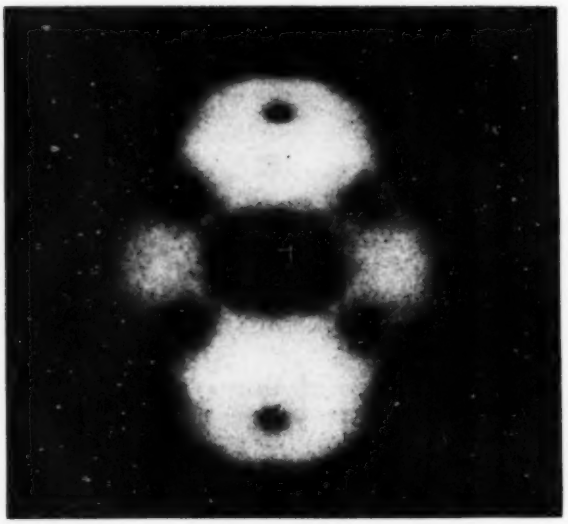

(a)

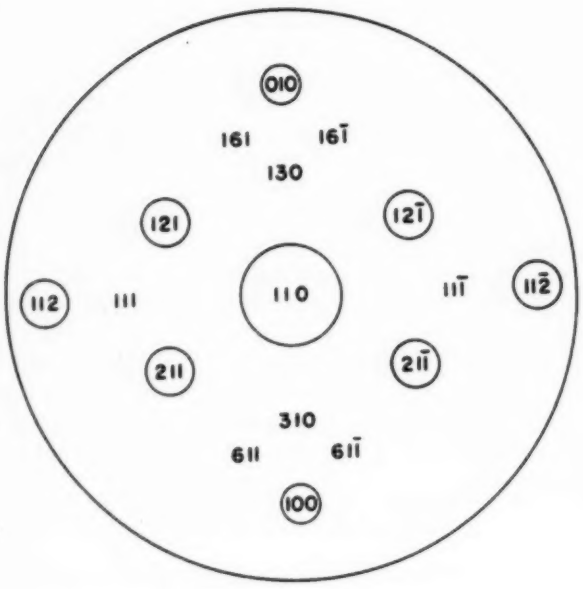

(b)

FIG. 1. Field-emission pattern of a clean tungsten cathode. (a) Photograph of projection-tube pattern; (b) Crystal surface diagram.

experienced with tubes of the conventional type. The cathode was a sharp point etched electrolytically from tungsten wire in a solution of sodium hydroxide. This point cathode was mounted on a tungsten hairpin so that it could be heated and outgassed. The phosphor (ZnS, silver activated) was sprayed on the inside of the glass envelope from a solution containing a nitrocellulose binder. Phosphor was deposited only on the top one-third of the bulb to eliminate reflected light reaching the pattern from the bottom part of the tube. Furthermore, only a very thin coating of phosphor was deposited to reduce to a minimum the diffusely scattered light from adjacent parts of the phosphor.

B. Vacuum Techniques

All experiments with field-emission projection tubes have indicated the necessity of extreme vacuum conditions in order to obtain a pattern of clean tungsten which remains stable with time. Since the point cathode is maintained at room temperature, any residual gas in the tube quickly adsorbs on the point, and the pattern produced by the field-emission electrons changes. With pressures of the order of 10^{-8} mm of Hg, after the point is cleaned by a high temperature "flash," the pattern changes so rapidly with time that it is difficult to determine the pattern representative of clean tungsten. The vacuum techniques used in this research were based on some earlier studies with field-emission projection tubes by Daniel[7] and Moore.[8] Data from extensive experiments by Nottingham[9] on ionization gauges were also extremely helpful.

An ion gauge was connected directly to the experimental tube so that it could be used after the tube was sealed off the vacuum system. Two types of ion gauges were used during the research: the conventional ion gauge; and the new style ion gauge[10] which has the elements inverted to reduce the x-ray limit of the gauge. Both types of gauges were equipped with flash filaments for approximating pressures below the limits of the gauge. The x-ray limit of the particular Bayard-Alpert gauge which was used was about 5×10^{-11} mm of Hg. The tube and ion gauge were processed very thoroughly on the vacuum system by repeating a specific cycle of outgassing.[6] This cycle, which included baking all the glassware for several hours, heating the metal parts to high temperatures by high frequency induced currents and electron bombardment, and bombarding the phosphor by thermionic electrons, was repeated until the rate of change of the field-emission pattern with time indicated no change between two successive cycles. The pressure in the tube at this time was about 10^{-11} mm of Hg. After the experimental tube was sealed off the vacuum system, the operation of the ion gauge served to clean up some of the residual gas. The pressure decreased slowly and, in about one week, it reached an equilibrium value of approximately 10^{-12} mm of Hg. At this final pressure in the sealed off tube, the rate of contamination of the point cathode was very slow, and the field-emission pattern changed very slowly with time. The stability of the pattern is shown in the sequence of photographs in Fig. 2. The first sign of contamination, which appears as an enlargement of the dark spots for crystallographic directions of the (112) classification, is seen in the photograph taken twenty-four hours after the point was cleaned.

[7] J. H. Daniel, thesis, Massachusetts Institute of Technology, 1940.
[8] N. H. Moore, thesis, Massachusetts Institute of Technology, 1941.
[9] W. B. Nottingham (private communication).
[10] R. T. Bayard and D. Alpert, Rev. Sci. Instr. **21**, 6, 571 (1950).

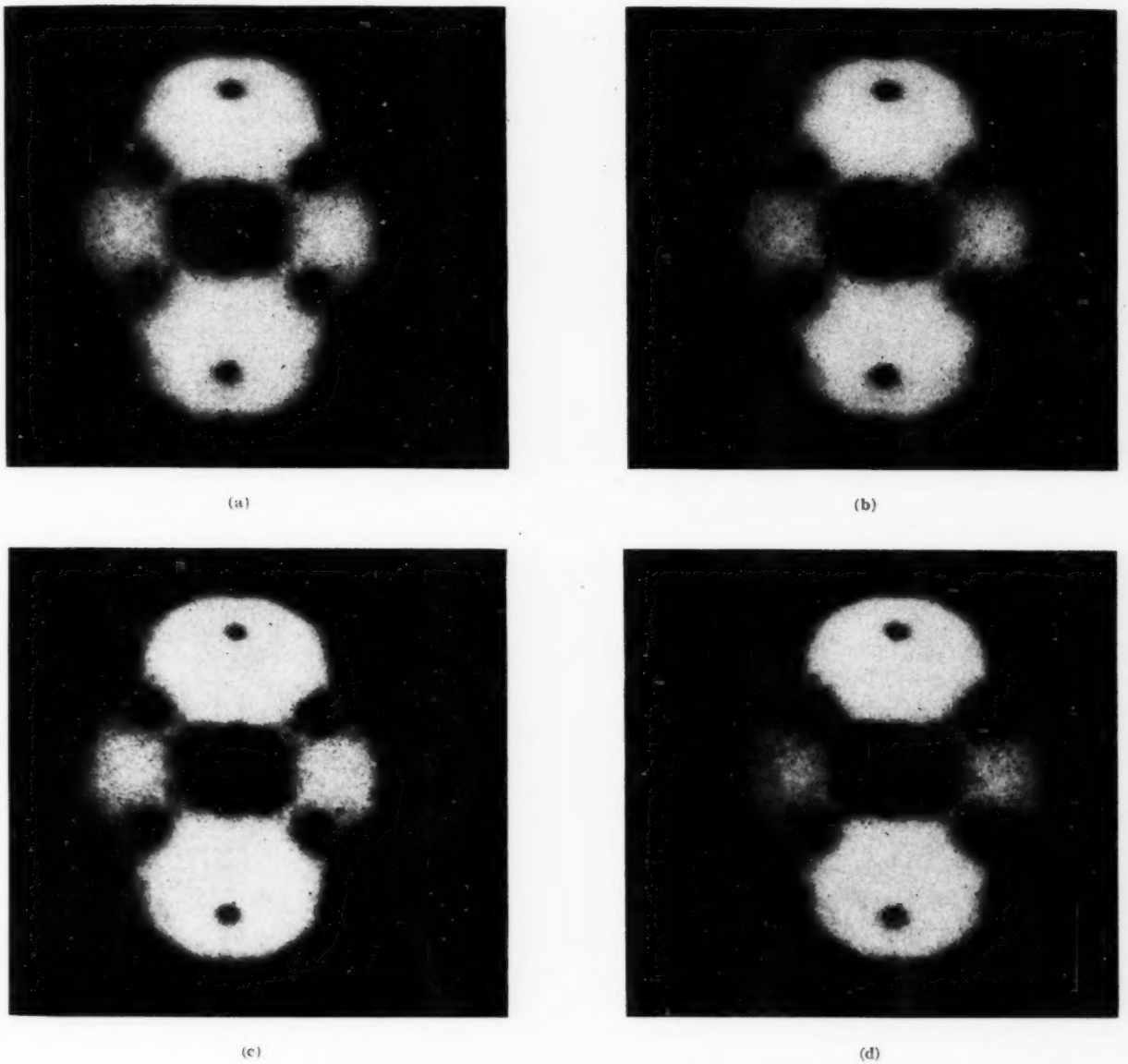

FIG. 2. Photographs showing rate of contamination of point cathode. (a) Immediately after flash; (b) 12 hours after flash; (c) 24 hours after flash; (d) 48 hours after flash.

C. Photometric Measurements

The photometric method of measurement was accomplished using a 931-A photomultiplier tube to measure the light output from the phosphor. Light from the desired crystallographic direction was focused by a simple lens on a small circular aperture in the photomultiplier housing. The currents produced in the 931-A photomultiplier were measured by a null method with the circuit shown schematically in Fig. 3. Conditions could be fulfilled easily to insure that the currents produced in the photomultiplier were directly proportional to the field-emission currents.

D. Relationship Between the Light Output from the Phosphor and the Potential of the Phosphor

Nottingham[11] has shown that the light output from a phosphor per unit current striking it, varies with the potential of the phosphor according to the relationship

$$L/I = kV^n \qquad (2)$$

where L is the light output from the phosphor, I is the electron current striking the phosphor, V is the potential of the phosphor, and k and n are constants. The value of n varies with the type of phosphor, and it may

[11] W. B. Nottingham, J. Appl. Phys. **10**, 73 (1939).

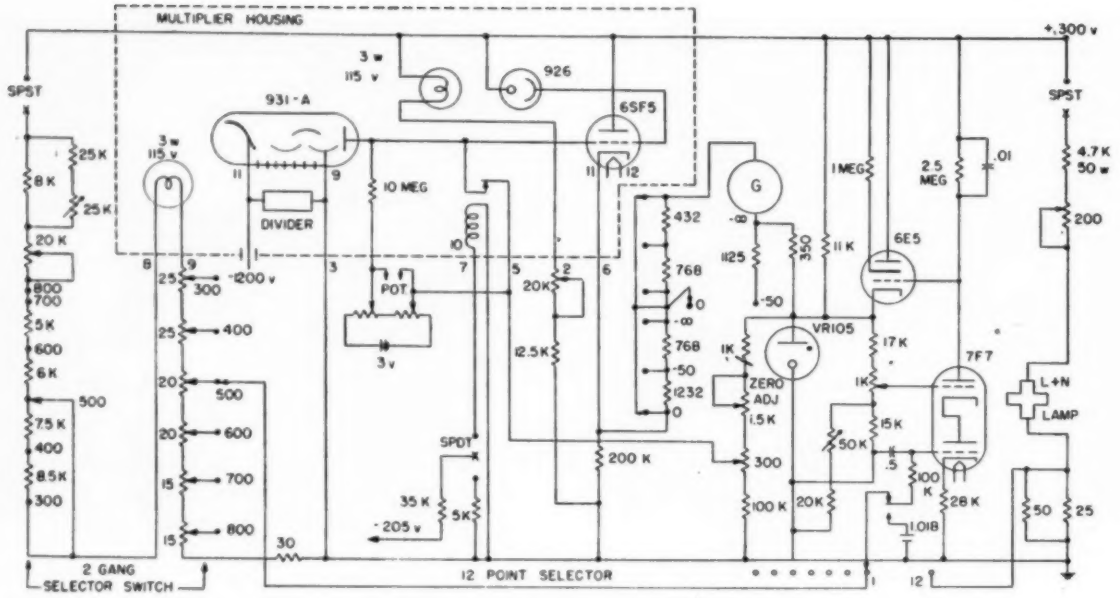

FIG. 3. Circuit diagram of photometer.

vary to a smaller degree for different samples of the same phosphor. An experimental determination of n was made after the tube had been processed and the final equilibrium pressure had been reached.

Data obtained from the final experimental tube with a ZnS:Ag screen are shown in Fig. 4. L_T represents a measurement of light which was proportional to the total light output from the experimental tube and I_T is the total collection current. The value of n, which is determined from the slope of the best straight line through the plotted data, is 2.5. Data were also obtained for a tube with a willemite screen, and the value of n was found to be 2.0.

E. Determination of the Radius of the Point

The radius of the point cathode was necessary for calculating the electric fields at the surface of the cathode and the emission current densities. Observations under an optical microscope of 1000 magnification indicated that the radius of the point used for the quantitative measurements was about one micron. An attempt was made to obtain a more accurate measurement with an electron microscope, but unfortunately the point was damaged when it was mounted.

III. EXPERIMENTAL RESULTS

A. Presentation of Experimental Data

In order to determine the value of electric field in a tube of this type, Benjamin and Jenkins[12] made a study of the equipotentials produced by a model of the point and filament system on a rubber membrane. They found that the electric field at the surface of the point cathode is given by the equation

$$F = \tfrac{1}{2}V/r, \tag{3}$$

where F is the electric field, V is the potential of the spherical envelope, and r is the radius of the point. Therefore, according to the field emission equation, a plot of log (J/V^2) against $1/V$ would give a straight

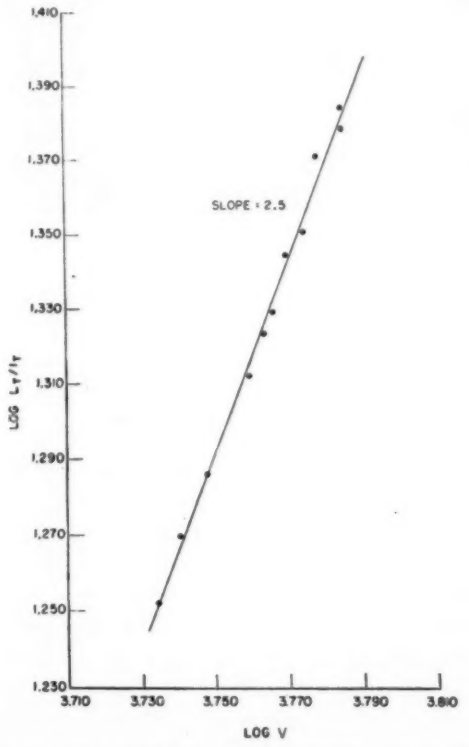

FIG. 4. Variation of the light output per unit current with the potential of a ZnS:Ag phosphor.

[12] M. Benjamin and R. O. Jenkins, Proc. Roy. Soc. (London) **A176**, 262 (1940).

line. Figure 5 represents such a plot showing the relationship between the total field-emission collection current and the applied voltage. Since the emitting area was constant, total current was plotted in place of the current density. The data indicate an excellent straight line over three orders of magnitude of current.

Figure 6 shows typical field emission plots which were obtained by photometering some of the main crystallographic directions. These data are also plotted with respect to applied voltage instead of electric field. The light output of the phosphor, L, is arbitrarily plotted in terms of the currents produced in the photomultiplier tube. It was necessary to plot $\log(L/V^{4.5})$ against $1/V$ to account for the fact that the light output per unit current for the zinc sulfide phosphor was proportional to $V^{2.5}$. Slopes of the straight lines are indicated in parentheses. Excellent straight lines were obtained for all the crystallographic directions which were photometered. These data were completely reproducible, indicating that the vacuum in the tube was sufficiently good to make contamination of the point negligible during the time data were taken. Sufficient measurements were made to establish a definite straight line, and photometric data from the darkest spots on the pattern were taken over almost two orders of magnitude of current.

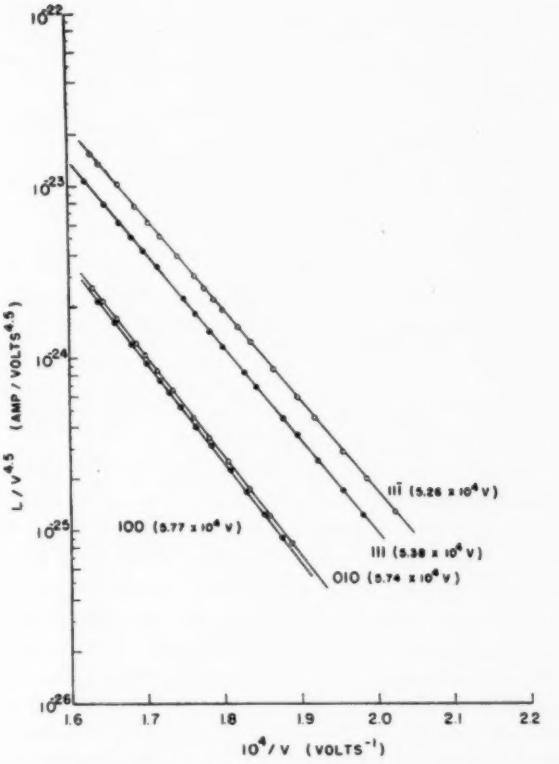

FIG. 6. Field-emission plots for the (100), (010), (111), and (11$\bar{1}$) crystallographic directions.

B. Discussion of Experimental Data

When a comparison of the field-emission plots for the various crystallographic directions is made, consideration must be given to the fact that these are not true field-emission characteristics. The plots are made with respect to the applied voltage, and the electric field at the surface of the point cathode for a specific applied voltage may have been different for the various directions. It is evident from the field emission equation that if the electric field is different, the absolute magnitude of the current will be different, but it should be emphasized that a difference in electric field also affects the slope of the straight line. This effect is indicated in Fig. 6, where data are plotted for the (111) and (11$\bar{1}$) crystallographic directions. Since these directions are essentially the same, they have the same value of work function, and the field-emission plots should be identical. However, it is seen that the values of the emission currents differ by about 40 percent, and the slopes differ by about 2 percent. A 2 percent difference in surface electric field for these two directions would cause this discrepancy. A similar comparison of the data for the other crystallographic directions showed that except for directions of the (112) classification, field-emission plots for directions of a certain Miller index classification had the same slope within 1 percent, and the magnitudes of the currents were very nearly the same. However, the data indicated that the surface electric field for the (12$\bar{1}$) and (21$\bar{1}$) directions was also about 2 percent higher than the field for the (121) and (211) directions. It is reasonable to assume that the shape of the point cathode was slightly different

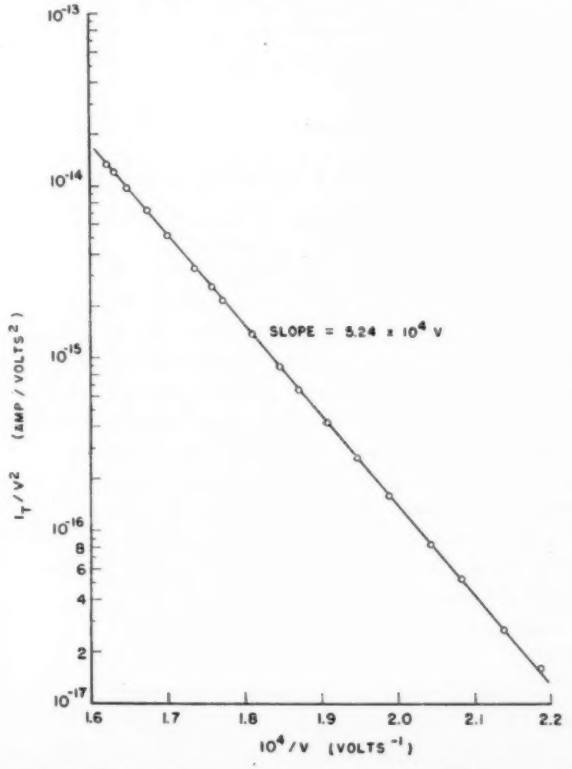

FIG. 5. Field-emission plot for the total emission current.

TABLE I. Slopes of field-emission plots and previously determined values of work functions.

Crystallographic direction	Slope (volts)	φ_N (ev)[a]	φ_M (ev)[b]
110	5.43×10^4	4.68	
121	5.71×10^4	4.69	4.50
100	5.77×10^4	4.56	
111	5.38×10^4	4.39	
$61\bar{1}$	5.21×10^4	4.39	
310	5.16×10^4		4.35

[a] Values of work functions determined thermionically by Nichols.
[b] Values of work functions determined photoelectrically by Mendenhall and DeVoe.

on the two sides, and that this asymmetry caused a small difference in the surface field.

Slopes of the field-emission plots for the classes of crystallographic directions which were photometered are tabulated in Table I. Only one direction of each Miller index classification is listed, since with the assumption of a slightly higher surface field at one section of the point cathode, the data for similar crystallographic directions agreed very closely. The values of work functions for the crystallographic directions which had been determined thermionically by Nichols[13] and photoelectrically by Mendenhall and DeVoe[14] are also tabulated. These data show that the crystallographic directions which are represented by dark spots on the field-emission pattern are those for which the field-emission plots have the greatest slopes. Furthermore, the percentage difference in the slopes for the various directions is sufficiently small that it may be explained by the difference in work function determined by other methods.

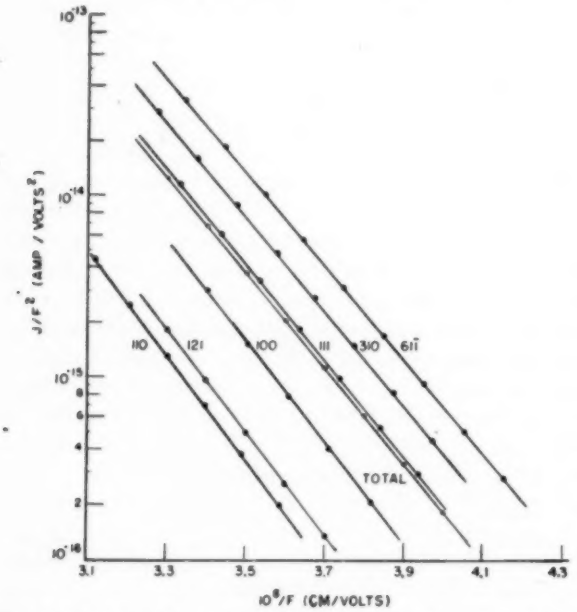

FIG. 7. Field-emission characteristics based on the assumed surface electric field.

[13] M. H. Nichols, Phys. Rev. **57**, 297 (1940). C. Herring and M. H. Nichols, Revs. Modern Phys. **21**, 185 (1949).
[14] C. E. Mendenhall and C. F. DeVoe, Phys. Rev. **51**, 346 (1937).

C. Field-Emission Characteristics

1. Assumption of the Surface Electric Field

In order to make a more careful comparison of the data with existing values of the work function, it was necessary to plot true field-emission characteristics. Such plots required a knowledge of the electric field distribution around the surface of the point cathode for a fixed applied voltage.

Since tungsten wire is drawn with the (110) direction along the axis of the wire, the angles which the various crystallographic directions formed with the axis of the cathode were calculated on this basis. Field-emission plots indicated that the surface electric field for the (112) crystallographic direction was 5 percent less than the field for the (121) direction, corresponding to an average decrease of 1 percent each 5°. This variation was assumed to be uniform and to occur at all angles with the axis. Measurements for the (112) crystallographic direction were not very accurate because the photometric currents were weak, but it is believed that the data gave a reasonable basis on which the electric field distribution could be assumed.

TABLE II. Variation of electric field with crystallographic direction based on the assumed electric field distribution.

Crystallographic direction	Angle with axis of point cathode[a]	Variation in field from the value. $F=\frac{1}{2}V/r$
110	0	+6%
121	30°	0
100	45°	−3%
111	35°16′	−1%
611	36°34′	−1.3%
310	26°34′	+0.7%

[a] These angles are actually angles between the 110 crystallographic direction and the other crystallographic directions listed.

The magnitude of the surface electric field for the total collection current was calculated from Eq. (3). Furthermore, since the field-emission patterns had indicated no appreciable emission from crystallographic directions which made angles larger than 60° with the axis of the point cathode, this equation was also used to calculate the surface field for the direction at an angle of 30° with the axis. Table II lists the angles which the various crystallographic directions formed with the axis of the cathode and the amount by which the surface electric field for each direction was changed from the value of the average field.

2. Conversion of Units

The arbitrary units of light measurement were converted to units of current by a comparison of the total light output of the pattern with the total collection current. Since the total light output was calculated by

numerical integration, the absolute current values are inaccurate except as an order of magnitude, but the relative values are unchanged. Current densities were calculated with the assumption that the point was semispherical and that no emission took place from surfaces of the cathode which formed an angle greater than 60° with the axis.

3. *Analysis of Field-Emission Characteristics*

The field-emission characteristics which are plotted in Fig. 7 resulted from the conversion of photometric units and the assumed surface electric field. The fact that the field-emission characteristic for the total emission current lies between the characteristics for the dark areas and light areas is an indication that the magnitudes of the current densities for the various crystallographic directions are reasonably correct even though the procedure used to convert units was not accurate.

The field-emission equation can be written in the form:

$$\log J/F^2 = \log A - B/F, \tag{4}$$

where B is the slope of the field-emission characteristic and $\log A$ is the intercept when $1/F$ is zero. Table III gives the values of $\log A$ and B for the data obtained in this research together with values of the work-functions as obtained by Nichols and by Mendenhall and DeVoe. As a matter of general interest, the values of current density are tabulated for an electric field of 3.0×10^7 volts/cm.

The values of B are seen to vary in the same general manner as the values of work functions obtained by other methods. According to the field-emission equation, a plot of the logarithm of B against the logarithm of the work function should give a straight line with a slope of $\frac{3}{2}$. The data are plotted in Fig. 8, and the straight line which is drawn with a slope of $\frac{3}{2}$ represents the plotted points quite well. Because of the uncertainty of the distribution in electric field over the surface of the point cathode, the data in Fig. 8 cannot be considered a verification that the theory predicts the correct dependence of the current density on the work function. However, for the particular electric field distribution which was assumed, the experimental data are in agreement with existing values of work function and the theoretical field-emission equation.

TABLE III. Slopes and intercepts of field-emission characteristics.[a]

Field-emission characteristic	Log A	B (volts/cm)	φ_N (ev)	φ_M (ev)	J[b] (amp/cm²)
110	−5.38	2.88×10^8	4.68		0.95
121	−5.33	2.85×10^8	4.69	4.50	1.3
100	−5.01	2.80×10^8	4.56		4.1
111	−5.08	2.66×10^8	4.39		10.3
$61\bar{1}$	−4.88	2.57×10^8	4.39		32.1
310	−5.03	2.60×10^8		4.35	18.6
Total Current	−5.26	2.62×10^8			9.2

[a] Only relative values in this table are significant. The numerical values depend on the accuracy of the measurement of the point radius and the validity of the factor ($\frac{1}{6}$) in Eq. (3).

[b] These values of current density occurred for an electric field of 3.0×10^7 volts/cm. The high voltage required to produce this field varied for the different directions but had an average value of 6000 volts.

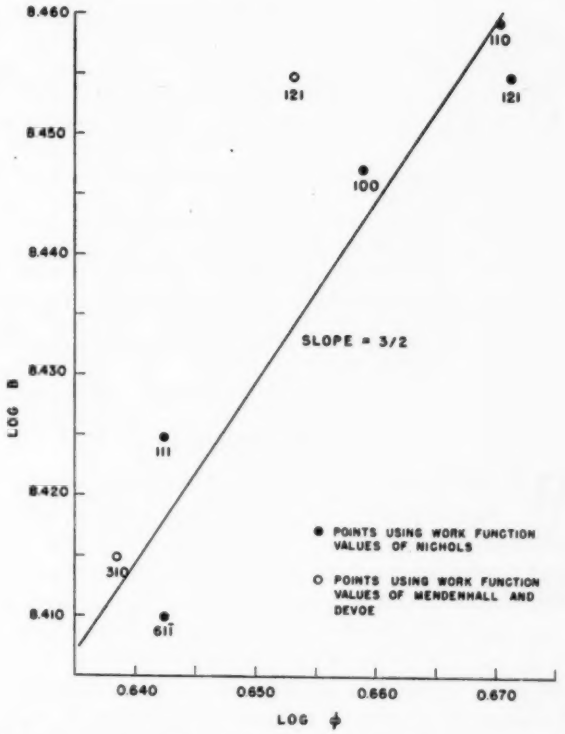

FIG. 8. Comparison of the field-emission data with existing values of work function.

Nichols and Smith[15] have recently obtained new values for the thermionic work functions of certain crystallographic directions. Except for the (110) direction, these values are in good agreement with the values previously obtained by Nichols. While the measured value for the (110) direction also agrees very closely with the previous value, experimental evidence indicates that this value is not correct and that the correct value should be much larger. The field-emission data obtained in this research would not be consistent with with such a value.

IV. ACKNOWLEDGMENTS

It is a pleasure for the author to express his gratitude to Professor W. B. Nottingham who suggested this study and gave his encouragement and helpful advice while guiding the work. The author is also indebted to the General Electric Company Research Laboratory for spraying the final experimental tube with "conducting glass," and to Dr. L. R. Koller for making the necessary arrangements. Mr. L. E. Sprague, Mr. L. W. Ryan, Mr. A. T. Velluto, and Mr. J. Palermo gave very able assistance in many aspects of the experimental procedures.

[15] M. H. Nichols and G. F. Smith, U. S. Office of Naval Research Report N6-onr-24433 (1952).

Static and Sliding Friction in Feedback Systems

J. Tou* and P. M. Schultheiss
Department of Electrical Engineering, Yale University, New Haven, Connecticut
(Received January 16, 1953)

One of the most common nonlinearities encountered in servomechanisms design is the friction phenomenon in electromechanical systems. Conventional linear theory fails to predict its effect upon system performance. This paper extends familiar techniques to the treatment of friction nonlinearity in servosystems. Frequency-response methods are employed throughout and the theoretical results are verified by means of an analog computer. Sliding friction and static friction are represented by describing functions which form the critical factors in determining system stability. The analysis indicates that certain series equalizers designed from linear theory may fail to achieve effective compensation in the presence of sliding and static friction. On the other hand, a subsidiary loop may avoid the stability problem while still realizing an essentially equivalent loop gain function.

I. INTRODUCTION

WHILE basic analysis and synthesis procedures for linear feedback systems have become well established during the last decade, there is no correspondingly broad approach to nonlinear problems. Except in very simple cases, no general solutions are possible, and the designer must rely either on machine computation or on various linear or quasi-linear approximations. A variety of such approximations has been developed to fit numerous types of systems and successful design procedures have been discovered for a great many practical problems. It is the purpose of this paper to extend one of these techniques so as to make it applicable to the analysis of feedback systems involving sliding and static friction. Particular attention will be paid to certain loop gain functions which appear to be quite satisfactory on the basis of linear analysis but are found to be unstable in practice as a result of friction phenomena. Methods of predicting, and hence presumably preventing, such behavior will be outlined.

II. REVIEW OF BASIC PROCEDURE

The technique to be employed was first devised by Kochenburger[1] for the analysis of contractor servomechanisms and subsequently adapted for use with other nonlinear devices.[2,3] The basic procedure has been described extensively in the literature[1-3] and will therefore be outlined only briefly. It is unique in that it permits use of the frequency domain in an approach to problems involving certain types of nonlinear elements. If a sinusoidal voltage is applied to a nonlinear device, the output is generally not sinusoidal. However, under rather general conditions the fundamental component of the output will be greater than any harmonic, a difference which will be further emphasized by effective low-pass filters such as servomotors. Adequate accuracy can therefore be obtained in many cases by considering only the fundamental component of the output.[1,2] Since the amplitude and phase of the fundamental component varies with the amplitude of the applied sinusoid, the approximate characteristics of the nonlinear device are represented by an "amplitude-describing function" $H_0(x)=f(x)e^{j\delta(x)}$ (see Fig. 1). If x represents the amplitude of a sinusoidal input signal, $f(x)$ is the ratio of the fundamental output to the input amplitude and $\delta(x)$ is the phase shift of the output fundamental relative to the input signal. Note that $H_0(x)$ is frequency invariant, it depends only on the input amplitude.

Once $H_0(x)$ is known, a stability analysis can proceed essentially as in the linear case. Consider the simple loop shown in Fig. 2. System stability is governed by the roots of the equation

$$1+H_0(x)H(s)=0 \tag{1}$$

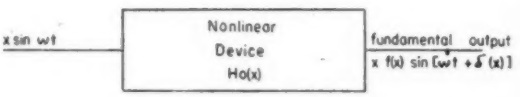

FIG. 1. Describing function of a nonlinear device.

or

$$H(s)=-1/H_0(x). \tag{2}$$

In the linear case $H_0(x)=1$ and the stability problem reduces to the conventional one, solved easily by means of a Nyquist plot. The only modification required for the nonlinear case under the assumptions stated is a change in the critical point which now becomes $-1/H_0(x)$ instead of -1. Thus the critical point changes with the signal amplitude, and it becomes necessary to plot an amplitude locus $-1/H_0(x)$ in addition to the frequency locus $H(s)$. If the amplitude locus lies completely outside the frequency locus, the system is stable under all conditions of operations.[4] Figure 3 shows intersecting loci. Here the system is unstable for small disturbances, but stable for large disturbances so

* Now with Philco Corporation, Philadelphia, Pennsylvania.
[1] R. J. Kochenburger, Elec. Eng. **69**, 687 (1950). See also Trans. Am. Inst. Elec. Engrs. **69**, 270 (1950).
[2] E. C. Johnson, dissertation, Massachusetts Institute of Technology, 1951; Trans. Am. Inst. Elec. Engrs. **71**II, 169 (1952).
[3] E. S. Sherrard, Trans. Am. Inst. Elec. Engrs. **71**II, 312 (1952).
[4] Frequently the inverse loci, $1/H(s)$ and $-H_0(x)$, are plotted. The choice is governed simply by computational convenience in particular instances.

that oscillations will tend to stabilize near the intersection point P which thus specifies the steady-state conditions, at least to a first approximation.[1]

In summary, analysis of the stability problem will require the following steps.

(a) Determination of the wave form at the output of the nonlinear device resulting from a sinusoidal input.

(b) Calculation of the describing function $H_0(x)$ from the wave shape obtained in (a).

(c) Plot and interpretation of the amplitude and frequency loci for the system under consideration. For the cases of particular interest here this step requires rearrangement of the conventional block diagram in order to secure effective separation of all transfer functions into two classes: The class of all linear but frequency sensitive components and that of all nonlinear but frequency insensitive elements.

The following definitions will be used throughout this paper. Static friction is the torque required to initiate rotation. Sliding friction is the velocity-independent component of the torque necessary to maintain such motion once started. Viscous friction is that component of the torque which is linearly proportional to the angular velocity of the rotating member.

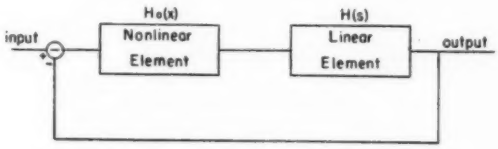

FIG. 2. Feedback loop with nonlinear element.

III. SLIDING FRICTION IN SERVOSYSTEMS

A. Wave Form Resulting from a Sinusoidal Input Torque to a System with Sliding Friction

If only sliding friction is considered the entire friction phenomenon can be represented by the characteristic curve of Fig. 4.

Consider a rotating member with moment of inertia J and angular acceleration $\ddot{\theta}$. Because of sliding friction the effective accelerating or decelerating torque τ_e is related to the applied torque τ_a through the equation

$$\tau_e=\tau_a\pm T_c, \tag{3}$$

where T_c is defined by Fig. 4. From Newton's law of motion,

$$\tau_a=T_c+J\ddot{\theta} \text{ for angular velocity } \dot{\theta}>0 \tag{4}$$

$$\tau_a=-T_c+J\ddot{\theta} \text{ for } \dot{\theta}<0. \tag{5}$$

From Eqs. (3), (4), and (5), the angular acceleration of the rotating member is given by

$$\ddot{\theta}(t)=\tau_e(t)/J. \tag{6}$$

Hence $\ddot{\theta}(t)$ has the same wave form as $\tau_e(t)$.

If the applied torque τ_a is sinusoidal,

$$\tau_a(t)=T_a\sin\omega t. \tag{7}$$

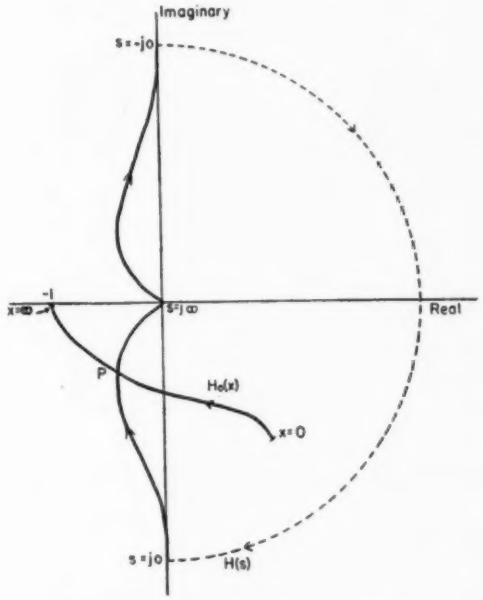

FIG. 3. Amplitude and frequency loci.

The corresponding steady-state wave forms are sketched in Figs. 5 and 6. The effective torque wave derived from Eq. (3) is shown in dotted lines. The discontinuities of the τ_e wave correspond to zeros of the $\dot{\theta}$ wave because the frictional torque T_c changes sign at those instants. On the $\dot{\theta}$ curve, point P is the point of inflection, corresponding to maximum acceleration. Since the steady state is of primary interest, the reference time is chosen after the oscillation has reached its steady-state value. $\ddot{\theta}(t)$ passes through zero at

$$\omega t=n\pi-\alpha, \quad n=0, 1, 2, 3\cdots,$$

while

$$\tau_a=T_c \quad \text{at} \quad \omega t=\alpha.$$

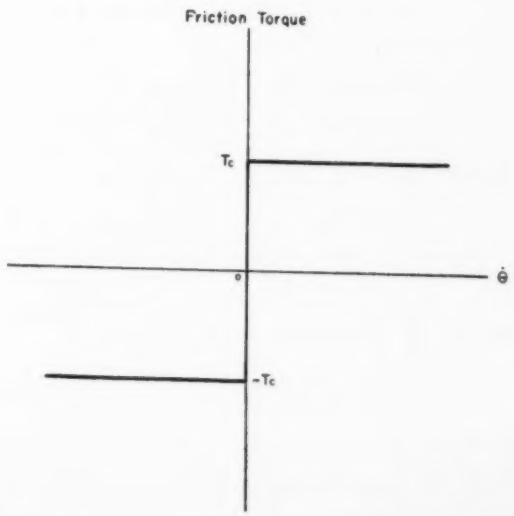

FIG. 4. Sliding friction characteristic.

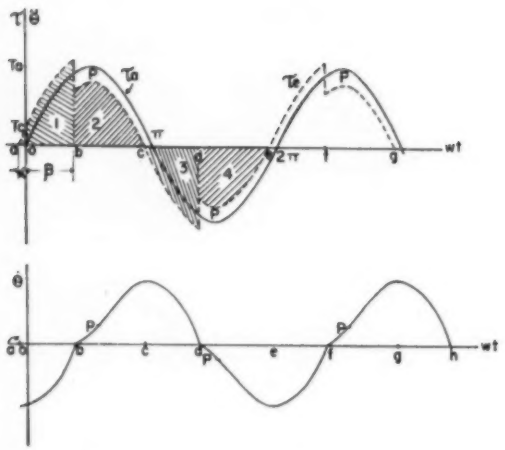

FIG. 5. Steady-state wave forms without dead zones.

It follows that

$$\alpha = \sin^{-1}\lambda, \tag{8}$$

where

$$\lambda = T_c/T_a. \tag{9}$$

Only the angle β corresponding to the first discontinuity point remains unknown. Once it has been evaluated in terms of λ, the wave form is completely determined. There are two possibilities: If $\alpha \leq \beta$, there is no dead zone in the τ_e wave (Fig. 5). If $\alpha > \beta$, there are dead zones as indicated in Fig. 6. These two cases will be considered separately.[5]

Mathematical Representation of the Steady-State Wave Forms

Case (1).—No dead zone. $\alpha \leq \beta$.

Refer to Fig. 5. In the absence of viscous friction, the following steady-state conditions exist.

Shaded area No. 1 = shaded area No. 2
= shaded area No. 3
= shaded area No. 4, etc.[6]

But between a and b,

$$\tau_e = T_a \sin\omega t + T_c = T_a(\sin\omega t + \sin\alpha) = T_a(\sin\omega t + \lambda); \tag{10}$$

and between b and c,

$$\tau_e = T_a \sin\omega t - T_c = T_a(\sin\omega t - \sin\alpha) = T_a(\sin\omega t - \lambda). \tag{11}$$

Then

$$\text{area No. 1} = \int_{-\alpha}^{\beta} T_a(\sin\omega t + \sin\alpha)\,d(\omega t) = T_a(-\cos\beta + \beta\sin\alpha + \cos\alpha + \alpha\sin\alpha), \tag{12}$$

and

$$\text{area No. 2} = \int_{\beta}^{\pi-\alpha} T_a(\sin\omega t - \sin\alpha)\,d(\omega t) = T_a[\cos\alpha - (\pi-\alpha)\sin\alpha + \cos\beta + \beta\sin\alpha]. \tag{13}$$

If Eqs. (12) and (13) are set equal and simplified, the result is

$$\cos\beta = \pi\sin\alpha/2$$

or

$$\beta = \cos^{-1}(\pi\lambda/2). \tag{14}$$

For the extreme case, $\beta = \alpha$, Eq. (14) becomes

$$\sin^{-1}\lambda = \cos^{-1}(\pi\lambda/2)$$

or

$$\lambda^2 + (\pi\lambda/2)^2 = 1.$$

A solution for λ yields

$$\lambda = \lambda_c = 0.536. \tag{15}$$

λ_c is the critical value of the quantity T_c/T_a. There is no dead zone for $\lambda \leq \lambda_c$, and there are dead zones for $\lambda > \lambda_c$.

Case (2).—With dead zones. $\alpha > \beta$.

In like manner, one obtains from Fig. 6:

shaded area No. 1 = shaded area No. 2
= shaded area No. 3
= shaded area No. 4, etc.

But, between a and b,

$$\tau_e = T_a(\sin\omega t + \lambda); \tag{16}$$

between b and c,

$$\tau_e = 0; \tag{17}$$

and between c and d,

$$\tau_e = T_a(\sin\omega t - \lambda). \tag{18}$$

Hence,

$$\text{area No. 1} = \int_{-\alpha}^{\beta} T_a(\sin\omega t + \lambda)\,d(\omega t) = T_a(-\cos\beta + \beta\lambda + \cos\alpha + \alpha\lambda), \tag{19}$$

$$\text{area No. 2} = \int_{\alpha}^{\pi-\alpha} T_a(\sin\omega t - \lambda)\,d(\omega t) = T_a[\cos\alpha - (\pi-\alpha)\lambda + \cos\alpha + \alpha\lambda]. \tag{20}$$

Equating (19) and (20) and simplifying

$$\lambda\beta - \cos\beta = (1-\lambda^2)^{\frac{1}{2}} - (\pi - \sin^{-1}\lambda)\lambda. \tag{21}$$

For the extreme case $\alpha = \beta = \sin^{-1}\lambda$,

$$\lambda\sin^{-1}\lambda - (1-\lambda^2)^{\frac{1}{2}} = (1-\lambda^2)^{\frac{1}{2}} - (\pi - \sin^{-1}\lambda)\lambda.$$

or

$$\lambda = \lambda_c = 0.536 \text{ as before.} \tag{15}$$

[5] Note that a dead zone or region of zero effective torque and velocity such as bc on Fig. 6 occurs whenever the applied torque T_a is smaller in magnitude than T_c at the instant when the velocity reaches zero.

[6] Velocity is proportional to the integral of torque in the absence of viscous friction.

B. Calculation of the Describing Function

Since $\tau_e(t)$ is a periodic function of time, it can be expressed in terms of a Fourier series:

$$\tau_e(t)=\frac{b_0}{2}+\sum_{n=1}^{\infty}(a_n \sin n\omega t+b_n \cos n\omega t). \tag{22}$$

It has been pointed out that, to a first approximation, $\tau_e(t)$ can be represented by the fundamental component of its Fourier series. From symmetry considerations, $b_0=0$. This implies oscillation about the rest position which is a condition of primary interest in stability analyses.[7] Then

$$\tau_e(t)\doteq a_1 \sin\omega t+b_1 \cos\omega t, \tag{23}$$

where

$$a_1=\frac{1}{\pi}\int_{\theta}^{2\pi+\theta}\tau_e(t)\sin(\omega t)d(\omega t) \tag{24}$$

and

$$b_1=\frac{1}{\pi}\int_{\theta}^{2\pi+\theta}\tau_e(t)\cos(\omega t)d(\omega t). \tag{25}$$

Evaluation of the Fourier Coefficients

Case (1).—No dead zone, $\lambda\leq\lambda_c$ or $\alpha\leq\beta$.

$$a_1=\frac{2}{\pi}\int_{-\alpha}^{\beta}T_a(\sin\omega t+\lambda)\sin(\omega t)d(\omega t)+\frac{2}{\pi}\int_{\beta}^{\pi-\alpha}T_a(\sin\omega t-\lambda)\sin(\omega t)d(\omega t)$$
$$=T_a(1-2\lambda^2). \tag{26}$$

Similarly

$$b_1=2T_a\lambda[(2/\pi)^2-\lambda^2]^{\frac{1}{2}}. \tag{27}$$

Equation (23) may also be written in the form

$$\tau_e(t)=C_1\sin(\omega t+\delta), \tag{28}$$

where

$$C_1=(a_1^2+b_1^2)^{\frac{1}{2}}=T_a\left[1-4\left(1-\frac{4}{\pi^2}\right)\lambda^2\right]^{\frac{1}{2}} \tag{29}$$

and

$$\delta=\tan^{-1}\frac{b_1}{a_1}=\tan^{-1}\frac{2\lambda[(2/\pi)^2-\lambda^2]^{\frac{1}{2}}}{1-2\lambda^2}. \tag{30}$$

Hence, with an applied torque $\tau_e(t)=T_a\sin\omega t$, the effective torque is

$$\tau_e(t)=T_a\left[1-4\left(1-\frac{4}{\pi^2}\right)\right]^{\frac{1}{2}}\times\sin\left[\omega t+\tan^{-1}\frac{2\lambda[(2/\pi)^2-\lambda^2]^{\frac{1}{2}}}{1-2\lambda^2}\right]. \tag{31}$$

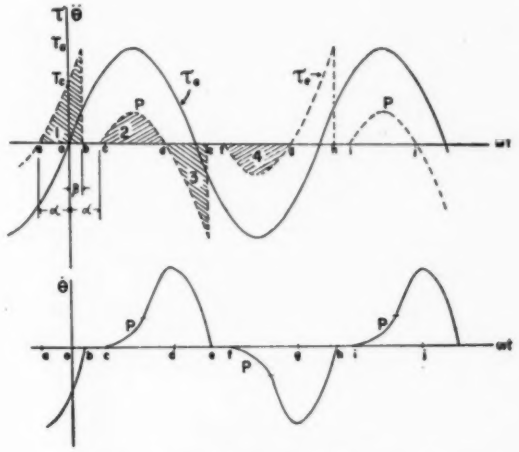

FIG. 6. Steady-state wave forms with dead zones.

In accordance with the definition of Sec. II, the describing function for the sliding-friction element is

$$H_0(\lambda)=f(\lambda)\angle\delta(\lambda)=\left[1-4\left(1-\frac{4}{\pi^2}\right)\lambda^2\right]^{\frac{1}{2}}\angle\tan^{-1}\frac{2\lambda[(2/\pi)^2-\lambda^2]^{\frac{1}{2}}}{1-2\lambda^2}. \tag{32}$$

Case (2).—With dead zones, $\lambda>\lambda_c$ or $\alpha>\beta$.

$$a_1=\frac{1}{\pi}\int_{\alpha}^{\pi+\beta}T_a(\sin\omega t-\lambda)\sin(\omega t)d(\omega t)+\frac{1}{\pi}\int_{\pi+\alpha}^{2\pi+\beta}T_a(\sin\omega t+\lambda)\sin(\omega t)d(\omega t)$$
$$=(T_a/\pi)[\pi-(\alpha-\beta)-\sin\alpha(\cos\alpha+\cos\beta)-\cos\beta(\sin\alpha+\sin\beta)]. \tag{33}$$

Similarly

$$b_1=(T_a/\pi)(\sin\alpha+\sin\beta)^2. \tag{34}$$

Hence in complete analogy with case (1) the friction-describing function is given by the expression

$$H_0(\lambda)=f(\lambda)\angle\delta(\lambda), \tag{35}$$

where

$$f(\lambda)=\frac{1}{\pi}\{[\pi-(\alpha-\beta)-\sin\alpha(\cos\alpha+\cos\beta)-\cos\beta(\sin\alpha+\sin\beta)]^2+[(\sin\alpha+\sin\beta)^2]^2\}^{\frac{1}{2}}$$

and

$$\delta(\lambda)=\tan^{-1}\frac{(\sin\alpha+\sin\beta)^2}{\pi-(\alpha-\beta)-\sin\alpha(\cos\alpha+\cos\beta)-\cos\beta(\sin\alpha+\sin\beta)}.$$

[7] Extensions to nonzero means are possible but complicate the analysis appreciably. See reference 1.

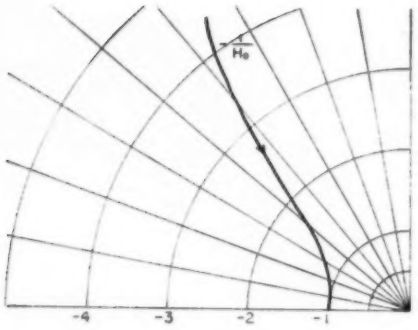

FIG. 7. The C locus.

C. C Locus

The C locus will be defined as a polar plot of the quantity $(-1/H_0)$. For any given system T_c is constant and H_0 is a function of T_a (because $T_a=T_c/\lambda$). For a fixed value of T_a, H_0 is a complex quantity which may be represented by a vector in the complex plane. The curve of $(-1/H_0)$, the C locus, forms the "critical locus" for system stability considerations, with the "critical point" $(-1, 0)$ as a special case for linear systems. The C locus is plotted in Fig. 7.

IV. SLIDING AND STATIC FRICTION IN SERVO SYSTEMS

A. Wave Form Resulting from a Sinusoidal Input Torque to a System with Sliding and Static Friction

If both sliding and static friction are considered, the friction phenomenon can be represented by the characteristic curve of Fig. 8. It will be satisfactory for most purposes to assume instantaneous transition from the static to the sliding friction value although this procedure does imply a degree of idealization.

Wave forms of $\tau_e(t)$ corresponding to an applied torque $\tau_a(t)=T_a \sin\omega t$ are easily sketched by a procedure identical with that used in Sec. III (Figs. 9 and 10). As before, there are two modes of oscillation, with and without dead zones. The latter is indistinguishable from the corresponding case discussed in Sec. III because the system is continually in motion. Thus only the former requires detailed discussion.

Mathematical Representation of the Steady-State Wave Forms

Case (1).—No dead zone, $\lambda\leq\lambda_c$, or $\alpha_2\leq\beta$.

From Sec. III, Eqs. (10) and (11), one immediately obtains the equations for $\tau_e(t)$,

$$\tau_e(t)=T_a(\sin\omega t+\lambda) \quad \text{for} \quad -\alpha_1<\omega t<\beta \tag{36}$$

$$\tau_e(t)=T_a(\sin\omega t-\lambda) \quad \text{for} \quad \beta<\omega t<\pi-\alpha_1, \tag{37}$$

where $\lambda=T_c/T_a$, $\alpha_1=\sin^{-1}\lambda$ and $\beta=\cos^{-1}(\pi\lambda/2)$.

Case (2).—With dead zones,

$$\lambda>\lambda_c \quad \text{or} \quad \alpha_2=\sin^{-1}T_s/T_a>\beta.$$

On Fig. 10,

shaded area No. 1

$$=\int_{\alpha_2}^{\pi-\alpha_1} T_a(\sin\omega t-\sin\alpha_1)d(\omega t)$$

$$=T_a[\cos\alpha_1-(\pi-\alpha_1)\sin\alpha_1+\cos\alpha_2+\alpha_2\sin\alpha_1], \tag{38}$$

shaded area No. 2

$$=\int_{\pi-\alpha_1}^{\pi+\beta} T_a(\sin\omega t-\sin\alpha_1)d(\omega t)$$

$$=T_a[\cos\beta-(\pi+\beta)\sin\alpha_1-\cos\alpha_1+(\pi-\alpha_1)\sin\alpha_1]. \tag{39}$$

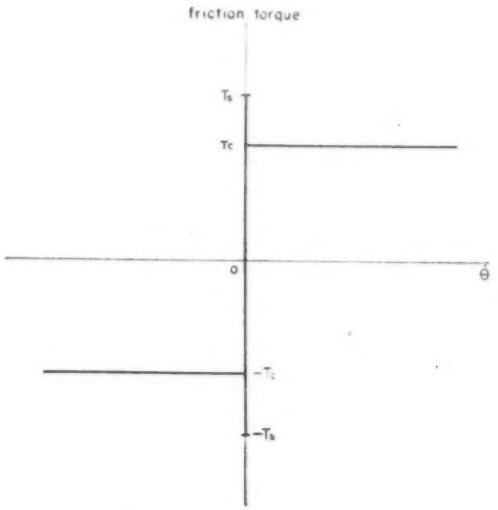

FIG. 8. Sliding and static friction characteristic.

With pure inertia load and under steady-state condition the shaded areas are equal. Equating (38) and (39) and simplifying,

$$\lambda\beta-\cos\beta=[1-(\lambda T_s/T_c)^2]^{\frac{1}{2}}-[\pi-\sin^{-1}(\lambda T_s/T_c)\lambda]. \tag{40}$$

Equation (40) defines β in terms of known parameters. It is clear that the system will not move at all if $\lambda>T_c/T_s$, for then $T_s>T_a$.

B. Calculation of the Describing Function

Approximate expressions for effective torque are obtained by reasoning similar to that in Sec. III.

$$\tau_e(t)\doteq a_1\sin\omega t+b_1\cos\omega t, \tag{23}$$

where a_1 and b_1 are given by Eqs. (24) and (25), respectively.

Case (1).—No dead zone. $\lambda\leq\lambda_c$, $\alpha_2\leq\beta$.

Since the equations for $\tau_e(t)$ are identical with those

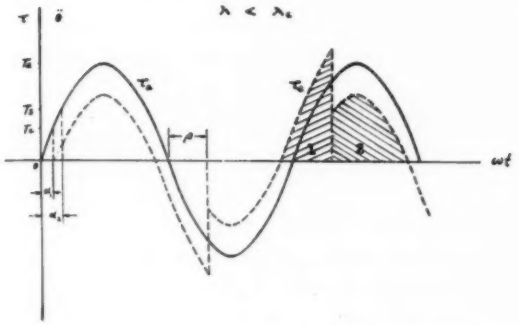

FIG. 9. Steady-state wave forms without dead zones.

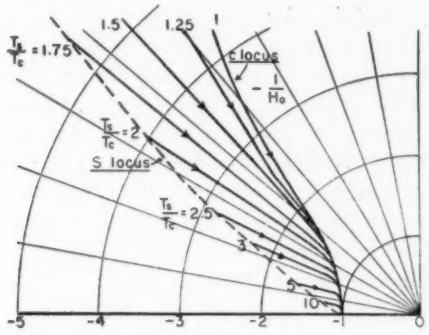

FIG. 11. Static friction loci, S locus.

in case (1) of Sec. III, the describing function $H_0(\lambda) = f(\lambda)\angle\delta(\lambda)$ is given by Eq. (32), and $f(\lambda)$ and $\delta(\lambda)$ have the following limiting values:

$$f(\lambda_c)=\frac{T_s/T_c}{[2.46+(T_s/T_c)^2]^{\frac{1}{2}}} \tag{41}$$

$$\delta(\lambda_c)=\tan^{-1}\frac{(4/\pi)(T_s/T_c)}{(\pi/2)^2+(T_s/T_c)^2-2[(\pi/2)^2+(T_s/T_c)^2]^{\frac{1}{2}}}. \tag{42}$$

Case (2).—With dead zones, $\lambda>\lambda_c$, $\alpha_2>\beta$.

$$a_1=\frac{1}{\pi}\int_{\alpha_2}^{\pi+\beta}2T_a(\sin\omega t-\lambda)\sin(\omega t)d(\omega t)$$

$$=(T_a/\pi)[\pi-(\alpha_2-\beta)+\cos\alpha_2(\sin\alpha_2-2\sin\alpha_1)-\cos\beta(2\sin\alpha_1+\sin\beta)] \tag{43}$$

in like manner

$$b_1=(T_a/\pi)[\sin\beta(2\sin\alpha_1+\sin\beta)+\sin\alpha_2(2\sin\alpha_1-\sin\alpha_2)]. \tag{44}$$

Hence the describing function for the static friction element is

$$H_0(\lambda)=f(\lambda)\angle\delta(\lambda),$$

where

$$f(\lambda)=\frac{1}{\pi}\{[\pi-(\alpha_2-\beta)-\cos\alpha_2(2\sin\alpha_1-\sin\alpha_2)-\cos\beta(2\sin\alpha_1+\sin\beta)]^2+[\sin\beta(2\sin\alpha_1+\sin\beta)+\sin\alpha_2(2\sin\alpha_1-\sin\alpha_2)]^2\}^{\frac{1}{2}} \tag{45}$$

and

$$\delta(\lambda)=\tan^{-1}\frac{\sin\beta(2\sin\alpha_1+\sin\beta)+\sin\alpha_2(2\sin\alpha_1-\sin\alpha_2)}{\pi-(\alpha_2-\beta)-\cos\alpha_2(2\sin\alpha_1-\sin\alpha_2)-\cos\beta(2\sin\alpha_1+\sin\beta)}. \tag{46}$$

C. Static Friction-Loci and S Locus

The static friction loci are polar plots of the quantity $(-1/H_0)$ for various ratios of static friction to sliding friction. The S locus is the locus of the termini of the static friction loci. The static friction loci and the S locus are plotted in Fig. 11.

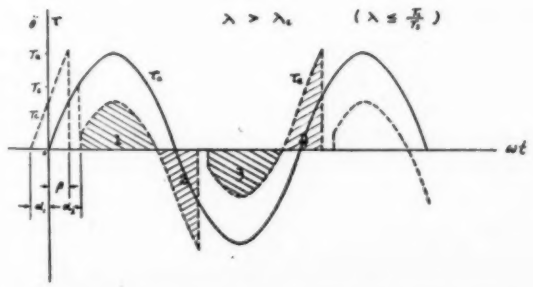

FIG. 10. Steady-state wave forms with dead zones.

V. PLOT AND INTERPRETATION OF THE AMPLITUDE AND FREQUENCY LOCI. EXAMPLES

Once the friction-describing function has been calculated, the desired stability information can be obtained easily by the method outlined in Sec. II. The procedure will be explained with the aid of a specific example which has been so chosen that a common type of corrective network will produce instability whereas another type of equalizer, apparently equivalent on a linear basis, will lead to a stable performance.

Consider the positioning loop shown in Fig. 12. In the absence of friction the loop gain function $A(s)$[8] has the form

$$A(s)=\frac{K_1}{s(1+Ts)}H_c(s). \tag{47}$$

A block diagram for this loop is shown in Fig. 13. The

[8] $A(s)$ is defined as the negative of the loop gain.

friction describing function relates applied torque to effective torque, neither of which appears as an explicit quantity in Fig. 13. This diagram therefore does not lend itself readily to the analysis of friction. However, it is easy to construct the equivalent block diagram of Fig. 14 by rearranging the basic equations describing motor performance. Torque now appears explicitly, and it is a simple matter to write the loop gain equation in terms of the friction-describing function and the system parameters defined in Fig. 12. The equation

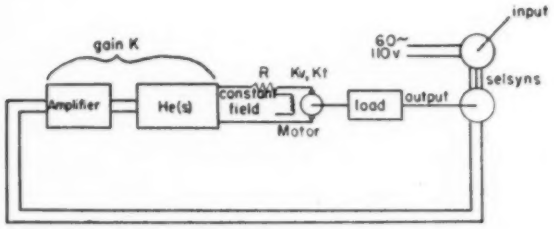

FIG. 12. Simple positioning system. $T=JR/K_vK_T$ = motor time constant; $H_e(s)$ = equalizer transfer function; K_T = motor torque per unit armature current; K_v = motor counter emf per unit speed; J = motor and load inertia; K_2 = gain of amplifier and selsyn $=K_1K_v$; R = armature loop resistance.

has the form

$$A(s)=H_0(\lambda)\frac{K_T}{Js^2}\left[\frac{K_vs}{R}+\frac{K_2}{R}H_e(s)\right]. \tag{48}$$

Note that viscous damping due to counter emf is represented by the additional feedback path rather than the conventional velocity-dependent load on the output member. This step is necessary because the friction-describing function was derived for the case of a pure inertia load. The procedure is obviously based on the assumption that a sinusoid applied to the nonlinear

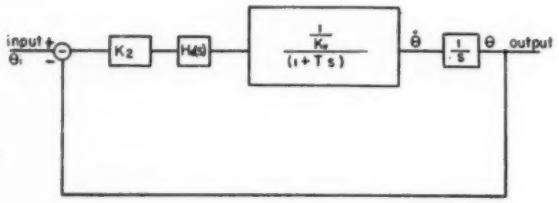

FIG. 13. Conventional block diagram.

device yields an output signal of which only the fundamental is significant in transmission around each loop, so that only sinusoids of the same frequency need be considered. This assumption becomes progressively poorer as damping, and hence the interior loop gain, increases. However, it will be seen that the method still leads to acceptable first approximations in cases of considerable practical interest.

Consider the system of Fig. 12 with the following arbitrary numerical parameters, all given in a consistent set of units.

$$K_T=K_v=0.1,\quad R=1,\quad J=0.001,\quad K_1=500,\quad K_2=50,\quad T=0.1. \tag{49}$$

Equation (47) now becomes

$$A(s)=\frac{500}{s(1+0.1s)}H_e(s). \tag{50}$$

In the absence of an equalizer $H_e(s)$ the loop would be close to instability. Let $H_e(s)$ be a two stage lag network or integral equalizer

$$H_e(s)=\left(\frac{1+0.5s}{1+5s}\right)^2. \tag{51}$$[9]

Without friction the system would exhibit a phase margin of 26° and a fairly well-damped transient response. The Nyquist diagram of Fig. 15 confirms that deduction. Note, however, that the sliding friction (C) locus intersects the Nyquist plot at two points. The system is evidently stable for exceedingly small disturbances; it becomes unstable as soon as a significant input signal is applied and then sustains oscillations at an amplitude

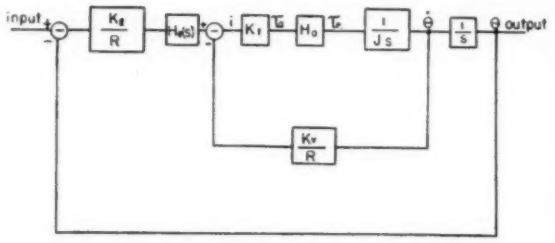

FIG. 14. Equivalent block diagram.

and frequency determined by the intersection point closer to the origin. An experimental check by analog computer resulted in oscillation at 1.6 rad/sec as compared to a theoretical value of about 2 rad/sec.

If a minor loop is used in place of the series equalizer (Fig. 16), the result is quite different. By a process entirely equivalent to that used in rearranging the block diagram of Fig. 13 the loop gain function may be written in the equivalent form

$$A(s)=H_0(\lambda)\frac{K_T}{Js}\left[\frac{K_v+H_b(s)}{R}+\frac{K_2}{Rs}\right]. \tag{52}$$

Using the equalizer transfer function[10]

$$H_b(s)=\frac{(5s)^2(1+0.1s)}{10(1+0.5s)^2(1+0.003s)} \tag{53}$$

[9] A more elaborate equalizer would probably be used in practice. This primitive form was chosen because it illustrates clearly the difficulties encountered because of friction effects.

[10] $H_b(s)$ has been chosen so as to yield a system with transfer from input to output as close as practical to the series equalized structure. Without the last denominator term (required for realizability) the two would be almost identical in the absence of friction. As it is, the step function responses are virtually indistinguishable.

and the same numerical values as in the previous case one obtains the Nyquist diagram shown along with the series equalizer case in Fig. 15. The plot does not intersect the C locus so that the system remains stable in the presence of friction. Measured results from an analog computer bear out this conclusion.

The equalizer used in the above example introduced attenuation with the third power of frequency over a 10:1 frequency range, so that the resultant frictionless system is conditionally stable. It may therefore not appear surprising that oscillations should develop when a nonlinear element is introduced into the loop. Similar results can, however, be obtained with a single-stage lag network and a resultant loop of absolute stability. Consider the series equalizer

$$H(s)=(1+0.25s)/(1+100s). \tag{54}$$

The gain factor K_2 is chosen as 100, all other parameters remain unchanged from the previous example. Figure 17

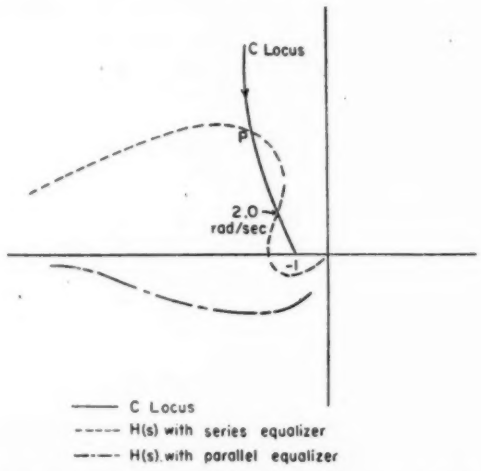

FIG. 15. Rough sketch of amplitude and frequency loci. Intersection at P is actually at a far greater distance from the origin.

shows the Nyquist plot as well as the curve for a corresponding minor loop structure. The latter is clearly stable. The Nyquist plot for the series equalizer case shows no intersection with the C locus and measurements in the presence of sliding friction alone indicate stability. However, the Nyquist diagram does cross the S locus twice, indicating that oscillations may occur when static as well as sliding friction is considered. Since the S locus traces the termini of the describing functions for various static-to-sliding-friction ratios, it is evident that stability depends critically on that ratio: only for values between those corresponding to the two intersection points can oscillations exist. It is also evident that the frequency of oscillations should rise from a theoretical minimum of 0.7 rad/sec to a maximum of 2.25 rad/sec. The corresponding range from computer measurement is 0.8 rad/sec to 2.0 rad/sec. The experimental correlation at intermediate values of the static-to-sliding-friction ratio is about equally close so that the method may be said to yield a reasonable first approximation.

VI. CONCLUSIONS

The describing function technique has been extended to cover problems of static and sliding friction in feedback systems. Under certain assumptions the stability problem can be handled adequately, and the frequency

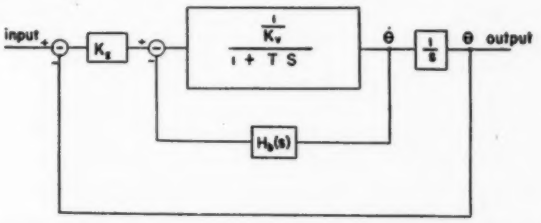

FIG. 16. Block diagram with minor loop (parallel equalizer).

of any sustained oscillations can be predicted to a first approximation. In particular it has been shown that the use of integral equalization in series with the loop may easily lead to instability when friction phenomena are important. Essentially equivalent minor loop equalizers may yield an entirely satisfactory system.

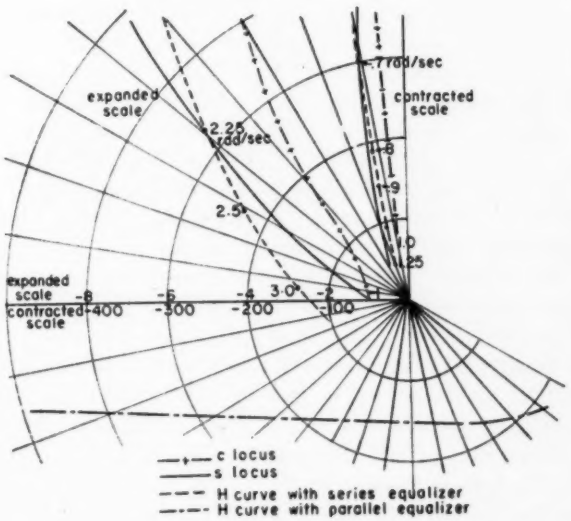

FIG. 17. Amplitude and frequency loci for an experimental system.

VII. ACKNOWLEDGMENT

The authors wish to acknowledge the aid of various members of the Electrical Engineering Department of Yale University, especially that of Professor F. B. Tuteur of the servomechanisms laboratory. The contents of this paper are taken in essence from a dissertation by Julius Tou presented to the faculty of the Yale School of Engineering in partial fulfilment of the requirements for the degree of Doctor of Engineering.

The Vector Wave Function Solution of the Diffraction of Electromagnetic Waves by Circular Disks and Apertures. I. Oblate Spheroidal Vector Wave Functions*

CARSON FLAMMER
Stanford Research Institute, Stanford, California
(Received January 30, 1953)

Rigorous solutions are presented of the problems of diffraction of plane electromagnetic waves by an infinitely thin, perfectly conducting, circular disk and by a circular aperture in a plane conducting screen. The analysis utilizes oblate spheroidal vector wave functions. In Part I these vector functions are defined and the expansions of plane-polarized waves in terms of them are obtained. Part II contains the solutions of the diffraction problems.

A. INTRODUCTION

THE vector wave functions considered here are the solenoidal solutions of the vector Helmholtz, or wave, equation. In the sequel we shall discuss vector wave functions which are derived from oblate spheroidal scalar wave functions. In Part II some of these vector functions will be used to obtain a rigorous solution of the diffraction of electromagnetic waves by circular disks and apertures. It is hoped that the same ones along with some of the other vector wave functions considered herein will also prove useful in other problems involving oblate spheroids.

The determination of vector wave functions from scalar wave functions was considered first by Hansen[1] for the cylindrical and spherical systems. The systematization and extension of Hansen's work by Stratton[2] culminated in the well-known vector wave-function formulation of the diffraction of electromagnetic waves by a spherical body. A much more general investigation has been made by Morse and Feshbach.[3] These authors have considered the problem of separability of the vector Helmholtz equation. In this connection the term separability implies, in addition to the usual reducibility of the original partial differential equation to a set of linear differential equations in the individual coordinates, that the solutions be of such a form as to permit the satisfying of the boundary conditions. At the present time, the spherical and cylindrical systems are the only coordinate systems for which a set of divergenceless solutions that satisfy the necessary separability conditions have been found.

It follows that no vector wave functions are known which enable one to solve the problem of the diffraction of electromagnetic waves by an arbitrary oblate spheroid in the same way as the diffraction by a sphere. Nevertheless, when the oblate spheroid is reduced to a perfectly conducting disk of vanishing thickness, the problem can be solved. This results from the fact that vector wave functions do exist which satisfy separability conditions on the faces of the disk. In Part II it will be shown that, because of the inherent singularities of these functions at the rim of the disk, a combination of two separate sets of vector functions must be used to satisfy the boundary conditions on the rim.

In the following section we shall define sixteen oblate spheroidal vector wave functions. Then in the succeeding section we shall derive the expansions of polarized plane waves in terms of these functions.

B. DEFINITIONS AND EXPRESSIONS OF THE FUNCTIONS

The solenoidal solutions of the vector Helmholtz equation,

$$(\nabla^2+k^2)\mathbf{A}=0, \tag{1}$$

satisfy the equation

$$\nabla\times\nabla\times\mathbf{A}-k^2\mathbf{A}=0. \tag{2}$$

The divergenceless nature of the solutions is ensured by writing them in the form

$$\mathbf{A}=\nabla\times\mathbf{a}\psi, \tag{3}$$

where ψ is a solution of the scalar Helmholtz equation

$$(\nabla^2+k^2)\psi=0. \tag{4}$$

The only known forms of the vector function $\mathbf{a}$ which generate solenoidal vectors $\mathbf{A}$, by means of Eq. (3), that satisfy Eq. (2) are a constant vector and the position vector $\mathbf{r}$.[2-4] In these cases Eq. (3) may be written in the form

$$\mathbf{A}=\nabla\psi\times\mathbf{a}, \quad \mathbf{a}=K_1\mathbf{e} \quad \text{or} \quad K_2\mathbf{r}, \tag{5}$$

where $\mathbf{e}$ denotes a constant unit vector. If $\mathbf{A}$ is a solution of Eq. (2), it is obvious that $\nabla\times\mathbf{A}$ is also a solution.

Spheroidal vector wave functions are obtained by expressing the quantities in Eq. (5) in terms of spheroidal coordinates. The oblate spheroidal coordinates η, ξ, ϕ shown in Fig. 1 are defined in terms of the

* This work was supported by the U. S. Air Force under Contract AF 19(604)-266.

[1] W. W. Hansen, Phys. Rev. 47, 139 (1935).

[2] J. A. Stratton, *Electromagnetic Theory* (McGraw-Hill Book Company, Inc., New York, 1941).

[3] P. M. Morse and H. Feshbach, *Methods of Theoretical Physics* (Technology Press, Massachusetts Institute of Technology, Cambridge, 1946).

[4] R. D. Spence and C. P. Wells, Commun. Pure Appl. Math. 4, 95 (1951).

rectangular coordinates by the relations

$$x=\frac{d}{2}[(1-\eta^2)(\xi^2+1)]^{\frac{1}{2}}\cos\phi,$$

$$y=\frac{d}{2}[(1-\eta^2)(\xi^2+1)]^{\frac{1}{2}}\sin\phi, \quad z=\frac{d}{2}\eta\xi, \quad (6)$$

where d is the diameter of the focal circle, $-1\leqslant\eta\leqslant 1$, $0\leqslant\xi\leqslant\infty$, and $0\leqslant\phi\leqslant 2\pi$. The metrical coefficients are given by

$$h_\eta=\frac{d}{2}\left(\frac{\xi^2+\eta^2}{1-\eta^2}\right)^{\frac{1}{2}}, \quad h_\xi=\frac{d}{2}\left(\frac{\xi^2+\eta^2}{\xi^2+1}\right)^{\frac{1}{2}},$$

$$h_\phi=\frac{d}{2}[(1-\eta^2)(\xi^2+1)]^{\frac{1}{2}}. \quad (7)$$

From the relations $\mathbf{e}_x\cdot\mathbf{e}_\eta=h_\eta^{-1}\partial x/\partial\eta$, etc., the transformation between the unit vectors in the two systems is found to be

$$\begin{aligned}\mathbf{e}_x&=-\eta\left(\frac{\xi^2+1}{\xi^2+\eta^2}\right)^{\frac{1}{2}}\cos\phi\mathbf{e}_\eta\\&\quad+\xi\left(\frac{1-\eta^2}{\xi^2+\eta^2}\right)^{\frac{1}{2}}\cos\phi\mathbf{e}_\xi-\sin\phi\mathbf{e}_\phi,\\ \mathbf{e}_y&=-\eta\left(\frac{\xi^2+1}{\xi^2+\eta^2}\right)^{\frac{1}{2}}\sin\phi\mathbf{e}_\eta\\&\quad+\xi\left(\frac{1-\eta^2}{\xi^2+\eta^2}\right)^{\frac{1}{2}}\sin\phi\mathbf{e}_\xi+\cos\phi\mathbf{e}_\phi,\\ \mathbf{e}_z&=\xi\left(\frac{1-\eta^2}{\xi^2+\eta^2}\right)^{\frac{1}{2}}\mathbf{e}_\eta+\eta\left(\frac{\xi^2+1}{\xi^2+\eta^2}\right)^{\frac{1}{2}}\mathbf{e}_\xi.\end{aligned} \quad (8)$$

The position vector $\mathbf{r}$ is given in the oblate spheroidal coordinate system by

$$\mathbf{r}=-\frac{d}{2}\eta\left(\frac{1-\eta^2}{\xi^2+\eta^2}\right)^{\frac{1}{2}}\mathbf{e}_\eta+\frac{d}{2}\xi\left(\frac{\xi^2+1}{\xi^2+\eta^2}\right)^{\frac{1}{2}}\mathbf{e}_\xi. \quad (9)$$

The eigenfunctions of the scalar Helmholtz equation, Eq. (4), in oblate spheroidal coordinates are expressible in the form

$$\begin{aligned}&\psi e,o_{mn}{}^{(i)}(\eta,\xi,\phi)\\&\quad=S_{mn}{}^{(1)}(-ic,\eta)R_{mn}{}^{(i)}(-ic,i\xi)_{\sin}^{\cos}m\phi,\end{aligned} \quad (10)$$

in which $c=\frac{1}{2}kd$. The functions $S_{mn}{}^{(1)}$ and $R_{mn}{}^{(i)}$ are respectively the angular oblate spheroidal functions of the first kind, and the radial functions of the ith kind, $i=1, 2, 3$, or 4, as defined by Stratton *et al.*,[5] except for the designation. The subscript l used by Stratton *et al.* is equal to $n-m$ as used here. The present designation is more consistent with that used by the majority of other writers.[6]

The angular functions are defined[5] by the series expansion

$$S_{mn}{}^{(1)}(-ic,\eta)=\sum_{r=0,1}{}'^{\infty} f_r{}^{mn}P_{m+r}{}^m(\eta), \quad (11)$$

where the prime over the summation sign denotes that the summation is to be taken over even or odd values depending upon whether $n-m$ is even or odd. Some values of $f_r{}^{mn}$ have been tabulated.[5] The angular functions are orthogonal over the interval $(-1, 1)$, namely,

$$\int_{-1}^{1}S_{ml}{}^{(1)}(-ic,\eta)S_{mn}{}^{(1)}(-ic,\eta)d\eta=\delta_{ln}N_{mn}, \quad (12)$$

with

$$N_{mn}=2\sum_{r=0,1}{}'^{\infty}\frac{(r+2m)!(f_r{}^{mn})^2}{r!(2r+2m+1)}. \quad (13)$$

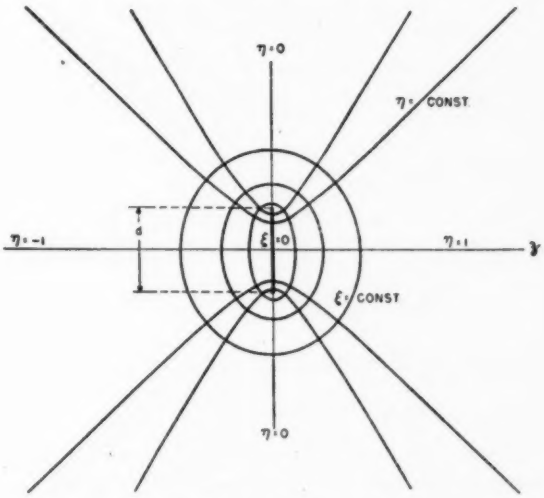

FIG. 1. The oblate spheroidal coordinate system.

The radial functions are defined[5] by the expansions

$$\begin{aligned}R_{mn}{}^{(i)}(-ic,i\xi)&=\frac{(\xi^2+1)^{m/2}}{\xi^m\sum_{r=0,1}{}'^{\infty}\dfrac{(r+2m)!}{r!}f_r{}^{mn}}\\&\quad\times\sum_{r=0,1}{}'^{\infty}(-1)^{r+m-n}\frac{(r+2m)!}{r!}f_r{}^{mn}z_{m+r}{}^{(i)}(c\xi),\end{aligned} \quad (14)$$

in which $z_n{}^{(i)}$ is the nth order spherical Bessel, Neumann, and Hankel functions of the first and of the second kind in the case $i=1$, 2, 3, and 4, respectively. When $c\xi$ is small, however, the series (14) for $R_{mn}{}^{(2)}$, and therefore also the series for $R_{mn}{}^{(3),(4)}$, converge slowly if at all. The following series in terms of associated Legendre func-

[5] Stratton, Morse, Chu, and Hutner, *Elliptic Cylinder and Spheroidal Wave Functions* (John Wiley and Sons, Inc., New York, 1941).

[6] See C. Flammer, Prolate Spheroidal Wave Functions, Tech. Report 16, S.R.I. Project 188, Air Force Contract No. AF 19(122)78.

tions of the second kind must be used in these cases:

$$R_{mn}^{(2)}(-ic, i\xi) = \frac{2(-ic)^{m-1}\left(\frac{n+m-1}{2}\right)!}{\left(\frac{n-m}{2}\right)!(m-\frac{3}{2})!f_{-2m}{}^{mn}\sum_{r=0}^{\infty}{}'\frac{(r+2m)!}{r!}f_r{}^{mn}} \times\sum_{-\infty}^{\infty}{}' f_r{}^{mn}Q_{m+r}{}^{m}(i\xi),\ (n-m)\text{ even}; \quad (15)$$

$$R_{mn}^{(2)}(-ic, i\xi) = \frac{-8(-ic)^{m-2}\left(\frac{n+m}{2}\right)!}{\left(\frac{n-m-1}{2}\right)!\left(m-\frac{5}{2}\right)!f_{1-2m}{}^{mn}\sum_{r=1}^{\infty}{}'\frac{(r+2m)!}{r!}f_r{}^{mn}} \times\sum_{-\infty}^{\infty}{}' f_r{}^{mn}Q_{m+r}{}^{m}(i\xi),\ (n-m)\text{ odd}. \quad (16)$$

The terms in Eqs. (15) and (16) with $r<-m$ are evaluated by the following limiting process in which $k>2m$:

$$\lim_{\rho\to 0} f_{-(k+\rho)}{}^{mn}Q_{m-(k+\rho)}{}^{m}(z) = \lim_{\rho\to 0}\frac{f_{-(k+\rho)}{}^{mn}P_{k-m-1}{}^{m}(z)}{\rho}$$

and

$$\lim_{\rho\to 0}\frac{f_{-(k+\rho)}{}^{mn}}{\rho} = \text{finite number}. \quad (17)$$

$R_{mn}^{(3),(4)}$ are obtained from the relations

$$R_{mn}^{(3),(4)} = R_{mn}^{(1)} \pm iR_{mn}^{(2)}. \quad (18)$$

In consonance with Eq. (5), we now define the following oblate spheroidal vector wave functions that are appropriate to diffraction problems in which the plane of incidence is the y, z plane:

$$\mathbf{M}e,\ o_{mn}{}^{u(i)}(\eta, \xi, \varphi) = \nabla\psi e,\ o_{mn}{}^{(i)}(\eta, \xi, \varphi-\tfrac{1}{2}\pi)\times\mathbf{e}_u,\quad u=x, y, z. \quad (19)$$

$$\mathbf{N}e,\ o_{mn}{}^{u(i)}(\eta, \xi, \varphi) = k^{-1}\nabla\times\mathbf{M}e,\ o^{u(i)}(\eta, \xi, \varphi), \quad (20)$$

$$\mathbf{m}e_{m\pm1,\,n}{}^{\pm(i)}(\eta, \xi, \varphi) = \tfrac{1}{2}[\mathbf{M}e_{mn}{}^{y(i)}(\eta, \xi, \varphi) \pm\mathbf{M}o_{mn}{}^{x(i)}(\eta, \xi, \varphi)], \quad (21)$$

$$\cdot\mathbf{m}o_{m\pm1,\,n}{}^{\pm(i)}(\eta, \xi, \varphi) = \tfrac{1}{2}[\mathbf{M}o_{mn}{}^{y(i)}(\eta, \xi, \varphi) \mp\mathbf{M}e_{mn}{}^{x(\lambda)}(\eta, \xi, \varphi)], \quad (22)$$

$$\mathbf{n}e,\ o_{m\pm1,\,n}{}^{\pm(i)}(\eta, \xi, \varphi) = k^{-1}\nabla\times\mathbf{m}e,\ o_{m\pm1,\,n}{}^{\pm(i)}(\eta, \xi, \varphi). \quad (23)$$

$$\mathbf{M}e,\ o_{mn}{}^{r(i)}(\eta, \xi, \varphi) = \nabla\psi e,\ o_{mn}{}^{(i)}(\eta, \xi, \varphi-\tfrac{1}{2}\pi)\times\mathbf{r}, \quad (24)$$

$$\mathbf{N}e,\ o_{mn}{}^{r(i)}(\eta, \xi, \varphi) = k^{-1}\nabla\times\mathbf{M}e,\ o_{mn}{}^{r(i)}(\eta, \xi, \varphi). \quad (25)$$

The explicit expressions of the vector wave functions utilized in Part II are given in Appendix B. For future reference it is to be noted that

$$\mathbf{M}e_{0n}{}^{y(i)}(\eta, \xi, \varphi) = 2\mathbf{m}e_{1n}{}^{+(i)}(\eta, \xi, \varphi),$$
$$\mathbf{N}e_{0n}{}^{y(i)}(\eta, \xi, \varphi) = 2\mathbf{n}e_{1n}{}^{+(i)}(\eta, \xi, \varphi). \quad (26)$$

It is of interest to observe that the solutions obtained by Page[7] upon separating the vector Helmholtz equation in prolate spheroidal coordinates are the analogs of our $\mathbf{M}e,\ o_{mn}{}^{z(i)}$ and $\mathbf{M}e,\ o_{mn}{}^{r(i)}$ functions for $m>0$, and of our $\mathbf{m}o_{0n}{}^{-(i)}$ and $\mathbf{n}_{0n}{}^{-(i)}$ functions when $m=0$.

None of the sets of spheroidal vector wave functions are orthogonal over the surface of a spheroid. We can obtain the expansions of plane waves in terms of them, however, by a circuitous method as shown in the following section.

C. EXPANSIONS OF PLANE POLARIZED WAVES

In this section we shall obtain expansions of plane polarized waves, which are propagating in the y, z plane, in terms of the appropriate vector wave functions. From the way in which the expansions are obtained, the derivations of the expansions for waves propagating in other planes will be obvious.

We take as our starting point the free space Green's function expansion

$$\frac{\exp(ik|\mathbf{r}-\mathbf{r}'|)}{4\pi|\mathbf{r}-\mathbf{r}'|} = \frac{ik}{2\pi}\sum_{m=0}^{\infty}\sum_{n=m}^{\infty}\frac{(2-\delta_{0m})}{N_{mn}} \times S_{mn}{}^{(1)}(-ic, \eta)S_{mn}{}^{(1)}(-ic, \eta') \cdot R_{mn}{}^{(1)}(-ic, i\xi)R_{mn}{}^{(3)}(-ic, i\xi') \times\cos m(\phi-\phi'),\quad \xi'>\xi. \quad (27)$$

Letting the source point go to infinity, $\xi'\to\infty$, in a direction such that the resulting plane wave propagates in the y, z plane with the positive direction of the propagation vector making an angle ζ with the positive z axis, we obtain the plane wave expansion,

$$e^{ik(y\sin\zeta+z\cos\zeta)} = \sum_{m,\,n}\gamma_{mn}(\zeta)\psi e_{mn}{}^{(1)}(\eta, \xi, \phi-\tfrac{1}{2}\pi), \quad (28)$$

with

$$\gamma_{mn}(\zeta) = 2(2-\delta_{0m})i^nN_{mn}{}^{-1}S_{mn}{}^{(1)}(-ic, \cos\zeta). \quad (29)$$

Several of the desired expansions can be obtained by applying vector operators to both sides of Eq. (28). The vector product of the gradient of both sides of Eq. (28) with $\mathbf{e}_x$, with $\mathbf{e}_y$, and with $\mathbf{e}_z$ leads respectively to the expansions

$$(\cos\zeta\mathbf{e}_y-\sin\zeta\mathbf{e}_z)e^{ik(y\sin\zeta+z\cos\zeta)} = (ik)^{-1}\sum_{m,\,n}\gamma_{mn}(\zeta)\mathbf{M}e_{mn}{}^{x(1)}(\eta, \xi, \phi), \quad (30)$$

[7] L. Page, Phys. Rev. **65**, 98 (1944).

$$\mathbf{e}_x e^{ik(y\sin\zeta+z\cos\zeta)} = -(ik\cos\zeta)^{-1}\sum_{m,n}\gamma_{mn}(\zeta)\mathbf{M}e_{mn}^{y(1)}(\eta,\xi,\phi), \quad (31)$$

$$\mathbf{e}_x e^{ik(y\sin\zeta+z\cos\zeta)} = (ik\sin\zeta)^{-1}\sum_{m,n}\gamma_{mn}(\zeta)\mathbf{M}e_{mn}^{z(1)}(\eta,\xi,\phi). \quad (32)$$

Application of the curl operator to both sides of Eqs. (30), (31), and (32) yields the further expansions

$$\mathbf{e}_x e^{ik(y\sin\zeta+z\cos\zeta)} = k^{-1}\sum_{m,n}\gamma_{mn}(\zeta)\mathbf{N}e_{mn}^{x(1)}(\eta,\xi,\phi), \quad (33)$$

$$(\cos\zeta\mathbf{e}_y-\sin\zeta\mathbf{e}_z)e^{ik(y\sin\zeta+z\cos\zeta)} = (k\cos\zeta)^{-1}\sum_{m,n}\gamma_{mn}(\zeta)\mathbf{N}e_{mn}^{y(1)}(\eta,\xi,\phi), \quad (34)$$

$$(\cos\zeta\mathbf{e}_y-\sin\zeta\mathbf{e}_z)e^{ik(y\sin\zeta+z\cos\zeta)} = -(k\sin\zeta)^{-1}\sum_{m,n}\gamma_{mn}(\zeta)\mathbf{N}e_{mn}^{z(1)}(\eta,\xi,\phi). \quad (35)$$

The limiting forms of Eqs. (30)–(34) as ζ becomes zero are obtained in a straightforward manner. The double summations reduce to single summations with $m=0$, since it follows from Eqs. (11) and (29) that

$$\gamma_{mn}(o)=0, \quad m\neq 0,$$
$$\gamma_{0n}(o)=-ia_{0n}=2iN_{0n}^{-1}\sum_{r=0,1}^{\infty}{}' f_r^{0n}. \quad (36)$$

Thus, for example,

$$\mathbf{e}_x\exp(ikz)=k^{-1}\sum_n a_{0n}\mathbf{M}e_{0n}^{y(1)}(\eta,\xi,\phi), \quad (37)$$

where a_{0n} is defined in Eq. (36).

To obtain the limiting form of Eq. (32) for $\zeta=0$, we note that when $\zeta=0$ the sum over n vanishes when $m=0$. This is seen by first putting $\zeta=0$ in Eq. (28), using Eq. (36), and then taking the vector product of the gradient of both sides with $\mathbf{e}_z$. Since, as is easily found from Eq. (11),

$$\lim_{\zeta\to 0}S_{1n}^{(1)}(-ic,\cos\zeta)/\sin\zeta=\sum_r{}' f_r^{1n}P_{r+1}'(1),$$
$$\lim_{\zeta\to 0}S_{mn}(-ic,\cos\zeta)/\sin\zeta=0, \quad m>1, \quad (38)$$

we obtain

$$\mathbf{e}_x\exp(ikz)=k^{-1}\sum_n b_{1n}\mathbf{M}e_{1n}^{z(1)}(\eta,\xi,\phi), \quad (39)$$

with

$$b_{1n}=2i^{n-1}N_{1n}^{-1}\sum_r{}' f_r^{1n}(r+2)!/r! \quad (40)$$

In Appendix A is given an independent derivation of Eq. (40), which utilizes the orthogonately properties of the angular functions upon equating components of Eq. (39). Equation (33) can be derived in a similar manner. The limiting form of Eq. (35) for $\zeta=0$ is obtained by taking the curl of Eq. (39).

The limiting form of Eq. (31) for $\zeta=\frac{1}{2}\pi$ is obtained in a manner similar to that used above in the derivation of Eqs. (39) and (40). By setting $\zeta=\frac{1}{2}\pi$ initially in Eqs. (28) and (29), one finds that the double summation over even values of $(n-m)$ in Eq. (31) vanishes in the limit $\zeta=\frac{1}{2}\pi$. Thus in this case the summation in Eq. (31) is over only odd values of $(n-m)$, and the limiting form of the coefficients is obtained with the aid of the relation

$$\lim_{\zeta\to\frac{1}{2}\pi}S_{mn}^{(1)}(-ic,\cos\zeta)/\sin\zeta = S_{mn}^{(1)}(-ic,o)=P_n^m(o), \quad (n-m)\text{ odd}. \quad (41)$$

APPENDIX A

The coefficients in the expansion

$$\mathbf{e}_x\exp(ikz)=k^{-1}\sum_n b_{1n}\mathbf{M}e_{1n}^{x(1)}(\eta,\xi,\phi) \quad (A\text{-}1)$$

may be obtained as follows. Utilizing Eqs. (6) and (8), and Table I, we obtain, by equating either the η or ξ components of Eq. (A-1), the relation

$$\sum_n b_{1n}R_{1n}^{(1)}(-ic,i\xi)S_{1n}^{(1)}(-ic,\eta) = c(\xi^2+1)^{\frac{1}{2}}(1-\eta^2)^{\frac{1}{2}}\exp(ic\eta\xi). \quad (A\text{-}2)$$

Multiplying both sides of Eq. (A-2) by $S_{1n}^{(1)}(-ic,\eta)$ and integrating over the range of the variable η, we get

$$R_{1n}^{(1)}(-ic,i\xi)N_{1n}b_{1n} = c(\xi^2+1)^{\frac{1}{2}}\int_{-1}^{1}\exp(ic\xi\eta)(1-\eta^2)^{\frac{1}{2}}S_{1n}^{(1)}(-ic,\eta)d\eta$$
$$= c(\xi^2+1)^{\frac{1}{2}}\sum_{r=0,1}^{\infty}{}' f_r^{1n}\times\int_{-1}^{1}\exp(ic\xi\eta)(1-\eta^2)^{\frac{1}{2}}P_{r+1}'(\eta)d\eta. \quad (A\text{-}3)$$

Substituting the relation

$$P_n'(\eta)=-P_n^{-1}(\eta)(n+1)!/(n-1)! = -\frac{(n+1)!}{(n-1)!}\frac{(1-\eta^2)^{-\frac{1}{2}}}{2^n n!}\frac{d^{n-1}(\eta^2-1)^n}{d\eta^{n-1}} \quad (A\text{-}4)$$

in Eq. (A-3) and then integrating by parts r times, we obtain

$$R_{1n}^{(1)}(-ic,i\xi)N_{1n}b_{1n} = -c(\xi^2+1)^{\frac{1}{2}}\sum_{r=0,1}^{\infty}{}'\frac{i^{r+2}f_r^{1n}(r+2)!(c\xi)^r}{2^{r+1}(r+1)!r!}\times\int_{-1}^{1}\exp(ic\xi\eta)(1-\eta^2)^{r+1}d\eta. \quad (A\text{-}5)$$

Since

$$\int_{-1}^{1}\exp(ic\xi\eta)(1-\eta^2)^{-k}d\eta=2^{k+1}k!\,j_k(c\xi)/(c\xi)^k, \quad \text{(A-6)}$$

Eq. (A-5) yields

$$R_{1n}^{(1)}(-ic,i\xi)N_{1n}b_{1n}$$
$$=2i^{n-1}(\xi^2+1)^{\frac{1}{2}}\xi^{-1}\times\sum_{r=0,1}^{\infty}{}'\,i^{r+1-n}\cdot f_r^{1n}j_{r+1}(c\xi)(r+2)!/r!$$
$$=2i^{n-1}R_{1n}^{(1)}(-ic,i\xi)\sum_{r=0,1}^{\infty}f_r^{1n}(r+2)!/r!, \quad \text{(A-7)}$$

whence

$$b_{1n}=2i^{n-1}N_{1n}^{-1}\sum_{r=0,1}^{\infty}{}'\,f_r^{1n}(r+2)!/r!. \quad \text{(A-8)}$$

This value of b_{1n} has been obtained by equating the η or ξ components of Eq. (A-1); either component yields the same relation, Eq. (A-2). But it is easily seen by subtracting the derivative of Eq. (A-2) with respect to ξ from the derivative of it with respect to η that the equality of the ϕ components of Eq. (A-1) is also guaranteed by Eq. (A-2). This actually follows from the solenoidal nature of both sides of Eq. (A-1).

APPENDIX B

TABLE I. $\mathbf{M}e,\,o_{mn}^{z(i)}(\eta,\xi,\varphi)=\nabla\psi e,\,o_{mn}^{(i)}(\eta,\xi,\varphi-\frac{1}{2}\pi)\times e_z$.

$$Me,\,o_{mn\eta}^{z(i)}=\pm\frac{2m\eta}{d(\xi^2+\eta^2)^{\frac{1}{2}}(1-\eta^2)^{\frac{1}{2}}}S_{mn}^{(1)}R_{mn}^{(i)}\begin{matrix}\sin\\\cos\end{matrix}m(\varphi-\tfrac{1}{2}\pi)$$

$$Me,\,o_{mn\xi}^{z(i)}=\mp\frac{2m}{d(\xi^2+\eta^2)^{\frac{1}{2}}(\xi^2+1)^{\frac{1}{2}}}S_{mn}^{(1)}R_{mn}^{(i)}\begin{matrix}\sin\\\cos\end{matrix}m(\varphi-\tfrac{1}{2}\pi)$$

$$Me,\,o_{mn\varphi}^{z(i)}=\frac{2(\xi^2+1)^{\frac{1}{2}}(1-\eta^2)^{\frac{1}{2}}}{d(\xi^2+\eta^2)}\times\left\{\eta\frac{dS_{mn}^{(1)}}{d\eta}R_{mn}^{(i)}-\xi S_{mn}^{(1)}\frac{dR_{mn}^{(i)}}{d\xi}\right\}\begin{matrix}\cos\\\sin\end{matrix}m(\varphi-\tfrac{1}{2}\pi)$$

TABLE II. $\mathbf{m}e,\,o_{m+1,n}^{+(i)}(\eta,\xi,\phi)=\frac{1}{2}\{\mathbf{M}e,\,o_{mn}^{y(i)}(\eta,\xi,\phi)\pm\mathbf{M}o,\,e_{mn}^{z(i)}(\eta,\xi,\phi)\}$.

$$me,\,o_{m+1,n\eta}^{+(i)}=\frac{1}{d(\xi^2+\eta^2)^{\frac{1}{2}}}\left\{\mp(\xi^2+1)^{\frac{1}{2}}S_{mn}^{(1)}\frac{dR_{mn}^{(i)}}{d\xi}\pm\frac{m\xi}{(\xi^2+1)^{\frac{1}{2}}}S_{mn}^{(1)}R_{mn}^{(i)}\right\}\begin{matrix}\sin\\\cos\end{matrix}(m+1)(\phi-\tfrac{1}{2}\pi)$$

$$me,\,o_{m+1,n\xi}^{+(i)}=\frac{1}{d(\xi^2+\eta^2)^{\frac{1}{2}}}\left\{\pm(1-\eta^2)^{\frac{1}{2}}\frac{dS_{mn}^{(1)}}{d\eta}R_{mn}^{(i)}\pm\frac{m\eta}{(1-\eta^2)^{\frac{1}{2}}}S_{mn}^{(1)}R_{mn}^{(i)}\right\}\begin{matrix}\sin\\\cos\end{matrix}(m+1)(\phi-\tfrac{1}{2}\pi)$$

TABLE II—*Continued*.

$$me,\,o_{m+1,n\phi}^{+(i)}=\frac{1}{d(\xi^2+\eta^2)}\left\{\xi(1-\eta^2)\frac{dS_{mn}^{(1)}}{d\eta}R_{mn}^{(i)}+\eta(\xi^2+1)S_{mn}^{(1)}\frac{dR_{mn}^{(i)}}{d\xi}\right\}\begin{matrix}\cos\\\sin\end{matrix}(m+1)(\phi-\tfrac{1}{2}\pi)$$

TABLE III. $\mathbf{m}e,\,o_{m-1,n}^{-(i)}(\eta,\xi,\phi)=\frac{1}{2}\{\mathbf{M}e,\,o_{mn}^{y(i)}(\eta,\xi,\phi)\mp\mathbf{M}o,\,e_{mn}^{z(i)}(\eta,\xi,\phi)\}$.

$$me,\,o_{m-1,n\eta}^{-(i)}=\frac{1}{d(\xi^2+\eta^2)^{\frac{1}{2}}}\left\{\pm(\xi^2+1)^{\frac{1}{2}}S_{mn}^{(1)}\frac{dR_{mn}^{(i)}}{d\xi}\pm\frac{m\xi}{(\xi^2+1)^{\frac{1}{2}}}S_{mn}^{(1)}R_{mn}^{(i)}\right\}\begin{matrix}\sin\\\cos\end{matrix}(m-1)(\phi-\tfrac{1}{2}\pi)$$

$$me,\,o_{m-1,n\xi}^{-(i)}=\frac{1}{d(\xi^2+\eta^2)^{\frac{1}{2}}}\left\{\mp(1-\eta^2)^{\frac{1}{2}}\frac{dS_{mn}^{(1)}}{d\eta}R_{mn}^{(i)}\pm\frac{m\eta}{(1-\eta^2)^{\frac{1}{2}}}S_{mn}^{(1)}R_{mn}^{(i)}\right\}\begin{matrix}\sin\\\cos\end{matrix}(m-1)(\phi-\tfrac{1}{2}\pi)$$

$$me,\,o_{m-1,n\phi}^{-(i)}=\frac{1}{d(\xi^2+\eta^2)}\left\{\xi(1-\eta^2)\frac{dS_{mn}^{(1)}}{d\eta}R_{mn}^{(i)}+\eta(\xi^2+1)S_{mn}^{(1)}\frac{dR_{mn}^{(i)}}{d\xi}\right\}\begin{matrix}\cos\\\sin\end{matrix}(m-1)(\phi-\tfrac{1}{2}\pi)$$

TABLE IV. $\mathbf{N}e,\,o_{mn}^{z(i)}(\eta,\xi,\phi)=k^{-1}\nabla\times\mathbf{M}e,\,o_{mn}^{z(i)}(\eta,\xi,\phi)$.

$$Ne,\,o_{mn\eta}^{z(i)}=\frac{4(1-\eta^2)^{\frac{1}{2}}}{kd^2(\xi^2+\eta^2)^{\frac{1}{2}}}\left\{\eta\frac{dS_{mn}^{(1)}}{d\eta}\frac{\partial}{\partial\xi}\left[\frac{(\xi^2+1)R_{mn}^{(i)}}{\xi^2+\eta^2}\right]-S_{mn}^{(1)}\frac{\partial}{\partial\xi}\left[\frac{\xi(\xi^2+1)}{\xi^2+\eta^2}\frac{dR_{mn}^{(i)}}{d\xi}\right]+\frac{m^2\xi S_{mn}^{(1)}R_{mn}^{(i)}}{(1-\eta^2)(\xi^2+1)}\right\}\begin{matrix}\cos\\\sin\end{matrix}m(\phi-\tfrac{1}{2}\pi)$$

$$Ne,\,o_{mn\xi}^{z(i)}=\frac{4(\xi^2+1)^{\frac{1}{2}}}{kd^2(\xi^2+\eta^2)^{\frac{1}{2}}}\left\{\xi\frac{\partial}{\partial\eta}\left[\frac{(1-\eta^2)S_{mn}^{(1)}}{\xi^2+\eta^2}\right]\frac{dR_{mn}^{(i)}}{d\xi}-\frac{\partial}{\partial\eta}\left[\frac{\eta(1-\eta^2)dS_{mn}^{(1)}}{(\xi^2+\eta^2)d\eta}\right]R_{mn}^{(i)}+\frac{m^2\eta S_{mn}^{(1)}R_{mn}^{(i)}}{(1-\eta^2)(\xi^2+1)}\right\}\begin{matrix}\cos\\\sin\end{matrix}m(\phi-\tfrac{1}{2}\pi)$$

$$Ne,\,o_{mn\phi}^{z(i)}=\mp\frac{4m(1-\eta^2)^{\frac{1}{2}}(\xi^2+1)^{\frac{1}{2}}}{kd^2(\xi^2+\eta^2)}\left\{\frac{\xi dS_{mn}^{(1)}R_{mn}^{(i)}}{(\xi^2+1)d\eta}+\frac{\eta S_{mn}^{(1)}}{(1-\eta^2)}\frac{dR_{mn}^{(i)}}{d\xi}\right\}\begin{matrix}\sin\\\cos\end{matrix}m(\phi-\tfrac{1}{2}\pi)$$

TABLE V. $\mathbf{ne}_{o_{m+1,n}}^{+(i)}(\eta,\xi,\phi)=k^{-1}\nabla\times\mathbf{me}_{o_{m+1,n}}^{+(i)}(\eta,\xi,\phi)$.

$$ne_{o_{m+1,n\eta}}^{+(i)}=\frac{2}{kd^2(\xi^2+\eta^2)^{\frac{1}{2}}}\left\{\eta S_{mn}^{(1)}\frac{\partial}{\partial\xi}\left[\frac{(\xi^2+1)^{\frac{1}{2}}}{\xi^2+\eta^2}\frac{dR_{mn}^{(i)}}{d\xi}\right]\right.$$
$$+(1-\eta^2)\frac{dS_{mn}^{(1)}}{d\eta}\frac{\partial}{\partial\xi}\left[\frac{\xi(\xi^2+1)^{\frac{1}{2}}R_{mn}^{(i)}}{\xi^2+\eta^2}\right]$$
$$-\frac{(m+1)}{(\xi^2+1)^{\frac{1}{2}}}\frac{dS_{mn}^{(1)}}{d\eta}R_{mn}^{(i)}$$
$$\left.-\frac{m(m+1)\eta S_{mn}^{(1)}R_{mn}^{(i)}}{(1-\eta^2)(\xi^2+1)^{\frac{1}{2}}}\right\}\begin{matrix}\cos\\ \sin\end{matrix}(m+1)(\phi-\tfrac{1}{2}\pi)$$

$$ne_{o_{m+1,n\xi}}^{+(i)}=-\frac{2}{kd^2(\xi^2+\eta^2)^{\frac{1}{2}}}\left\{\xi\frac{\partial}{\partial\eta}\left[\frac{(1-\eta^2)^{\frac{1}{2}}}{\xi^2+\eta^2}\frac{dS_{mn}^{(1)}}{d\eta}\right]R_{mn}^{(i)}\right.$$
$$+(\xi^2+1)\frac{\partial}{\partial\eta}\left[\frac{\eta(1-\eta^2)^{\frac{1}{2}}S_{mn}^{(1)}}{\xi^2+\eta^2}\right]\frac{dR_{mn}^{(i)}}{d\xi}$$
$$+\frac{(m+1)}{(1-\eta^2)^{\frac{1}{2}}}S_{mn}^{(1)}\frac{dR_{mn}^{(i)}}{d\xi}$$
$$\left.-\frac{m(m+1)\xi S_{mn}^{(1)}R_{mn}^{(i)}}{(1-\eta^2)^{\frac{1}{2}}(\xi^2+1)}\right\}\begin{matrix}\cos\\ \sin\end{matrix}(m+1)(\phi-\tfrac{1}{2}\pi)$$

$$ne_{o_{m+1,n\phi}}^{+(i)}=\pm\frac{2(1-\eta^2)^{\frac{1}{2}}(\xi^2+1)^{\frac{1}{2}}}{kd^2(\xi^2+\eta^2)}\left\{\frac{d}{d\eta}\left[(1-\eta^2)^{\frac{1}{2}}\frac{dS_{mn}^{(1)}}{d\eta}\right]\frac{R_{mn}^{(i)}}{(\xi^2+1)^{\frac{1}{2}}}\right.$$
$$+\frac{S_{mn}^{(1)}}{(1-\eta^2)^{\frac{1}{2}}}\frac{d}{d\xi}\left[(\xi^2+1)^{\frac{1}{2}}\frac{dR_{mn}^{(i)}}{d\xi}\right]$$
$$+m\frac{d}{d\eta}\left[\frac{\eta S_{mn}^{(1)}}{(1-\eta^2)^{\frac{1}{2}}}\right]\frac{R_{mn}^{(i)}}{(\xi^2+1)^{\frac{1}{2}}}$$
$$\left.-\frac{mS_{mn}^{(1)}}{(1-\eta^2)^{\frac{1}{2}}}\frac{d}{d\xi}\left[\frac{\xi R_{mn}^{(i)}}{(\xi^2+1)^{\frac{1}{2}}}\right]\right\}\begin{matrix}\sin\\ \cos\end{matrix}(m+1)(\phi-\tfrac{1}{2}\pi)$$

TABLE VI. $\mathbf{ne}_{o_{m-1,n}}^{-(i)}(\eta,\xi,\phi)=k^{-1}\nabla\times\mathbf{me}_{o_{m-1,n}}^{-(i)}(\eta,\xi,\phi)$.

$$ne_{o_{m-1,n\eta}}^{-(i)}=\frac{2}{kd^2(\xi^2+\eta^2)^{\frac{1}{2}}}\left\{\eta S_{mn}^{(1)}\frac{\partial}{\partial\xi}\left[\frac{(\xi^2+1)^{\frac{1}{2}}}{\xi^2+\eta^2}\frac{dR_{mn}^{(i)}}{d\xi}\right]\right.$$
$$+(1-\eta^2)\frac{dS_{mn}^{(1)}}{d\eta}\frac{\partial}{\partial\xi}\left[\frac{\xi(\xi^2+1)^{\frac{1}{2}}R_{mn}^{(i)}}{\xi^2+\eta^2}\right]$$
$$+\frac{(m-1)}{(\xi^2+1)^{\frac{1}{2}}}\frac{dS_{mn}^{(1)}}{d\eta}R_{mn}^{(i)}$$
$$\left.-\frac{m(m-1)\eta S_{mn}^{(1)}R_{mn}^{(i)}}{(1-\eta^2)(\xi^2+1)^{\frac{1}{2}}}\right\}\begin{matrix}\cos\\ \sin\end{matrix}(m-1)(\phi-\tfrac{1}{2}\pi)$$

$$ne_{o_{m-1,n\xi}}^{-(i)}=-\frac{2}{kd^2(\xi^2+\eta^2)^{\frac{1}{2}}}\left\{\xi\frac{\partial}{\partial\eta}\left[\frac{(1-\eta^2)^{\frac{1}{2}}}{\xi^2+\eta^2}\frac{dS_{mn}^{(1)}}{d\eta}\right]R_{mn}^{(i)}\right.$$
$$+(\xi^2+1)\frac{\partial}{\partial\eta}\left[\frac{\eta(1-\eta^2)^{\frac{1}{2}}S_{mn}^{(1)}}{\xi^2+\eta^2}\right]\frac{dR_{mn}^{(i)}}{d\xi}$$
$$-\frac{(m-1)}{(1-\eta^2)^{\frac{1}{2}}}S_{mn}^{(1)}\frac{dR_{mn}^{(i)}}{d\xi}$$
$$\left.-\frac{m(m-1)\xi S_{mn}^{(1)}R_{mn}^{(i)}}{(1-\eta^2)^{\frac{1}{2}}(\xi^2+1)}\right\}\begin{matrix}\cos\\ \sin\end{matrix}(m-1)(\phi-\tfrac{1}{2}\pi)$$

$$ne_{o_{m-1,n\phi}}^{-(i)}=\mp\frac{2(1-\eta^2)^{\frac{1}{2}}(\xi^2+1)^{\frac{1}{2}}}{kd^2(\xi^2+\eta^2)}\left\{\frac{d}{d\eta}\left[(1-\eta^2)^{\frac{1}{2}}\frac{dS_{mn}^{(1)}}{d\eta}\right]R_{mn}^{(i)}\right.$$
$$+\frac{S_{mn}^{(1)}}{(1-\eta^2)^{\frac{1}{2}}}\frac{d}{d\xi}\left[(\xi^2+1)^{\frac{1}{2}}\frac{dR_{mn}^{(i)}}{d\xi}\right]$$
$$-m\frac{d}{d\eta}\left[\frac{\eta S_{mn}^{(1)}}{(1-\eta^2)^{\frac{1}{2}}}\right]R_{mn}^{(i)}$$
$$\left.+\frac{mS_{mn}^{(1)}}{(1-\eta^2)^{\frac{1}{2}}}\frac{d}{d\xi}\left[\frac{\xi R_{mn}^{(i)}}{(\xi^2+1)^{\frac{1}{2}}}\right]\right\}\begin{matrix}\sin\\ \cos\end{matrix}(m-1)(\phi-\tfrac{1}{2}\pi)$$

The Vector Wave Function Solution of the Diffraction of Electromagnetic Waves by Circular Disks and Apertures.* II. The Diffraction Problems

CARSON FLAMMER
Stanford Research Institute, Stanford, California
(Received January 30, 1953)

Rigorous solutions are presented of the problems of diffraction of plane electromagnetic waves by an infinitely thin, perfectly conducting, circular disk and by a circular aperture in a plane conducting screen. A unique solution is obtained in each case when two separate groups of the appropriate oblate spheroidal vector wave functions discussed in Part I are combined to fulfill the condition that the φ component of the electric field vanish on the rims of the disk and aperture.

A. INTRODUCTION

THE classical boundary value problems of the diffraction of electromagnetic waves by a circular aperture in a plane conducting screen and by the complementary circular disk have, until lately, defied accurate solutions. It is true that the Kirchoff diffraction theory, so widely used in optics,[1] leads to adequate results when $ka \to \infty$, where k is the wave number $2\pi/\lambda$ and a is the radius of the disk or aperture. It is also true that at the other extreme, $ka \to 0$, the quasi-static method of Lord Rayleigh[2] yields satisfactory solutions.[3] However, the assumptions made in each method are such as to preclude its yielding even qualitatively correct results, except in the limiting cases stated.

Of late, these problems have received considerable attention. By virtue of the electromagnetic form of Babinet's principle,[4,5] the solution of the one diffraction problem entails the solution of the other. Thus Bouwkamp[6] has given power series solutions in powers of k (with $a=1$) for the field components in both problems for the case of normal incidence. Bouwkamp[7] has also shown that the work of Bethe[8] and of Copson[4] is in error. Variational expressions for the transmission cross section of an arbitrary aperture in a plane conducting screen have been given by Levine and Schwinger,[9] and applied by them to the case of a circular aperture with normal incidence. Variational aspects of the problem have also been considered by Miles.[10] Two procedures for obtaining a rigorous solution have been proposed. The one by Meixner[5] has been criticized, however, by Bouwkamp.[11] The other, by Meixner and Andrejewski,[12] seems to lead to a valid solution.

Many of the authors referred to in the preceding paragraph utilize potential functions in their analyses of the diffraction by a circular disk. Thus Bouwkamp employs the vector potential, Meixner uses a pair of Dedeye potential functions, while Meixner and Andrejewski use two rectangular components of a Hertzian vector. It is significant that all of these authors have to make explicit use of the so-called edge condition in order to obtain a unique solution of the diffraction problem. The edge condition is the condition which qualifies the form of the scattered electromagnetic field in the neighborhood of sharp edges of a diffracting body, to wit: the field strengths of the scattered wave may become infinite at the sharp edges of a diffracting body only to such a degree as leads to an integrable energy density. That is, the scattered electromagnetic field energy must be finite in any arbitrarily small volume of space, since there are no real sources in the physical problem. This is tantamount to the requirement that the field components may become infinite at most as $s^{-\frac{1}{2}}$, where s is the distance from the field point to the edge. More explicit information on the general behavior of the total field near the rim of a disk has been ascertained by Bouwkamp.[4] By examining the singularities along the rim in Sommerfeld's famous diffraction problem of the half-plane for the two independent cases of polarization, Bouwkamp has shown that the order relations for the tangential field components near the rim of a disk are

$$E_t = 0(s^{\frac{1}{2}}), \quad H_t = 0(1), \quad (s \to 0), \tag{1}$$

while all other components become infinite as $s^{-\frac{1}{2}}$. These relations will be verified in the sequel.

In this paper a rigorous solution for each of the problems of diffraction by perfectly conducting circular disk and by a circular aperture in a perfectly conducting plane screen is obtained with the use of the oblate spheroidal vector wave functions discussed in Part I. The present formulation deals directly with the electromagnetic field strengths and is, therefore, much more straightforward than those employing potential functions. A unique solution is obtained from the requirement that the ϕ component of the electric field vanish on the rim of the conducting circular disk and on the rim of the circular aperture. The validity of this re-

* This work was supported by the U. S. Air Force under Contract AF 19(604)-266.

[1] See M. Born, *Optik* (Verlag Julius Springer, Berlin, 1933).
[2] Lord Rayleigh, Phil. Mag. **44**, 28 (1897).
[3] C. T. Tai, Trans. Inst. Radio Engrs. PGAP **1**, 13 (1951).
[4] E. T. Copson, Proc. Roy. Soc. (London) **A186**, 100 (1946).
[5] J. Meixner, Z. Naturforsch. **3a**, 506 (1948).
[6] C. J. Bouwkamp, Philips Research Rep. **5**, 401 (1950).
[7] C. J. Bouwkamp, Philips Research Rep. **5**, 321 (1950).
[8] H. A. Bethe, Phys. Rev. **66**, 163 (1944).
[9] H. Levine and J. Schwinger, Commun. Pure Appl. Math. **3**, 355 (1950).
[10] J. W. Miles, J. Appl. Phys. **20**, 760 (1949).
[11] C. J. Bouwkamp, Physica **16**, 1 (1950).
[12] J. Meixner and W. Andrejewski, Ann. Physik **7**, 157 (1950).

quirement which seems to be obvious from continuity considerations, is demonstrated in the Appendix.

Previous attempts to solve the problem of diffraction by a circular disk by means of vector wave functions appear to have failed because of the obtainment of edge singularities of too high an order and the lack of uniqueness.[13] In the present work, the method consists, in essence, of formulating the problem in terms of two separate groups of appropriate vector wave functions. Each group can be used by itself to satisfy the condition of vanishing tangential electric field on the face of the disk. But the separate use of either one leads to a non-vanishing tangential component of the electric field and associate violations of the edge condition at the rim of the disk. The two groups of vector wave functions are therefore combined in such a way that the boundary conditions are satisfied on the rim. This leads to a unique solution which, in the case of normal incidence, reduces exactly to Bouwkamp's series solution when the power series expansions of the relevant spheroidal functions are used.

In the sequel, the case of normal incidence is considered first in detail. Then the formal extension to arbitrary incidence is given. Numerical computations have been deferred for the present.

B. NORMAL INCIDENCE

1. Diffraction by a Circular Disk

We assume an infinitesimally thin, perfectly conducting disk of diameter d, which lies in the plane $z=0$. The center of the disk is the point $\mathbf{r}=0$. In terms of the oblate spheroidal coordinates η, ξ, ϕ shown on Fig. 1 of Part I, the disk is completely specified by the coordinate $\xi=0$.

A plane-polarized electromagnetic wave, which is traveling in the positive z direction, is assumed to impinge upon the disk. Without any loss in generality, we may consider the incident field to be that described by the equations

$$\mathbf{E}^i=\mathbf{e}_x E_0 e^{ikz}, \quad \mathbf{H}^i=\mathbf{e}_y H_0 e^{ikz}, \quad H_0=(\epsilon/\mu)^{\frac{1}{2}}E_0. \tag{2}$$

The harmonic time dependence $e^{-i\omega t}$ is omitted throughout. By means of the Eqs. (I-37) and (I-39) the incident field of Eq. (2) can be expanded as follows:

$$\mathbf{e}_x E_0 e^{ikz}=E_0 k^{-1}\Big[\alpha\sum_{n=0}^{\infty} a_{0n}\mathbf{M}e_{0n}{}^{y(1)}(\eta,\xi,\phi) + \beta\sum_{n=1}^{\infty} b_{1n}\mathbf{M}e_{1n}{}^{z(1)}(\eta,\xi,\phi)\Big], \tag{3}$$

$$\mathbf{e}_y H_0 e^{ikz}=-iH_0 k^{-1}\Big[\alpha\sum_{n=0}^{\infty} a_{0n}\mathbf{N}e_{0n}{}^{y(1)}(\eta,\xi,\phi) + \beta\sum_{n=1}^{\infty} b_{1n}\mathbf{N}e_{1n}{}^{z(1)}(\eta,\xi,\phi)\Big], \tag{4}$$

where α and β are arbitrary constants subject to the condition

$$\alpha+\beta=1. \tag{5}$$

The coefficients a_{0n} and b_{1n} are given by the Eqs. (I-36) and (I-40).

The scattered[14] electric field corresponding to the incident field of Eq. (3) may be assumed to be

$$\mathbf{E}^s(\eta,\xi,\phi)=E_0 k^{-1}\Big[\alpha\sum_{n=1}^{\infty}{}' A_{0n}\mathbf{M}e_{0n}{}^{y(3)}(\eta,\xi,\phi) + \beta\sum_{n=1}^{\infty}{}' B_{1n}\mathbf{M}e_{1n}{}^{z(3)}(\eta,\xi,\phi)\Big] \tag{6}$$

with

$$A_{0n}=-a_{0n}R_{0n}{}^{(1)\prime}(-ic,io)/R_{0n}{}^{(3)\prime}(-ic,io), \tag{7}$$

$$B_{1n}=-b_{1n}R_{1n}{}^{(1)}(-ic,io)/R_{1n}{}^{(3)}(-ic,io). \tag{8}$$

Here and in the sequel a prime over a spheroidal function denotes differentiation with respect to the coordinate on which the function depends. The primes over the summation signs in Eq. (6) denote summations over only odd values of n. From the asymptotic behavior of the $R_{mn}{}^{(3)}(-ic,i\xi)$ functions, namely,

$$R_{mn}{}^{(3)}(-ic,i\xi)\xrightarrow[c\xi\to\infty]{}\frac{1}{c\xi}\exp\left[i\left(c\xi-\frac{n+1}{2}\pi\right)\right], \tag{9}$$

it is seen that the expression, Eq. (6) satisfies the radiation condition. Furthermore, from Tables I and II and Eq. (26) of Part I, it is easily seen that the tangential components of the total electric field vanish on the faces of the disk, as required by the boundary condition

$$\mathbf{e}_z\times\mathbf{E}(\eta,0,\phi)=0, \quad \mathbf{E}=\mathbf{E}^i+\mathbf{E}^s. \tag{10}$$

But it is also seen that $\mathbf{E}_\phi$ does not vanish on the rim of the disk for arbitrary α and β. The satisfaction of the requirement that E_ϕ vanish on the rim determines α and β and leads to a unique solution of the problem. Thus we require that

$$\lim_{\xi\to 0,\eta\to 0}\Bigg\{\alpha\frac{\xi(1-\eta^2)}{\xi^2+\eta^2}\sum_{n=1}^{\infty}{}' a_{0n}S_{0n}{}^{(1)\prime}(-ic,\eta) \times\left[R_{0n}{}^{(1)}(-ic,i\xi)-\frac{R_{0n}{}^{(1)\prime}(-ic,io)}{R_{0n}{}^{(3)\prime}(-ic,io)}R_{0n}{}^{(3)}(-ic,i\xi)\right] -\beta\frac{\xi(\xi^2+1)^{\frac{1}{2}}(1-\eta^2)^{\frac{1}{2}}}{\xi^2+\eta^2}\sum_{n=1}^{\infty}{}' b_{1n}S_{1n}{}^{(1)}(-ic,\eta) \times\left[R_{1n}{}^{(1)\prime}(-ic,i\xi)-\frac{R_{1n}{}^{(1)}(-ic,io)}{R_{1n}{}^{(3)}(-ic,io)}\times R_{1n}{}^{(3)}(-ic,i\xi)\right]\Bigg\}=0. \tag{11}$$

[13] R. D. Spence and C. P. Wells, Commun. Pure Appl. Math. 4, 95 (1951).

[14] As used here, the term "scattered field" includes both the waves actually reflected or scattered by the disk and the corrective field which compensates the unperturbed incident field in the shadow. But the spheroidal functions employed herein are practical only when $kd/2<10$, in which range the corrective field is negligible. For an illuminating discussion of these concepts see L. Brillouin, J. Appl. Phys. 20, 1110 (1949).

With the aid of the Wronskian relation

$$R_{mn}^{(1)}(-ic, i\xi)R_{mn}^{(3)\prime}(-ic, i\xi) - R_{mn}^{(3)}(-ic, i\xi)R_{mn}^{(1)\prime}(-ic, i\xi)=i/c(\xi^2+1), \quad (12)$$

and power series expansions of the spheroidal functions,[15] we find that Eq. (11) is satisfied when

$$\alpha\sum_{n=1}^{\infty}{}' a_{0n}\left[\frac{R_{0n}^{(1)\prime}(-ic, o)}{R_{0n}^{(3)\prime}(-ic, io)}\right] +\beta\sum_{n=1}^{\infty}{}' b_{1n}\left[\frac{S_{1n}^{(1)}(-ic, o)}{R_{1n}^{(3)}(-ic, io)}\right]=0. \quad (13)$$

From Eqs. (5) and (13) we obtain

$$\alpha=\frac{\sum_{n=1}^{\infty}{}' b_{1n}\left[\frac{S_{1n}^{(1)}(-ic, o)}{R_{1n}^{(3)}(-ic, io)}\right]}{\sum_{n=1}^{\infty}{}' b_{1n}\left[\frac{S_{1n}^{(1)}(-ic, o)}{R_{1n}^{(3)}(-ic, io)}\right]-\sum_{n=1}^{\infty}{}' a_{0n}\left[\frac{S_{0n}^{(1)\prime}(-ic, o)}{R_{0n}^{(3)\prime}(-ic, io)}\right]}, \quad (14)$$

$$\beta=1-\alpha.$$

With these values of α and β, the scattered electric field is given exactly by Eq. (6). The expression for the scattered magnetic field follows from the Maxwell equation $\nabla\times\mathbf{E}=i\omega\mu\mathbf{H}$, and is

$$\mathbf{H}^s(\eta, \xi, \phi)=-iH_0k^{-1}\{\alpha\sum_{n=1}^{\infty}{}' A_{0n}\mathbf{N}e_{0n}^{y(3)}(\eta, \xi, \phi) +\beta\sum_{n=1}^{\infty} B_{1n}\mathbf{N}e_{1n}^{z(3)}(\eta, \xi, \phi)\}. \quad (15)$$

The total field is given by the sums of Eqs. (3) and (6) and Eqs. (4) and (15).

It is readily verified that the total field satisfies the edge condition and the order relations given in Eq. (1) and the first line thereafter. In the plane of, but outside, the disk, for example, where the distance from the rim of the disk is given by

$$s=d\xi^2/4, \quad \eta=0, \quad \xi\to 0 \quad (16)$$

we find that, in cylindrical coordinates (ρ, ϕ, z),

$$E_\rho=0(s^{-\frac{1}{2}})\cos\phi, \quad E_\phi=0(s^{\frac{1}{2}})\sin\phi, \quad E_z=0,$$
$$H_\rho=0(1)\sin\phi, \quad H_\phi=0(1)\cos\phi, \quad H_z=0(s^{-\frac{1}{2}})\sin\phi. \quad (17)$$

On the disk itself, where

$$s=d\eta^2/4, \quad \xi=0, \quad \eta\to 0 \quad (18)$$

we find

$$E_\rho=0, \quad E_\phi=0, \quad E_z=0(s^{-\frac{1}{2}})\cos\phi,$$
$$H_\rho=0(s^{-\frac{1}{2}})\sin\phi, \quad H_\phi=0(1)\cos\phi, \quad H_z=0. \quad (19)$$

[15] A. Leitner and R. D. Spence, J. Franklin Inst. **249**, 299 (1950).

It is worthy of note that, for arbitrary α and β, the z-component of the magnetic field as given by Eq. (15) does not satisfy the edge condition. But the same values of α and β which insure the vanishing of E_ϕ on the rim of the disk, also insure the satisfaction of the edge condition by H_z. This relationship is a consequence of the interdependence of the electric and magnetic field components as given by Maxwell's equations, and also of the nature of the vector wave functions employed. We shall discuss this further in Section C.

The far-zone scattered field is obtained in spherical coordinates (r, θ, ϕ) with the use of the asymptotic forms Eq. (9) and

$$\eta\to\cos\theta, \quad \mathbf{e}_\eta\to-\mathbf{e}_\theta, \quad c\xi\to kr, \quad (\xi\to\infty). \quad (20)$$

Thus

$$\mathbf{E}^s(r, \theta, \phi) \simeq iE_0k^{-1}\{\mathbf{e}_\theta\alpha\sum_{n=1}^{\infty}{}' i^{n-1}A_{0n}S_{0n}^{(1)}(-ic, \cos\theta)\cos\phi -\mathbf{e}_\phi[\alpha\sum_{n=1}^{\infty}{}' i^{n-1}A_{0n}S_{0n}^{(1)}(-ic, \cos\theta)\cos\theta -\beta\sum_{n=1}^{\infty}{}' i^{n-1}B_{1n}S_{1n}^{(1)}(-ic, \cos\theta) \times\sin\theta]\sin\phi\}e^{ikr}/r, \quad (21)$$

$$\mathbf{H}^s(r, \theta, \phi) \simeq iH_0k^{-1}\{\mathbf{e}_\theta[\alpha\sum_{n=1}^{\infty}{}' i^{n-1}A_{0n}S_{0n}^{(1)}(-ic, \cos\theta)\cos\theta -\beta\sum_{n=1}^{\infty}{}' i^{n-1}B_{1n}S_{1n}^{(1)}(-ic, \cos\theta)\sin\theta]\sin\phi +\mathbf{e}_\phi\alpha\sum_{n=1}^{\infty}{}' i^{n-1}A_{0n}S_{0n}^{(1)}(-ic, \cos\theta)\cos\phi\}e^{ikr}/r. \quad (22)$$

In those cases for which the present formulation is suited, the total scattering cross section is given to a good approximation by[16]

$$\sigma_s=\lim_{r\to\infty}\frac{\int_0^{2\pi}\int_0^{\pi}[\mathbf{E}^s(r, \theta, \phi)\times\mathbf{H}^{s*}(r, \theta, \phi)r^2\sin\theta d\theta d\phi]}{E_0H_0}. \quad (23)$$

In order to carry out the integration over θ in Eq. (23), it is necessary to use the series expansions of the angular functions in Eqs. (21) and (22) and integrate the resulting quadruple sum term by term. This will be relegated to another paper, along with numerical computations. In the next section, however, we shall give the series expansion of σ_s in powers of c.

2. Power Series Solution

In order to show that the present solution reduces exactly to Bouwkamp's solution for the case of small

[16] See footnote 14 and the reference cited there.

disks, we shall obtain the expressions for the far-zone scattered field components in powers of c. To do this we need the expansions in powers of c of the coefficients f_r^{mn} [see Eqs. (I-11) to (I-16)]. These are easily obtained from the recursion relation for the f_r^{mn} once the power series expansions of the eigenvalues have been obtained. The required coefficients have been given by Meixner (when h is γ is replaced by $-ic$) in decimal form, so that we shall not include a table of the fractional forms which we have calculated and used here.

In the calculation of the power series expansions of α, β, A_{0n}, and B_{1n}, the following expressions, which are valid for odd n, are needed:

$$S_{1n}^{(1)}(-ic, o)=S_{0n}^{(1)\prime}(-ic, o)=\frac{i^{n-1}(n+1)!}{2^n[(n-1)/2]![(n+1)/2]!}, \quad (24)$$

$$R_{1n}^{(1)}(-ic, io)=\frac{i^{n-1}2cf_0^{1n}}{3\sum_{r=0}^{\infty}{}' f_r^{1n}(r+2)!/r!}, \quad (25)$$

$$R_{0n}^{(1)\prime}(-ic, io)=\frac{i^{n-1}cf_1^{0n}}{3\sum_{r=1}^{\infty}{}' f_r^{0n}}, \quad (26)$$

$$R_{1n}^{(2)}(-ic, io)=\frac{i^{n-1}\pi}{2f_{-2}^{1n}\sum_{r=0}^{\infty}{}' f_r^{1n}(r+2)!/r!\times\left[\sum_{r=0}^{\infty}{}'\frac{i^r(r+2)!f_r^{1n}}{2^{r+1}(r/2)![(r+2)/2]!}\right]^2}, \quad (27)$$

$$R_{0n}^{(2)\prime}(-ic, io)=\frac{i^{n-1}3\pi}{2c^2f_1^{0n}\sum_{r=1}^{\infty}{}' f_r^{0n}\times\left[\sum_{r=1}^{\infty}{}'\frac{i^{r-1}(r+1)!f_r^{0n}}{2^r[(r-1)/2]![(r+1)/2]!}\right]^2}. \quad (28)$$

The calculations are straightforward though tedious. The results are:

$$\alpha=2+\frac{2}{3}c^2+\frac{2}{15}c^4+\cdots+i\frac{4}{3\pi}c^3\left(1+\frac{34}{45}c^2+\cdots\right), \quad (29)$$

$$\beta=-\left\{1+\frac{2}{3}c^2+\frac{2}{15}c^4+\cdots+i\frac{4}{3\pi}c^3\left(1+\frac{34}{45}c^2+\cdots\right)\right\}, \quad (30)$$

$$f_1^{01}A_{01}=-i\frac{2}{3\pi}c^3\left(1+\frac{4}{25}c^2+\frac{3}{245}c^4+\cdots\right)+\frac{4}{27\pi^2}c^6\left(1+\frac{7}{25}c^2+\cdots\right), \quad (31)$$

$$f_3^{03}A_{03}=i\frac{128\times10^{-4}}{63\pi}c^7+\cdots. \quad (32)$$

$$f_1^{11}B_{11}=i\frac{4}{3\pi}c^3\left(1-\frac{7}{25}c^2+\frac{6}{49}c^4+\cdots\right)-\frac{16}{27\pi^2}c^6\left(1-\frac{16}{25}c^2+\cdots\right), \quad (33)$$

$$f_3^{13}B_{13}=i\frac{512\times10^{-4}}{189\pi}c^7+\cdots. \quad (34)$$

With the use of Eqs. (29) through (34), the power series expansions of the far-zone field components are found from Eqs. (21) and (22) to be

$$E_\theta=(\mu/\epsilon)^{\frac{1}{2}}H_\phi\simeq\frac{4c^3E_0}{3\pi k}\left\{1+\frac{13}{30}\left(1+\frac{3}{13}\cos^2\theta\right)c^2+\frac{29}{280}\left(1+\frac{38}{87}\cos^2\theta+\frac{1}{29}\cos^4\theta\right)c^4+\frac{i8c^3}{9\pi}\left[1+\frac{39}{50}\left(1+\frac{5}{39}\cos^2\theta\right)c^2\right]+O(c^6)\right\}\cos\theta\cos\phi\frac{e^{ikr}}{r}, \quad (35)$$

$$E_\phi=-(\mu/\epsilon)^{\frac{1}{2}}H_\theta\simeq-\frac{4c^3E_0}{3\pi k}\left\{1+\frac{11}{30}\left(1+\frac{5}{11}\cos^2\theta\right)c^2+\frac{17}{280}\left(1+\frac{70}{51}\cos^2\theta+\frac{7}{51}\cos^4\theta\right)c^4+\frac{i8c^3}{9\pi}\left[1+\frac{17}{25}\left(1+\frac{5}{17}\cos^2\theta\right)c^2\right]+O(c^6)\right\}\sin\phi\frac{e^{ikr}}{r}. \quad (36)$$

If $\cos^2\theta$ is replaced by $1-\sin^2\theta$ in Eqs. (35) and (36), the resulting expressions are identical with those obtained by Bouwkamp[6] for a disk of unit radius and an incident electric field of unit amplitude. The leading terms of Eqs. (35) and (36) are contained in Lord Rayleigh's paper[2] on the scattering by small ellipsoids.

Substitution of Eqs. (35) and (36) in Eq. (23) leads to the power series expansion of the total scattering

cross section. The scattering coefficient (scattering cross section/area of disk) τ is thus found to be

$$\tau=\frac{128c^4}{27\pi^2}\left\{1+\frac{22}{25}c^2+\frac{7312}{18375}c^4+0(c^6)\right\}, \tag{37}$$

which again is in agreement with Bouwkamp's result.

The power series expansions of the scattered field components on and near a small disk have been given by Bouwkamp and need not be repeated here. For a larger disk the exact forms of Eqs. (6) and (15) must be used.

3. Diffraction by a Circular Aperture in a Plane Conducting Screen

The solution of the problem of diffraction by a circular aperture in a plane conducting screen can be obtained immediately from that of the complementary disk problem by the application of the electromagnetic form of Babinet's principle, as formulated by Copson[4] and by Meixner.[5] The electromagnetic form of Babinet's principle states that if $\mathbf{E}_1^s$, $\mathbf{H}_1^s$ is the diffracted field when a wave $\mathbf{E}_1^i$, $\mathbf{H}_1^i$ is incident in the positive z direction on a finite, perfectly conducting, plane screen lying in the plane $z=0$, then

$$\begin{aligned}&\mathbf{E}_2^s=-(\mu/\epsilon)^{\frac{1}{2}}\mathbf{H}_1^s, \quad \mathbf{H}_2^s=(\epsilon/\mu)^{\frac{1}{2}}\mathbf{E}_1^s, \qquad z\gtrless 0\\ &\mathbf{E}_2^s=(\mu/\epsilon)^{\frac{1}{2}}\mathbf{H}_1^s, \qquad \mathbf{H}_2^s=-(\epsilon/\mu)^{\frac{1}{2}}\mathbf{E}_1^s, \quad z\lessgtr 0\end{aligned} \tag{38}$$

are the diffracted fields when the wave

$$\mathbf{E}_2^i=(\mu/\epsilon)^{\frac{1}{2}}\mathbf{H}_1^i, \quad \mathbf{H}_2^i=-(\epsilon/\mu)^{\frac{1}{2}}\mathbf{E}_2^i, \tag{39}$$

is incident in the positive z direction on the complementary, perfectly conducting, plane screen. In the latter case, the total field in the half-space $z\lessgtr 0$ is formed from a superposition of the incident wave, the reflected wave in the absence of an aperture, and the diffracted wave; in the half-space $z\gtrless 0$, it is equal to the diffracted wave.

We shall identify the fields $\mathbf{E}_1^s$, $\mathbf{H}_1^s$ and $\mathbf{E}_1^i$, $\mathbf{H}_1^i$ in Eqs. (38) and (39) with those of Eqs. (6), (14) and (3). Then $\mathbf{E}_2^s$, $\mathbf{H}_2^s$ in Eq. (38) is the diffracted field when the incident wave $\mathbf{E}_2^i$, $\mathbf{H}_2^i$ of Eq. (39) impinges normally upon a perfectly conducting, plane screen with a circular aperture of diameter d centered about the origin. Let us now rotate the coordinate system about the z axis through a positive angle of 90 degrees. We thus find that when the incident wave is

$$\mathbf{E}^i=\mathbf{e}_x E_0 e^{ikz}, \quad \mathbf{H}^i=\mathbf{e}_y H_0 e^{ikz},$$

the diffracted field $\mathbf{E}^{(+)}$, $\mathbf{H}^{(+)}$ in the half-space $z\gtrless 0$ behind the aperture is

$$\mathbf{E}^{(+)}(\eta,\xi,\phi)=iE_0k^{-1}\{\alpha\sum_{n=1}^{\infty}{}'A_{0n}\mathbf{N}e_{0n}{}^{y(3)}(\eta,\xi,\phi+\tfrac{1}{2}\pi)+\beta\sum_{n=1}^{\infty}{}'B_{1n}\mathbf{N}e_{1n}{}^{z(3)}(\eta,\xi,\phi+\tfrac{1}{2}\pi)\}, \tag{40}$$

$$\mathbf{H}^{+}(\eta,\xi,\phi)=H_0k^{-1}\{\alpha\sum_{n=1}^{\infty}{}'A_{0n}\mathbf{M}e_{0n}{}^{y(3)}(\eta,\xi,\phi+\tfrac{1}{2}\pi)+\beta\sum_{n=1}^{\infty}{}'B_{1n}\mathbf{M}e_{1n}{}^{z(3)}(\eta,\xi,\phi+\tfrac{1}{2}\pi)\}, \tag{41}$$

with α, β, A_{0n}, and B_{1n} given by Eqs. (14), (7), and (8).

It should be remarked that the formulation of the problem as expressed by Eqs. (40), (41) and the corresponding ones for the half-space $z\lessgtr 0$, can also be obtained directly without recourse to the electromagnetic form of Babinet's principle. By starting with the expansion of Eq. (I-33) and the relation $\mathbf{N}e_{0n}{}^{x(i)}(\eta,\xi,\phi)=-\mathbf{N}e_{0n}{}^{y(i)}(\eta,\xi,\phi+\frac{1}{2}\pi)$ along with the expansion of Eq. (I-35) with ϕ replaced by $\phi+\frac{1}{2}\pi$, one is lead to the formulation of Eqs. (40) and (41) upon satisfying the conditions of vanishing electric field on the screen and continuity of the fields across the aperture. The values of α and β given by Eq. (14) insure the vanishing of the ϕ component of the electric field on the rim of the circular aperture.

An alternative formulation can also be written down directly with $\mathbf{E}^s$ and $\mathbf{H}^s$ expressed, respectively, in terms of the same type of vector wave functions as in the disk problem, but with different coefficients A_n, B_n, and with the summations extended over only even values of n. The latter formulation also follows from the application of the electromagnetic form of Babinet's principle to the case of the following section when $\mathbf{E}^i$ is in the plane of incidence.

The far-zone field components in the half-space $z\gtrless 0$ are found from Eqs. (40) and (41) to be

$$\begin{aligned}&E_\theta^{(+)}(r,\theta,\phi)\\ &=(\mu/\epsilon)^{\frac{1}{2}}H_\phi(r,\theta,\phi)\simeq -ikE_0\\ &\quad\times\{\alpha\sum_{n=1}^{\infty}{}'i^{n-1}A_{0n}S_{0n}{}^{(1)}(-ic,\cos\theta)\cos\theta\\ &\quad-\beta\sum_{n=1}^{\infty}{}'i^{n-1}B_{1n}S_{1n}{}^{(1)}(-ic,\cos\theta)\sin\theta\}\cos\phi\frac{e^{ikr}}{r},\end{aligned} \tag{42}$$

$$\begin{aligned}&E_\phi^{(+)}(r,\theta,\phi)\\ &=-(\mu/\epsilon)^{\frac{1}{2}}H_\phi^{(+)}(r,\theta,\phi)\simeq iE_0k^{-1}\alpha\\ &\quad\times\sum_{n=1}^{\infty}{}'i^{n-1}A_{0n}S_{0n}{}^{(1)}(-ic,\cos\theta)\sin\phi\frac{e^{ikr}}{r}.\end{aligned} \tag{43}$$

The power series expansion of $E_\theta^{(+)}(r,\theta,\phi)$ is given by Eq. (36) with $\sin\phi$ replaced by $\cos\phi$, while that of $E_\theta^{(+)}(r,\theta,\phi)$ is given by Eq. (35) with $\cos\phi$ replaced by $\sin\phi$; these agree with those given by Bouwkamp. The

power series expansions of the field components in and near the aperture have also been given by Bouwkamp. Finally, the power series expansion of the transmission coefficient t of a circular aperture for a normally incident, plane-polarized wave is equal to $\frac{1}{2}\tau$, where τ is given by Eq. (37).

C. ARBITRARY INCIDENCE

In the case of arbitrary incidence, the formal solutions of the diffraction problems can be obtained in the same general manner as in the case of normal incidence. As before we shall derive the form of the scattered field in the disk problem. The solution for the circular aperture then follows immediately upon the application of the electromagnetic form of Babinet's principle.

There are two independent cases to be considered since the incident wave can be polarized with the electric vector either perpendicular to or parallel with the plane of incidence (the y, z plane). We shall distinguish the quantities pertaining to the two cases by appending a $\perp$ or $\parallel$ sign to them.

For the expansion of the incident electric field we have available the expansions (I-31) and (I-32) in the one case, and (I-34) and (I-35) in the other. But the ϕ dependence of the various components of $\mathbf{M}e_{mn}^{y(i)}$ and $\mathbf{N}e_{mn}^{y(i)}$ differs from that of the components of $\mathbf{M}e_{mn}^{z(i)}$ and $\mathbf{N}e_{mn}^{z(i)}$. We shall replace, therefore, the functions $\mathbf{M}e_{mn}^{y(i)}$ and $\mathbf{N}e_{mn}^{y(i)}$ by

$$\mathbf{M}e_{mn}^{y(i)}(\eta,\xi,\phi)=\mathbf{m}e_{m-1,n}^{-(i)}(\eta,\xi,\phi)+\mathbf{m}e_{m+1,n}^{+(i)}(\eta,\xi,\phi), \quad (44)$$

$$\mathbf{N}e_{mn}^{y(i)}(\eta,\xi,\phi)=\mathbf{n}e_{m-1,n}^{-(i)}(\eta,\xi,\phi)+\mathbf{n}e_{m+1,n}^{+(i)}(\eta,\xi,\phi). \quad (45)$$

From Tables II, III, V, and VI it is seen that in each case we now have available two separate expansions in terms of vector wave functions whose components have the same ϕ dependence. In each pair of expansions the coefficients of the same ϕ-dependent trigonometrical function must be equal, component by component. Therefore we may expand the incident field as follows:

$$\mathbf{E}_\perp{}^i=\mathbf{e}_x E_0 e^{ik(y\sin\zeta+z\cos\zeta)}$$
$$=E_0k^{-1}\sum_{m=0}^{\infty}\{\alpha_{m-1}{}^\perp\sum_{n=m}^{\infty}a_{mn}(\zeta)\mathbf{m}e_{m-1,n}^{-(1)}(\eta,\xi,\phi)+\alpha_{m+1}{}^\perp\sum_{n=m}^{\infty}a_{mn}(\zeta)\mathbf{m}e_{m+1,n}^{+(1)}(\eta,\xi,\phi)+\beta_m{}^\perp\sum_{n=m}^{\infty}b_{mn}(\zeta)\mathbf{M}e_{mn}^{z(1)}(\eta,\xi,\phi)\}, \quad (46)$$

$$\mathbf{H}_\perp{}^i=(\cos\zeta\mathbf{e}_y-\sin\zeta\mathbf{e}_z)H_0e^{ik(y\sin\zeta+z\cos\zeta)}, \quad (47)$$

and

$$\mathbf{E}_\parallel{}^i=(-\cos\zeta\mathbf{e}_y+\sin\zeta\mathbf{e}_z)E_0e^{ik(y\sin\zeta+z\cos\zeta)}$$
$$=iE_0k^{-1}\sum_{m=0}^{\infty}\{\alpha_{m-1}{}^\parallel\sum_{n=m}^{\infty}a_{mn}(\zeta)\mathbf{n}e_{m-1,n}^{-(1)}(\eta,\xi,\phi)+\alpha_{m+1}{}^\parallel\sum_{n=m}^{\infty}a_{mn}(\zeta)\mathbf{n}e_{m+1,n}^{+(1)}(\eta,\xi,\phi)+\beta_{m+1}{}^\parallel\sum_{n=m}^{\infty}b_{mn}(\zeta)\mathbf{N}e_{mn}^{z(1)}(\eta,\xi,\phi)\}, \quad (48)$$

$$\mathbf{H}_\parallel{}^i=\mathbf{e}_xH_0e^{ik(y\sin\zeta+z\cos\zeta)} \quad (49)$$

with

$$\alpha_{-1}=\alpha_1;\quad \alpha_m+\beta_m=1,\quad m\geqslant 0, \quad (50)$$

in both cases. The coefficients $a_{mn}(\zeta)$ and $b_{mn}(\zeta)$ are

$$a_{mn}(\zeta)=i\gamma_{mn}(\zeta)/\cos\zeta,\qquad b_{mn}(\zeta)=-i\gamma_{mn}(\zeta)/\sin\zeta, \quad (51)$$

where $\gamma_{mn}(\zeta)$ is given by Eq. (I-29).

Treating the two cases together, we let the scattered fields be as follows:

$$\mathbf{E}_\perp{}^s(\eta,\xi,\phi)$$
$$=E_0k^{-1}\sum_{m=0}^{\infty}\{\alpha_{m-1}{}^\perp\sum_{n=m+1}^{\infty}{}'A_{mn}{}^\perp(\zeta)\mathbf{m}e_{m-1,n}^{-(3)}(\eta,\xi,\phi)+\alpha_{m+1}{}^\perp\sum_{n=m+1}^{\infty}{}'A_{mn}{}^\perp(\zeta)\mathbf{m}e_{m+1,n}^{+(3)}(\eta,\xi,\phi)+\beta_m{}^\perp\sum_{n=m}^{\infty}{}'B_{mn}{}^\perp(\zeta)\mathbf{M}e_{mn}^{z(3)}(\eta,\xi,\phi)\}, \quad (52)$$

$$\mathbf{E}_\parallel{}^s(\eta,\xi,\phi)$$
$$=iE_0k^{-1}\sum_{m=0}^{\infty}\{\alpha_{m-1}{}^\parallel\sum_{n=m}^{\infty}{}'A_{mn}{}^\parallel(\zeta)\mathbf{n}e_{m-1,n}^{-(3)}(\eta,\xi,\phi)+\alpha_{m+1}{}^\parallel\sum_{n=m}^{\infty}{}'A_{mn}{}^\parallel(\zeta)\mathbf{n}e_{m+1,n}^{+(3)}(\eta,\xi,\phi)+\beta_m{}^\parallel\sum_{n=m+1}^{\infty}{}'B_{mn}{}^\parallel(\zeta)\mathbf{N}e_{mn}^{z(3)}(\eta,\xi,\phi)\}, \quad (53)$$

$$\mathbf{H}_{\perp,\parallel}{}^s(\eta,\xi,\phi)=-i(\epsilon_0/\mu_0)^{\frac{1}{2}}k^{-1}\nabla\times\mathbf{E}_{\perp,\parallel}{}^s(\eta,\xi,\phi), \quad (54)$$

with

$$A_{mn}{}^\perp(\zeta)=-\frac{R_{mn}^{(1)\prime}(-ic,io)}{R_{mn}^{(3)\prime}(-ic,io)}a_{mn}(\zeta),\qquad B_{mn}{}^\perp(\zeta)=-\frac{R_{mn}^{(1)}(-ic,io)}{R_{mn}^{(3)}(-ic,io)}b_{mn}(\zeta), \quad (55)$$

$$A_{mn}{}^\parallel(\zeta)=-\frac{R_{mn}^{(1)}(-ic,io)}{R_{mn}^{(3)}(-ic,io)}a_{mn}(\zeta),\qquad B_{mn}{}^\parallel(\zeta)=-\frac{R_{mn}^{(1)\prime}(-ic,io)}{R_{mn}^{(3)\prime}(-ic,io)}b_{mn}(\zeta). \quad (56)$$

With the scattered fields given by Eqs. (52) through (54), the total tangential electric field vanishes on the faces of the disk in both cases. But, for arbitrary α_m and β_m, the E_ϕ component does not vanish on the rim of the disk, with accompanying violations of the edge condition. As in the case of normal incidence, a unique and rigorous solution is obtained in each case when α_m and β_m are chosen such that E_ϕ vanishes on the rim of the disk.

The determination of α_m and β_m is carried out, in general, in the same way as the determination of α and β in Sec. B-1 for the case of normal incidence. Therefore, we shall not include the details. However, the determination of α_0'' and β_0'' requires a separate discussion because in this case E_ϕ has no ϕ-independent term. The simplest way to determine α_0'' and β_0'' is to consider the problem of the complementary aperture in a plane conducting screen. By interchanging the expressions for $\mathbf{E}$ and $\mathbf{H}$ and requiring the vanishing of E_ϕ on the rim of the circular aperture, we obtain the required relation between α_0'' and β_0''. The results are

$$\alpha_0^{\perp}=\frac{\sum_{n=0}^{\infty}{}' b_{0n}(\zeta)\dfrac{S_{0n}^{(1)}(-ic,o)}{R_{0n}^{(3)}(-ic,ic)}}{\sum_{n=0}^{\infty}{}' b_{0n}(\zeta)\dfrac{S_{0n}^{(1)}(-ic,o)}{R_{0n}^{(3)}(-ic,ic)}-\frac{1}{2}\sum_{n=2}^{\infty}{}' a_{1n}(\zeta)\dfrac{S_{1n}^{(1)\prime}(-ic,o)}{R_{1n}^{(3)\prime}(-ic,ic)}}, \tag{57}$$

$$\alpha_1^{\perp}=\frac{\sum_{n=1}^{\infty}{}' b_{1n}(\zeta)\dfrac{S_{1n}^{(1)}(-ic,o)}{R_{1n}^{(3)}(-ic,ic)}}{\sum_{n=1}^{\infty}{}' b_{1n}(\zeta)\dfrac{S_{1n}^{(1)}(-ic,o)}{R_{1n}^{(3)}(-ic,ic)}-\sum_{n=1}^{\infty}{}' a_{0n}(\zeta)\dfrac{S_{0n}^{(1)\prime}(-ic,o)}{R_{0n}^{(3)\prime}(-ic,ic)}-\frac{1}{2}\sum_{n=2}^{\infty}{}' a_{2n}(\zeta)\dfrac{S_{2n}^{(1)\prime}(-ic,o)}{R_{2n}^{(3)\prime}(-ic,ic)}}, \tag{58}$$

$$\alpha_m^{\perp}=\frac{\sum_{n=m}^{\infty}{}' b_{mn}(\zeta)\dfrac{S_{mn}^{(1)}(-ic,o)}{R_{mn}^{(3)}(-ic,ic)}}{\sum_{n=m}^{\infty}{}' b_{mn}(\zeta)\dfrac{S_{mn}^{(1)}(-ic,o)}{R_{mn}^{(3)}(-ic,ic)}-\frac{1}{2}\sum_{n=m}^{\infty}{}' a_{m-1,n}(\zeta)\dfrac{S_{m-1,n}^{(1)\prime}(-ic,o)}{R_{mn}^{(3)\prime}(-ic,ic)}-\frac{1}{2}\sum_{n=m+2}^{\infty}{}' a_{m+1,n}(\zeta)\dfrac{S_{m+1,n}^{(1)\prime}(-ic,o)}{R_{m+1,n}^{(3)\prime}(-ic,ic)}}, \tag{59}$$

$$m\geq 2,$$

$$\alpha_0''=\frac{\sum_{n=1}^{\infty}{}' b_{0n}(\zeta)\dfrac{S_{0n}^{(1)\prime}(-ic,o)}{R_{0n}^{(3)\prime}(-ic,ic)}}{\sum_{n=1}^{\infty}{}' b_{0n}(\zeta)\dfrac{S_{0n}^{(1)\prime}(-ic,o)}{R_{0n}^{(3)\prime}(-ic,ic)}+\frac{1}{2}\sum_{n=1}^{\infty}{}' a_{1n}(\zeta)\dfrac{S_{1n}^{(1)}(-ic,o)}{R_{1n}^{(3)}(-ic,ic)}}, \tag{60}$$

$$\alpha_1''=\frac{\sum_{n=2}^{\infty}{}' b_{1n}(\zeta)\dfrac{S_{1n}^{(1)\prime}(-ic,o)}{R_{1n}^{(3)\prime}(-ic,ic)}}{\sum_{n=2}^{\infty}{}' b_{1n}(\zeta)\dfrac{S_{1n}^{(1)\prime}(-ic,o)}{R_{1n}^{(3)\prime}(-ic,ic)}+\sum_{n=0}^{\infty}{}' a_{0n}(\zeta)\dfrac{S_{0n}^{(1)}(-ic,o)}{R_{0n}^{(3)}(-ic,ic)}+\frac{1}{2}\sum_{n=2}^{\infty}{}' a_{2n}(\zeta)\dfrac{S_{2n}^{(1)}(-ic,o)}{R_{2n}^{(3)}(-ic,ic)}}, \tag{61}$$

$$\alpha_m''=\frac{\sum_{n=m+1}^{\infty}{}' b_{mn}(\zeta)\dfrac{S_{mn}^{(1)\prime}(-ic,o)}{R_{mn}^{(3)\prime}(-ic,ic)}}{\sum_{n=m+1}^{\infty}{}' b_{mn}(\zeta)\dfrac{S_{mn}^{(1)\prime}(-ic,o)}{R_{mn}^{(3)\prime}(-ic,ic)}+\frac{1}{2}\sum_{n=m-1}^{\infty}{}' a_{m-1,n}(\zeta)\dfrac{S_{m-1,n}^{(1)}(-ic,o)}{R_{m-1,n}^{(3)}(-ic,ic)}+\frac{1}{2}\sum_{n=m+1}^{\infty}{}' a_{m+1,n}(\zeta)\dfrac{S_{m+1,n}^{(1)}(-ic,o)}{R_{m+1,n}^{(3)}(-ic,ic)}}, \tag{62}$$

$$m\geq 2,$$

$$\beta_m^{\perp,\parallel}=1-\alpha_m^{\perp,\parallel}. \tag{63}$$

With these values of α_m and β_m, the fields scattered by the disk are given uniquely and rigorously by Eqs. (52) through (54). In the case of normal incidence, the solution of the $\mathbf{E}_\perp{}^i$ case reduces to the one given in Sec. B-1, while the solution of the $\mathbf{E}_\parallel{}^i$ case provides an alternative formulation.

The solution of the diffraction by a circular aperture in a plane conducting screen of an arbitrarily incident wave follows immediately from Eqs. (38) and (39) and need not be written out explicitly.

In the foregoing we have appeared to require only the satisfaction, at the rim of the disk or aperture, of the boundary condition on the component of the electric field parallel to the rim. A unique solution which fulfills the requirements of the edge condition has then ensued. It should be pointed out, however, that this is a result of the nature of the vector wave functions employed. Not all vector wave functions are so proper. If, for example, the vector functions $\mathbf{M}_{mn}{}^{r}(\eta, \xi, \phi)$ and $\mathbf{N}_{mn}{}^{r}(\eta, \xi, \phi)$ are used in conjunction with one of the other sets of vector wave functions, it is possible to satisfy the condition on E_ϕ at the rim. But the other field components do not satisfy the edge condition, indicating an incorrect solution. Thus the satisfaction of the boundary condition on the component of the electric field parallel to the rim is not, in general, sufficient. This is seen above, in fact, where we consider the disk and aperture problems concurrently in order to determine α_{0ll} and β_{0ll}. These quantities can also be obtained without considering both problems together by invoking the edge condition explicitly.

D. CONCLUSION

We have given rigorous solutions of the problems of diffraction by a circular conducting disk and by a circular aperture in a plane conducting screen in terms of oblate spheroidal vector wave functions. This form of solution has been found useful in the application of the electromagnetic extension of the cellular method of solid state physics to an artificial dielectric composed of an array of conducting disks.[17] The same method, but with the employment of additional vector wave functions, has been used in an analysis of the radiation characteristics of electric and magnetic dipoles in the presence of a conducting disk. This will be presented in a future paper.

APPENDIX

In a recent paper on diffraction by an edge, Jones[18] has found that conditions on the induced current and charge densities plus an extra condition, which makes the components of the field parallel to the edge finite, (i.e., not infinite), are sufficient to ensure a unique solution. It is worthy of note that instead of our premise that E_ϕ vanishes on the rim of the conducting disk, we need to presuppose only Jones' condition that E_ϕ is finite on the rim. That E_ϕ actually vanishes on the rim can then be ascertained in the case of normal incidence, for example, as follows.

If E_ϕ is finite on the rim, the right-hand side of Eq. (11) is replaced by a constant and the equation becomes of the form

$$\lim_{\xi \to 0} \xi^{-1} f(c, \xi) = \text{constant}. \tag{A-1}$$

This requires that $f(c, \xi)$ vanish, as before, which is ensured by Eq. (13). But the coefficient of the linear term in the expansion of $f(c, \xi)$ in powers of ξ is found to vanish. Thus the constant of the right-hand side of Eq. (A-1) is zero. Similar results are found to obtain in the case of arbitrary incidence for both the disk and circular aperture. This proves that E_ϕ does vanish on the rim, as assumed originally.

The author would like to acknowledge conversations with Dr. C. T. Tai which incited the present work.

[17] C. Flammer, Phys. Rev. **89**, 1298 (1953).
[18] D. S. Jones, Quart. J. Mech. Appl. Math. **5**, 363 (1952).

Laminar Flow in Channels with Porous Walls*

ABRAHAM S. BERMAN
K-25 Laboratories, Carbide and Carbon Chemicals Company, Oak Ridge, Tennessee
(Received March 20, 1953)

The Navier-Stokes equations have been solved to obtain a complete description of the fluid flow in a channel having a rectangular cross section and two equally porous walls. The scope has been limited to two-dimensional incompressible steady-state laminar flow.

The solution of the flow equations leads to detailed expressions for the dependence of the velocity components and the pressure on position coordinates, channel dimensions, and fluid properties.

INTRODUCTION

THE solution of problems involving diffusion phenomena in a flowing gas stream requires a knowledge of the details of the flow. More specifically, one must know the magnitude and direction of the velocity at any point in the flow channel. The effect of wall porosity on the velocity and pressure distributions in a channel has not, to the author's knowledge, been investigated previously, although considerable theoretical effort has been devoted to the boundary-layer flow over a porous flat plate.[1] In this case, however, the boundary-layer equations have been used which are approximations to the Navier-Stokes equations and are not applicable to fully developed channel flow.

Several treatments, relating the over-all pressure drop to the flow rate in a channel with porous walls, have appeared in the literature, notably those of Olson[2] and Van Der Hegge Zijnen.[3] However, in these cases, the problem was simplified by neglecting kinetic-energy effects or restricting the discussion to a one-dimensional flow.

For these reasons, it seemed desirable to investigate the possibility of obtaining a solution to the Navier-Stokes equations for channel flow under the condition where fluid is being withdrawn through the channel walls.

REDUCTION OF THE FLOW EQUATIONS

A channel of rectangular cross section is to be considered. One side of the cross section, representing the distance between the porous walls, is taken to be much smaller than the other. This condition enables one to treat the problem as a case of two-dimensional flow. Both channel walls are taken to have equal permeability.

The following flow conditions are imposed: (1) a steady state prevails; (2) the fluid is incompressible; (3) no external forces act on the fluid; (4) the flow is laminar; and (5) the velocity of the fluid leaving the walls of the channel is independent of position.

A coordinate system is chosen with the origin at the center of the channel. The y axis is perpendicular to the channel walls and the x axis is in a plane parallel to the channel walls. The distance between the walls is taken to be $2h$ and the channel length is L.

Under the assumed conditions and choice of axes, the Navier-Stokes equations are

$$u\frac{\partial u}{\partial x}+\frac{v}{h}\frac{\partial u}{\partial \lambda}=-\frac{1}{\rho}\frac{\partial p}{\partial x}+\nu\left(\frac{\partial^2 u}{\partial x^2}+\frac{1}{h^2}\frac{\partial^2 u}{\partial \lambda^2}\right), \tag{1}$$

$$u\frac{\partial v}{\partial x}+\frac{v}{h}\frac{\partial v}{\partial \lambda}=-\frac{1}{h\rho}\frac{\partial p}{\partial \lambda}+\nu\left(\frac{\partial^2 v}{\partial x^2}+\frac{1}{h^2}\frac{\partial^2 v}{\partial \lambda^2}\right), \tag{2}$$

and the continuity equation is

$$\frac{\partial u}{\partial x}+\frac{1}{h}\frac{\partial v}{\partial \lambda}=0 \tag{3}$$

where the dimensionless variable

$$\lambda=y/h \tag{4}$$

has been introduced.

The boundary conditions are

$$u(x,\pm 1)=0 \tag{5}$$

$$(\partial u/\partial \lambda)_{\lambda=0}=0 \tag{6}$$

$$v(x,0)=0 \tag{7}$$

$$v(x,\pm 1)=v_w=\text{constant}. \tag{8}$$

For a two-dimensional incompressible flow a stream function ψ exists such that

$$u(x,\lambda)=(1/h)(\partial\psi/\partial\lambda), \tag{9}$$

$$v(x,\lambda)=-(\partial\psi/\partial x), \tag{10}$$

and the continuity equation, (3), is satisfied.

Since the flow is symmetrical about a plane midway between the walls, the solution will be investigated over half the channel, i.e., from the midplane to one wall.

For constant wall velocity v_w and the given boundary conditions, a suitable choice of stream function is

$$\psi(x,\lambda)=[h\bar{u}(0)-v_w x]f(\lambda), \tag{11}$$

* This document is based on work performed for the U. S. Atomic Energy Commission by Union Carbide and Carbon Corporation at Oak Ridge, Tennessee.

[1] H. Schlichting, *Grenzschicht-Theorie* (G. Braun, Karlsruhe, 1951), p. 213 ff.

[2] F. C. Olson, J. Appl. Mech. **16**, 53 (1949).

[3] B. G. Van Der Hegge Zijnen, Appl. Sci. Research, **A3**, 144 (1951).

giving for the velocity components by Eqs. (9) and (10)

$$u(x,\lambda)=[\bar{u}(0)-(v_w x/h)]f'(\lambda), \tag{12}$$

$$v(\lambda)=v_w f(\lambda). \tag{13}$$

In these equations $f(\lambda)$ is some function, yet to be determined, of the distance parameter λ. It is noted that under the assumption of constant wall velocity v_w, the y component of velocity v becomes a function of λ only.

If Eqs. (12) and (13) are substituted into the equations of motion (1) and (2), there result

$$-\frac{1}{\rho}\frac{\partial p}{\partial x}=\left[\bar{u}(0)-\frac{v_w x}{h}\right]\left\{-\frac{v_w}{h}[f'^2-ff'']-\frac{\nu}{h^2}f'''\right\}, \tag{14}$$

$$-\frac{1}{h\rho}\frac{\partial p}{\partial \lambda}=\frac{v}{h}\frac{dv}{d\lambda}-\frac{\nu}{h^2}\frac{d^2v}{d\lambda^2}. \tag{15}$$

The right-hand side of (15) is seen to be a function of λ only, hence differentiation with respect to x yields

$$(\partial^2 p/\partial x\partial\lambda)=0 \tag{16}$$

so that upon differentiating (14) with respect to λ, one obtains

$$\left[\bar{u}(0)-\frac{v_w x}{h}\right]\frac{d}{d\lambda}\left\{\frac{v_w}{h}[f'^2-ff'']+\frac{\nu}{h^2}f'''\right\}=0. \tag{17}$$

If (17) is to be satisfied for all x, then

$$\frac{d}{d\lambda}\left\{\frac{v_w}{h}[f'^2-ff'']+\frac{\nu}{h^2}f'''\right\}=0 \tag{18}$$

or integrating and defining

$$R\equiv(v_w h/\nu),\ \text{(a Reynolds number)}, \tag{19}$$

one obtains

$$R[f'^2-ff'']+f'''=k, \tag{20}$$

where k is the constant of integration.

The boundary conditions on the function $f(\lambda)$ and its derivatives are readily obtained from Eqs. (5) through (8) and Eqs. (12) and (13). Thus

$$f(0)=f'(1)=f''(0)=0, \tag{21}$$

$$f(1)=1. \tag{22}$$

The third-order, nonlinear, ordinary differential equation, (20), together with the associated boundary conditions (21) and (22) constitute an exact solution to the equations of motion and continuity as formulated. Four boundary conditions are needed since the integration constant k is still to be determined.

Formally, Eq. (20) appears similar to a general boundary-layer equation investigated first by Falkner and Skan[4] and later, more thoroughly, by Hartree.[5] However, the differences between the equations† are of such a nature that the author did not find it possible to make use of the solutions already available for the boundary-layer problem.

If one considers the limiting form of Eq. (20) as v_w, and hence R tends to zero (the order of the equation is unchanged), a simple third-order equation, $f'''=k$, results. The solution to this equation subject to the boundary conditions (21) and (22) leads to a function f describing the well-known Poiseuille flow in a rectangular channel. In view of this, it seemed reasonable that the deviations from Poiseuille flow, brought about by the permeable walls, could best be studied by a perturbation treatment in which the wall Reynolds number R is used as a perturbation parameter. Such a solution will be valid for sufficiently small values of R and is outlined in the next section.

For large values of R, it is not possible to investigate the nature of the solution by considering the limiting form assumed by Eq. (20). This is so since, contrary to the case for small R, the order of the equation is reduced by unity if the terms not multiplied by R are neglected. Thus, one must first obtain a general solution to the unmodified equation and then investigate the behavior of this solution as R increases. No suitable technique has as yet been found enabling one to obtain such a solution which would be expected to be valid for all values of R.

PERTURBATION SOLUTION

Expanding the function $f(\lambda)$ and the constant of integration k of Eq. (20),

$$f(\lambda)=f_0(\lambda)+f_1(\lambda)R+f_2(\lambda)R^2+\cdots+f_n(\lambda)R^n+\cdots \tag{23}$$

and

$$k=C_0+C_1R+C_2R^2+\cdots+C_nR^n+\cdots. \tag{24}$$

Here the f_n's and C_n's are taken to be independent of R. Substitution of (23) and (24) into (20) and collecting powers of R leads to the following set of equations:

$$\text{Zero order, } f_0'''=C_0 \tag{25}$$

$$\text{First order, } f_1'''=C_1+f_0f_0''-f_0'^2 \tag{26}$$

$$\text{Second order, } f_2'''=C_2+f_0f_1''+f_1f_0''-2f_0'f_1'. \tag{27}$$

[4] V. M. Falkner and S. W. Skan, Phil. Mag. **12**, 865 (1931).

[5] D. R. Hartree, Proc. Cambridge Phil. Soc. **33**, Part II, 223 (1937).

† The differences between the Falkner and Skan equation and Eq. (20) of this paper arise from the fundamentally different physical situations that are involved. The Falkner and Skan equation results from the consideration of a system wherein the "boundary layer" occupies only a very small portion of the region of interest whereas in the case of the present equation, the "boundary layer" fills the whole domain. This difference is reflected in the different coefficients of the two equations, in a finite interval of integration compared to an infinite interval, in four instead of three boundary conditions, and in boundary conditions which are not the same. The fact that there are four boundary conditions, two of which are specified at the upper limit ($\lambda=1$), makes a series solution, of the type used by Falkner and Skan, less advantageous than the perturbation method used here.

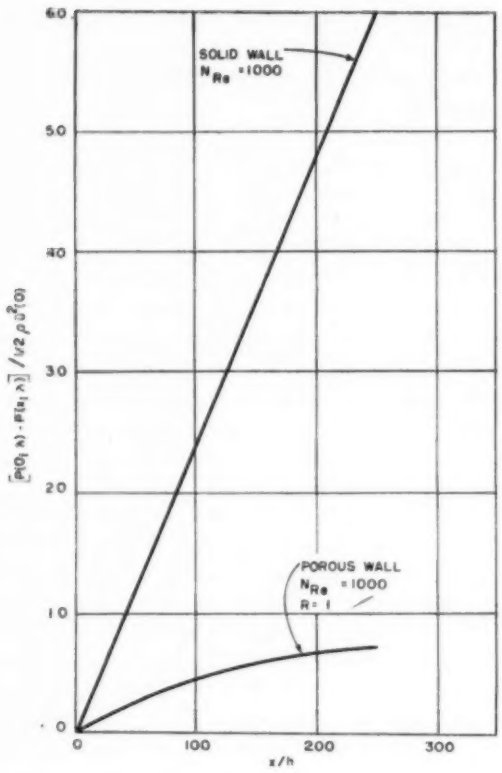

FIG. 1. Pressure drop in channels with rectangular cross section.

The boundary conditions to be satisfied by the f_n's are from (21) and (22)

$$f_n(0)=f_n'(1)=f_n''(0)=0 \tag{28}$$

$$\left.\begin{aligned} &f_0(1)=1 \\ &f_n(1)=0; \quad n\geqq 1 \end{aligned}\right\}. \tag{29}$$

Equations (25), (26), etc., are ordinary linear third-order equations which are readily solved to give successive approximations to $f(\lambda)$.

THE EFFECT OF POROUS WALLS ON CHANNEL FLOW

The first-order perturbation solution gives for $f(\lambda)$ and k

$$f^{(1)}(\lambda)=\tfrac{1}{2}\lambda(3-\lambda^2)+(R/280)(3\lambda^3-2\lambda-\lambda^7), \tag{30}$$

$$k^{(1)}=-3+(81/35)R. \tag{31}$$

Since the correction term in (31) seemed rather large, a second-order perturbation calculation was carried through and the coefficient of the R^2 term in the expression for k was found to be about 0.02.

Equation (30) and its derivative along with Eqs. (12) and (13) yield the following expressions for the velocity components:

$$u(x,\lambda)=\left[\bar{u}(0)-\frac{v_w x}{h}\right]\left[\tfrac{3}{2}(1-\lambda^2)\right] \times\left[1-\frac{R}{420}(2-7\lambda^2-7\lambda^4)\right], \tag{32}$$

$$\frac{v(\lambda)}{v_w}=\frac{\lambda}{2}(3-\lambda^2)-\frac{R}{280}\lambda(2-3\lambda^2+\lambda^6). \tag{33}$$

From Eq. (32) it is seen that the velocity profile is flatter than the Poisueille parabola at the channel center $\lambda=0$, and steeper close to the channel walls.

The pressure distribution in the channel is readily obtained from Eq. (14). Thus, multiplying (14) by $(-h^2/\nu)$ one obtains

$$+\frac{h^2}{\rho\nu}\frac{\partial p}{\partial x}=\left[\bar{u}(0)-\frac{v_w x}{h}\right]\{R[f'^2-ff'']+f'''\}. \tag{34}$$

Using (20) and rearranging gives

$$\frac{\partial p}{\partial x}=\frac{k\mu}{h^2}\left[\bar{u}(0)-\frac{v_w x}{h}\right]. \tag{35}$$

Further from (15),

$$\frac{\partial p}{\partial\lambda}=\frac{\mu}{h}\frac{d^2v}{d\lambda^2}-\rho v\frac{dv}{dx}. \tag{36}$$

Integrating (35) and (36) and making use of (33), one finally obtains

$$p(x,\lambda)=p(0,0)-\rho\frac{v_w^2}{2}f^2(\lambda) +\frac{k\mu}{h^2}\left[\bar{u}(0)x-\frac{v_w x^2}{2h}\right]+\frac{v_w\mu}{h}[f'(\lambda)-f'(0)]. \tag{37}$$

Using the first-order results for $f(\lambda)$ and its derivative one can complete the evaluation of the pressure distribution.

It is interesting to calculate the pressure drop in the major flow direction. From (37)

$$p(0,\lambda)-p(x,\lambda)=-\frac{k\mu}{h^2}\left[\bar{u}(0)x-\frac{v_w x^2}{2h}\right]. \tag{38}$$

In dimensionless form, this becomes

$$\frac{p(0,\lambda)-p(x,\lambda)}{\tfrac{1}{2}\rho\bar{u}^2(0)}=\left(\frac{24}{N_{Re}}-\frac{648}{35}\frac{R}{N_{Re}}\right) \times\left(1-\frac{2R}{N_{Re}}\frac{x}{h}\right)\left(\frac{x}{h}\right), \tag{39}$$

where the entrance Reynolds number has been introduced as

$$N_{Re}=4h\bar{u}(0)/\nu \tag{40}$$

and the first-order value for k has been used.

The values assigned to (x/h) are limited by the fact that at some value of x in the channel, all the gas has been removed through the channel walls. From Eq. (3), it can be shown that the range of allowable values for (x/h) is

$$0\leqq x/h\leqq N_{Re}/4R. \tag{41}$$

Equation (39) is shown graphically in Fig. 1 for an arbitrary choice of $R=1$ and $N_{Re}=1000$. Also illustrated in the same figure is the x dependence of pressure in a solid wall channel having the same entrance Reynolds number.

To help visualize the flow, the streamlines for the upper half-channel are shown in Fig. 2 for a choice of $R=1$, and $N_{Re}=1000$. The first-order result for $f(\lambda)$ was used and the stream function was plotted in dimensionless form. Thus from Eq. (11),

$$\Psi(x,\lambda)=[\psi(x,\lambda)/h\bar{u}(0)]$$
$$=[1-(4R/N_{Re})(x/h)]f(\lambda). \tag{42}$$

The technique used for obtaining a solution for this case of two porous walls having the same permeability can be readily extended to obtain solutions for the cases of a channel having porous walls of different permeability or for a porous tube.

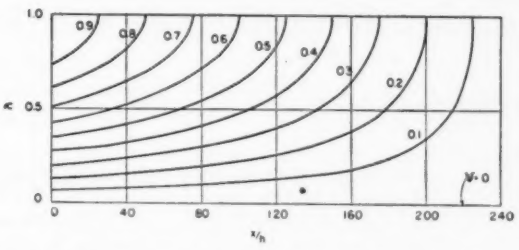

FIG. 2. Flow lines in the upper half of a channel with porous walls. $R=1$; $N_{Re}=1000$.

SUMMARY

The effect of wall porosity on the two-dimensional steady-state incompressible laminar flow of a fluid in a channel having rectangular cross section has been investigated in detail by the solution of the Navier-Stokes equations.

With the assumption of uniform suction at the walls, an exact solution of the flow equations is obtained leading to a third-order nonlinear differential equation with appropriate boundary conditions. For small flows through the porous walls, this latter equation is solved by a perturbation method. First-order expressions for the dependence of the velocity components and the pressure on positional coordinates, channel dimensions, and fluid properties are obtained.

The velocity "profile" in the major flow direction is found to deviate from the Poiseuille parabola by being flatter at the center of the channel and steeper in the region close to the walls, the degree of deviation depending on a Reynolds number for the flow through the channel walls.

The pressure drop in the direction of the main flow is found to be appreciably less in the porous wall channel than that in a solid wall channel having the same dimensions and the same entrance Reynolds number.

NOMENCLATURE

$2h$ = distance between the channel walls.
k = an integration constant.
$p(x,\lambda)$ = the pressure in the channel at the point (x,λ).
$u(x,\lambda)$ = the velocity component in the x direction at the point (x,λ) in the channel.
$\bar{u}(x)$ = the x component of velocity averaged over the channel cross section at position x along the channel.
$v(x,\lambda)$ = the λ component of velocity at the point (x,λ) in the channel.
v_w = the velocity of the fluid leaving the channel walls.
R = a Reynolds number for the flow through the channel wall, $R=hv_w/\nu$.
N_{Re} = a Reynolds number for the flow entering the channel, $N_{Re}=4h\bar{u}(0)/\nu$.
λ = dimensionless distance parameter, $\lambda=(y/h)$.
μ = the fluid viscosity.
ν = the kinematic viscosity (μ/ρ).
ψ = the stream function.
Ψ = the dimensionless stream function.

ACKNOWLEDGMENT

Dr. R. F. Fledderman's‡ contributions, in the form of suggestions concerning various methods of attack on the problem, are gratefully acknowledged.

Appreciation and thanks are extended to Dr. L. Geller, Dr. J. D. Justice, Dr. F. A. Ficken, and Mr. H. L. Weissberg for many stimulating discussions during the course of this work.

The author wishes particularly to express his indebtedness to Dr. L. Geller for his suggestions leading to the clarification and simplification of the mathematical arguments.

‡ Under U. S. Atomic Energy Commission contract with the State Engineering Experiment Station at the Georgia Institute of Technology. Project No. 202-146. Dr. M. J. Goglia, Project Director.

Electron Flow Through Small Tubes With Magnetic Focusing*

JOHN L. STEWART
Electronics Research Laboratory, Stanford University, Stanford, California
(Received March 16, 1953)

When a uniform finite magnetic field passing through the cathode is used for focusing a beam of electrons, random emission at the cathode results in the electrons traveling down the beam in a helical manner. Such a rotational motion severely limits the amount of current that can be made to travel through a small tube or between closely spaced parallel plates. The amount of current transmitted through such structures is calculated in this paper and presented in the form of normalized curves. It is assumed that the current initially fills the tube or the region between the parallel plates.

If an alternating electric field having a frequency comparable to the rotational frequency of the electrons is applied normal to the beam, the average electron radius of motion is increased. Should the electron beam be made to flow through a tube after the application of such an alternating electric field, the current transmission through the tube will be reduced over that when no electric field exists. The first-order correction term for this case is calculated and presented in the form of normalized curves. The fact that the average electron radius is increased when an electric field is present implies added energy and leads to the formulation of a conductance expression relating the power in the rotational motion of the beam to the electric field normal to the beam.

The current interception and the equivalent beam conductance are important in many electronic devices such as traveling-wave tubes. The beam conductance may be quite large in some cases—on the order of that present off the axis of a helix.

ELECTRON EQUATIONS OF MOTION

ASSUME a set of rectangular coordinates (x, y, z) with an electron traveling at a constant velocity v in the z direction in the presence of a finite magnetic field also in the z direction. At some reference plane $(t=0, z=0)$, the initial z directed velocity is v, and the x and y velocity components are $\dot{x}_0$ and $\dot{y}_0$, respectively. The initial x and y positions at this reference plane will be arbitrarily selected to yield the greatest simplicity to the equations of motion. It will be assumed that no steady electric fields exist, e.g., space charge will be neglected. This does not introduce as serious a limitation as might at first be supposed. The analysis of this paper is applicable mainly to fairly high electron rotational frequencies and to the case where an electron beam passes between closely-spaced parallel plates or within a small tube where the space charge is often small enough to be considered negligible.[1,2] The effect of finite space charge can be partly accounted for as will be mentioned later.

From the general equation of motion for an electron in both electric and magnetic fields,

$$m(d\mathbf{v}/dt) = -e(\mathbf{E}+\mathbf{v}\times\mathbf{B}), \tag{1}$$

where m = mass of electron, e = magnitude of charge on electron, $B = z$ directed magnetic flux density, t = time, and $E(t) = x$ directed alternating electric field. Three component equations can be written, one for motion in each coordinate. The solution for the z motion shows the electron to travel at a constant velocity $v = (2eV/m)^{\frac{1}{2}}$ in the z direction where V is the voltage equivalent of the velocity v. (The rationalized mks system of units will be used exclusively.)

Assuming that the field $E(t)$ is given by

$$E(t) = -E\sin(\omega t - \beta z), \tag{2}$$

where β and E are real constants and where ω is the ferquency, a solution for the x and y components of motion can be obtained. The phase constant β will be important only to the extent of affecting the frequency of the electric field as seen by the moving electrons. Its effect can be taken into account by calculating the resulting Doppler shift by simple means; consequently, β will be considered zero here. (The analysis of this report is not applicable should β be a function of z.)

Solving for the x and y motion of the electron as a function of time and finding the radius of the resulting electron spiral motion (assuming $z=0$ at $t=0$), one obtains

$$r^2 = x^2+y^2 = r_0^2 + \left\{\left(\frac{eEz}{2m\omega_0 v}\right)\left[\frac{\sin(\omega_c z/2v)}{(\omega_c z/2v)}\right]\right\}^2 + \left(\frac{eEz}{m\omega_0 v}\right)\left[\frac{\sin(\omega_c z/2v)}{(\omega_c z/2v)}\right] r_0\sin\alpha, \tag{3}$$

where $z = v/t$ has been substituted for the time, and where r = radius of electron spiral at time $t = z/v$, r_0 = initial radius of spiral (at time $t=0$), ω_0 = cyclotron frequency, ω_c = difference frequency. Hence

$$\omega_0 = eB/m, \tag{4}$$

$$\omega_c = \omega - \omega_0. \tag{5}$$

It is assumed that initial velocities in the x and y directions are due only to cathode emission. Thus, the

* The work reported in this paper was made possible through generous support extended jointly by the Navy Department (U. S. Office of Naval Research), the U. S. Air Force, and the U. S. Army (Signal Corps) under ONR Contract N6onr-25132.

[1] A. V. Haeff, Proc. Inst. Radio Engrs. **27**, 586–602 (1939).

[2] J. R. Pierce, *Theory and Design of Electron Beams* (D. Van Nostrand Company, Inc., 1949), Chaps. 8 and 9.

angle α, expressed as

$$\alpha=\arctan \dot{y}_0/\dot{x}_0$$
$$\dot{x}_0/\omega_0=r_0\cos\alpha \tag{6}$$
$$\dot{y}_0/\omega_0=r_0\sin\alpha$$

is a random variable with equal likelihood of being found anywhere in the interval $(0, 2\pi)$. In terms of the quantities of (6), r_0 can be expressed as

$$r_0^2=\dot{x}_0^2/\omega_0^2+\dot{y}_0^2/\omega_0^2=X_1^2+Y_1^2, \tag{7}$$

where $\dot{x}_0$ and $\dot{y}_0$ are independent random variables.

In obtaining (3), certain approximations have been made, namely, the difference frequency ω_c is small by comparison to ω_0 giving the approximation

$$\omega^2-\omega_0^2\cong 2\omega_0\omega_c, \tag{8}$$

and the radius r is of interest only after the lapse of a considerable amount of time compared to the cyclotron period which implies $\omega_0 t\gg 1$.

The mean-squared values of (3) and (7) can be taken to make the preceding equations for a single electron applicable when a large number of electrons exist. These mean squared values are

$$\langle r^2\rangle_{Av}=\langle r_0^2\rangle_{Av}+\left[\left(\frac{eEz}{2m\omega_0 v}\right)\left(\frac{\sin(\omega_c z/2v)}{(\omega_c z/2v)}\right)\right]^2, \tag{9}$$

$$\langle r_0^2\rangle_{Av}=\langle\dot{x}_0^2\rangle_{Av}/\omega_0^2+\langle\dot{y}_0^2\rangle_{Av}/\omega_0^2$$
$$=\langle 2\dot{x}_0^2\rangle_{Av}/\omega_0^2=2\langle\dot{y}_0^2\rangle_{Av}/\omega_0^2. \tag{10}$$

Equation (9) has the form of a standing wave having minima $\langle r_0^2\rangle_{Av}$ and maxima which become closer together as ω_c increases. If a velocity spread exists because of space charge (or because of random initial velocities in the z direction about a mean value v), the standing wave pattern will tend to be smoothed out—the result of integrating (3) over a spread of velocities. This is a way of accounting for the most important effects of a finite space charge should it exist.

For small u, the variable $(\sin u)/u$ becomes unity. The previous equations are valid for this case.

If E is not constant but is a function of distance z, it may accurately be taken as an average value with respect to z at resonance (where $\omega_c\to 0$) as long as the electric field varies very slowly compared to the distance traveled by an electron during one cyclotron period. Off resonance, the situation is more complex but can be solved by using E as a function of time and distance, $E(z, t)=E(vt, t)$, in the original differential equations. (For some functions, the use of the Laplace transformation methods allows the solution to be obtained most directly and easily.) However, an estimate in this case can be fairly accurate. For example, should the field vary as a half sine wave along the electron beam, the average value would be used for $E(2/\pi$ times the value at the center) and the variable u in the term $(\sin u)/u$ (but not elsewhere) could be multiplied by $1-(2/\pi)\times\arcsin(2/\pi)=0.56$ which corresponds to the ratio of the distance between the average points on the half sine wave variation to the full distance π.

PROBABILITY DENSITY FUNCTIONS OF RADII

It is well known that the probability density functions of the components of electron velocity tangential to a plane cathode are normal functions given by[3]

$$P(\dot{x}_0)=(2\pi\langle\dot{x}_0^2\rangle_{Av})^{-\frac{1}{2}}\exp(-\dot{x}_0^2/2\langle\dot{x}_0^2\rangle_{Av}), \tag{11}$$

where the function for $\dot{y}_0$ is of identical form, and where

$$\langle\dot{x}_0^2\rangle_{Av}=\langle\dot{y}_0^2\rangle_{Av}=kT/m=\omega_0^2\lambda. \tag{12}$$

The quantity k is Boltzmann's constant and T is the absolute cathode temperature in degrees Kelvin.

The orthogonal components of velocity are independent random variables; hence, the virtual cathode (if such exists) will affect only the normal component of velocity.

The radius of motion of any electron having initial transverse velocities $\dot{x}_0$ and $\dot{y}_0$ has been given by (7). The probability density function of radii is then obtained through

$$P(X_1, Y_1)dX_1dY_1=P(X_1)P(Y_1)dX_1dY_1$$
$$=(dX_1dY_1)/(2\pi\lambda)\exp(-X_1^2/2\lambda-Y_1^2/2\lambda), \tag{13}$$

where the value of λ is indicated in (12).

Substituting

$$X_1=r\cos\theta$$
$$Y_1=r\sin\theta \tag{14}$$
$$dX_1dY_1=rdrd\theta,$$

and integrating θ over the interval $(0, 2\pi)$, the probability density function for the radii of electrons emitted from the cathode is obtained,

$$P(r)=(r/\lambda)\exp(-r^2/2\lambda). \tag{15}$$

The probability density function of (15) is termed a Rayleigh function and results whenever the magnitude of two orthogonal independent random variables, each normally distributed, is desired. It is the same function as that pertaining to the envelope of noise in an intermediate frequency amplifier.[4,5]

If the electron stream experiences an alternating electric field normal to its path and having a relative frequency equal to the cyclotron frequency ω_0, the x motion of the electrons can be written as

$$x(t)=R\cos\omega_0 t+x_n(t), \tag{16}$$

where $R\cos\omega_0 t$ is the part correlated with the electric field and $x_n(t)$ is a random time function by virtue of initial thermal radii. The quantity $x_n(t)$ can be broken

[3] E. H. Kennard, *Kinetic Theory of Gases* (McGraw-Hill Book Company, New York, 1938).
[4] S. O. Rice, Bell System Tech. J. **23** (1944); **25** (1945).
[5] J. L. Lawson and G. E. Uhlenbeck, *Threshold Signals* (McGraw-Hill Book Company, New York, 1950) Vol. 24, Mass. Inst. Technol. Radiation Lab. Series.

into parts in phase and in phase quadrature with $\cos\omega_0 t$,

$$x_n(t)=x_c\cos\omega_0 t+x_s\sin\omega_0 t=\sum_{i=1}^{N}C_i\cos(\omega_0 t+\phi_i). \quad (17)$$

C_i and ϕ_i are random numbers referring to the ith electron. The number of electrons N can be assumed to approach infinity.

From (17),

$$x_c=\sum_{i=1}^{N}C_i\cos\phi_i;\quad x_s=\sum_{i=1}^{N}C_i\sin\phi_i. \quad (18)$$

By virtue of the central limit theorem of statistics and the above equations, the C_i are normally distributed

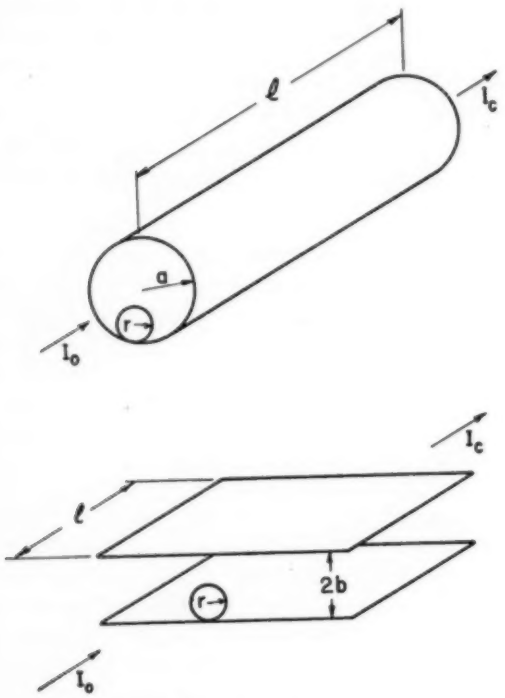

FIG. 1. Geometry of structures.

with variance

$$\langle x_n^2\rangle_{Av}=\langle x_s^2\rangle_{Av}=\langle x_c^2\rangle_{Av}=\lambda. \quad (19)$$

Consider the variables

$$X_2=R+x_c;\quad Y_2=Y_1=x_s. \quad (20)$$

Since $Y_2=x_s$ and $X_2-R=X_1=x_c$ are normally distributed independent random variables,

$$P(X_2, Y_2)dX_2dY_2=(dX_2dY_2)/(2\pi\lambda)\times\exp\left[-\frac{(X_2-R)^2+Y_2^2}{2\lambda}\right]. \quad (21)$$

Substituting the variables of (14) and integrating θ over $(0, 2\pi)$, the probability density function of electrons emitted from the cathode and subjected to a transverse alternating electric field of frequency ω_0 is obtained.

$$P(R, r)=(r/\lambda)I_0(rR/\lambda)\exp\left[-\frac{r^2+R^2}{2\lambda}\right], \quad (22)$$

where I_0 is the Bessel function with imaginary argument

The radius of motion is given by

$$r^2=X_2^2+Y_2^2=(x_c+R)^2+x_s^2=x_c^2+x_s^2+R^2+2x_cR=r_0^2+R^2+2x_cR. \quad (23)$$

From a comparison of (3) and (23), it is apparent that

$$R^2=\left[\left(\frac{eEz}{2m\omega_0 v}\right)\left(\frac{\sin(\omega_c z/2v)}{(\omega_c z/2v)}\right)\right]^2. \quad (24)$$

The nth moments of the probability density function of (22) are given by

$$\langle r^n\rangle_{Av}=\int_0^\infty r^nP(R, r)dr=(2\lambda)^{n/2}\Gamma(1+n/2)\,{}_1F_1(-n/2, 1; -R^2/2\lambda), \quad (25)$$

where Γ is the gamma function and ${}_1F_1$ is the confluent hypergeometric function defined by

$${}_1F_1(a, b; z)=1+\frac{a}{b}\cdot\frac{z}{1!}+\frac{a(a+1)}{b(b+1)}\cdot\frac{z^2}{2!}+\cdots. \quad (26)$$

It is to be noted that *all* the moments have a first-order correction term due to the alternating electric field proportional to the *square* of the field strength. It can be further noted that all even order moments are expressible as polynomials in R^2.

The limiting behavior of (22) for large R is of interest. Substituting the asymptotic expression for the Bessel function, one obtains

$$\lim_{R\to\infty}P(R, r)=(\tfrac{1}{2}\pi\lambda)^{\frac{1}{2}}(r/R)^{\frac{1}{2}}\exp\left[-\frac{(r-R)^2}{2\lambda}\right], \quad (27)$$

which behaves as a normal function of mean R and variance λ for those values of r where the value of the exponential is appreciable.

FLOW THROUGH HOLES AND BETWEEN PLATES

Consider an electron stream approaching and entering either a long tube or the gap between parallel plates as in Fig. 1.

If it is assumed that l, the length of the tube (or plates) is larger than p, the pitch of the helix described by the motion of the electrons traveling in the magnetic field B, the ratio of I_c/I_0 (current passing through the system to current incident to the system) can be readily obtained (geometrically) for electrons all of which have

the same radius of motion r as

$$(I_c/I_0)_{\text{tube}}=(1-r/a)^2; \quad (I_c/I_0)_{\text{plates}}=1-r/b. \quad (28)$$

From these equations, the probability density functions in unnormalized form for electrons after they have passed through the tube or between the plates can be obtained (by classifying electrons as to radii) as

$$P_c(R, r)_{\text{tube}}=(1-r/a)^2P(R, r), \quad r\leqslant a \quad (29)$$

$$P_c(R, r)_{\text{plates}}=(1-r/b)P(R, r), \quad r\leqslant b, \quad (30)$$

where it is assumed that the alternating electric field acts upon the electrons before they enter the system.

The intergral of these functions from $r=0$ to $r=a$ or b is then the ratio of currents which is desired. For $R=0$, the solution is not difficult and is expressed in terms of elementary integrals and the error integral. For R not zero, the general solution is difficult. The solution can be obtained in terms of an infinite series in R^2 by expanding $I_0(rR/\lambda)\exp(-R^2/2\lambda)$ in the integrand and evaluating each coefficient by again making use of elementary integrals and the error integral. The result for the lower-order terms for the *tube* is

$$\frac{I_c(R, a)}{I_0}=\left[1+\frac{-\exp(-\sigma^2)}{\sigma^2}-\frac{\pi^{\frac{1}{2}}Erf(\sigma)}{\sigma}\right]$$
$$-\left(\frac{R^2}{2\lambda}\right)\left[\frac{\pi^{\frac{1}{2}}Erf(\sigma)}{2\sigma}-\frac{1-\exp(-\sigma^2)}{\sigma^2}\right]$$
$$+\frac{1}{8}\left(\frac{R^2}{2\lambda}\right)^2\left[\frac{\pi^{\frac{1}{2}}Erf(\sigma)}{2\sigma}-\exp(-\sigma^2)\right]-\frac{1}{48}\left(\frac{R^2}{2\lambda}\right)^3$$
$$\times\left[\frac{\pi^{\frac{1}{2}}Erf(\sigma)}{2\sigma}-\exp(-\sigma^2)+\tfrac{2}{3}\sigma^2\exp(-\sigma^2)\right]$$
$$+\text{terms of order } (R^2/2\lambda)^4 \text{ and higher}, \quad (31)$$

where

$$\sigma=a/(2\lambda)^{\frac{1}{2}}=a/\langle r_0^2\rangle_{Av}^{\frac{1}{2}} \quad (32)$$

is a normalized dimension.

A similar derivation for the parallel plates yields

$$\frac{I_c(R, b)}{I_0}=\left[1-\frac{\pi^{\frac{1}{2}}Erf(\gamma)}{2\gamma}\right]$$
$$-\left(\frac{R^2}{2\lambda}\right)\left[\frac{\pi^{\frac{1}{2}}Erf(\gamma)}{4\gamma}-\frac{\exp(-\gamma^2)}{2}\right]$$
$$+\text{terms of order } (R^2/2\lambda)^2 \text{ and higher}, \quad (33)$$

where

$$\gamma=b/(2\lambda)^{\frac{1}{2}}=b/\langle r_0^2\rangle_{Av}^{\frac{1}{2}}. \quad (34)$$

The value for $R=0$ for both tubes and plates is plotted as a function of the normalized dimensions in Fig. 2. Similarly, the coefficient of $-R^2/2\lambda$ is plotted in Fig. 3 for both tubes and plates.

The asymptotic forms of (31) and (33) for both small and large normalized dimensions σ and γ can readily be obtained.

Should the pitch of the electron helix be larger than l (the length of the tube or the plates), some electrons will have only l/p as much chance of being intercepted. Others have different probabilities of being intercepted. Unfortunately, the expressions become most complex if such a situation exists. A rough approximation can be

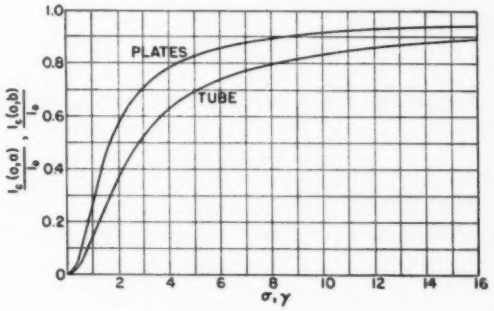

FIG. 2. Field-free current transmission.

obtained if an equivalent dimension (to σ or γ) is assumed such that

$$\sigma_{eq}\sim(p/l)\sigma=\frac{2\pi v}{\omega_0 l}\cdot\frac{a\omega_0}{(2kT/m)^{\frac{1}{2}}}=(2\pi a/l)(eV/kT)^{\frac{1}{2}}. \quad (35)$$

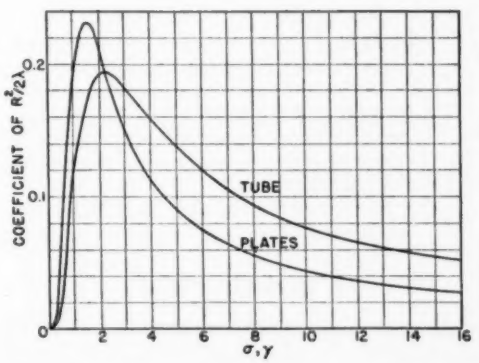

FIG. 3. First-order correction to current transmission.

EQUIVALENT BEAM CONDUCTANCE TO TRANSVERSE ELECTRIC FIELDS

If there exists an alternating electric field normal to the electron beam and at the cyclotron resonance frequency ω_0 (accounting for any Doppler shift in frequency which may be considerable in such devices as slow-wave structures with relatively high electron velocities), the electrons acquire an average radius which is greater than that when no electric field is present. This added radius represents additional energy possessed by the electrons which must have been acquired from the

transverse electric field. With respect to the electric field applied to a structure through which an electron beam passes, a power loss component or conductance exists.

The rotational energy of a single electron is $\frac{1}{2}m\omega_0^2r^2$. That of a stream of electrons passing a given point is

$$P_T=\tfrac{1}{2}m\omega_0^2gI_0\langle r^2\rangle_{Av}, \tag{36}$$

where $g=6.29\times10^{18}$ electrons per second per ampere of current flow, I_0 is the beam current, and the mean-squared value of r has been taken in order to account for a large number of electrons having various radii.

But, from (9) or (25),

$$\langle r^2\rangle_{Av}=\langle r_0^2\rangle_{Av}+R^2. \tag{37}$$

Thus, the power *added* to the beam by the transverse field is

$$P_0=\tfrac{1}{2}m\omega_0^2gI_0R^2. \tag{38}$$

Substituting for R^2 from (24) and defining a conductance G_0 as the ratio of P_0 to the mean-squared value of the electric field $E^2/2$,

$$G_0=2P_0/E^2=\frac{gI_0}{m}\left(\frac{ez}{2v}\right)^2\left(\frac{\sin(\omega_c z/2v)}{(\omega_c z/2v)}\right)^2. \tag{39}$$

The value of z can be taken as that when the electrons leave the structure of interest. For some values, $G_0\cong0$. For such values, the standing-wave pattern in the structure yields a minimum when the electrons leave; although the electrons had at one time absorbed energy, they returned it to the structure before passing entirely through. But note the maxima and minima are functions of the difference frequency ω_c. The ripples in the amplitude function of traveling-wave tubes may be partially describably by such a phenomenon. It can be stated that the conductance given by (39) can easily be as large or larger than the reciprocal of the impedance of a structure such as the helix of a traveling-wave tube depending upon the various operating conditions of beam velocity, magnetic field, and so forth.

JOURNAL OF APPLIED PHYSICS VOLUME 24, NUMBER 9 SEPTEMBER, 1953

Epicentral Displacement Caused by Elastic Waves in an Infinite Slab*

ALAN G. MENCHER
University of California, Los Angeles, California

(Received January 5, 1953)

The displacement is determined at the epicenter of a homogeneous isotropic infinitely long elastic slab containing a point source of pressure waves. The source is centrally located between the slab surfaces and is taken to have a step function time dependence.

The formal solution for the Laplace transform of the displacement is obtained as an infinite integral. The integration and the inversion are simultaneously accomplished by an infinite series expansion of the integrand and transformation of variables for each term of the expansion. The resultant integrated series consists of terms having the mathematical form of reflected waves which diverge individually but combine to give a finite resultant.

In view of the fact that the expansion of the integrand is not valid at the upper limit of integration, a justification of the method and of the results is given.

I. INTRODUCTION

UNTIL recent years, an important phase of the field of theoretical seismology remained largely neglected. Attention was directed principally toward steady-state problems, while the question of the transient response to impulsive sources was mostly ignored until operational methods had been placed on a rigorous basis in the form of an extended theory of the Laplace transform.

Considerable work with transform methods has been done by Japanese[1] and Russian[2] investigators. The most complete contribution, however, was made by L. Cagniard[3] who investigated displacements in a system consisting of two different homogeneous isotropic half-spaces separated by a plane surface of contact, with a point source having a step function time dependence imbedded in one of the media. Cagniard only obtained formal results, and it remained for Pinney,[4] using different methods, to obtain numerical solutions for a special case of Cagniard's problem where one of the half-spaces is vacuum.

Effort may now be usefully concentrated on investigations of layered media which form a more realistic model of the earth than a half-space. The simplest layered

* Taken from part of a thesis submitted to the faculty of the University of California at Los Angeles in partial fulfillment of the requirements for the Ph.D. degree in physics.

[1] K. Sezawa and K. Kanai, Bull. Earthquake Research Inst., Tokyo Univ. **19**, Part 2, 151–161 (1941).

[2] S. Sobolev, Acad. Sci. URSS, Publ. Inst. Seis. No. 18, 1–41 (1932).

[3] L. Cagniard, *Reflexion et Refraction des Ondes Seismiques Progressives* (Gauthier-Villars, Paris, 1939).

[4] E. Pinney, J. Math. and Phys. **30**, 1–10 (1951), and private communication.

medium is an infinite slab, a solid of given thickness bounded on both surfaces by infinite planes which separate it from vacuum. The present work considers the motion resulting from a step function point source of pressure waves at the epicenter of the slab only, since the general problem of the displacement anywhere on the surface is considerably more complicated.

II. SOLUTIONS OF THE WAVE EQUATIONS

Consider a point source of longitudinal waves having a step function time dependence located midway between the surfaces of a homogeneous isotropic infinite slab characterized by the Lamé constants λ, μ, and the density, δ. The surfaces separate the slab from vacuum. We ask for the displacement as a function of time of the epicenter (the surface point directly above the source). The geometry is shown in Fig. 1.

The equation of motion of a point in a homogeneous isotropic elastic medium is

$$(\lambda+\mu)\nabla\nabla\cdot\mathbf{s}+\mu\nabla^2\mathbf{s}=\delta(\partial^2\mathbf{s}/\partial t^2), \tag{1}$$

where $\mathbf{s}$ is the vector displacement of the point from equilibrium and the other quantities are defined above. It is convenient to express $\mathbf{s}$ in terms of a scalar potential ϕ and a vector potential $\mathbf{A}$ by defining

$$\mathbf{s}=\nabla\phi+\nabla\times\mathbf{A}. \tag{2}$$

A proper choice of gauge permits one to set $\nabla\cdot\mathbf{A}=0$. Substituting Eq. (2) into (1), using the divergence condition and requiring that ϕ satisfy the scalar wave equation, one arrives at the following equations for ϕ and $\mathbf{A}$:

$$\nabla^2\phi=\frac{1}{V_L{}^2}\frac{\partial^2\phi}{\partial t^2}$$
$$\nabla^2\mathbf{A}=\frac{1}{V_T{}^2}\frac{\partial^2\mathbf{A}}{\partial t^2}, \tag{3}$$

where $V_L{}^2=(\lambda+2\mu)/\delta$, and $V_T{}^2=\mu/\delta$. The subscripts L and T denote the well-known fact that the scalar wave is to be identified with a longitudinal or pressure disturbance while the vector wave is to be identified with a transverse or shear disturbance. These equations must be satisfied subject to the boundary conditions, namely, that the normal and shear stress vanish on the surfaces of the slab.

Taking the Laplace transform of the scalar wave equation gives

$$\nabla^2\langle\phi\rangle=\frac{p^2}{V_L{}^2}\langle\phi\rangle,$$

where $\langle\phi\rangle$ is the Laplace transform of ϕ and p is the transform variable, under the conditions that $\phi_{t=0}=0=\phi'_{t=0}$.

Because of the azimuthal symmetry of the problem, cylindrical coordinates are a convenient choice. The displacement then has no θ component, while $\mathbf{A}$ has a θ component only. With the origin at the source, the general solution to Eqs. (3) subject to conditions of symmetry is

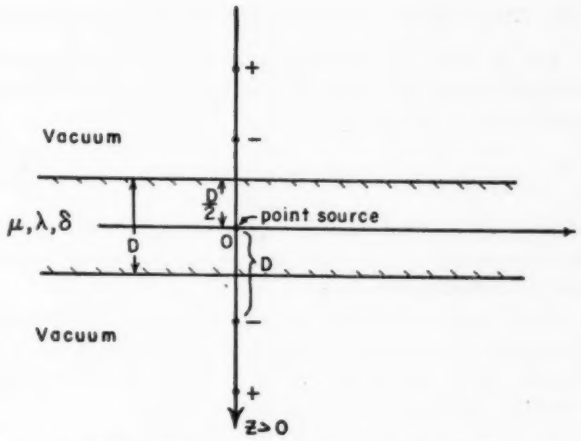

FIG. 1. Infinite elastic slab. The plus and minus signs denote positions of images.

$$\langle\phi\rangle=\int_0^\infty C(m)\cosh K_L z J_0(m\rho)dm, \tag{4}$$

where

$$K_L{}^2=m^2+p^2/V_L{}^2 \tag{5}$$

An exactly similar procedure leads to the general solution of the transformed vector wave equation

$$\langle A_\theta\rangle=\int_0^\infty B(m)\sinh K_T z J_1(m\rho)dm, \tag{6}$$

where

$$K_T{}^2=m^2+p^2/V_T{}^2.$$

The functions $C(m)$ and $B(m)$ are to be determined by the boundary conditions.

The Laplace transform of the potential of a spherically symmetric source is

$$\langle\phi_s\rangle=N(p)\frac{e^{-pr/V_L}}{r}, \tag{7}$$

where $N(p)$ is determined by the time dependence of the source and is simply N/p in the case of a step function.

An integral representation of Eq. (7) is given by[5]

$$\langle\phi_s\rangle=\frac{N}{p}\int_0^\infty\frac{mdm}{K_L}e^{-K_L z}J_0(m\rho). \tag{8}$$

Thus the total expression for the scalar wave is

$$\langle\phi_t\rangle=\int_0^\infty C(m)\cosh K_L z J_0(m\rho)dm+\langle\phi_s\rangle. \tag{9}$$

and the vector wave is given by Eq. (6).

[5] A. Sommerfeld, *Partial Differential Equations in Physics* (Academic Press, Inc., New York, 1949), p. 242.

III. STATEMENT OF THE BOUNDARY CONDITIONS

The generalized Hooke's law for a homogeneous, isotropic medium may be written in a curvilinear coordinate system as[6]

$$\tau_{ij}=\lambda\delta_{ij}e_{kk}+2\mu e_{ij}, \tag{10}$$

where e is the strain tensor, τ the stress tensor, and δ_{ij} the Kronecker delta. Summations are to be performed over all repeated subscripts.

The boundary conditions are given by the fact that no stress may be transmitted across the surfaces $z=\pm D/2$. In cylindrical coordinates the following conditions are required at $z=\pm D/2$

$$\tau_{zz}=0, \quad \tau_{z\rho}=0. \tag{11}$$

Equations (11) may be expressed in terms of the scalar and vector waves by means of Eqs. (10), (2), and expressions relating the components of strain to the components of displacement.[6] Making the necessary substitutions into Eq. (11), taking the Laplace transform, and using the transformed scalar wave equation for simplification, one obtains straightforwardly

$$\tau_{zz}=\delta p^2\langle\phi\rangle-2\delta V_T^2\left\{\frac{p^2}{V_L^2}\langle\phi\rangle-\frac{\partial^2\langle\phi\rangle}{\partial z^2}-\frac{\partial}{\partial z}\left[\frac{1}{\rho}\frac{\partial}{\partial\rho}(\rho\langle\phi_A\rangle)\right]\right\}=0$$

$$\tau_{z\rho}=\mu\left\{2\frac{\partial^2\langle\phi\rangle}{\partial z\partial\rho}-\frac{\partial^2\langle A_\theta\rangle}{\partial z^2}+\frac{\partial}{\partial\rho}\left[\frac{1}{\rho}\frac{\partial}{\partial\rho}(\rho\langle\phi_A\rangle)\right]\right\}=0. \tag{12}$$

Equations (12) indicate the complexity of the boundary conditions even for a case of simple geometry. A coupling between the scalar and vector waves is revealed by Eqs. (12). This undesirable feature severely restricts the geometrical arrangements for which solutions are feasible.

It may be noted at this point that, although Eqs. (12) apply at both boundary surfaces and thus consist of four equations, Eqs. (6) and (9) involve only two functions which are to be determined by the boundary conditions. This implies an overdetermined system. However, the same symmetry considerations which permitted solutions of the wave equations to be written in the form (4) and (6) insure the fact that the same set of two equations results from application of the boundary conditions at either surface.

It is now possible to substitute Eqs. (6) and (9) into (12) and solve the resultant set of simultaneous linear equations for the functions $A(m)$ and $B(m)$. However, a very helpful simplification occurs if one expresses the solution of the scalar wave equation in a slightly different form. The possibility exists of setting up the expression for the scalar wave in terms of an infinite set of images as well as the source term and the integral term in Eq. (9) which may be interpreted as a perturbation caused by the boundary. This possibility is suggested more obviously in the case of a point source in a semi-infinite elastic medium; in this case there is but one image term, which may be readily identified.[3]

IV. THE SET OF IMAGES

As indicated in the previous section, the scalar wave may be expressed as the sum of two terms, one representing the source and an infinite set of images, and the other, analogous to the integral in (9), representing a perturbation caused by the presence of the boundaries. Thus,

$$\langle\phi\rangle=\int_0^\infty A(m)\cosh K_L z J_0(m\rho)dm+\langle\phi_{sI}\rangle. \tag{13}$$

Here $\langle\phi_{sI}\rangle$ denotes the contribution of the source and the infinite set of images. Comparison with Eq. (9) shows that the effect of *not* extracting the images would manifest itself in a change of $A(m)$ to $C(m)$ and a corresponding change of $\langle\phi_{sI}\rangle$ to $\langle\phi_s\rangle$.

Figure 1 shows schematically only the first two images on either side of the slab, although the sequence continues to infinity in both directions.

Introducing the change of variable

$$m=pu$$

and letting $a=(u^2+1/V_L^2)^{\frac{1}{2}}$ and $b=(u^2+1/V_T^2)^{\frac{1}{2}}$ we have

$$K_L=pa \quad \text{and} \quad K_T=pb.$$

The source term (8) then becomes

$$\langle\phi_s\rangle=\int_0^\infty\frac{Nu}{pa}e^{-paz}J_0(m\rho)dm \quad (z>0) \tag{14a}$$

$$\langle\phi_s\rangle=\int_0^\infty\frac{Nu}{pa}e^{paz}J_0(m\rho)dm \quad (z<0), \tag{14b}$$

where the integrands have been written in a form mixing m and u for reasons of future convenience. Expressions representing the infinite sequence of images shown in Fig. 1 may now be written down. For $z>0$, we have

$$-e^{-pa(D+z)}+e^{-pa(2D+z)}-e^{-pa(3D+z)}+\cdots, \tag{15a}$$

while for $z<0$,

$$-e^{-pa(D-z)}+e^{-pa(2D-z)}-e^{-pa(3D-z)}+\cdots, \tag{15b}$$

[6] I. S. Sokolnikoff, *Mathematical Theory of Elasticity* (McGraw-Hill Book Company, Inc., New York, 1946).

where each term in the series is an abbreviation for an integral of the form (14a) or (14b). The result is obtained by summing the geometric series given by the sum of Eqs. (15a), (15b), and the appropriate term of Eq. (14).

$$\langle\phi_{sI}\rangle=\int_0^\infty \frac{Nu}{pa}\frac{\sinh pa\left(z+\frac{D}{2}\right)}{\cosh\frac{paD}{2}}J_0(m\rho)dm, \quad z<0 \tag{16a}$$

$$\langle\phi_{sI}\rangle=\int_0^\infty \frac{Nu}{pa}\frac{\sinh pa\left(\frac{D}{2}-z\right)}{\cosh\frac{paD}{2}}J_0(m\rho)dm, \quad z>0. \tag{16b}$$

V. APPLICATION OF THE BOUNDARY CONDITIONS

The boundary conditions (12) must be satisfied at both surfaces $z=\pm D/2$. As has been pointed out, however, this gives two duplicate pairs of equations so that it is sufficient to consider only the surface $z=-D/2$. Substituting Eqs. (6) and (13) into (12), using (16a) and simplifying the result, one arrives at the following pair of simultaneous equations for $A(m)$ and $B(m)$.

$$\begin{aligned}
&A(m)U\cosh\frac{K_LD}{2}+B(m)2mK_TV_T^2\cosh\frac{K_TD}{2}=0,\\
&-A(m)2mK_LV_T^2\sinh\frac{K_LD}{2}-B(m)U\sinh\frac{K_TD}{2}\\
&\qquad=\frac{2NumV_T^2}{\cosh(K_LD/2)},
\end{aligned} \tag{17}$$

where U is defined by

$$U=p^2+2m^2V_T^2.$$

Thus,

$$\begin{aligned}
A(m)&=\frac{4Nu^3bV_T^4p^3}{\mathfrak{D}}\frac{\cosh(K_TD/2)}{\cosh(K_LD/2)}\\
B(m)&=-\frac{2NUuV_T^2p^3}{\mathfrak{D}},
\end{aligned} \tag{18}$$

where $U_p=U/p=1+2u^2V_T^2$ and

$$\begin{aligned}
\mathfrak{D}=&-U_p^2\sinh\frac{K_TD}{2}\cosh\frac{K_LD}{2}\\
&+4m^2K_LK_TV_T^4\sinh\frac{K_LD}{2}\cosh\frac{K_TD}{2}.
\end{aligned}$$

Substituting Eqs. (13), (16a) and (9b) into (2) and specializing to the epicenter $\rho=0$, $z=-D/2$, we obtain

$$\frac{\langle s_z\rangle}{p}=\int_0^\infty \frac{-NuU_p\sinh(pbD/2)du}{-U_p^2\sinh(pbD/2)\cosh(paD/2)+4u^2abV_T^4\sinh(paD/2)\cosh(pbD/2)} \tag{19}$$

$$\langle s_\rho\rangle=0.$$

If we had not specialized to the epicenter, the presence of $J_0(pu\rho)$ would introduce even more serious difficulties than those presented by Eq. (19). Equation (19) is the formal solution of the problem. The integration over u and the Laplace inversion remain to be performed.

VI. EXPANSION OF THE INTEGRAND

As already noted, Eq. (19) presents many difficulties. The variable of integration u occurs in the arguments of the hyperbolic functions (more precisely in a and b), and the determination of the roots of the denominator for the purpose of evaluating Eq. (19) as part of a contour integral is a formidable task. If the Laplace inversion is attempted prior to the integration over u, the difficulties are just as great, since the transform variable p also appears in the argument of the hyperbolic functions. However, one observes in Eq. (19) that the transform variable p occurs *only* in the arguments of the hyperbolic functions. This suggests the possibility of writing the hyperbolic functions in exponential form and in some way expanding the denominator into a series of negative exponentials. Since according to the translation theorem of the Laplace transform a negative exponential corresponds to a delay in time determined by the exponent, one intuitively expects a sequence of this sort to represent the series of waves which are successively reflected from the bottom surface of the slab.

Every wave incident upon a surface of discontinuity gives rise, in general, to both longitudinal and transverse reflected waves. Consequently, the sequence of exponentials will be infinite and will contain terms corresponding to all possible combinations of longitudinal and transverse reflections. The method of successively reflected waves, successfully used in one-dimensional problems,[7] will be applied to the present case of spherical waves.

Equation (19) may be written as

$$\frac{\langle s_z\rangle}{p}=2N\int_0^\infty \frac{e^{-paD/2}udu}{U_p(1+e^{-paD})\left(1-\bar{R}\frac{\tanh(paD/2)}{\tanh(pbD/2)}\right)}, \tag{20}$$

[7] H. S. Carslaw and J. C. Jaeger, *Operational Methods in Applied Mathematics* (Clarendon Press, Oxford, 1941).

where $\bar{R}=4u^2abV_T^4/U_p^2$. By virtue of the definitions of a and b, and the fact that $V_T^2<V_L^2$, it follows that

$$\frac{\tanh(paD/2)}{\tanh(pbD/2)}<1 \quad \text{for } u<\infty,\ p \text{ real.}$$

Also,

$$\lim_{u\to\infty}\frac{\tanh(paD/2)}{\tanh(pbD/2)}=1.$$

It is readily seen that

$$\bar{R}<1 \quad \text{for } u<\infty$$

and

$$\lim_{u\to\infty}\bar{R}=1.$$

We may therefore expand

$$\frac{1}{1-V}=1+V+V^2+\cdots \quad V<1, \tag{21}$$

where

$$V=\bar{R}\frac{\tanh(paD/2)}{\tanh(pbD/2)}. \tag{22}$$

Also,

$$\frac{1}{1+e^{-paD}}=1-e^{-paD}+e^{-2paD}-\cdots. \tag{23}$$

Since Eqs. (21) and (23) are both absolutely and uniformly convergent, their product also possesses these properties. The reason for emphasizing this fact is that the justification of a subsequent rearrangement of the order of the terms requires absolute convergence, while an interchange of the order of summation and integration will necessitate uniform convergence.[8]

The restriction to real p may be questioned. It can be shown that if the Laplace transform of a function is known at the points $p=n, n+1, n+2, \cdots\infty$, where n is a finite integer, the function is uniquely determined;[9] consequently, p may be confined to the positive real axis with no loss in generality.

By expanding the ratio of hyperbolic tangents in Eq. (22) in terms of exponentials, it is possible to express Eq. (20) as a series of integrals

$$\frac{\langle s_z\rangle}{p}=2N\sum_{i=1}^{\infty}\int_0^{\infty}f_i(u)e^{-pg_i(u)}du, \tag{24}$$

where summation and integration have been interchanged. It is to be noted that p appears only as a factor in the exponential, and nowhere else in the integral. This is a fortuitious occurrence and permits an explicit determination of the Laplace inversion.

Consider the general term of the series

$$I_i=\int_0^{\infty}f_i(u)e^{-pg_i(u)}du. \tag{25}$$

Make the change of variable

$$t=g_i(u). \tag{26}$$

Then

$$I_1=\int_{g_i(0)}^{g_i(\infty)}q(t)e^{-pt}dt,$$

where $q(t)$ is the result of substituting u in terms of t in Eq. (25). It turns out in every case that $g_i(\infty)=\infty$. Thus we have

$$I_i=\int_0^{\infty}q(t)H[t-g_i(0)]e^{-pt}dt,$$

where $H(t-t')$ is the unit step function. Since by definition of the Laplace transform

$$I_i=\mathfrak{L}\{q(t)H[t-g_i(0)]\}=\int_0^{\infty}q(t)H[t-g_i(0)]e^{-pt}dt,$$

we have

$$\mathfrak{L}^{-1}I_i=q(t)H[t-g_i(0)].$$

In this way one obtains the inversion of Eq. (24) by inspection. The above artifice, first used by Cagniard[3] permits the utilization of the integration over u in Eq. (25) in such a way that two integrations, that over u and the inversion integral, are obviated. Each term in Eq. (24) may be treated by the same straightforward procedure, although the algebra is rather complicated.

In making the change of variables Eq. (26), the lower limit of the integral Eq. (25) is changed from zero to a positive number which corresponds to an arrival time of one of the infinite number of waves successively reflected from the lower surface. That is, for $t<g_i(0)$, $I_i=0$, while for $t>g_i(0)$, $I_i\neq 0$. This strongly suggests that each integral is the mathematical representation of one of the reflected waves.

Each term of the series (24) will be designated according to the wave which has the same arrival time. For example, LL denotes the longitudinal wave first reflected from the lower surface and so on. The angular brackets surrounding the designating letters denote the transform of the quantity. The first four terms of the series are

$$\frac{\langle L\rangle}{P}=-2N\int_0^{\infty}\frac{U_pe^{-paD/2}}{\Delta_0}udu, \tag{27}$$

$$\frac{\langle LT\rangle}{P}=2N\int_0^{\infty}\frac{U_p\Delta_+}{\Delta_0^2}e^{-paD/2}e^{-pbD}udu+2N\int_0^{\infty}\frac{U_pe^{-paD/2}e^{-pbD}}{\Delta_0}udu, \tag{28}$$

[8] The writer wishes to thank the referee for pointing out the incompleteness of the argument of absolute convergence as presented in this paper. The series expansion is actually a doubly infinite series while the theorems invoked here apply only to the usual singly infinite series. A rigorous convergence proof is being constructed since it is important to have a firm foundation for the unexpected results. The rigorous proof will be given at a later date. Meanwhile, the justification will have to be on physical grounds.

[9] This can be shown with the help of D. V. Widder, *The Laplace Transform* (Princeton University Press, Princeton, 1941), pp. 59–63.

$$\frac{\langle LL\rangle}{P}=-2N\int_0^\infty \frac{U_p\Delta_+}{\Delta_0^2}e^{-\frac{3}{2}paD/2}udu, \tag{29}$$

$$\frac{\langle LLL\rangle}{P}=-2N\int_0^\infty \frac{U_p\Delta_+^2}{\Delta_0^3}e^{-\frac{5}{2}paD/2}udu, \tag{30}$$

where the quantities in Eqs. (27) through (30) are expressed in terms of $x=u^2V_L^2$ as follows:

$$\Delta_0=-(1+2x/3)^2+4x/9(1+x)^{\frac{1}{2}}(3+x)^{\frac{1}{2}},$$

$$\Delta_+=(1+2x/3)^2+4x/9(1+x)^{\frac{1}{2}}(3+x)^{\frac{1}{2}},$$

$$\Delta_0'=-4/3(1+2x/3)+4/9\left[\frac{2x^2+6x+3}{(1+x)^{\frac{1}{2}}(3+x)^{\frac{1}{2}}}\right],$$

$$\Delta_+'=4/3(1+2x/3)+4/9\left[\frac{2x^2+6x+3}{(1+x)^{\frac{1}{2}}(3+x)^{\frac{1}{2}}}\right],$$

$$U_p=1+2x/3.$$

These quantities depend upon the ratio V_L/V_T, and therefore upon Poissons' ratio σ, since

$$\sigma=\frac{\frac{1}{2}-(V_T/V_L)^2}{1-(V_T/V_L)^2}.$$

The above expressions for Δ_0, Δ_+, Δ_0', Δ_+', and U_p hold for the special case $\sigma=0.25$. Calculations for other values of σ are underway.

The transformations (26) may now be applied to Eqs. (27) through (30) and the Laplace inversion along with the corresponding arrival time determined for each integral in the manner described above. The resulting expressions must then be differentiated with respect to time, because of the factor $1/p$ on the left side of Eqs. (27) through (30). Although the presence of the step function in the inverted expression leads upon differentiation to a delta-function singularity, this is an artificial effect introduced by the idealization of the source as a step function. The delta function may thus be disregarded. The first four terms finally become

$$L=-\frac{16N}{D^2}\left\{\frac{7+6x}{6\Delta_0}-\frac{(3+5x+2x^2)\Delta_0'}{3\Delta_0^2}\right\}, \tag{31}$$

$$LL=-\frac{16N}{9D^2}(1+x)\left\{\frac{2}{3}\frac{\Delta_+}{\Delta_0^2}+\frac{U_p\Delta_+'}{\Delta_0^2}-\frac{2U_p\Delta_+\Delta_0'}{\Delta_0^3}+\frac{1}{2}\frac{U_p\Delta_+}{\Delta_0^2(1+x)}\right\}, \tag{32}$$

$$LLL=-\frac{16N}{25D^2}(1+x)\left\{\frac{2}{3}\frac{\Delta_+^2}{\Delta_0^3}+\frac{2U_p\Delta_+\Delta_+'}{\Delta_0^3}-\frac{3U_p\Delta_0'\Delta_+^2}{\Delta_0^4}+\frac{1}{2}\frac{U_p\Delta_+^2}{\Delta_0^3(1+x)}\right\}, \tag{33}$$

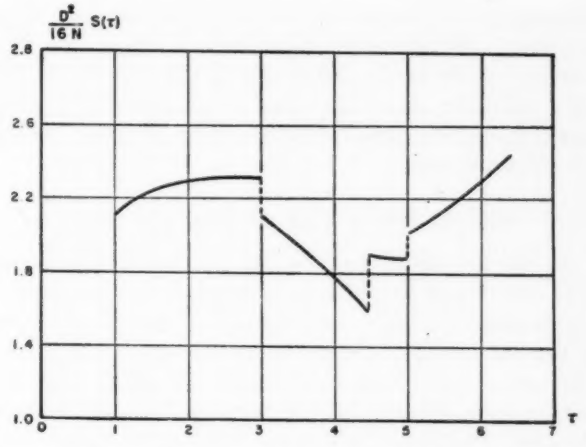

FIG. 2. Displacement at the epicenter of the slab for Poisson's ratio equal to 0.25.

$$LT=\frac{128N}{27D^2}\left\{\frac{\delta}{\Delta_0^2\alpha^2}-\frac{2\Delta_0'\gamma}{\Delta_0^3\alpha^2}-\frac{1}{2}\frac{\beta\gamma}{\Delta_0^2\alpha^3(1+x)^{\frac{1}{2}}(3+x)^{\frac{1}{2}}}\right\}(1+x)^{\frac{1}{2}}(3+x)^{\frac{1}{2}}, \tag{34}$$

where

$$\alpha=(3+x)^{\frac{1}{2}}+2(1+x)^{\frac{1}{2}},$$

$$\beta=2(3+x)^{\frac{1}{2}}+(1+x)^{\frac{1}{2}},$$

$$\gamma=2x^4+11x^3+18x^2+9x,$$

$$\delta=8x^3+33x^2+36x+9.$$

Expressions (31) through (34) are plotted in Fig. 2 as a function of a dimensionless time $\tau=2V_Lt/D$. Because of the difference in the various changes of variable (26) for the four terms (31) through (34), the relation between τ and x is different for each of the 4 cases, namely,

$$\tau=(1+x)^{\frac{1}{2}}, \qquad x=\tau^2-1, \tag{31a}$$

$$\tau=3(1+x)^{\frac{1}{2}}, \qquad x=\tau^2/9-1, \tag{32a}$$

$$\tau=5(1+x)^{\frac{1}{2}}, \qquad x=\tau^2/25-1, \tag{33a}$$

$$\tau=(1+x)^{\frac{1}{2}}+2(3+x)^{\frac{1}{2}}, \qquad x=1/18\{10\tau^2-66-8\tau(\tau^2-6)^{\frac{1}{2}}\}. \tag{34a}$$

In all cases, of course, $x\geq 0$.

The first term (31) is just the result one obtains for the problem of a point source in a semi-infinite elastic medium rather than in a slab. This provides a check on the result. The absolute values of the other terms (32), (33), and (34), however, increase without limit as time increases, although the terms themselves combine to give a well-behaved result.

One very important point has been disregarded in the above discussion, namely, that the upper limit of each

integral in the series is infinite. The expansion (21) is therefore not valid at the upper limit of integration, thus casting doubt on the legitimacy of the procedure. The fact that the procedure may nonetheless be carried through to give correct results will be demonstrated in the next section.

VII. JUSTIFICATION OF THE METHOD

It can be shown that the integral before expansion, Eq. (20), leads to a finite displacement as $t\to\infty$. The establishment of this convergence is important in view of the divergence of the individual terms (32), (33), and (34) as $t\to\infty$. It then only remains to prove that the results of Sec. 6 are correct even though the expansion of the integrand of Eq. (20) is not valid at the upper limit of integration. Write Eq. (20) as

$$\frac{\langle s_z\rangle}{p}=\int_0^\infty \frac{f(u,p)e^{-puD/2}du}{1-V(u,p)}, \tag{35}$$

where $V(u,p)$ is given by Eq. (22) and

$$f(u,p)=\frac{2Nu}{U_p(1+e^{-puD})}.$$

Now $V\to 1$ as $u\to\infty$ so that the expansion (21) breaks down at the upper limit. If the upper limit is changed from ∞ to a finite value Ω, Eq. (25) becomes

$$\frac{\langle s_z'\rangle}{p}=\int_0^\Omega \frac{f(u,p)e^{-puD/2}du}{1-V(u,p)}$$

$$=\int_0^\infty \frac{f(u,p)H(\Omega-u)e^{-puD/2}du}{1-V(u,p)}. \tag{36}$$

The expansion is now permissible everywhere so that the change of variable corresponding to Eq. (26) may be made for each term and the Laplace inversion performed by inspection. Equation (36) may now be regarded as the exact solution to a different physical problem, which, in the limit $\Omega\to\infty$, becomes identical with the original problem. To determine the other physical problem one must investigate the changes which occur in the original formulation of the problem as a result of the alteration made in the upper limit of the integral. The only change required occurs in the source term, Eq. (8a), since the free wave terms (4) and (6) could just as well involve an integral from zero to Ω as one from zero to infinity. The source of the new problem differs from the source of the original problem by an additive term

$$\int_\Omega^\infty \frac{mdm}{(m^2+p^2/V_L^2)^{\frac{1}{2}}}J_0(m\rho)e^{-K_L|z-l|}.$$

The exponential term causes the integral to become arbitrarily close to zero for sufficiently large Ω. Thus, by taking Ω large enough, the difference between the sources for the two problems may be made vanishingly small.

It is now shown that the result is exact. Equation (36) is a function of p and Ω. For a given p, Eq. (36) may be plotted as a function of Ω, $0<\Omega<\Omega_1$, where $\Omega_1>\Omega_0$. Then the value of the function for $\Omega\leq\Omega_0$ is independent of the value of Ω_1. Since the sources of the two problems differ by a vanishingly small amount for Ω_1 sufficiently large, the result is exact.

Another method of justifying the expansion makes use of a convergence factor $e^{-\epsilon u}$, where ϵ is a positive number small enough so that $e^{-\epsilon u}$ has no influence except as $u\to\infty$. One then writes Eq. (35) as

$$\frac{\langle s_z\rangle}{p}=\int_0^\infty \frac{f(u,p)e^{-puD/2}du}{1-V(u,p)e^{-\epsilon u}}.$$

As $u\to\infty$, the convergence factor insures the fact that $V'=Ve^{-\epsilon u}<1$, thus making an expansion of $1/1-V'$ valid over the entire range of integration including its end points. One must verify that the introduction of $e^{-\epsilon u}$ does not alter the value of the integrand at the point at which difficulty occurs. This condition is fulfilled, for $f(u,p)$ behaves as $(1/u)$ for large u, so that

$$\lim_{u\to\infty} f(u,p)=0.$$

The introduction of the convergence factor does not change this result and the limit is approached in the same way. If now the procedure leading to Eqs. (31) through (34) is retraced with the convergence factor included in the definition of $\bar{R}$, everything proceeds as before so that in the limit $\epsilon\to 0$, the result agrees with that previously obtained.

ACKNOWLEDGMENT

The author wishes to express his sincere thanks to Dr. W. Garvin for interesting him in this problem and for calling his attention to the work of L. Cagniard. He is grateful to Professor A. Banos, Dr. L. Knopoff, Professor David Saxon, and Dr. Garvin for discussions and suggestions and to Professor L. B. Slichter and the Institute of Geophysics at the University of California at Los Angeles for financial aid in the form of a research assistantship which made this work possible.

Letters to the Editor

Spatially Alternating Magnetic Fields for Focusing Low-Voltage Electron Beams

J. R. PIERCE
Bell Telephone Laboratories, Murray Hill, New Jersey
(Received June 10, 1953)

WHEN Livingston, Courant, and Snyder[1] of the Brookhaven National Laboratory published their paper on the "Strong Focusing Effect," A. M. Clogston and R. W. Sears of these Laboratories suggested that the principle of alternating field focusing was quite general and should equally well apply to low-velocity electron beams in the presence of space charge. Analysis and experimental work carried out through the joint efforts of several people have indicated that while systems such as those described[1] might indeed be used to focus low-voltage electron beams, axially symmetrical periodic magnetic fields, which are everywhere converging, may be more advantageous.[2] The equations for electron motion in such periodic axially symmetrical fields have been solved using the differential analyzer at the Bell Laboratories. The solutions confirm that a dense electron beam can be stable in such fields. In such fields, stable flow occurs when the rms value of the field is nearly equal to the uniform "Brillouin" field which is associated with conventional electron flow.[3] The use of periodic axially symmetrical magnetic fields has been found to have hitherto unrecognized advantages. If electromagnets are used, a somewhat higher mean-square field can be attained with a given number of ampere turns by using a periodic field than by a uniform field, but the practical advantage may not be great. However, when permanent magnets are used the advantage of a periodic field in which the direction of the axial field reverses periodically, so that the average axial field is zero, is very marked, as one can see from the following argument:

Consider the work done in assembling a series of short permanent magnets. When they are assembled alternately N−S, S−N, N−S, work must be done on the system to overcome their mutual repulsion, whereas if they are assembled N−S, N−S, N−S, work is done by the system on the mutual attraction of the magnets. Thus, in the former case of an alternating field, energy is added to the field by assembling the magnets, and this leads to a higher field intensity for a given set of magnets. Comparing alternating *versus* unidirection fields in another way, alternating fields die off at a much faster rate in the transverse direction than do unidirectional fields, and this means that for alternating fields there is less magnetic stored energy away from the axis. Thus, one can produce a given mean-square magnetic field with a much smaller magnet, and at the same time reduce the stray field external to the structure. As an illustration of this weight-saving feature, we have in the past focused an electron beam 6 in. in length and 0.080 in. in diameter having a current of 20 ma at 1700 volts, using a uniform field magnet which weighed 38 pounds. The same beam was focused using a series of ring magnets which produced a periodic field of the same rms value, with a magnet weight of 1 pound 5 ounces. This alternating field was down to 2 percent of its maximum value $\frac{1}{2}$ in. from the magnets, compared with 15 in. for the magnets giving a uniform field.

A feature of periodic focusing which was brought out in the experimental work is the existence of "stop bands." When the current transmitted through the tube is plotted *versus* magnetic field, one obtains a curve which begins at zero and reaches a maximum at an optimum value of magnetic field somewhat above the Brillouin value. However, as the magnetic field is increased further the transmitted current begins to decrease until at a critical value of the magnetic field the current drops suddenly to zero. If the magnetic field is increased still further, the transmitted current will again rise to its maximum value in a second "pass band."

As the magnetic field is increased above the optimum value, the beam radius varies along the beam length with a period related to the Larmor frequency associated with the rms value of the magnetic field. When the period of the radial variations approaches the period of the magnet structure, the resonance causes the amplitude of the radial variations to increase without limit, resulting in zero collector current at the "stop band."

[1] Livingston, Courant, and Snyder, Phys. Rev. **88**, 1190–1196 (1952).
[2] Periodic electric focusing has been used, notably: W. C. Hahn and G. F. Metcalf, Proc. Inst. Radio Engrs. **27**, 106–116 (1939). All axially symmetrical electric lenses have succeeding regions of convergence and divergence.
[3] J. R. Pierce, *Theory and Design of Electron Beams* (D. Van Nostrand Company, Inc., New York), 1949, Chapter IX.

Mach Reflexion of Shocks at Arbitrary Incidence*

H. F. LUDLOFF AND M. B. FRIEDMAN
Guggenheim School of Aeronautics, New York University, New York, New York
(Received April 30, 1953)†

ALTHOUGH the problem of Mach reflexion at glancing incidence may be considered as solved by linearized theories developed by Bargman, Lighthill and by Ting and Ludloff, the Mach reflection of shocks from finite corners (see Fig. 1) leads to a difficult nonlinear boundary value problem which may be stated, in conical coordinates $\xi=x/t$, $\eta=y/t$, as follows:

(a) Differential equations
Conservation of mass:

$$(\rho U)_\xi+(\rho V)_\eta+2\rho=0, \tag{1}$$

Conservation of momentum:

$$U\cdot U_\xi+V\cdot U_\eta+U=-p_\xi/\rho, \tag{2}$$

$$U\cdot V_\xi+V\cdot V_\eta+V=-p_\eta/\rho, \tag{3}$$

Conservation of energy:

$$U\cdot S_\xi+V\cdot S_\eta=0. \tag{4}$$

Here $U=u-\xi$, $V=v-\eta$ are the components of vector $\bar{Q}$ and u, v, are the fluid velocities at an point ξ, η.

From Eq. (4) it follows that the "streamlines"

$$V/U=(d\eta/d\xi)_S. \tag{5}$$

are isentrops. After substituting the entropy S in terms of p and ρ, the above system represents four equations for the four unknown dependent variables U, V, p and ρ. Of the four characteristics, two are a real double root, namely the isentrops, the other two are imaginary.

(b) Boundary Conditions. The location of the reflected and Mach shocks and that of the slipstream are not known *a priori*.

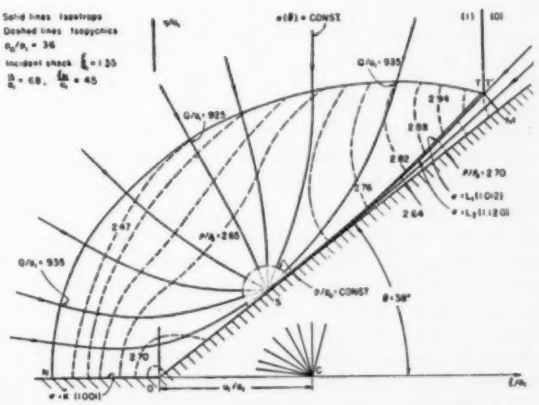

FIG. 1.

At these boundaries of unknown location, the four conservation laws must be fulfilled. This yields four conditions on the shocks and two conditions on the slipstream, the other two being automatically fulfilled. On the symmetry-line and on the wall only one condition is to be imposed, namely, the usual requirement of tangential flow velocity. To solve the problem, a shock and slipstream configuration has to be assumed. The problem would be overdetermined, if the fulfillment of all four conservation laws would be required at the selected boundary. Consequently, one boundary condition has to be dropped temporarily; it will serve later on as a check for the assumed boundary form. Taking the preceding considerations into account, there must be *three* conditions on the shocks, *one* on the wall and *one* on the slipstream.

To carry out a numerical solution of this nonlinear system, the afore mentioned *true* boundary conditions have to be supplemented by so-called *dependent* conditions, which are an expression of the validity of the differential equations at the boundary.

Hence, on the reflected and Mach shocks, the *three true* boundary conditions may be written:

$$\begin{aligned}(q_n)_B &= A_{0,1}(\xi, \eta, \alpha, \rho_{0,1}, p_0, q_{0,1}),\\ (q_\tau)_B &= B_{0,1}(\xi, \eta, \alpha, \rho_{0,1}, p_0, q_{0,1}),\\ (\rho)_B &= C_{0,1}(\xi, \eta, \alpha, \rho_{0,1}, p_0, q_{0,1}),\end{aligned} \tag{6}$$

where B = boundary, 0 = in front of incident shock, 1 = behind incident shock, and the quantities on the right are known.

A linear combination of the momentum equations yields the following *one dependent* boundary condition for the boundary value p_B:

$$\left(\frac{\partial p}{\partial n}\right)_B = -\rho\cdot\cos^2\alpha\cdot\left\{[(u-\xi)+(v-\eta)\cdot\operatorname{tg}\alpha]\times\left[\frac{\partial u}{\partial s}\cdot\operatorname{tg}\alpha-\frac{\partial v}{\partial s}\right]+[(u-\xi)\cdot\operatorname{tg}\alpha-(v-\eta)]\times\left[\frac{\partial u}{\partial n}\cdot\operatorname{tg}\alpha-\frac{\partial v}{\partial n}\right]\right\}, \tag{7}$$

where s is parallel, n perpendicular to the boundary. Since, in difference form, $(\partial p/\partial n)_B = (p_B - p_i)/\Delta n$, p_B may be expressed by (7) in terms of the pressure in the interior p_i and determinable and known quantities.

On wall and slipstream, the *one true* boundary condition is

$$\frac{V}{U} = \operatorname{tang}\theta(\xi,\eta) = V\left(\frac{d\eta}{d\xi}\right)_S;\ \theta = \text{angle of boundary, with } \xi\text{-axis}, \tag{8}$$

because for both boundaries $Q_n = 0$, by definition. This proves that wall and slipstream are isentrops.

The *three dependent* conditions are, at the wall,

$$\left(\frac{\partial p}{\partial n}\right)=0;\ \left(\frac{\partial p}{\partial s}\right)=-\rho U\cdot(U_s+\xi_s)\cdot\sec^2\theta,\quad\text{and}\quad p/\rho^\gamma=\sigma_1. \tag{9}$$

For the slipstream, the three analogous conditions are slightly more complicated.

The preceding formulation of the problem is sufficient to carry through a numerical difference scheme (to be described elsewhere), if a plausible boundary configuration is assumed. The isentrops shown in the diagram have been computed by using the experimental isopycnics. By this procedure, Eqs. (1) to (4) may be reduced to two equations for U and V, by eliminating p from (2) and (3) and considering the ρ field as known. The result of the computations confirms the following general properties derived analytically.

(1) By (8), the slipstream is an isentrop; more exactly two isentrops because of different values for σ on either side. The symmetry-line and wall section *NOS* represent another isentrop, which meets the slipstream at S. The value of σ on all three isentrops can be seen to differ due to different strengths of the shocks at N, T, and T'. Outside the disturbed region *NOST*, the streamlines $\bar{Q}$ are rays converging toward C. In the linearized case of a shallow corner ϵ, in which the disturbance is of $0(\epsilon)$, these rays continue radially all the way through. For large corners the radial character of the isentrops will be disturbed. Since the resulting curves can not turn around and continue outwardly, they have to meet all at the intersection point of slipstream and wall. In other words, at S, there is a directional singularity of the entropy.

(2) The "ray behavior" of the isentrops in this vicinity may be written as $V/U = (\eta-\eta_0)/(\xi-\xi_0)$. If this is substituted into the momentum equations, it follows that $V/U = -(d\xi/d\eta)_{p=C}$, i.e., the isobars are circles about this point, of the form: $p = p_0 + p_1\cdot r^3$, so that $(\partial p/\partial r)_{r=0}=0$. This means that the intersection of slipstream and wall should occur at a minimum of the pressure distribution of the wall; this feature is confirmed by many of Bleakney's interferograms. Furthermore note that $Q=0$ for any isentrop at S; otherwise, there would be a Q_n component perpendicular to the wall. Hence the Q values along any isentrop increase from 0 to approximately 0.9.

(3) The vicinity of the singular point S has been investigated analytically, by resolving the four dependent variables into radial and tangential components and expanding them in terms of polar coordinates. In this way a recursion formula between the various coefficients is obtained. While the pressure field is seen to be regular near S, the density field can be shown to have a directional singularity, represented by

$$\rho=\left[\frac{p_0}{\sigma(\theta)}\right]^{1/\gamma}\cdot\left[1+\frac{p_1(\theta)}{\gamma\cdot p_0}\cdot r^3+\cdots\right].$$

This means that several isopycnics should originate at S. This is not visible in the experimental diagram, because the variation of $\sigma(\theta)$ is extremely small, so that the flow inside *TSON* is almost irrotational here. However, in other of Bleakney's interferograms, where $\sigma(\theta)$ varies widely, the "ray behavior" of the isopycnics can be clearly discerned.

* Investigation supported by Mechanics Branch of the U. S. Office of Naval Research and Applied Mathematics Division of the Naval Ordinance Laboratory.
† Received in Editorial Office on May 11, 1953.

Effect on Distribution of Lattice Defects within Crystals of Linear Expansion and X-Ray Lattice Constant*

P. H. Miller, Jr., and B. R. Russell
Department of Physics, University of Pennsylvania, Philadelphia, Pennsylvania
(Received June 24, 1953)

CONCERNING the difference between the change in x-ray lattice constant and in linear dimensions produced by lattice defects discussed in our previous article[1] it seems clear that an error was made in one of the original calculations for single defects located near the surface which led us to draw an incorrect conclusion in the case of randomly distributed defects. For the case of randomly distributed Frenkel defects the relative changes in x-ray lattice constant and in linear dimensions are virtually the same. Detailed calculations taking into account the total distortion produced by 10 random defects in an idealized crystal of 729 atoms have been carried out with a card program calculator and indicate a difference in the two relative expansions of only 10 or 20 percent on the average. Thus an appreciable difference is to be expected only if Schottky defects occur.

The only cases in which Frenkel defects might give rise to an x-ray expansion differing from the macroscopic linear expansion are those for which the distribution of defects is spatially nonuniform within the crystal. Thus, when the crystals are small so that the x-rays penetrate them quite completely and at the same time due to incomplete diffusion of the defects to or from the surface there is a larger concentration of defects near the centers of the crystals, then the x-ray expansion may be as much as a factor of two larger than that calculated from density changes. Thus, while the x-ray expansion may be appreciably larger in this

special case, it is not generally true that it would be larger. Indeed, the detailed calculations show that for the opposite case (larger concentration of defects near the surfaces) the x-ray expansion may be slightly smaller. In experiments with large crystals it must be remembered that the x-ray measurements depend on the concentration of defects near the reflecting surface on account of the slight penetration of the x-rays while the macroscopic expansion measurements involve the average concentration throughout the crystal; therefore, comparisons of the two expansions are quite meaningless unless the experimental conditions are such that the spatial distribution of defects within the crystal may be considered as known.

The authors are indebted to J. D. Eshelby whose work prompted us to make these further calculations and to locate our original error. We wish also to acknowledge the assistance of Lester Spandorfer and Betty Schoff of the University of Pennsylvania Computing Center.

* This work was supported by Contract AF 18(600)-561 with the Air Force.

[1] P. H. Miller, Jr., and B. R. Russell, J. Appl. Phys. 23, 1163 (1952).

Geometrical and Apparent X-Ray Expansions of a Crystal Containing Lattice Defects*

J. D. Eshelby
Department of Physics, University of Illinois, Urbana, Illinois
(Received June 24, 1953)

THE results reported by Miller and Russell[1] may be illustrated by a direct calculation for a spherical crystal. Using the notation of their previous paper[2] the displacement caused by a point imperfection is $\Delta\mathbf{r}=A(a/r)^3\mathbf{r}$, and the geometrical volume change it produces is $\Delta V_G=\int\Delta\mathbf{r}\cdot nd\mathbf{S}=4\pi a^3A$, being proportional to the solid angle subtended by the surface of the crystal at the imperfection. The relative expansion as determined by x-rays is equal to the relative contraction of the reciprocal lattice, $-[\Delta h_1(100)+\Delta h_2(010)+\Delta h_3(001)]$. This may be evaluated with the help of reference 2, Appendix 1, if we allow ourselves to replace sums like ΣL_1^2 and $\Sigma\Delta L_1L_1$ by $a^2\int x^2dv$ and $a^2\int(\Delta r)_x xdv$. The integrals are of the type occurring in potential theory. For an imperfection with position vector ξ relative to the center of a spherical crystal of radius R we easily find the following expression for the apparent volume change as determined by x-rays:

$$\Delta V_X=10\pi Aa^3(1-\xi^2/R^2). \tag{1}$$

When $\xi=0$, $\Delta V_X=2\cdot5\Delta V_G$ as in reference 2, but when $\xi>\sqrt{(3/5)}R$, $\Delta V_X<\Delta V_G$. If there are a large number of defects scattered randomly through the sphere, the mean ΔV_X per defect will be given by replacing ξ^2 in (1) by its mean value over the sphere, namely, $3R^2/5$. Thus the mean ΔV_X is equal to ΔV_G, and the total geometrical and x-ray expansions are equal.

We have neglected the fact that the displacement $\Delta\mathbf{r}=A(a/r)^3\mathbf{r}$ leads to nonvanishing stresses at the surface of the crystal, and so cannot be correct. It happens that for the problem above the necessary additional "image terms" affect ΔV_G and ΔV_X equally. The relation $\Delta V_G=\Delta V_X$ can in fact be established for a body of arbitrary shape uniformly filled with point defects, but only if the image terms are included. These terms make an important contribution. In fact,

$$\Delta V_G=\Delta V_X=4\pi a^3A\cdot\frac{3(1-\sigma)}{1+\sigma} \tag{2}$$

times the number of imperfections. The factor involving σ (Poisson's ratio) is about 1.5 for metals and 1.8 for alkali halides. For ΔV_G the result (2) has been given by Seitz.[3]

We hope to publish a more detailed account later.

* Work supported by the U. S. Office of Naval Research.
[1] P. H. Miller, Jr., and B. R. Russell, J. Appl. Phys. 24, 1248 (1953).
[2] P. H. Miller, Jr., and B. R. Russell, J. Appl. Phys. 23, 1163 (1952).
[3] Frederick Seitz, Revs. Modern Phys. 18, 384 (1946).

Combustion Rate of Artificial Graphites from 700°C to 2000°C in Air

Jun Okada and Tatsuo Ikegawa
Technical Research Laboratory, Tokai Electrode Manufacturing Company, Fujisawa, Japan
(Received May 18, 1953)

THE combustion rate of artificial graphites, which are self-heated from 700°C up to 2000°C in 1-atmos air of room temperature, were measured.

The cylindrical specimens of artificial graphites, which have 10 mm in diameter and 100 mm in length, were held horizontally between two artificial graphite electrodes and heated up to 2000°C in 1-atmos air by passing the electric current through the specimen and the electrodes. Heat was produced uniformly along the specimen by the resistance of the specimen itself, and also at both ends of the specimen where contact resistance prevailed. The temperature distribution along the specimen was comparatively uniform except for the parts of 2 cm length from both ends of the specimen. After the temperature of the specimen had been increased rapidly up to the desired temperature, it was kept at this temperature for a time of 5–15 minutes. The temperatures were directly measured along the specimen by an optical pyrometer and the average temperature of the part where the combustion rate should be measured [i.e., except for the sections of 2 cm in length from both ends of the specimen] was determined. The specimens were placed in an extensive air space, so the air about the specimen flowed by convection. After cooling the specimen, the ashes were cleaned off, the sections of 2 cm length from both ends were cut off and the weight of the remaining specimen was measured. Initial weight of that part was determined in proportion to the length from the weight of the initial total specimen.

The combustion rate, which was expressed by the weight loss per unit apparent surface area and unit time, was calculated from the measured weight loss percent by the following equation in this case of cylindrical specimens:

$$\text{weight loss percent}/100=2kt/r_0\rho_{0_2}-(kt/r_0\rho_0)^2,$$

where k is the combustion rate gram/cm/sec, r_0 is the initial radius of the specimen in cm, ρ_0 is the apparent density of the specimen in gram/cm³, and t is the combustion time in sec.

Typical curves among the many similar curves measured for several grades of artificial graphites are indicated in Fig. 1.

Generally, the combustion rate of carbon is controlled by the chemical activity and diffusion velocity. Recently, A.C. Riddiford[1] reported that the equation for the rate of heterogeneous reaction as a function of the temperature, (which is based on the assumption that the measured rate of the reaction depends on the rate of the chemical reaction and the rate of diffusion of the reactant) agrees with the earlier results[2] measured by Tu, Davis, and Hottel for the

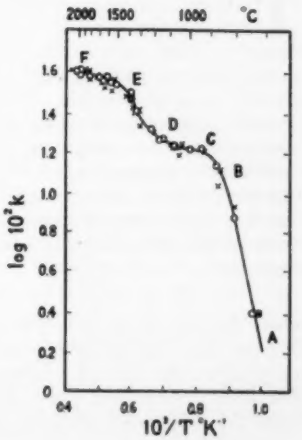

FIG. 1. Log 10^2k vs $1/T$ for the combustion of artificial graphites in air. k = combustion rate in mg/cm²/sec; T = absolute temperature.

combustion rate of a carbon sphere in air stream up to 1450°C. Results measured under our conditions agree with Riddiford's equation to about 1200°C, but do not agree with it from 1200°C to 2000°C.

This deviation from Riddiford's equation (*DE* indicated in Fig. 1) cannot be explained by the fact that the air velocity about the specimen increases somewhat by convection, because, if it depends on this fact, the curves should continuously increase without a step *DE-EF* (indicated in Fig. 1). It also cannot be explained by a turbulent flow.

Recently, measurements of the combustion rate for several kinds of carbon powders up to 1200°C were reported by H. Honda.[3] According to his reports, the similarity to our results was found for charcoal at lower temperatures, and similar omens were indicated for the other carbons at about 1200°C. H. Honda had described for his results that the transition from "the transport" to "the chemical" control occurs again at the middle temperature range. His explanation, however, seems to be improbable, for the transport control should always act strongly at higher temperatures.

Although the same number of the reactant gas molecules are transported to the surface of the graphite specimen under the same transport control, if a reaction of a different type occurs, the number of carbon atoms removed from the surface should be changed. The transition of the type of reaction with increasingly higher temperatures (1200°C–1600°C) was indicated by L. Meyer,[4] and E. Wicke,[5] although these should be discussed further. In Riddiford's equation, only the increase of the rate of chemical reaction was considered, but the type of reaction was not considered.

Therefore, it may be predicted that the deviation from Riddiford's equation depends on the fact that the transition of the type of reaction from one to another occurs under the condition of transport control. It is interesting that the slope of *CD* is approximately equal to that of *EF* in Fig. 1. This fact indicates that the rate of combustion follows Riddiford's equation in the range of the uniform type reaction.

Further investigation is necessary to confirm our prediction, however the above mentioned results are industrially useful.

[1] A. C. Riddiford, J. Phys. Chem. **56**, 745 (1952).
[2] Tu, Davis, and Hottel, Ind. Eng. Chem. **26**, 749 (1934).
[3] H. Honda, J. Fuel Soc. Japan **30**, 231 (1951).
[4] L. Meyer, Z. Elektrochem. **17**, 385 (1932).
[5] E. Wicke, Z. Elektrochem. **56**, 414–20 (1952).

A Simplified Calculation for Dolph-Tchebycheff Arrays

G. J. VAN DER MAAS
Division of Radio and Electrical Engineering, National Research Council, Ottawa, Canada
(Received April 13, 1953)

THE methods given by Dolph[1,2] and by Barbiere[3] for finding the current distribution in an equispaced broadside array require a great deal of calculation with numbers having many significant figures, even though in the final result only engineering accuracy may be required. The amount of computational labor becomes prohibitive when the number of radiators exceeds about twenty-four. The main difficulty in using Barbiere's series to calculate the currents in individual elements arises from the fact that the terms in the series are large and alternate in sign. Barbiere's series is given in terms of powers of a quantity Z_0, which in terms of the side-lobe ratio r and the number of radiators N is given by:

$$T_{N-1}(z_0)=r, \tag{1}$$

where $T_{N-1}(z_0)$ is the Tchebycheff polynomial of degree $(N-1)$. In most practical arrays the value of z_0 differs very little from unity, especially when N is large. This is another reason for the difficulties encountered when the number of radiators is large. From the differential equation for the currents in the radiators the writer has derived a series which is more suitable for numerical calculation than that given by Barbiere, because it is not alternating and written in terms of powers of a variable α, constrained to the interval $0\leq\alpha\leq 1$, while in the practical case where N becomes large, α becomes very small.

If we number the N radiators from left to right $1, 2, \cdots K, \cdots N$, this series for the relative current in the Kth radiator I_N^K, is given by

$$\left.\begin{aligned} &I_N^K=\frac{N-1}{N-K}\sum_{s=0}\begin{bmatrix}N-K\\ s+1\end{bmatrix}\begin{bmatrix}K-2\\ s\end{bmatrix}\alpha^{s+1} \text{ for } K\neq 1 \text{ and } K\neq N;\\ &I_N^K=1 \text{ for } K=1 \text{ and } K=N.\end{aligned}\right\} \tag{2}$$

The variable α is given by

$$\alpha=\frac{z_0^2-1}{z_0^2}=\tanh\left[\frac{\ln[r+(r^2-1)^{\frac{1}{2}}]}{N-1}\right]. \tag{3}$$

The series terminates for $s=N-K-1$ if $K\geqq(N+1)/2$ and for $s=K-2$ if $K\leqq(N+1)/2$. For long arrays and for practical sidelobe levels $\alpha\ll 1$. The special case $\alpha=1$ gives the binomial distribution

$$I_N^K=\begin{bmatrix}N-1\\ K-1\end{bmatrix}.$$

For large N and small α the current distribution approaches a limiting function $L(\xi)$ defined by:

$$L(\xi)\equiv\frac{I_1[v(1-\xi^2)^{\frac{1}{2}}]}{(1-\xi^2)^{\frac{1}{2}}I_1(v)} \text{ for } |\xi|\neq 1,$$
$$L(\xi)\equiv\frac{(N-1)}{2vI_1(v)} \text{ for } |\xi|=1. \tag{4}$$

In this formula, $\xi=(2K-N-1)/N-1$, $v=\ln[r+(r^2-1)^{\frac{1}{2}}]$, and $N=$number of radiators. $I_1(v)=j^{-1}J_1(jv)$ is a modified Bessel function of first order. For practical sidelobe levels $(10<r<100)$ the Eq. (4) is a good approximation even for arrays with as few as 20 radiators.

It is clear from the calculations that the two end radiators play a very important role in the regulation of sidelobe levels and that they must be adjusted very accurately. A complete report of our investigations will be published soon.

[1] C. L. Dolph, Proc. Inst. Radio Engrs. **34**, 335 (1946).
[2] H. J. Riblet and C. L. Dolph, Proc. Inst. Radio Engrs. **35**, 489 (1947).
[3] D. Barbiere, Proc. Inst. Radio Engrs. **40**, 78 (1952).

Some Relations between the Modulus of Rigidity and the Surface and Sublimation Energies

G. C. KUCZYNSKI
Metallurgy Department, University of Notre Dame, Notre Dame, Indiana
(Received May 13, 1953)

THE surface energy of a solid is defined as the energy required to enlarge the surface of a solid by one square centimeter under isothermal conditions. Such an enlargement can be accomplished by shearing a crystal along a certain crystallographic plane. If the energy of a unit shear (such as a single edge dislocation) is denoted by E, the surface energy by γ, and the number of units shears required to produce two surfaces, by n, then

$$nE/2=2\gamma, \tag{1}$$

and

$$E=G\delta^2/2, \tag{2}$$

where G is the modulus of rigidity and δ the interatomic distance (Buerger's vector, if the operation is contemplated as motion of dislocations). Equations (1) and (2) give

$$G\delta/\gamma\cong 8. \tag{3}$$

For actual metals this quotient seems to remain close to the theoretical value 8, as can be seen from Table I. The discrepancies

TABLE I.

Metal	$\gamma \frac{\text{ergs}}{\text{cm}^2}$ [a]	$G \frac{\text{dynes}}{\text{cm}^2}$ [b]	δ(cm)	$\frac{G\delta}{\gamma}$
Cu	1120	4.24×10^{11}	2.55×10^{-8}	9.65
Ag	909	2.80	2.88	9.90
Au	1120	2.80	2.88	7.20
Pt	1820	6.40	2.77	9.70
Sn	538	1.67	2.80	8.80
Zn	772	2.90	2.66	10.00
Cd	546	2.00	3.00	11.00

[a] The values of γ for molten metals close to the melting points, taken from Smithells, *Metals Reference Book*, p. 416.
[b] Smithells, *Metals Reference Book*, p. 414.

can be explained by the fact that the surface energies of molten metals are always lower than those for solid ones. The values of γ for solid copper,[1] silver,[2] and gold[3] are available and they are 1370, 1140, and 1017 ergs/cm², respectively. The quotients $G\delta/\gamma$ computed on this basis are 7.90 for copper, 7.10 for silver, and 7.95 for gold.

Equation (3) can be used further to obtain the relationship between the modulus of rigidity G and energy of sublimation L. From the definition of surface energy

$$\gamma \cong \left(\frac{Z-a}{Z}\right)\frac{L}{N\delta^2},$$

where N is Avogadro's number, Z the number of nearest neighbors in the bulk material, and a the number of nearest neighbors on the surface. This equation together with Eq. (3) yields

$$\frac{L}{GV_0}=\frac{Z}{8(Z-a)},$$

where V_0 is the atomic volume.

The figures in Table II seem to indicate that, for face-centered

TABLE II.

Metal	$G \frac{\text{dynes}}{\text{cm}^2}$	$L \frac{\text{kg cal}}{\text{mole}}$	FV_0(cc)	$\frac{L}{GV_0}$
Cu	4.24×10^{11}	81.7	7.1	1.13
Ag	2.80	69.4	10.0	1.04
Au	2.80	83.0	10.0	1.24
Al	2.70	67.6	10.0	1.04
Pt	6.40	125.0	9.0	0.91
Pd	5.00	110.0	9.3	0.99
Ni	7.00	98.1	6.7	0.89
Sn[a]	1.67	68.0	16.3	1.04

[a] Body-centered tetragonal.

cubic metals,

$$G \cong L/V_0,$$

and that the number of nearest neighbors of the atoms on the surface of these metals is about 10.

[1] Udin, Shaler, and Wulff, Trans. Am. Inst. Mining Met. Engrs. **185**, 186 (1949).
[2] Funk, Udin, and Wulff, Trans. Am. Inst. Mining Met. Engrs. **191**, 1206 (1951).
[3] Buttner, Udin, and Wulff, Trans. Am. Inst. Mining Met. Engrs. **191**, 1209 (1951).

X-Ray Measurements of Radiation Damage in Black Phosphorus*

D. L. CHIPMAN AND B. E. WARREN, *Massachusetts Institute of Technology, Cambridge, Massachusetts*
AND
G. J. DIENES, *Brookhaven National Laboratory, Upton, Long Island, New York*
(Received May 28, 1953)

ORTHORHOMBIC black phosphorus has a layer structure,[1] the layers being perpendicular to the c axis. Interest was centered on the broadening of the (00l) diffraction peaks, and any possible change in the c axis length. To increase the diffracted intensity in the (00l) reflections, the samples were prepared with a high degree of preferred orientation, by taking advantage of the layer structure of the material. The samples were irradiated in the Brookhaven reactor for one month at a temperature of about 50°C.

X-ray measurements show a definite but small broadening of the (00l) peaks. Two sets of measurements of the c spacing were made with CuKα radiation; the first using the peak positions of (006) and (0010) damaged and undamaged, and the second using (002), (004), (006), (008), and (0010). In both cases the percentage change $(\Delta c)/(c)\times100$ computed from the different orders was plotted against the function

$$\tfrac{1}{2}\left(\frac{\cos^2\theta}{\sin\theta}+\frac{\cos^2\theta}{\theta}\right),$$

and an extrapolation made to zero value of this function. Both sets of measurements gave an expansion $(\Delta c)/(c)\times100=0.03$ percent ±0.02 percent.

These preliminary results are of interest because at this, or even at considerably higher, level of pile irradiation close-packed metallic crystals do not exhibit any observable line broadening or lattice parameter change.[2] Wittels[3] observed recently, however, strong anisotropic expansion in the a direction of α quartz upon neutron bombardment. It is tempting to speculate that displaced atoms trapped in open spaces in the black phosphorus and quartz crystals are responsible for the observed effects. The c direction in black phosphorus is expected to be elastically soft so that relatively small disturbances between the planes may lead to rather large strains in the c direction.

In addition to the foregoing effects, there was produced, apparently by the irradiation, a large number of extra lines not belonging to the pattern of black phosphorus, and not seen in the pattern of the undamaged material. Agreement of several of the stronger extra lines with lines of one or another of the forms of red phosphorus[4] suggested that under irradiation black phosphorus was reverting to its more stable form. However, some of the observed lines could not be correlated, and some of the expected strong lines of red phosphorus were not observed. It is definite that the material is changing under irradiation, but the nature of the change is uncertain. In addition it was noticed that the irradiated sample was stronger and harder and showed less tendency to absorb water from the air. We are indebted to Professor P. W. Bridgman for the black phosphorus used in these studies.

* Research sponsored by the U. S. Atomic Energy Commission.
[1] Hultgren, Gingrich, and Warren, J. Chem. Phys. **3**, 351 (1935).
[2] B. E. Warren, U. S. Atomic Energy Commission Document NYO-3731, NYO-3732 (1952).
[3] M. Wittels, Phys. Rev. **89**, 657 (1953).
[4] Roth, DeWitt, and Smith, J. Am. Chem. Soc. **69**, 2881 (1947).

Test for Zeros in the Unit Circle

LOUIS WEINBERG
Hughes Research and Development Laboratories, Culver City, California
(Received June 10, 1953)

THE use of transfer functions for digital computers is coming more and more into use, and just as in the case of analog systems the problem of stability is of prime importance. For some unfathomable reason the stability test for determining whether a polynomial is of Hurwitz character, that is, has all its roots in the left half-plane, is most often presented to nonmathematicians in the determinant form. The writer has observed that many engineers experience difficulty in setting up the determinants and finally in desperation send the problem to the computing room. There a heinous crime is committed: in order to determine whether the system is stable, the roots are found! If the polynomial has roots in the right half-plane, a physical parameter and consequently a coefficient may be changed and the problem returned by the engineer to the computing room. When sampled-

data systems are encountered this folly becomes even more prevalent.

In this note no new procedures for determining stability are advanced. An attempt is made merely to demonstrate a simple direct procedure for determining the stability of a physical system, particularly a sampled-data system. This method, in addition to more complicated tests, appears in the literature, but it seems that the simple method is not so widely used as it should be. Only the main outlines will be presented here, the details being available in the references.

It is well known that the relation between the output and input of any physical system (linear, time-invariant, and possessing lumped parameters) may be expressed by the rational function,

$$H(s)=\frac{O(s)}{I(s)}=\frac{p(s)}{q(s)}, \tag{1}$$

where $O(s)$ and $I(s)$ are, respectively, the Laplace transforms of the output and input, while p and q are real polynomials in s. For stability of the system it is necessary and sufficient that the zeros of $q(s)$ lie in the left half-plane.

For sampled-data systems the program transfer function may be represented by

$$K(e^{-Ts})=\frac{O(e^{-Ts})}{I(e^{-Ts})}=\frac{g(e^{-Ts})}{h(e^{-Ts})}, \tag{2}$$

where g and h are real polynomials in e^{-Ts}, s is the complex frequency variable, and T is the sampling period. For stability it is, of course, again necessary that the denominator h have all its s roots in the left half-plane. If the substitution $z=e^{-Ts}$ is made, the transfer function then becomes the rational function in z,

$$K(z)=g(z)/h(z). \tag{3}$$

Since the above substitution maps every point in the right half-plane of s into the interior of the unit circle of z, the condition for stability in terms of the polynomial in z now becomes: *$h(z)$ must have no zeros in the unit circle.* The test for this condition, as will be explained subsequently, is made to depend on the simple Hurwitz test.

Explanation of the method.—In Eq. 1 it is desired to test the denominator $q(s)$ for Hurwitz character. The procedure[1] is simple. It consists of forming a continued fraction. If the degree of q is even, we form the fraction m/n, where m and n are the even and odd parts of q respectively. If it is odd, the reciprocal n/m is formed. One step in a long division process is then carried out. After the fractional remainder has been inverted, the step in division is repeated. This process is continued until r quotients are obtained, where r is the degree of q. If any coefficient of the r quotients is negative, the polynomial has roots in the right half-plane; the number of such roots is equal to the number of negative quotients. For example, using the fourth-degree polynomial, $s^4+s^3+3s^2+s+1$, we obtain

$$\begin{array}{l} s^3+s \;\overline{)\,s^4+3s^2+1\,}\;\; s \\ \qquad\; s^4+s^2 \\ \hline \qquad\; 2s^2+1 \;\overline{)\,s^3+s\,}\;\; s/2 \\ \qquad\qquad\; s^3+s/2 \\ \hline \qquad\qquad\; s/2 \;\overline{)\,2s^2+1\,}\;\; 4s \\ \qquad\qquad\qquad\; 2s^2 \\ \hline \qquad\qquad\qquad\; 1 \;\overline{)\,s/2\,}\;\; s/2 \\ \qquad\qquad\qquad\qquad\; s/2 \\ \hline \end{array} \tag{4}$$

Since all the quotients have positive coefficients, the roots are all in the left half-plane. If the procedure had been carried out for the general fourth-degree polynomial,

$$\sum_{r=1}^{4} c_r s^r,$$

the necessary and sufficient conditions for stability would have been obtained as

$$\begin{gathered} c_0>0,\ c_1>0,\ c_2>0,\ c_3>0,\ c_4>0 \\ c_2c_3-c_1c_4>0 \\ c_1c_2c_3-c_1^2c_4-c_0c_3^2>0. \end{gathered} \tag{5}$$

Now for the case of the digital computer program, since we would like to apply this simple Hurwitz test, a substitution is needed that will map all points in the interior of the unit circle of z into the right half-plane of a new variable x. Such a substitution[2] is

$$z=(1-x)/(1+x). \tag{6}$$

It is straightforward and almost trivially simple to substitute this in the $h(z)$ of Eq. (3). It now becomes clear: *if the numerator of the new function obtained from the substitution has no zeros in the right half-plane, then $h(z)$ has no zeros in the unit circle and K represents a stable program.* Thus substitution in the general fourth-degree polynomial yields

$$h(z)=\sum_{r=1}^{4} a_r z^r=\sum_{r=1}^{4} a_r\left(\frac{1-x}{1+x}\right)^r, \tag{7}$$

and clearing of fractions gives the polynomial to be tested for Hurwitz character,

$$f(x)=\sum_{r=1}^{4} a_r(1-x)^r(1+x)^{4-r}=\sum_{r=1}^{4} b_r x^r, \tag{8}$$

where

$$\begin{aligned} b_0&=a_0+a_1+a_2+a_3+a_4 \\ b_1&=4a_0+2a_1-2a_3-4a_4 \\ b_2&=6a_0-2a_2+6a_4 \\ b_3&=4a_0-2a_1+2a_3-4a_4 \\ b_4&=a_0-a_1+a_2-a_3+a_4. \end{aligned} \tag{9}$$

But Eq. 5 gives the Hurwitz conditions on the general fourth-degree polynomial so that the test can now be made on the b coefficients almost by inspection.

It should be clear that the fourth-degree polynomial has only been used for illustrative purposes. A polynomial of any degree may be tested similarly.

The user of the procedure for sampled-data systems may often desire to apply some quick checks on $h(z)$ before he substitutes the new variable. For example, the following theorem[3] is frequently useful:

If $0<a_r<a_{r-1}<\cdots<a_0$, then $h(z)$ has no roots in or on the unit circle.

Similar theorems are given in the reference cited.

It has been demonstrated that a computationally simple and useful test for the stability of a pulsed-data system is given by a bilinear transformation and the continued-fraction form of the Hurwitz test. ■

[1] E. A. Guillemin, *The Mathematics of Circuit Analysis* (John Wiley and Sons, Inc., New York, 1949), pp. 401 ff.
[2] M. Marden, *The Geometry of the Zeros of a Polynomial in a Complex Variable* (American Mathematical Society, New York, 1949), pp. 148 ff.
[3] See reference 2, p. 151, example 4.

Response of Undamped Systems to Noise

D. B. Duncan
Electro-Mechanical Engineering Department, North American Aviation, Inc., Downey, California
(Received April 24, 1953)

It is well known that the steady-state mean-square response of a stable linear system to a random input is given by the integral over-all frequencies of the product of the spectral density and the square of the absolute value of the transfer function.[1] There are occasions, however, when the physical system under consideration is most reasonably approximated by a transfer

function without damping. In this case the output will usually increase with the square root of time and the standard methods cannot be used. The conditions under which the rms response will be proportional to the square root of time are developed and a simple expression for the constant of proportionality is derived.

We shall consider the case of a linear system excited by a random variable of known autocorrelation function satisfying the usual conditions which permit interchanging the limiting processes of integration and ensemble averaging.[2] We shall use the following notation:

$f(t)$—input to system;
$\phi(t)$—autocorrelation function of $f(t)$;
$\Phi(j\omega)$—spectral density of the input, equal to the Fourier transform of $\phi(t)$;
$\Theta(s)$—Laplace transform of a function equal to $\phi(t)$ for $t>0$ and equal to zero for $t<0$;
$w(t)$—weighting function of system;
$w(s)$—transfer function of system, equal to Laplace transform of $w(t)$;
$x(t)$—output of system; and
$\langle x^2(t)\rangle_{Av}$—ensemble average of $x^2(t)$.

From the convolution integral, the output is given by

$$x(t)=\int_0^t w(u)f(t-u)du. \tag{1}$$

Squaring this expression, carrying out an averaging process over the ensemble, and using the definition of the autocorrelation function, we obtain an expression for the mean-square response

$$\langle x^2(t)\rangle_{Av}=\int_0^t\int_0^t w(u)w(v)\phi(u-v)dudv. \tag{2}$$

This equation gives a completely general solution to the problem of determining the mean-square response. However, for high-order systems which are frequently encountered it is very laborious to apply. What would be desirable is an expression comparable to the one used for obtaining steady-state values for stable systems which can be used to obtain the dominant term for the response of conditionally stable systems.

Because $\phi(t)$ is an even function, it can be shown that Eq. (2) can be written

$$\langle x^2(t)\rangle_{Av}=2\int_0^t w(u)\int_0^u w(v)\phi(u-v)dvdu. \tag{3}$$

Taking the Laplace transform of this equation, we obtain

$$L[\langle x^2\rangle_{Av}]=\frac{1}{\pi js}\int_{-j\infty}^{j\infty}W(p)W(s-p)\Theta(p)dp. \tag{4}$$

This particular expression is probably a more useful form for obtaining the general transient solution than either Eqs. (2) or (3).

If the system is stable, we can use the final limit theorem of Laplace transform theory to obtain the standard form

$$\lim_{t\to\infty}\langle x^2(t)\rangle_{Av}=\frac{1}{2\pi}\int_{-\infty}^{\infty}|W(j\omega)|^2\Phi(j\omega)d\omega. \tag{5}$$

For conditionally stable systems this result does not apply. However, we can obtain an expression for the term which dominates where t is large. Let us restrict ourselves to the case where there are only first-order poles on the imaginary axis. The generalization to higher-order poles on this axis can be made with only algebraic modifications. We can then write $W(p)$ in the form

$$W(p)=\frac{K_0}{p}+\sum_{n=1}^{N}\left[\frac{K_r}{p-j\lambda_n}+\frac{K_n^*}{p+j\lambda_n}\right]+G(p), \tag{6}$$

where $G(p)$ is a function which has poles only in the left half-plane, λ_n is a characteristic angular frequency, K_0 is the residue of $W(p)$ at the origin (if the origin is a singular point), K_n is the residue at $p=j\lambda_n$, and K_n^* is its complex conjugate. We can substitute this form into Eq. (4) and write out the expression for the Laplace transform of the mean-square output as the integral of a double sum. By considering the terms individually, it can be shown that almost all of the integrals approach constant values as s approaches zero. These terms will contribute constant errors at large t. The only terms whose integrals do not have this property are those in the double sum for which $n=m$ and the K_0^2 term. From these integrals we obtain terms with s in the denominator. We can therefore write the equation in the form

$$L[\langle x^2\rangle_{Av}]=\frac{2}{s}\left[\frac{1}{s}\left\{K_0^2\Phi(0)+\sum_{n=1}^{N}K_nK_n^*[\Theta(j\lambda_n)+\Theta(-j\lambda_n)]\right\}+C+O(s)\right], \tag{7}$$

where C is a constant whose value has not been determined explicitly and the remaining terms are of order s. These terms will transform into functions that do not increase with time and which may be neglected for values of t that are sufficiently large. As in the case of Eq. (5), we can identify $[\Theta(j\lambda_n)+\Theta(-j\lambda_n)]$ as the spectral density or the Fourier transform of $\phi(t)$, We therefore obtain, for large t,

$$\langle x^2(t)\rangle_{Av}=2t\left[\tfrac{1}{2}K_0^2\Phi(0)+\sum_{n=1}^{N}K_nK_n^*\Phi(j\lambda_n)\right]. \tag{8}$$

It is seen that in the case of conditionally stable systems with isolated singularities on the imaginary axis that there is a term in the rms error which increases as the square root of time which will be the dominant term for large values of time and that the coefficient of this term can be simply calculated from the spectral density of the input and the transfer function of the system.

The following simple examples illustrate the usefulness of the method:

(1) Simple Integrator. The transfer function $W(p)$ is $(1/p)$ which, when expanded in the form of Eq. (6), gives $K_0=1$. Substituting in Eq. (8), we obtain

$$\langle x^2\rangle_{Av}=\Phi(0)t.$$

(2) Simple Harmonic Oscillator. The transfer function $W(p)$ is $(p^2+a^2)^{-1}$, where a is the angular frequency. When expanded in the form of Eq. (6), this gives $\lambda_1=a$, $K_1=(1/2aj)$. Substituting in Eq. (8), we obtain

$$\langle x^2\rangle_{Av}=\tfrac{1}{2}a^{-2}\Phi(ja)t.$$

(3) Brownian Motion. The equation relating displacement and force is

$$m\frac{d^2x}{dt^2}+6\pi\eta a\frac{dx}{dt}=f(t),$$

where m is the mass of the particle, a is the radius of the particle, η is the coefficient of viscosity, x is the displacement of the particle, and f is the force acting. The transfer function between force and displacement therefore is $(mp^2+6\pi\eta ap)^{-1}$. There is a single pole on the imaginary axis at the origin with a residue of $(6\pi\eta a)^{-1}$.

Comparing the time constant of this system and the average time between molecular collisions, it can be shown that the force can be approximated by white noise. The amplitude of the spectral density can be obtained by calculating the ensemble average of the velocity squared by standard methods and requiring that

$$\tfrac{1}{2}m\left\langle\left(\frac{d^2x}{dt^2}\right)^2\right\rangle_{Av}=\tfrac{1}{2}kT,$$

where k is Boltzmann's constant and T is absolute temperature. We therefore find that

$$\Phi(j\omega)=12\pi\eta akT.$$

Substituting into Eq. (8), we obtain

$$\langle x^2\rangle_{Av}=\frac{\Phi(0)t}{36\pi^2\eta^2a^2}=\frac{kT}{3\pi\eta a}t,$$

which is the standard expression for Brownian motion.

[1] James, Nichols, and Phillips, *Theory of Servomechanisms* (McGraw-Hill Book Company, Inc., New York, 1947) p. 313.
[2] N. Wiener, *Extrapolation, Interpolation and Smoothing of Stationary Time Series* (The Technology Press and John Wiley and Sons, Inc., New York, 1949) p. 15.

Announcements

Dr. Conrad Longmire and **Dr. Albert S. Eisenstein** will be visiting professors of physics at Cornell. Dr. Longmire will do research in Cornell's Laboratory of Nuclear Studies and will teach a graduate course in theoretical physics in the Department of Physics. Dr. Eisenstein will teach in the advanced laboratory in the Department of Physics and do research in solid state physics.

Dr. Norman Rostoker, former research physicist at Carnegie Institute of Technology, is now a full physicist at Armour Research Foundation of Illinois Institute of Technology. Dr. Rostoker is from Toronto, Canada.

Fred T. Harris, Joseph M. Kirshner, and **Edward G. Spencer** have joined the staff of the National Bureau of Standards. Mr. Harris will engage in research and development of proximity fuzes and Mr. Kirshner in investigations of the theoretical aspects of guided missile fusing. Mr. Spencer, a specialist in microwave spectroscopy and magnetic resonance, is staff member of the Ordnance Electronics Division of NBS.

New officers elected by the **Operations Research Society of America** during its 1953 meeting were **Dr. Robert Rinehart** of the Case Institute of Technology, President, and **Dr. Jacinto Steinhardt,** Director of the Navy's Operations Evaluation Group, Vice-President.

Edward J. Albert of Thwing-Albert Instrument Company, Philadelphia, was elected President of the **Scientific Apparatus Makers Association** at the group's annual meeting held at The Greenbrier, White Sulphur Springs, West Virginia.